ABSTRACT

Title of dissertation: THE STAR-FORMING PROPERTIES OF AN ULTRA-HARD X-RAY SELECTED SAMPLE OF ACTIVE GALACTIC NUCLEI

Thomas Taro Shimizu, Doctor of Philosophy, 2016

Dissertation directed by: Professor Richard Mushotzky
Department of Astronomy

This thesis provides a comprehensive examination of star formation in the host galaxies of active galactic nuclei or AGN. AGN are bright, central regions of galaxies that are powered through accretion onto a supermassive black hole (SMBH). Through accretion and the loss of gravitational potential energy, AGN emit powerful radiation over all wavelengths of the electromagnetic spectrum. This radiation can influence the AGN's host galaxy through what is known as AGN "feedback" and is thought to suppress star formation as well as stop accretion onto the SMBH leading to a co-evolution between the SMBH and its host galaxy. Theoretical models have long invoked AGN feedback to be able reproduce the galaxy population we see today but observations have been unclear as to whether AGN actually have an effect on star formation.

To address this question, we selected a large sample of local ($z < 0.05$) AGN based on their detection at ultra-hard X-ray energies (14–195 keV) with the *Swift* Burst Alert Telescope (BAT). Ultra-hard X-ray selection frees our sample from selection effects and biases due to obscuration and host galaxy contamination that can

hinder other AGN samples. With these 313 BAT AGN we conducted a far-infrared survey using the *HerschelSpace Observatory*. We use the far-infrared imaging to probe the cold dust that traces recent star formation in the galaxy and construct spectral energy distributions (SEDs) from 12–500 μm. We decompose the SEDs to remove the AGN contribution and measure infrared luminosity which provides us with robust estimates of the star formation rate (SFR).

Through a comparison with a stellar-mass matched non-AGN sample, we find that AGN host galaxies have larger dust masses, dust temperatures, and SFRs, confirming the results of previous studies that showed the optical colors of the BAT AGN are bluer than non-AGN. We find that the AGN luminosity as probed by the 14–195 keV luminosity is not related to the SFR of the host galaxy suggesting global, large scale star formation on an individual basis is not affected by the AGN. However, after a thorough analysis comparing our AGN to star-forming main sequence, a tight relationship between the SFR and stellar mass of a galaxy, we discover that our AGN as a whole show systematically lower specific SFRs (SFR/stellar mass). We confirm that AGN host galaxies, as a population, are transitioning between the star-forming and quiescent populations. This result supports the theory that AGN feedback has suppressed star formation, but we also consider other models that could reproduce our observations. Finally we conclude with a summary of this thesis and describe several ongoing and future projects that will push forward the exciting field of AGN research.

THE STAR-FORMING PROPERTIES OF AN ULTRA-HARD X-RAY SELECTED SAMPLE OF ACTIVE GALACTIC NUCLEI

by

Thomas Taro Shimizu

Dissertation submitted to the Faculty of the Graduate School of the
University of Maryland, College Park in partial fulfillment
of the requirements for the degree of
Doctor of Philosophy
2016

Advisory Committee:
Professor Richard Mushotzky, Chair/Advisor
Professor Sylvain Veilleux
Professor Stuart Vogel
Professor Amy Barger
Professor Robert Hudson, Graduate Dean's Representative

Preface

The work in this thesis has largely been published in peer-reviewed journals and presented at international conferences. Chapter 2 was published in *The Monthly Notices of the Royal Astronomical Society* as "*Herschel* Far-Infrared Photometry of the Swift Burst Alert Telescope Active Galactic Nuclei Sample of the Local Universe. II. SPIRE Observations" (Shimizu et al., 2016). Chapter 4 was also published in *The Monthly Notices of the Royal Astronomical Society* as "Decreased specific star formation rates in AGN host galaxies" (Shimizu et al., 2015). Chapter 3 is in preparation to be submitted to *The Monthly Notices of the Royal Astronomical Society*. Results from Chapter 2 was presented at the conference *The Universe Explored by Herschel* October of 2013 at ESA/ESTEC in Noordwijk, Netherlands. Preliminary and final results in Chapters 2, 3, and 4 have been presented at *The Fate of the Gas in Galaxies: AGN vs. Star Formation* August of 2014 at Durham University in Durham, England and *The Physics of Supermassive Black Hole Formation and Feedback* October of 2015 in Annapolis, MD U.S.A. *Herschel* data were obtained as part of the Cycle 1 Guest Observing program (PI: Mushotzky) and WISE data were taken from the IRSA online database.

Dedication

To Kim, my Mom, and my Grandma

Acknowledgments

Completing a Ph.D. in astronomy has been a dream of mine since grade school and I can't thank enough the many people that have helped and encouraged me along the way. The road was tough but with all of the guidance and support I have accomplished a huge life goal of mine.

Thank you first and foremost to my advisor, Richard Mushotzky. You took a chance on a young, raw, budding astronomer halfway through his first year of graduate school and introduced him to the exciting world of AGN. These last 6 years you have been a great advisor, mentor, and friend. I have enjoyed our many long conservations about not just science but life in general. Your enthusiasm and passion for astronomy is unrivaled and every time I entered your office feeling down about my research, you somehow always managed to cheer me up and get me excited again. Perhaps most of all what I will remember are all the little emails that showed me you recognized me as not just your student but also a person: the "Happy Birthdays", "Happy Anniversarys," and "Get well soons" were always appreciated and made me grateful you were my advisor.

Thank you to Stuart Vogel for not just serving on my thesis committee, but also for being a great chair of the department. As Grand Poobah, you were so easy to work with and always made time to hear the concerns of the graduate students. I can't express how nice it was to have a chair who cared as much as you did about our well-being.

Thank you to the rest of my committee members, Sylvain Veilleux, Amy

Barger, and Robert Hudson for patiently waiting for my thesis and taking the time to read it carefully. A special thank you to Amy for waking up early for my defense, working with me on my papers, and writing all those letters of recommendation when I was applying for jobs. Thank you to Sylvain for keeping your door open and letting me pop-in from time to time to get your opinion or ask a question.

My time at the University of Maryland has been amazing and I thank everyone in the Department of Astronomy for a creating a wonderful environment to work in. Thank you to all of the professors who taught my graduate classes, Eve Ostriker, Andy Harris, Massimo Ricotti, Alberto Bolatto, Richard, Sylvain, and Drake Deming for helping to build the foundation of my research, especially since I had never taken an astronomy class before. A special thank you to Marcio Melendez for helping and guiding me so much during the early parts of working on this thesis. Thank you to my classmates, Ashlee Wilkins, Maxime Rizzo, John Capone, Kim Nguyen, Alice Olmstead, and Kory Kreimeyer. I will always remember that first night you all came over to my house to work on our very first Radiative problem set and then our epic celebration after finishing the qualifying exam. Thank you to the rest of the graduate students for all of your friendship and support over the years including Alex McCormick, Jithin George, Katie Jameson, Jonathan Fraine, Vicki Toy, Krista Smith, Johnny Vanlandingham, Ron Ballouz, Gabriele Betancourt-Martinez, and my Poobah successor Drew Hogg. I had such a good time exploring D.C. with you all and you helped make getting a Ph.D. less stressful and more enjoyable. I want to especially mention my Poobah predecessor, Hannah Krug. You shared in my love of sports and immediately made me feel welcome by inviting me to watch

a Rams-Redskins game at your apartment. I can't thank you enough for entrusting me to take over after you and I hope I was half as good a Poobah as you were. Thank you to all the staff, Maryann Phillips, Barbara Hansborough, Eric McKenzie, Adrienne Newman, and Susan Lehr, for making the department run so smoothly and being so kind to me whenever I came to you for help.

Thank you to all my family and friends back in St. Louis and elsewhere around the U.S. Your support and encouragement have kept me going and I'm grateful for your understanding when this journey has led me to miss get-togethers, weddings, and birthdays. Thank you to my Grandma for helping raise me and for reading all of those books to me. Thank you to my Mom. You worked so hard to give me the best education, always supported me and encouraged me, and never questioned the direction I was taking my life in. You have helped me so much through your love and generosity that I know I would not be here without you.

Finally, thank you to my amazing wife, Kim. Who knew we'd be preparing to move to Germany when we first met working in a little frozen custard stand in St. Louis? Thank you for joining me on this journey and moving halfway across the country so that I could pursue my dream. Thank you for being understanding when I had to work late. Thank you for traveling with me to conferences. Thank you for convincing me to adopt Sam. Thank you for all the work you did the past few months preparing for our move and keeping the apartment in order while I finished this thesis. Thank you for loving me, always encouraging me, and always believing in me. I can't imagine having done this without you.

Table of Contents

List of Tables

List of Figures

List of Abbreviations

AGN	Active Galactic Nucleus/Nuclei
SMBH	Supermassive Black Holes
ISM	Interstellar Medium
ΛCDM	Λ Cold Dark Matter
z	Redshift
SFR	Star Formation Rate
BAT	Burst Alert Telescope
$M_{\rm star}$	Stellar Mass
$\rm M_\odot$	Solar Mass
$\rm L_\odot$	Solar Luminosity
c	Speed of light
k	Boltzmann's constant
h	Planck's constant
$B(\nu)$	Blackbody function
ν	Frequency
λ	Wavelength
μm	Microns (i.e. 10^{-6} meters
LIRG	Luminous Infrared Galaxy, $10^{11} < L_{\rm IR} < 10^{12}$ $\rm L_\odot$
ULIRG	Ultraluminous Infrared Galaxy, $L_{\rm IR} > 10^{12}$ $\rm L_\odot$

Chapter 1: Motivation and Background

Galaxy evolution is inherently an extremely complicated process that involves the mutual interactions of dark matter, photons, gas, and stars over the entire history of the universe. While gravity is the main driving force behind the evolution of galaxies, early large-scale cosmological simulations indicated that simple gravitational collapse within a Λ Cold Dark Matter (ΛCDM; the current well-accepted cosmological model for governing the evolution of the universe) framework struggles to reproduce some key observables in today's universe ($z = 0$).

One important observable is the mass and luminosity function (i.e. the number of galaxies per volume as a function of mass or luminosity) of galaxies. Semi-analytic models and simulations where the growth of galaxies is left unchecked produced an overabundance of high-mass galaxies[1] also have increasing amounts star formation. This follows cleanly from the ΛCDM model which implies hierarchical growth of structure through clustering and merging of smaller dark matter haloes into larger ones thus leading to a dominant population of massive, star-forming galaxies in

[1]Models and simulations also produced an overabundance low-mass galaxies. I choose to focus on the high-mass end because this is where AGN likely have the greatest effect. The problem at the low mass end seems to be solved by the inclusion of supernova feedback that reduces the efficiency of star formation (e.g. Benson et al., 2003; White & Frenk, 1991)

the local universe. However, observations at both high and low redshift revealed a nearly opposite scenario. Rapid star-formation is instead more prevalent in massive galaxies at earlier times (Cowie et al., 1996), while in the local universe the majority of the most massive galaxies display an old stellar population with little ongoing star formation (Kauffmann et al., 2003a).

The remedy to the problem of "cosmic downsizing" seems to lie in the interaction between the central supermassive black hole (SMBH) and its host galaxy. Once thought to just be insignificant bystanders, it has become apparent in the past two decades that SMBHs can play a large role in shaping the evolution of the galaxies they live in.

1.1 The Co-evolution of Galaxies and SMBHs

The first evidence for a connection between the evolution of SMBHs and their host galaxies came in the form of strong correlations between the SMBH mass and various host galaxy properties. Such a connection seemed infeasible given the enormous difference between the small physical scale within which a SMBH can gravitationally influence its environment and the large physical scale of a galaxy. Assuming a 10^8 $M_\odot$ SMBH, its sphere of gravitational influence only has a radius of $\sim 10pc$ compared to the roughly 10 kpc size of the galaxy, therefore it seemed unlikely for the SMBH to affect any meaningful change to the galaxy over 3 orders of magnitude in size.

Nonetheless, repeated studies kept finding tight relationships between the mass

of the SMBH and the large scale properties of the galaxy's bulge, most notably the stellar velocity dispersion (Ferrarese & Merritt, 2000; Gebhardt et al., 2000; Gültekin et al., 2009; McConnell & Ma, 2013), luminosity (Gültekin et al., 2009; Magorrian et al., 1998; McConnell & Ma, 2013), and mass (Häring & Rix, 2004; Kormendy & Richstone, 1995; Marconi & Hunt, 2003; McConnell & Ma, 2013). Figure 1.1 shows one of the most recent measurements of the correlation between SMBH mass and stellar velocity dispersion, now known as the $M_{\rm BH} - \sigma$ relation. These correlations immediately suggested a sustained co-evolution between the galaxy and central SMBH such that the growth of one follows the growth of the other. Otherwise, there is no natural reason to expect the size of the SMBH to so closely match the properties of the galaxy.

To explain the co-evolution, there must be in place a mechanism that can affect, in the same manner, both the growth of the SMBH and the host galaxy. SMBHs grow through the accretion of material while galaxies largely grow by forming stars, therefore this mechanism has to be able to regulate the SMBH accretion rate and star formation rate (SFR) of the galaxy. As it turns out, the very act of material accreting onto the SMBH can provide the necessary energy to simultaneously shut down star formation as well as prevent future growth of the SMBH.

1.2 What is an Active Galactic Nucleus?

As Osterbrock & Ferland (2006) recounts, the first identification of an active galactic nucleus came from a spectroscopic study of the central regions of galaxies

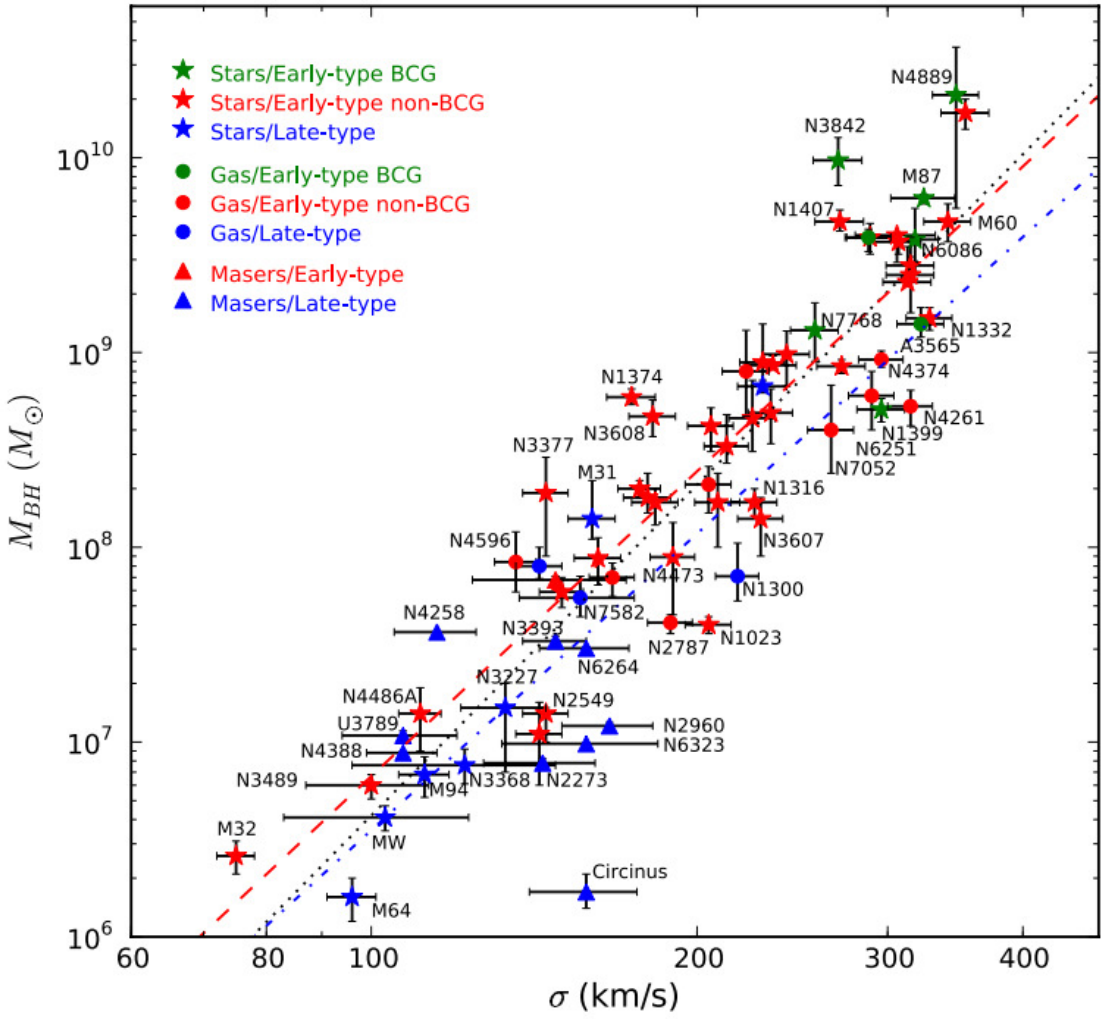

Figure 1.1: Observed tight relationship between the SMBH mass and stellar velocity dispersion in the bulge of the galaxy. Taken from McConnell & Ma (2013).

("spiral nebulae" at the time) when Edward Fath in 1908 noticed one galaxy (now one of the most well-studied AGN, NGC 1068) exhibited bright, broad emission lines compared to the usual slew of stellar absorption lines. Carl Seyfert in 1943 published his seminal paper noting that a small fraction of galaxies exhibit these same broad emission lines indicative of highly ionized gas that are also coincident with relatively bright "semi-stellar" nuclei (Seyfert, 1943). Today, the term "Seyfert galaxy" is synonymous with an AGN. While AGN seemed to only appear in a small fraction of galaxies, their enormous energy output (sometimes more than the whole galaxy itself) made them interesting targets for research into their nature and makeup. Since then, AGN have been found to emit over nearly the entire range of the electromagnetic spectrum from high energy gamma-rays and X-rays through the ultraviolet, optical, and infrared, and down to long wavelength radio.

Originally it was thought AGN consisted of dense nuclear star clusters, but the combined observations of their high luminosity, compact size, rapid variability, and broad emission lines all pointed toward a different process powering AGN. Just taking the large luminosities ($\sim 10^9 - 10^{12}$ $L_\odot$) and assuming it is gravitationally bound leads to incredibly large lower limits on the mass ($M > 10^7\,M_\odot$) based on the Eddington limit (i.e. radiation pressure must balance gravitational collapse). Thus a highly energetic, highly massive object is contained within a small compact region. The efficiency needed to reproduce these conditions far outweighs that of thermonuclear reactions that produces the light in stars. Lynden-Bell (1969) first proposed that gravitational infall of matter onto a SMBH could reasonably produce the power output seen in AGN. With only a roughly 10% efficiency for the conversion

from mass into energy, an accretion rate of only 1 $M_{\odot}yr^{-1}$ is needed for an AGN to shine at 10^{12} $L_{\odot}$.

1.2.1 Observational Characteristics

Decades later, it is now widely accepted that mass accretion onto a SMBH ($M = 10^6 - 10^{10}$ $M_{\odot}$) is the power source for AGN. Much work has gone into determining the exact processes and physics involved in accretion that lead to radiation at the various wavelengths. AGN are particularly bright in the UV and optical and their spectral energy distributions (SED) show a characteristic "big, blue bump" produced by thermal emission from the disk of material (i.e. accretion disk) falling into the SMBH. Extending the accretion disk down to the innermost stable orbit increases the temperature of the gas likely leading to the low energy X-ray emission as well. Higher energy X-ray emission however requires non-thermal processes. The current best explanation invokes the presence of a "corona" above the accretion disk consisting of high energy electrons. UV and optical photons from the accretion disk then are inverse Compton scattered inside the corona that increases their energy to above 1 keV and leading to the characteristic powerlaw continuum seen in X-ray spectra. The powerlaw continuum also illuminates the (relatively) cold accretion disk which can lead to an observable "reflection hump" peaking at 30 keV. The "reflection hump" is primarily due to photoelectric absorption of lower energy incident X-ray photons and Compton scattering of high energy X-rays to lower energies. Radio emission is largely due to synchrotron emission from jets.

Moving further away from the SMBH is what is known as the Broad Line Region (BLR) where high velocity ionized gas produces the characteristic broad emission lines seen in UV and optical spectra of AGN. The high velocities of these lines as well as observed lags between the strength of the lines and the continuum indicate radii of about 0.1 pc. Even further is the Narrow Line Region (NLR), which by its name, indicates the region where ionized gas emits relatively narrow lines. The velocities of the gas in the NLR are several hundred km s^{-1} and do not show any time-lags with the continuum. Moreover, the NLR has been spatially resolved in some nearby AGN indicating sizes of a few 10s of pc up to kpc scales.

Spectral studies of AGN in the optical revealed two broad classes: Type 1 and Type 1 (also sometimes referred to as Seyfert 1 and Seyfert 2 galaxies). Type 1 AGN show broad permitted lines of H I, He I, and He II as well as narrower (but still broader than expected from ionized gas in star-forming regions) forbidden lines (i.e [OIII], [NeII], [SII]) whereas Type 2 AGN only show narrow forbidden and permitted lines. This led to speculation as to why some AGN seem to only contain a NLR and others both a NLR and BLR and directly led to development of the unified model of AGN.

1.2.2 The Unified Model of AGN and the Importance of the Dusty Torus

The unified model (Antonucci, 1993; Urry & Padovani, 1995) attempts to explain the observational differences between different classes of AGN as an effect of

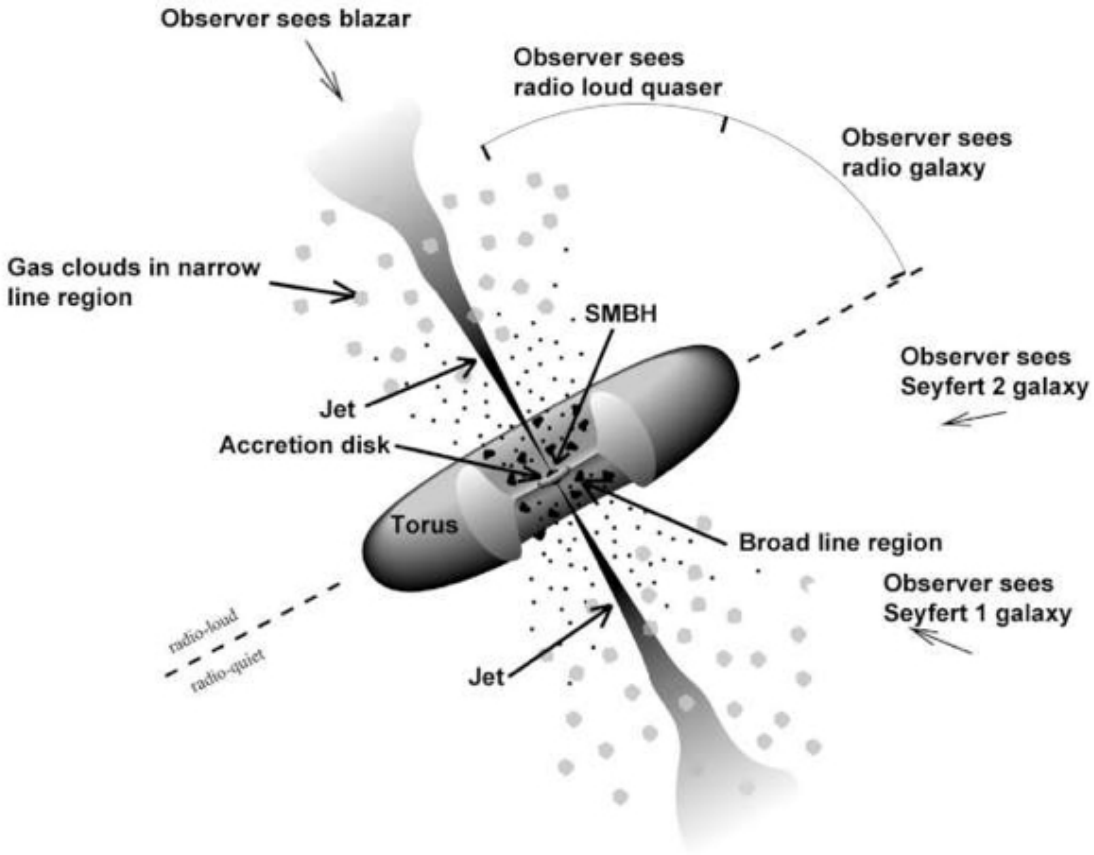

Figure 1.2: An illustration of the main components of an AGN including the SMBH, accretion disk, jets, BLR, NLR, and dusty torus. The unified model argues that all AGN classes contain the same components but the line of sight to the AGN changes the observed properties. Reproduced from http://fermi.gsfc.nasa.gov/science/eteu/agn/.

the observer's line of sight towards the AGN. Figure 1.2 shows an illustration of an AGN and the various components previously mentioned. The important addition to the AGN within the unified model is the presence of the torus.

The torus consists primarily of cold, molecular gas and is shown in Figure 1.2 as the thick donut shape surrounding the accretion disk and SMBH. Within the torus, though, is copious amounts of dust along with the molecular gas that render the torus completely optically thick. Dust, likely composed of silicates and graphite, preferentially absorb the UV and optical emission originating from the accretion disk and reemits the energy as thermal emission in the infrared. Analogous to the "big blue bump," the SEDs of AGN also show a broad mid-infrared bump that can peak between 20 and 60 μm.

The torus then fundamentally leads to the observed dichotomy of Type 1 and Type 2 AGN. Lines of sight that avoid peering through dusty torus have an obstructed view of not just the accretion disk, but also the BLR revealing the strong broad permitted lines. Type 2 AGN, on the other hand, are the result of lines of sight through the dusty torus that obscures the accretion disk and BLR. Since the NLR exists at much larger radii, the torus and therefore viewing angle does not have an effect on the observation of narrow lines. The unified model has also been used to link other classes of AGN, such as Blazars where the line of sight is looking "down the barrel" of the jet and the radio-loud/radio quiet dichotomy.

The exact structure of the dusty torus has been a matter of debate. At first it was assumed to be smoothly varying distribution of dust and gas just as the illustration in Figure 1.2 shows (e.g. Pier & Krolik, 1992). These models predict a

strong anisotropy of infrared radiation between Type 1 and Type 2 AGN. However, recent studies have shown the anisotropy is not as strong, particularly with regards to the 10 μm silicate feature. This has led to development and popularity of clumpy torus models where dust and gas is distributed as extremely optically thick clouds ($\tau_V \sim 100$) (Nenkova et al., 2002) which match observed infrared spectra much better (e.g. Nenkova et al., 2008b; Nikutta et al., 2009).

1.3 AGN Feedback and The Starburst-AGN Connection

With a better understanding of what constitutes an AGN, we can come back to the possible effect they could be having on their host galaxy and their role in shaping its evolution. Given the energies involved while a SMBH is in an AGN phase and actively fueling, the tremendous range in physical scales between the SMBH and galaxy can easily be overcome. Fabian (2012) puts forth a fairly simple argument based on the observed scalings between the mass of the galaxy and SMBH mass, the observed stellar velocity dispersion, and the energy output of the AGN to show that the accretion power can overwhelm the binding energy of the galaxy. Silk & Rees (1998) and Fabian (1999) similarly showed that Eddington limited growth of the SMBH that prevents accretion of gas onto the galaxy leads to an expression between the SMBH mass and stellar velocity dispersion remarkably similar to that found observationally ($M_{\rm BH} \propto \sigma^4$). Therefore energetic "feedback" from the AGN can possibly explain the observed tight scaling relations between galaxy properties and the SMBH mass.

AGN feedback has thus been a fixture in models of galaxy evolution. The prevailing theoretical framework involves the funneling of gas to the central regions of galaxies through the instabilities induced by massive mergers. The build-up of gas leads to a burst of circumnuclear star-formation as well as the ignition of an obscured AGN. Sanders et al. (1988a) first observed the coincidence of starburst activity and dust enshrouded AGN in a small sample of Ultraluminous Infrared Galaxies (ULIRGs). Due to the availability of large amounts of cold gas, the necessary fuel for both star formation and AGN, both the galaxy and SMBH grow in concert. Eventually the AGN grows powerful enough to sweep away the remaining gas effectively cutting off the growth of both the SMBH and galaxy (Di Matteo et al., 2005; Hopkins et al., 2006; Springel et al., 2005a,b).

Within numerical and semi-analytical models, AGN feedback solved the problem of an overabundance of high-mass star-forming galaxies. As Croton et al. (2006) and Bower et al. (2006) showed, models with the addition of AGN feedback effectively reproduce the local galaxy luminosity function as well as the observed "downsizing" of galaxies over the history of the universe. AGN feedback is a featured component in today's most sophisticated and complex cosmological simulations such as Illustris (Vogelsberger et al., 2014) and EAGLE (Schaye et al., 2015).

Strong observational evidence for AGN feedback has proven elusive. While winds, outflows, and jets (the primary mechanisms for AGN feedback) are nearly ubiquitous in AGN, the actual effect on the galaxy itself is hard to measure as well as discerning whether the outflows are being driven by the AGN or stellar processes. Recent studies have started to indicate that powerful AGN can boost the velocities

of molecular outflows (Cicone et al., 2014; Veilleux et al., 2013) leading to more efficient gas-depletion which should result in suppressed star formation.

The big question at hand though is "Do we observe AGN host galaxies with reduced levels of star formation as a result of AGN feedback?" To answer this question requires two things: 1) A reliable method to find and construct a large sample of AGN and 2) A reliable method to then measure the star formation rate in the galaxy. This thesis aims to mitigate the pitfalls that can arise with each of these hurdles by conducting a far-infrared survey of a large sample of ultra-hard X-ray selected AGN.

1.4 AGN Selection Techniques

As briefly discussed in Section 1.2, AGN can be bright over nearly the entire electromagnetic spectrum. This feature has led to numerous methods for efficiently finding AGN that aim to reduce selection effects and limit false positives. Because AGN exist deep inside galaxies, the problem in finding AGN boils down to determining how its emission (as captured by either spectra, imaging, or broadband photometry) is different from the surrounding various stellar and ISM processes. One of the simplest methods is to use optical colors as AGN tend to be much bluer than expected for a galaxy due to the aforementioned "big blue bump" associated with thermal emission from the accretion disk (Richards et al., 2001). Color selection however will depend on the luminosity of the AGN as it must outshine the host galaxy behind it and impose its color on the total SED. Type 2 AGN also will likely

be undersampled using optical color selection since the dusty torus inherently reddens or completely obscures the accretion disk emission. Finally, intense starburst activity will also produce blue colors.

Today, one of the most popular methods to select AGN is through the use of optical line ratios. Baldwin et al. (1981) were one of the first develop a classification scheme to distinguish between the spectra of galaxies dominated by star-forming regions (i.e. HII regions) and AGN. The scheme works off the basis that the ionization mechanism responsible for producing narrow emission lines in galaxies is significantly different. HII regions are photoionized by hot O and B stars while the NLR in AGN is photoionized by a powerlaw continuum that extends to much higher energies. The harder continuum of the AGN produces stronger low-ionization emission lines relative to high ionization lines compared to the line ratios of HII regions allowing for easy separation. Since 1981, the scheme has been revised, updated, and tested to reflect better modeling and data (Kauffmann et al., 2003b; Kewley et al., 2001, 2006; Veilleux & Osterbrock, 1987). The Sloan Digital Sky Survey (SDSS; York et al., 2000), with its database of over 3 million spectra that contain measurements of the line intensities, have made selection via line ratios very easy and quick. However just like optical color selection, the AGN must overwhelm the emission from HII regions. Weak lines are another issue that can cause ambiguous classification.

Seeing the dusty torus as an advantage rather than a hindrance, mid-infrared color selection has become prominent especially after the launch of the *Wide-field Infrared Survey Explorer* that mapped the sky and produced catalogs at 3.4, 4.6,

12, and 22 μm(Donley et al., 2012; Stern et al., 2012). Mid-infrared selection avoids the effects of obscuration and thus will find AGN even in the face of high column densities. But again, star formation heated dust, especially in starbursts, can complicate selection and possibly lead to a bias against highly star-forming AGN host galaxies.

Luminous radio selection, one of the first ways AGN were found, are biased towards low star-forming "red and dead" ellipticals especially for "radio-loud" objects (Hickox et al., 2009). At lower radio luminosities, synchrotron radiation from relativistic electrons in supernova remnants (i.e. star formation) contributes strongly and will contaminate samples of AGN with starbursts (Mushotzky, 2004).

To avoid all of these biases and selection effects, especially ones related to star formation, we have constructed our AGN sample based on high energy X-ray detection. Because of the extreme environments necessary to produce X-ray emission, compact, nuclear, and luminous X-ray emission is a near certain indicator of an AGN. In the low redshift universe (where this thesis focuses on), no galaxy without an AGN achieves an X-ray luminosity greater than 10^{42} ergs s^{-1}. Below this luminosity and at softer X-ray energies ($E < 2$ keV), contamination from starburst galaxies can creep in, but pushing to higher X-ray energies essentially nullifies any possibility. Obscuration due to intervening dust and gas which plague optical and UV selection is also only a problem at low X-ray energies. High energy X-ray emission ($E > 10$ keV) is virtually unchanged except for extremely high column densities above the Compton thin limit ($N_{\rm H} > 10^{24}$ cm^{-2}. Finally, the X-ray luminosity by itself can be used as a measure of the overall bolometric luminosity of the

AGN (Vasudevan & Fabian, 2007; Winter et al., 2012). These combined advantages of unambiguous identification, obscuration independence, and strong correlation to overall AGN strength make X-ray surveys one of the best ways to formulate large unbiased samples of AGN and are the reasons why we chose the *Swift Burst Alert Telescope* catalog as our parent AGN sample.

1.5 The *Swift Burst Alert Telescope*

In November of 2004, the *Swift* satellite (Gehrels et al., 2004) was launched with a suite of instruments and telescopes with the primary goal of studying gamma-ray bursts (GRBs). One of the instruments, the *Burst Alert Telescope* (BAT; Barthelmy et al., 2005), was designed to continuously monitor the sky at ultra-hard X-ray energies (14–195 keV) for GRBs. Instead of normal focusing optics that are standard for astronomical telescopes, BAT uses a 5200 cm^2 coded-aperture mask above an array of 32768 CdZnTe detectors. Ultra-hard X-ray sources illuminate the BAT producing a distinct "shadow" on the detector array that changes as a function of position in sky. When a GRB is detected, complex algorithms involving Fourier techniques can locate the position to within 1-4' and slew the satellite to provide rapid followup from the other instruments (XRT and UVOT)

In between GRBs, *Swift* is used for preplanned targets but BAT is always monitoring, taking snapshot images of nearly 1/6 of the entire sky ($\sim$ 2 steradians) every 20 minutes. BAT's wide field of view combined with the random positions of GRBs then results in nearly uniform sky coverage and leads to the most sensitive

all-sky survey at ultra-hard energies. Survey data have been reduced and analyzed multiple times throughout BAT's lifetime, each time generating larger and larger catalogs of sources as the integrated exposure increases and the flux limit reduced. At the time of this writing, the most recent one is the 70 month catalog (Baumgartner et al., 2013) with over 1100 sources, over 700 of which are AGN. Details of the current analysis pipeline and catalog generation procedure can be found in Tueller et al. (2010) and (Baumgartner et al., 2013).

At the start of this thesis, however, the 58 month catalog[2] was the latest catalog produced with 1092 sources at a flux limit of 1.1×10^{-11} ergs s^{-1} cm^{-2}. Over 600 of those sources were identified as AGN. The flux limit, while still the most sensitive at energies above 10 keV, quickly leads to severe incompleteness at low luminosities as redshift increases. Thus, while there are some extremely luminous AGN at redshifts greater than 2.0, the overall median redshift is only 0.03 or about 130 Mpc. What this amounts to though is a very complete and very local sample of AGN that will be largely free from any possible effects related to the overall evolution of galaxies or AGN as a population. The local nature of the AGN sample also ensures maximum spatial resolution for imaging which is crucial in studies of the host galaxies of AGN. With its selection at such high energies, the AGN in the BAT catalog guarantees little bias against Compton-thin Type 2 AGN and no selection effects related to star formation in the host galaxy.

[2] http://swift.gsfc.nasa.gov/results/bs58mon/

1.6 Measuring Star Formation in Galaxies

There are many ways to measure the SFR of a galaxy and a large body of literature exists detailing the intricacies, advantages, and disadvantages of each one (see Kennicutt & Evans, 2012; Kennicutt, 1998, for extensive overviews). Each method (besides directly counting stars and measuring their ages) relies on the assumption that stars do not form in isolated environments but rather in stellar clusters that result in a population of stars with a distribution of masses (the initial mass function or IMF). The initial mass of a star largely determines its overall evolution including luminosity and lifetime. While the total number of stars formed is dominated by low mass stars, the luminosity and color of a single stellar population, especially at early times, is dominated by high mass stars. The short lifetimes of high mass stars then make diagnostics sensitive to their presence a powerful tool in determining the recent SFR.

The UV continuum luminosity is the best direct measure of a galaxy's recent SFR because it traces emission that originates from the photospheres of high mass (several solar masses) stars. High mass stars are hot with temperatures above $10^{4.5}$ K that firmly place the peak of their spectra in the UV and blue end of the visible regime. This is the reason star-forming galaxies are described as "blue" due to the increased ratio of high mass to low mass stars. After star formation shuts off, the high mass stars die off leaving behind a stellar population consisting of mainly lower mass stars and shifting the color of the galaxy to "red." UV continuum measurements however are highly sensitive to the internal extinction of the galaxy

caused by intervening gas and dust. Calibrations have been developed to estimate this effect using the UV slope (e.g. Calzetti et al., 1994) but assumptions must be made about the intrinsic color, geometry and distribution of the dust, and the extinction curve.

The intensity of recombination lines is another accurate and popular tracer of the SFR, but instead of directly measuring stellar emission it measures the re-processed emission by gas. Stellar clusters form within giant clouds of gas and dust that will immediately respond to the influx of radiation from the newly formed stars. Very massive stars (> 10 $M_\odot$) will produce a large flux of high energy photons ($h\nu > 13.6$ eV) able to ionize hydrogen in the surrounding region (HII regions). As electrons recombine with protons and decay down to lower energy levels they emit radiation at characteristic energies producing spectral lines with the most prominent one in ionized hydrogen being the Hα line. Therefore, the integrated Hα luminosity of a galaxy can easily be calibrated to the nearly instantaneous SFR by assuming all of the ionizing flux originates from recently formed high mass stars (Kennicutt et al., 1994; Madau et al., 1998). Just as with the UV continuum, the Hα luminosity is susceptible to extinction which can be accounted for by the Balmer decrement in normal galaxies but performs poorly in starbursts. It is also much more sensitive to the specific shape of the IMF at the high mass end and age of the system.

While both the UV and Hα have been extensively used to study large samples of normal star-forming galaxies to large success, these tracers are problematic when applying them to galaxies hosting an AGN. As discussed above in Section 1.2, the peak of the SED from the accretion disk is in the UV. The hard continuum from the

accretion disk and corona also produces large amounts of ionizing flux, more-so than high mass stars, leading to bright Hα emission from the BLR and NLR. There are certainly ways around these complications such as limiting the sample to only Type 2 AGN where the UV due to the accretion disk is almost completely obscured by the torus or detailed image decomposition to remove central AGN. These methods thought could introduce systematic biases by not including Type 1 AGN as well as uncertainties involving the spatial resolution of the image and the reliability of the removal of a bright unresolved source against a fainter extended galaxy.

To avoid strong AGN "contamination" in the SFR tracer, this thesis utilizes dust emission in the infrared. Long the bane of optical astronomers, dust is an important component of a galaxy's ISM even though it only makes up approximately 1% of the mass. Interstellar dust is thought to be composed of a combination of silicates, graphites, and polycyclic aromatic hydrocarbons (PAHs) with a size distribution between 0.35 nm up to 1 μm (Draine, 2003). Dust is thought to play a crucial role in the chemistry of the ISM by locking up heavy elements as well as serving as the location for the formation of molecular hydrogen (Gould & Salpeter, 1963). In the presence of high energy radiation, photoelectric emission from dust can be an important heating mechanism.

For our purposes, we are more interested in dust's cooling abilities. Photoelectric absorption by dust can be important all the way up to the mid-infrared, however the absorption efficiency is strongest in the UV and optical (Draine, 2011). After absorbing a photon, dust grains will transfer the energy into vibrational modes, effectively heating the grain. Dust grains then cool radiatively by reemitting in

the infrared. Because dust is distributed through out a galaxy, especially near star-forming regions, a typical galaxy can have between one-third to one-half of its stellar emission absorbed by dust and reemitted in the infrared with the bulk of the thermal radiation between 5 and 1000 μm. Figure 1.3 shows an average infrared SED for a normal galaxy. The mid-infrared (MIR) continuum ($\lambda < 20$ μm) is produced by smaller, hotter grains that are likely surround young star-forming regions. Superposed onto the continuum are broad, emission features due to the vibrational modes of PAHs. The bulk of the radiation however occurs in the far-infrared (FIR) where a distinct, broad, featureless peak can be seen in the SED. Emission in the FIR is due to larger grains with cold temperatures in thermal equilibrium with the interstellar radiation field (Draine, 2003). Interstellar dust then essentially serves as a calorimeter for measuring the SFR in a galaxy. Numerous calibrations exist in the literature for converting infrared luminosity (either total luminosity from 8–1000 μm, or strictly FIR luminosity from 40–120 μm) into a SFR.

Observing in the infrared however is difficult due to absorption by Earth's atmosphere. Infrared telescopes also necessarily need to be cooled as thermal radiation from the mirror and instruments themselves with an effective temperature of about 10–90 K can overwhelm the signal. Therefore the biggest leap in infrared astronomy and in particular the FIR came in 1983 when the *Infrared Astronomical Satellite* (IRAS Neugebauer et al., 1984) was launched and performed an all-sky survey at wavelengths 12, 25, 60, and 100 μm. IRAS revolutionized the field opening up a whole new window to the universe. For extragalactic astronomers, IRAS discovered a whole population of never before seen dusty starburst galaxies that directly led to

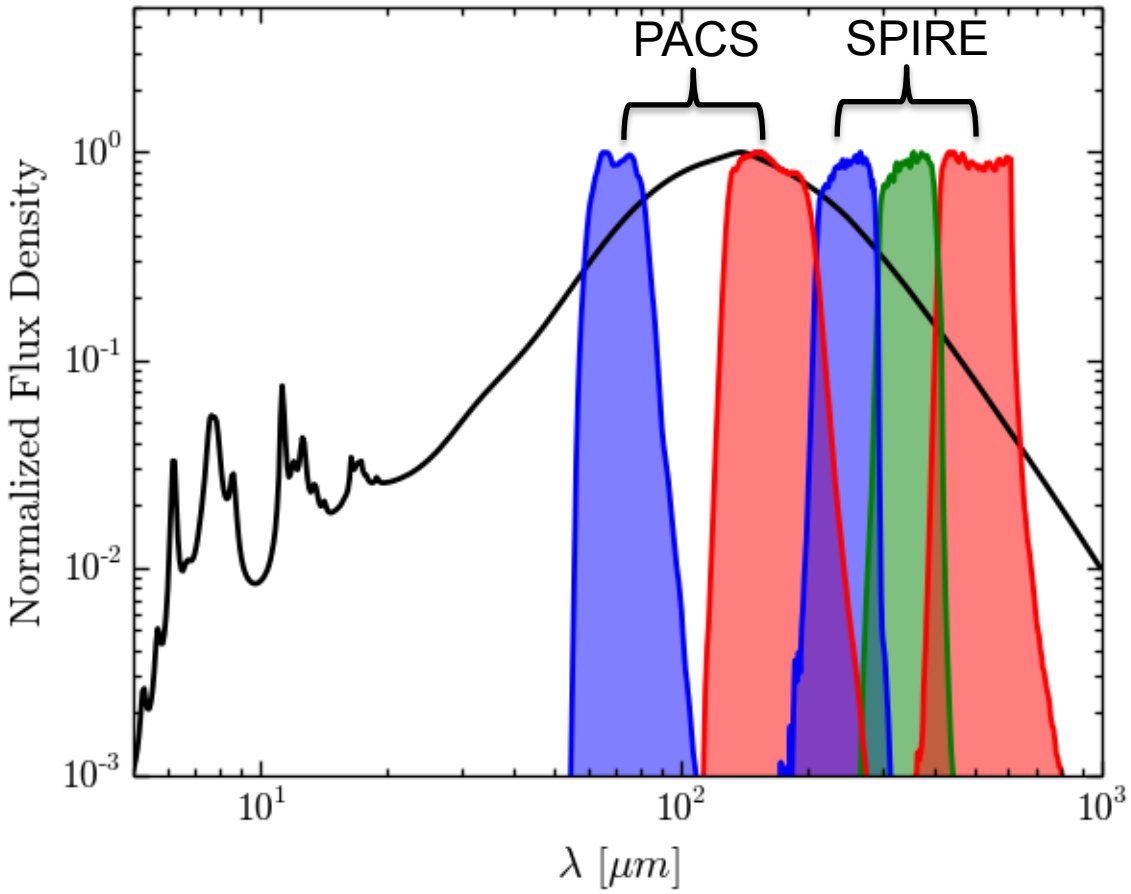

Figure 1.3: Spectral energy distribution for average star-forming galaxy taken from Ciesla et al. (2014a). The SED peaks in the far-infrared regime where the *Herschel* observations lie for our AGN sample. The left blue and red shaded regions indicate the filters for the PACS instrument at centered at 70 and 160 μm and the right blue, green, and red shaded regions show the filters for the SPIRE instrument at 250, 350, and 500 μm.

the development of the model linking AGN activity, merging galaxies, and quenching of star formation (Sanders & Mirabel, 1996; Sanders et al., 1988a,b). Since IRAS, a number of infrared telescopes have launched including the *Infrared Space Observatory* (ISO), the *Spitzer Space Telescope*, WISE, *Akari*, and *The Herschel Space Observatory* making the infrared regime a fixture and an almost necessity for studying star formation in galaxies.

Besides being a strong indicator of the SFR, the FIR is also routinely considered to contain little to no contribution from the AGN. The obscuring torus which contains large amounts of dust is bright in the mid-infrared due to the hard continuum of the AGN heating the dust to large temperatures ($\sim$ 100-100K) (Jaffe et al., 2004; Mor & Netzer, 2012; Nenkova et al., 2008a; Pier & Krolik, 1992). The high luminosities at short wavelengths routinely outshine emission from the galaxy and show strong correlations with the X-ray luminosity (Ichikawa et al., 2012). At FIR wavelengths, however, the situation becomes complicated because cold dust due to stellar heating is much more prominent. While early models of the torus that incorporated a "flared disk" could produce significant FIR emission from AGN heating, the most recent clumpy torus models generally show a rapidly declining SED longward of about 40 μm (Hönig & Kishimoto, 2010; Nenkova et al., 2002, 2008a; Schartmann et al., 2008). Observations have also pointed to low contamination of the AGN at FIR wavelengths. Netzer et al. (2007), using a sample of high luminosity AGN with combined *Spitzer* and IRAS data, showed that by assuming the FIR was solely due to star formation heated dust, subtraction of a starburst template produces very similar SEDs among all the AGN no matter whether they were strong

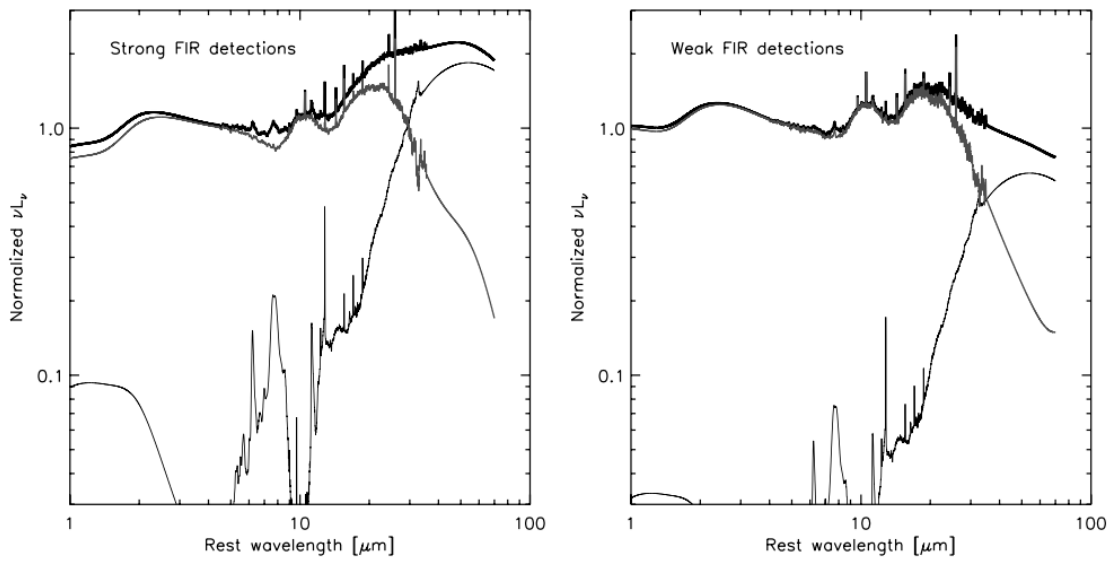

Figure 1.4: Average infrared SEDs for high luminosity AGN with strong FIR detections (left) and weak FIR detections (right) are shown as thick black lines. The lowest thin line is the starburst template to subtract the star-forming component and produce the intrinsic infrared AGN SED shown in the middle. Taken from Netzer et al. (2007)

or weak in the FIR. All of the resulting SEDs feature a peak around 20 μm with a rapid downturn towards longer wavelengths (see Figure 1.4). Mullaney et al. (2011) followed up the work of Netzer et al. (2007) using a sample of BAT detected AGN to develop a so-called "intrinsic AGN SED." The SED similarly showed decreasing emission at long wavelengths but a peak at 40 μm. However, Mullaney et al. (2011) did find 11 sources with SEDs dominated by the AGN at 60 μm.

What all of this highlights is that even though its likely the FIR is mostly due to star formation related emission, SED decomposition is necessary to accurately measure the SFR in the presence of an AGN. If the AGN can dominate out to 60 μm then even using just the 40–120 μm luminosity will overestimate the SFR. To be able to properly account for the AGN contribution, well-sampled SEDs are needed. The *Herschel Space Observatory* filled just that need.

1.7 The *Herschel Space Observatory*

In May of 2009, the European Space Agency launched the *Herschel Space Observatory* (Pilbratt et al., 2010). *Herschel* operated at the second Lagrange point positioning itself far away from the infrared radiation due to the Earth and Moon. Further, the elimination of orbits around the Earth removed the effect of constant heating and cooling as the satellite moves into and out of the Earth's shadow.

Herschel flew with three main instruments, two imaging cameras[3] and one high resolution spectrometer, each cooled to 2 K by liquid helium. For this thesis, we took advantage of the two imaging cameras: the Photodetecting Array Camera and Spectrometer (PACS; Poglitsch et al., 2010) and Spectral and Photometric Imaging Receiver (SPIRE Griffin et al., 2010). PACS had three bands centered at 70, 100, and 160 μm with the ability to observe with two simultaneously. SPIRE contained three bands centered at 250, 350, and 500 μm.

With its 3.5 m mirror, *Herschel* is the largest infrared telescope ever launched, providing unprecedented angular resolution in the FIR. At the PACS 70 μm waveband, the FWHM was 6″ compared to several arcminutes for IRAS at 60 μm. Figure 1.5 shows the PACS 70 μm image for one our sources, NGC 2992. The contours indicate the IRAS 60 μm image for the same region. Notice IRAS was completely unable to resolve the NGC 2992 (central source) from its companion NGC 2993 (source in bottom left). *Herschel* also provided much improved sensitivity, able to

[3]PACS and SPIRE both were a combined camera and low resolution spectrometer but this thesis only makes use of their imaging capabilities

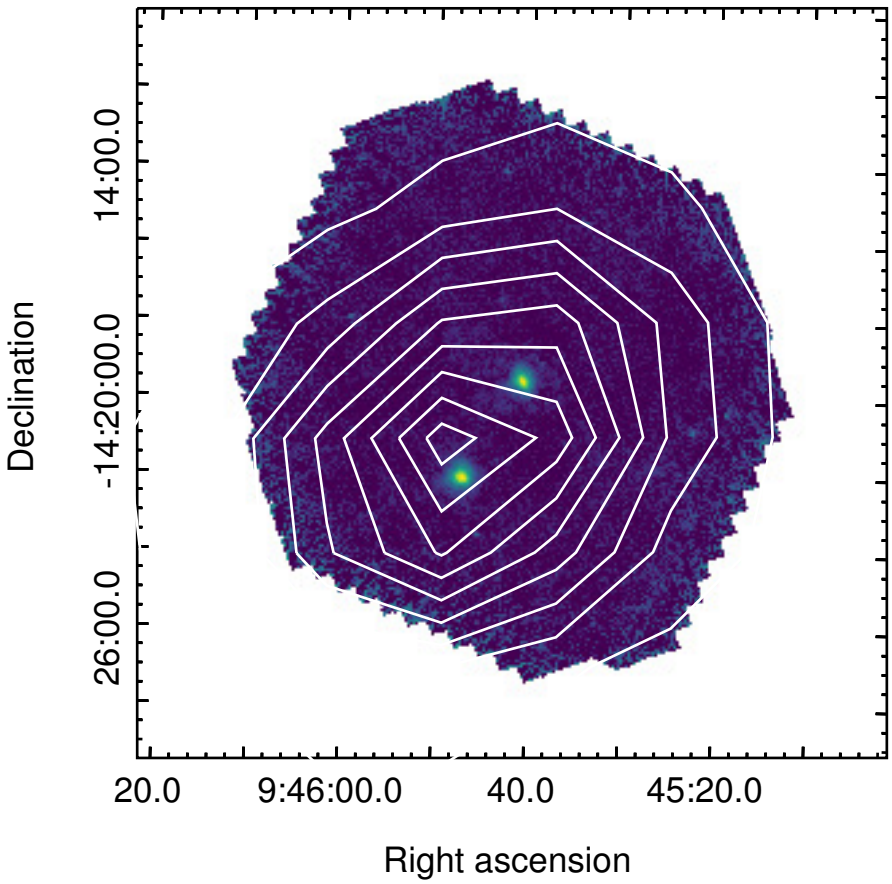

Figure 1.5: Example 70 μm image of NGC 2992 from our sample shown in log scale. White contours superimposed on top show the IRAS 60 μm image for the same region.

reach a detection limit at the milliJansky level for PACS and the confusion limit for SPIRE. This enabled *Herschel* to study some of the coldest objects in the universe as well as push to the high redshift universe since the FIR peak is shifted to longer wavelengths.

To accomplish the goals of this thesis and measure the star-forming properties of a large, unbiased sample of AGN, we selected 313 AGN from the 58 month *Swift*/BAT catalog with a redshift cutoff of 0.05 for imaging with *Herschel*. All 313

were imaged by PACS at 70 and 160 μm, and all three bands of SPIRE. At such low redshifts, the 5-band imaging adequately samples the expected FIR SED, covering not just the peak but the Rayleigh-Jeans tail as well (see Figure 1.3).

1.8 Outline of Thesis

This thesis is focused on exploring the star-forming properties of AGN host galaxies. Using ultra-hard X-ray selection that reduces selection effects and biases, we have assembled a large sample of 313 nearby AGN for study with *Herschel* imaging in the FIR. The main goal is to determine whether AGN host galaxies systematically display quenched SFRs as a result of AGN feedback by taking advantage of the host galaxy dust emission as an effective tracer of recent star formation.

In Chapter 2, we detail the analysis of the SPIRE images to measure the 250, 350, and 500 μm photometry. For the first time, we measure correlations between the 250, 350, and 500 luminosities and the X-ray luminosity to determine any link between the AGN and long wavelength emission. We compare the SPIRE flux ratios of our AGN with a large sample non-AGN as a quick test on whether the broad shape of the SED matches star-forming galaxies.

In Chapter 3, we combine the SPIRE photometry from Chapter 2 with the previously measured PACS photometry and archival WISE photometry to construct the mid-to-far infrared SEDs for our entire AGN sample. We decompose the SED using an analytical model that provides measurements of the SFR, dust mass, dust temperature, and infrared AGN luminosity for every source and compare the dis-

tributions of these properties to a mass-matched non-AGN sample. We determine optimum mid-far infrared colors for efficient AGN selection and assess their completeness and sensitivity to the AGN contribution to the infrared SED. We also test the unified model by comparing the dust properties and SFRs between Type 1 and Type 2 AGN. Finally, we measure the relationship between host galaxy SFR and AGN luminosity, compare to previously measured relationships, and discuss the consequences of our results in the context of galaxy evolution.

Chapter 4 focuses on star formation in AGN host galaxies in relation to the star forming main sequence, a tight correlation between SFR and stellar mass for non-AGN galaxies. We use previously published stellar masses for a subsample of our AGN with the SFRs from Chapter 3 to determine whether AGN host galaxies display suppressed specific SFRs (SFR normalized by stellar mass). We split the sample by morphology and compare with a high-mass non-AGN sample to measure the morphological dependence on location in the SFR-stellar mass plane. We also test whether the AGN luminosity is related to distance from the main sequence and discuss whether AGN feedback is driving the evolution in these galaxies. Finally, in Chapter 5 I summarize our findings and provide a brief description of ongoing work with the rich *Herschel* data as well as future prospects in the study of star formation in AGN.

Chapter 2: *Herschel* Far-Infrared Photometry of the Swift Burst Alert Telescope Active Galactic Nuclei Sample of the Local Universe. II. SPIRE Observations

2.1 Introduction

The star formation rate (SFR) of galaxies sets the rate at which galaxies grow and evolve and is the one of the most important measures for understanding the hierarchical build-up of our universe over cosmic time. Large scale simulations, however, have shown that unregulated star formation leads to an overabundance of high mass galaxies (e.g. Bower et al., 2006; Croton et al., 2006; Silk & Mamon, 2012). Therefore some process (or processes) must be able to stop, or "quench," star formation before the galaxy grows to be too big.

The answer seems to lie in supermassive black holes (SMBH) which nearly all massive galaxies harbor in their centers. SMBHs grow through accretion of cold material (Active Galactic Nuclei; AGN), and the huge loss of gravitational energy of the cold material is converted into radiation that is evident across the whole electromagnetic spectrum and manifests itself as a bright point source in the nucleus of galaxies. The AGN can deposit this energy into the ISM of its host galaxy through

jets (e.g. Best, 2007; Fabian et al., 2003; Lanz et al., 2015) or powerful outflows that either heat the gas or remove it altogether, i.e. "feedback" processes (e.g Alatalo et al., 2011; Harrison et al., 2014; Tombesi et al., 2015; Veilleux et al., 2013).

Indirect evidence of this "feedback" has been observed through the simple, scaling relationships between the mass of the SMBH and different properties of the host galaxy such as the stellar velocity dispersion in the bulge, the bulge mass, and the bulge luminosity (e.g. Ferrarese & Merritt, 2000; Gültekin et al., 2009; Häring & Rix, 2004; Kormendy & Ho, 2013; Kormendy & Richstone, 1995; Marconi & Hunt, 2003). The relative tightness of these relationships suggests a strong coevolution of the host galaxy and SMBH. Much debate remains however as to the exact mechanism of AGN feedback and whether or not it plays a dominant role in the overall evolution of galaxies especially in light of new observations at both low and high $M_{\rm BH}$ that seem to deviate from the well-established relationships (see Kormendy & Ho, 2013, for a detailed review).

Evidence for AGN feedback though should also manifest itself in the SFR of its host galaxy, therefore much work has also focused on the so-called starburst-AGN connection (e.g. Chen et al., 2013; Cid Fernandes et al., 2001; Diamond-Stanic & Rieke, 2012; Dixon & Joseph, 2011; Esquej et al., 2014; Hickox et al., 2014; LaMassa et al., 2013; Mushotzky et al., 2014; Rovilos et al., 2012; Sanders et al., 1988a). The problem lies in determining accurate estimates of the SFR in AGN host galaxies. Well-calibrated indicators, such as Hα emission and UV luminosity, are significantly, if not completely, contaminated by the central AGN. Many studies therefore turn to the infrared (IR) regime ($1 < \lambda < 1000$ μm) where dust re-emits the stellar light

from young stars.

Dust fills the interstellar medium (ISM) of galaxies and plays an important part in the heating and cooling of the ISM and the general physics of the galaxy. While dust contributes very little to the overall mass of a galaxy ($< 1\%$), the radiative output, mainly in the infrared (IR) regime, can, on average, constitute roughly half of the bolometric luminosity of the entire galaxy (Boselli et al., 2003; Burgarella et al., 2013; Dale et al., 2007; Hauser & Dwek, 2001), although there is an enormous range in the fraction. Dust efficiently absorbs optical and UV emission and re-radiates it in the mid- and far-infrared (MIR, FIR) depending on the temperature as well as grain size (Draine, 2003). Recently formed O and B stars produce the majority of the optical and UV light in galaxies, therefore measuring the total IR light from dust provides insights into the current (< 100 Myr) star formation rate (SFR) (e.g. Kennicutt & Evans, 2012), although for very passive galaxies where the current SFR is much lower than it was earlier, IR emission can be an overestimate due to dust heating by an older stellar population.(e.g. Bendo et al., 2015)

However, dust is also the key component in obscuring our view of AGN. Dust heated by the AGN is thought to primarily live in a toroidal-like structure that encircles the AGN and absorbs its radiative output for certain lines of sight. The dusty torus is used to explain the dichotomy of AGN into Seyfert 1 (Sy 1) and Seyfert 2 (Sy 2) within a unified model (Antonucci, 1993; Urry & Padovani, 1995). Like O and B stars in star-forming regions, the AGN outputs heavy amounts of optical and UV light, and like dust in the ISM the dusty torus absorbs and re-emits this as IR radiation. Spectral energy distribution (SED) models (Barvainis, 1987;

Efstathiou & Rowan-Robinson, 1995; Fritz et al., 2006; Nenkova et al., 2002; Pier & Krolik, 1992) as well as observations (Elvis et al., 1994; Mor & Netzer, 2012; Mullaney et al., 2011; Netzer et al., 2007; Spinoglio et al., 2002) suggest the torus mainly emits in the MIR ($3 < \lambda < 40$ μm) with the flux density dropping rapidly in the FIR ($\lambda > 40$ μm). Further the SED for stellar dust re-radiation peaks in the FIR (Calzetti et al., 2000; Dale & Helou, 2002; Draine et al., 2007), making the FIR the ideal waveband to study star-formation in AGN host galaxies.

Space-based telescopes such as the *Infrared Astronomical Satellite* (IRAS; Neugebauer et al., 1984), *Spitzer Space Telescope* (Werner et al., 2004), and *Infrared Space Observatory* (Kessler et al., 1996) greatly expanded our knowledge of the IR universe and provided a window into the FIR properties of galaxies. But, before the launch of the *Herschel Space Observatory* (Pilbratt et al., 2010), the FIR SED was limited to $\lambda < 200$ μm, except for studies of small samples of the brightest galaxies using ground-based instruments such as *SCUBA* (e.g. Papadopoulos & Allen, 2000; Papadopoulos & Seaquist, 1999). *Herschel* with the Spectral and Photometric Imaging Receiver (SPIRE; Griffin et al., 2010) has pushed into the submillimeter range with observations in the 250, 350, and 500 μm wavebands, probing the Rayleigh-Jeans tail of the modified blackbody that accurately describes the broadband FIR SED of galaxies (e.g. Calzetti et al., 2000; Cortese et al., 2014; Dale et al., 2012). These wavebands are crucial for measuring dust properties (i.e. temperature and mass) as Galametz et al. (2011) and Gordon et al. (2010) show. Further, Ciesla et al. (2015) found that FIR and submillimeter data are important for estimating the SFR of AGN host galaxies.

Recent studies, such as Petric et al. (2015) and Xu et al. (2015), focusing on the dust and star-forming properties of AGN have shown the power of long wavelength *Herschel* data to better constrain the SFR, dust mass, and dust temperature in AGN host galaxies. Petric et al. (2015) analyzed the IR SEDs of low redshift ($z < 0.5$), quasi-stellar objects (QSOs) broadly finding most of the FIR emission can be attributed to thermally-heated dust. Xu et al. (2015) looked at the IR SEDs of 24 μm selected AGN at slightly higher redshift ($0.3 < z < 2.5$) around galaxy clusters finding a strong correlation between the AGN and star-forming luminosity which could be due to their shared correlation with galaxy stellar mass. Both studies, however, rely on AGN selection using different wavebands (optical vs. mid-infrared) and generally probe the higher AGN luminosity population.

Therefore, we have assembled a large (~ 300), low redshift ($z < 0.05$) sample of AGN selected using ultra-hard X-ray observations with the *Swift/Burst Alert Telescope* (BAT) and imaged each one with *Herschel*. This sample focuses on moderate luminosity Seyfert galaxies ($10^{42} < L_{\rm AGN} < 10^{46}$). In Meléndez et al. (2014), we presented the PACS data of the *Herschel*-BAT AGN which provided photometry at 70 and 160 μm. In this Chapter, we complete the FIR SED of the BAT AGN with the creation and analysis of the SPIRE images. We focus on the overall luminosity distributions at the SPIRE wavebands as well as the SPIRE colors (F_{250}/F_{350} and F_{350}/F_{500}) to determine the likely heating sources of cold dust in AGN host galaxies. We also look for correlations with a proxy for the bolometric AGN luminosity to potentially reveal any indication that AGN heated dust is contributing to the FIR SED. This Chapter sets us up for a complete study of the mid-far IR SED to

fully explore the star-forming properties of AGN host galaxies and reveal the global starburst-AGN connection in the nearby universe (Chapter 3). Throughout this Chapter we assume a ΛCDM cosmology with $H_0 = 70$ km s^{-1} Mpc^2, $\Omega_m = 0.3$, and $\Omega_\Lambda = 0.7$. Luminosity distances for each AGN were calculated based on their redshift and assumed cosmology, except for those with $z < 0.01$ where we referred to the *Extragalactic Distance Database*[1].

2.2 The *Swift*/BAT AGN Sample

Swift/BAT (Barthelmy et al., 2005; Gehrels et al., 2004) operates in the 14–195 keV energy range, continuously monitoring the sky for gamma-ray bursts. This constant monitoring has also allowed for the most complete all-sky survey in the ultra-hard X-rays. To date, BAT has detected 1171 sources at $> 4.8\sigma$ significance corresponding to a sensitivity of 1.34×10^{-11} ergs s^{-1} cm^{-2} (Baumgartner et al., 2013). Over 700 of those sources have been identified as a type of AGN (Seyfert, Blazar, QSO, etc.)

We selected our sample of 313 AGN from the 58 month *Swift*/BAT Catalog[2], imposing a redshift cutoff of $z < 0.05$. All different types of AGN were chosen only excluding Blazars/BL Lac objects which most likely introduce complicated beaming effects. To determine their AGN type, for 252 sources we used the classifications from the BAT AGN Spectroscopic Survey (Koss et al, in preparation) which compiled and analyzed optical spectra for the *Swift*/BAT 70 month catalog (Berney et al., 2015).

[1] http://edd.ifa.hawaii.edu/

[2] https://swift.gsfc.nasa.gov/results/bs58mon

Seyfert classification was determined using the standard scheme from Osterbrock (1977) and Osterbrock (1981). For the remaining 61 AGN we used the classifications provided in the 70 month catalog. In total the sample contains 30 Sy 1, 30 Sy 1.2, 79 Sy 1.5, 1 Sy 1.8, 47 Sy 1.9, 121 Sy 2, 4 LINERs, and 1 unclassified AGN. For the purpose of broad classification, in the rest of this Chapter we choose to classify all Sy 1-1.5 as Sy 1's, and all Sy 1.8-2 as St 2's. In Table A.1 we list the entire *Herschel*-BAT sample along with positions and redshifts taken from the *NASA/IPAC Extragalactic Database* (NED)[3].

Selection of AGN by ultra-hard X-rays provides multiple advantages over other wavelengths. Due to their high energy, ultra-hard X-rays easily pass through Compton-thin gas or dust in the line of sight providing a direct view of the AGN. Using optical or mid-infrared selection can be problematic due to contamination by the host galaxy. Also, ultra-hard X-rays are unaffected by any type of absorption by material obscuring the AGN provided it is optically thin to Compton scattering ($N_{\rm H} \lesssim 10^{24}$ cm^{-2}) which is a concern for hard X-rays in the 2-10 keV energy range.

Numerous studies have been done on the BAT sample in the past that span nearly the entire electromagnetic spectrum. Weaver et al. (2010) and Meléndez et al. (2008) used *Spitzer*/IRS spectra to study the mid-infrared properties of the BAT AGN. Winter et al. (2009) and Vasudevan et al. (2013) studied the X-ray spectral properties for a subsample, while Koss et al. (2011) looked at the optical host galaxy properties and Winter et al. (2010) analyzed the optical spectra. Along with these, many of the BAT AGN are detected at radio wavelengths with the FIRST (Becker

[3] http://ned.ipac.caltech.edu/

et al., 1995) and NVSS (Condon et al., 1998) survey as well. One key ingredient missing though is the far-infrared (FIR) where emission from ultraviolet-heated dust peaks.

2.3 *Herschel* SPIRE Observations and Data Reduction

The Spectral and Photometric Imaging Receiver (SPIRE) (Griffin et al., 2010) onboard *Herschel* observed in small map mode 293 of our objects between operational days (OD) 722 and 1265 as part of a Cycle 1 open time program (OT1_rmushotz_1, PI: Richard Mushotzky). 20 other objects with public data from separate programs are also included to complete our sample. Within each observation from our program, two scans were performed at nearly orthogonal angles with the nominal 30" s^{-1} scan speed that resulted in a $\sim$5' diameter area of homogeneous coverage in all three SPIRE wavebands centered at 250, 350, and 500 μm. Table 1 lists the OD and OBSID for each source.

The SPIRE raw data ("Level 0") were reduced to "Level 1" using the standard pipeline contained in the *Herschel Interactive Processing Environment* (HIPE) version 13.0 (Ott, 2010). The pipeline performs a host of steps including, but not limited to, glitch removal, electrical crosstalk correction, and brightness conversion, which results in timeline data (brightness vs. time) for each bolometer and each scan.

The Level 1 timelines were then input into *Scanamorphos* v24.0 (Roussel, 2013) to create image maps for each source. *Scanamorphos* was effectively designed

to take advantage of the built-in redundancy of the detectors to subtract the low frequency noise caused by temperature drifts of the telescope as a whole (correlated noise) and each bolometer. The drifts are determined from the data themselves without the use of any noise model and thus more accurately take into account any time variation of the drifts. The final output of *Scanamorphos* is a FITS image cube or series of FITS files containing the image, 1σ pixel error, drifts, weights, and clean map. Each map has pixel sizes equal to $\sim$1/4 times the point spread function (PSF) full width at half maximum (FWHM) of each waveband. For the 250 (18" FWHM), 350 (24" FWHM), and 500 μm (36" FWHM) maps, this means 4.5", 6.25", and 9" pixel sizes respectively. The brightness units for the maps are Jy/beam. Fig. B.1 shows the resulting maps, centered on the known positions of the AGN from Table A.1.

2.4 SPIRE Flux Extraction

Because of the large beams of SPIRE, a subsample of sources remain unresolved even though all are fairly nearby ($z < 0.05$). We employed two different methods depending on whether a source is resolved (aperture photometry) or unresolved (timeline fitting).

2.4.1 Timeline Fitting

Timeline fitting involves modeling the response of a point source in the Level 1 data as a Gaussian and determining the best fit parameters for the Gaussian. The

peak of the Gaussian then corresponds to the flux density of the source. Because this method is performed on the Level 1 data, instead of the image maps, it avoids any potential artifacts or biases involved with the mapmaking procedure and is the highly recommended procedure for determining the photometry of point sources by the SPIRE Data Reduction Guide (DRG, section 5.7.1)[4].

To determine which sources are unresolved, we fit the Level 1 data using the `sourceExtractorTimeline` task within HIPE to measure the best-fit Gaussian where one of the free parameters is the size of the source, represented by the FWHM of the Gaussian. A source is then considered unresolved in a waveband if its best fit FWHM is less than 21", 28", or 40" at 250, 350, or 500 μm respectively, the upper limit for the nominal ranges of FWHM expected for point sources. We also visually inspected the images to ensure no extended sources were falsely classified as a point source. This occurred when an extended galaxy contained a bright point source in the nucleus. To avoid combining different flux extraction techniques for a single source, we only used the timeline flux densities if that source was unresolved at all wavebands in which it is visually detected.

We used the timeline fluxes for 82 (26%), 62 (20%), and 12 (13%) sources in each of the three wavebands. These sources are indicated in Table C.1 with a "TF". The discrepancy is due to some of the sources being undetected at longer wavelengths because of the rapid fall-off of the SED as well as the decreasing sensitivity of SPIRE. For the sources that are undetected we used aperture photometry to determine their 5σ upper limit, therefore if a source is detected as a point source at 250 μm but

[4] http://herschel.esac.esa.int/hcss-doc-11.0/index.jsp#spire_drg:_start

undetected at 350 and 500 μm, it would be listed as having a timeline flux for 250, but not for 350 and 500. For reference all but three of the 82 sources for which we used timeline fitting to determine the 250 μm photometry are also point-like in both PACS wavebands. The exceptions, however are only partially resolved at 70 μm and point-like at 160 μm.

2.4.2 Aperture Photometry

For the rest of the sources, we perform aperture photometry to measure the flux densities directly from the *Scanamorphos*-produced SPIRE maps. The first step in aperture photometry is to determine the size and shape of the aperture from which to extract the flux from. To determine the local background, we also used a concentric annulus around the source aperture as well as a series of apertures within the annulus to calculate the background root-mean-square (RMS).

Instead of choosing apertures manually by visually inspecting each image, we used the publicly available, Python based `photutils`[5] package. `photutils` provides open-source functions that perform tasks such as detecting sources, measuring their size and shape, and performing aperture photometry. The process we used for the aperture photometry of the BAT AGN in the SPIRE maps involved the following key steps and is very similar to the method employed in the popular `Sextractor` software (Bertin & Arnouts, 1996) especially in regards to the use of a segmentation image.

[5] http://photutils.readthedocs.org/en/stable/

1. Convert the maps from Jy/beam to Jy/pixel.

2. Measure the standard deviation and median of the global background level.

3. Detect sources above a given threshold using a segmentation image–details are given in the next section.

4. Find the associated BAT source.

5. Measure the size and shape of associated source.

6. Create the source and background annulus from the size and shape of the source.

7. Create a series of background apertures around the source aperture to measure the RMS of the background.

8. Measure the fluxes within all apertures and calculate a background-subtracted flux and uncertainty.

2.4.2.1 Source Detection

The first step in the process is converting the SPIRE map units from Jy/beam to Jy/pixel. The images must be divided by the beam area specific to the waveband and calibration version (spire_cal_13_1) used to create the maps. For this work the beam areas are 469.7, 831.7, and 1793.5 arcsec^2 for the 250, 350, and 500 μm wavebands respectively and taken from the latest version of the SPIRE DRG. Each

pixel of the map is converted to Jy/pixel using the following formula.

$$I\,[Jy/pixel] = \frac{I\,[Jy/beam] \times P^2}{B} \tag{2.1}$$

I is the intensity value of the pixel, P is the pixel size of the map (see Section 2.3), and B is the beam area stated above. After converting all of the pixels, we use an iterative procedure to measure the median and standard deviation of the background over the whole map. For this, we use two tools: sigma-clipping and a segmentation image. Sigma-clipping involves measuring the median and standard deviation of data (in this case pixel values of the SPIRE maps) and removing pixels that are above a clipping limit. The process is then repeated until there are no more pixels above the clipping limit. We chose a clipping limit of 3 standard deviations above the measured median. The function used to perform the sigma-clipping is `sigma_clipped_stats` that is provided within the `Astropy` (Astropy Collaboration et al., 2013) package.

Sigma-clipping however can still be affected by sources in the field and provides a biased estimate of the background. A better process is to iteratively run sigma-clipping, each time masking out pixels associated with a source. To determine which pixels will be masked, we use a segmentation image. A segmentation image is a map, the same size as the input map, that identifies groups of connected pixels that are above a certain threshold. For a threshold we use $MD + 2 \times SD$ where MD and SD are the median and standard deviation of the map determined through sigma-clipping. A source is identified in the map as a group of 5 interconnected pixels that are above this threshold value. The `Photutils` function `detect_sources` was

used to create all segmentation images. All of the pixels that are associated with a source are then masked out and sigma-clipping is re-run on the remaining pixels. This process is repeated until the percentage change in the sigma-clipped median is less than 1×10^{-6} or a maximum of 10 iterations. A final sigma-clipped median (MD_{final}) and standard deviation (SD_{final}) is measured from the masked map.

We then produce a new segmentation image to find the associated BAT source in the SPIRE map using a threshold of $MD_{final} + 1.5 \times SD_{final}$. Through tests of various extended sources, we found $1.5 \times SD_{final}$ to best incorporate the fainter outer regions of the galaxies. The `Photutils` function `segment_properties` is then used to measure centroid, semimajor axis length, semiminor axis length, and position angle of all sources detected from the segmentation image. We identify the BAT source as the closest detected source within one FWHM (see Section 2.3) of the known positions (Table A.1).

2.4.2.2 Target and Background Apertures

After the SPIRE source that is associated with the BAT source is found, we used the measured size and shape from `segment_properties` to construct a target and background aperture. The target aperture is an ellipse and the background aperture is an elliptical annulus. The semimajor and semiminor radii of the target aperture are calculated as 3.5 times the semimajor and semiminor sigma values from `segment_properties`. The sigma values are measured from the second-order central moments of the detected source and represent the standard deviations along

each axis of a 2D Gaussian that has the same second-order moments. The central position of the target aperture is the centroid of the source and the orientation is the same as the measured orientation.

The background annulus has the same central position and orientation as the target aperture. For the inner radius, we increase the semimajor and semiminor axis of the target aperture by 3 pixels. The outer radius is then 1.5 times the inner radius.

In addition to the background annulus, we also construct a series of circular apertures that encircle the target aperture. These have a size of 22", 30", and 42", the recommended size of an aperture (see the SPIRE DRG) for measuring the flux of a point source in the 250, 350, and 500 μm maps respectively. While the background annulus is used to measured the local background level, these circular apertures are used to measure the background noise. The SPIRE DRG recommends using local background apertures for the calculation of the background noise because calculating the RMS within the background annulus will underestimate the noise. We construct as many apertures as can fit just outside the target aperture without overlapping but impose a minimum of 6 apertures. Figure 2.1 shows an example of the apertures used in calculating the photometry as well as the segmentation image that was used to find the source and determine its properties to construct the apertures.

One exception to all of this occurs for small sources. If the constructed target aperture has a semimajor axis smaller than 22", 30", or 42" for 250, 350, and 500 μm maps, then we use a circular aperture with these radii. This indicates the source is

likely a point source that was either missed using the results from the timeline fitting (Section 2.4.1) or is extended at other SPIRE wavelengths which automatically identifies it as extended at all wavelengths. For these aperture photometry point sources, the background annulus used has a 60" inner radius and a 90" outer radius, the recommended annulus for point source photometry from the SPIRE DRG. The circular background apertures are still constructed in the same way as for extended sources.

The other exception is for sources that lie in maps dominated by foreground cirrus emission. Cirrus emission comes from cold dust in the Milky Way galaxy that is along our line of sight to the AGN. It is identified as bright smooth patches that occur over large spatial scales. We visually identified 25 sources that are likely contaminated by Milky Way cirrus. We used point source apertures for the photometry, however instead of placing the background annulus 60–90" away, we placed it right outside the target aperture to get a more accurate estimate of the local background.

2.4.2.3 Flux Extraction

We calculate the raw source flux (F_{raw}) by summing the values of the pixels within the target aperture. Pixels that are on the border are used by determining the fraction of the pixel area that is inside the aperture and using that fraction of the pixel value in the sum. The background level is determined by estimating the mode of the pixel values within the background annulus using a Python version of the "MMM" routine which is the method used in the popular photometry package

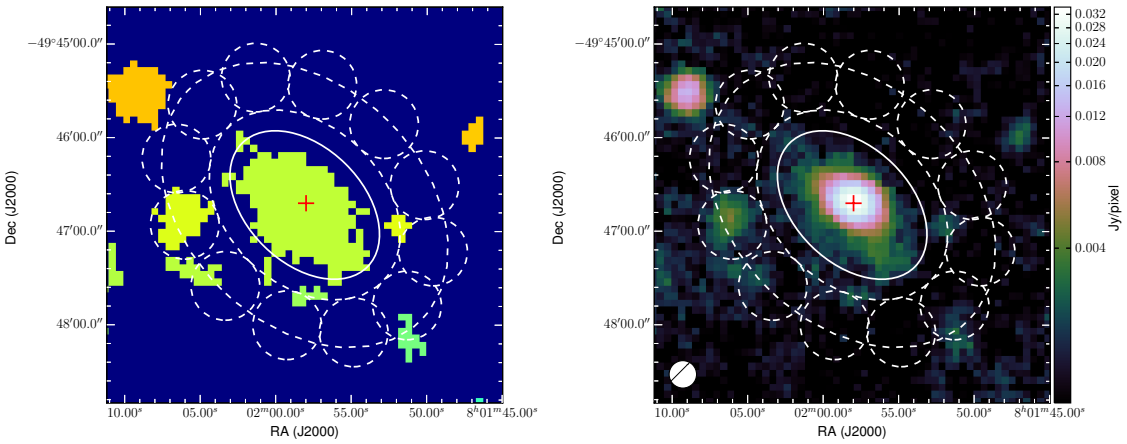

Figure 2.1: An example of the segmentation image (left) and apertures used in the aperture photometry procedure. The solid white line indicates the target aperture whose size and shape were determined from the centroid and second order moments of the source (central light green group of pixels) detected in the segmentation image. The dashed annulus shows the background annulus used to calculate the local background level. The dashed circular apertures are used to determine the background noise. The right image is the actual SPIRE map of the BAT source ESO 209-G012 using an arcsinh stretch. The red cross in both images shows the known location of ESO 209-G012 from Table A.1.

`DAOPHOT`. The mode (F_{bkg-an}) then represents the per-pixel background level so we multiply it by the pixel area of the target aperture (A_{src}) to calculate the total background flux within the target aperture. The background flux is then subtracted from the raw source flux. The whole procedure can be represented with the following equation:

$$F_{\rm bkg-sub} = F_{\rm raw} - F_{bkg-an} \times A_{src} \tag{2.2}$$

For extended sources, $F_{\rm bkg-sub}$ represents the final measured flux density. However for sources which used the point source aperture, we applied the necessary aperture corrections as given in the SPIRE DRG. For the 250, 350, and 500 μm bands, these corrections are 1.2697, 1.2271, and 1.2194 respectively.

Both Ciesla et al. (2012) and Dale et al. (2012) found aperture corrections for extended emission to be small and unnecessary. To confirm this, we convolved our PACS 160 μm images (PSF FWHM 12") to the 250, 350, and 500 μm angular resolution using the convolution kernels from Aniano et al. (2011). This makes the assumption that the 160 μm emission is generated by the same material as that producing the SPIRE emission. Aperture corrections were calculated by dividing the total flux within an aperture from the original PACS image by the flux within the exact same aperture applied to the convolved image. The same aperture sizes were used in this calculation as the ones used in this SPIRE analysis. Median aperture corrections of 1.01, 0.98, and 0.98 were found consistent with a value of 1 and confirming that extended emission aperture corrections are not necessary.

2.4.3 Uncertainty Calculation

For sources where we used aperture photometry, three components were factored into the total error budget for the SPIRE aperture photometry of our sample. These were the instrumental error ($err_{\rm inst}$), background error ($err_{\rm bkg}$), and calibration error ($err_{\rm cal}$). $err_{\rm cal}$ is fixed at 6.5% of the measured background-subtracted flux density for sources which used aperture photometry. The calibration error is the combination of the 4% uncertainty in the Neptune (which is the primary calibrator source for SPIRE) flux model, the 1.5% uncertainty from repeated measurements of Neptune, and the 1% uncertainty in the beam areas (Bendo et al., 2013). To determine $err_{\rm inst}$, we summed in quadrature all of the 1σ pixel uncertainties from

the error map contained in the target aperture. For $err_{\rm bkg}$, we measured the flux within the circular background apertures placed around the source aperture. The standard deviation of the fluxes was calculated after using sigma-clipping with a 3σ cutoff to remove fluxes possibly contaminated with a bright, background source. This was then scaled to the area of the target aperture to represent $err_{\rm bkg}$. The three error components are then summed in quadrature to form the total 1σ uncertainty ($err_{\rm tot}$) of the measured flux density for each source.

For sources where we used the timeline fitting, only two components are needed. The output from the timeline fitting contains an estimate of the statistical uncertainty in the flux density. This is combined in quadrature with a 5.5% calibration error, which is the same as the calibration error for aperture photometry minus the 1% uncertainty in the beam areas that are not needed in the timeline fitting.

2.5 The *Herschel*-BAT SPIRE Catalog

Table C.1 represents our final SPIRE catalog for the *Herschel*-BAT AGN. For each waveband three columns are provided. The first column contains the flux density ($F_{bkg-sub}$ and 1σ uncertainty (err_{tot}). The second column provides the photometry method used to determine the flux density, either timeline fitting ("TF") point source aperture photometry ("PAP"), or extended source aperture photometry ("EAP"). The third column provides flags to assist in assessing the reliability of the photometry. We decided to impose a strict 5σ threshold for reporting the pho-

tometry, so for all sources where $5err_{\rm tot} > F_{\rm bkg-sub}$, only the 5σ upper limit is given as the flux density for that band and a flag of "U" is used. For sources above 5σ a flag of "A" is used. Alongside these two flags we also indicate those sources that are contaminated by foreground cirrus emission with a flag of "C". Finally a flag of "d" or "D" is used for sources that have a nearby companion that could possibly be affecting the photometry of the main BAT source. "d" represents companions that are either relatively faint compared to the BAT source or are far enough away where contamination to the SPIRE photometry is minimal. "D" represents nearby bright companions that are completely contaminating the source photometry, and we recommend using these flux densities as only upper limits. In total 17 and 10 sources have a "d" and "D" classification for the 250 μm waveband, 20 and 13 for the 350 μm waveband, and 13 and 21 for the 500 μm waveband. The changing numbers with wavelength represents the degrading resolution as wavelength increases. Many of the sources with a "d" or "D" flag have previously been identified as merging or companion systems in Koss et al. (2010).

2.5.1 Comparison with *Herschel* Reference Survey

The *Herschel* Reference Survey (HRS, Boselli et al. (2010b)) is a guaranteed time key project that surveyed 323 nearby ($15 < D < 25$ Mpc) galaxies using SPIRE to explore the dust content in early and late-type galaxies. Cross-correlating our sample with HRS, we found four sources (NGC 3227, NGC 4388, NGC 4941, and NGC 5273) that are a part of both. We compared the fluxes published in Ciesla

et al. (2012) to our own and find a mean ratio $F_{\rm BAT}/F_{\rm HRS}$ of 0.88, 0.92, and 0.87 for the 250, 350, and 500 μm wavebands respectively.

However, there are several distinct differences between the HRS analysis and ours with the major difference being the beam area sizes. Ciesla et al. (2012) used beam areas of 423, 751, and 1587 arcsec^2 compared with 469.7, 831.7, and 1793.5 arcsec^2 for our analysis. To correct for this, we multiplied the HRS fluxes for the galaxies by 423/469.7, 751/831.7, and 1587/1793.5 for the 250, 350, and 500 μm bands respectively. After this correction the flux comparison ratios change to 0.97, 1.02, and 0.99. The remaining few percent differences we attribute to the differences in observing mode, map maker (Scanamorphos vs. naive map), data reduction, and photometry techniques. The ratios are also well within the uncertainties, therefore we conclude our photometry is consistent with the HRS.

2.5.2 Comparison with *Planck*

We also compared our fluxes with those from the *Planck* Catalog of Compact Sources (PCCS; Planck Collaboration et al., 2014). The *Planck* telescope performed an all-sky survey at nine submillimeter and radio wavebands to primarily measure the cosmic microwave background. The highest frequency band centered at 857 GHz matches the SPIRE 350 μm waveband and the 545 GHz (550 μm) overlaps the SPIRE 500 μm waveband allowing for independent measurements of the flux density of our sources. We searched the PCCS for our sources at each frequency using a 4' search radius and found 60 matches at 350 μm and 37 at 500 μm. To be

consistent with our work we chose the aperture fluxes to compare with ours except for Centaurus A, NGC 1365, and M106 in which we chose the fluxes from fitting a Gaussian. These three sources are resolved even with *Planck*'s poor spatial resolution, so the aperture fluxes will underestimate the true flux because the aperture sizes are equal to the resolution at each frequency.

We applied color corrections to the *Planck* fluxes to account for the differences in both central wavelength and spectral response. These were downloaded from the NHSC website[6] and provides corrections for different temperature greybodies with an assumed emissivity of 1.8. Also provided are F_{545}/F_{847} flux ratios that correspond to each temperature, which we compare with each observed flux ratio to find the right color correction for each source. Therefore we also restricted our comparison to only include sources that were detected in both the 545 and 857 GHz band giving a total of 27 sources.

After correcting the *Planck* fluxes, we compare them to our SPIRE fluxes and find a median SPIRE-to-*Planck* ratio of 0.90 and 1.00 for the 350 and 500 μm band respectively. This shows a relatively good agreement between the SPIRE and *Planck* instruments, especially in the 500 μm band and especially given all the assumptions and corrections that were made to compare the flux densities.

[6] https://nhscsci.ipac.caltech.edu/sc/index.php/Spire/PhotDataAnalysis

2.6 FIR Properties of the *Herschel*-BAT Sample

2.6.1 Detection Rate and Luminosity Distributions

Meléndez et al. (2014) in analyzing the PACS photometry found 95% and 83% of the BAT sample had a 5σ detection at 70 and 160 μm, indicating a largely complete survey of AGN for those wavelengths. Our SPIRE analysis finds a 5σ completeness of 86%, 72%, and 46% for 250, 350, and 500 μm respectively. The decreasing completeness reflects both the decreasing sensitivity of SPIRE with increasing wavelength as well as the rapid fall-off of the SED at longer wavelengths. Even with the relatively low detection rate at 500 μm, this still results in 143 AGN having complete FIR SEDs from 70–500 μm, representing a great step forward in advancing the study of the mid-far IR SED of AGN.

After splitting the sample into Sy 1's and Sy 2's, we find a distinct difference in the detection rate (Figure 2.2). Sy 2's, for all 3 wavebands, are detected at a significantly higher rate than Sy 1's (95% vs. 81% for 250 μm, 85% vs. 62% for 350 μm, 58% vs. 34% for 500 μm).

As we discuss in Meléndez et al. (2014) with the PACS photometry, this most likely is a result of the different redshift distribution between Sy 1's and Sy 2's. In the *Swift*/BAT catalog, Sy 2's are found preferentially at lower redshifts than Sy 1's. Without taking into account the redshifts, the higher detection rate for Sy 2's would indicate Sy 2's favoring higher FIR luminosities. However, as Figure 2.3 shows, this is not the case. Figure 2.3 displays the kernel density estimates (KDE)

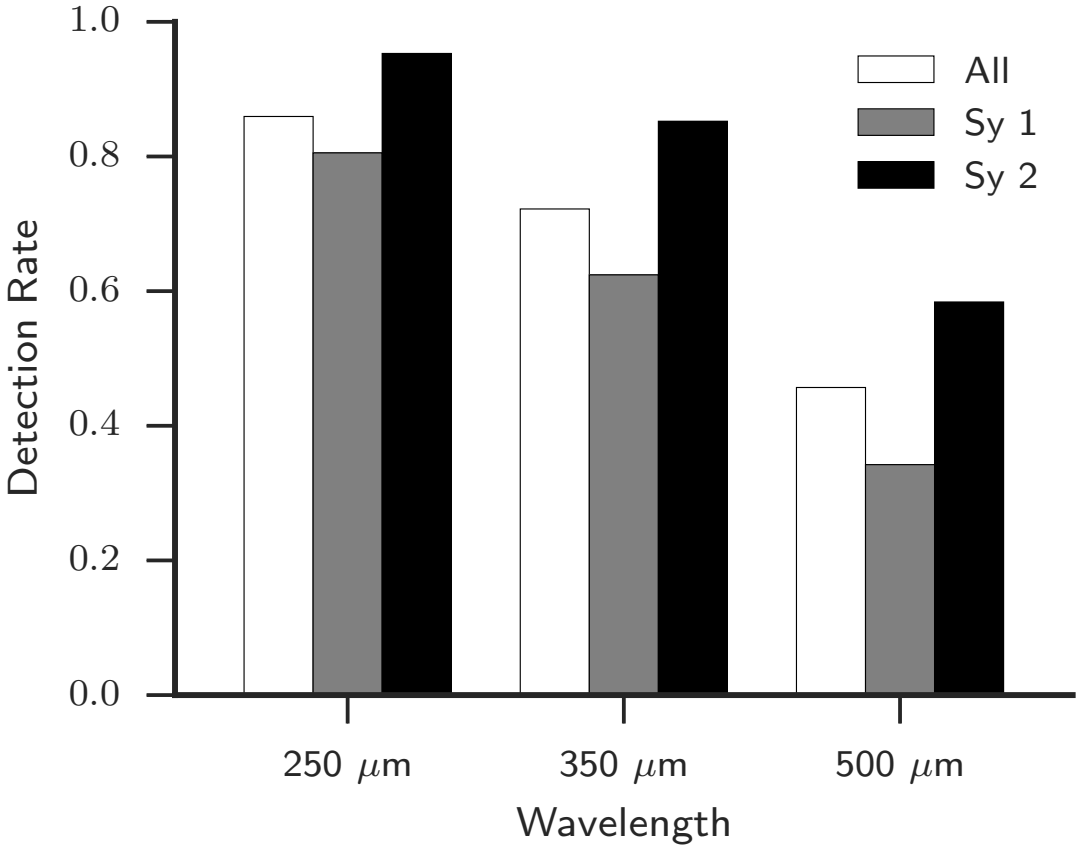

Figure 2.2: Detection fractions for the whole BAT sample (313 AGN), Sy 1's (139 AGN), and Sy 2's (169 AGN) in each SPIRE waveband. Sy 1's show significantly lower detection fractions than Sy 2's.

of the SPIRE luminosity distributions for the total sample, Sy 1's, and Sy 2's. KDE's are a better way to represent distributions of data than histograms due to the histogram's dependence on both bin size and bin centers. A KDE represents each data point using a user-specified shape and sums all of them together. In this Chapter, the shape we use is a Gaussian that has a width defined by "Scott's Rule" (Scott, 1992).

Sy 1's and Sy 2's have identical 250 and 350 μm luminosity distributions. At 500 μm the luminosity distributions for Sy 2's actually peak at a *lower* luminosity than Sy 1's. Again, this is due to Sy 2's occurring at lower redshifts where it is easier to detect the lower luminosities at longer wavelengths.

Figure 2.3 however does not account for the undetected galaxies at each wavelength. For this, we use "survival analysis" to calculate the Kaplan–Meier product-limit estimator, a non-parametric representation of the survival function, $S(t) = P(T \geqq t)$. The Kaplan–Meier estimator then allows for an accurate estimate of mean, median, and standard deviation of a sample including censored values.

To perform the survival analysis, we utilized the software package ASURV (Feigelson & Nelson, 1985; Isobe et al., 1990). The only inputs necessary are the measured luminosities and upper limits for each wavelength. In Table 2.1 we outline the mean, 25th, 50th, and 75th percentiles of the luminosity distribution at each SPIRE wavelength. We give values for the entire sample as well as just the Sy 1's and Sy 2's.

The mean and medians for Sy 1's and Sy 2's are similar, however Sy 2's do seem to have slightly higher luminosities at each wavelength. The mean luminosities

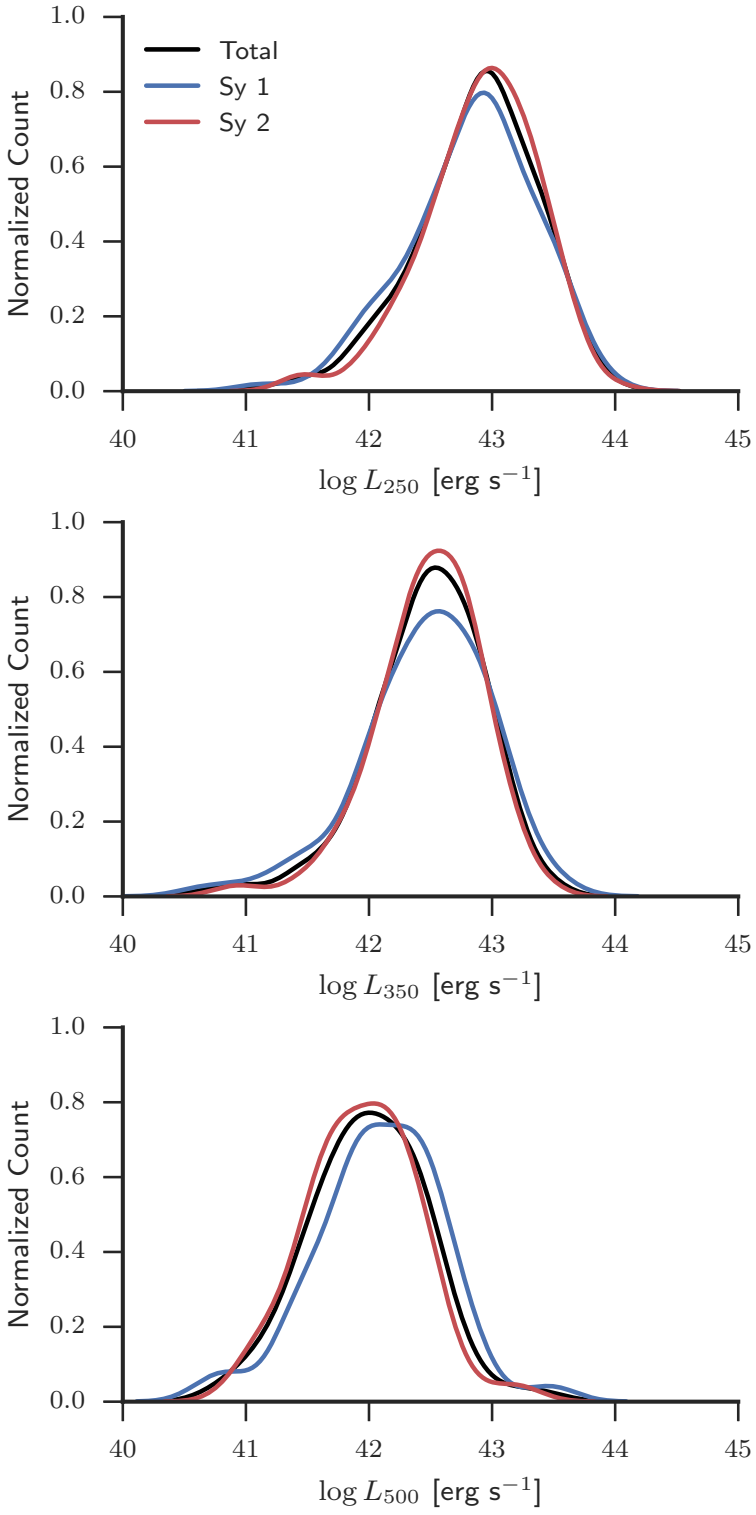

Figure 2.3: Kernel density estimates (KDE, see text for explanation) of the luminosity distribution at each SPIRE wavelength for the total sample (black), Sy 1's (blue), and Sy 2's (red). At 250 μm Sy 1's and Sy 2's are nearly identical while at 350 and 500 μm Sy 2's seem to shift towards lower luminosities.

Table 2.1: SPIRE Luminosity Distributions

Sample	Mean	25th %tile	50th %tile	75th %tile
250 μm				
Total	42.8±0.03	42.5	42.9	43.2
Sy 1	42.6±0.07	42.2	42.8	43.1
Sy 2	42.8±0.05	42.6	42.9	43.2
350 μm				
Total	42.3±0.04	42.0	42.4	42.7
Sy 1	41.9±0.1	40.9	42.2	42.6
Sy 2	42.3±0.05	42.0	42.4	42.7
500 μm				
Total	41.6±0.06	41.3	41.7	42.0
Sy 1	41.2±0.1	26.7	41.1	41.9
Sy 2	41.4±0.09	40.6	41.6	42.0

deviate between 0.2–0.4 dex and the median deviates between 0.1–0.5 dex. We test for differences between the two samples using the Peto & Prentice Generalized Wilcoxon test, which is similar to the standard Kolmogorov-Smirnov test but allows for censoring (i.e. upper limits). The test indicates that the probability that Sy 1's and Sy 2's are drawn from the same parent population is 5%, 3%, and 14% for 250, 350, and 500 μm respectively. The usual cutoff for significant differences between two samples is 5%, therefore we consider the luminosity distributions of Sy 1's and Sy 2's to be statistically the same at 500 μm and marginally different at 250 and 350 μm. This echoes the same small differences seen in Meléndez et al. (2014) for the 160 μm band where Sy 2's displayed slightly higher luminosities as well, suggesting that Sy 2's do indeed exhibit either larger dust masses or higher rates of star formation.

2.6.2 *Herschel* Undetected Sources

With the photometry for all five wavebands of our *Herschel* study now measured, we can identify sources that are completely undetected at the 5σ limit. In total, we find 11 sources that are completely undetected or about 4%. These sources are 2MASS J17485512-3254521, 2MASX J08032736+0841523, 2MASX J09360622-6548336, 2MASX J12475784-5829599, 2MASX J13512953-1813468, 2MASX J14080674-3023537, 2MASX J14530794+2554327, 2MASX J20183871+4041003, Arp 151, LEDA 138501, and PG 2304+042.

The images for three of these sources (2MASS J17485512-3254521, 2MASX J12475784-5829599, and 2MASX J20183871+4041003) are dominated by foreground cirrus emission so it is possible they would have been detected in the SPIRE wavebands without the cirrus contamination. The other eight *Herschel*-BAT AGN, however, are clear non-detections at all five wavebands.

We examined SDSS optical images (Figure 2.4) for four of the eight sources that are not detected in any *Herschel* waveband. 3/4 of the host galaxies appear to be quite red in color, indicating a lack of young stars and older stellar population. Further their morphologies are either elliptical or cigar shaped, indicative of early-type galaxies which are known to be faint in the FIR and contain little dust (e.g. di Serego Alighieri et al., 2013). The only exception is ARP 151, which seems to be involved in a merger, displaying a long and narrow tidal tail. It is possible the merger process has removed large amounts of gas and dust from the galaxy causing it to be faint in the FIR. Given 75% of the undetected sources with optical images

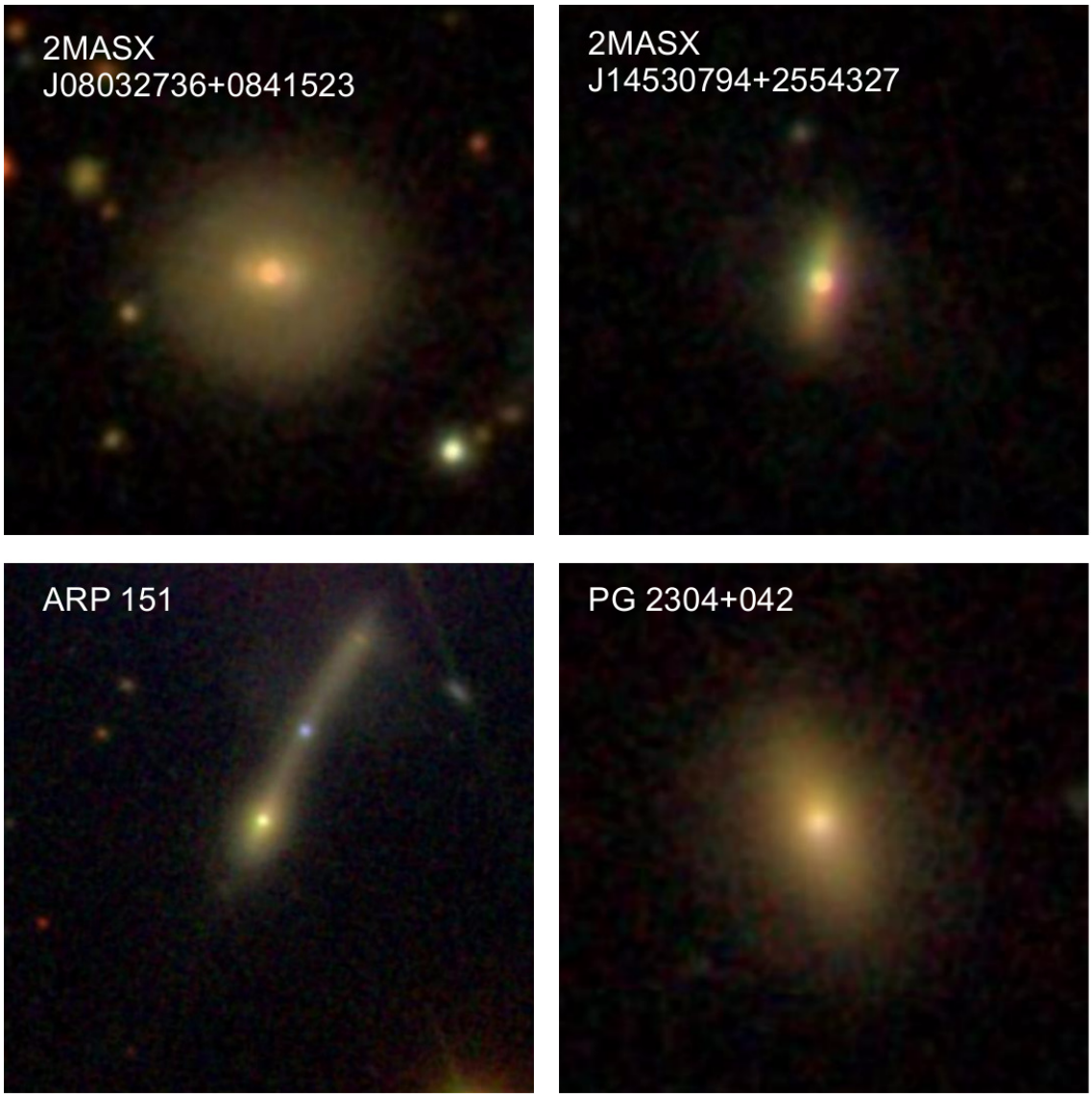

Figure 2.4: SDSS *gri* images of 4/8 the *Herschel*-BAT AGN that are undetected at all five *Herschel* wavebands.

are early-type galaxies, it is likely the remaining four AGN host galaxies are also early-type galaxies with relatively little cold dust and star formation occurring.

2.6.3 Wavelength–Wavelength Luminosity Correlations

Thermally heated dust is thought to produce the mid-far IR SED (e.g. Draine, 2003). Shorter wavelength emission corresponds to both hotter and smaller dust grains and vice versa for longer wavelengths. Both the amount of dust (i.e. dust mass) heated to a specific temperature as well as the relative intensity of the heating process determine the strength of the emission at a particular wavelength. If the same process (e.g. young star formation) is heating all of the dust and producing the entire FIR SED, we would expect strong correlations between each wavelength, however if two or more disjointed processes contribute to the SED (e.g. star formation and AGN emission), correlations will become weaker.

Three processes could contribute to the heating of dust in the BAT AGN. Recent star formation in the galaxy will produce OB stars with a high intensity of UV light that can heat nearby dust to large temperatures. UV light can also escape the star-forming regions and heat dust further away to colder temperatures. Older stellar populations, however, also produce an interstellar radiation field that can heat diffuse dust to temperatures around 15 K which would contribute most heavily at the longest wavelengths (e.g. Bendo et al., 2010, 2012, 2015; Boselli et al., 2012). Finally, the UV light from the AGN itself can heat dust in the torus.

We ran a correlation analysis between each *Herschel* waveband. Two effects

Table 2.2: Luminosity Partial Correlation Coefficients

	250 μm	350 μm	500 μm
Total			
70 μm	0.54±0.03 ($\ll$ 0.01)	0.45±0.03 ($\ll$ 0.01)	0.27±0.03 ($\ll$ 0.01)
160 μm	0.74±0.02 ($\ll$ 0.01)	0.62±0.02 ($\ll$ 0.01)	0.34±0.03 ($\ll$ 0.01)
250 μm	...	0.75±0.02 ($\ll$ 0.01)	0.41±0.03 ($\ll$ 0.01)
350 μm	...	...	0.42±0.03 ($\ll$ 0.01)
14–195 keV	0.06±0.03 (0.05)	0.06±0.03 (0.06)	0.02±0.02 (0.52)
Sy 1			
70 μm	0.55±0.04 ($\ll$ 0.01)	0.43±0.04 ($\ll$ 0.01)	0.23±0.04 ($\ll$ 0.01)
160 μm	0.71±0.03 ($\ll$ 0.01)	0.57±0.04 ($\ll$ 0.01)	0.29±0.04 ($\ll$ 0.01)
250 μm	...	0.66±0.04 ($\ll$ 0.01)	0.32±0.04 ($\ll$ 0.01)
350 μm	...	...	0.32±0.04 ($\ll$ 0.01)
14–195 keV	0.13±0.05 (0.003)	0.10±0.04 (0.02)	0.04±0.04 (0.23)
Sy 2			
70 μm	0.51±0.04 ($\ll$ 0.01)	0.44±0.04 ($\ll$ 0.01)	0.30±0.04 ($\ll$ 0.01)
160 μm	0.74±0.03 ($\ll$ 0.01)	0.64±0.03 ($\ll$ 0.01)	0.40±0.04 ($\ll$ 0.01)
250 μm	...	0.81±0.03 ($\ll$ 0.01)	0.48±0.04 ($\ll$ 0.01)
350 μm	...	...	0.50±0.04 ($\ll$ 0.01)
14–195 keV	0.02±0.04 (0.69)	0.03±0.05 (0.54)	-0.004±0.04 (0.91)

must be taken into account to establish reliable correlation coefficients: censoring and confounding variables. The confounding variable in this case is distance. Since our sample is flux-limited, higher luminosity objects are more likely to be found at larger distances. Therefore it can produce the effect of an intrinsic correlation when comparing two luminosities. To mitigate the effects of censoring and the luminosity-distance relationship, we calculated the partial Kendall-τ correlation coefficient as presented in Akritas & Siebert (1996). Table 2.2 displays all of the correlation coefficients (ρ_τ) as well as the probability of zero correlation (P_τ).

While all the relationships show some amount of correlation with very low ($\ll$ 1%) probabilities of occurring by chance, the strongest ones occur between

wavelengths that are nearest each other. The 160 vs. 250 μm and 250 vs. 350 μm correlations have a correlation coefficient > 0.7. This makes sense within the context of multiple temperature components. Photometry from nearby wavelengths should be produced from closely related temperature components.

The weak correlation between 70 and 500 μm indicates the emission in these wavebands does not originate from closely related processes. 70 μm emission comes from much hotter and smaller dust grains than 500 μm and several processes could provide an explanation. Since this is an AGN sample, there could be a strong contribution from AGN heated dust at 70 μm, whereas at 500 μm, AGN related emission would likely be negligible. This is supported by our findings in Meléndez et al. (2014) where we showed that the 70 μm luminosity is weakly correlated with AGN luminosity. Further, in Mushotzky et al. (2014) we found that the BAT AGN morphologies at 70 μm were concentrated in the nucleus potentially indicating an AGN contribution.

The weak correlation, however, can also be explained if non-star-forming processes also contribute to the 500 μm emission. While in non-AGN galaxies, the majority of 70 μm emission is most likely due to small, stochastically heated dust grains around HII regions, > 250 μm emission is likely produced by the heating of larger dust grains in the diffuse ISM by older stars (e.g. Bendo et al., 2015). Therefore, the disconnect between the stellar populations would produce significant scatter in the correlation between 70 and 500 μm.

A third possibility is that synchrotron radiation produced by radio jets associated with AGN can contribute to the FIR, especially the longest wavelengths

as seen in some radio-loud galaxies (Baes et al., 2010; Boselli et al., 2010a). This non-thermal emission would be completely unrelated to the thermal emission at 70 μm, thereby producing a weaker correlation between the luminosities at those wavebands. In a later section we will show there are indeed some radio-loud sources in our sample where synchrotron emission dominates the SPIRE emission, although the fraction of sources is quite low.

When we break the sample down into Sy 1's and 2's we do not find much difference between the correlation coefficients. This shows that Sy 1's and 2's are not different in terms of their overall FIR emission and the same processes are likely producing the FIR emission. Sy 1's do show a slightly weaker correlation between the *Herschel* luminosities especially the ones involving 500 μm. This is likely due to the fact that most radio-loud AGN are classified as Sy 1's so synchrotron emission is contributing strongest at 500 μm compared to the other wavebands.

2.6.4 Correlation With Ultra-Hard X-ray Luminosity

Ultra-hard X-ray luminosity directly probes the current strength of the AGN because it likely originates very close to the SMBH. The 14–195 keV luminosity then provides an unambiguous measure of the AGN power especially for Compton-thin sources. If we want to determine whether the AGN contributes in any way to the FIR luminosity, the first check would be to correlate the 14–195 keV luminosity with each waveband's luminosity. Meléndez et al. (2014) ran correlation tests for the PACS wavebands finding a weak, but statistically significant correlation between

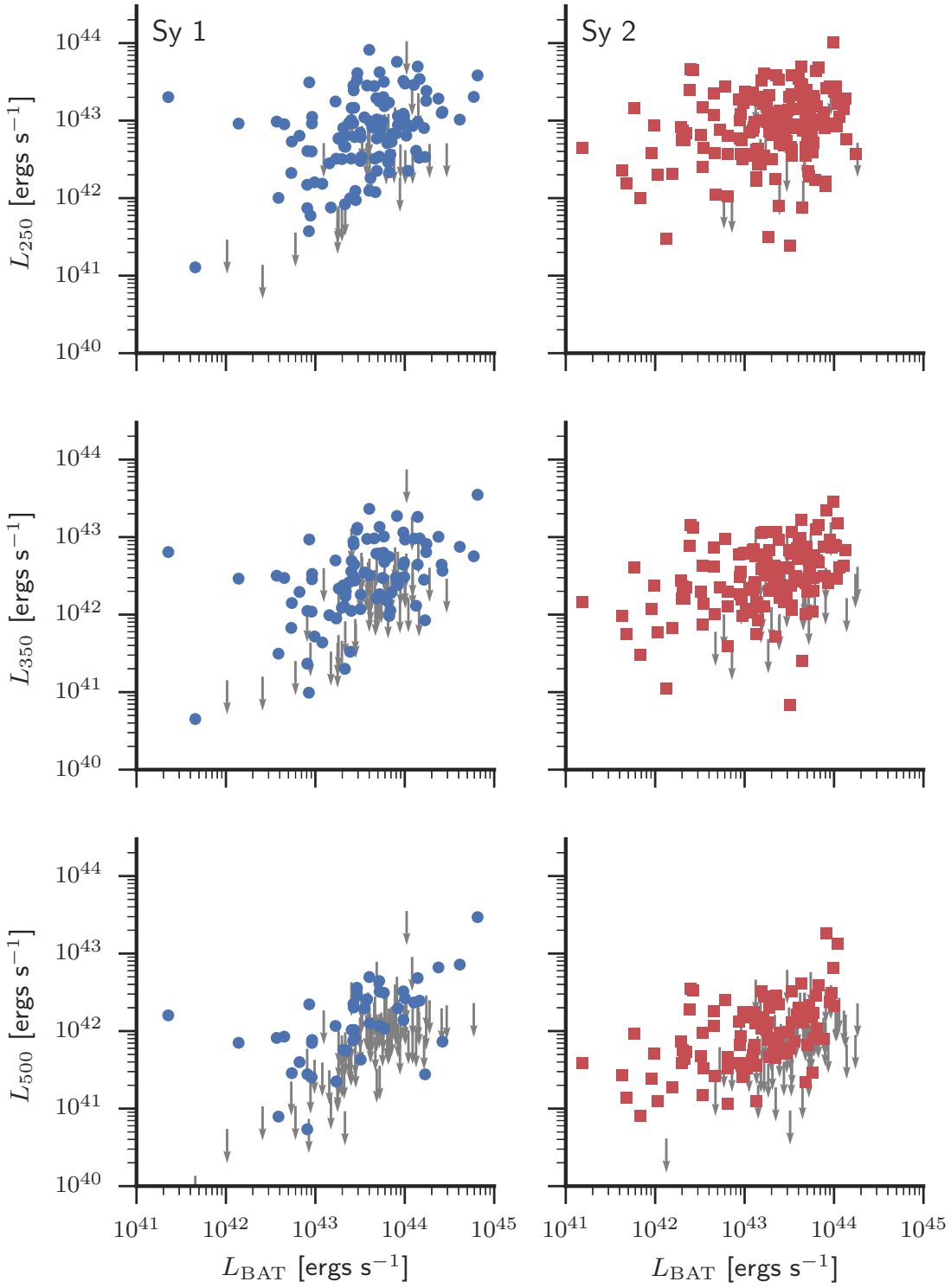

Figure 2.5: Correlations between each SPIRE waveband luminosity and the BAT 14–195 keV luminosity. Blue circles in the left column represent Sy 1's. Red squares in the right column are Sy 2's. Sources with gray arrows indicate 5σ upper limits.

the 70 and 160 μm luminosity and the 14–195 keV luminosity for Sy 1's but not for Sy 2's.

Using the same methods as we did to measure strengths of the correlations between each *Herschel* luminosity, we measured the correlation between each SPIRE and 14–195 keV luminosity. The last lines of each section of Table 2.2 lists the results of the correlation tests and Figure 2.5 plots the correlations with gray arrows indicating upper limits.

For the AGN sample as a whole, no significant correlation exists between the SPIRE and 14–195 keV luminosity. All of the ρ_τ, after accounting for the partial correlation with distance, are below 0.1 with P_τ either at or above 5%. However, when we break the sample up into Sy 1's and Sy 2's and redo the correlation tests, we find a very weak correlation between the 250 and 350 μm luminosity and ultra-hard X-ray luminosity for Sy 1's only ($\rho_\tau = 0.13$ and 0.10). Sy 2's ρ_τ are consistent with no correlation with $P_\tau > 54\%$ for all three wavebands. This continues the trend with what was found in Meléndez et al. (2014) where only Sy 1's were found to have a weak correlation between the BAT luminosity and the PACS waveband luminosities. The partial correlation coefficients were 0.20 ± 0.04 and 0.12 ± 0.04 for Sy 1s and 0.08 ± 0.04 and -0.005 ± 0.04 for Sy 2's at 70 and 160 μm respectively (see Table 3 of Meléndez et al., 2014).

We note however that except for the 70 μm waveband, none of the correlation coefficients are $> 3\sigma$ away from a null correlation coefficient. So even though $P_\tau < 5\%$, these are all quite weak correlations between the *Herschel* wavebands and BAT luminosity for Sy 1's. At 500 μm, the correlation completely disappears.

As we discuss in Meléndez et al. (2014), this extends the trend observed in the MIR where strong correlations have been measured between the 9, 12, and 18 μm luminosities and the BAT luminosity (Gandhi et al., 2009; Ichikawa et al., 2012; Matsuta et al., 2012) but moving towards longer wavelengths the correlation degrades rapidly as shown in Ichikawa et al. (2012) for 90 μm emission.

Clearly then, at long wavelengths ($\lambda > 40$ μm), emission from dust unrelated to the AGN dominates most galaxies. However, we must still explain why Sy 1's retain a weak correlation while Sy 2's do not. Meléndez et al. (2014) discussed in detail several theories for why Sy 1's would show a different correlation between the *Herschel* luminosities and BAT luminosity. These included an intrinsically different BAT luminosity distribution for Sy 1's and Sy 2's and the addition of Compton-thick (CT) AGN in the Sy 2 sample.

Several authors have found that the Sy 2 luminosity function breaks at a significantly lower luminosity than for Sy 1s (e.g. Burlon et al., 2011; Cowie et al., 2003; Hasinger et al., 2005). At low BAT luminosity, then, there are more Sy 2's than Sy 1's as is evident in Figure 2.5. Rosario et al. (2012) showed that at low AGN luminosity the correlation between SFR and AGN luminosity flattens. This can be explained one of two ways: 1.) Only at high AGN luminosity is there a direct connection between star formation and AGN activity. 2.) At high AGN luminosity, the IR-related AGN emission overwhelms any star-forming related IR emission even at long wavelengths. Regardless of the physical reason, the flattening of the SF-AGN relationship at low luminosity could explain the correlation differences seen between Sy 1s and Sy 2s since Sy 2s are preferentially found at lower luminosity

than Sy 1s.

Meléndez et al. (2014) tested this for the PACS wavebands and found that only using high luminosity objects did not improve the X-ray-to-IR correlation for Sy 2's. We repeated this test with the SPIRE luminosities and limited the samples to only AGN with BAT luminosity greater than $10^{43.5}$ ergs s^{-1}. For both Sy 1's and Sy 2's the correlations become insignificant, likely because of the reduction in number of sources used in the analysis. It is then inconclusive whether or not a difference in intrinsic AGN luminosity is the cause of the differences in correlations between X-ray and IR luminosity for Sy 1's and Sy 2's.

The other possibility is that CT sources are contaminating the Sy 2 sample. This would have an effect if the high column density ($N_{\rm H} > 10^{24}$ cm^{-2}) material obscuring the AGN scatters 14-195 keV photons out of our line sight causing a lower measured BAT luminosity. Meléndez et al. (2014) identified 44 either confirmed CT AGN or likely CT AGN based on X-ray hardness ratios in our sample. We removed these likely CT sources and redid the correlation tests, finding no difference from before just as Meléndez et al. (2014) found. Therefore, it is unlikely that CT sources are the cause of the difference between the Sy 1 and Sy 2 correlations.

Given the inconclusiveness of the first test limiting the sample to high luminosity objects, we can only speculate about the reason for the difference in correlations. However, Meléndez et al. (2014) did find that restricting the sample to high luminosity objects increased the strength of the correlation for Sy 1's but not Sy 2's in the PACS wavebands. It is possible then that either a direct physical link between the SFR and AGN luminosity that is only evident in high luminosity AGN or in-

creased contamination of the AGN to the IR SED is causing the relatively stronger correlation in Sy 1s but not Sy 2s.

What is conclusive is that the SPIRE emission from the AGN host galaxies on average is not strongly contaminated by AGN-related emission given the small values for the correlation coefficients even for Sy 1's.

2.6.5 SPIRE Colors

While in the previous sections, we examined the absolute luminosities of each SPIRE waveband and the correlations between each other and other wavebands (PACS and BAT), in this section we examine the SPIRE colors (i.e. flux ratios). Colors in general provide measures of the shape of the SED. Different objects and mechanisms produce significantly different SED shapes across the same wavelength regime, therefore colors can be used to separate distinct populations from each other especially when groups display the same absolute brightnesses. We investigate two colors, F_{250}/F_{350} and F_{350}/F_{500}, that probe the Rayleigh Jeans tail of a modified blackbody if the dominant process producing the emission is cold dust.

2.6.5.1 BAT AGN SPIRE colors are similar to high-mass non-AGN galaxies

Figure 2.6 plots the KDE of the two colors. The top row compares the distribution of the colors (F_{250}/F_{350} on the left and F_{350}/F_{500} on the right) from the BAT AGN and HRS samples. While the HRS galaxies are local like the BAT AGN, one

major difference is the stellar mass distribution. The HRS sample contains more low stellar mass galaxies while the BAT AGN are strictly found in galaxies with stellar mass (M_*) values above $10^{9.5}$ $M_\odot$ (Koss et al., 2011).

As Boselli et al. (2012) show, FIR colors can be affected by the physical properties of the galaxy, especially the colors probing the cold dust such as the ones we are investigating here. Therefore, we broke the HRS sample into two groups, a high mass group ($M_* > 10^{9.5}$ $M_\odot$) and low mass one ($M_* > 10^{9.5}$ $M_\odot$) indicated in Figure 2.6 by the solid and dashed green lines. Stellar masses for the HRS were obtained from Cortese et al. (2012b).

We also plot the theoretical color of the modified blackbody with a dust temperature of 20 K and emissivity (β) of 2.0 and 1.5, values typical of normal, star-forming galaxies (e.g. Calzetti et al., 2000; Cortese et al., 2014; Dale et al., 2012; Galametz et al., 2012; Smith et al., 2012). The HRS high mass group and BAT AGN display nearly identical color distributions for both colors whereas the HRS low mass group is skewed toward lower colors. Results of a K-S test show that the HRS high mass group and BAT AGN colors are drawn from the same parent population with a $P_{K-S} = 49\%$ and 22% for F_{250}/F_{350} and F_{350}/F_{500} respectively. On the other hand the HRS low mass group colors are significantly different from the BAT AGN with P_{K-S} values much less than 1%.

This is consistent with what was found in Boselli et al. (2012), who showed that the SPIRE colors for the HRS sample were affected by the metallicity of the galaxy with metal rich galaxies displaying larger flux ratios and a higher β than metal poor ones. Given the strong, positive relationship between metallicity and M_* (e.g.

Tremonti et al., 2004), this is exactly in line with what is seen in Figure 2.6. The HRS high mass group and BAT AGN display colors closer to the ones expected for a modified blackbody with $\beta \sim 2.0$ while the low mass HRS group are closer to $\beta \sim 1.5$.

In Figure 2.7 we plot both colors together for the HRS and BAT AGN. Nearly all of the HRS galaxies are concentrated along a main locus as well as many of the BAT AGN. We also plot the expected colors for a modified blackbody with varying temperature between 10 and 60 K and an emissivity of either 2.0 (green line and squares) or 1.5 (purple line and diamonds). Each square or diamond represents an increase of 5 K starting at 10 K in the lower left. The main locus for both samples is clearly aligned with a modified blackbody with temperatures between 15–30 K. Cortese et al. (2014) fit the FIR SED of the HRS sample using a single temperature modified blackbody finding exactly this range of temperatures and an average emissivity of 1.8. Further these values are consistent with dust in the Milky Way, Andromeda, and other nearby galaxies (Boselli et al., 2012; Galametz et al., 2012; Smith et al., 2012).

2.6.5.2 Sy 1s and Sy 2s show the same SPIRE colors

In the bottom rows, we compare Sy 1's and Sy 2's. Based on the results of our analysis in Section 2.6.1, we would expect Sy 1's and Sy 2's to show the same distribution of colors. Indeed this is the case as both distributions in both colors peak at nearly the same values and have nearly the same spread. K-S tests reveal

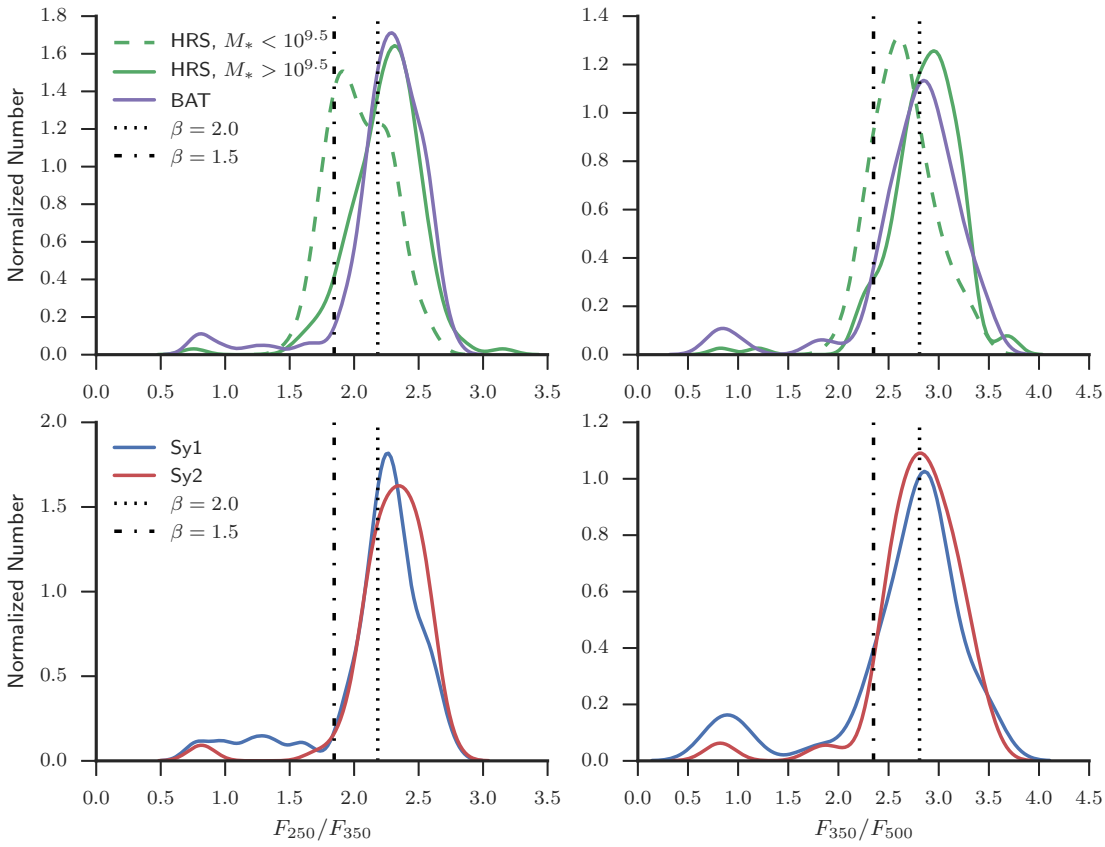

Figure 2.6: *top row:* KDE of the F_{250}/F_{350} (left) and F_{350}/F_{500} (right) colors for the BAT AGN (purple) and HRS (green). For the HRS galaxies, we split the sample into high ($M_* > 10^{9.5}$ $M_\odot$; solid line) and low ($M_* < 10^{9.5}$ $M_\odot$, dashed linje) stellar mass groups. A K-S test indicates the SPIRE color distributions for the BAT AGN and HRS high-mass group are statistically the same with $P_{K-S} = 49\%$ for F_{250}/F_{350} and $P_{K-S} = 22\%$ for F_{350}/F_{500}. *bottom row:* KDEs for the colors of the BAT AGN separated into Sy 1s (blue) and Sy 2s (red). K-S tests indicate the two Seyfert types are drawn from the same parent population with $P_{K-S} = 17\%$ and 37% for F_{250}/F_{350} and F_{350}/F_{500} respectively. In both rows we also plot the expected color for a modified blackbody with a dust temperature of 20 K and an emissivity of 2.0. (dotted line) and 1.5 (dot-dash line)

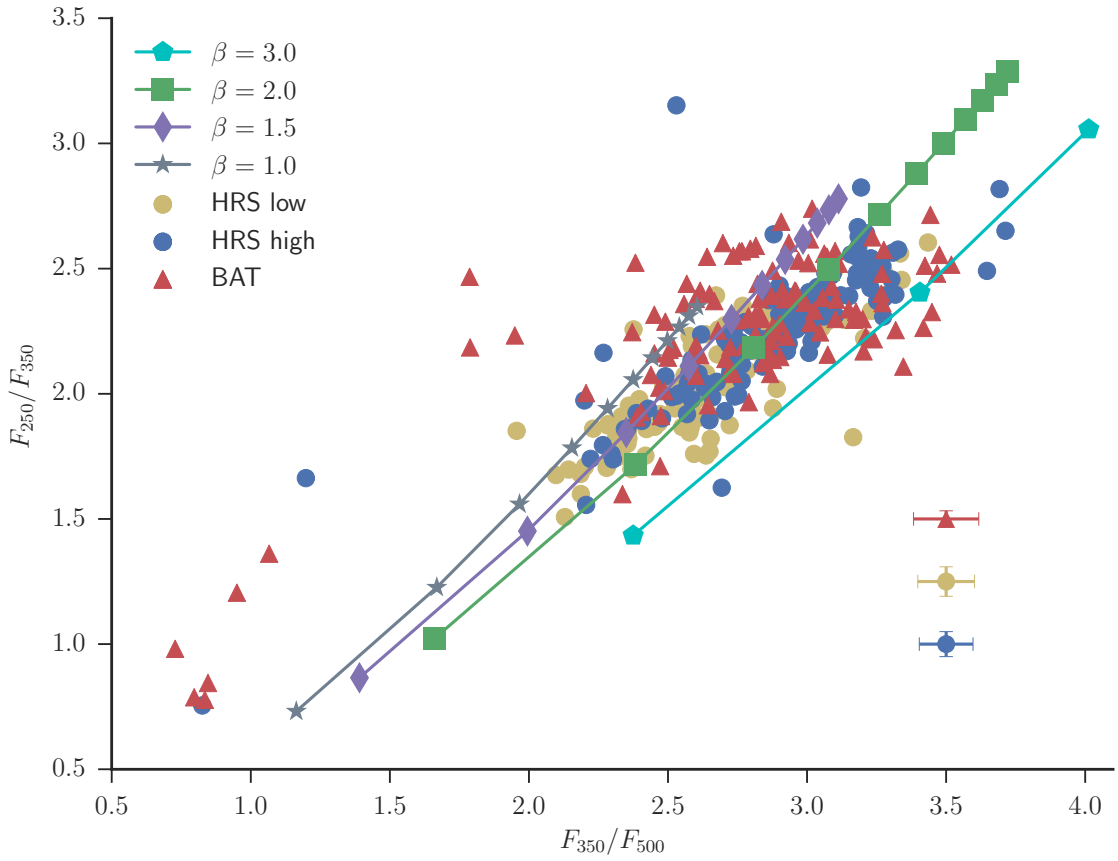

Figure 2.7: SPIRE color-color plot of the BAT AGN (red triangles) and HRS high and low M_* group (blue and yellow circles). The lines with markers represent theoretical colors assuming a modified blackbody ($F_\nu \propto \nu^\beta B(\nu, T)$) with emissivity, $\beta = 3.0, 2.0, 1.5,$ and 1.0. Each marker represents a different temperature from 10 K (lower left) to 60 K (upper right) in increments of 5 K, except for $\beta = 3.0$ for which we only show markers for 10, 15, and 20 K. The main locus for both the BAT AGN and HRS is concentrated around the theoretical colors between 15–30 K and $\beta = 1.5 - 2.0$. Representative error bars are shown in the lower right corner.

the colors for the two Seyfert types are drawn from the same parent population with $P_{K-S} = 0.2$ for F_{250}/F_{350} and $P_{K-S} = 0.3$ for F_{350}/F_{500}.

2.6.5.3 Outliers in SPIRE color-color space: Radio-loud AGN and excess 500 μm emission

While the bulk of the SPIRE colors are very similar between the HRS and BAT, and the two Seyfert types, one noticeable difference is a distinct bump in the color distribution around 0.75. This bump is absent in the HRS sample and mainly is made up of Sy 1s. With both flux ratios less than one, this indicates a monotonically rising SED that is in stark contrast with the rapidly declining SED characteristic of a modified blackbody. The equation for a modified blackbody is

$$F_\nu \propto \nu^\beta B(\nu, T) \tag{2.3}$$

where $B(\nu, T)$ is the standard Planck blackbody function with a temperature of T.

The bump seen in Figure 2.6 is very evident in Figure 2.7 as a separate population in the lower left-hand corner. Specifically 6 BAT AGN and one HRS galaxy occupy the region of color-color space where $F_{250}/F_{350} < 1.5$ and $F_{350}/F_{500} < 1.5$. Based on the theoretical curves, these exceptional colors cannot be explained as either a different temperature or emissivity. Rather an entirely different process is producing the FIR emission in these galaxies and since the colors indicate essentially a rising SED, we suspected synchrotron radiation as the likely emission mechanism with its characteristic increasing power law shape with wavelength.

Further there seems to be a horizontal spread in the distribution of the BAT

AGN in Figure 2.7 that is clearly not evident in the HRS. Also this effect is not seen Figure 2.6 and the KDEs because it only becomes evident when analyzing the two colors together. Both samples span the same range of colors, however their distribution in color-color space is different. This is characterized by a large group of BAT AGN above and to the left of the main locus and $\beta = 1.5$ line (purple) as well as a smaller group of AGN below and to the right of the main locus and $\beta = 2.0$ line (green). The latter group can be explained simply from a decrease in temperature and increase in emissivity up to a beta value of 3.0 (cyan line in Figure 2.6), indicating the prevalence of large amounts of cold dust. The former group could be explained by a decrease in the emissivity closer to around values of 1.0 (gray line), however this would require the dust temperature to increase to values above 60 K, not typical of regular star-forming galaxies.

Rather these high temperatures (70–100 K) are near the expected temperatures for dust heated by the AGN, which show characteristic peaks in their SED between 20–40 μm (Mullaney et al., 2011; Netzer et al., 2007; Richards et al., 2006). If the AGN is affecting the colors of these sources more than the ones on the main locus then there should be some correlation between the offset from the main locus and an indicator of AGN strength such as X-ray luminosity.

To quantify the offset from the main locus, we fit the SED of all of the sources in Figure 2.7 using a modified blackbody (Eq. 2.3) with a fixed emissivity of 2.0 to measure the excess or deficiency of observed 500 μm emission compared to the model.

With the emissivity fixed at 2.0, there are only two free parameters, the dust

temperature and normalization. We fit the sources within a Bayesian framework using uniform priors for the logarithm of the normalization and dust temperature and a standard Gaussian likelihood function. To sample the posterior probability density function, we use the `emcee`[7] package (Foreman-Mackey et al., 2013) that implements the affine-invariant ensemble sampler for Markov chain Monte Carlo (MCMC) originally proposed by Goodman & Weare (2010)[8].

For the model fitting, we only use 160, 250, and 350 μm flux densities. We exclude the 500 μm data point because our aim is to compare the expected 500 μm emission from the model with the observed one and do not want the fitting influenced by the observed emission. We also exclude the 70 μm flux density because it can be dominated by emission from hotter dust heated by young stars in dense star-forming regions or the AGN itself (Bendo et al., 2010; Boquien et al., 2011; Calzetti et al., 2000; Meléndez et al., 2014; Smith et al., 2012).

Each sample from the MCMC chain contains values for the parameters of the modified blackbody that are likely given the posterior distribution. From all of these parameters, we calculated 40000 modeled 500 μm emission and "excess" using the following equation:

$$E_{500} = \frac{F_{obs} - F_{model}}{F_{model}} \tag{2.4}$$

[7]Available at `http://dan.iel.fm/emcee/current/`

[8]The MCMC ensemble sampler is essentially multiple MCMC chains running in parallel and each chain is called a "walker". We chose to use 50 walkers that run for 1000 steps each. The first 200 steps of each walker are discarded as a "burn-in" period that allows each walker time to move away from the initial guesses for the parameters and begin exploring the full posterior probability distribution.

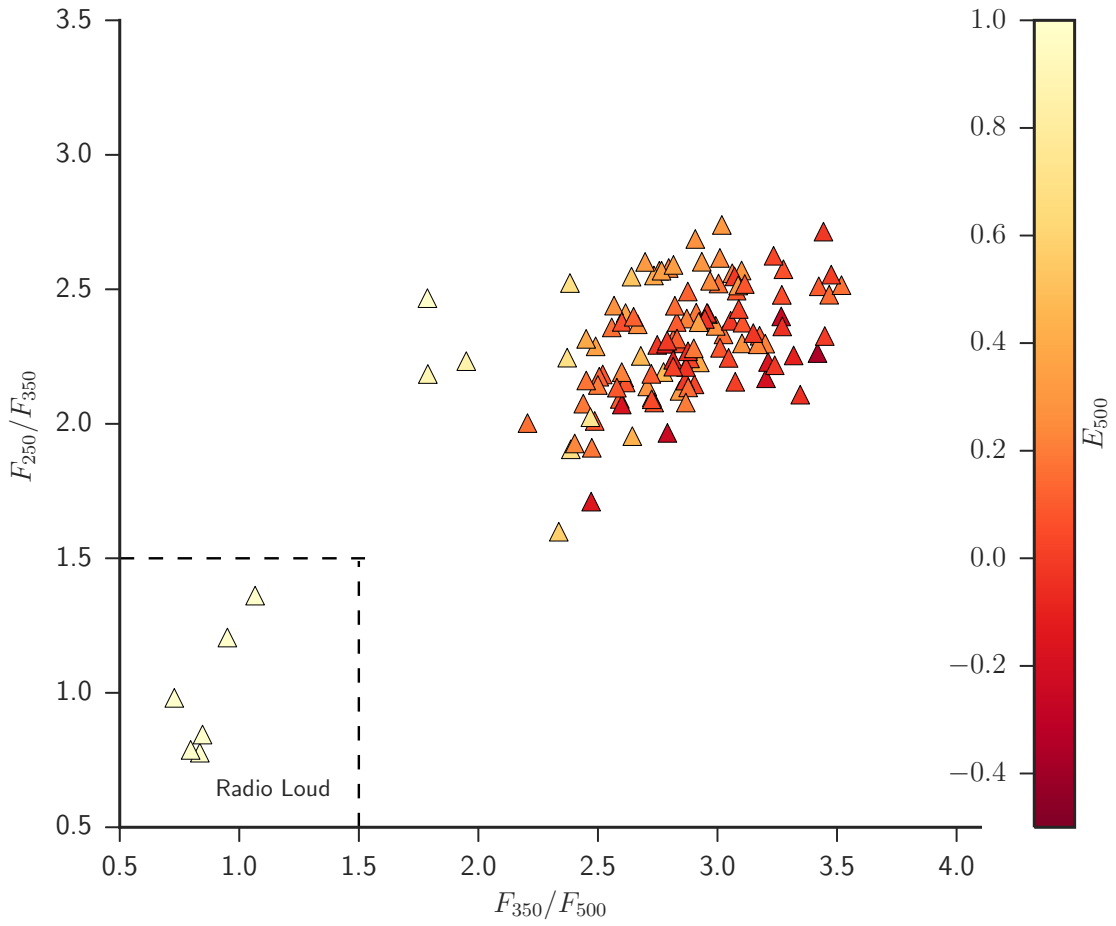

Figure 2.8: Same as Figure 2.7 but only showing the BAT AGN. The points are colored by F_{excess}, the measured 500 μm excess emission compared to a modified blackbody. The two dashed lines delineate the color cutoff for radio loud AGN, $F_{250}/F_{350} < 1.5$ and $F_{350}/F_{500} < 1.5$.

E_{500} then represents a fractional excess (or deficiency) as compared to the model emission. A deficiency would be indicated by a negative value for E_{500}. The final excess value associated with the source is then determined as the median of all of the excess values. In Figure 2.8 we plot the same color-color diagram as in Figure 2.7 with each point colored by its measured E_{500}.

In general, points with low values of the F_{350}/F_{500} color show high values of E_{500} and vice versa for high values of the F_{350}/F_{500} color. Points along the main

locus are scattered around $E_{500} = 0$. Thus, E_{500} can quantify a source's distance from the main locus and allows us to study possible causes for this excess emission at 500 μm.

We first measure the correlation between E_{500} and radio loudness. AGN historically have been classified into two groups based on how bright their radio emission is compared to another waveband, usually optical. These groups are "radio-loud" and "radio-quiet" AGN with the former group showing bright radio emission and the latter faint radio emission relative to the optical or X-ray emission (Kellermann et al., 1989; Xu et al., 1999). While originally radio-loud and radio-quiet AGN seemed to form a dichotomy, the consensus now seems to be that there is a broad distribution of radio-loudness rather than a bimodality (Cirasuolo et al., 2003a,b; Laor, 2003; White et al., 2000). Further, the original radio loudness parameter, $R = L_{\rm radio}/L_{\rm opt}$ which measured the ratio of the radio to optical luminosity, was shown to underestimate the radio loudness especially for low-luminosity Seyfert galaxies (Terashima & Wilson, 2003). Rather $R_{\rm X} = L_{\rm radio}/L_{\rm X}$ which measures the nuclear radio to X-ray luminosity ratio was confirmed to be a better radio-loudness indicator given X-rays are less affected by obscuration and contamination from the host galaxy. Therefore, for the BAT AGN, we use $R_{\rm X}$ to measure the radio-loudness with $L_{\rm radio} = L_{1.4\,\rm GHz}$ and $L_{\rm X} = L_{14-195\,\rm keV}$.

For $L_{1.4\,\rm GHz}$ we first cross-correlated the BAT AGN with the FIRST and NVSS databases which provide 1.4 GHz flux densities over all of the northern sky. FIRST flux densities were preferred over NVSS due to the much better angular resolution (5" vs. 45"). Since *Swift*/BAT was an all-sky survey, nearly half of the BAT AGN

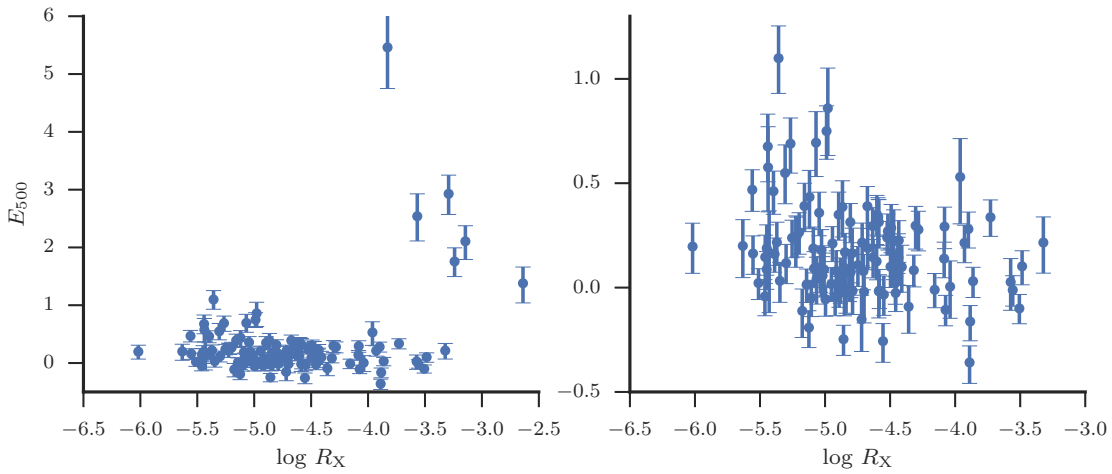

Figure 2.9: The correlation between radio loudness defined as $R_X = L_{1.4\,GHz}/L_{14-195\,keV}$ and the 500 μm excess emission, E_{500}. The left panel displays all sources, while the right panel zooms in on the majority of the BAT AGN with $E_{500} < 1.0$. Error bars encompass the 68% confidence region for E_{500}.

were not included in either FIRST or NVSS. For these southern sources we turned to the Sydney University Molonglo Sky Survey (SUMSS; Bock et al., 1999) which surveyed the southern sky at 843 MHz. Finally, for the remaining sources missing radio data, we performed a literature search and found 5 GHz fluxes from various other studies (Becker et al., 1991; Griffith & Wright, 1993; Ho & Peng, 2001; Rush et al., 1996; Shi et al., 2005). To convert all flux densities to 1.4 GHz, we assumed a power-law spectrum, $F_\nu \propto \nu^{-0.7}$, that is typical for synchrotron emission.

Figure 2.9 plots E_{500} against R_X to test our hypothesis that the excess 500 μm emission is related to the radio loudness of the AGN. In the left panel we plot all of the sources together to show the full range of E_{500}. Indeed, the six AGN with the largest values of E_{500} exhibit high values of radio loudness ($\log R_X > -4.0$). These six AGN are HB 890241+622, 2MASX J23272195+1524375, 3C 111.0, 3C

120, Pictor A, and PKS 2331-240 and all are well known radio-loud AGN. They correspond to the six sources in Figures 2.7 and 2.8 that lie in the lower left hand corner. Further, the lone HRS galaxy seen in Figure 2.7 among the six BAT AGN is the radio galaxy M87, whose jets and radio activity have been studied extensively. Based on this, we prescribe color cutoffs that can easily separate radio-loud AGN from radio-quiet AGN and normal star-forming galaxies: $F_{250}/F_{350} < 1.5$ and $F_{350}/F_{500} < 1.5$ (see dashed lines in Figure 2.8).

While radio-loudness can explain the most extreme values of E_{500}, it does not explain the more moderate ones. In the right panel of Figure 2.9, we zoom in on the AGN with $E_{500} < 1.0$. Visually there does not appear to be any strong correlation between $R_{\rm X}$ and E_{500} and the Spearman rank correlation coefficient between them is -0.15, weak and in the opposite sense of what would be expected if synchrotron emission was contaminating the 500 μm emission.

To explore even further, we analyzed the correlations between E_{500} and two AGN-related indicators, the *Swift*/BAT luminosity, $L_{14-195\,keV}$, and the 3.4 to 4.6 μm flux ratio ($W1/W2$). The 3.4 ($W1$) and 4.6 ($W2$) μm fluxes for the BAT AGN were obtained from the *Wide-field Infrared Survey Explorer* (*WISE*; Wright et al., 2010) AllWISE catalog accessed through the *NASA/IPAC* Infrared Science Archive (IRSA)[9]. Details of the compilation of *WISE* fluxes for the BAT AGN will be available in an upcoming publication (Shimizu et al. in preparation).

Winter et al. (2012) showed that $L_{14-195\,keV}$ can be used as a measure of the intrinsic bolometric luminosity of the AGN, unaffected by host galaxy contamination

[9] http://irsa.ipac.caltech.edu/Missions/wise.html

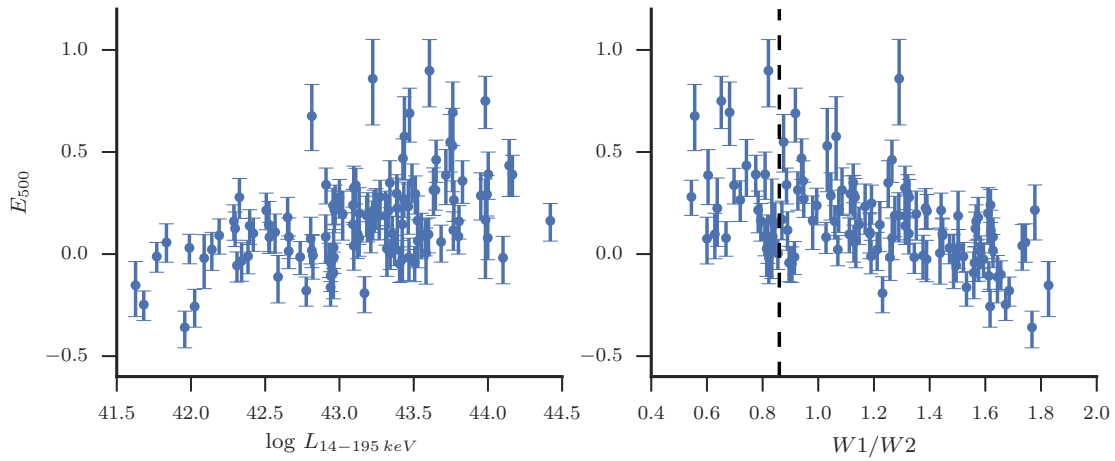

Figure 2.10: Relationships between E_{500} and the hard X-ray luminosity (left), $L_{14-195\,\mathrm{keV}}$, as a proxy for the intrinsic AGN strength, and $W1/W2$ (right), the ratio of the 3.4 and 4.6 μm flux densities, as a proxy for the relative strength of the AGN to host galaxy emission. In the right panel we also plot as a dashed line, the cutoff (0.86) for AGN-dominated galaxies prescribed by Stern et al. (2012) after converting to flux densities. In both panels we removed sources with $E_{500} > 1.0$ that are associated with radio-loud AGN. Error bars encompass the 68% confidence region for E_{500}.

or line-of-sight absorption. $W1/W2$ has been shown to be an effective discriminator between AGN-dominated and normal star-forming galaxies that has both high reliability and completeness (Stern et al., 2012)[10]. Stern et al. (2012) also show that as the fraction of emission coming from the host galaxy increases $W1/W2$ increases as well making it a good measure of the relative contribution of the AGN to the infrared luminosity.

Fig. 2.10 shows the relationships between both $L_{14-195\,\mathrm{keV}}$ (left panel) and $W1/W2$ (right panel) with E_{500} after removing the six radio-loud AGN. Both parameters display noticeable correlations with E_{500} with $L_{14-195\,\mathrm{keV}}$ positively corre-

[10]Stern et al. (2012) prescribe a cutoff of $W1 - W2 \geq 0.8$ in magnitude units for selecting AGN. In flux units this changes to $W1/W2 \leq 0.86$

lated and $W1/W2$ negatively correlated. We calculated Spearman rank correlation coefficients finding values of 0.49 and -0.49 respectively. Pearson correlation coefficients are 0.30 and -0.50 respectively reflecting the more linear relationship between E_{500} and $W1/W2$ than the one between E_{500} and $L_{14-195\,\mathrm{keV}}$. All correlations have a probability of a null correlation less than 0.01%. In the right panel we also plot the Stern et al. (2012) cutoff for AGN-dominated galaxies where values to the left of this line indicate AGN-dominated colors.

Both panels indicate that the strength of the AGN in the host galaxy is possibly having an effect on the SPIRE colors. A stronger AGN in relation to the host galaxy is causing deviations from a standard modified blackbody in the form of a small but noticeable 500 μm offset.

Without longer wavelength data, however, its impossible to determine the exact cause of the 500 μm excess so we can only speculate. Submillimeter excess emission has been observed in a number of objects including dwarf and normal star-forming galaxies (e.g. Dale et al., 2012; Galametz et al., 2011, 2009; Rémy-Ruyer et al., 2013) as well as the Small and Large Magellanic Clouds (Bot et al., 2010; Gordon et al., 2010) and even our own Milky Way (Paradis et al., 2012). Various explanations have been proposed including the presence of a very cold ($T \sim 10$ K) component (Galametz et al., 2011, 2009; O'Halloran et al., 2010), grain coagulation that causes the emissivity to increase for colder temperatures (Paradis et al., 2009), fluctuations in the Cosmic Microwave Background (Planck Collaboration et al., 2011), and an increase in magnetic material in the ISM (Draine & Hensley, 2012). While all of these explanations are certainly still possible to explain the excess seen

in the BAT AGN, they lack any direct connection to the strength of the AGN. Further, a key result from all of the previous work is that the submillimeter excess is more prevalent in very metal-poor galaxies ($12+\log(\mathrm{O/H} \lesssim 8.3$). Because dust is composed of metals, its likely the dust properties of metal-poor galaxies are different than those of higher metallicity galaxies. Whether the excess is caused by a changing emissivity, very cold dust, or spinning dust is still a matter of debate. Nevertheless, all of the BAT AGN reside in high stellar mass galaxies (Koss et al., 2011) and given the mass-metallicity relationship (Tremonti et al., 2004) should also be quite metal rich, therefore we should not expect excess emission.

Rather, we speculate the excess is related to radio emission more closely associated with the AGN itself. Several studies of the radio properties of AGN have revealed a millimeter excess around 100 GHz (Behar et al., 2015; Doi et al., 2005, 2011; Scharwächter et al., 2015) that is likely due to either an inverted or flat SED between cm and mm wavelengths. Because Doi et al. (2011) found the excess mainly in low luminosity AGN similar to Sgr A*, they invoked advection dominated accretion flows (ADAF) that produce compact nuclear jets to explain the inverter or flat SEDs. However the sample of Behar et al. (2015) was composed of X-ray bright AGN including high Eddington ratio ($L_{\mathrm{bol}}/L_{\mathrm{Edd}}$, a measure of the accretion rate relative to the Eddington limit) sources where an ADAF is unlikely. Behar et al. (2015) instead use the radio-to-X-ray luminosity ratio to argue that the high-frequency radio emission originates near the X-ray corona of the accretion disk given the ratio's similarity to that found for stellar coronal mass ejections (e.g Bastian et al., 1998) as well as the compact nature of the radio emission. Magnetic activity around the

accretion disk in the core of the AGN would then be responsible for the excess and if magnetic activity increases with $L_{\rm bol}/L_{\rm Edd}$, this could explain the relationship seen with $L_{14-195\,\rm keV}$ as well as $W1/W2$. This strengthens the need for a more comprehensive survey of AGN in the mm wavelength range as it could clearly reveal interesting physics possibly occurring near the accretion disk.

2.7 Conclusions

We have produced the *Herschel*/SPIRE maps for 313 AGN selected from the *Swift*/BAT 58 month catalog in three wavebands: 250, 350, and 500 μm. Combined with the PACS photometry from Meléndez et al. (2014), the SPIRE flux densities presented in this Chapter form the complete FIR SEDs for a large, nearby, and relatively unbiased sample of AGN. We used two methods for measuring the flux densities: timeline fitting for point sources and aperture photometry for extended and undetected sources. We summarize below the results of our statistical analysis and comparison to the *Herschel* Reference Survey sample of normal star-forming galaxies.

- Sy 2s are detected at a higher rate than Sy 1s, and after accounting for upper limits, Sy 2's have slightly higher SPIRE luminosities than Sy 1's. However the effect is small and indicates that on average, the global FIR properties of AGN are independent of orientation.

- Using a partial correlation survival analysis to account for the luminosity-distance effect and upper limits, we find all of the *Herschel* luminosities are

correlated with each other suggesting the process (or processes) producing the emission from 70–500 μm is connected. Luminosities with the smallest wavelength difference (i.e. 160 and 250 μm) are much more correlated than pairs further apart (i.e. 70 and 500 μm), in agreement with different temperature components associated with different wavebands. While this could point to the AGN affecting the shorter wavebands more than the longer ones and increasing the scatter, it can also be explained by an increased contribution from older stellar populations to the emission at longer wavelengths.

- None of the SPIRE luminosities are well correlated with the 14–195 keV luminosity, a proxy for the bolometric AGN luminosity. The AGN, in general, is unlikely to be strongly affecting either the 250, 350, or 500 μm emission, however Sy 1s do show a very weak correlation at 250 and 350 μm. Removing CT sources does not improve the correlation for Sy 2's. It remains to be seen what the exact explanation is for the difference in correlations between Sy 1s and Sy 2s but possible explanations include a direct link between star-formation and AGN luminosity that is evident only at high luminosity or increased contamination by the AGN.

- We compared the SPIRE colors, F_{250}/F_{350} and F_{350}/F_{500}, with the colors of the HRS galaxies. The BAT AGN have statistically similar SPIRE color distributions as the high stellar mass ($\log M_* > 9.5$ $M_\odot$) HRS galaxies. This further emphasizes that on average, the FIR emission of AGN host galaxies is likely produced by cold dust in the ISM heated by stellar radiation just as in

normal star-forming galaxies without an AGN.

- We did find anomalous colors for 6 BAT AGN with $F_{250}/F_{350} < 1.5$ and $F_{350}/F_{500} < 1.5$. The FIR SEDs for these AGN are dominated by synchrotron emission from a radio jet rather than thermally heated dust.

- Another group of AGN with less anomalous colors but still removed from the main locus were analyzed by fitting the SEDs with a modified blackbody and calculating a 500 μm excess. We found the 500 μm excess is not related to radio loudness, but is well correlated with the 14–195 keV luminosity and $W1/W2$ (3.4/4.6 μm) color from *WISE*. We speculate this is possibly related to the millimeter excess emission recently seen in AGN caused by coronal emission above the accretion disk.

Chapter 3: *Herschel* far-infrared photometry of the Swift Burst Alert Telescope active galactic nuclei sample of the local universe–III. Global star-forming properties and the connection to nuclear activity

3.1 Introduction

Ever since the discoveries that the large scale properties of galaxies are related to the mass of the supermassive black holes (SMBH) they host (Ferrarese & Merritt, 2000; Gebhardt et al., 2000; Gültekin et al., 2009; Häring & Rix, 2004; Kormendy & Ho, 2013; Magorrian et al., 1998; Marconi & Hunt, 2003; McConnell & Ma, 2013), studies have intensely focused on finding the link between the evolution and growth of both the galaxy and SMBH. Theoretical arguments (eg. Silk & Rees, 1998) as well as cosmological simulations (e.g Bower et al., 2006; Croton et al., 2006) support the idea that SMBHs, while accreting material in their active galactic nuclei (AGN) phase, can affect both their own growth and the growth of their host galaxy through a mechanism that shuts down accretion and star formation (i.e. negative feedback).

Early evidence backing this theory seemed to be found in the observation that the SFR density and accretion rate density of the universe evolve similarly with

redshift (Aird et al., 2010; Boyle & Terlevich, 1998; Franceschini et al., 1999; Merloni & Heinz, 2013; Silverman et al., 2008, 2009). Further, AGN host galaxies were found to predominantly lie in the "green valley" of the color-magnitude diagram, in between the blue, star-forming galaxies and "red-and-dead" quiescent ones (Koss et al., 2011; Martin et al., 2007; Nandra et al., 2007; Schawinski et al., 2010; Silverman et al., 2008), suggesting that nuclear activity plays a role in transitioning its host galaxy from star-forming to quiescence.

While suggestive, optical colors can be strongly affected by extinction due to dust that might move a galaxy from "blue" to "green" (Cardamone et al., 2010). Other measures of the SFR including emission line, ultra-violet (UV), and mid-infrared (MIR) luminosities that are extensively used for normal, non-AGN galaxies suffer from varying degrees of contamination in the presence of an AGN, especially unabsorbed ($N_{\rm H} < 10^{22}$ cm^{-2}) Type I AGN.

This problem was solved with the advent of far-infrared (FIR; $\lambda = 40-500$ μm) telescopes, including the *Infrared Astronomical Satellite* (*IRAS*), the *Infrared Space Observatory* (*ISO*), the *Spitzer Space Telescope*, and most recently the *Herschel Space Observatory* (Pilbratt et al., 2010). FIR emission remains the ideal waveband to study star formation in AGN host galaxies for two reasons: (1) the rapidly declining spectral energy distribution (SED) associated with AGN heated dust in the FIR regime (Fritz et al., 2006; Mullaney et al., 2011; Netzer et al., 2007; Shi et al., 2014) ensures little AGN contamination at long wavelengths (2) thermal emission of large grains heated by the ionizing emission of recently formed massive stars (Devereux & Young, 1990; Lonsdale Persson & Helou, 1987) creates a strong FIR

"bump" and provides a reliable measure of the recent (10–100 Myr) SFR (Kennicutt, 1998).

Even though the FIR can provide a reliable SFR tracer, individual investigations into the connection between AGN activity and star-formation have produced conflicting and even contradictory results. Some studies (Barger et al., 2015; Page et al., 2012) have reported lowered SFRs for the highest luminosity AGN, indicative of a suppression of star formation due to AGN feedback. Others have found weak or flat relationships (Azadi et al., 2015; Diamond-Stanic & Rieke, 2012; Mullaney et al., 2012a; Rosario et al., 2012; Rovilos et al., 2012; Stanley et al., 2015) especially at more moderate AGN luminosities. Finally, some find an overall positive correlation (Chen et al., 2013; Dai et al., 2015; Lutz et al., 2008; Netzer, 2009; Rosario et al., 2012; Rovilos et al., 2012).

Many of the studies possibly however suffer from one or more problems that include small number statistics either due to a small area survey or low sensitivity, an inaccurate scaling from monochromatic luminosities to a total SFR, and source confusion due to the relatively large beam size of *Herschel*, especially at longer wavelengths.

In this Chapter, we aim to test these findings on the AGN-star formation relationship in the low redshift universe. We have performed a *Herschel* survey of a sample of AGN from the *Swift* Burst Alert Telescope 58 month catalogue which selected sources over the entire sky in the 14–195 keV energy range. At this high of energy, we are nearly unbiased with respect to any host galaxy properties including SFR as well as obscuration below a hydrogen column density ($N_{\rm H}$) of 10^{24} cm^{-2}.

The *Swift*/BAT AGN sample has been extensively studied since the release of the first 9-month catalogue (Tueller et al., 2008). Most relevant to our work, Koss et al. (2011) performed an optical survey of over 170 AGN using combined *Sloan Digital Sky Survey* (SDSS) and *Kitt Peak National Observatory* imaging to study their host galaxy properties. They found that the *Swift*/BAT AGN are dominated by massive ($M_{\rm star}> 10^{9.5}$ $M_{\odot}$) spirals with bluer colors than a mass-matched sample of non-AGN galaxies. Koss et al. (2011) further found that AGN showed enhanced FIR luminosities, using 90 μm photometry from *Akari* compared to the mass-matched sample.

With 5 band imaging with *Herschel* along with archival photometry from the *Wide-field Infrared Survey Explorer* (*WISE*), we have constructed MIR-FIR SEDs for over 300 AGN, allowing us to accurately measure the SFR in a robust manner. Because of the low-redshift nature of our sources, every AGN is easily able to be identified and there is no concern over source confusion. These SEDs not only allow us to calculate SFRs but also to test varying SED decomposition methods and models as well as measure other properties of the host galaxies such as the dust mass and dust temperature to compare with non-AGN samples. With a high detection rate (95, 83, 86, 72, and 46 per cent at 70, 160, 250, 350, and 500 μm), our measured properties from the SEDs are well constrained, removing much of the uncertainty due to censoring.

The Chapter is organized as follows: in Section 2 we briefly describe the *Herschel*-BAT AGN sample; in Section 3 we detail our *WISE* and *Herschel* datasets. Section 4 introduces our non-AGN comparison sample. Section 5 qualitatively ex-

amines the SEDs and determines calculates the average SED as a function of AGN luminosity, while Section 6 outlines our fitting methods. Sections 7 and 8 then discusses our results, compares with other studies, and concludes the Chapter. Throughout, we use a cosmology with $H_0 = 70$ km s^{-1} Mpc^{-1}, $\Omega_{\rm M} = 0.3$, and $\Omega_\Lambda = 0.7$ to calculate luminosity distances from redshifts.

3.2 *Herschel*-BAT Sample

Because *Swift*/BAT continuously monitors the entire sky in the energy range 14–195 keV for gamma ray bursts, it simultaneously provides an all-sky survey at ultra high X-ray energies. This allows for the creation of complete catalogues with increasing sensitivity the longer *Swift*/BAT remains in operation. Given the extreme environments necessary to produce strong 14–195 keV emission, the majority of sources in the *Swift*/BAT catalogues are AGN at high galactic latitude.

We chose 313 AGN from the parent sample of ~ 720 AGN detected in the 58 month catalogue[1] after imposing a redshift cutoff of $z < 0.05$ and excluding Blazars and BL Lac objects to form our *Herschel*-BAT AGN sample. With a mean redshift of $\langle z \rangle = 0.025$, our AGN sample provides a comprehensive view of the properties of AGN host galaxies in the local universe. Our selection at ultra high X-ray energies further removes biases and selection effects due to host galaxy contamination and obscuration (Mushotzky, 2004) that can influence samples at other wavelengths.

The demographics of our sample are nearly evenly split between Type I (43

[1] https://swift.gsfc.nasa.gov/results/bs58mon

per cent) and Type II (53 per cent) with the remaining 4 per cent (5 objects) either a Low-Ionization Nuclear Emission-line Region (LINER) or unclassified. The *Herschel*-BAT sample spans nearly four orders of magnitude in 14–195 keV luminosity ($10^{41} < L_{14-195\,\mathrm{keV}} < 10^{45}$ ergs s^{-1}) allowing for a robust determination of the connection between AGN strength and SFR. For a complete listing of our sample with names, luminosity distances, redshifts, and AGN type, we point the reader to Meléndez et al. (2014) or Shimizu et al. (2016).

3.3 Data

3.3.1 *Herschel* Photometry

293 of the *Herschel*-BAT AGN were observed with *Herschel* as part of a Cycle 1 open time program (OT1_rmushotz_1, PI: Richard Mushotzky). The remaining 20 sources were part of the other programs with public archival data. *Herschel* observed all 313 AGN using both the Photoconductor Array Camera and Spectrometer (PACS; Poglitsch et al., 2010) and Spectral and Photometric Imaging Receiver (SPIRE; Griffin et al., 2010) producing images in five wavebands: 70, 160, 250, 350, and 500 μm.

Detailed descriptions of the data reduction process and photometric flux extraction can be found in Meléndez et al. (2014) for PACS and Shimizu et al. (2016) for SPIRE. The following is a short description of the flux extraction procedure. We measured fluxes at each waveband directly from the images using aperture photometry with a concentric annulus to define the local background. We applied

aperture corrections for sources where we used a point source aperture as defined in the respective PACS and SPIRE data reduction guides. Fluxes for sources that were unresolved at all three wavebands in SPIRE were determined using the SPIRE Timeline Fitter within the *Herschel* Interactive Processing Environment. All fluxes have a signal-to-noise ratio of at least 5, otherwise we provided a 5σ upper limit.

In Shimizu et al. (2016), using the SPIRE flux ratios, we found 6 radio-loud objects which have a large contribution to their FIR emission from synchrotron radiation due to their jets. These sources are Pictor A, 3C 111.0, 3C 120, 2MASX J23272195+1524375, PKS2331-240, and [HB89] 0241+622. For this work we remove these sources from all analysis, however we still provide figures of their SED fits in Appendix D and list their best-fit parameters in Table D.1.

Also in Shimizu et al. (2016), we flagged objects with a "D" that likely had strong contamination due to a nearby source. For these sources, we treat the SPIRE fluxes as upper limits. For a small number of very nearby galaxies with large angular size (NGC 2655, NGC 3718, NGC 4939, NGC 4941, NGC 5033, and NGC 6300), the PACS FOV of our observations did not encompass the entirety of the galaxy leading to possible underestimations of the 70 and 160 μm flux densities. Therefore, for this work, we chose to conservatively increase the uncertainty in the flux to 50 per cent.

3.3.2 *WISE* Photometry

To extend the SEDs into the mid-infrared (MIR), we supplemented our *Herschel* data with archival *Wide-field Infrared Survey Explorer* (WISE; Wright et al., 2010) photometry. WISE performed a broadband all-sky survey at 3.4 (W1), 4.6 (W2), 12 (W3), and 22 (W4) μm with angular resolution comparable to *Herschel*/PACS at 70 μm for W1, W2, and W3 and 160 μm for W4. We queried the AllWISE catalogue through the NASA/IPAC Infrared Science Archive[2] to search for coincident sources within 6". Counterparts were found for all but one AGN (Mrk 3) at every waveband. The catalogue only contained W1 and W2 fluxes for Mrk 3 due to differences in the depth of coverage for W1/W2 and W3/W4, therefore Mrk 3 is not included as part of the sample in this work.

The AllWISE catalogue provides magnitudes determined using multiple extraction methods. We consider only the profile-fitting magnitudes (wN*mpro* where N is 1, 2, 3, or 4) and the elliptical aperture magnitudes (wN*gmag*). Profile-fitting magnitudes were determined by fitting the position dependent point spread function using deblending procedures when necessary to decompose overlapping sources. The wN*mpro* magnitudes therefore are only relevant for unresolved sources.

If a WISE source is associated with a source in the *Two Micron All Sky Survey* (2MASS) Extended Source Catalog (XSC), then wN*gmag* magnitudes were also measured using an elliptical aperture with the same shape from the XSC and sizes scaled given the larger WISE beam. Thus, wN*gmag* magnitudes are more appropri-

[2] http://irsa.ipac.caltech.edu/frontpage/

ate for extended sources. For details of all of the WISE magnitude measurements we point the reader to the All-Sky Release Explanatory Supplement[3].

Given the low-redshift nature of our sample, using only the wN*mpro* magnitudes would severely underestimate the flux for large extended sources. To decide which magnitude to include in the SED for each source, we used the reduced χ^2 value (wN*rchi2*) from the profile-fitting. If wN*rchi2*< 3 then we chose the wN*mpro* magnitude, otherwise wN*gmag* was chosen.

3.4 Comparison Sample

To test whether the AGN has any effect on the star-forming properties of their host galaxies, we need samples of galaxies which contain little evidence for nuclear activity. These samples also need to occupy the same redshift range to mitigate against evolutionary effects and have been observed with nearly the same instruments so the properties can be compared on an equal level. Three low-redshift samples exist that satisfy these constraints. They are the *Herschel Reference Survey* (HRS; Boselli et al., 2010b), *Key Insights on Nearby Galaxies: a Far-Infrared Survey with Herschel* (KINGFISH; Kennicutt et al., 2011), and the *Herschel Stripe 82 Survey* (HerS; Viero et al., 2014). While the KINGFISH sample has been observed with all of the same wavelengths as the *Herschel*-BAT AGN, the sample was selected in a heterogeneous manner and only contains 61 galaxies that does not allow for stellar mass matching. The HerS sample is numerous and covers a large range in

[3] http://wise2.ipac.caltech.edu/docs/release/allsky/expsup/

mass, however the sample was only observed with SPIRE. Further, the catalog was built based on SPIRE detections which imposes a selection effect associated with the SFR. We therefore chose the HRS as our comparison sample to the *Herschel*-BAT AGN.

The HRS was a guaranteed time key *Herschel* program dedicated to studying the dust content of "normal" galaxies. The 323 galaxy sample is volume limited ($15 < D < 25$ Mpc) to avoid distance effects and K-band flux limited to avoid selection effects due to dust and provide a representative population of local galaxies. The size of the HRS as well as the local nature make it an ideal sample to compare to the *Herschel*-BAT galaxies.

The HRS galaxies also were imaged using both PACS and SPIRE, although the 100 μm filter was used instead of the 70 μm filter. Cortese et al. (2014) and Ciesla et al. (2012) measured the PACS and SPIRE flux densities respectively using similar techniques as the *Herschel*-BAT galaxies. WISE 12 and 22 μm photometry for HRS were provided in Ciesla et al. (2014a). The available data for the HRS SEDs are nearly identical as our sample.

The only issue in comparing the HRS galaxies to the *Herschel*-BAT AGN concerns the stellar mass ($M_{\rm star}$) distribution. Because the near-infrared is most strongly effected by the mass of the older stellar population, the HRS K-band selection produces a $M_{\rm star}$ distribution that is representative of the naturally occurring $M_{\rm star}$ distribution. However, many recent studies have shown that detected AGN prefer high $M_{\rm star}$ galaxies (e.g. Schawinski et al., 2010; Xue et al., 2010), a feature that is also found in the BAT AGN (Koss et al., 2011). Figure 3.1 displays the $M_{\rm star}$

distributions for the *Herschel*-BAT and HRS sample (dashed line). The *Herschel*-BAT galaxies have an average $\log M_{\rm star}$ of 10.6 $M_{\odot}$, whereas the average $\log M_{\rm star}$ for HRS is 9.8 $M_{\odot}$, nearly a ten-fold difference.

To account for possible stellar mass effects, we decided to produce a mass-matched HRS sample in the following way. Stellar masses for the *Herschel*-BAT AGN were calculated based on the AGN-subtracted *ugriz* photometry from (Koss et al., 2011) and the $g-i$ calibrated stellar mass relation from Zibetti et al. (2009). This is the same method that stellar masses were calculated for the HRS sample, given in Cortese et al. (2012b). For each of the 122 *Herschel*-BAT AGN which have stellar mass estimates, we chose all HRS galaxies which have a stellar mass within 0.15 dex of the *Herschel*-BAT mass. We then randomly selected an HRS galaxy from this pool. Because high-mass galaxies are relatively rare in the HRS sample, some matches are duplicated. We find though 97/122 of the matched HRS galaxies are unique, representing 80% of the sample so the duplicating effects should not be large. The red solid line in Figure 3.1 now shows the mass-matched HRS sample which overlaps with the *Herschel*-BAT mass distribution. Throughout the rest of this Chapter, we refer to the HRS mass-matched sample as simply the HRS sample unless otherwise noted.

3.5 The IR SEDs of $z = 0$ AGN

Before fitting the SEDs and comparing to a non-AGN sample, we begin with a qualitative look at the SEDs of the 313 AGN. Figure E.1 shows the 12–500 μm SED

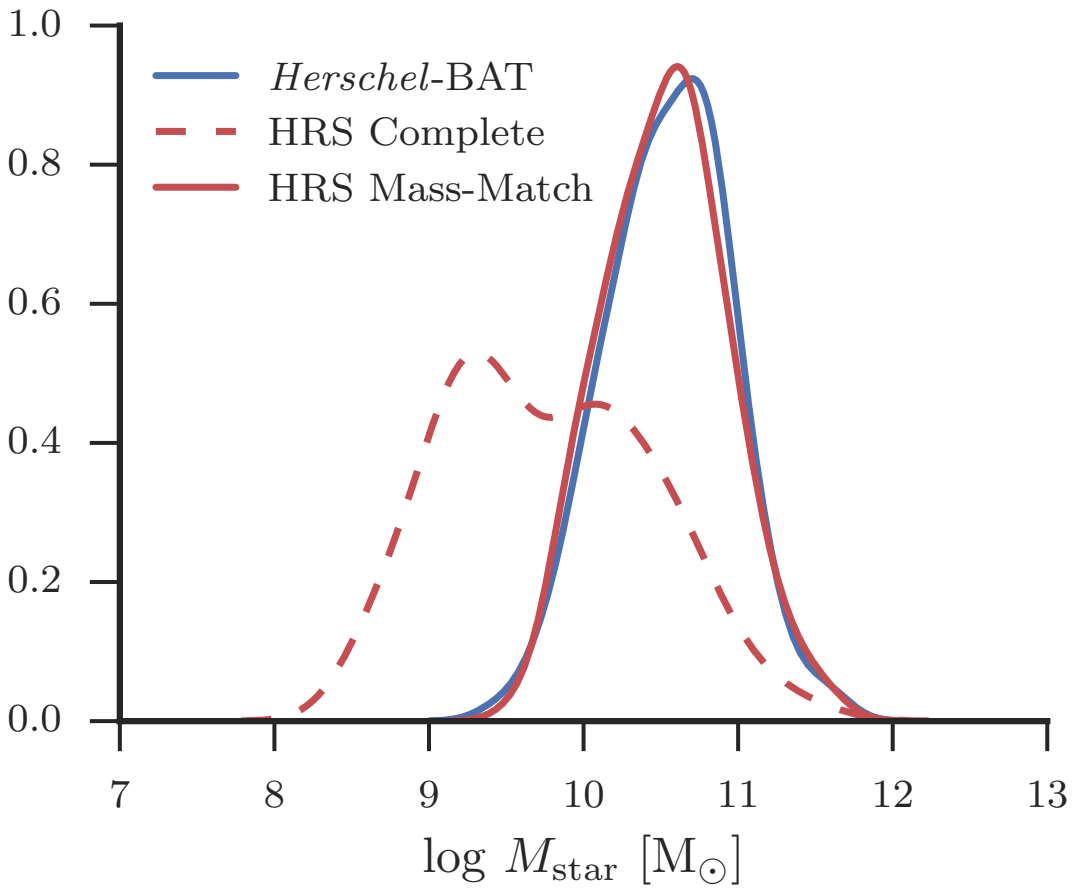

Figure 3.1: Kernel Density Estimates (KDE) of the $M_{\rm star}$ distribution for the BAT AGN (blue), full HRS sample (red), and mass-matched HRS sample(red dashed). The *Herschel*-BAT AGN probe a higher $M_{\rm star}$ galaxy population than the full samples, however with mass-matching we can reproduce the stellar-mass distribution of the *Herschel*-BAT AGN with non-AGN.

for every source in the *Herschel*-BAT sample. Immediately noticeable is the varied SED shapes. Some of the SEDs (e.g. 2MASX J07595347+2323241, Cen A, ESO 005-G004, NGC 4051, NGC 4138, NGC 6814) feature a very prominent FIR bump that is recognizable in nearly all star-forming galaxies and is indicative of thermally heated dust from recently formed massive stars as well as cirrus emission heated by an older population. The general shape is usually well fit by a blackbody modified by a frequency dependent optical depth (e.g. Bianchi, 2013; Calzetti et al., 2000; Cortese et al., 2014; Smith et al., 2012; Symeonidis et al., 2013).

These star formation dominated objects represent one extreme end of the shapes we observe. The other extreme are SEDs whose shapes seem to peak shortward of 70 μm and display rapidly falling emission with increasing wavelength. Examples include 2MASX J06561197-4919499, 2MASX J210990996-0940147, ESO 103-035, IC 4329A, MCG -05-23-016, and Mrk 335. Emission in the MIR dominates these SEDs and is likely associated with hotter dust heated by the AGN. MIR colors are commonly used to select AGN samples because they display strong red (i.e. increasing SED with wavelength) colors compared to non-AGN galaxies (Donley et al., 2012; Lacy et al., 2004; Stern et al., 2012) due to the dust in the obscuring torus heated by the optical and UV emission from the accretion disk. Monochromatic MIR luminosities, especially for sources dominated by an unresolved central component, show near linear correlations with the X-ray luminosity (e.g Asmus et al., 2012; Gandhi et al., 2009; Lutz et al., 2004) providing more evidence that much of the MIR in AGN host galaxies is associated with the AGN.

The remaining *Herschel*-BAT AGN display SEDs somewhere in between MIR-

dominated and FIR-dominated as a result of competing contributions between the AGN and star formation. The varied shapes of the SED emphasizes the need for SED decomposition, especially at shorter wavelengths, to accurately determine the IR luminosity associated with either star formation or the AGN.

If star formation suppression occurs at high AGN luminosity then we expect the IR SEDs for the most X-ray luminous sources to resemble the MIR-dominated SEDs as Barger et al. (2015) observed. To test this, we binned the SEDs by logarithmic 14–195 keV luminosity. Five bins ($\log L_{14-195\,\mathrm{keV}} > 42.5$, $\log L_{14-195\,\mathrm{keV}} = 42.5 - 43.0$, $43.0 - 43.5$, $43.5 - 44.0$, and $\log L_{14-195\,\mathrm{keV}} > 44.0$) were chosen with 0.5 dex widths to ensure enough sources occupied each one. The number of sources in each bin is 22, 39, 94, 116, and 35.

We then calculated the median luminosity density within each X-ray luminosity bin. We used the ASURV (Feigelson & Nelson, 1985) package which applies the principles of survival analysis to astronomical data. Information contained in the upper limits can be then included in the measurement of statistical properties of samples without biasing results towards brighter sources that are more likely to be detected. Specifically, ASURV calculates the non-parametric Kaplan-Meier product-limit (KMPL) estimator for a sample distribution. The KMPL estimator is an estimate of the survival function which is simply 1−CDF (cumulative distribution function). Using the KMPL, we calculate for each waveband the median luminosity density (50th percentile) and estimate the uncertainty using the 16th and 84th percentiles.

Figure 3.2 shows the median IR SED for sources in each X-ray luminosity bin.

From visual inspection, the median SED as a function of X-ray luminosity seems to be driven more by an increasing MIR hot dust component. There does not seem to be any indication that star formation is being suppressed at the highest luminosities. The wavebands that show the largest change with X-ray luminosity are the MIR bands. At wavelengths longer than 160 μm, the SED shows no significant change, consistent with the correlations we measured in Meléndez et al. (2014) and Shimizu et al. (2016). If we make the assumption that the longer wavelengths are mainly associated with star-formation, then the lack of change indicates star-formation is unrelated to X-ray luminosity within the range probed by our sample. We can also compare the AGN SEDs with the median SED for the HRS sample plotted as red squares and a dashed line. While the median HRS SED occurs at a lower normalization, suggesting lower levels of star formation, the shape is nearly identical to the SED for our lowest X-ray luminosity bin showing that at the lowest AGN luminosities, the IR SED is completely dominated by star formation. However, to definitively test this we need to decompose the SED into star-forming and AGN components to accurately calculate SFRs.

3.6 SED Fitting

Many models and templates exist in the literature to fit the broadband SEDs of galaxies. We chose a model that allowed us to both decompose the SED into star-forming and AGN components as well as provide estimates on the dust temperature and dust mass.

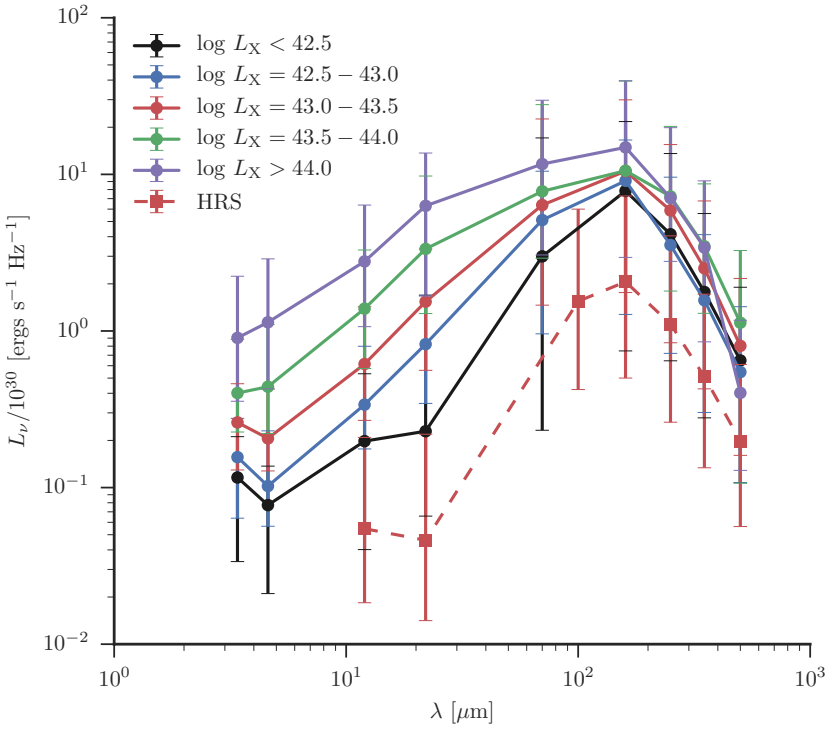

Figure 3.2: Median IR SEDs in units of 10^{30} ergs s^{-1} Hz^{-1} for the *Herschel*-BAT AGN binned by $L_{14-195\,\mathrm{keV}}$. Each point in the SEDs is the median L_ν for the whole sample including upper limits calculated using the Kaplan-Meier product-limit estimator. The error bars represent the 68% confidence interval determined from the 16th and 84th percentiles. For reference we also show the median IR SED for the HRS sample as red squares and a dashed line. Photometry was only available at 12 and 22 μm.

3.6.1 Casey 2012 Model

One of the most widely used models for fitting the FIR SED of galaxies is a single modified blackbody (MBB). The simple model consists of a normal, single temperature blackbody that represents isotropic dust emission combined with a frequency dependent opacity given that dust is not a perfect blackbody.In the optically thin limit, the opacity can be approximated as a powerlaw, $\tau_\nu = (\nu/\nu_0)^\beta$. The form of the single modified blackbody for the flux density at each frequency is then

$$S(\nu) \propto \nu^\beta B_\nu(T_\mathrm{d}) \tag{3.1}$$

where β is the spectral emissivity index and $B_\nu(T_\mathrm{d})$ is the standard Planck blackbody function for an object with temperature T_d. This simple model has been shown to fit well the prominent FIR bumps for large samples of star-forming galaxies and provides estimates of the dust temperature, dust mass, and SFR (e.g. Bianchi, 2013; Calzetti et al., 2000; Cortese et al., 2014).

To calculate the dust mass, we must assume a particular dust absorption coefficient, κ_0 at a particular frequency, ν_0. For this work, we assume $\kappa_0 = 0.192\,\mathrm{m^2\,kg^{-1}}$ and $\nu_0 = 857\,\mathrm{GHz}$ (i.e. 350 μm) from Draine (2003). However, as Bianchi (2013) shows, by assuming a specific κ_0, we must also fix the spectral emissivity index to the value used to measure κ_0. In this work, we fix $\beta = 2.0$ to match the spectral emissivity index used by Draine (2003).[4] The final full form of the single MBB

[4]We have tested the effect of allowing β to be a free parameter by re-fitting sources which were detected in all wavebands. We find a median $\beta = 1.8 \pm 0.3$, consistent with our choice to fix

model is then

$$S_{\rm MBB}(\nu) = \frac{M_{\rm d}\kappa_0}{D_{\rm L}^2}\left(\frac{\nu}{\nu_0}\right)^{\beta}\frac{2h\nu^3}{c^2}\frac{1}{e^{h\nu/kT_{\rm d}}-1} \tag{3.2}$$

where $M_{\rm d}$ is the dust mass, $D_{\rm L}$ is the luminosity distance, c is the speed of light, h is the Planck constant, and k is the Boltzmann constant. The two free parameters then are $M_{\rm d}$ and $T_{\rm d}$, the dust mass and dust temperature respectively.

The simple assumption that dust emission in the IR can be modeled with a single temperature greybody works well for "normal" star-forming galaxies. However for galaxies with large amounts of hot dust either due to a compact starburst or central AGN, this assumption can quickly break down. To account for this hot dust we also fit our sample using the model described in Casey (2012, hereafter C12) which is the combination of a single MBB and an exponentially cutoff powerlaw. The C12 model takes the form

$$S_{\rm C12}(\nu) = N_{\rm pl}\left(\frac{\nu}{\nu_{\rm c}}\right)^{-\alpha}e^{-\nu_{\rm c}/\nu} + S_{\rm MBB}(\nu) \tag{3.3}$$

where $\nu_{\rm c}$ represents the turnover frequency and $N_{\rm PL}$ is a normalization constant. C12 illustrated using the *Great Origins All-Sky LIRG Survey* (GOALS) sample that this model provides better estimates of the cold dust temperature, dust mass, and IR luminosity compared to both a single temperature modified blackbody and template libraries.

The C12 model introduces three more free parameters ($N_{\rm PL}$, α, and $\nu_{\rm c}$), how-

$\beta = 2.0$. Further we find that all of the derived parameters, especially the integrated luminosities, are consistent within measurement uncertainty with their values when β is fixed at 2.0.

ever, within the implementation used by C12, $N_{\rm PL}$ and $\nu_{\rm c}$ are tied to the normalization of the modified blackbody component and dust temperature to produce a smoothly varying SED and reduce the number of free parameters from five to three.

But, after early tests using this initial setup, we found that fixing $N_{\rm PL}$ and $\nu_{\rm c}$ as a function of the other parameters produced unreliable fits. This is because AGN SEDs from the MIR to FIR are not as smooth as those seen in (U)LIRGS, likely due to the disconnect between star-formation and AGN heating. Within starbursting galaxies both the hot and cold dust are related through the same heating process, i.e. star formation, while much of the MIR emission in AGN host galaxies originates from dust around the AGN with no strong connection to global star formation in the galaxy. Therefore, we chose to leave both $N_{\rm PL}$ and $\nu_{\rm c}$ as free parameters resulting in a total of five for the entire model.

3.6.2 SED Parameter Estimation

To find the best fitting parameters in our SED modeling, instead of standard least squares analysis, we used a Bayesian framework along with Monte Carlo Markov Chains to probe the posterior probability distribution functions for each parameter. The Bayesian framework allows for robust estimates of the uncertainty and for explicit statements about prior knowledge of the parameters. It also makes it relatively easy to include information contained in the undetected photometry of the SED.

3.6.3 Likelihood Representation

The likelihood defines the probability of observing a set of data given a specific model. In SED fitting, this translates to the combined probability of measuring all the photometric data points in the observed SED given a model for the SED (whether based on templates or analytic models). The total likelihood can then be expressed as the product of the probabilities of observing each single photometric point:

$$\mathcal{L}(F|M) = \prod_i P(F_i|M) \tag{3.4}$$

where F is the set of photometric fluxes, F_i and M is the model. For our analysis, we assume the probability of our observations follows a Gaussian distribution with mean equal to M and standard deviations equal to the measurement errors, σ_i.

$$P(F_i|M) = \frac{1}{\sqrt{2\pi\sigma_i^2}}\exp\left(\frac{-(F_i - M)^2}{2\sigma_i^2}\right) \tag{3.5}$$

Equation 3.5 only defines the probability for detected fluxes. To use the information contained in the undetected photometry, U_i, we define a different probability under the assumption that all of the upper limits are 5σ.

$$\begin{aligned} P(U_i|M) &= \int_{-\infty}^{U_i} \frac{1}{\sqrt{2\pi\sigma_i^2}}\exp\left(\frac{-(x - M)^2}{2\sigma_i^2}\right) dx \\ &= \frac{1}{2}\left(1 + \mathrm{erf}\left[\frac{U_i - M}{\sigma_i\sqrt{2}}\right]\right) \end{aligned} \tag{3.6}$$

where $\sigma_i = \frac{U_i}{5}$ and erf is the standard error function. For numerical accuracy and simplicity, it is customary to minimize the negative log-likelihood. Supposing we

have N total SED points with D detections and $D - N$ non-detections then the total negative log-likelihood combining Equations 3.4, 3.5, and 3.6 is:

$$-\log \mathcal{L} = \frac{1}{2} \sum_{i=0}^{D} \left[\log(2\pi\sigma_i^2) - \left(\frac{F_i - M}{\sigma_i} \right)^2 \right] + \sum_{j=0}^{D-N} \log \left[1 + \mathrm{erf} \left(\frac{U_j - M}{\sigma_j \sqrt{2}} \right) \right] \tag{3.7}$$

It is important to recognize here how M is calculated, no matter whether it represents a template or analytic model. Each data point in an SED is the observer-frame flux density measured over a defined wavelength range. Therefore, to determine the model flux densities we first redshifted the full rest-frame model SED into the observer frame using the known redshifts of all of our sources. This observer-frame SED was then convolved with each instrument filter transmission curve to produce model flux densities that can be accurately compared to the observed ones.

3.6.4 Bayesian MCMC Analysis

Within the Bayesian framework, the important probability is the probability of the model given the data at hand, i.e. the most probable SED model given the observed fluxes. This probability can be determined using Bayes theorem:

$$P(M|F) = \frac{P(F|M)P(M)}{P(F)} \tag{3.8}$$

and is known as the posterior probability distribution. $P(F|M)$ is proportional to the likelihood (Equation 3.4), $P(M)$ codifies our prior knowledge about the model,

and $P(F)$ is the model evidence and can be disregarded as a simple normalization term.

The reader may notice that assuming a flat prior, $P(M) \propto 1$, reduces Equation 3.8 to $P(M|F) \propto \mathcal{L}$ verifying our use of maximum likelihood in determining the best template models.

For the C12 model, we used flat priors for the dust temperature and dust mass. We placed conservative limits on both the dust temperature and $\log M_{dust}$ to be between 1 and 100 K and 1 and 10 $M_{\odot}$respectively. Within the powerlaw component for the C12 model, we also used flat priors for the powerlaw slope between -5 and 5 and the log of the normalization between -10 and 10. Based on previous work attempting to measure the intrinsic AGN SED and modeling the dusty torus, we expect the SED to turnover anywhere in the range between 20-70 μm. Therefore we imposed a Gaussian prior centered at 45 μm with a standard deviation of 20 μm. We found that imposing this prior resulted in better and more realistic fits to the SEDs. On a few individual SEDs, this choice had a large effect in the resulting parameters compared to simply using a flat prior for the turnover wavelength. In some cases, using a flat prior resulted in the PL component reaching into the submillimeter regime and made the MBB component negligible. For these sources by imposing a Gaussian prior, we have pushed the PL component to largely reside in the MIR. For the whole sample, however, we found that the distribution of best-fit parameters did not change dramatically between using a flat prior and Gaussian prior and the results of this Chapter are largely unchanged. The major difference is the removal of very cold dust temperatures ($T_{\rm dust} < 15$ K) and very large dust masses which

are unphysical. The need for a Gaussian prior for better SED fitting would be removed with more photometry between 22 and 70 μm where our fits show the largest uncertainty.

We used the PYTHON package EMCEE (Foreman-Mackey et al., 2013) to perform MCMC and sample the posterior probability distribution function (Equation 3.8). EMCEE runs an implementation of the Affine-Invariant MCMC sampler from Goodman & Weare 2010. Instead of one single MCMC chain, it samples the posterior PDF with multiple "walkers", each with their own chain. For our analysis, we used 50 walkers that each produced a 1000 step chain. To allow for each chain to stabilize and move away from the initial guesses for the parameters, we imposed a 200 step "burn-in". In total, this resulted in 40000 steps to define the full posterior PDF.

To determine the best fit parameters, we first marginalized the posterior PDF over all other parameters and then calculated the median. All quoted uncertainties represent the 68% confidence interval determined from the 16th and 84th percentile of the marginalized posterior PDF.

For the 35 sources with less than four detected points, the parameters of the MBB component are unconstrained. These sources are undetected for several reasons. Either they are a.) intrinsically faint, b.) at relatively large distances, or c.) located in a region with high foreground cirrus emission. This last reason causes problems because it produces high upper limits on the fluxes for the SPIRE wavebands which give the appearance that a substantial amount of FIR emission could exist. Therefore, we tested our modeling with three fixed dust temperatures:

15, 23, and 40K. 15 and 40 K are the extreme low and high temperatures we find for the whole sample, while 23 K is the median dust temperature. We fit only the 70 – 500 μm points/upper limits and let the dust mass increase until the model SED exceeded one of the points/upper limits.

We find that using a dust temperature of either 23 or 40 K produces consistent MBB luminosities. Using a 15 K dust temperature produces MBB luminosities *lower* than the 23 K and 40 K ones. Therefore its reasonable to assume conservative upper limits on the MBB luminosity can be constrained with a higher dust temperature. The parameter most affected by the choice of temperature is the dust mass. Lower temperatures produce higher upper limits on the dust mass. In fact moving from a 15 K temperature to a 40 K temperature changes the dust mass by two orders of magnitude. Given these tests we choose to run our modeling by fixing the dust temperature at 23 K, the median temperature of our whole sample. We acknowledge that for some of the undetected sources, we might be underestimating the upper limit on the dust mass. Since this subsample is only $\sim$ 10 per cent of the whole, we do not anticipate any large effect on the overall results.

We fit all 313 of the *Herschel*-BAT AGN using the C12 model and report the best fitting parameters in Table D.1. Best-fit model SEDs are shown along with the observed SEDs in Figure E.1. We also fit HRS galaxies using the exact same model so we can accurately compare the star-forming properties between non-AGN and AGN host galaxies. For the 23 HRS sources with less than four detected points we fix the dust temperature at 21 K, the median dust temperature for the whole HRS sample. This represents 19% of the sample.

3.6.5 Luminosities and AGN Fractions

In addition to the parameters associated with the model, we also calculated several luminosities and an AGN fraction. For this work, we define three luminosities: 1) $L_{\rm IR}$ will represent the total infrared luminosity determined by integrating the full SED from 8–1000 μm. 2) $L_{\rm SF}$ will represent the 8–1000 μm luminosity due to star formation in the host galaxy. 3) $L_{\rm AGN,IR}$ will represent the 8–1000 μm luminosity due to AGN-heated dust.

$L_{\rm IR}$ for each source was calculated by integrating the best fit model SED from 8–1000 μm. To determine $L_{\rm SF}$ and $L_{\rm AGN,IR}$ we first start with $L_{\rm PL}$ and $L_{\rm MBB}$, the 8–1000 μm luminosities of the separate PL and MBB components from our SED decomposition. If we made the assumption that the PL component is completely dominated by the AGN in all sources then we could simply represent $L_{\rm PL}$ as the $L_{\rm AGN,IR}$ and $L_{\rm MBB}$ as $L_{\rm SF}$. However, the PL component for some AGN host galaxies can have a strong contribution from dust heated by stars. Therefore a correction factor must be applied to convert $L_{\rm PL}$ and $L_{\rm MBB}$ into $L_{\rm AGN,IR}$ and $L_{\rm SF}$.

We make this correction using the results of the C12 modeling for the HRS sample. Since all of the galaxies in this sample has either no or low-luminosity AGN, the MIR emission is primarily the result of stochastically heated grains near star-forming regions. In Figure 3.3, we show the distribution of $L_{\rm MBB}/L_{\rm PL}$, the ratio of the MBB component luminosity to the MIR powerlaw component. The ratio for the HRS sample is narrowly distributed around a single value, indicating that for our lower mass non-AGN comparison sample the energy contained in the PL and

MBB components are tightly connected. We find a median $\log(L_{\rm MBB}/L_{\rm PL}) = 0.48 \pm 0.13$, which transforms to $L_{\rm PL,SF} \approx \frac{1}{3} L_{\rm MBB}$ where we now indicate the contribution to the PL component from star formation as $L_{\rm PL,SF}$. We can calculate the AGN contribution for the *Herschel*-BAT AGN then by assuming the star-forming emission follows the same ratio.

$$L_{\rm AGN,\,IR} = L_{\rm PL} - L_{\rm PL,SF} = L_{\rm PL} - \frac{1}{3} L_{\rm MBB} \tag{3.9}$$

$$f_{\rm AGN} = L_{\rm AGN,\,IR}/L_{\rm IR} \tag{3.10}$$

$$L_{\rm SF} = L_{\rm MBB} + L_{\rm PL,SF} = \frac{4}{3} L_{\rm MBB} \tag{3.11}$$

The uncertainty on the correction factor leads to an uncertainty on $f_{\rm AGN}$ using this method which we estimate by measuring $f_{\rm AGN}$ for the HRS sample. Figure 3.4 shows the distribution of "$f_{\rm AGN}$" for HRS. As expected the distribution is centered around 0. We estimate the spread of the distribution by calculating the standard deviation, finding an uncertainty of 0.1. Therefore we add in quadrature an uncertainty of 0.1 to all of our $f_{\rm AGN}$ estimates. Further, any $f_{\rm AGN}$ below 0.1 are converted to upper limits with a value of 0.1.

3.7 Comparison between different models

In this section we compare the results for the total luminosity, IR AGN luminosity, and star forming luminosity between the C12 model and two other models to decompose the SED. We exclude from this analysis objects which were only detected by *Herschel* in ≤ 1 waveband given the strong uncertainties associated with their

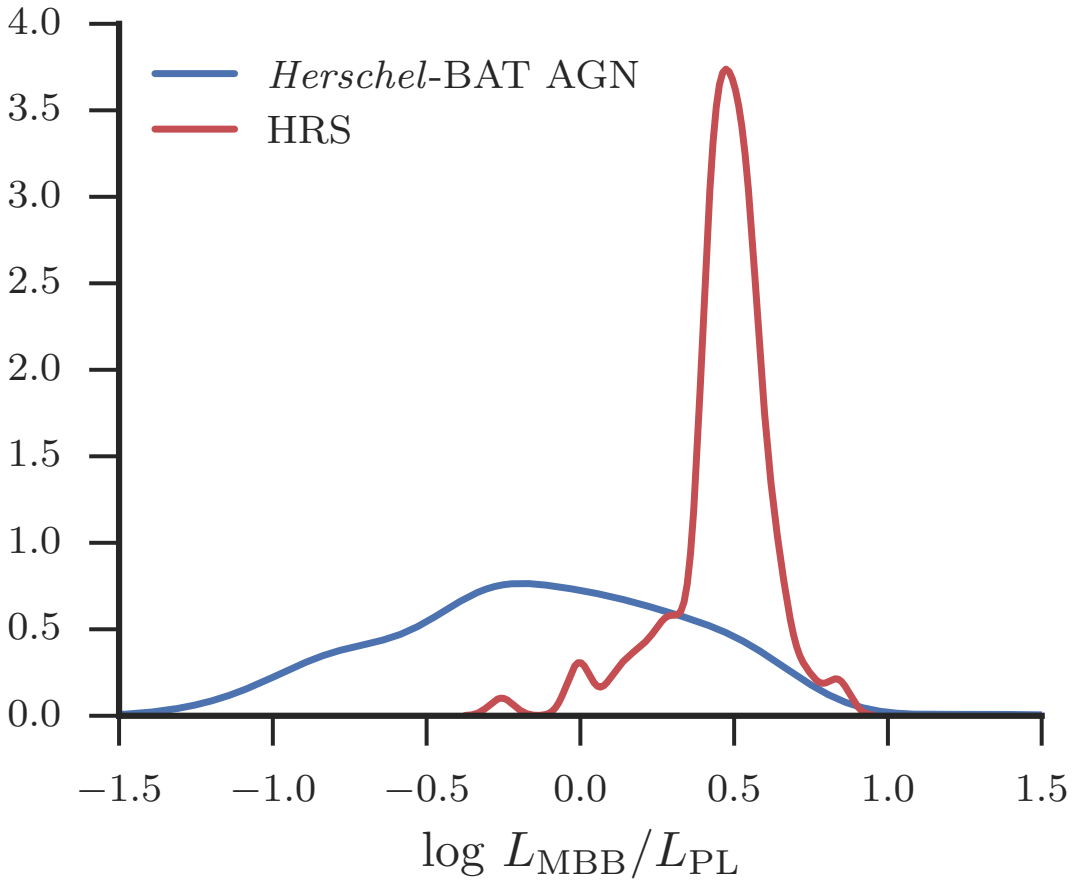

Figure 3.3: Histograms and Kernel Density Estimates (KDE) of the $L_{\mathrm{MBB}}/L_{\mathrm{PL}}$ distribution for the *Herschel*-BAT AGN (blue), and HRS (red) samples. The HRS galaxies have a narrowly distributed ratio whereas the BAT AGN span a wide range due to the AGN contribution.

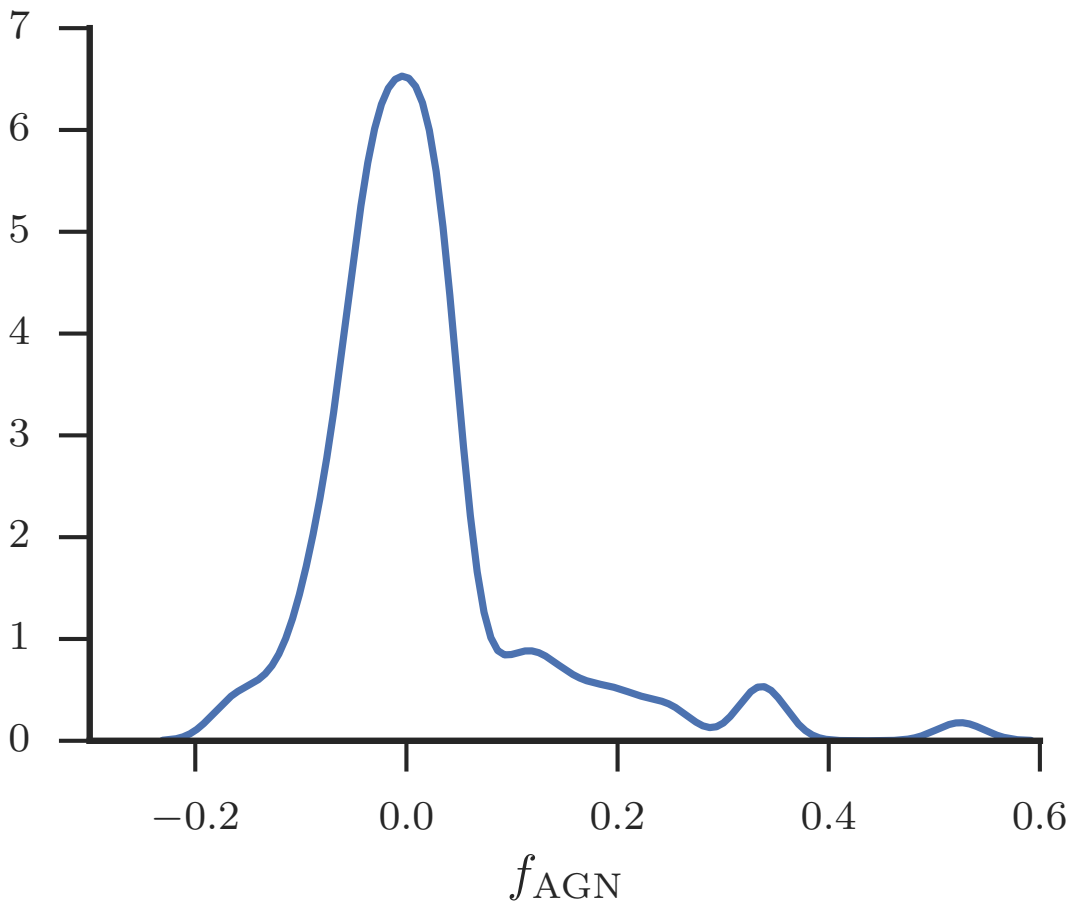

Figure 3.4: f_{AGN} distribution for mass-matched HRS sample. The standard deviation of this distribution quantifies the uncertainty on f_{AGN} associated with the correction factor used to calculate f_{AGN}.

properties. We also exclude as before the 6 radio-loud objects and Mrk 3 (for lack of WISE data).

3.7.1 DecompIR model

Besides analytic models, another popular method is the use of template SEDs. Templates are constructed based on well-sampled SEDs of large samples of galaxies and usually parameterized according to a known property such as infrared luminosity.

For galaxies known to host an AGN, recent studies have often used the DecompIR (Mullaney et al., 2011) templates. DecompIR consists of five host galaxy templates that span the IR color and luminosity range of the original Brandl et al. (2006) starburst galaxy templates. Mullaney et al. (2011) constructed the AGN templates based on a subsample of the *Swift*/BAT AGN which had AGN dominated *Spitzer*/IRS spectra determined by the equivalent width of the 11.3 μm feature being < 0.03 μm. The *Spitzer*/IRS spectra were combined with *IRAS* photometry at 60 and 100 μm to define the "intrinsic" AGN SED from 6–100 μm.

Mullaney et al. (2011) created three different AGN templates: one based only on high AGN luminosity objects, low AGN luminosity objects, and a median of the entire sample. For this work, we only consider the median AGN template given our SEDs only contain two points in the MIR where AGN-related emission is expected to dominate.

3.7.2 Dale et al 2014 model

The third model we chose to test on our sample is the semi-empirical templates from Dale et al. (2014, hereafter D14). These templates also contain two components, one for dust emission in the host galaxy and one for the AGN. The host galaxy components were built from an updated version of the Dale & Helou (2002) model. Each component represents an SED produced using a different value of α_{SF}, which is the powerlaw slope of the intensity distribution for the interstellar radiation field that is heating the dust. These SEDs contain a mixture of emission from PAHs, small stochastically heated grains, and thermally radiating large grains.

For the AGN component, D14 chose the median SED of the Palomar-Green quasars from Shi et al. (2013) citing the care with which any star-forming component was removed and the prominence of several AGN related MIR features such as the [OIV] fine structure line and the broad 10 and 18 μm silicate emission bumps. At long wavelengths the AGN template falls as a blackbody.

Instead of two separate templates for the AGN and host galaxy, D14 provided a single set of templates based on different combinations of α_{SF} and f_{AGN}, the fractional contribution of the AGN to the 5–20 μm emission. In total there are 1365 templates that range in $\alpha_{SF} = 0.0625 - 4.0$ in 0.0625 intervals and $f_{AGN} = 0 - 1$ in 0.05 intervals.

3.7.3 SED Fitting for the template models

For each template in a model set, Equation 3.7 was minimized to determine the best fit normalization. We then chose the normalized template with the lowest $-\log\mathcal{L}$ as the best fitting model for a source. For the DecompIR set, this meant first simultaneously optimizing over a normalization for the AGN component and each host galaxy component, then choosing the combined template that resulted in the minimum $-\log\mathcal{L}$. For D14, this meant calculating $-\log\mathcal{L}$ over the entire set of α and f_{AGN} templates.

Uncertainties using the maximum likelihood method were determined by generating 1000 simulated SEDs for each source. These data points in the simulated SEDs were calculated by assuming each detected point followed a Gaussian distribution with mean equal to the observed flux density and a standard deviation equal to the measured error. Each of the simulated SEDs were re-fit using the same method. The standard deviation on the set of best fit parameters from the simulated SEDs then was used as the uncertainty. In this way both statistical and systematic errors can be taken into account in assessing the reliability of our best fit parameters.

3.7.4 $L_{\rm IR}$ Comparison

The measured property that should be most model independent is the total infrared luminosity, $L_{\rm IR}$. Assuming each model was able to fit well the broadband SEDs and reproduce the observed photometry, $L_{\rm IR}$ is simply the total integrated energy underneath the SED, irregardless of how the SED is decomposed. In Fig-

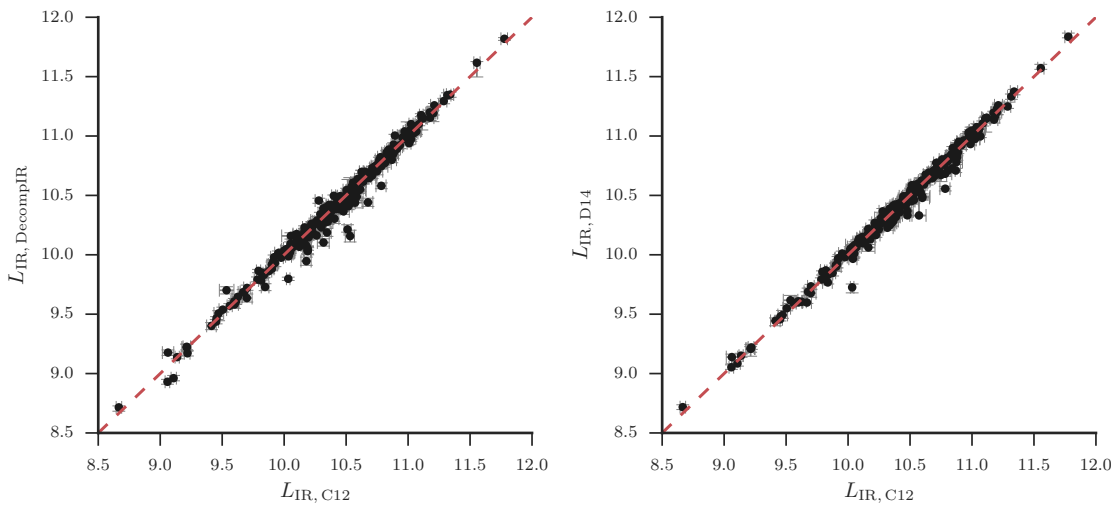

Figure 3.5: Correlations of total $L_{\rm IR}$ between the C12 model and DecompIR and D14. The red dashed line indicates a 1-to-1 correspondence.

ure 3.5, we plot the correlations between the C12 model and DecompIR and D14 models for$L_{\rm IR}$.

The median log $L_{\rm IR}$ for the C12, DecompIR, and D14 models for our sample are all 10.39 $L_{\odot}$with a spread of 0.5 dex. Clearly, based on Figure 3.5, each model well fits the broadband SED of our sample with a small scatter around the 1-to-1 correspondence line. The average difference in the luminosities from each model is only $\sim$ 0.01 dex with a standard deviation between 0.05 and 0.08 dex, slightly higher than the median statistical uncertainty for the C12 model of 0.03 dex.

3.7.5 $L_{\rm SF}$, $L_{\rm AGN,IR}$, and $f_{\rm AGN}$ Comparison

Where the models begin to disagree more, is in the actual decomposition of the SED. In particular, we compare $L_{\rm SF}$, $L_{\rm AGN,IR}$, and$f_{\rm AGN}$. Calculating these parameters for the template models is relatively easy compared to the corrections we had to make for the C12 model. For the DecompIR template set, $L_{\rm IR}$, $L_{\rm SF}$,

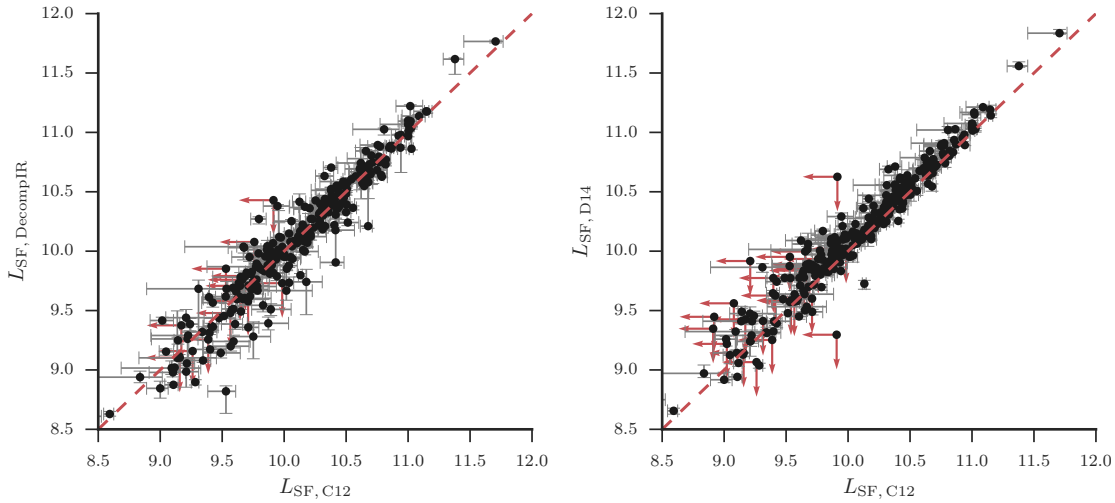

Figure 3.6: Same as Figure 3.5 but for L_{SF}

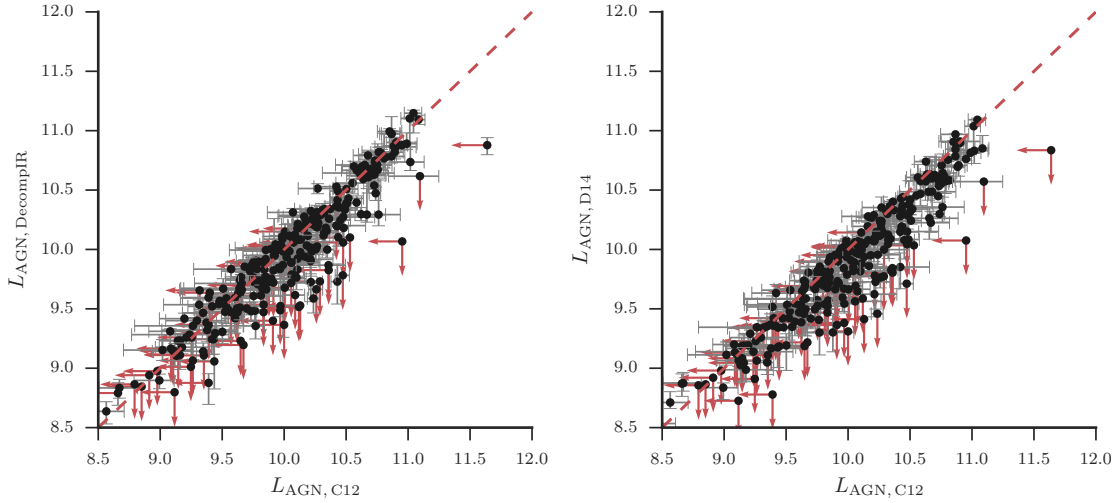

Figure 3.7: Same as Figure 3.5 but for $L_{\mathrm{AGN,\,IR}}$

and $L_{\rm AGN,IR}$ were simply calculated from the best fit total, host galaxy, and AGN SEDs. For the D14 model set, $L_{\rm IR}$ was measured from the best fitting template and $L_{\rm SF}$ and $L_{\rm AGN,IR}$ were calculated based on the best fit $f_{\rm AGN}$.[5] Uncertainties on all of these luminosities were determined with the same Monte Carlo method used to determine the uncertainties on the best fitting parameters.

Figures 3.6, 3.7, and 3.8 display the relationship between each model's $L_{\rm SF}$, $L_{\rm AGN,IR}$, and, $f_{\rm AGN}$. Out of the three parameters, $L_{\rm SF}$ is most consistent between the three models. The C12, DecompIR, and D14 models have a median $L_{\rm SF}$ of 10.12, 10.12, and 10.19 $L_{\odot}$ respectively. The average difference between C12 and DecompIR is only 0.006 dex with a standard deviation of 0.16 dex while the average difference between C12 and D14 is -0.07 dex with a standard deviation of 0.11 dex. Based on these differences, we assign a conservative uncertainty of 0.2 dex for $L_{\rm SF}$ to account for model dependence.

The comparison for $L_{\rm AGN,IR}$ shows increased scatter compared to the two previous luminosities. The median $L_{\rm AGN,IR}$ for the three models is 10.04, 9.9, and 9.85 $L_{\odot}$ for the C12, DecompIR, and D14 models respectively. The average difference between C12 and DecompIR is 0.10 dex with a standard deviation of 0.20 dex while the average difference between C12 and D14 is 0.14 dex with a standard deviation of 0.20 dex. It is likely that the more flexible C12 model which allows the PL component to extend to longer wavelengths creates the discrepancy between it and the

[5] Dale et al. (2014) only provides $f_{\rm AGN}$ calculated between 5–15 μm, however D. Dale graciously provided the authors with $f_{\rm AGN}$ calculated between 8–1000 μm through private communication in August 2015.

template based models. Our implementation of DecompIR and D14 adheres to a strict single template for the intrinsic AGN SED. Adding the offset and spread in the differences in quadrature indicates an uncertainty of 0.25 dex in the determination of $L_{\rm AGN,IR}$.

The relatively large uncertainty in $L_{\rm AGN,IR}$ then leads to a large scatter in $f_{\rm AGN}$ as shown in Figure 3.8. The average difference between C12 and DecompIR is only 0.02 however the standard deviation is 0.13. The average difference between C12 and D14 is 0.1 with a standard deviation of 0.11. Given the spread in $f_{\rm AGN}$ is comparable to the average statistical uncertainty (0.14) from our C12 modeling, we do not add any more uncertainty onto our estimates.

The 15 per cent uncertainty between the three models represents our general lack of knowledge about the details of decomposing broadband SEDs of AGN host galaxies. The estimated $f_{\rm AGN}$ is only 10–15% dependent on the assumed models of both the host galaxy and AGN, and currently at best we can only constrain to within 15 per cent. This influences then the calculations of both the SFR (based on $L_{\rm SF}$) and the IR portion of AGN luminosity ($L_{\rm AGN,IR}$). Studies relying on calculating the SFR of AGN host galaxies using the infrared need to take these discrepancies into account or else risk over-interpreting results based on broad SED decomposition. This also highlights the need for high angular resolution studies of AGN, to determine the true shape of the AGN IR SED.

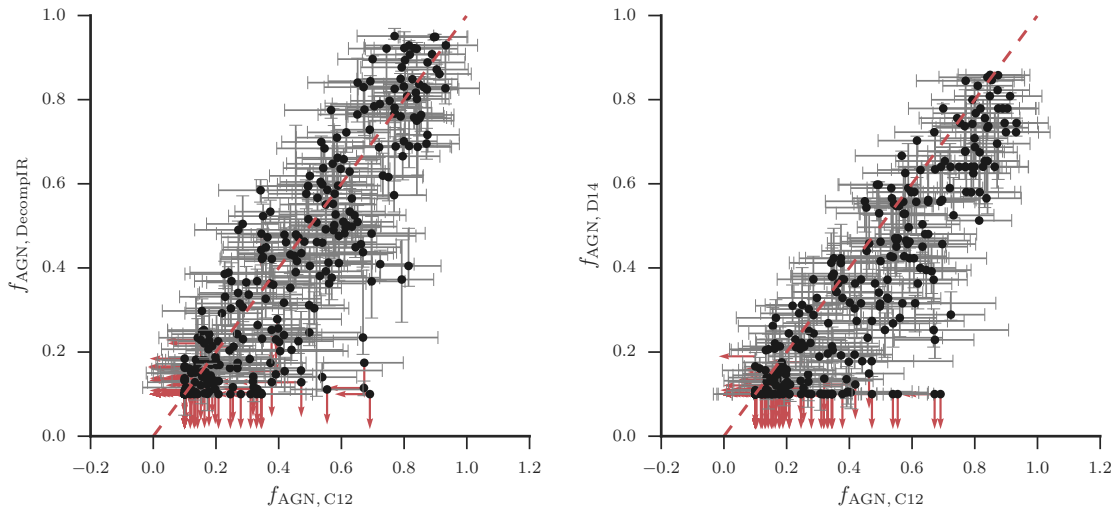

Figure 3.8: Correlations of f_{AGN} from the three SED models. Error bars represent the 68% confidence interval. Upper limits are indicated as red downward pointing arrows. The red dashed line indicates a 1-to-1 correspondence.

3.8 Results and Discussion

3.8.1 Comparison of L_{SF} with PAH measurements

To test our estimates of the star-forming luminosity (L_{SF}), we compare them with estimates of the star-forming luminosity calculated from the PAH 11.3 and 7.7 μm luminosity. PAH features are thought to be caused by the vibrations of complex hydrocarbons (Draine & Lee, 1984; Puget & Leger, 1989) and have been shown to be reliable tracers of the SFR (Roussel et al., 2001; Sargsyan & Weedman, 2009; Shipley et al., 2016; Treyer et al., 2010) even for AGN (Diamond-Stanic & Rieke, 2010). Therefore, comparing our L_{SF} with the 11.3 and 7.7 μm PAH luminosity provides a further check on our SED decomposition.

To measure the 7.7 and 11.3 μm luminosities we first searched the Cornell Atlas of Spitzer IRS Sources (Lebouteiller et al., 2011, CASSIS;) for low-resolution

Spitzer/IRS spectra of the *Herschel*-BAT AGN. We found 120/313 AGN on CASSIS and downloaded their reduced spectra using the default extraction method. Due to the different sizes of the Short-Low (SL) slit and Long-Low (LL) slit, the continuum of each can be offset mainly from extended emission not captured by the SL slit. Therefore spectral orders were stitched together by fitting a line to the ends of each order and scaling to match the overlapping regions. SL2 and LL2 were first matched and scaled to SL1 and LL1 respectively. Then the combined SL1/SL2 spectra was matched to the combined LL1/LL2 spectra to produce the final full Spitzer/IRS low resolution spectra.

We fit each spectra using small spectral windows centered on 7.7 and 11.3 μm. Following Smith et al. (2007) and the popular spectral fitting software package, PAHFIT, we modeled the PAH features using a Drude profile and any emission lines contained in the spectral windows as narrow Gaussians. The full-width-at-half-maximum (FWHM) and central wavelength of the emission lines were kept fixed at the values in Table 2 of Smith et al. (2007). The 7.7 and 11.3 μm features are actually complexes with multiple subfeatures. PAHFIT models these with multiple Drude profiles chosen to reproduce the observed features and we follow this method using the values for the fractional contribution and FWHM as given in Table 3 of Smith et al. (2007). We model the continuum as a simple third-order polynomial. This allows the continuum to take on many shapes that is more necessary for AGN spectra which can show broad silicate absorption and emission and varying continuum slopes (Baum et al., 2010; Spoon et al., 2007; Wu et al., 2009). While silicate absorption is included within PAHFIT, silicate emission is absent prompting the need for our

own modeling. Finally, to determine the best-fit model, we again use the Bayesian methodology and MCMC described in Section 3.6.2. This allows us to treat the continuum and other nearby features as nuisance parameters and robustly determine uncertainties on the 7.7 and 11.3 μm luminosities.

Figure 3.9 shows the correlation between $L_{\rm SF}$ and $L_{\rm PAH}$ for both the 7.7 (right) and 11.3 μm (left) complexes. We chose to use the KINGFISH galaxies (red squares) as a comparison here rather than HRS given the available PAH measurements. $L_{\rm SF}$ was determined using the C12 model in the same way as the HRS sample and $L_{\rm PAH}$ is from Smith et al. (2007). The $L_{\rm PAH}$ for KINGFISH were measured using PAHFIT, but given the large similarity with our method, we do not expect large differences.

Based on Figure 3.9, both the KINGFISH and *Herschel*-BAT samples seem to follow broadly the same correlation indicating we are neither over nor under estimating $L_{\rm SF}$ from our SED decomposition for the *Herschel*-BAT AGN. Using LINMIX, we measured the relationship for both samples and both PAH luminosities. The median correlations with 95% confidence intervals are shown in Figure 3.9 with the blue and red solid lines and shaded regions corresponding to the *Herschel*-BAT AGN and KINGFISH samples respectively. For the *Herschel*-BAT AGN we find slopes of 1.26 ± 0.1 (11.3 μm) and 1.32 ± 0.11 (7.7 μm) with correlation coefficients of 0.92 and 0.93 while for the KINGFISH galaxies we find slopes of 1.02 ± 0.15 and 1.11 ± 0.16 with correlation coefficients of 0.82 for both. In all four cases the probability of a null correlation is extremely small with the largest probability being 10^{-10}. The *Herschel*-BAT AGN show a slightly steeper relationship than the KINGFISH galaxies, however they are still within $\sim 1.5\sigma$ of each other. The steepness of the correlation

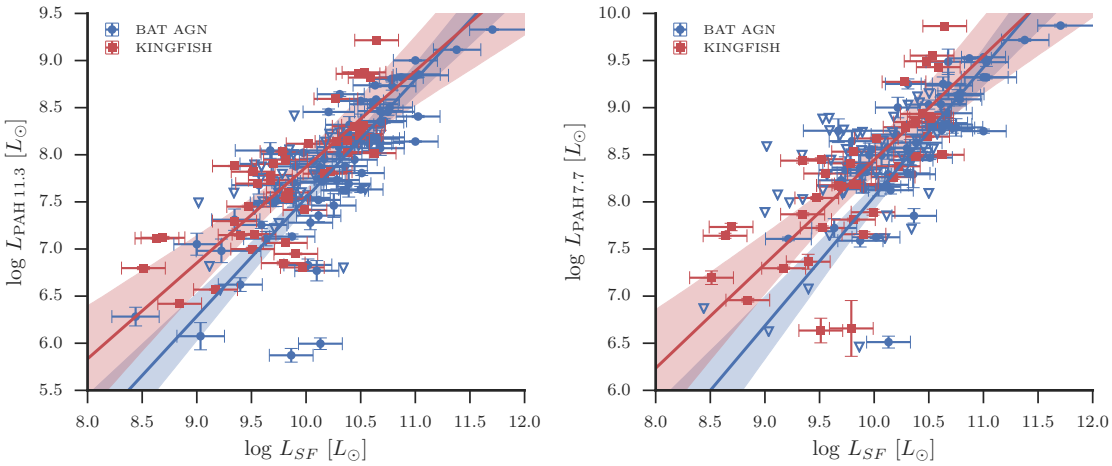

Figure 3.9: Correlation between $L_{\rm SF}$ and the 11.3 (left) and 7.7 μm (right) luminosity. Blue points correspond to the *Herschel*-BAT AGN and red squares correspond to the KINGFISH galaxies. Sources with upper limits on $L_{\rm PAH}$ are shown as open triangles. Measured correlations between $L_{\rm SF}$ and the 11.3 and 7.7 μm luminosity are shown as solid blue and red lines for the *Herschel*-BAT AGN and KINGFISH samples respectively. The shaded region around the median correlations indicate the 95% confidence interval. The broad consistency of the correlation for both the KINGFISH and *Herschel*-BAT samples shows that SFRs determined from $L_{\rm SF}$ are comparable without any systematic bias.

for the *Herschel*-BAT AGN could be driven by the large number of upper limits for the PAH luminosities. Indeed, when excluding these from the analysis we find slopes of 1.13 ± 0.09 and 1.15 ± 0.12, much closer to the KINGFISH galaxies.

For the purposes of this work, Figure 3.9 indicates that our SED decomposition of the *Herschel*-BAT AGN has produced reliable estimates of the star-forming luminosity consistent with measurements of the PAH 11.3 and 7.7 μm luminosity. A more detailed analysis on the exact correlation between broadband IR luminosity and PAH emission for AGN is beyond the scope of this Chapter and has no bearing on our results.

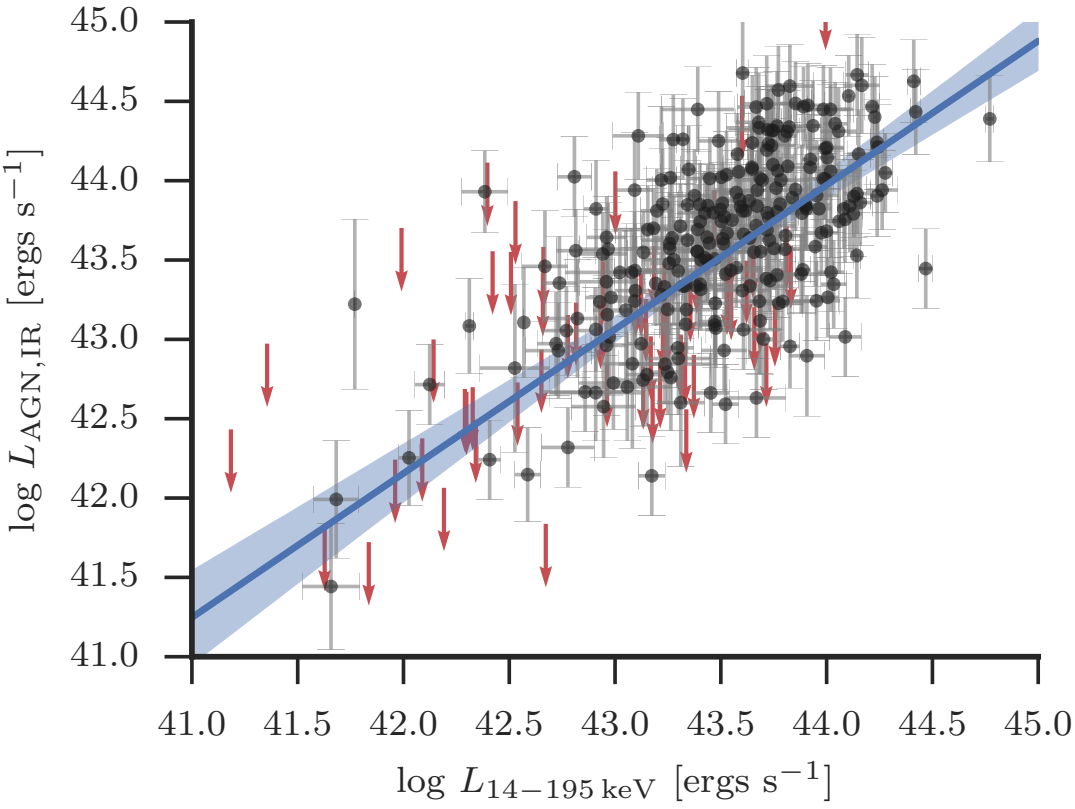

Figure 3.10: Correlation between $L_{\rm AGN,IR}$ and $L_{14-195\,\rm keV}$ for the *Herschel*-BAT sample (blue points). The solid black line shows the result of Bayesian linear regression with the grey shaded region indicating the 95 per cent confidence interval. The strong correlation between the two luminosities provides evidence our SED decomposition performed well in measuring the IR luminosity associated with AGN heated dust.

3.8.2 Correlation between $L_{\rm AGN,IR}$ and $L_{14-195\,\rm keV}$

In Figure 3.10, we plot the relationship between the 14–195 keV luminosity and $L_{\rm AGN,IR}$. As expected, we find a strong correlation between the two luminosities indicating we have measured $L_{\rm AGN,IR}$ accurately from the C12 model and our correction factor. To quantify the relationship, we performed linear regression using a PYTHON implementation of LINMIX_ERR[6] (Kelly, 2007), a Bayesian method for linear regression that incorporates errors in both independent and dependent variables as well as non-detections. Kelly (2007) showed through simulations that LINMIX_ERR outperforms other popular linear regression methods such as ordinary least squares and FIT_EXY. LINMIX_ERR outputs marginalized posterior probability distributions for the slope, intercept, and intrinsic scatter between the two variables as well as the correlation coefficient, ρ. Our reported best fit parameters here and throughout the rest of the Chapter will be the median of the marginalized posterior probability distribution with an uncertainty equal to the standard deviation. The linear model assumed is of the form:

$$Y = mX + b + \epsilon_{\rm int} \tag{3.12}$$

where Y and X are the dependent and independent variables, m is the slope, b is intercept, and $\epsilon_{\rm int}$ represents intrinsic scatter in the relationship beyond that related to measurement error. $\epsilon_{\rm int}$ is modeled as a Gaussian random variable with mean 0 and a variance of σ^2.

[6] https://github.com/jmeyers314/linmix

We plot the best fit linear regression for the whole sample in Figure 3.10 as a black line with grey shading to indicate the 95 per cent confidence interval. The best-fit line corresponds to the following relationship:

$$\log(L_{\rm AGN,IR}) = (0.91 \pm 0.06)\log(L_{14-195\,\rm keV}) - (4.03 \pm 2.6) \tag{3.13}$$

The correlation coefficient from LINMIX_ERR is 0.8±0.03 and the intrinsic scatter is 0.15 dex. The probability of zero correlation is only 10^{-77}. Our measured slope of 0.91 is slightly flatter than the slope measured in Gandhi et al. (2009) ($m = 1.1$) using sub-arcsecond 12 μm imaging for 16 nearby Seyferts. However, given our very simple method for determining the AGN MIR luminosity from broadband SED decomposition, a slope close to 1.0 and high correlation coefficient provides confidence that the decomposition has performed reasonably well. Further, Equation 3.13 will provide future studies with estimates of the full 8–1000 μm AGN contribution and allow better estimates of IR-based SFRs for AGN as long X-ray data is available.

Because we are comparing luminosities and the *Swift*/BAT sample if flux-limited, the correlation we see could simply be due to a confounding variable, in this case distance. To investigate this possibility, we performed a partial correlation test with ASURV using distance as our third variable along with the 14–195 keV luminosity and AGN-related IR luminosity. The partial correlation test calculates Kendall's-τ rank correlation coefficient between all three variables, then estimates the intrinsic correlation coefficient after removing the dependence on the third variable (i.e. distance).

We find $\tau = 0.30 \pm 0.03$ and the probability of a null correlation of only 10^{-23}. While the value of the correlation coefficient is less than the correlation coefficient from LINMIX_ERR, the partial correlation test does not account for scatter due to measurement error.

14–195 keV luminosities are only available for our low redshift sample, therefore Equation 3.13 is useless at higher redshifts. We can convert 14–195 keV luminosity to the more accessible 2–10 keV luminosity by making the simple assumption that the shape of the X-ray spectrum of AGN is a powerlaw with a photon index of 1.8 (e.g. Vasudevan et al., 2013). The ratio of L_{14-195}/L_{2-10} is then ~ 2.7. Switching to L_{2-10} changes Equation 3.13 to

$$\log(L_{\rm AGN,IR}) = (0.91 \pm 0.06) \log(L_{2-10\,\rm keV}) - (3.64 \pm 2.6) \tag{3.14}$$

$L_{2-10\,\rm keV}$ assumes the luminosity has been absorption-corrected. Differences in the assumed photon index only change the intercept by at most 0.3 dex.

3.8.3 IR colors as a predictor of $f_{\rm AGN}$ and selecting AGN

We utilize our broad coverage of the IR SED for AGN host galaxies to test the viability of different IR colors for predicting the AGN IR luminosity fraction (i.e. $f_{\rm AGN}$). For large surveys and/or high redshift studies, coverage from 12–500 μm might not be available or possible. FIR colors have also been readily used in the past ever since the launch of *IRAS* to select "warm" sources which might be powered by an AGN. In particular, the 25/60 μm color, which is very similar to

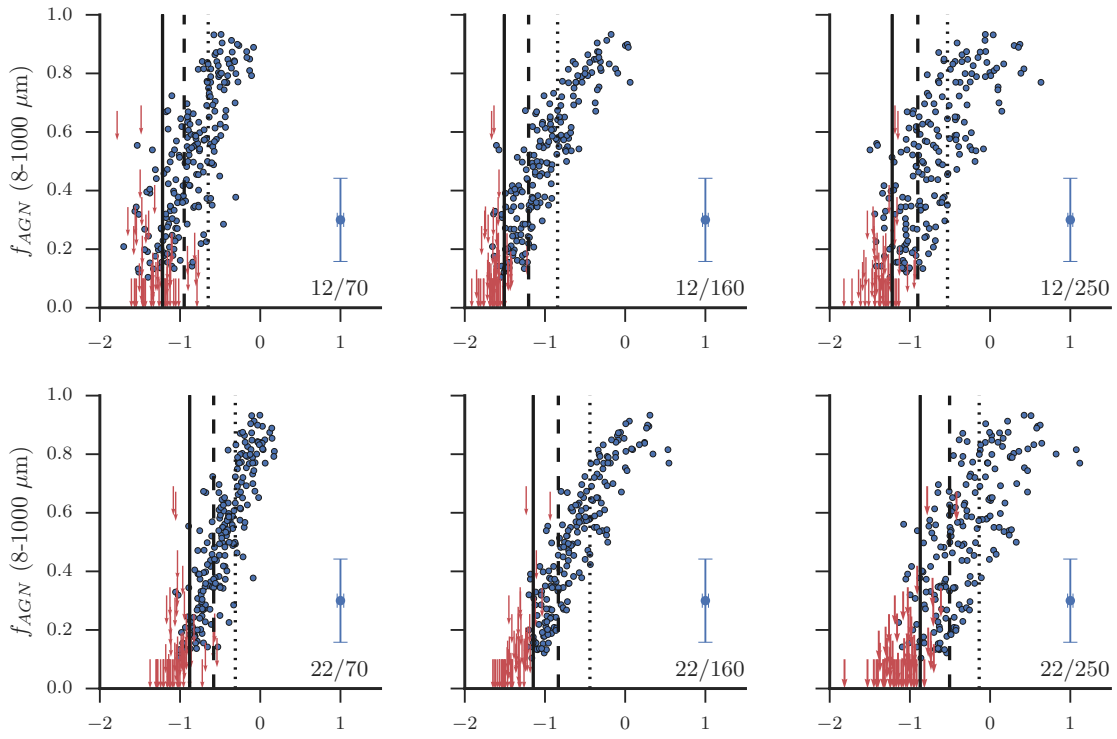

Figure 3.11: Relationship between different IR colors and the $f_{\rm AGN}$, the fraction of the 8–1000 μm luminosity attributed to AGN heated dust. The IR colors (x-axis) are in logarithmic units. Upper limits on $f_{\rm AGN}$ are indicated as red arrows and are at 95% confidence. We also display the 75th, 50th, and 25th percentile colors for the *Herschel*-BAT AGN as solid, dashed, and dotted vertical lines, respectively. Choosing a sample with colors *above* these would result in 75, 50, and 25 per cent completeness for the *Herschel*-BAT AGN.

the 22/70 color we test below, was shown nearly thirty years ago to be an excellent indicator of AGN activity (de Grijp et al., 1985). With our sample and data we can test this color as well as others to determine their effectiveness in both choosing AGN as well as indicating the AGN contribution.

In Figure 3.11, we plot six MIR/FIR flux ratios (12/70, 12/160, 12/250, 22/70, 22/160, 22/250) against the measured $f_{\rm AGN}$ for the *Herschel*-BAT AGN. The flux ratios are all in log units to better visualize the relationships. Upper limits on $f_{\rm AGN}$ are shown as downward-pointing arrows. In the lower right corner of each subplot, we show representative error bars. We fit a linear model between each flux ratio and $f_{\rm AGN}$ with the following form

$$f_{\rm AGN} = m \log(F_1/F_2) + b + \epsilon_{\rm int} \tag{3.15}$$

where F_1/F_2 represents each flux ratio. To calculate the best fitting parameters, we again used LINMIX_ERR.

Table 3.1 outlines the best fit parameters for each relationship. Each flux ratio is highly correlated with $f_{\rm AGN}$ (all $\rho > 0.87$). It is clear however that the worst indicators are the flux ratios involving the 250 μm flux with ρ less than 0.9 as well as showing significant scatter in Figure 3.11.

Based on the slope of the linear regressions, the 22/70 μm, with a slope of 0.8, overall seems to be the best flux ratio to use as an indicator of the AGN contribution to the IR SED. These two wavebands bracket the region where the intrinsic AGN SED is thought to turnover (e.g. Mullaney et al., 2011; Netzer et al., 2007) and seems

to be the crucial transition region where the SED shifts from AGN-dominated to host galaxy dominated.

Table 3.1. Linear Regression Between Flux Ratios and $f_{\rm AGN}$

F_1/F_2	m	b	$\sigma_{\rm int}$	ρ	75th %tile (%tile for HRS)	50th %tile (%tile for HRS)	25th %tile (%tile for HRS)
12/70	0.67 ± 0.04	1.02 ± 0.03	0.016 ± 0.004	0.89 ± 0.02	-1.23 (90)	-0.97 (50)	-0.66 (21)
12/160	0.58 ± 0.02	1.05 ± 0.03	0.002 ± 0.002	0.99 ± 0.01	-1.51 (31)	-1.21 (5.2)	-0.85 (2.2)
12/250	0.51 ± 0.03	0.84 ± 0.03	0.019 ± 0.004	0.87 ± 0.03	-1.22 (28)	-0.91 (5.2)	-0.57 (1.5)
22/70	0.79 ± 0.03	0.86 ± 0.02	0.001 ± 0.001	0.99 ± 0.01	-0.89 (32)	-0.60 (16)	-0.32 (12)
22/160	0.58 ± 0.02	0.85 ± 0.02	0.0004 ± 0.0005	0.997 ± 0.003	-1.14 (5.6)	0.83 (1.2)	-0.45 (0)
22/250	0.49 ± 0.03	0.65 ± 0.02	0.016 ± 0.004	0.90 ± 0.02	0.87 (6.8)	-0.51 (0.02)	-0.18 (0)

We further test how well each IR color exclusively selects AGN host galaxies. In Figure 3.11 we plot the 75th, 50th, and 25th percentile color for the *Herschel*-BAT sample as blue dashed (for the 25th and 75th percentiles) and blue solid (for the 50th percentile) vertical lines. In Table 3.1, the last three columns list the colors in logarithmic units for the 75th, 50th, and 25th percentiles. These colors mean that by selecting galaxies with a color above this one, the sample will be 75, 50, and 25 per cent complete based on the *Herschel*-BAT sample.

While these colors are useful for selecting AGN host galaxies, we also want to know what percentage of non-AGN galaxies would be selected with these color cuts as contamination for a sample. Therefore, we also calculated the percentile of HRS galaxies that would be selected. For this analysis, we used the complete HRS sample since it represents the natural field galaxy population and we do not want to restrict to only high-mass non-AGN galaxies. The HRS sample unfortunately was not observed at 70 μm, therefore to calculate the 12/70, and 22/70 colors, we simply used the 70 micron flux from the best-fit model. The percentiles for HRS are given in parentheses next to the values of the colors in Table 3.1.

We find that the best color to use in selecting an AGN-only sample would be the 22/160 color. Using the 75th percentile color (-1.14), we would only select 5.6 per cent of the HRS sample. To get only around 1 per cent of the HRS sample, we would have to use the 50th percentile 22/160 or 22/250 color, however this would only select half of a complete AGN sample. To select no non-AGN galaxies would require pushing to the 25th percentile colors and risk severe incompleteness and a selection bias of only AGN-dominated galaxies. In a forthcoming publication,

we will evaluate these colors along with other MIR color selection techniques (e.g. Donley et al., 2012; Stern et al., 2012) to determine the biases and selection effects with regards to the SFR of the galaxy and strength of the AGN.

3.8.4 The AGN contribution to the 70 μm emission

Many studies examining the relationship between nuclear activity and star formation rely on single monochromatic luminosities as an indicator of star formation (e.g. Netzer, 2009; Netzer et al., 2007; Rosario et al., 2012). The most widely used indicator has been the 60 μm luminosity given its availability from the all-sky *IRAS* survey.

With our *Herschel*-BAT sample and SED modeling we can test how often and at what level AGN emission contributes to different wavelength bands. We test the AGN contribution to the 70 μm emission. Based on visual inspection of all of the SED fits, we found this waveband is the only *Herschel* band with a noticeable AGN contribution. All other longer wavelength bands were dominated by the MBB component. We restrict this analysis to only those sources with well-determined SEDs longwards of 70 μm, excluding those objects with less than four detected SED points. We note that the majority of these objects are likely AGN dominated at 70 μm, however the uncertainty in their FIR SED, especially their dust temperature results in a largely unconstrained calculation.

To determine the AGN contribution to the 70 μm emission, we first estimated the PL component associated with star formation. We assumed the shape of the

star-forming PL component followed the average power law slope ($\alpha = 0.0$ and turnover wavelength ($\lambda_c = 50$ μm) from the HRS sample. We then adjusted the normalization such that the integrated luminosity would equal $1/3 L_{\rm MBB}$. We combined the estimated star forming PL component with the measured MBB component to form each of the *Herschel*-BAT AGN's total star-forming component. The 70 μm AGN contribution was then calculated as the excess 70 μm emission leftover after subtracting the star-forming contribution from the total 70 μm emission from the best-fit SED. We denote the fraction contributed by the AGN as $f_{\rm AGN,70}$.

Figure 3.12, *left* shows the distribution of $f_{\rm AGN,70}$. We find that for 48 per cent of the sample, $f_{\rm AGN,70} < 0.2$ but for 24 per cent of the sample $f_{\rm AGN,70} > 0.5$. Using the 70 μm luminosity as a single SFR indicator would overestimate values by at least a factor of 2 for almost one-third of an AGN sample.

In the right panel of Figure 3.12 we show $f_{\rm AGN,70}$ as a function of the 14–195 keV luminosity. The grey points indicate the individual points while the blue points with error bars are binned averages with a 68 per cent confidence interval determined through bootstrapping. Its abundantly clear that at log $L_{14-195\,\rm keV} < 42.5$), $f_{\rm AGN,70}$ is largely negligible with only two sources with $f_{\rm AGN,70} > 0.2$. These AGN are NGC 1052 and NGC 4941. Both are quite pointlike, possibly unresolved at 70 μm, while at long wavelengths show large-scale extended emission.

Above log $L_{14-195\,\rm keV} = 42.5$, the AGN contribution at 70 μm varies nearly uniformly between 0 and 1. This indicates that the AGN contribution is not a simple function of high AGN luminosity, rather it is due to the competing interplay between AGN emission and star-formation. This reinforces the need for SED decomposition

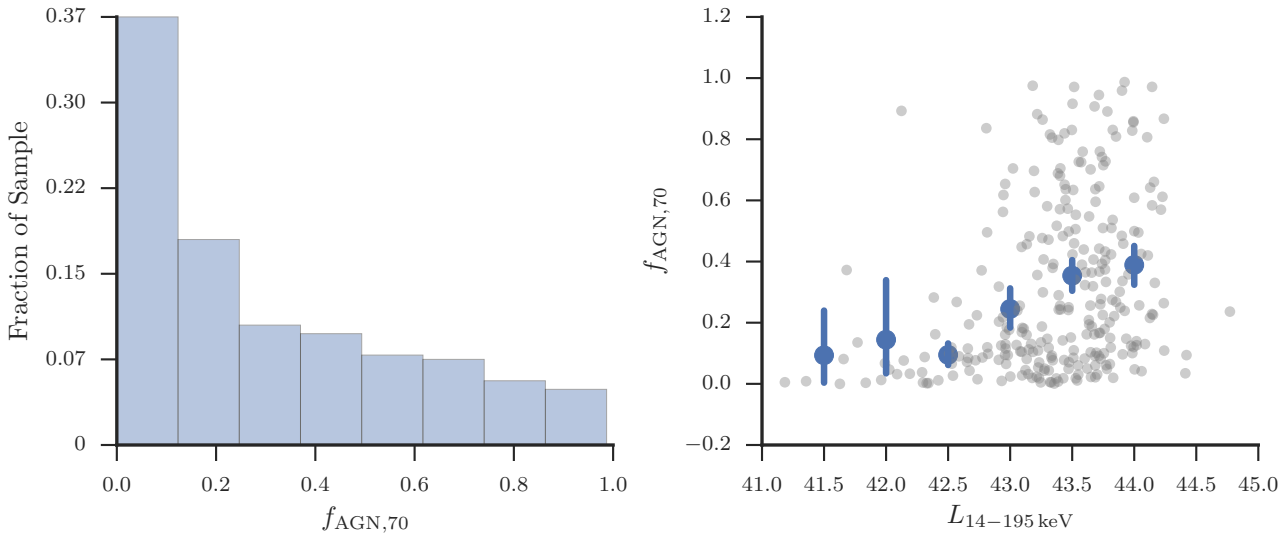

Figure 3.12: *left:* Histogram of the estimated 70 μm contribution by AGN-heated dust. Each bar is a bin with a width of 0.1 and a height equal to the fraction of the total sample. *right:* Relationship between the 14–195 keV luminosity and 70 μm AGN contribution. Grey dots represent each individual source while the blue dots with error bars are averages within bins according to 14–195 keV luminosity. Error bars indicate the 68 percent confidence interval determined using bootstrap analysis.

Table 3.2. Mean M_{dust}, T_{dust}, and SFR

Sample	log M_{dust} [$\mathrm{M}_{\odot}$]	T_{dust} [K]	log SFR [$\mathrm{M}_{\odot}$ yr^{-1}]
Herschel-BAT	7.36 (6.56–7.90)	23.8 (19.4–27.5)	0.23 (-0.57–0.81)
HRS	7.08 (5.12–7.70)	21.5 (19.4–24.6)	-0.23 (-1.57–0.36)

to determine accurate SFRs when an AGN is present. We did repeat this process at 160 μm, finding no source indicated an AGN contribution above the 5 per cent level.

3.8.5 M_{dust}, T_{dust}, and SFR of local AGN host galaxies

Figure 3.13 compares the distribution of M_{dust}, T_{dust}, and SFR for our three samples of galaxies. We calculated SFRs using the conversion from 8–1000 μm

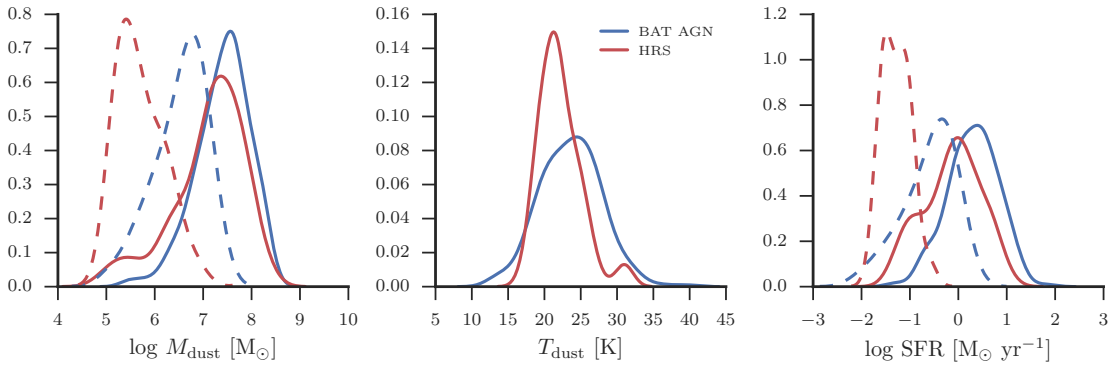

Figure 3.13: Comparison of $M_{\rm dust}$, $T_{\rm dust}$, and SFR between the *Herschel*-BAT AGN (blue), and HRS mass-matched sample (red). The distributions with dashed lines indicate sources with only upper limits on these values.

star-forming luminosity using the following equation from Murphy et al. (2011)

$$\mathrm{SFR} = \frac{\mathrm{L_{SF}}}{2.57 \times 10^{43}} \tag{3.16}$$

The solid lines show the KDE for sources which have firm measurements while the dashed lines show the KDE for the sources with only upper limits. We remind the reader that the *Herschel*-BAT sample contains 35 (11%) sources with upper limits while the mass-matched HRS sample contains 23 (19%). Table 3.2 displays the median for these three properties and each sample. The values inside parentheses indicate the 16th and 84th percentiles for each distribution. The median, 16th, and 84th percentiles were calculated using survival analysis and the KMPL as in Section 3.5 to account for upper limits.

We find that the *Herschel*-BAT AGN have higher dust masses than the HRS sample, slightly higher dust temperatures, and higher SFRs. Because we have mass-matched the HRS sample to the *Herschel*-BAT sample, there should be no effects due to stellar mass. To confirm that the distributions are statistically different

we run the Peto-Prentice two-sample test. The Peto-Prentice two sample test is comparable to the Kolmogorov-Smirnov (K-S) test which calculates the probability that two separate samples were drawn from the same parent population. The Peto-Prentice test, however, allows for the inclusion of censored data.

For the comparison of dust masses, we find the probability that the *Herschel*-BAT AGN and HRS galaxies are drawn from the same parent distribution is 1.8×10^{-5}. The probability for the dust temperatures is 4×10^{-4}, while the probability for the SFRs is 8.4×10^{-11}. All three probabilities are less than 0.05, the standard cutoff for declaring two samples are inconsistent with being drawn from the same parent population.

Because of the strong dependence of the dust mass on the dust temperature, we checked to ensure the results were unchanged by excluding the sources with only upper limits. Excluding the upper limits for both the *Herschel*-BAT and HRS, we still find that the *Herschel*-BAT AGN display higher dust masses than the HRS galaxies. The probability that the dust mass distributions are drawn from the same parent distribution is only 0.0008, still under the standard cutoff of 0.05. We are then confident that the result of higher dust masses for AGN host galaxies is not influenced by our choice of fixed dust temperature for undetected sources.

The increased SFRs for the *Herschel*-BAT sample compared to the mass-selected HRS sample are consistent with the results of Koss et al. (2011). Koss et al. (2011), using optical colors, found that the *Swift*/BAT AGN displayed bluer colors compared to a mass-matched sample of Sloan Digital Sky Survey (SDSS) galaxies, indicative of increased levels of star formation.

These results may seem contradictory with our previous work in Shimizu et al. (2015) where we detail using the SFRs calculated here that AGN host galaxies are experiencing decreased levels of star formation given their stellar mass. However, the discrepancy lies in the comparison being done. In Shimizu et al. (2015) we compare the *Herschel*-BAT AGN to the so-called star-forming "main sequence," a tight nearly linear correlation between SFR and $M_{\rm star}$(Brinchmann et al., 2004; Noeske et al., 2007; Salim et al., 2007), finding the AGN are falling off and transitioning towards quiescence. In this work as well as in Koss et al. (2011), simple mass-matching is used to form comparison samples which leads to selecting only high stellar mass non-AGN galaxies due to the high stellar masses of the BAT AGN. Based on previous studies of the color-magnitude relation, however, selection of high mass galaxies will result in a large quiescence fraction (Kauffmann et al., 2003a; Wuyts et al., 2011) especially at low redshifts (Bell et al., 2012). Therefore, since the *Herschel*-BAT AGN show both intermediate optical colors and SFRs, it makes sense that a mass-selected non-AGN sample with indicate bluer colors and higher SFRs for AGN host galaxies given quiescent galaxies are largely red with low SFRs.

Further, looking into the details of our mass-selected HRS sample, we find that 47/122 (50%) are morphologically classified as early type (E/S0), the dominant morphology for quiescent galaxies (Bell et al., 2012; Wuyts et al., 2011). The *Herschel*-BAT AGN, though, are largely late type spirals (Koss et al., 2011) and even the few ellipticals in our sample show higher SFRs than expected for quiescent galaxies (Shimizu et al., 2015). Thus, it seems clear that we can reconcile the results of Koss et al. (2011), Shimizu et al. (2015), and this work by understanding that

mass-matching preferentially selects low star-forming, red galaxies in contrast to the intermediate star-forming, blue AGN.

The higher SFRs immediately explain slightly larger dust masses observed for the *Herschel*-BAT AGN.[7] The *Herschel*-BAT AGN have a median $\log M_{\rm dust}$ of 7.38 $M_\odot$ vs. 7.0 $M_\odot$ for the HRS. The 16th percentiles also extend to much lower dust masses for the HRS. Cortese et al. (2012a) showed using the full HRS sample that the dust-to-stellar mass ratio is anti-correlated with $NUV - r$ color, a proxy for specific SFR and decreases strongly when moving from late type to early type galaxies. da Cunha et al. (2010) also showed, using over 3000 galaxies from SDSS, a strong correlation between the cold dust mass of galaxies and their SFR.

The increased dust temperatures observed in the *Herschel*-BAT AGN could also be explained by the increased SFRs. Dust temperatures are known to increase with both infrared luminosity and specific SFR (e.g Chapman et al., 2003; Cortese et al., 2014; Magnelli et al., 2014; Symeonidis et al., 2013), although both of those studies did not extend to the low luminosities and specific SFR we observe in our samples. Because we know our sample contains an AGN, it is possible at least some of the increased dust temperatures could be to AGN heating. Recently, García-González et al. (2016) spatially decomposed the FIR images of a small sample of nearby Seyfert galaxies and found that nuclear emission shows markedly higher dust temperatures than the host galaxy (as probed through the 70/160 μm color).

[7]Excluding the objects with only upper limits on the dust mass, which are dependent on the assumed fixed dust temperature we used in the modeling (see Section 3.6 produces the same overall trend of higher dust masses in the *Herschel*-BAT AGN sample)

Sources that are dominated by nuclear emission should then show higher temperatures that do not match with the overall correlation between SFR and $T_{\rm dust}$.

In Figure 3.14, we show the relationship between SFR and $T_{\rm dust}$ for the *Herschel*-BAT AGN and HRS galaxies. The bulk of both samples follow in general a broad positive correlation. There exists a group of HRS galaxies at low SFR ($\log \mathrm{SFR} < -1.0$) that show a flat relationship with $T_{\rm dust}$. All but one of these galaxies are early type which are known to show dust temperatures up to 30 K (Temi et al., 2007). The encircled *Herschel*-BAT AGN at $T_{\rm dust} > 30$ K and $\log \mathrm{SFR} < 0.5$ seem to represent distinct outliers from both samples. These sources are 2MASX J09235371-3141305, 2MASXJ 15462424+6929102, ESO 103-035, ESO 417-G006, MCG –05-23-016, MCG –06-30-015, Mrk 841, and NGC 3516. Except for 2MASX J09235371-3141305, these sources also all have $f_{\rm AGN} > 0.5$, indicating the MIR PL component is quite dominant. ESO 103-035, MCG –05-23-016, and Mrk 841 show SEDs that peak around 20 μm, highly indicative of an SED dominated by IR emission from the AGN. For these seven AGN, then, it is possible that the large dust temperatures are due to AGN heating, rather than star formation.

Besides the seven sources listed, though, the bulk of the *Herschel*-BAT AGN seem to show $T_{\rm dust}$largely consistent with star-formation heated dust and coincides with our results for $M_{\rm dust}$ and the SFR.

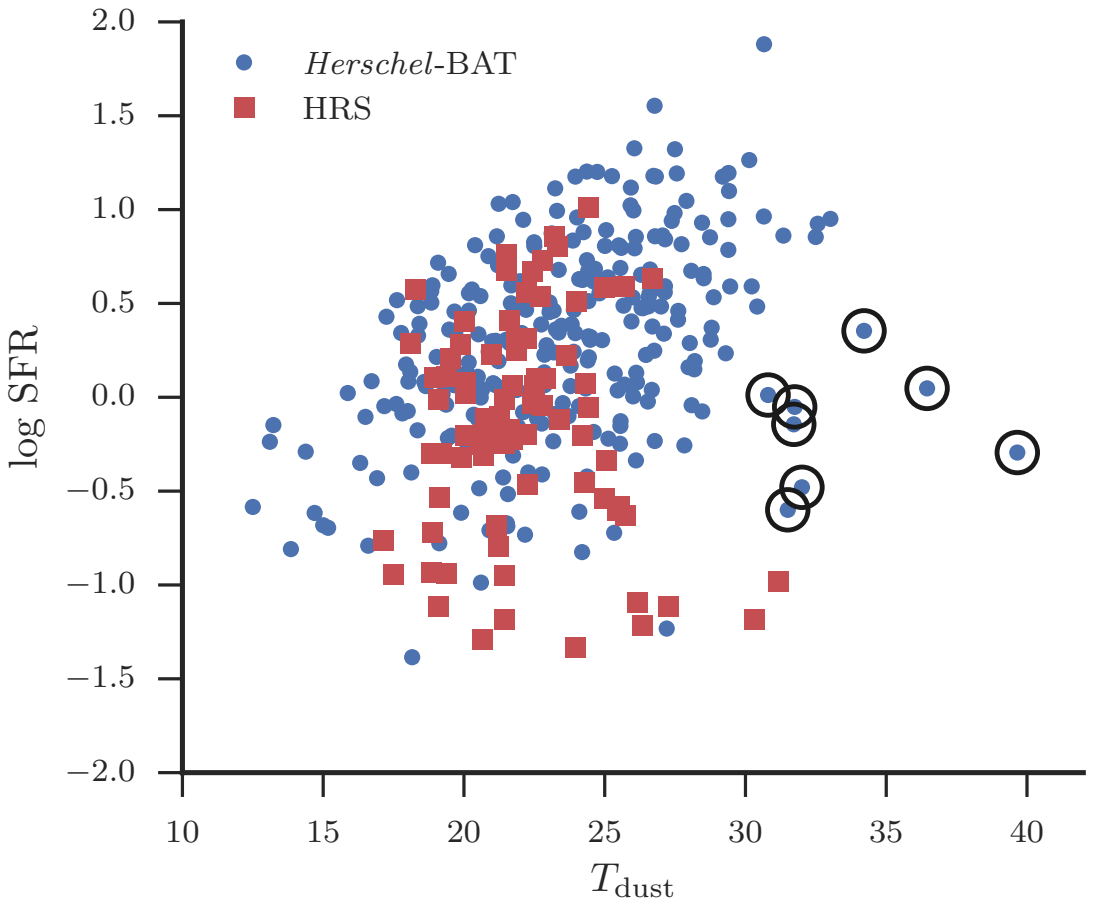

Figure 3.14: Correlation between dust temperature and SFR for the *Herschel*-BAT AGN (blue points) and HRS galaxies (red squares). Circled blue points indicate possible sources that are dominated by AGN-heated dust.

Table 3.3. Comparison of Star-Forming and SED Properties of Type 1 and Type 2 AGN

	log $M_{\rm dust}$ [$M_\odot$]	$T_{\rm dust}$ [K]	log SFR [$M_\odot$ yr^{-1}]	log $L_{\rm AGN,IR}$ [ergs s^{-}1]
Type 1	7.10±0.08	23.3±0.4	-0.07±0.08	10.00±0.06
Type 2	7.34±0.05	23.8±0.3	0.26±0.05	9.68±0.07
Peto-Prentice Probability	0.06	0.64	0.01	0.001

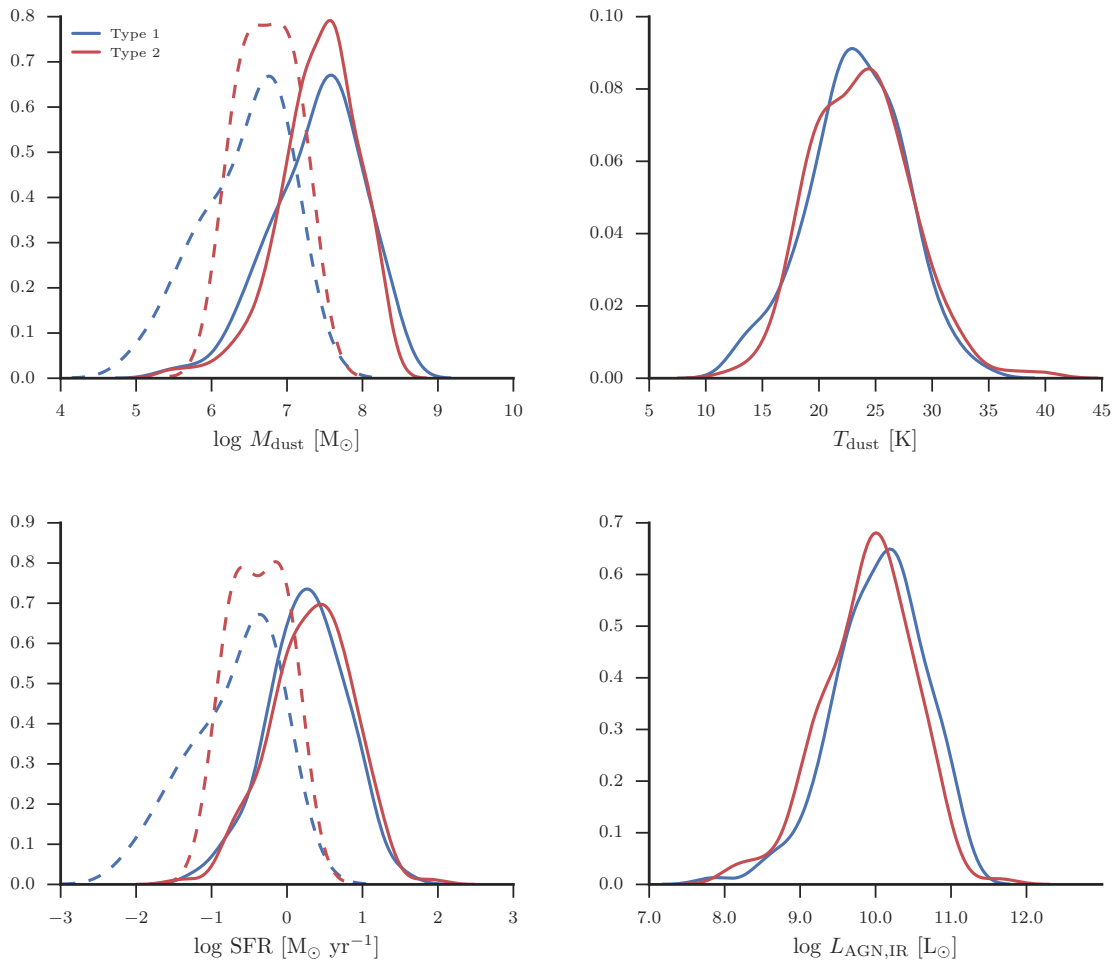

Figure 3.15: Comparison of $M_{\rm dust}$, $T_{\rm dust}$, SFR, and $L_{\rm AGN,IR}$ between the *Herschel*-BAT AGN Type 1 (blue) and Type 2 (red) samples. Dashed lines indicate the distribution for sources with only upper limits.

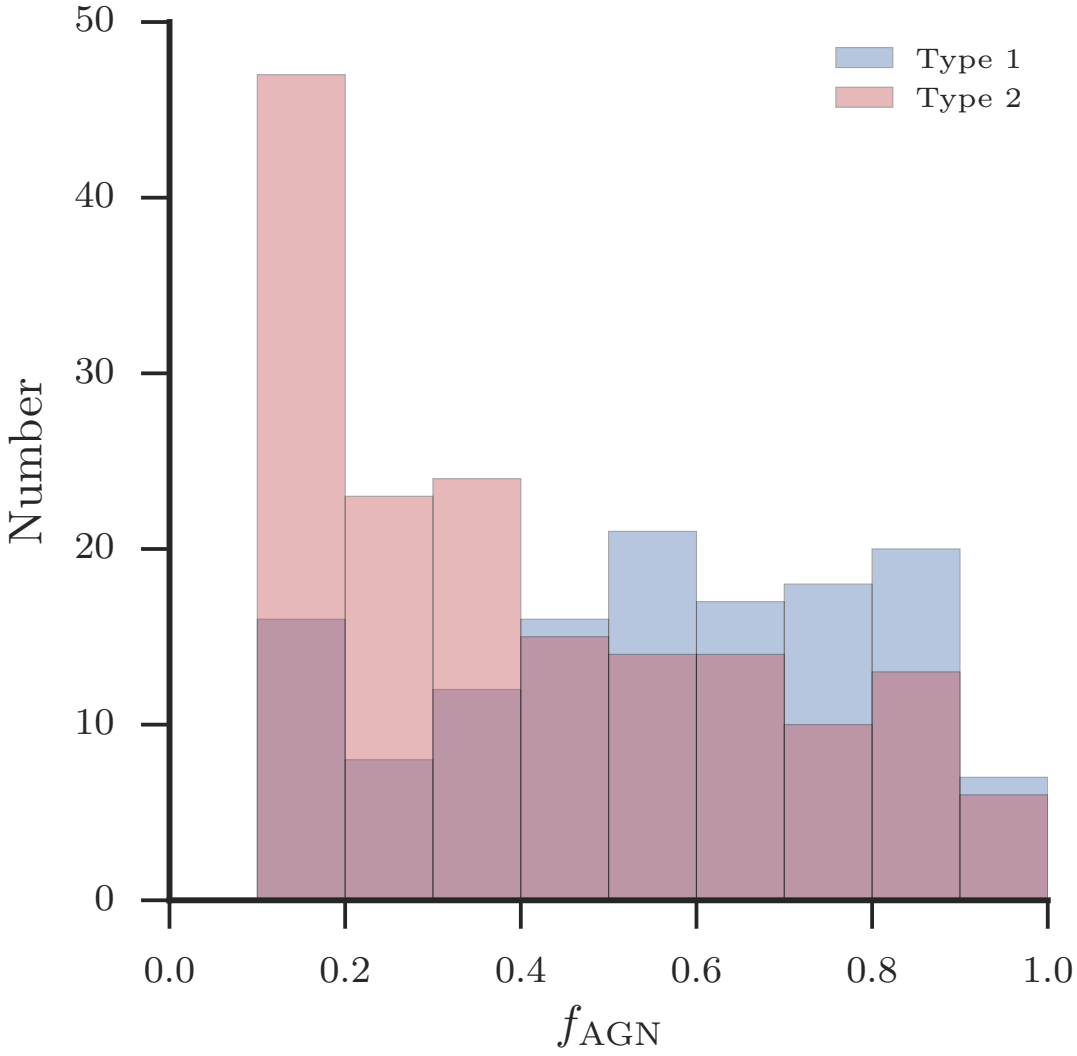

Figure 3.16: Histogram of $f_{\rm AGN}$ for Type 1s (blue) and Type 2s (red). Type 2s on average have much lower $f_{\rm AGN}$ than Type 1s.

3.8.6 Comparison between Type 1s and 2

In this Section, we compare the properties of unabsorbed (Type 1) vs absorbed (Type 2) AGN. According to the unified model (Antonucci, 1993; Urry & Padovani, 1995), Type 1 and Type 2 AGN are two manifestations of the same object. The only difference between the two is the viewing angle towards the central AGN. Due to a dusty structure, lines of sight at low angle are obscured causing the broad line region to be hidden while high angle lines of sight allow an unobstructed view of both the accretion disk and broad line region. Type 1 AGN therefore exhibit broad emission lines and low hydrogen absorption while the opposite is true of Type 2 AGN.

Because the differences in AGN types is related to the central obscuring structure, global star-forming properties of Type 1 and Type 2 AGN should be the same. In the top row of Figure 3.15, we compare the distribution of $M_{\rm dust}$, $T_{\rm dust}$, and SFR between Type 1s and Type 2s. Visually the distributions for the detected sources look identical. However the distributions for the sources with upper limits on $M_{\rm dust}$ and SFR are different between Type 1s and Type 2s. In Table 3.3, we show the average of these properties (including upper limits) as well as the Peto-Prentice probability that Type 1s and Type 2s are drawn from the same distribution. The only property with a probability greater than 0.05 is $T_{\rm dust}$, meaning that the cold dust temperature associated with star formation is the same in Type 1s and Type 2s.

Surprising are the results of the Peto-Prentice test for $M_{\rm dust}$ and SFR. Survival

analysis seems to indicate that Type 1s are skewed more strongly towards galaxies with lower $M_{\rm dust}$ and SFR. Type 1s have 0.24 dex lower average $M_{\rm dust}$ and 0.33 dex lower average SFR. This difference is caused by the population of sources with only upper limits on both $M_{\rm dust}$ and SFR. 25/35 of the AGN with upper limits are classified as Type 1. Further, the actual values of the upper limits for the Type 1 AGN are lower compared to Type 2 AGN. Of the 25 Type 1 AGN with upper limits, 5 have $\log M_{\rm dust} < 6.0$ and $\log {\rm SFR} < -1.0$ compared to none of the Type 2 AGN and form the bump and long tail in the distribution of upper limits seen in Figure 3.15.

These Type 1 AGN with little to no dust and no recent star formation seem to form a separate sample away from the main population of AGN host galaxies. If we restrict the samples to only those sources with $\log M_{\rm dust} > 6.0$ and $\log {\rm SFR} > -1.0$, the Peto-Prentice probability changes to 0.25 for $M_{\rm dust}$ and 0.09 for the SFR. The new probabilities are both above the standard threshold of 0.05, indicating they originate from the same parent population. These anomalous Type 1 AGN could be an interesting subsample for future study, but our main result is that for the bulk of Type 1 and Type 2 AGN, their host galaxies display the same star-forming properties in agreement with the unified model.

Regarding the AGN related properties of the IR SED, we see differences between Type 1 and Type 2 AGN even before including sources with upper limits. Both the Type 1 α and $L_{\rm AGN,IR}$ distributions are visually different from Type 2 AGN with Type 2 AGN having higher α and lower $L_{\rm AGN,IR}$. Survival analysis and calculation of their means confirm the visual differences as shown in Table 3.3. Type

1 AGN have an average α of 1.46 compared to 1.73 for Type AGN and an average log $L_{\rm AGN,IR}$ of 10.00 compared to 9.71.

The difference in log $L_{\rm AGN,IR}$ between Type 1 and Type 2 AGN can be explained by the different X-ray luminosity distributions of Type 1 and Type 2 *Herschel*-BAT AGN. It has been well documented (e.g. Burlon et al., 2011; Meléndez et al., 2014) that within the *Swift*/BAT AGN sample, Type 2 AGN are more prevalent at lower luminosities compared to Type 1 AGN. This has been given as evidence for luminosity dependent obscuration and perhaps the torus receding at high AGN luminosity (e.g. Toba et al., 2014). Toba et al. (2014) found that the average covering factor of the torus decreased with increasing AGN luminosity which explains the increasing Type 1 AGN fraction with luminosity since a higher covering factor means more of a chance of observing a Type 2 AGN. Because $L_{\rm AGN,IR}$ is strongly related to the X-ray luminosity that probes the overall bolometric AGN luminosity, we would expect Type 2s to show a shifted distribution of $L_{\rm AGN,IR}$ towards lower values. This is what is seen in Figure 3.15.

The combination of lower $L_{\rm AGN,IR}$ and relatively similar SFR distributions produces a strong difference in the $f_{\rm AGN}$ distribution for Type 2s and Type 1s as shown in Figure 3.16. Type 2s have much lower $f_{\rm AGN}$ compared to Type 1 AGN which agrees with Meléndez et al. (2008) who found that Type 2s have colder 25/60 μm colors. Our interpretation however is that the lower $f_{\rm AGN}$ is not indicative of larger SFRs in Type 2 AGN but rather lower AGN luminosities. Because Type 2 AGN are more likely to be observed in lower AGN luminosity systems, their intrinsic MIR luminosities are going to be lower assuming the MIR simply scales with the

bolometric luminosity (as shown in Section 3.8.2). Since the SFR distributions are the same (apart from the very low star-forming Type 1s), then the ratio between AGN MIR luminosity and star-forming luminosity will naturally be lower in Type 2 AGN host galaxies. This means that Type 2 AGN on average are more likely to be found in host galaxy dominated systems at least in terms of their IR SED.

These results are in agreement with Diamond-Stanic & Rieke (2012) who found no statistically significant differences between the SFRs of Type 1 and Type 2 AGN on all physical scales using the 11.3 μm PAH feature and 24 μm continuum emission. Moreover, Imanishi & Wada (2004), using the 3.3 μm PAH feature as a measure of star-forming activity found no differences between Type 1 and Type 2 AGN; and Pereira-Santaella et al. (2010), using the [NeIII] emission line, determined Type 1 and Type 2 AGN exhibit the same star-forming activity. Thus, nearly all measures of SFR in the infrared (FIR, PAH features, ionization lines) seem to confirm that moderate luminosity Type 1 and Type 2 AGN are actively star-forming at the same level.

Previous studies that indicated Type 2 AGN have enhanced star formation occurring in their host galaxies, such as Maiolino et al. (1995) and Mouri & Taniguchi (2002) reached these conclusions based on analysis of the colors and luminosity ratios which we have shown to be more indicative of the different AGN fractions of the IR SED of Type 1 and Type 2 AGN rather than a difference in their SFRs.

In conclusion, we find that Type 1 and Type 2 AGN broadly show the same star-forming properties in terms of their dust masses, dust temperatures, and SFRs. We do find a small subset of Type 1 AGN that occur in very low star-forming systems

and nearly dustless galaxies that causes the total distribution of Type 1 AGN host galaxy properties to skew towards lower dust masses and SFRs. This could be an evolutionary effect, that after galaxies have been quenched, Type 1 AGN are more likely to occur given the lack of gas and dust available in the galaxy to form a strong torus and cause obscuration. Apart from this subsample, however, the main difference seen between Type 1 and Type 2 AGN is in $L_{\rm AGN,IR}$ and $f_{\rm AGN}$ where Type 2 AGN show lower values for both properties. This is caused by the preference for Type 2 AGN to be found in lower AGN luminosity systems which decreases both $L_{\rm AGN,IR}$ and $f_{\rm AGN}$ and produces more host galaxy dominated IR SEDs.

3.8.7 The Correlation Between SFR and AGN Luminosity

Our main goal in this Chapter is to assess the observational evidence for a connection between AGN and star formation in their host galaxy. To accomplish this, we analyze the correlation between the AGN strength and SFR. We assume the 14–195 keV luminosity ($L_{14-195\rm keV}$) linearly probes the bolometric AGN luminosity as shown by Winter et al. (2012). $L_{\rm SF}$ measures the SFR using Equation 3.16.

Figure 3.17 plots the correlation between the SFR and $L_{14-195\rm keV}$ for the *Herschel*-BAT AGN. Black points with error bars indicate all of our detected sources, while red arrows show 95 per cent confidence upper limits for objects with less four SED points. We determine parameters for the following linear model:

$$\log \mathrm{SFR} = m \log L_{14-195\,\rm keV} + b + \epsilon_{\rm int} \tag{3.17}$$

using LINMIX_ERR as before. The black line and grey shaded region in Figure 3.17 represents the best-fit line and 95 percent confidence interval. We find a best fitting $m = 0.18 \pm 0.07$, $b = -7.85 \pm 2.93$, and $\sigma^2 = 0.37 \pm .04$ with a correlation coefficient of only 0.17±.06, but is still significant at >99.9% level. We also split the sample into Type 1 and 2 samples to test if there is a difference. We find for Type 1 AGN$m = 0.34 \pm 0.13$, $b = -15 \pm 6$, and $\sigma^2 = 0.49 \pm .08$ with a correlation coefficient of 0.25±.09 and significance level >99.9%. For Type 2 AGN we find $m = 0.19 \pm 0.08$, $b = -8 \pm 3$, and $\sigma^2 = 0.26 \pm .04$ with a correlation coefficient of 0.21±.09 and significance level >99.9%. The Type 1 and Type 2 AGN SFR-AGN luminosity relations are also shown in Figure 3.17 as blue and red lines and shaded regions.

None of the three samples show a strong correlation between the SFR and 14–195 keV luminosity. With slopes between 0.18–0.34 and correlation coefficients between 0.17 and 0.25, even though they are inconsistent with 0, the evidence for a connection between the strength of the AGN and global star formation is fairly weak.

Type 1 AGN do show a slightly stronger correlation than the whole sample and Type 2 AGN which is consistent with our findings in Meléndez et al. (2014) and Shimizu et al. (2016) using the monochromatic *Herschel* luminosities. However, the significance of the differences are not more than 2σ therefore we must conclude that Type 1 AGN show a similar relationship between their SFR and 14–195 keV luminosity.

Our measured AGN-SFR relationship agrees mainly with the previous studies that found a flat or weak relationship (Azadi et al., 2015; Diamond-Stanic & Rieke,

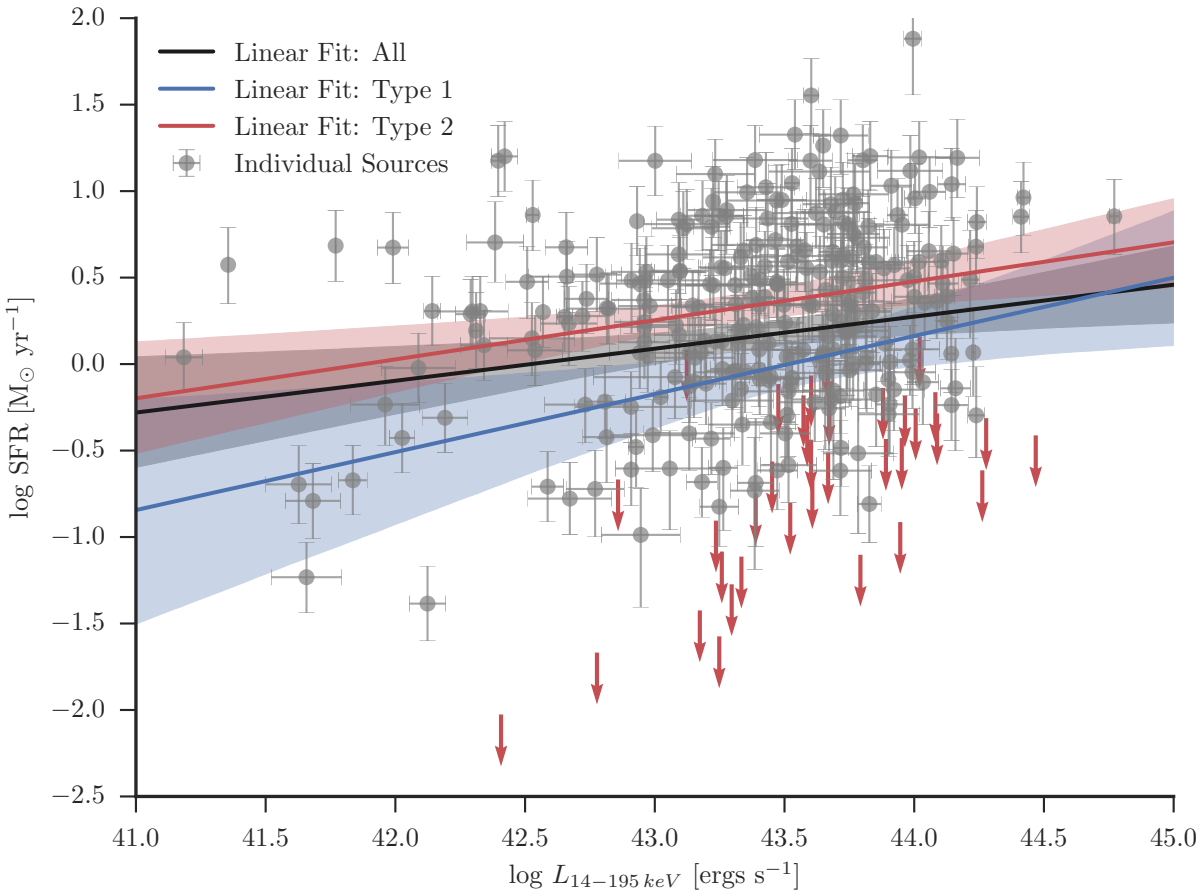

Figure 3.17: Correlation between AGN luminosity as probed by $L_{14-195\,\mathrm{keV}}$ and SFR. Error bars on $L_{14-195\,\mathrm{keV}}$ correspond to the 90 percentile confidence interval from the 58 month BAT catalogue. Error bars on the SFR correspond to the 68 percentile confidence interval from our SED fitting. Downward pointing red arrows plot 95 percent confidence upper limits on the SFR. The solid black line with shading plots the best fit line and 95 percentile confidence interval for our AGN-SFR relationship from LINMIX_ERR for the entire sample. The blue and red lines show the relationship for only Type 1 and Type 2 AGN respectively.

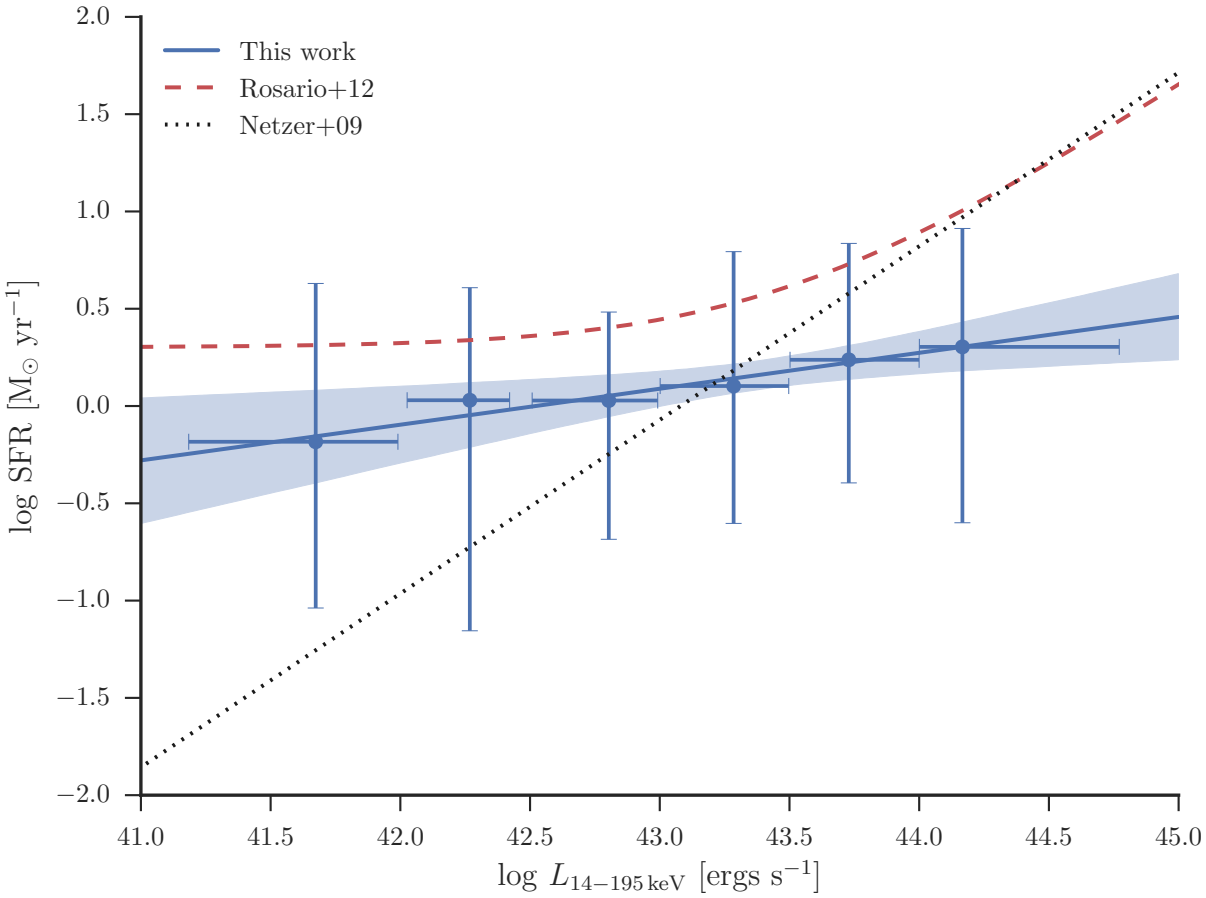

Figure 3.18: Comparison between the measured SFR-$L_{14-195\,\mathrm{keV}}$ from the *Herschel*-BAT sample (blue line with shaded region) and previous relationships from Netzer (2009) (dotted line) and Rosario et al. (2012) (red dashed line). The points with error bars are the median SFRs binned by $L_{14-195\,\mathrm{keV}}$ from the *Herschel*-BAT sample. Error bars represent the 68 per cent confidence interval.

2012; Mullaney et al., 2012a; Silverman et al., 2009; Stanley et al., 2015). The scatter in the relationship is high covering nearly 2 orders of magnitude in SFR for a given AGN luminosity. In Figure 3.18, we compare our correlation with previous measured relationships at low redshift from Rosario et al. (2012) (red dashed line) and Netzer (2009) (black dashed line). The blue points show the median log SFR in bins of 14–195 keV luminosity with error bars indicating the 16th and 84th percentiles.

Our correlation does not agree with either Rosario et al. (2012) or Netzer (2009) showing both a lower normalization, no upturn at high luminosities and a much flatter slope.The slope of the Netzer (2009) relationship is 0.8 which also coincides with the slope of the Rosario et al. (2012) relationship at high luminosities. Both studies, however, used the 60 μm luminosity as a measure of the SFR which we showed in Section 3.8.4 can be strongly influenced by the AGN. Netzer (2009) also chose to only measure the relationship in AGN-dominated objects leading to an even greater effect of the AGN contribution. Interestinly, Netzer (2009) also only used Type 2 AGN which we show to have a flatter relationship than Type 1 AGN, so a difference in Type 1 and Type 2 distribution between our samples cannot explain the strong linear relationship seen in Netzer (2009).

The upturn seen in the Rosario et al. (2012) relationship could be due to Malmquist bias. Even though their sample was based on the *Swift*/BAT AGN, no redshift cutoff was applied. Due to the flux-limited nature of the *Swift*/BAT catalogue, there is a strong selection bias where the highest luminosity objects are preferentially at high redshift which will introduce a correlation based on distance rather than an intrinsic one. Rosario et al. (2012) also only used *IRAS* detected

sources. The lower sensitivity of *IRAS* compared to *Herschel* can explain the reduced normalization we see. Combined with the work of Azadi et al. (2015) and Stanley et al. (2015), we can firmly say that for all redshifts including the local universe, individual SFRs are not related to the current AGN strength at moderate luminosities.

It is however still possible that our sample did not extend to high enough AGN luminosity to reveal a trend. While the upturn can be explained by Malmquist bias, it can also be explained by the lack quasars ($L_{\rm AGN} > 10^{46}$ ergs s^{-1}). The upper error bars on our binned points do still extend to the Rosario et al. (2012) relationship making the difference between our relationship and Rosario et al. (2012) only $\sim 1\sigma$ although the 95% confidence interval on our relationship clearly does not overlap with Rosario et al. (2012). Nevertheless, perhaps with more sources at higher AGN luminosity, an upturn could be revealed. The highest AGN luminosities are where we expect the AGN to have the greatest influence and the strongest link to current star formation as seen in merger simulations (e.g. Di Matteo et al., 2005). Treister et al. (2012) further showed that major mergers trigger only the most luminous AGN while moderate luminosity AGN seem to be triggered by secular process like disk instabilities.Therefore, perhaps the moderate luminosity AGN that comprise our sample is simply not probing the stage in an AGN host galaxy's lifetime where global star formation and nuclear activity are linked.

In terms of the weak relationship we observe, two different but not mutually exclusive explanations have been proposed to explain the lack of relationship seen between the strength of the AGN and SFR. Diamond-Stanic & Rieke (2012) suggest

that the AGN only influences star formation in the nuclear regions of galaxies and find that when restricting their measurements to only the inner 1kpc, a stronger relationship appears. Esquej et al. (2014), probing even smaller scales ($r < 100$ pc) using MIR interferometry, also found a nearly linear relationship between the nuclear SFR and SMBH accretion rate, and LaMassa et al. (2013), utilizing the fixed aperture of the SDSS fiber, found that only within 1.7 kpc a positive relationship between the SFR and accretion rate occurs. These are all in agreement with hydrodynamical simulations (Hopkins & Quataert, 2010; Thacker et al., 2014) that predict an increasingly linear relationship as the star formation size scale decreases. We are currently working on spatially decomposing the SFRs of the *Herschel*-BAT sample to determine whether the relationship strengthens near the nucleus.

The second explanation involves the varying timescales associated with star formation and accretion onto the SMBH. Measuring the SFR from the IR luminosity results in an average SFR over nearly 100 Myr (Kennicutt & Evans, 2012) while the X-ray luminosity is more aligned with the instantaneous AGN luminosity especially given the observations that the X-ray emission likely originates very near to the SMBH (e.g Chen et al., 2011). Therefore, if the AGN luminosity can vary over 100 Myr, while the SFR is relatively stable, this will cause any intrinsic relationship between the two to weaken. Hickox et al. (2014) explored this using a simple model for the Eddington ratio distribution for an AGN and a linear relationship between the AGN luminosity and SFR, finding that a powerlaw Schechter function matches the observed weak AGN-SFR relationship. However this was based on the upturns seen in the relationships from Rosario et al. (2012) which we clearly do not observe

suggesting that adjustments need to be made to conform with our observations.

Neither explanation however needs to invoke AGN feedback. An intrinsically positive correlation between the SFR and AGN luminosity, whether on small spatial scales or long timescales can simply be explained by the availability of their common fuel, namely cold gas. Large amounts of cold gas will spur both high accretion rates and high SFRs. Certainly observations that X-ray detected AGN lie below the star-forming main sequence Matsuoka et al. (2015); Mullaney et al. (2015); Shimizu et al. (2015) is suggestive that the AGN plays some role in quenching. AGN-driven outflows that are likely suppressing star formation have been observed in small samples (Cicone et al., 2014; Tombesi et al., 2015; Veilleux et al., 2013); but in a recent study of 50 nearby *Swift*/BAT AGN, Stone et al. (2016) found only four objects with evidence for a molecular outflow, strengthening the argument that AGN only contribute to driving gas out of the galaxy at high luminosity ($L_{\rm AGN} > 10^{45}$ ergs s^{-1}). Instead its equally possible that at least some of our galaxies are going through passive quenching, whereby gas is simply being slowly depleted through star-formation and star-formation driven outflows after accretion onto the galaxy has slowed or been shut off (Peng et al., 2015). This scenario agrees with the so-called "bathtub" model for galaxy evolution first proposed in Lilly et al. (2013). The fact we observe the majority of AGN host galaxies in transition would simply be a consequence that AGN activity is more likely in gas-rich galaxies (Vito et al., 2014) but there is a delay between the peak of star formation and accretion onto the SMBH (Davies et al., 2007; Schawinski et al., 2014). This is supported by our results that AGN have higher dust masses along with higher SFRs than mass-matched field

galaxies, assuming the dust-to-gas ratio is constant. On an individual galaxy basis, however, there does exist evidence that some form of AGN feedback is necessary. Even though (Peng et al., 2015) conclude that slow quenching is likely the dominant quenching mechanism, they note that to obtain the α-element enhancement observed in massive ellipticals, fast quenching must have occurred. They also suggest that AGN feedback could work in concert with slow quenching or even be the catalyst to jumpstart the quenching process.

It is clear then that situation is quite complicated. Because our sample is not extending to quasar luminosities, we might be missing the phase of an AGN's lifetime where the strongest link between star formation and AGN luminosity should exist. Further, the AGN influence might only work over small physical scales and AGN variability might be smearing any intrinsic relationship that exists. Future work will involve remedying two of these problems by combining our sample with low redshift quasar samples like the Palomar-Green quasar sample and utilizing the relatively high spatial resolution of the *Herschel* images to look for a connection at smaller scales.

3.9 Conclusions

Using our high quality *Herschel* photometry from Meléndez et al. (2014) and Shimizu et al. (2016) combined with archival *WISE* 12 and 22 μm photometry, we have constructed and modeled the SEDs for over 300 AGN. Our sample is unique given its nearly unbiased selection based on ultra-hard X-ray detection as well as its

local nature that eliminates possible biases and source confusion. The following is a summary of our results and conclusions.

1. After correcting for host galaxy contribution, we find a nearly linear correlation between the estimated 8–1000 μm luminosity due to the AGN and the 14–195 keV luminosity signifying our decompositions are accurate.

2. We determined relationships between various MIR and FIR colors as a proxy for the AGN contribution to the total 8–1000 μm luminosity ($f_{\rm AGN}$), finding that the 22/70 and 22/160 colors follow the best relationship with $f_{\rm AGN}$.

3. We investigated the AGN contribution to the 70 μm emission of a galaxy and showed that for nearly 30 per cent of our sample, more than half of the 70 μm flux is likely due to AGN heating.

4. We calculated a median dust mass of $10^{7.36}$ $M_\odot$, dust temperature of ~ 24 K, and SFR of 1.7 $M_\odot$ yr^{-1} for AGN host galaxies. In a comparison with a mass-matched sample of non-AGN, we find all three properties are systematically higher by a factor 2 for the dust mass, 2 K in dust temperature, and a factor of 3 in SFR. This can be explained as a consequence of high mass non-AGN samples largely being composed of quiescent early type galaxies.

5. Confident in our measures of the SFR, we find a nearly flat (slope = 0.18$\pm$0.07) relationship between the SFR and AGN luminosity, in agreement with previous studies at higher redshift. Our flat relationship is in contrast to previous low redshift studies that find either a nearly linear relationship or an upturn at

high luminosities. We suspect this is due to either AGN contamination or Malmquist bias. If nuclear activity is related to global star formation, it is only on long timescales, however another possible explanation is that the relationship strengthens only as the physical scales probed decrease.

It is abundantly clear now that AGN activity is not related to the global SFR as probed by the X-ray luminosity and FIR emission at least for moderate AGN luminosity host galaxies. It is currently unclear whether at the highest AGN luminosities (i.e. the quasar regime) a correlation exists when the AGN would have the largest influence on the galaxy. We are working to determine whether spatial decomposition combined with our SED decomposition can illuminate the exact nature of the relationship between the AGN and nuclear star formation. This will also further test our simple decomposition methods and help expand our knowledge of the intrinsic AGN infrared SED into the FIR regime.

Chapter 4: Decreased Specific Star Formation Rates in AGN Host Galaxies

4.1 Introduction

The link between supermassive black holes (SMBH) and their host galaxies has been evident for many years through the study of correlations between large scale host galaxy properties and SMBH mass. Tight correlations were found with bulge stellar velocity dispersion (Ferrarese & Merritt, 2000; Gebhardt et al., 2000; Gültekin et al., 2009), bulge luminosity (e.g. Magorrian et al., 1998), and bulge mass (Häring & Rix, 2004; Kormendy & Richstone, 1995; Marconi & Hunt, 2003) suggesting a coevolution of the SMBH with the host galaxy. The question that remains however is how two seemingly disjoined objects can influence each other over an extremely large range of physical scales. Using a simple estimate of the sphere of influence for a SMBH ($r_{sph} = GM/\sigma^2$; Peebles (1972)) and a typical SMBH mass of $10^8 M_\odot$ and stellar velocity dispersion, $\sigma = 200$ km s^{-1}, $r_{sph} \sim 10$ pc whereas the size of the bulge is roughly several kpc (e.g. Simard et al., 2011). Therefore any influence from the SMBH must be able to extend over 3 orders of magnitude in physical scale.

Active galactic nuclei (AGN), the phase where the SMBH is vigorously accret-

ing material and growing, are thought to supply the necessary energy to influence the galaxy on large scales (e.g. Silk & Rees, 1998). This leads to a feedback cycle wherein the galaxy supplies cold gas that ignites the AGN and fuels star formation, and the AGN then returns energy and/or momentum to the galaxy that shuts off both accretion and star formation. The explicit feedback mechanism that runs this cycle is currently not well understood but is thought to be either large scale outflows (Cimatti et al., 2013; Harrison et al., 2014; Kaviraj et al., 2011; Veilleux et al., 2013) or radio jets Best (2007); Dubois et al. (2013)(for a review see Fabian, 2012). Theoretical simulations have also shown that adding AGN feedback reproduces well the observed mass and luminosity functions while an absence produces too many blue, high mass galaxies (e.g. Croton et al., 2006).

Early evidence for the quenching of star formation due to AGN came from studying the colors and stellar masses of large samples of both non-AGN and AGN host galaxies. Whereas the non-AGN sample clearly separates into two populations on a color-magnitude or color-mass diagram, one with red colors (i.e. red sequence thought to be quiescent galaxies) and one with blue (i.e. blue cloud thought to be strongly star-forming galaxies) (Strateva et al., 2001), AGN host galaxies were found to be concentrated between them, displaying "green" colors (e.g Hickox et al., 2009; Nandra et al., 2007; Silverman et al., 2008). Initially, this was interpreted as AGN preferentially occurring in galaxies that have had their star formation recently quenched (Martin et al., 2007; Salim et al., 2007; Schawinski et al., 2009) and are in transition from the blue cloud to the red sequence. Optical colors, however, can be imprecise tracers of star formation, especially in the presence of strong intrinsic dust

absorption (e.g. Cardamone et al., 2010) that obscures recent star formation and causes a reddening of the colors that is not due to a reduction of star-formation. Green colors can also just be an indication of a mixture of old and new stellar populations and not necessarily a "transition" between the two population. Further, recent studies that mass-match non-AGN galaxy samples to AGN host galaxies reveal that the difference in optical colors virtually disappear (Pierce et al., 2010; Rosario et al., 2013a,b; Silverman et al., 2009)

Far-infrared (FIR) emission ($\lambda > 40$ μm) is essentially immune to reddening effects while also being a direct tracer of recent star formation. Dust in the galaxy is heated by UV photons from recently formed OB stars, that then reemit in the mid-far infrared regime (Draine, 2003) creating a strong correlation between the FIR luminosity and SFR of a galaxy (Kennicutt & Evans, 2012; Kennicutt, 1998). Furthermore, AGN are not thought to strongly affect the FIR (e.g. Netzer et al., 2007), and thus the FIR is more robust compared to other SFR indicators such as UV continuum and Hα line emission that are mainly used in non-AGN galaxy studies.

The *Herschel Space Observatory* (Pilbratt et al., 2010) opened a window into the FIR universe with the unprecedented sensitivity of both the Photodetector Array Camera and Spectrometer (PACS; Poglitsch et al. (2010)) and Spectral and Photometric Imaging Receiver (SPIRE; Griffin et al. (2010)) instrument extending the broad band spectral energy distributions out to 500 μm and allowing an accurate estimate of the FIR luminosity of more objects than allowed by previous FIR telescopes (i.e. *Infrared Astronomical Satellite (IRAS)*; Neugebauer et al. (1984)).

In this study we utilize *Herschel* to measure the SFRs of a large and relatively unbiased sample of AGN and compare their location on the SFR-stellar mass ($M_{\rm star}$) diagram with that of the general star-forming galaxy population, which forms a "main sequence".

The main sequence is the observed tight correlation between the stellar mass and SFR of a normal star-forming galaxy and has been confirmed in depth by many studies (e.g. Brinchmann et al., 2004; Elbaz et al., 2007, 2011; Magnelli et al., 2014; Noeske et al., 2007; Rodighiero et al., 2010; Whitaker et al., 2012). This correlation seems to exist up to at least $z \sim 2$ (e.g. Elbaz et al., 2011; Whitaker et al., 2012) and possibly all the way to $z \sim 4$ (Bouwens et al., 2012; Heinis et al., 2014), with only the normalization changing as a function of redshift, shifting to higher SFRs at earlier epochs. This discovery has changed theories of galaxy evolution from one that is merger-driven to one that is driven more by internal secular processes. Elbaz et al. (2011) showed that galaxies that live above the main sequence are much more compact with a higher SFR surface density, indicative of a major merger. Main sequence galaxies, though, have disk-like morphologies inconsistent with a recent merger (Wuyts et al., 2011) that suggests star formation is triggered by internal processes such as disk instabilities.

In the past, the question of where AGN fit into the picture was unclear because most main sequence studies purposely excluded AGN due to its messy contribution to SFR indicators. However, with *Herschel*, more accurate estimates of the SFRs for AGN host galaxies can be calculated as well as better detection rates. For example, both Mullaney et al. (2012b) and Rosario et al. (2013a), using deep observations of

large fields examined the star-forming properties of X-ray selected AGN. Both came to the conclusion that AGN primarily reside in main sequence galaxies, calling into question the long-held idea that AGN host galaxies are in the process of quenching star formation. If most AGN are in main sequence galaxies, this could indicate that moderate luminosity AGN are simply coincidental with a large cold gas reservoir that also fuels star formation (Vito et al., 2014).

In this Chapter, we seek to fully investigate the location of AGN on the SFR-$M_{\rm star}$ plane using *Herschel* observations of *Swift*/BAT selected AGN. These are ultra-hard X-ray confirmed AGN at low redshift using a selection method that is unbiased with respect to both obscuration and host galaxy contamination. We calculate SFRs using *Herschel* photometry and a simple model to disentangle star formation and AGN contributions and combine them with estimates of the stellar mass using AGN subtracted SDSS photometry from Koss et al. (2011). The SFRs and $M_{\rm star}$'s are then compared to a local normal star-forming galaxy sample to define the main sequence as well as a sample of galaxies purely selected on stellar mass. Finally we discuss the implications of our results and compare them to previous studies. Throughout this Chapter we use a ΛCDM cosmology with $H_0 = 70 {\rm km\,s^{-1}\,Mpc^2}$, $\Omega_m = 0.3$, and $\Omega_\Lambda = 0.7$. Luminosity distances were calculated using this cosmology along with redshifts taken mainly from the *NASA/IPAC* Extragalactic Database (NED)[1], except for those objects with $z < 0.01$ where we used measured distances from the Extragalactic Distance Database[2]. We either use

[1] http://ned.ipac.caltech.edu/

[2] http://edd.ifa.hawaii.edu/

or correct for a Chabrier or Kroupa initial mass function (IMF) for all star formation rate calculations.

4.2 Samples and Observations

4.2.1 *Swift*/BAT AGN

Our parent sample of AGN was drawn from the 58 month *Swift* Burst Alert Telescope (BAT) (Barthelmy et al., 2005; Gehrels et al., 2004) catalog (Baumgartner et al., 2013) with a redshift cutoff of $z < 0.05$, totaling 313 AGN (149 Seyfert 1-1.5s, 157 Seyfert 1.8-2s, 6 LINERs, and 1 unidentified AGN). The catalog is the result of continuous monitoring by *Swift*/BAT of the entire sky in the 14–195 keV energy range. These high energies allow for an unambiguous detection of AGN with little to no contamination from the host galaxy and significantly reduced selection effects due to obscuration.

All 313 AGN were observed by the *Herschel Space Observatory* with 291 part of our program (PI: R. Mushotzky, PID: OT1_rmushotz_1) and the remaining 22 obtained from other programs publicly available on the *Herschel* Science Archive. The sample was imaged by both the PACS and SPIRE instruments providing, for the first time, sensitive FIR photometry from 70–500 μm for a large, ultra-hard X-ray selected sample of AGN. Detailed descriptions of the reduction and analysis of the PACS and SPIRE images are given in Meléndez et al. (2014) and Shimizu et al (2015, in preparation), but we provide a brief summary here.

PACS and SPIRE together imaged the sample in 5 broad bands: 70 and 160

μm (PACS) and 250, 350, and 500 μm (SPIRE). Level 0 (raw) data were reduced to Level 1 using the standard pipeline provided by the *Herschel* Interactive Processing Environment (Ott, 2010) v8.0. Maps were produced from the Level 1 data using *Scanamorphos* (Roussel, 2013) v19.0, a software package that takes advantage of the redundancy inherent in the scanning procedure of *Herschel* to remove both thermal and non-thermal low-frequency noise. Circular and elliptical apertures with radii chosen visually to encompass the entirety of the FIR emission were then used to extract the photometry for each waveband. 1σ errors for the photometry were determined using a combination of the pixel-by-pixel errors in the aperture, an estimate of the root-mean-square of the background, and calibration uncertainty.

In addition to *Herschel* observations, Koss et al. (2011) analyzed optical images of 185 BAT AGN from the *Sloan Digital Sky Survey* (SDSS) and Kitt Peak National Observatory. Using GALFIT (Peng et al., 2002), they were able to accurately measure the host galaxy light by subtracting out the central point source due to the AGN. Reliable stellar masses for the BAT AGN host galaxies were then estimated using standard stellar population models. Because the Koss et al. (2011) BAT sample was chosen from the 22 month catalog (Tueller et al., 2010), 45/185 were not observed with *Herschel*, reducing the sample to 140 AGN. Furthermore, Koss et al. (2011) flagged 18/140 objects for incomplete PSF-subtraction from the *griz* images, so we choose not to include these sources resulting in a final sample of 122 AGN, including 46 Sy 1s, 72 Sy 2s, and 4 LINERs, where we define a Sy 1 as Sy 1-1.5 and Sy 2 as Sy 1.8-2. The reason for the discrepancy between the number of Sy 1s and Sy 2s is that all 18 of the objects that were flagged for incomplete

PSF-subtraction are Sy 1s.

4.2.2 *Herschel* Reference Survey

To form the main sequence, we need a large and complete sample of star-forming galaxies that do not host an AGN but have been observed at the same wavelengths allowing for a consistent determination of both the SFR and stellar mass. For these reasons we chose the *Herschel Reference Survey* (HRS; Boselli et al. (2010b)), a guaranteed time *Herschel* key project that imaged 323 K-band selected galaxies from 100–500 μm. The HRS spans all morphological types and was volume limited to contain galaxies between 15 and 25 Mpc away. Even though our sample stretches out to $z = 0.05$ ($\sim$200 Mpc), the HRS represents the best sample of local star-forming galaxies to compare with given that both have been observed by *Herschel* as well as other telescopes including the *Wide-Field Infrared Survey Explorer* (Wright et al., 2010, WISE), the *Galaxy Evolution Explorer* (GALEX Martin et al., 2005), and *SDSS*.

The HRS PACS and SPIRE images were analyzed in Cortese et al. (2014) and Ciesla et al. (2012) producing photometry at 100, 160, 250, 350, and 500 μm. We applied the same corrections to the SPIRE photometry as described in Cortese et al. (2014) due to changes in the SPIRE calibration and beam size. The corrections reduce the SPIRE flux densities by 7, 6, and 9 per cent at 250, 350, and 500 μm respectively.

A subset of the HRS are galaxies within the Virgo Cluster and have been

affected by the dense environment through the stripping of their gas (Boselli et al., 2006). The dust content of these galaxies has also been shown to be affected by the environment (Cortese et al., 2010, 2012a). Therefore, following Ciesla et al. (2014b), we restrict the HRS sample to only those galaxies that aren't "HI-deficient" as defined in Boselli et al. (2012) which reduces the sample to 146 galaxies.

4.2.3 COLD GASS

While the HRS represents a sample that was observed using the same telescopes, it is limited in its range of stellar mass especially above $10^{10} M_{\odot}$. For a complete comparison to the BAT AGN, we supplemented HRS with the *CO Legacy Database for GASS* (COLD GASS; Saintonge et al., 2011a), a 366 galaxy subsample of the *GALEX Arecibo SDSS Survey* (GASS; Catinella et al., 2010). The GASS sample consists of ∼1000 galaxies randomly selected such that every galaxy lies within the footprint of the SDSS spectroscopic survey, the ALFALFA survey, and the *GALEX* Medium Imaging Survey. The galaxies also were selected to have a redshift range $0.025 < z < 0.05$ and a stellar mass between 10^{10} and $10^{11.5}$, both of which match very well to the BAT AGN. 366 galaxies were randomly selected from GASS to form the COLD GASS sample and have deep CO(1–0) imaging with IRAM. COLD GASS then represents a completely unbiased sample of galaxies above $10^{10} M_{\odot}$.

As described in Catinella et al. (2010) and Saintonge et al. (2011a), both GASS and COLD GASS were selected to have a uniform $\log M_{\rm star}$ distribution. The stellar

mass distribution that is observed, however, is more heavily weighted towards lower mass galaxies (see Figure 1 of Saintonge et al. (2011a)). Therefore, Saintonge et al. (2011a) constructed 50 representative subsamples of COLD GASS that matches the observed $M_{\rm star}$ distribution. Each subsample contains between 200-260 galaxies and can be used to test the robustness of any relation that might be observed. Throughout this Chapter, we explicitly note whether the full COLD GASS sample, an average of the representative subsamples, or a single representative subsample is being used.

Because COLD GASS was selected in an unbiased way, the sample contains a mixture of galaxy types from star-forming to quiescent to AGN. To determine the type of each galaxy in COLD GASS, we cross-matched the sample with the MPA-JHU SDSS DR7 spectroscopic catalog.[3] In this catalog, galaxies that have SDSS optical spectra were classified according to their location on the standard BPT diagram (Baldwin et al., 1981). Brinchmann et al. (2004) describes the details of the classification[4]. Galaxies were separated into 6 groups: Star-forming, Low S/N Star-forming, AGN, Composite, LINER, and Quiescent. For the purposes of comparison with the BAT AGN, we combined the Star-forming and Low S/N Star-forming groups into a single Star-forming group and the AGN and Composite

[3] http://www.mpa-garching.mpg.de/SDSS/DR7/ and http://home.strw.leidenuniv.nl/~jarle/SDSS/

[4] We note that Saintonge et al. (2012) used a more conservative method to classify AGN in the COLD GASS. A galaxy was considered an AGN if $\log[\mathrm{NII}/\mathrm{H}\alpha] > -0.22$ and $\log[\mathrm{OIII}/\mathrm{H}\beta] > 0.48$. This led to a much lower fraction of AGN in their analysis (6 per cent) compared to this work (30 per cent).

groups into a single AGN+Composite group. We combine the AGN and Composite group because after cross-matching the BAT AGN with the same SDSS DR7 sample, we find that almost all are classified as an AGN or Composite galaxy. The COLD GASS AGN+Composite subsample then represents an ideal optically selected sample of AGN to compare with the BAT AGN, while the Star-forming and Quiescent sample represent ideal non-AGN samples. We denote the different subsamples in the following way: Star-forming as CGS, AGN+Composite as CGA, LINERs as CGL, and Quiescent as CGQ.

4.2.4 *Herschel* Stripe 82 Survey

With the HRS and COLD GASS samples we have one that matches the photometry available to the BAT AGN (HRS) and one that more closely matches the physical properties of the BAT AGN host galaxies (COLD GASS). HRS lacks galaxies at the high stellar mass of the BAT AGN whereas COLD GASS lacks *Herschel* and *WISE* photometry to allow for a consistent comparison between SFRs. Therefore, we use a third comparison sample to the BAT AGN, the *Herschel* Stripe 82 survey (HerS; Viero et al., 2014)that bridges the gap between HRS and COLD GASS.

HerS is a 79 deg^2 survey of SDSS Stripe 82 with *Herschel*/SPIRE at 250, 350, and 500 μm. Viero et al. (2014) produced the catalog of HerS sources while Rosario et al (2015, in preparation) calculated SFRs based on FIR luminosities. Given its small area, the volume covered at low redshift is smaller than that of both

the COLDGASS and BAT samples which means HerS is rather incomplete at high stellar masses ($> 10.5 M_{\odot}$). However it is still better than the HRS and has *Herschel* photometry available, albeit only from the SPIRE instrument.

We selected our HerS sample from Rosario et al (2015, in preparation), who matched HerS sources from Viero et al. (2014) with the SDSS MPA-JHU DR7 catalog. Because the HerS catalog assumes all galaxies are point sources, Rosario et al (2015, in preparation) limited their sample to $z > 0.02$. We further limit the sample to $z < 0.08$ to match the BAT AGN while also pushing out to a slightly larger volume to populate the high mass end better without a significantly affecting our results. After cutting sources which do not have a measured stellar mass as well as sources with low S/N (< 3) emission lines (only 5 objects) this results in a final HerS sample of 517 objects. Due to the combined magnitude cut from the SDSS and the limited sensitivity of SPIRE from which the HerS catalog was built, Malmquist bias can be a problem. However, because of the relatively low redshift nature of our sample we do not expect it to largely bias our results.

The HerS sample was also split into some of the same classifications as COLDGASS using the BPT diagram. HerS contains both a star-forming and AGN population and will be designated as HerS SF and HerS AGN. The HerS AGN, just as CGA, is a combination of the AGN and Composite classifications. Within HerS, there is also an Uncertain classification which indicates a galaxy that is missing or has upper limits for at least one of the 4 key lines needed to classify it using the BPT diagram.

4.3 Star Formation Rate Estimation

The unique *Herschel* data provides a means for determining accurate star formation rates (SFR). IR emission has long been used as a calibrator for star formation (see Kennicutt, 1998, for a review), because it probes the dust population that reprocesses the UV emission from young stars (e.g. Draine, 2003). The specific wavelength range of *Herschel* covers the bulk of the IR emission from dust including the characteristic FIR bump typically seen in star-forming galaxies (e.g. Dale et al., 2007) allowing for precise measures of the total IR luminosity and thus the star formation rate, especially for AGN host galaxies where many of the often used SFR indicators (e.g. Hα, UV continuum) can be substantially contaminated by AGN-related emission.

Many SED-fitting packages exist in the literature ranging from template based models to full dust radiative transfer models. However, given the low number of data points for our SEDs (at most seven), we chose to fit our SEDs with the model described in Casey (2012), which is a combination of an exponentially cutoff mid-infrared (MIR) power law and a single temperature greybody. Details and results of the SED fitting for the BAT AGN are in Chapter 3. In Section 4.6.1 we discuss extensively and test whether this model introduces systematic biases especially related to the decomposition of the SED.

The *Herschel* photometry constrains the greybody component, but we need additional shorter wavelength data to constrain the power law component. Therefore, we cross-correlated our sample with the *Wide-field Infrared Survey Explorer*

(Wright et al., 2010, *WISE*) All-Sky Release Catalog on the IRSA website.[5] We only use the 12 (W3) and 22 (W4) μm photometry to avoid contamination by the stellar population in the host galaxy. *WISE* photometry for the HRS were taken from Ciesla et al. (2014b).

For consistency, we fit both the BAT AGN and HRS galaxies using the Casey (2012) model even though the HRS galaxies do not host an AGN or are classified as ULIRGs. In this way, we can account for a portion of MIR emission that is due to normal star formation rather than AGN heated dust. We fit all BAT AGN and HRS galaxies with at least four detected photometric points. This restriction ensures quality photometry for each galaxy and removes only a further 9 and 11 galaxies from the BAT AGN and HRS sample respectively for final sample sizes of 113 and 135. We determine three luminosities for each galaxy: a total IR luminosity ($L_{\rm TIR}$), a MIR power law luminosity ($L_{\rm MIR}$) and a greybody luminosity ($L_{\rm Grey}$). Each one was calculated by integrating the best-fitting model from 8–1000 μm. $L_{\rm TIR}$ is the luminosity from integrating over the total model while $L_{\rm MIR}$ is from only integrating the MIR power law component, and $L_{\rm Grey}$ is from the greybody component.

Star formation rates are then calculated using one of these IR luminosities and the equation from Murphy et al. (2011).

$$\mathrm{SFR_{IR}} = \frac{\mathrm{L_{IR}\ [erg\ s^{-1}]}}{2.57 \times 10^{43}} \tag{4.1}$$

For the HRS galaxies $L_{\rm IR} = L_{\rm TIR}$ since there is no AGN to contribute to the IR emission. For the BAT AGN, however, we use $L_{\rm IR} = 4/3 L_{\rm Grey}$. The 4/3 is a

[5] http://irsa.ipac.caltech.edu/Missions/wise.html

correction factor to account for MIR emission from star formation. To determine it, we calculated the average ratio of $L_{\rm MIR}/L_{\rm Grey}$ for the HRS sample, which contain no AGN, and found it to be narrowly distributed around 1/3. This means that only using $L_{\rm Grey}$ to determine the SFR underestimates it by 1/3 so we need to multiply $L_{\rm Grey}$ by 4/3 as a correction.

While FIR emission probes dust obscured star formation, the UV continuum is a measure of unobscured star formation by tracing the direct light from young massive stars. Hence, a complete census of star formation can be found by combining measurements from both wavebands. AGN are strong emitters in the UV though, so only Seyfert 2 galaxies will have reliable UV photometry to combine with the FIR for a SFR. Using *GALEX* far-UV data from the GCAT catalog (Bianchi et al., 2014) for the BAT AGN Seyfert 2's and the same from Boselli et al. (2013) for the HRS, we calculated dust-corrected UV SFRs. We found that using UV SFRs for both the HRS and BAT AGN Seyfert 2s had no effect on the results of this Chapter. Thus, we choose to use the FIR only SFRs to allow a larger BAT AGN sample (Seyfert 1's and 2's).

The COLD GASS sample unfortunately was not observed with *Herschel* and does not allow for the same calculation of the SFR. We use the SFRs provided in Saintonge et al. (2011b) which were calculated by fitting SDSS and *GALEX* photometry to Bruzual & Charlot (2003) models. Saintonge et al. (2011b) compared these SFRs to those inferred from combined *GALEX* FUV and *Spitzer* 70 μm data finding a strong correlation with only a scatter of 0.22 dex and indicating FIR-based SFRs are consistent with optical-UV ones. We recognize that the Saintonge

et al. (2011b) comparison however did not use any *Herschel* photometry, but three calibration analyses[6][7][8] show that *Spitzer* and *Herschel* produce consistent fluxes. Further Domínguez Sánchez et al. (2014) recently showed that SFRs calculated from FIR SED fitting are consistent (with large scatter especially for pure AGN and quiescent galaxies) with the SFRs inferred from the MPA-JHU SDSS spectral analysis. Based on all these indirect tests, we are confident that the COLD GASS SFRs are consistent with the SFRs based on *Herschel* we use for the HRS and BAT AGN in a way that does not effect the results of this Chapter.

For the HerS sample, the SFRs were estimated by fitting the SPIRE 250 μm and *WISE* 22 μm fluxes to the Dale & Helou (2002) (DH02) templates. Each of the 64 templates represents a different value of α where α is the power law index for the distribution of dust mass over heating intensity in a galaxy. χ^2 minimization was used to scale each of the 64 templates to the observed fluxes in the HerS sample, then the template with the lowest χ^2 was chosen as the best fit. The best-fit template was integrated between 8–1000 μm to calculate $L_{\rm IR}$ and converted to a SFR using the SFR–L_{IR} relation from Kennicutt (1998) adjusted for a Chabrier IMF (lowered by a factor of 1.7). In the absence of *WISE* 22 μm photometry, α was fixed at -2.0.

This is a slightly different method than the one used for the HRS and BAT AGN. To test for systematics we fit the HRS galaxies with 250 μm and 22 μm

[6] http://herschel.esac.esa.int/twiki/pub/Public/PacsCalibrationWeb/ExtSrcPhotom.pdf

[7] http://herschel.esac.esa.int/twiki/bin/viewfile/Public/PacsCalibrationWeb?rev=1;filename=PICC-NHSC-TN-029.pdf

[8] https://nhscsci.ipac.caltech.edu/pacs/docs/Photometer/PICC-NHSC-TR-034.pdf

detections using the DH02 method and compared the SFRs. A linear fit to the two SFRs reveals a slope of 1.0 and an offset of 0.11 dex with the SFRs determined from the Casey (2012) and Equation 4.1 higher than the ones from DH02 and the relation from Kennicutt (1998). Therefore we adjust all of the HerS SFRs by adding a constant of 0.11 dex.

4.4 Stellar Mass Estimates

SFRs are only one-half of the main sequence; stellar masses are also needed for the galaxies. Cortese et al. (2012b) calculated the stellar masses of the HRS using the relation from Zibetti et al. (2009):

$$\log(M_*/L_i) = -0.963 + 1.032(g - i) \tag{4.2}$$

where M_* is the stellar mass and L_i is the i-band luminosity, both in solar units. To be consistent we also used this equation for the BAT AGN. The $g - i$ color was calculated using the PSF-subtracted photometry from Koss et al. (2011). The stellar masses determined here correlate very well with the stellar masses from Koss et al. (2011) with a Pearson correlation coefficient, $r_{\rm P} = 0.85$ indicating a highly linear relationship. However the Koss et al. (2011) values are systematically larger by a factor of ~ 2[9] Since the goal of this Chapter is to compare AGN with nor-

[9]This is most likely due to the different stellar population models used in Zibetti et al. (2009). They used the 2007 version of the Bruzual & Charlot (2003) models that included a new presciption for thermally pulsing AGB stars. This decreases the stellar mass by a factor of 2 especially for star-forming galaxies. This has no effect on our results as long as all samples are on the same stellar mass scale.

mal star-forming galaxies and not absolute measures of stellar mass and SFR, we choose to use Equation 4.2 for the BAT AGN stellar masses. We performed the same calculation for the COLD GASS galaxies and compared these $M_{\rm star}$ with those provided in Saintonge et al. (2011b). We find the same strong correlation and the same systematic offset as the BAT AGN stellar masses so we choose to also use the stellar masses calculated in this Chapter for COLD GASS as well. The HerS stellar masses are taken from the MPA-JHU database which used the same method as both Koss et al. (2011) and Saintonge et al. (2011b). However, we do not have g or i photometry for HerS so we apply a factor of 2 correction to them to match the stellar mass scale from Equation 4.2.

4.5 Results

4.5.1 Location of AGN in SFR-M_* Plane

One key issue in this analysis is which main sequence to use. Many authors have published main sequence relations (for a nice compilation see: Speagle et al., 2014), however each relation was determined differently using different stellar mass estimates, SFR indicators, and redshift ranges. This has resulted in a large spread of values for both the slope and normalization of the main sequence, especially in the local universe. Therefore, we choose to calculate our own main sequence relation using only the HRS galaxies and the HerS star-forming galaxies since both the stellar masses and SFRs were calculated with comparable methods as for the BAT AGN. We use a linear bisector (Isobe et al., 1990) to fit the HRS+HerS data, resulting in

the following equation:

$$\log(\mathrm{SFR_{IR}}) = 1.01\log(\mathrm{M_*}) - 9.87 \tag{4.3}$$

The scatter of the relation is 0.36 dex, similar to the scatter seen in other studies (e.g Noeske et al., 2007; Peng et al., 2010). The slope and the normalization are slightly steeper and smaller respectively than that found in Peng et al. (2010), who analyzed the SFRs and stellar masses of the entire local ($0.02 < z < 0.085$) SDSS population. The slope is much steeper than the $z = 0$ slope predicted using the Speagle et al. (2014) relation (0.5). This is possibly due to the addition of lower mass objects from HRS as well differences in the measurement of the SFR and M_{star}. Further, due to the large scatter in MS relations measured at low redshift, Speagle et al. (2014) specifically did not include low redshift studies in formulating their redshft-dependent MS relation. This is the reason we set out to formulate our own main sequence relation that uses a well-defined star-forming galaxy sample and measures of the SFR and stellar mass that are consistent between the non-AGN and AGN host galaxy samples.

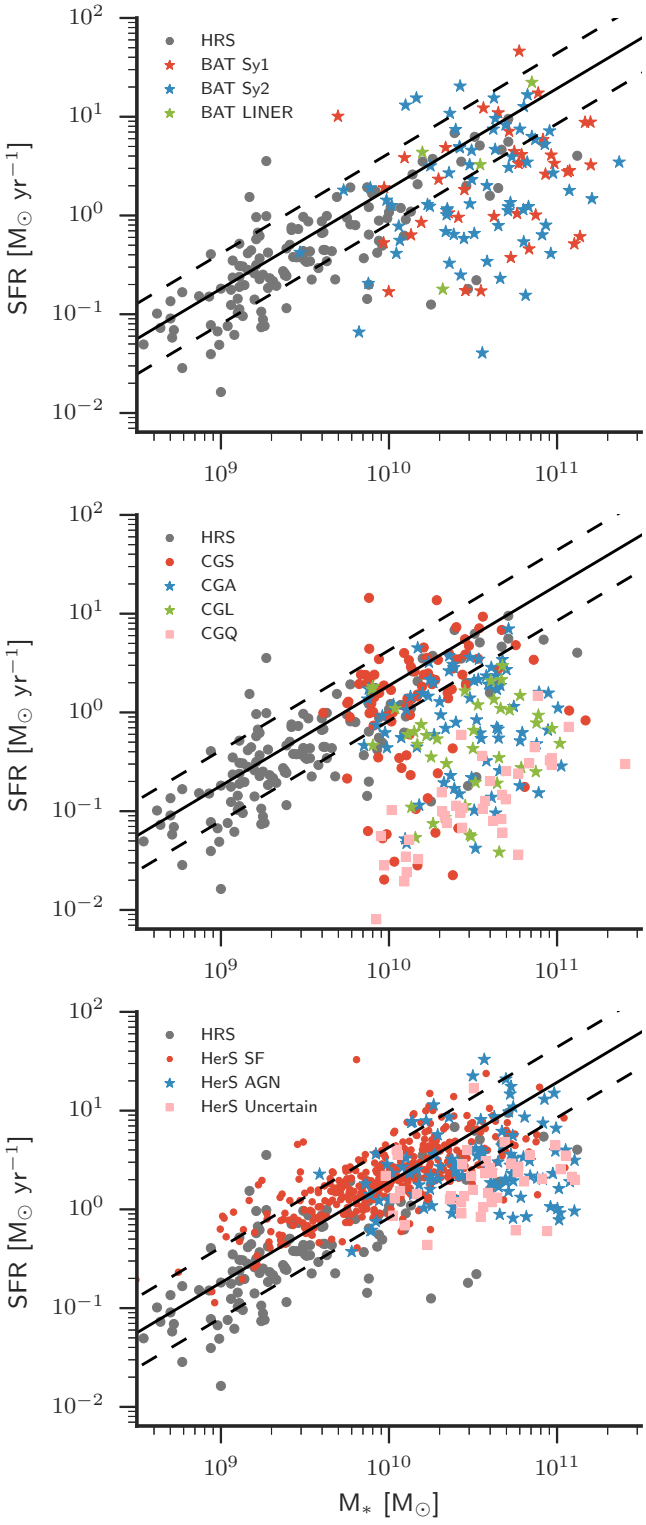

Figure 4.1: The relationship between SFR and M_* for the HRS (black dots), BAT AGN (*top:* colored stars), a representative subsample of COLD GASS (*middle:* colored symbols), and the HerS sample (*bottom:* colored symbols). The solid line represents the main sequence relationship calculated using the IR-based HRS+HerS SFRs (Equation 4.3). The dashed lines are the measured 1σ (0.32 dex) scatter in the relationship.

Table 4.1: Location of BAT AGN and COLD GASS Relative to the Main Sequence

Sample	Total	Above MS	Inside MS	$1-2\sigma$ Below	$2-3\sigma$ Below	$>3\sigma$ Below
(1)	(2)	(3)	(4)	(5)	(6)	(7)
BAT AGN						
All	...	0.05	0.28	0.28	0.18	0.20
Sy 1	0.35	0.05	0.20	0.35	0.20	0.20
Sy 2	0.61	0.06	0.30	0.26	0.17	0.20
LINER	0.04	0.00	0.75	0.00	0.00	0.25
COLD GASS (CG)						
All	...	0.02	0.33	0.15	0.12	0.39
Star-Forming (CGS)	0.37	0.04	0.62	0.12	0.05	0.16
AGN+Comps (CGA)	0.30	0.02	0.28	0.23	0.15	0.34
LINER (CGL)	0.17	0.00	0.07	0.18	0.25	0.50
Quiescent	0.15	0.00	0.00	0.00	0.03	0.97
***Herschel* Stripe 82 (HerS)**						
All	...	0.12	0.67	0.14	0.05	0.02
Star-Forming	0.72	0.14	0.78	0.07	0.01	0.00
AGN+Comps	0.19	0.08	0.48	0.25	0.10	0.09
Uncertain	0.08	0.02	0.21	0.42	0.28	0.07

Notes (1) Sample and subsample names for the BAT AGN and COLD GASS. (2) Fraction of the total sample (i.e. BAT AGN and COLD GASS) that each subsample occupies. (3) Fraction of sample that is above the main sequence (MS) ($\Delta \log \mathrm{SFR} > 1\sigma$; $\sigma = 0.32$ dex). (4) Fraction of sample that is inside the MS ($1\sigma > \Delta \log \mathrm{SFR} > -1\sigma$). (5) Fraction of sample that is between 1σ and 2σ below the MS ($-1\sigma > \Delta \log \mathrm{SFR} > -2\sigma$). (6) Fraction of sample that is between 2σ and 3σ below the MS ($-2\sigma > \Delta \log \mathrm{SFR} > -3\sigma$). (7) Fraction of sample that is greater than 3σ below the MS ($\Delta \log \mathrm{SFR} < -3\sigma$). The COLD GASS fractions represent the average fractions over all 50 representative subsamples. Due to round-off errors, the sums across each row are not exactly equal to 1.

Figure 4.1 plots the HRS, BAT AGN, a randomly chosen representative subsample of COLD GASS, and the HerS sample on the SFR-$M_{\rm star}$ plane along with Equation 4.3 and its scatter. Visually it is clear that a large fraction of the BAT AGN and COLD GASS lie either inside or below the MS. Table 4.1 quantifies the exact fraction of galaxies in five different regions. The different regions are divided according to $\Delta \log {\rm SFR} = \log {\rm SFR}_{\rm obs} - \log {\rm SFR}_{\rm MS}$ where ${\rm SFR}_{\rm obs}$ is ${\rm SFR}_{\rm IR}$ and ${\rm SFR}_{\rm MS}$ is the SFR expected given the M_* of the galaxy using Equation 4.3. $\Delta \log {\rm SFR}$ represents the distance a source is from the main sequence and given the nearly linear MS relation is proportional to specific SFR (sSFR = SFR/$M_{\rm star}$). The five regions are defined as: above the main sequence ($\Delta \log {\rm SFR} > 1\sigma$), inside the main sequence ($1\sigma > \Delta \log {\rm SFR} > -1\sigma$), 1–2$\sigma$ below the main sequence ($-1\sigma > \Delta \log {\rm SFR} > -2\sigma$), 2–3$\sigma$ below the main sequence ($-2\sigma > \Delta \log {\rm SFR} > -3\sigma$), and 3$\sigma$ below the main sequence ($\Delta \log {\rm SFR} < -3\sigma$) with σ equal to the observed scatter in the main sequence relationships (i.e. 0.36 dex). We break the "below" region in three separate regions to judge how the sample is clustered. If all of the sources below the main sequence are in the 1σ region, then it could be argued that most of the AGN are main sequence galaxies and simply display a larger scatter. The fractions for the different COLD GASS subsamples are the average fraction over all 50 representative subsamples.

The numbers confirm the visual impression seen in Figure 4.1 that the BAT AGN mainly live inside the main sequence or below it. 28 per cent lie inside the main sequence and 66 per cent lie below it from adding together the three "below" regions. Only 5 per cent of the sample is above the main sequence. The sources

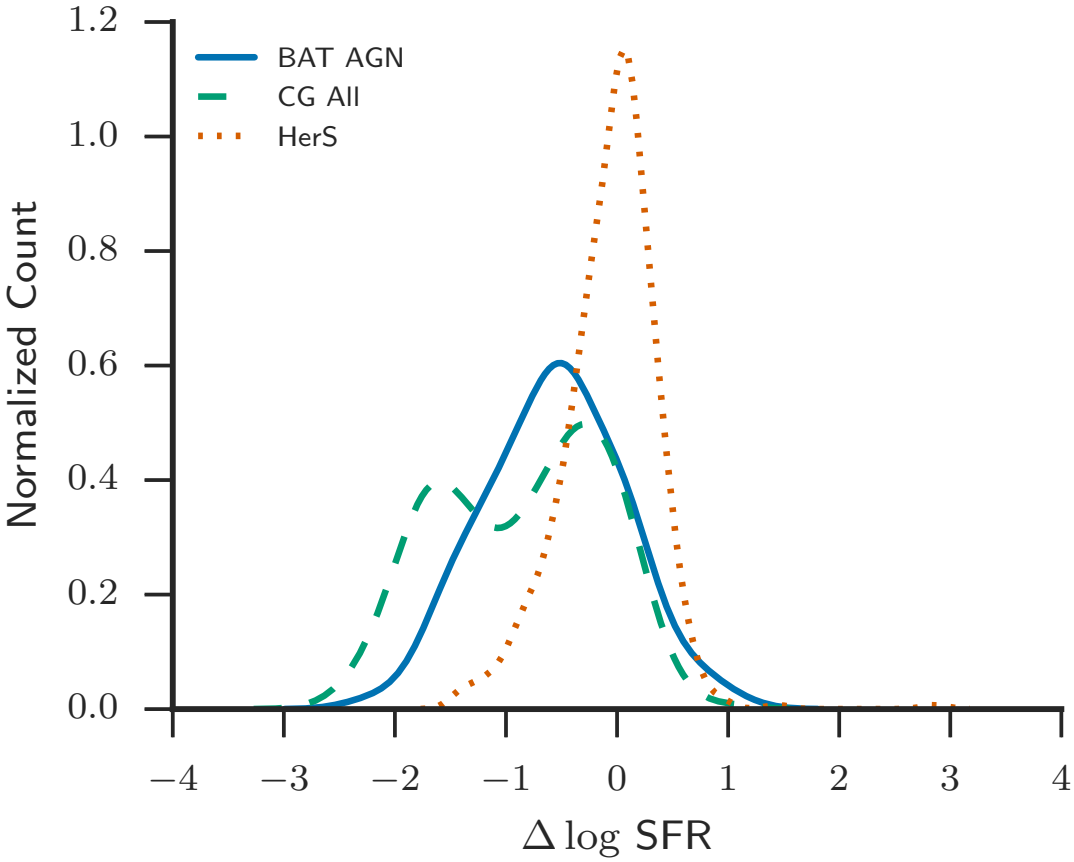

Figure 4.2: Kernel density estimate (KDE) of the logarithmic distance (Δ log SFR) from the main sequence for the BAT AGN, a representative subsample of COLD GASS, and the HerS sample.

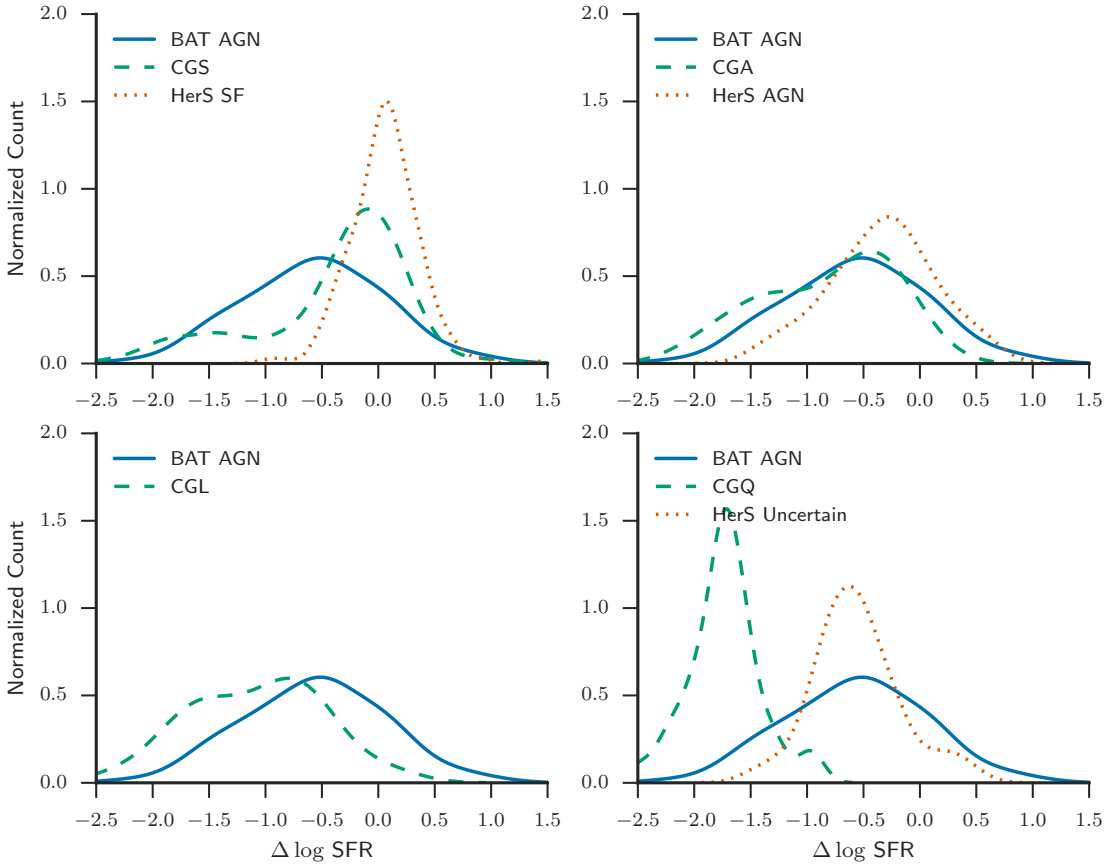

Figure 4.3: Same as Figure 4.2 but with the COLD GASS subsample split into 4 classifications based on their location in the BPT diagram. CGS: Star-forming galaxies. CGA: AGN and composite galaxies. CGL: LINERs. CGQ: Quiescent galaxies. The HerS sample was split into 3 classifications (Star-forming, AGN and composite, and Uncertain). The BAT AGN galaxies show a similar distribution in Δ log SFR as the CGA and HerS AGN sample (upper right).

below the main sequence are also well spread out between the 1σ, 2σ, and 3σ regions, showing the BAT AGN do not cluster near the edge of the main sequence and in fact a significant percentage (20 per cent) display SFRs more than 3σ below what is expected given their stellar masses.

For the COLD GASS sample as a whole, there seems to be a bimodal distribution with 33 per cent of galaxies inside the main sequence and 39 per cent $> 3\sigma$ below it. This mirrors what has been extensively seen using optical colors and is another representation of the split into the blue cloud and red sequence. The BAT AGN do not display the same bimodality and overall have a very different distribution of $\Delta \log \mathrm{SFR}$ as shown in Figure 4.2[10] We ran K-S tests to compare the BAT AGN with each COLD GASS representative subsample (see Section 4.2.3 for a description of the subsamples) and found that 0/50 tests returned a probability > 5 per cent verifying that the two samples are not drawn from the same parent distribution.

The HerS sample differs from the COLD GASS and BAT AGN samples and is sharply peaked around $\Delta \log \mathrm{SFR} = 0$, signifying most of the galaxies are on the MS. Indeed, 67% of the total HerS sample lie inside the main sequence, while only 12 per cent are above and 21 per cent below. HerS likely does not reach as

[10]We take this opportunity to explain that we choose to represent distributions of values using a Kernel Density Estimate (KDE) rather than a histogram. This is due to the visualization of a histogram being highly dependent on the bin size, number of bins chosen, and the edges of the bins. A KDE represents each point in a data set with a specific kernel and sums all of them together. In this Chapter we use a Gaussian kernel. The only tunable parameter is the kernel width for which we use "Scott's Rule" (Scott, 1992), $width = N^{-1/5}$, where N is the number of data points.

far below the main sequence as COLD GASS given the parent sample was selected based on a SPIRE 250 μm detection. Using the Viero et al. (2014) 5σ depth for SPIRE 250 μm of 65 mJy and assuming a greybody with $T_{dust} = 25$ K and $\beta = 2.0$, the minimum SFR detectable is 0.5 $M_{\odot}$ yr^{-1}, much higher than the level reached by COLD GASS and the BAT AGN. Even so, we again ran a K-S test between the BAT AGN and HerS and found a $P_{K-S} << 0.01$ indicating they are drawn from different populations.

It is only when we separate the COLD GASS and HerS sample into their different classifications do we find a similarity. Figure 4.3 shows the KDEs of $\Delta \log \mathrm{SFR}$ for the BAT AGN and each COLD GASS and HerS classification. The COLD GASS KDEs were calculated from a randomly chosen representative subsample. The BAT AGN are most similar to the CGA (e.g. the AGN population of COLD GASS), displaying lower values of $\Delta \log \mathrm{SFR}$ than CGS/HerS SF and higher values than CGL and especially CGQ. In fact the percentages in each region for the BAT AGN and CGA are nearly identical except in the $> 3\sigma$ region where there is a larger fraction of CGA. We again ran K-S tests for each of the 50 representative subsamples for COLD GASS and found 48/50 CGA subsamples returned a probability > 5 per cent indicating that the BAT AGN and CGA are consistent with the same parent population. 0/50 of the CGS, CGL, and CGQ subsamples returned a probability > 5 per cent of being consistent with the BAT AGN. The K-S test between the BAT AGN and HerS AGN returned a $P_{K-S} = 0.002$ while the ones with HerS SF and HerS Uncertain returned $P_{K-S} << 0.001$ and $P_{K-S} = 0.07$. Using the standard 5 per cent cutoff to determine if the samples originate from the same population

would indicate that the BAT AGN are most similar to the HerS Uncertain galaxy population. However as we discuss above, this is most likely due to the lower SFR depth reached in HerS. Also the HerS Uncertain classification is a more conservative classification and includes many galaxies that would have been classified using the Brinchmann et al. (2004) system including AGN and LINERs. The HerS AGN still show lower SFRs than the HerS SF sample with 48 per cent inside the MS compared to 78 per cent and 44 percent below it compared to 8 per cent. Therefore, both an optically selected sample of AGN and an ultra-hard X-ray selected sample of AGN display the same property: **they lie in between a strongly star-forming and quiescent group and suggests that AGN host galaxies are in transition between the two populations.**

We note that while the K-S tests confirm that the BAT AGN and CGA are from the same population, both Table 4.1 and Figure 4.3 show that the BAT AGN contain slightly more galaxies with higher SFRs while CGA contains slightly more quiescent galaxies. We hypothesize this is due to the selection method for the two groups. The BAT AGN are X-ray selected, a method that is completely independent from the star-forming properties of the host galaxy while the CGA are selected by optical emission line ratios whose origin can be a mixture of AGN and star-formation. If a galaxy is highly star-forming, optical emission line ratios are more likely to classify it as a star-forming galaxy rather than AGN or even composite (see Trump et al. (2015) for biases associated with line ratio selection of AGN). Indeed, many of the BAT AGN above the main sequence are either involved in a merger or are known starburst galaxies (e.g. Mrk 18, NGC 3079, NGC 7679).

Because the BAT survey is flux-limited, it is biased against weak AGN, while COLD GASS, due to its selection from SDSS, can reach to lower AGN luminosities. If low-luminosity AGN are more associated with quiescent, early-type galaxies (e.g. Kauffmann et al., 2003b), this would explain the larger fraction of the CGA group in the $> 3\sigma$ region compared to the BAT AGN. In Section 4.5.4 we show that the CGA contain a larger fraction of elliptical galaxies than the BAT sample which have lower values of sSFR.

We also note that the BAT AGN and CGS have essentially the same fraction of galaxies in the $> 3\sigma$ below region (16 per cent vs. 14 per cent). This is seen in Figure 4.3 as the long tail towards low $\Delta \log \mathrm{SFR}$ for CGS. However, this does not change the general result that the BAT AGN in general show lower levels of sSFR than the star-forming sample due to the much higher percentages in the $1-2\sigma$ and $2-3\sigma$ below regions. BAT AGN occur in the $1-2\sigma$ region at a > 3 times higher rate than the CGS and more than 2 times in the $2-3\sigma$ below region. Further 64% of the CGS occur inside the main sequence compared to only 40% of the BAT AGN. So over the entire population, AGN are more likely to be found in host galaxies that have lower SFRs than the main sequence.

4.5.2 Differences Between Seyfert 1s and 2s

According to the unified model (Antonucci, 1993; Urry & Padovani, 1995), orientation distorts our view of AGN and causes the differences seen between Sy 1s and 2s. Current models invoke an anisotropic dusty and possibly clumpy torus

(e.g. Hönig & Kishimoto, 2010; Nenkova et al., 2008a) that absorbs and scatters the nuclear optical/UV/X-ray emission. Two regions of ionized gas produce optical emission lines, one at relatively close distances to the central AGN that produces broad emission lines (i.e. broad line region, BLR) and one at further distances that produces narrow emission lines (i.e. narrow line region, NLR). Under the unified model, Sy 1 galaxies, which display very bright nuclear point sources as wells as broad optical emission lines are viewed along lines of sight through the opening angle of the torus allowing access to the BLR and accretion disk. Sy 2 galaxies on the other hand display weaker or even absent central point sources and only narrow emission lines are viewed through the dusty torus that only allows access to the NLR and obscures emission from the BLR and accretion disk. However, assuming orientation is the only difference means Sy 1s and Sy 2s should display virtually the same host galaxy properties since the torus only affects the very central regions and not the galaxy-wide properties. With our focus on the main sequence, this means Sy 1s and Sy 2s should not separate out in Figure 4.1.

Indeed, both Figure 4.1 and Table 4.1 suggest this is the case. Sy 1s compared to Sy 2s in each region show a percent difference of +1, +10, -9, -3, and -0 per cent. Assuming Poisson statistics, these differences are all well within the 1σ error bars. Only the 10 and 9 per cent differences for the inside the MS and 1–2σ regions have a marginal 1σ significance.

To investigate further, we compared the $\Delta \log \mathrm{SFR}$ distribution for both Sy 1s and Sy 2s and Figure 4.4 displays their histograms. Apart from the increased absolute numbers of Sy 2s, Sy 1s and Sy 2s have similar distributions of $\Delta \log \mathrm{SFR}$.

Using a K-S test to test whether they are drawn from the same parent population, we find a p-value of 0.36, again indicating Sy 1s and Sy 2s are similar in terms of their $\Delta \log \mathrm{SFR}$. This is in agreement with Koss et al. (2010) who found no difference in $u - r$ colors between broad and narrow line AGN. This is in disagreement with previous studies (e.g. Buchanan et al., 2006; Heckman et al., 1989; Maiolino et al., 1995) that found Sy 2s reside in more highly star-forming galaxies. However, these samples and conclusions are based on smaller samples as well as different selection criteria. Samples selected using optical or mid-infrared emission will inherently be influenced by the level of star-formation in the host galaxy and bias samples towards higher star-forming objects, especially for Sy 2's that are fainter at these wavelengths due to obscuration.

4.5.3 Correlation of $\Delta \log \mathrm{SFR}$ with host galaxy and AGN properties

Given the large percentage of AGN host galaxies below the main sequence compared with normal, main sequence galaxies, we examined the relationship between $\Delta \log \mathrm{SFR}$ and various AGN and host galaxy properties. Because our entire sample consists of AGN, the immediate reaction is to assume the AGN has influenced star formation in the host galaxy through some mechanism and slowed it down. From this scenario, the expectation is for more powerful AGN to have a greater effect on the host galaxy and occur further from the main sequence. To test this, we binned the sample according to the regions described in Section 4.5.1. Within each bin we calculated the mean 14–195 keV luminosity (L_{X}) since Winter

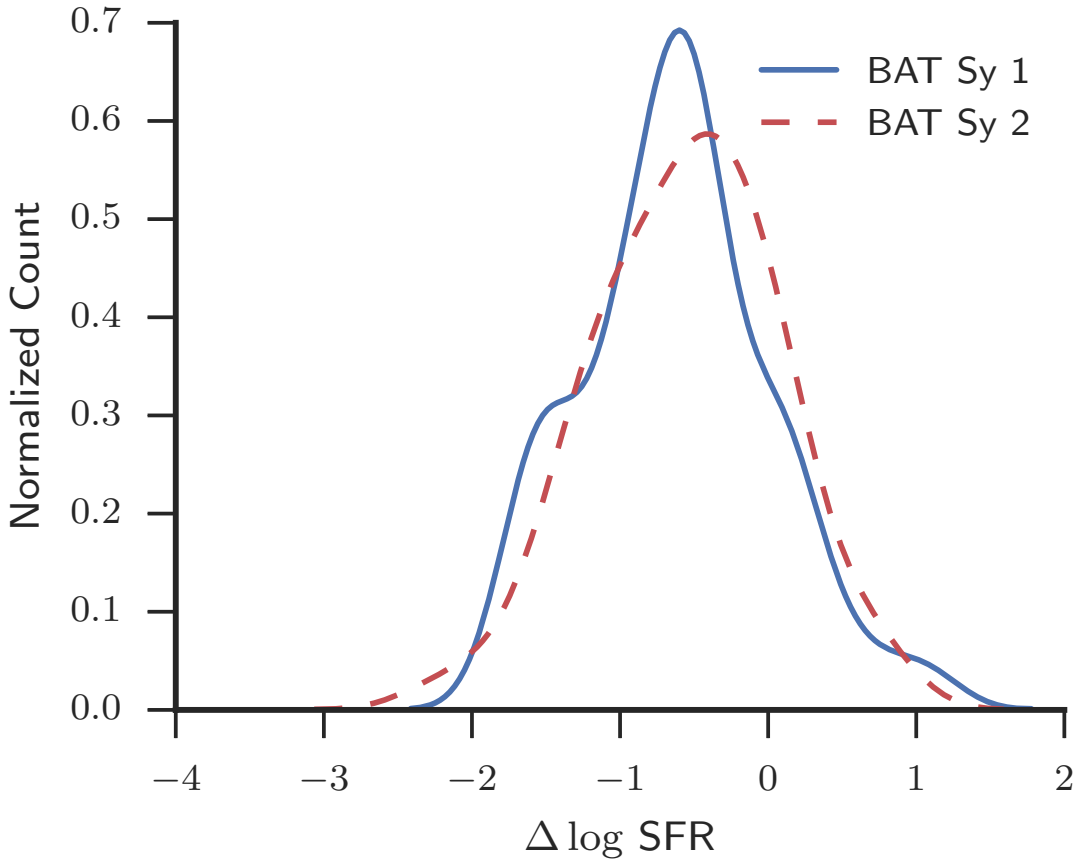

Figure 4.4: KDE of Δ log SFR for Sy 1s (solid, blue line) and Sy 2s (dashed red line) showing the similarity between the two.

et al. (2012) found the 14–195 keV luminosity to be a very good probe of the overall bolometric luminosity and strength of the AGN.

The top left plot of Figure 4.5 shows the resulting relationship between $\Delta \log \mathrm{SFR}$ and L_{X}. We found **no** clear correlation between the strength of the AGN and $\Delta \log \mathrm{SFR}$. Over the entire range of $\Delta \log \mathrm{SFR}$, the mean L_{X} only changes by < 0.4 dex with a large spread in each region. We calculated the Spearman rank correlation coefficient (ρ_s) and used bootstrap analysis to determine the 95 per cent confidence interval. We found $\rho_s = -0.1$ with a 95 percent confidence interval of -0.3–0.1 consistent with $\rho_s = 0$. This would seem to argue against the AGN having any effect on star-formation in the host galaxy. However Hickox et al. (2014) argues that AGN variability will smear out any intrinsic correlations between star-formation and AGN activity due to the much shorter timescales of AGN activity compared to star-formation. The ultra-hard X-rays used to calculate the luminosity for the BAT AGN presumedly originate very near the SMBH and represent an instantaneous strength while the SFRs are averaged over $\sim$100 Myr. The null correlation and large scatter we see between L_{X} and $\Delta \log \mathrm{SFR}$ then is most likely a product of the large variability that AGN typically exhibit.

The middle plot indicates there is a positive correlation between $L_{\mathrm{Grey}}/L_{\mathrm{MIR}}$ and $\Delta \log \mathrm{SFR}$. $L_{\mathrm{Grey}}/L_{\mathrm{MIR}}$ is the ratio of the luminosity of the greybody component to the luminosity of the MIR power-law component used in our SED model. The MIR power law luminosity strongly correlates with the AGN luminosity (Shimizu et al. 2015, in preparation) and is assumed to be produced by the AGN, while the greybody luminosity is assumed to be a product of star formation. The ratio of their

luminosities is a measure of which component dominates the SED. Far below the MS, the IR SED should be dominated by the AGN, while the IR SEDs of MS galaxies as well as those above the MS are dominated by star formation. We expect this trend due to the null correlation of $L_{\rm X}$ with $\Delta \log {\rm SFR}$. Since $L_{\rm MIR}$ is strongly correlated with $L_{\rm X}$, a decrease in $\Delta \log {\rm SFR}$ is then mostly due to a decrease in SFR which was directly calculated from $L_{\rm grey}$. We again calculated ρ_s finding $\rho_s = 0.6$ [0.46–0.7] where the range in brackets is the 95 per cent confidence interval determined using a bootstrap analysis. This strongly suggests a real positive correlation between $L_{\rm Grey}/L_{\rm MIR}$ and $\Delta \log {\rm SFR}$ and confirms that far below the main sequence the IR SED is most likely dominated by the AGN.

The greybody dust temperature also suggests a positive correlation with $\Delta \log {\rm SFR}$ with galaxies at larger $\Delta \log {\rm SFR}$ having a higher temperature (Figure 4.5, right). This has been observed before (e.g. Magnelli et al., 2014) and can easily be explained given that an increase in SFR increases the number of OB stars that produce the UV photons to heat the dust. We found $\rho_s = 0.6$ [0.45–0.7], very similar to the correlation with $L_{\rm Grey}/L_{\rm MIR}$ showing that the true property determining an AGN host galaxy's location within the main sequence diagram is star-formation rather than the strength of the AGN.

Both of these effects can also be seen in Figure 4.6 where we plot the mean SEDs for each region after normalizing to the 12 μm flux density. Because some of the observed SEDs contain upper limits especially at the longest wavelengths, we use the Kaplan-Meier product-limit estimator (Feigelson & Nelson, 1985), a maximum likelihood estimate of the distribution function, to calculate the mean

and its standard error. Using only the detected flux densities would bias the mean towards larger values, with an increasing bias at longer wavelengths as the number of upper limits increases. This would then lead to an artificial flattening of the SED.

The peak of the SED is seen to shift to longer wavelengths as sSFR decreases, indicating colder temperatures (i.e. Wien's Displacement Law) while the overall amplitude decreases along with a flattening of the slope of the SED between 4.6 and 160 μm. In their analysis of *Spitzer* IRS spectra for Seyfert galaxies, both Wu et al. (2009) and (Baum et al., 2010) found that AGN host galaxies with lower amounts of star formation display bluer SEDs in 15–40 μm regime, in agreement with our mean SEDs and an increase in the AGN contribution. We also see a general increase in the W1/W2 *WISE* color moving towards lower sSFR, an indication that the host galaxy (in particular older stars) begins to contribute to the MIR, similar to what is observed in many quenched galaxies. The long wavelength IR regime, though, seems to be completely unaffected by the sSFR. All five of the SEDs essentially display the same slope and relative flux density at 250, 350, and 500 μm. Indeed a comparison of the BAT AGN SPIRE colors with the HRS colors shows there is little difference between the two samples (Shimizu et al 2015, in preparation), verifying the same process (i.e. star formation) is producing most of the long wavelength emission.

4.5.4 Host Galaxy Morphology

Koss et al. (2011) closely analyzed the host galaxy morphologies of the BAT AGN, finding that at all stellar masses a larger percentage of AGN are hosted by

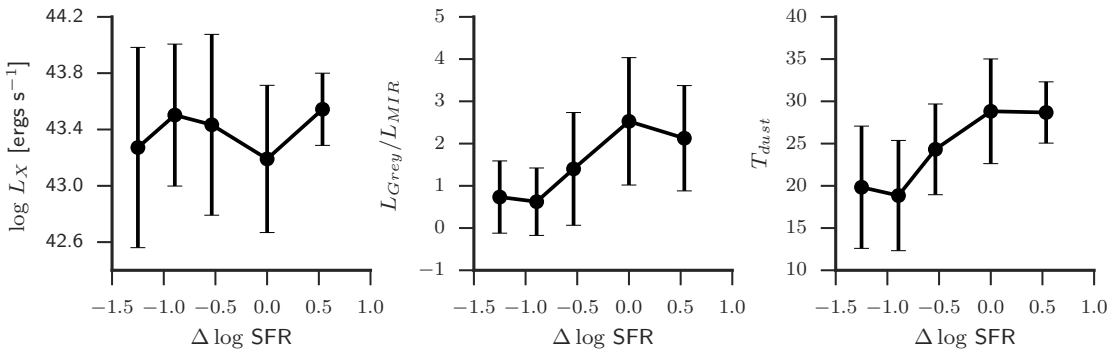

Figure 4.5: Correlations between different properties of the galaxies/AGN as a function of $\Delta \log \mathrm{SFR}$. *left*: 14–195 keV luminosity, *middle*: ratio of the MIR power law luminosity and greybody luminosity, *right*: Dust temperature. For each property, we binned the sources according to whether they were above, inside, or below the main sequence (split into 3 separate regions). For each MS region we calculated the mean AGN/galaxy property. Error bars are the standard deviation within each bin.

spiral galaxies compared to a matched sample of normal galaxies. Using these morphologies, we can assess if we observe a change in the host galaxy morphology as a function of sSFR. Koss et al. (2011) classified the BAT AGN into three categories: spirals, ellipticals, and intermediate based on the results from the Galaxy Zoo Project (Lintott et al., 2008). Each galaxy was independently classified numerous times by the public. A spiral or elliptical morphology was chosen for the galaxy if > 80 per cent people selected the type, or else intermediate was chosen. Mergers were defined in the same way as Patton & Atfield (2008) and Koss et al. (2010), requiring a projected distance of at most 30 kpc and a radial velocity difference of < 500 km s^{-1} between the galaxy and its companion. We used the same method for the COLD GASS sample as well for the spiral/elliptical/intermediate classification. Merger classifications for the COLD GASS sample were determined in Saintonge et al. (2012) where they visually classified each galaxy as a merger/interaction if it

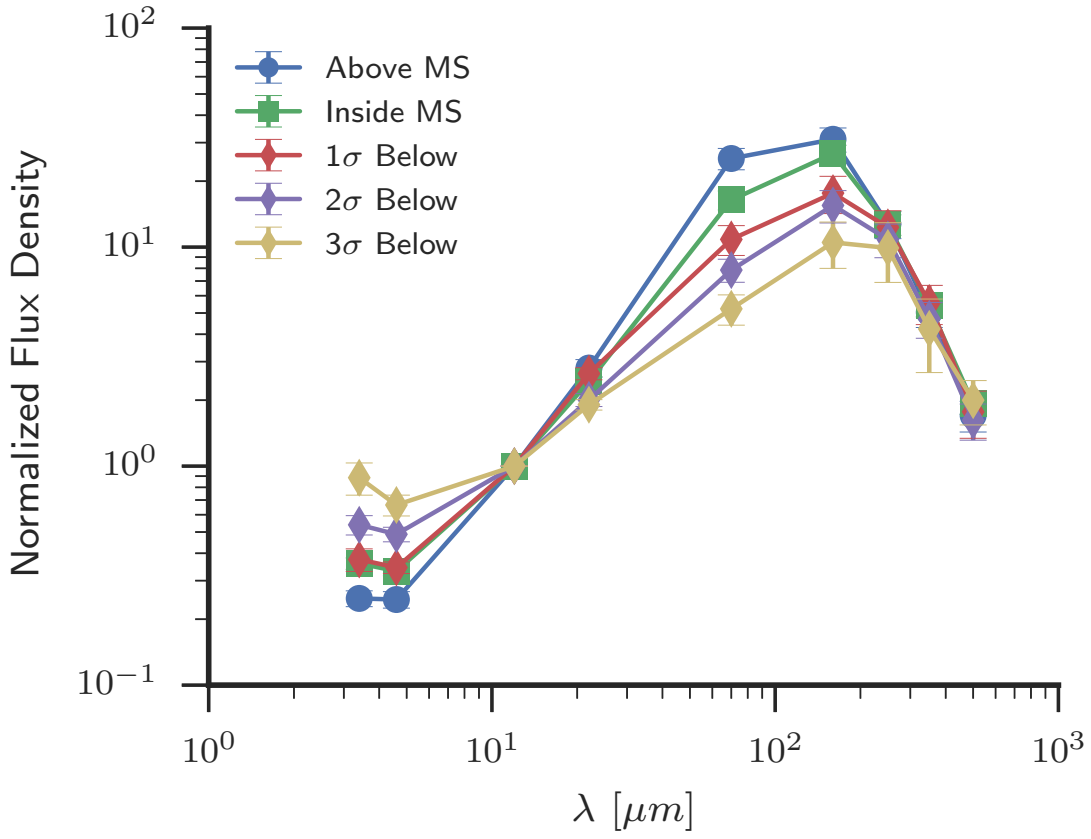

Figure 4.6: Mean SED of the sources in each region of the main sequence plot. The individual SEDs were first normalized to the 12 μm flux density. Error bars represent the standard error of the mean normalized flux.

had a nearby companion ($< 1'$) and/or evidence of a disturbed morphology, tidal tails, etc (see Appendix A of Saintonge et al. (2012)). Each galaxy that looked like a merger was given a merger rating from 2–5 with 2 representing galaxies that only had a nearby companion and a 5 representing galaxies with very strong signs of a merger. After looking through the images of the COLD GASS mergers we decided to exclude all of the galaxies with a merger rating of 2 because they would not have been classified as a merger using the method from Koss et al. (2011). We chose to only compare the BAT AGN morphologies with the COLD GASS sample given COLD GASS's better mass completeness and larger SFR depth.

In the "Total" column of Table 4.2 and Figure 4.7 we outline the total fraction of galaxies that are spirals, intermediates, and ellipticals over the whole sample. Spiral galaxies dominate ($\sim$ 60 per cent) the population of both the BAT AGN and CGS similar to what was found in Koss et al. (2011) whereas for the CGA they represent $\sim$ 50 per cent of the population and for the CGL they are 35 per cent. There are virtually no spiral galaxies in the quiescent group (CGQ).

On the other hand the CGQ are dominated by elliptical galaxies ($\sim$ 60 per cent). The CGL are $\sim$ 26 per cent elliptical, CGA 20 per cent, and the BAT AGN and CGS 10 per cent elliptical. Overall in terms of the whole population the BAT AGN more closely resemble the morphology distribution of the CGS rather than the CGA. However a closer look at the sSFR for each morphology shows that the BAT AGN and CGA are more similar. This is shown in Figure 4.7, right panel, where we plot the average sSFR for each morphology. BAT AGN spirals and intermediates show decreased levels of sSFR compared to the CGS and more in line with the CGA.

If we examine the distribution of spirals, ellipticals, and intermediates as shown in Figure 4.8, we can again see that the BAT AGN and CGA are almost identical in terms of the fraction of spirals and ellipticals in each MS region. The biggest difference seems to occur with intermediates; however there is much uncertainty concerning the nature of intermediates given they are simply defined as objects where there was no consensus on whether it was a spiral or elliptical.

Interestingly for both the BAT AGN and CGA, ellipticals show increased levels of sSFR compared to those within the CGS and CGQ groups. This could be an indication that AGN within early-type galaxies actually stimulate star-formation rather than quench it. With such large error bars, though, the significance of this result is unclear.

In agreement with Koss et al. (2010) we find that the merger fraction of the BAT AGN (28 per cent) is much higher than that of the CGS (3 per cent) and CGA (3 per cent). There are no mergers in the CGL and CGQ samples. Mergers have long been known to increase the SFR in the interacting galaxies (Sanders et al., 1988a) as evidenced by the majority of ultra-luminous infrared galaxies (ULIRGS) involved in one. Elbaz et al. (2011) found that the nearly all of the local galaxies above the main sequence are IR-compact starbursts that were most likely triggered by a merger. Thus, we expect to see a large fraction of mergers occurring above the main sequence. Indeed, this is the case especially for the CGS where 34 per cent of the mergers are above the MS and the rest are inside the MS. Further for both the BAT AGN and CGS, mergers have the greatest average sSFR (Figure 4.7). This could also explain the extremely low merger fraction for the CGA. If mergers

are associated with highly star-forming galaxies, then emission line ratios would indicate a star-forming galaxy rather than an AGN as any AGN signatures would be overwhelmed. With ultra-hard X-rays though, we can peer through the obscuring gas and detect the AGN.

In Figure 4.9, we plot the fraction of all galaxies of a sample in a MS region that is a merger. This is different than Figure 4.8 where we plot the fraction of all mergers that is in each region. Here we can see that the merger incidence rate rises with $\Delta \log \mathrm{SFR}$ as expected. Above the MS, the CGA show the highest merger rate at roughly 80 per cent, but this is based on small number statistics and is reflected in the large error bars. The BAT AGN have a 50 per cent merger rate and CGS are at 30 per cent. For all three samples the above the MS region represents the largest merger rate. Inside, and below the MS the BAT AGN clearly show much larger merger rates than that of CGS and CGA. In fact the merger fraction for the BAT AGN is roughly flat from above the MS to the 2–3σ region. This could be evidence that mergers and interactions are important in triggering AGN at low redshift even before the star burst ignites and those below the MS are in fact moving up the SFR-M_{star} plane. Another explanation is that these are late stage mergers and have moved past the initial burst of star formation and are slowly falling off the main sequence. A confirmation of this would be if all of the mergers in the $> 1\sigma$ region are in the early stages whereas the ones above the MS are near coalescence. In either case, the BAT AGN mergers occur across nearly the whole SFR-M_{star} plane at a high rate compared to local non-active galaxies and optically selected AGN. This is in disagreement with recent higher-redshift studies of the merger rate in

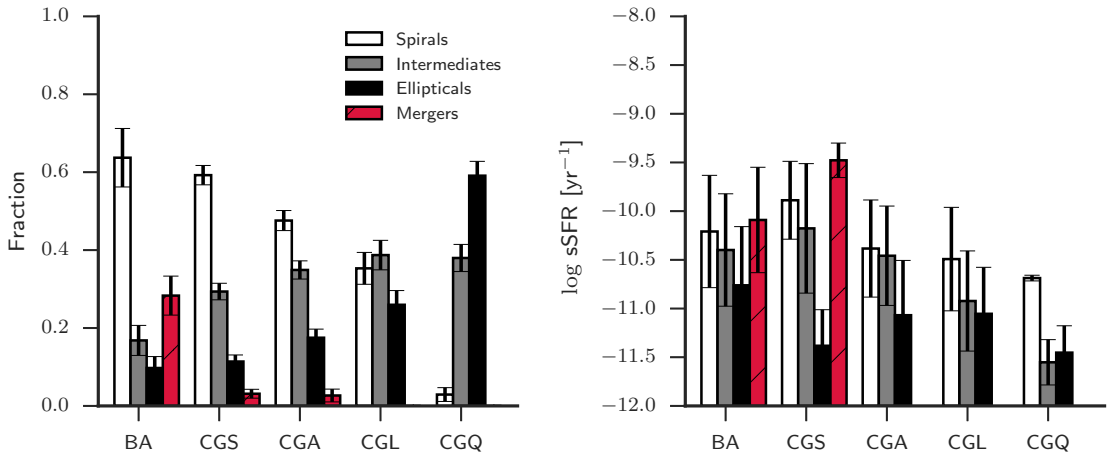

Figure 4.7: *Left:* The distribution of spirals, intermediates, and ellipticals for all of the galaxy samples. For the COLD GASS samples, the fractions represent the mean fraction of all 50 representative subsamples. 1σ error bars for the BAT AGN (BA) were calculated assuming Poisson statistics while the error bars for the COLD GASS samples represent the standard deviation of the fractions for the 50 representative subsamples. *Right:* The average sSFR for the different morphologies within each sample. For the COLD GASS samples we randomly chose one representative subsample which for the CGA in this case did not contain any mergers. Error bars are the standard deviation of sSFR within each group.

X-ray selected galaxies (e.g. Kocevski et al., 2012; Villforth et al., 2014) that find no difference in the merger rates between AGN and non-AGN galaxies.

4.6 Discussion

4.6.1 Selection Effects and Model Dependence

Due to the flux-limited nature of our parent AGN sample, there is a strong dependence on the X-ray luminosity (i.e. AGN luminosity) with distance, limiting the inclusion of low luminosity AGN especially at higher redshifts. However this would only affect our results if they were related to either the SFR or $M_{\rm star}$ of the host galaxy. X-ray luminosity has been shown to only have a weak correlation with

Table 4.2: Host Galaxy Morphology Distribution in SFR-$M_{\rm star}$ Plane

Sample	Total	Above MS	Inside MS	$1-2\sigma$ Below	$2-3\sigma$ Below	$>3\sigma$ Below
(1)	(2)	(3)	(4)	(5)	(6)	(7)
BAT AGN						
Spirals	0.64	0.06	0.33	0.26	0.21	0.14
Ellipticals	0.10	0.00	0.18	0.18	0.09	0.55
Intermediates	0.17	0.05	0.11	0.42	0.16	0.26
Mergers	0.28	0.09	0.34	0.28	0.22	0.06
CG All						
Spirals	0.43	0.03	0.52	0.20	0.12	0.13
Ellipticals	0.23	0.00	0.03	0.03	0.08	0.86
Intermediates	0.34	0.03	0.28	0.16	0.13	0.41
Mergers	0.02	0.41	0.40	0.00	0.19	0.00
CGS						
Spirals	0.59	0.04	0.74	0.16	0.04	0.03
Ellipticals	0.11	0.00	0.06	0.00	0.11	0.84
Intermediates	0.29	0.06	0.60	0.11	0.07	0.18
Mergers	0.03	0.34	0.66	0.00	0.00	0.00
CGA						
Spirals	0.48	0.02	0.34	0.25	0.14	0.25
Ellipticals	0.18	0.00	0.08	0.06	0.14	0.72
Intermediates	0.35	0.02	0.29	0.28	0.15	0.26
Mergers	0.03	0.49	0.01	0.00	0.50	0.00
CGL						
Spirals	0.35	0.00	0.21	0.27	0.26	0.27
Ellipticals	0.26	0.00	0.00	0.08	0.17	0.76
Intermediates	0.39	0.00	0.00	0.18	0.30	0.53
Mergers	0.00	0.00	0.00	0.00	0.00	0.00
CGQ						
Spirals	0.03	0.00	0.00	0.00	1.00	0.00
Ellipticals	0.59	0.00	0.00	0.00	0.00	1.00
Intermediates	0.38	0.00	0.00	0.00	0.00	1.00
Mergers	0.00	0.00	0.00	0.00	0.00	0.00

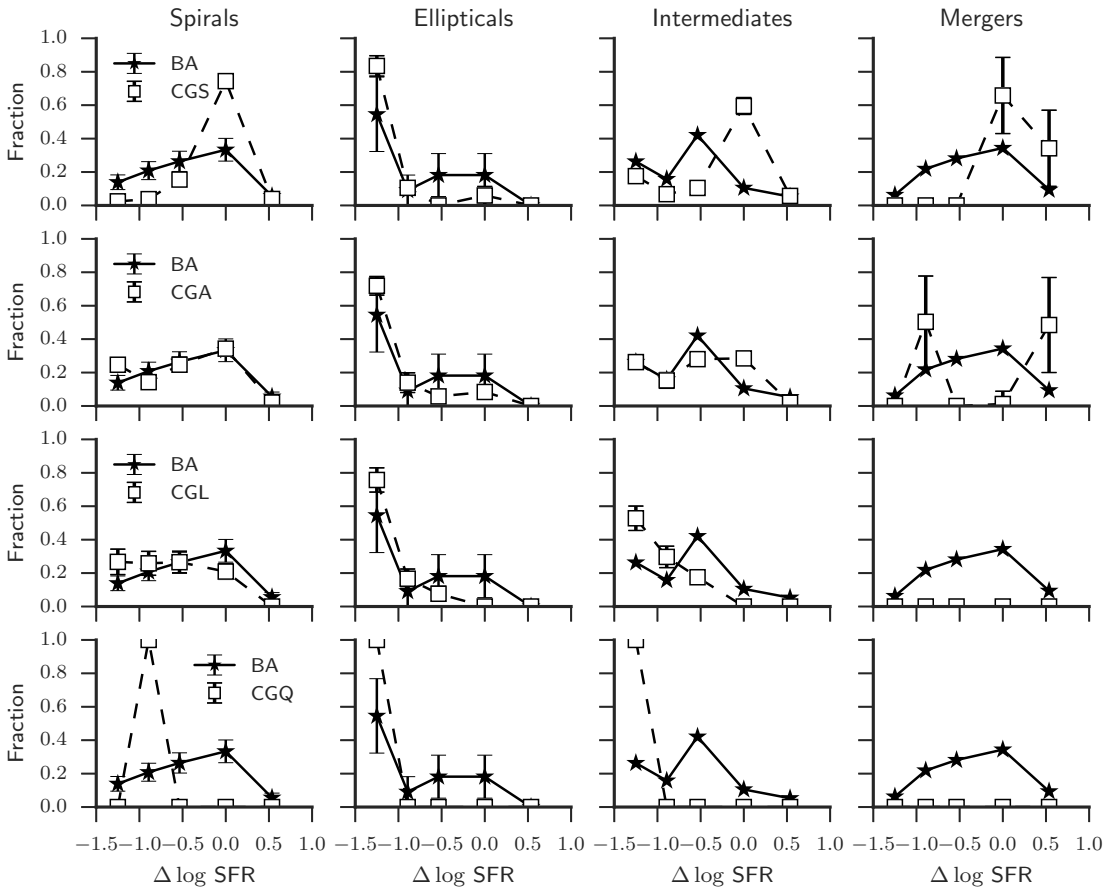

Figure 4.8: Comparison of the fraction of spirals, ellipticals, intermediates, and mergers that are in each main sequence region for the BAT AGN (BA) and COLD GASS samples (CGS, CGA, CGL, and CGQ). The fractions for the COLD GASS samples are the average fractions over the 50 representative subsamples. Errors for the BAT AGN are calculated assuming Poisson statistics while the errors for the COLD GASS samples are the standard deviation of the fraction for the 50 representative subsamples.

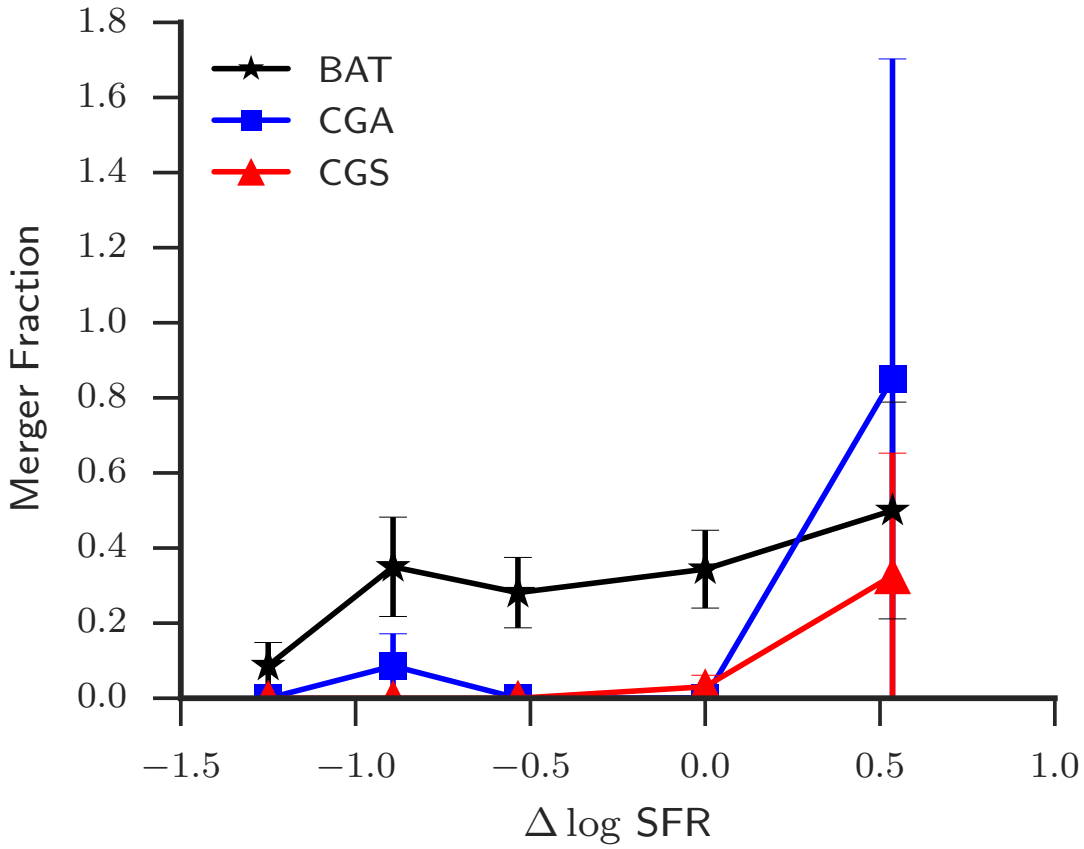

Figure 4.9: Fraction of galaxies in each MS region that are mergers for the different samples.. Errors for the BAT AGN (black stars) are calculated assuming Poisson statistics for the merger fraction. Errors for the CGA (blue squares) and CGS (red triangles) are the standard deviation of the fraction over all 50 representative subsamples.

SFR (e.g Mullaney et al., 2012a; Rosario et al., 2012; Shao et al., 2010; Silverman et al., 2009). Furthermore, the correlations are positive implying the absence of low AGN luminosity in our sample only removes objects with even lower SFR that would enhance our result that a large fraction of AGN lie below the main sequence. Mullaney et al. (2012a) found a very weak correlation of intrinsic AGN luminosity with stellar mass where a two order increase in AGN luminosity results in only a factor 2 greater stellar mass. This combined with the weak correlation of SFR shows that we are not biased towards low sSFR galaxies in our sample.

The choice of model to fit the SEDs of our galaxies could greatly influence the results, given that the SFRs are directly calculated from the measured FIR luminosity. It is possible that we are assigning too much of the 8–1000 μm luminosity to the AGN and underestimating the SFR. We have tested this effect in two ways. First, we implemented the SED fitting routine, DECOMPIR, described and developed by Mullaney et al. (2011). DECOMPIR utilizes a set of 5 host galaxy templates and an intrinsic AGN template to fit the IR SED's of galaxies. Although there is the option to let the parameters of the AGN template vary, given our sample, we only used the mean intrinsic AGN SED found in Mullaney et al. (2011). Each BAT AGN was fit with each host galaxy template allowing the normalizations of both the AGN and host galaxy to vary. The host galaxy template that resulted in the minimum χ^2 was chosen as the best fit. SFRs were then calculated by integrating the best fit host galaxy SED from 8–1000 μm and using Equation 4.1. Using the DECOMPIR SFRs combined with the same stellar masses and main sequence relation (defined by Equation 4.3) we find 6, 35, 28, 14, and 18 per cent of the AGN in the Above MS,

Inside MS, $1-2\sigma$ Below, $2-3\sigma$ Below, and $>3\sigma$ Below regions respectively. These fractions are extremely similar to those using the Casey (2012) model (Table 4.1) with only a slightly higher incidence of AGN inside the main sequence and lower number below it.

The second way we tested the model dependency was by using just the monochromatic 160 μm luminosity as a pure SFR indicator. The 60 or 70 μm luminosity has been used extensively in the literature as a SFR indicator; however, based on the modeling of the BAT sample, 70 μm is a poor choice due to the AGN contribution especially at higher AGN luminosities (Meléndez et al., 2014). 160 μm however seems to be relatively free from any AGN contribution. Therefore we simply used the 160 μm luminosity to convert to a SFR using the relation from (Calzetti et al., 2010) for both the HRS sample and BAT AGN and recalculated the main sequence based only on the HRS since we do not have 160 μm data for the HerS sample. This results in 6, 37, 25, 12, and 20 per cent of the BAT AGN in the Above MS, Inside MS, $1-2\sigma$ Below, $2-3\sigma$ Below, and $>3\sigma$ Below regions respectively, comparable to both the values in Table 4.1 and using DECOMPIR. This confirms our main result that a large fraction of AGN lie below the main sequence and is not a product of over-subtracting the AGN component of the SED. Three separate techniques for estimating the SFR agree that >50 per cent of AGN have lower sSFRs than normal galaxies for the same stellar mass.

4.6.2 Comparison with previous studies

We have substantiated that our results are not due to selection effects or are model dependent. The BAT AGN, COLD GASS AGN, and HerS AGN span a large range in sSFR that extends over two orders of magnitude. Many previous studies have suffered from low detection rates ($<$ 40 per cent) in the FIR and needed to resort to stacking techniques (e.g. Mullaney et al., 2012a) to achieve a reasonable dynamic range. Our *Herschel*-BAT AGN sample provides a unique opportunity to compare to previous work and whether assumptions made remain valid. In particular we will focus on the work from Mullaney et al. (2012a) who used deep *Herschel* observations of the GOODS-South and GOODS-North fields to study the star-forming properties of AGN selected from 2 Ms and 4Ms *Chandra* Deep Field South and North. Their AGN sample spans the same luminosity range as the BAT AGN, but a much higher redshift range ($0.5 < z < 3$) with an overall detection fraction in the FIR of $\sim$ 40 per cent. To enhance their sample to low redshifts, they utilize a sample of the BAT AGN, however with much poorer FIR photometry from *IRAS* and again only a detection fraction of 40 per cent compared to our 95 per cent and 83 per cent detection fraction at 70 and 160 μm respectively, the two wavelength bands closest to the longest *IRAS* bands.

For the FIR undetected AGN in the GOODS fields, they utilized stacking analysis to find the weighted average sSFR in three different redshift bins. Using a Monte Carlo approach and assuming a lognormal distribution of sSFR, they estimated 15 per cent of all (FIR detected and undetected) AGN reside in quenched

galaxies, 79 per cent are in main-sequence galaxies, and 7 per cent in starburst galaxies. While the starburst percentage (i.e. above the main sequence) is comparable to the fraction presented here, the main sequence and quenched (i.e. below the main sequence) percentages seem to be in disagreement. However this is merely due to a difference in definition of being inside or below the main sequence. Mullaney et al. (2012a) define starbursts as galaxies that have sSFRs > 3 times that of main sequence galaxies and quenched galaxies as ones that have 10 per cent the sSFR of main sequence galaxies. All others are then considered normal star-forming galaxies which include transitioning galaxies in the "green valley." Using these criteria for our BAT sample, we then find 14 per cent starburst galaxies, 73 per cent main sequence galaxies, and 13 per cent quenched galaxies. While we seem to see a factor of 2 greater incidence of starburst galaxies, the fraction of main sequence galaxies and quenched galaxies are completely in line with Mullaney et al. (2012a).

To further check the agreement between the two studies, we simulated samples of AGN at higher redshifts by assuming our BAT AGN sample is representative of the AGN population at all redshifts. To simplify the process, we also assumed every AGN has a host galaxy SED exactly that of the SB5 template from DECOMPIR at $z = 0$. The template was then scaled to have the same observed 160 μm flux. For each redshift bin probed by Mullaney et al. (2012a) (0.5–1.0, 1–2, and 2–3) we simulated 1000 samples of AGN by randomly assigning a redshift from that bin to each of the AGN in our BAT sample. After a redshift was assigned, we simulated the increase in SFR with increasing redshift using Equation 13 from (Elbaz et al., 2011). From this, we obtained a multiplicative factor to boost the IR SED of the

AGN for a specific redshift. Finally, after redshifting the SED, we employed the same detection wavelengths (100 μm for $0.5 < z < 1.5$ and 160 μm for $1.5 < z < 3.0$) and thresholds (0.8 mJy for 100 μm and 2.4 mJy for 160 μm) to determine whether the source would be detected. The detection fractions for all 1000 sets of AGN were averaged to find the estimated detection fraction for each redshift bin.

Overall for the entire redshift range of 0.5–3 we found a detection fraction of $\sim$ 35 per cent, very near to the observed one of 42 per cent. However when splitting up into the redshift bins we find detection fractions of 71, 30, and 6 per cent compared to 60, 42, and 29 per cent found by Mullaney et al. (2012a) in redshift bins of 0.5–1.0, 1–2, and 2–3 respectively. This could be a sign of an evolution of AGN host galaxies where at higher redshifts, more AGN live in main sequence galaxies than what is seen at low redshift. The discrepancy could also be caused by the lack of an AGN contribution used in our simulations. At 100 and 160 μm, there is very little contamination from the AGN, but at the rest frame wavelengths being probed (40–67 μm) it could have a profound effect. To test this we repeated the simulations, adding in the average AGN SED from DECOMPIR such that 25 per cent of the observed frame 100 or 160 μm is due to the AGN. Doing this increases the detection fraction to 77, 38, and 10 per cent in the same redshift bins, much closer in the middle bin but still far off the 30 per cent in the highest redshift bin. However, we have not included any AGN luminosity evolution with redshift. Ueda et al. (2014) find that $L_{\rm X}$ is a strong function of redshift especially between $z = 0-2$. This would increase the fluxes especially in the higher redshift bins and subsequently increase the detection fractions.

4.6.3 Comparison with SDSS sample

All three AGN samples, one X-ray selected (BAT AGN) and two optically selected (CGA and HerS AGN) have reduced levels of star-formation compared to the main sequence. All of these samples, however, are relatively small in number so we decided to test a much larger sample of both star-forming and AGN galaxies from the SDSS.

The SDSS DR7 spectroscopic catalog mentioned previously contains 818,333 unique galaxies with optical spectra that were analyzed in a consistent manner by the MPA-JHU team (Brinchmann et al., 2004). SFRs and stellar masses were measured for every galaxy. Stellar masses are based on fits to the five SDSS photometry using the technique described in Salim et al. (2007). SFRs were derived in two separate ways. For star-forming galaxies, the SDSS spectra were fit using the Charlot & Longhetti (2001) models with an additional aperture correction to account for light outside the fiber (Salim et al., 2007). For the other classifications, emission lines are not reliable either due to low S/N or unknown AGN contribution (composite and AGN dominated). The SFRs for these groups were estimated using the 4000 Åbreak (D_n4000) which has been shown to correlate with sSFR, albeit with large scatter (Brinchmann et al., 2004).

We restricted the SDSS sample to only those galaxies with well measured redshifts ($z_{conf} > 0.9$) and in the redshift range $0.01 < z < 0.05$. The upper limit matches the upper redshift of our BAT AGN sample and the lower limit is to avoid very nearby galaxies that the SDSS pipeline can shred into multiple sources. We

further included an absolute magnitude cut of $M_z < -19.5$ to ensure mass completeness and only used galaxies with well measured SFRs (sfr_flag = 0). These restrictions resulted in 21,091 star-forming galaxies; 8,189 low-SFR galaxies; 12,190 composite; and 9,421 AGN-dominated systems. We combined the star-forming and low-SFR galaxies to form the SDSS normal galaxy sample. Figure 4.10 shows the distribution of sSFR for the SDSS normal galaxies. There is a clear bi-modality in sSFR that matches the bi-modality seen with optical colors and in the COLD GASS sample. The threshold between the two populations occurs at sSFR $\sim 10^{-11}\mathrm{yr}^{-1}$ shown by the vertical dashed line. We use this threshold to split the SDSS normal galaxy sample into an actively star-forming population and passive population, hereafter referred to as $\mathrm{SDSS_{SF}}$ and $\mathrm{SDSS_{passive}}$.

In Figure 4.11 we plot the number density of the SDSS galaxies on the SFR-M_* diagram separated into the various classifications. In the left panel of Figure 4.11, we plot the SDSS_{SF} galaxies (blue contours) along with the $\mathrm{SDSS}_{passive}$ galaxies. The black solid line is the MS relation found by Peng et al. (2010) using the same data while the dashed line corresponds to a constant sSFR= 10^{-11} yr^{-1}. The SDSS_{SF} galaxies follow the Peng et al. (2010) MS relation just as the HRS galaxies follow their own MS relation with the passive galaxies far below. In the right panel of Figure 4.11 we plot the SDSS composite (magenta contours) and AGN-dominated galaxies (green contours). The same effect is seen as when comparing the BAT AGN, CGA, and HerS AGN with the main sequence, CGS, and HerS SF. **AGN host galaxies systematically have lower rates of star formation than normal star-forming galaxies.** SDSS AGN and composites, BAT AGN, CGA, and HerS

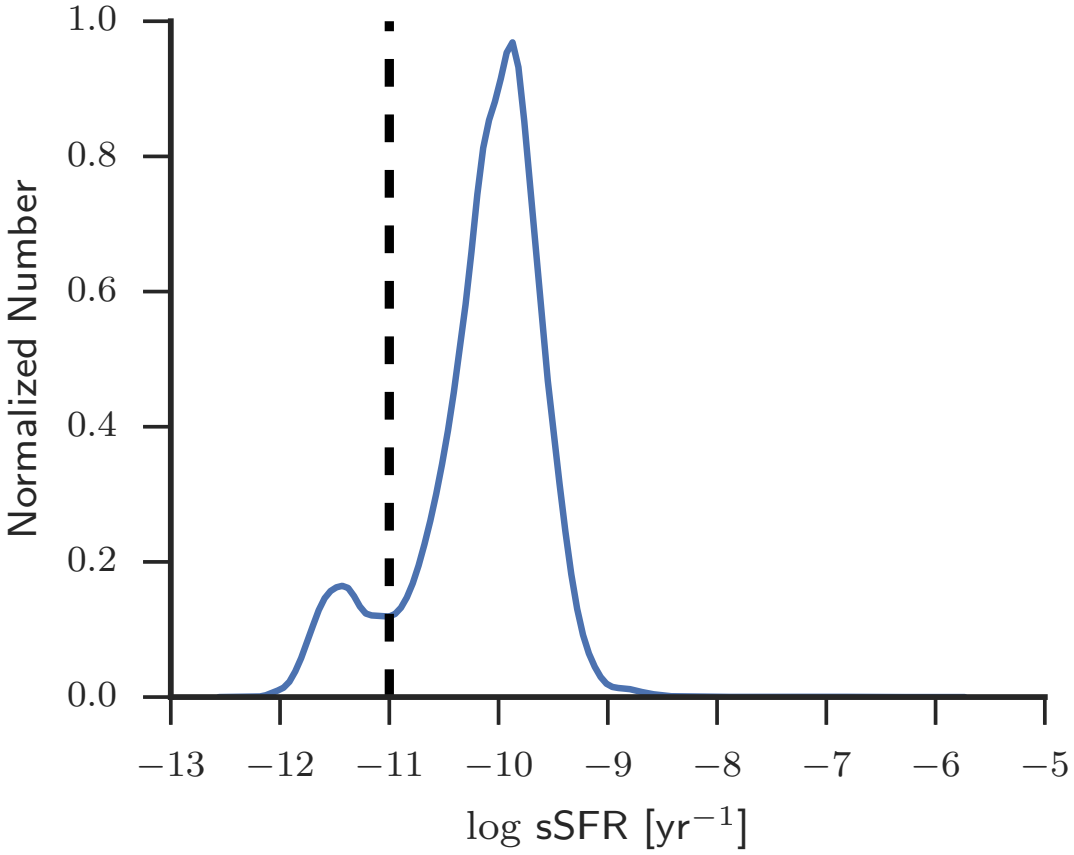

Figure 4.10: KDE of the sSFR for the SDSS DR7 sample. There is a clear bi-modality in sSFR defining the two populations of actively star forming and passive galaxies with a transition around 10^{-11} yr^{-1} (dashed line).

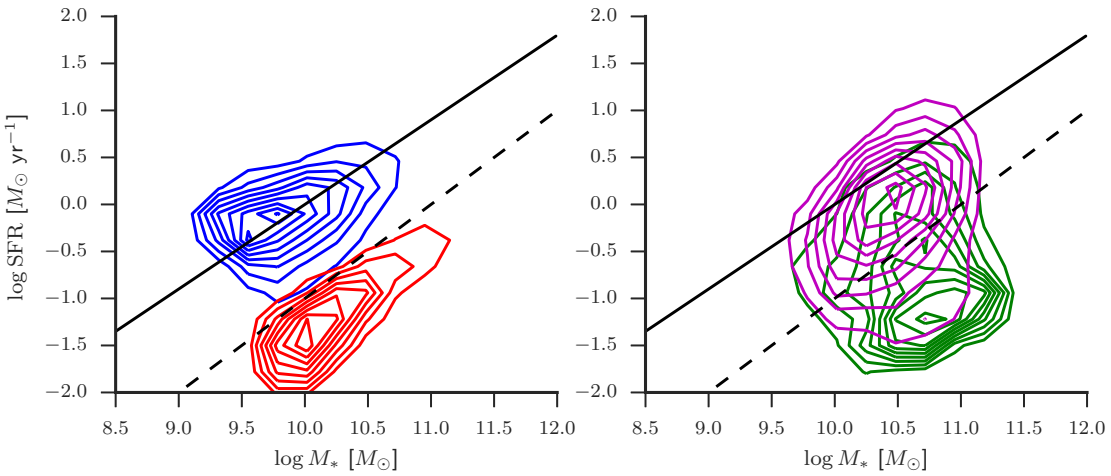

Figure 4.11: SFR–M_* diagram for the spectroscopic SDSS DR7 sample. *left panel:* SDSS non-AGN galaxies split into "SF" (blue contours) and "passive" (red contours) based on the sSFR. The black line indicates the sSFR= 10^{-11} yr^{-1} threshold to split the sample into "active" and "passive". *right panel:* Same as left panel with contours representing the SDSS composite (magenta contours) and AGN-dominated galaxies (green contours). Contours enclose 10–90 per cent of the specified sample in increments of 10 per cent.

AGN definitively lie in between the actively star-forming and completely quenched population signaling these galaxies are possibly transitioning from one stage to the next.

4.6.4 Implications for Galaxy Evolution and AGN Feedback

In this Chapter, we have rigorously shown that Seyfert galaxies display lower levels of star formation than that expected from the main sequence by comparing normal galaxy samples with an ultra-hard X-ray selected AGN sample using the same methods for measuring the SFR and stellar mass. Optically selected AGN from the COLD GASS and HerS sample also show the same effect even though their SFRs were measured using a different method. Extending the comparison to large numbers with the SDSS further emphasizes the difference between AGN and

non-AGN galaxies and confirms our results with the much smaller samples.

Just because AGN host galaxies have systematically lower sSFRs than non-AGN galaxies however does not directly imply that AGN feedback is taking place. Two scenarios can possibly explain our results. 1.) AGN actively quench star formation through short outbursts during the late life of the galaxy. 2.) AGN are simply the result of the availability of cold gas in a galaxy.

High-mass star-forming galaxies on the main sequence are gas rich especially in molecular gas (Saintonge et al., 2012). This large cold gas supply can fuel both star-formation and AGN activity. If we prescribe to the "bathtub" model of gas regulation (Lilly et al., 2013), the SFR is simply proportional to the mass of the gas reservoir in the galaxy. The two processes that regulate the mass are the accretion rate from the halo and a wind outflow, which in Lilly et al. (2013) is proportional to the SFR.

In the first scenario we can imagine the AGN significantly adding to the decrease of gas mass in the galaxy through several ways such as halo heating and powerful winds. All of these feedback processes work to reduce the mass of gas in the galaxy, which then reduces the SFR and produces the shift in sSFR we see compared to non-AGN star-forming galaxies (Figure 4.3). However based on Figure 4.5 we know the SFR is not connected to the *instantaneous* AGN strength, rather the SFR is correlated with the *average* AGN strength over 100 Myr timescales (Chen et al., 2013). So if AGN feedback is working it must be only over relatively short periods of time probably while undergoing a powerful outburst. This is supported by findings of molecular outflows in powerful AGN (Cicone et al., 2014; Veilleux et al.,

2013) where the mass outflow rate was shown to rise with increasing AGN luminosity. It is also supported by the discovery of "voorwerpje" (Keel et al., 2012, 2014; Lintott et al., 2009), highly ionized clouds at kpc scales around currently dormant SMBH that indicate AGN outbursts on timescales of $\sim 100,000$ years. Tombesi et al. (2015) recently were able to show that a fast accretion-disk wind is driving a molecular outflow in a ULIRG. Within this framework, this means all of the BAT AGN lying below the MS have gone through at least one powerful phase or possibly more to be able to significantly deplete the galaxy of molecular gas. The AGN still inside the MS perhaps are still waiting for that outburst or haven't gone through enough to move off the MS.

In the second scenario, the existence of an AGN is the consequence of the large availability of cold gas in high mass galaxies. If there is enough cold gas, eventually enough will find its way to the centers to trigger an AGN. AGN would likely turn on while the galaxy is still on the MS. A quenching process unrelated to the AGN, possibly shock heating of the accreting halo gas, slowly shuts down star formation beginning in the outskirts of the galaxy. This would be supported by our findings that the BAT AGN are more compact in the FIR than normal star-forming galaxies (Mushotzky et al., 2014). The AGN persists as the galaxy falls off the MS, eventually turning off as the remaining cold gas runs out. This scenario is still supported by the findings of Chen et al. (2013). The long timescale average accretion rate is tightly connected to the SFR through the available gas reservoir. It would only require that gas accretion onto the SMBH not be a smooth and constant process but more intermittent and variable which is supported by high resolution

simulations (Hopkins & Quataert, 2010; Novak et al., 2011).

There is one component we are currently ignoring however: mergers and interactions. With 30 per cent of the BAT AGN involved in one, in both scenarios mergers could be the key ingredient for funneling cold gas to the nuclei of galaxies and igniting an AGN. Schawinski et al. (2014) cites major mergers as the mechanism to cause fast quenching in early type galaxies whereas late type galaxies are slowly quenched through a drying up of their gas reservoir. Perhaps both quenching mechanisms are at play in the BAT AGN. The majority are contained in massive spirals (Figure 4.7) where AGN feedback (scenario 1) or external processes (scenario 2) are slowly suppressing star-formation while the ones involved in a merger have had their SFRs and SMBH accretion rates briefly elevated before rapidly falling off the main sequence. This could also explain why we still see a large fraction of mergers just below the main sequence.

Which scenario is dominant is still a matter of debate and at present we are unable to distinguish between these concepts. One thing that is clear though is that massive galaxies go through an AGN phase as they fall off the main sequence. This is shown in Figure 4.12 where we plot the fraction of all galaxies that are classified as an AGN/Composite (blue line) or AGN/Composite/LINER (magenta line, if we suppose LINERs also contain an AGN) as a function of distance from the MS in the COLD GASS sample. The fractions are the average across all 50 representative subsamples. Both lines peak in the $1-2\sigma$ and $2-3\sigma$ below regions with close to 80 per cent of the galaxies in these regions containing an AGN or LINER. The question that remains is whether these AGN have had a substantial effect on the SFR in their

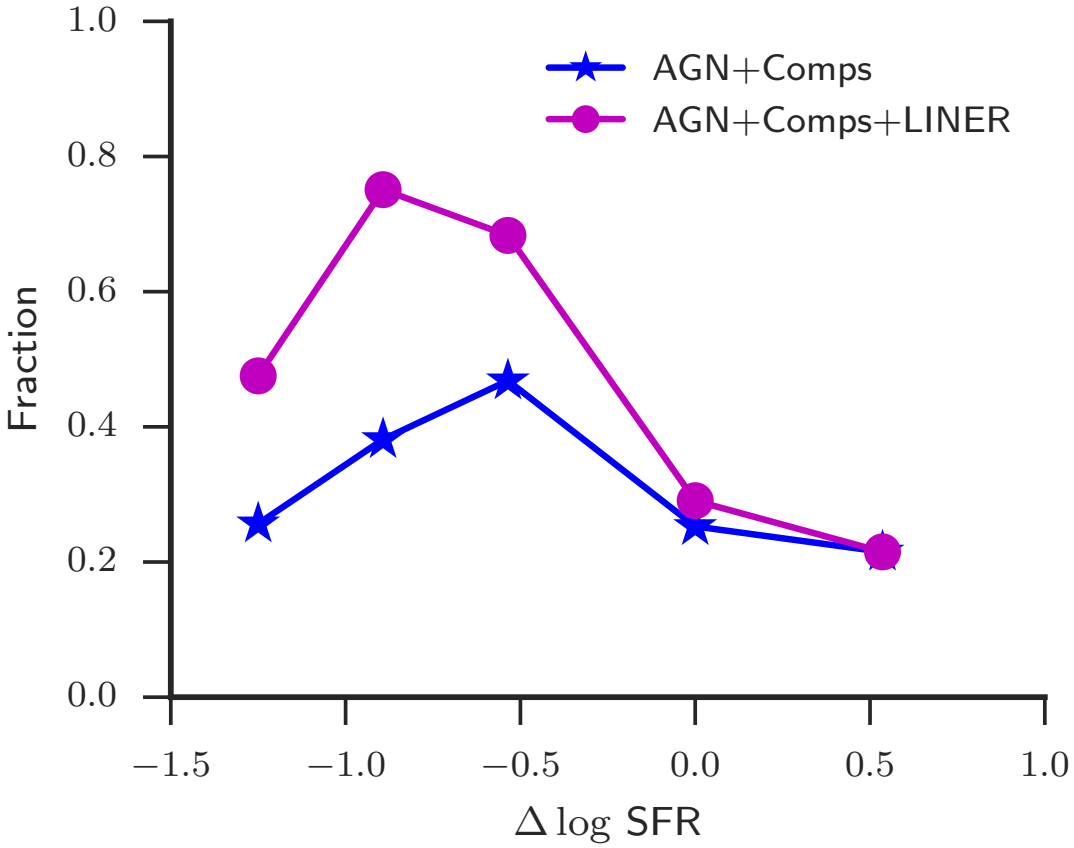

Figure 4.12: Fraction of all COLD GASS galaxies that are AGN or Composite galaxies (blue star) and AGN, Composite, or LINERs (magenta circles) as a function of distance from the main sequence. The fractions shown are the average fractions of all 50 representative subsamples.

host galaxy or they are just "along for the ride" off the main sequence. An answer could possibly come from surveys using integral field unit (IFU) spectroscopy such as MaNGA[11] and CALIFA (Sánchez et al., 2012) that provide spatially resolved spectra across the entire galaxy.

[11] https://www.sdss3.org/future/manga.php

4.7 Summary and Conclusions

Using consistent measures of both stellar mass and SFR, we compared three samples of galaxies, one a set of local, non-AGN star-forming galaxies (HRS), one a complete set of AGN host galaxies selected from the *Swift*/BAT catalog, and one a mass-selected sample of both star-forming and AGN host galaxies (COLD GASS). From the HRS, we constructed our own "main sequence" relation and systematically analyzed the location of the samples with respect to the main sequence. Our main conclusions are as follows:

1. AGN host galaxies, both X-ray selected and optically selected, systematically lie below the main sequence, indicating reduced levels of star-formation.

2. After splitting the AGN sample into regions of increased offset from the main sequence of star formation, we found no dependence of the offset on hard X-ray luminosity.

3. Analysing the morphologies of the samples, we find that while the fraction of BAT AGN that are in spirals most closely resembles the star-forming sample, the sSFR's are more closely related to the optically selected AGN. The distribution of sSFR for spirals and ellipticals in the BAT AGN also best match the distribution for spirals and ellipticals for optically selected AGN. We find a significant increase in the merger fraction from 0.1 well below the main sequence up to 0.4 near, inside, and above it. The merger fractions for the BAT AGN are much higher than those for the COLD GASS AGN and star-forming

galaxies.

4. These results are both model independent as well as unaffected by our selection criteria. A detailed comparison with Mullaney et al. (2012a) does not find any discrepancy between the two studies, and evolving our population of AGN to higher redshifts agrees well with their detection fractions.

5. Expanding the analysis to the larger SDSS sample of galaxies shows the effect of AGN host galaxies lying below the main sequence also occurs in larger optically selected samples and confirms the previous findings of AGN preferentially occurring in galaxies in transition from star-forming to quiescence.

6. We discussed how the trend in sSFR can be explained by AGN feedback that reduces the supply of cold gas in the galaxy. This slowly suppresses star-formation through short periodic outbursts. It can also be explained if the occurrence of AGN is simply the result of the availability of cold gas. As star formation is quenched through other processes the AGN follows along and eventually fades as the cold gas runs out. In either case it is clear AGN are prevalent in massive galaxies currently falling off the main sequence.

Chapter 5: Summary, Conclusions, and Future Work

This thesis explored the global star-forming properties of an unbiased, ultra-hard X-ray selected sample of AGN in an effort to find evidence for AGN feedback. Our AGN selection method ensured no bias exists in terms of the host galaxy SFR or obscuration towards the AGN. Our sample is one of the largest local AGN samples that allows for robust statistical analysis into the nature of AGN host galaxies. The studies contained in this thesis have provided strong conclusions into the relationship between AGN activity and star formation and strengthened previous hints about the AGN's role in galaxy evolution.

In Chapter 2, we detailed the procedure for analyzing the SPIRE images for the entire *Herschel*-BAT sample. After producing the largest local AGN catalog of fluxes out to 500 μm, we robustly measured for the first time the relationship between sub-millimeter emission and AGN luminosity. We found no strong correlation, confirmation that rest-frame long wavelength radiation is largely dominated by dust heated in the host galaxy rather than the AGN. This result was further strengthened by comparing the SPIRE flux ratios with a non-AGN galaxy sample on a color-color plot where the bulk of the AGN colors followed the behavior of the non-AGN. Intriguingly, however, we did find a small subset of our AGN which

showed anomalous colors, consistent with a 500 μm excess and suggestive of possible contamination by synchrotron emission from the corona of the AGN. Follow-up observations at longer wavelengths of these sources could have significant impact on our knowledge of the physics of AGN.

Chapter 3 utilizes the SPIRE catalog created in Chapter 2 to build the 12–500 μm SED for each *Herschel*-BAT AGN. SPIRE fluxes were combined with the PACS fluxes from Meléndez et al. (2014) and WISE photometry from the AllWISE catalog. We fit the SEDs using an analytical model composed of an exponentially cutoff powerlaw with a modified blackbody to measure the SFR, dust mass, and dust temperature for each source. We compared our modeling with two other popular models that incorporate templates to decompose the SED, finding general agreement between all three. Our model comparison resulted in tight constraints on the uncertainty in measuring the star-forming luminosity, AGN IR luminosity, and fraction of AGN contribution to the 8–1000 μm luminosity. We compared the infrared luminosity due to AGN heating with the 14–195 keV X-ray luminosity finding a very strong linear correlation that both suggests our SED decomposition methods were successful and provides an easy calibration for estimating the 8–1000 μm AGN luminosity. Using a stellar-mass matched sample from the *Herschel* Reference Survey, we compared the dust mass, dust temperature, and SFR of AGN host galaxies with non-AGN galaxies. We found that on average, AGN tend to reside in host galaxies with significant star formation. Because of the greater star formation compared to our comparison sample, the dust masses and dust temperatures also tend to be higher as well. This result confirmed the previous findings of Koss et al. (2011) who

found the BAT AGN to be bluer than non-AGN galaxies. Finally, we found zero evidence for any connection between the intrinsic AGN luminosity and the global SFR of its host galaxy.

Following up on the results of Chapter 3, Chapter 4 heavily focused on the main sequence of star-formation and the AGN population's place in relation to it. We discovered that AGN systematically lie below the main sequence, evidence for ongoing quenching of star-formation. We found, by comparing the *Herschel*-BAT AGN to the COLD GASS sample, that AGN host galaxies lie firmly between the star-forming population and quenched population, confirmation that AGN largely lie in the "green valley" and are transitioning towards the "red sequence." Just as we did for the absolute SFR, we find no correlation between how far below the main sequence a galaxy is and its AGN luminosity. While this seems to be in contradiction with our results from Chapter 3, the problem lies in the mass-matched sample. Because the majority of AGN are located in high-mass galaxies, a non-AGN mass-matched sample without taking into account morphology will preferentially select quiescent ellipticals leading to results that show AGN host galaxies to be more star-forming. However, in Chapter 3, we show that in fact AGN host galaxies are in between normal, star-forming galaxies and the quiescent ellipticals.

The results of this thesis support a model of galaxy evolution that involves AGN feedback, however the model must account for the lack of relationship between the AGN luminosity, which should be driving whatever mechanism feedback works through, and the SFR, the parameter that should be most affected by feedback. Its clear that combining our work in this study with that of Stanley et al. (2015) shows

that during any narrow epoch the individual SFRs of galaxies containing moderate luminosity AGN is not related to its SFR. Rather the bulk distribution of SFRs in AGN host galaxies is systematically shifted to lower SFRs, quantified by their location against the main sequence. Since our discovery, numerous studies have confirmed this phenomenon at a range of redshifts (Leslie et al., 2016; Matsuoka et al., 2015; Mullaney et al., 2015). The Hickox et al. (2014) model whereby short-term AGN variability is washing away any intrinsic relationship certainly has strong potential, but it seems it must be adjusted to account for the lack of an upturn at high AGN luminosity that was previously seen in earlier studies. If the model can be adjusted by either flattening the slope or lowering the normalization, there is still the question of what its physical cause is. Is it AGN feedback or is it a simple scaling that naturally arises as a consequence of gas availability? Both of those scenarios can also explain the decreased specific SFR as we discuss at the end of Chapter 4.

Clearly there is still lots of work left in understanding the AGN's influence on its host galaxy. This thesis though has certainly made a big step forward confirming AGN are in the process of transitioning to quiescence through a close analysis of their FIR SEDs. The *Herschel* data too still have much to offer to in the way of AGN science and in the rest of this Chapter I highlight several ongoing or future projects.

5.1 The Far-Infrared Size Distribution in AGN Host Galaxies and Nuclear Far-Infrared Emission

One of the key upgrades of *Herschel* compared to previous FIR telescopes is its angular resolution. As shown in Chapter 1, the increase in resolution from IRAS to *Herschel* is dramatic changing from several arcminutes to 6″ at 70 μm. Combined with the necessary sensitivity to detect low surface brightness emission and a low redshift sample, we can measure for the first time the extent of star formation in AGN host galaxies and spatially decompose the emission into nuclear and extra-nuclear components. Lutz et al. (2016) measured FIR sizes for a sample of normal star-forming galaxies and Palomar-Green (PG) QSOs finding similar sizes between the two samples. However, the PG QSOs are at higher redshift than the *Herschel*-BAT AGN and were only partially resolved whereas we can explicitly measure the sizes for AGN host galaxies over a larger range of AGN luminosity. They further found that galaxies with higher specific SFR compared to the main sequence show decreased FIR sizes and higher FIR surface brightnesses indicating more compact star formation. With the main sequence measurements from Chapter 4, we can test this result as well for AGN host galaxies.

After first creating the maps for the sample, we immediately noticed that much of the *Herschel*-BAT AGN are compact, even at 70 μm with its relatively high angular resolution. However, at the highest redshift of our sample, $z = 0.05$, 6″ corresponds to 6 kpc so its possible the compact sources were simply only partially

resolved and at higher redshifts. Therefore, we decided to test their compactness using several methods.

The first test we did was to simply measure the fraction of the flux contained within a small aperture (6″, 12″, and 18″ for 70, 160, and 250μm) centered on the nucleus. We compared these nuclear fluxes ($F_{\rm nuc}$) to the total fluxes ($F_{\rm total}$ and only used sources for which the S/N in the aperture photometry flux was greater than 5 (i.e. all of the "detected" sources in the catalogs). Figure 5.1 shows the KDE of the distribution and histograms for the nuclear fraction ($F_{\rm nuc}/F_{\rm total}$) at each waveband.

The reason the peaks of the distributions are less than 1.0 is due to the wings of the PSF. In the calculation of $F_{\rm total}$, we applied aperture corrections to point-like objects to account for flux missed by the aperture. In Figure 5.1, we show the corresponding aperture corrections of 0.64, 0.68, and 0.77 for a 6″, 12″, and 18″aperture at 70, 160, and 250 μm. If we use an arbitrary cutoff of 0.5 to denote "point-source-dominated" sources, we find that 78, 77, and 73% of the sample are "point-source-dominated." Applying the aperture corrections to the nuclear fluxes changes the percentages to 92, 87, and 83%. Using either numbers indicates that for a large fraction of the *Herschel*-BAT sample, the FIR emission largely originates within a small angular region. Based on this simple analysis, it seems that the FIR emission, especially at 70 μm, is concentrated near the nucleus. To confirm this, we used 2D spatial decomposition to measure the sizes and nuclear fluxes of our sources.

To model the FIR surface brightness of our sample, we used *GALFIT* (Peng et al., 2002), a popular 2D surface brightness decomposition software package. We

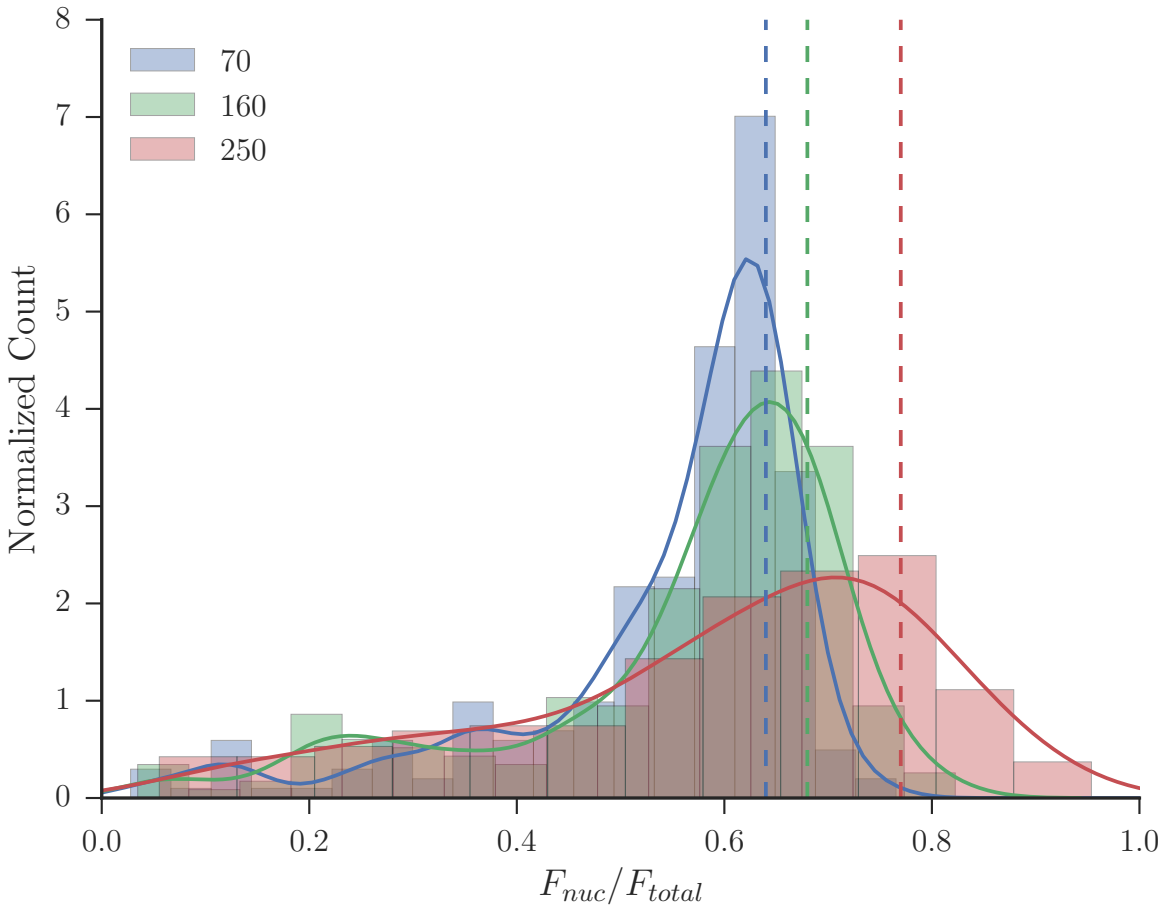

Figure 5.1: The distribution of the fraction of the flux contained within a 6″, 12″, and 18″aperture centered on the nucleus for the 70 μm (blue), 160 μm (green), and 250 μm (red) *Herschel* images. The vertical dashed lines correspond to the encircled energy fraction for an unresolved source at each waveband (0.64, 0.68, and 0.77 for 70, 160, and 250 μm).

used three separate models: an unresolved point source (PS), a Sèrsic profile (S), and a combined Sèrsic and point source (S+PS). These three models correspond to the broad categories we found by looking through the images. A Sèrsic profile is a general radial profile often used in fitting galaxies and is parameterized primarily by the Sèrsic index (n, a measure of the "cuspiness") and the half-light radius, r_e.

Just from the number of purely unresolved sources, we confirm our previous qualitative results that the 70 μm emission is more compact than 160 and 250 μm. At 70 μm, we find 108/270 (40%) of the sample are completely unresolved, with no indication of any extended emission while at 160 μm there are 71/270 (26%) and at 250 μm, 82/270 (30%). Even including the undetected sources as also unresolved, (3, 12, and 16 sources at 70, 160, and 250 μm), does not affect the results although it does bring the 250 μm numbers near that of 70 μm, but still less than 70 μm even though the spatial resolution is a factor of 3 worse.

Looking at the distribution of the physical sizes spanned at each wavelength (Figure 5.2), the same effect can be seen even for the sources which have a detectable extended component (solid lines). While each waveband shows approximately the same shape (peak at small radii with long tail towards large radii), the 70 μm distribution is clearly peaked at much smaller radii than the 160 μm and 250 μm distributions. The median effective radius at 70 μm is 1.7 kpc while at 160 μm it is 4.0 kpc and 250 μm it is 5.4 kpc. For all unresolved sources, we calculated an upper limit to the source size by fitting the source with a single extended component and iteratively increasing the effective radius until χ^2 changed by 3σ. The median upper limit to the effective radius for unresolved objects is 0.9 kpc at 70 μm, 2.4 kpc at

160 μm, and 3.4 kpc at 250 μm. The increase in the upper limits on the unresolved sizes with wavelength is due to the decreasing resolution.

In Mushotzky et al. (2014), we reported these results and discussed the possibility that AGN live inside compact starburst-like regions given the small sizes, especially at 70 μm. Since 70 μm has been shown to more closely follow the hot dust distribution associated with star-formation compared to longer wavelengths which can be effected by heating by the older stellar population (Bendo et al., 2012; Boquien et al., 2011; Calzetti et al., 2010; Li et al., 2010, 2013). Therefore we calculated SFRs based solely on the 70 μm luminosity and used the 70 μm sizes as an estimate of the surface area of star formation. We found that between 30% and 50% of our sample have high SFR surface densities, above the empirical threshold for driving galactic winds, $\Sigma_{\rm SFR} > 0.1$ M$_\odot$ yr^{-1} kpc^{-2} (Heckman, 2001). We suggested that this could be an indication for how feedback works, where central starbursts produce winds that can then be boosted by radiation from the AGN. The other possibility is that AGN feedback has preferentially shut down star formation in the extended outer regions of the galaxy, leaving behind only compact nuclear star formation.

We have updated these results to reflect the SFR measured through our SED fitting which corrects for possible AGN contribution. We still use the 70 μm sizes., determined by calculating the radius at which 90% of the emission is contained in which varies as a function of n. In total we find 90/270 (33%) AGN host galaxies have $\Sigma_{\rm SFR} > 0.1$ M$_\odot$ yr^{-1} kpc^{-2}. Within the sample, it is about an even split between unresolved sources (44) and extended sources (46). If we include the rest of the unresolved population, the number jumps up to 152/270 (56%) however this is a

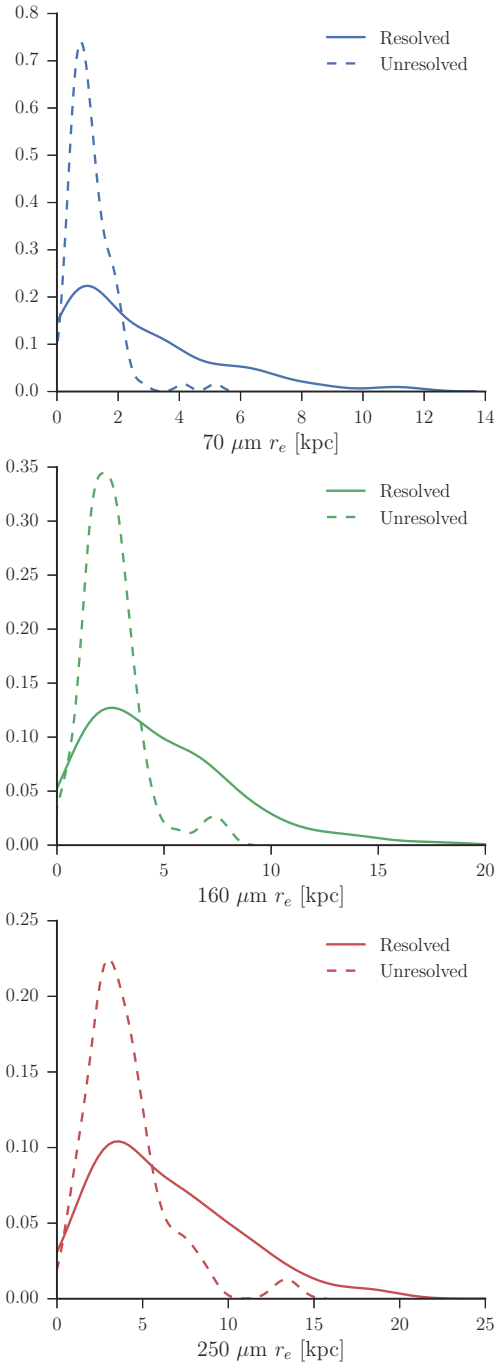

Figure 5.2: Distributions of the effective radius at 70 (top), 160 (middle), and 250 μm (bottom) for the *Herschel*-BAT AGN. Solid lines correspond to resolved sources which were able to be fit with a Sérsic component, while the dashed line is the distribution of 3σ upper limits for the unresolved population.

highly conservative upper limit given 17 of these sources have upper limits on their SFR as well. Then it is reasonable to conclude that between 33 – 56% of AGN host galaxies have $\Sigma_{\rm SFR}$ indicative of starburst driven winds, the same range we found in Mushotzky et al. (2014).

I want to extend this analysis in two separate ways. 1) Use a subset of our sample which are very nearby to spatially resolve the FIR emission on small scales. Combining our *Herschel* imaging with archival or new imaging at near-infrared and mid-infrared wavelengths will allow us to investigate the specific heating mechanisms within the internal structure of each source. We'll be able show just how extended star formation is in each galaxy and use correlations between different wavelengths and flux ratios to determine whether young stars, old stars, or the AGN is heating the dust. This method has been used extensively in the literature but largely ignoring AGN host galaxies (Bendo et al., 2012; Boquien et al., 2011; Hunt et al., 2015; Kirkpatrick et al., 2014). Bendo et al. (2010) used *Herschel* to study resolved FIR emission in M81, noting that within 2 kpc there seemed to be high dust temperatures which could be heated by the AGN or a compact starburst. By comparing with non-AGN, this project would reveal any effect the AGN could be having on the heating of dust and star formation in their galaxy. We would also be able to compare the extended structure with their location with respect to the main sequence to determine where star formation is shutting down. This would inform models of quenching and help assess the impact of AGN feedback.

2) The second project would specifically focus on the extracted nuclear FIR fluxes obtained through our *GALFIT* analysis. We can use these and combine them

with either infrared spectroscopy or high resolution photometry to investigate nuclear infrared SED out to long wavelengths. We can then test whether clumpy torus models or previous templates are able to reproduce the observed long wavelength emission. If not, we can test other models such as a dusty wind (Hönig et al., 2013; Keating et al., 2012) or dust associated with NLR. Asmus et al. (2014) recently found that extended nuclear MIR emission aligns with previously observed ionization cones which should be resolvable in the FIR for our most nearby AGN. This would lead to better templates for the intrinsic AGN SED out to longer wavelengths and possibly reveal relationships with the AGN luminosity. I've recently began work on this and specifically looked at the 70/14 μm flux ratio for sources where the *Spitzer* IRS spectra are likely dominated by the AGN determined with the DeblendIRS method from Hernán-Caballero et al. (2015). Intriguingly I find a negative correlation between the flux ratio and X-ray luminosity as shown in Figure 5.3. The reduced flux ratio would indicate relatively more cold dust in low luminosity AGN, a possible indication that at high luminosities the AGN has cleared the nearby environment.

5.2 Merger Induced Star Formation and AGN Activity

This thesis focused on the SFRs of AGN host galaxies and their relationship to the AGN luminosity. One important piece of the puzzle though is mergers and interactions. In Chapter 4, we did show that the merger fraction in the *Herschel*-BAT sample increases as the specific SFR increases, in line with the theory that mergers induce enhanced star formation (e.g. Di Matteo et al., 2007; Patton et al.,

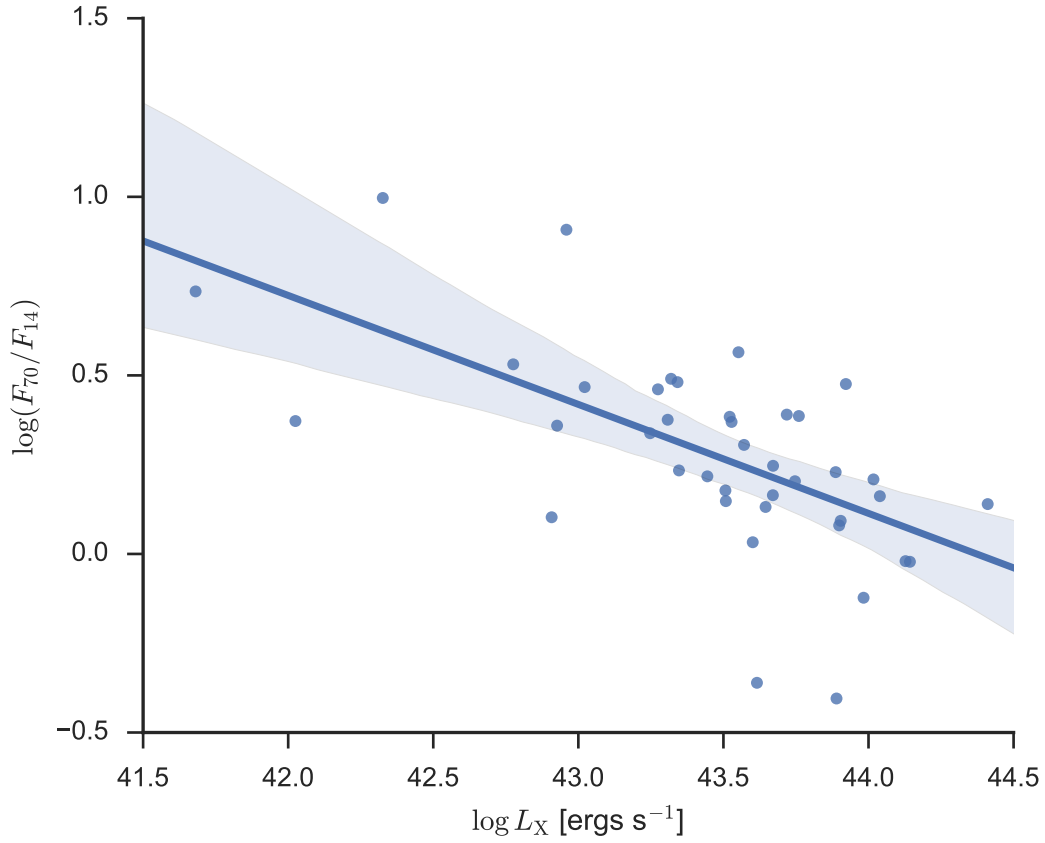

Figure 5.3: The nuclear 70/14 μm flux ratio, a measure of the bulk dust temperature, as a function of X-ray luminosity. Nuclear 70 μm fluxes were calculated based on spatial decomposition using GALFIT while the 14 μm flux is from *Spitzer* IRS spectra.

2013). As Koss et al. (2010) showed in previous work on the BAT AGN, mergers seem to be an important mechanism for triggering AGN. Ellison et al. (2011) also showed a clear increase in the AGN fraction for close pairs of interacting galaxies.

With our *Herschel* data, we can explore the SFRs of the interacting galaxies in the *Herschel*-BAT sample. Key questions we could answer are: 1) Which of the galaxies (AGN or non-AGN) show stronger star-formation? 2) Does the SFR increase as a function of projected distance between the galaxy pairs? 3) Does the relationship between AGN luminosity and SFR get stronger as the projected distance between them decreases? 4) Are merging AGN host galaxies more compact than their partner?

Answers to these questions would provide great insight into the merger induced fueling and triggering of both star formation and the AGN. An increasing connection between the SFR and AGN luminosity and/or Eddington ratio with decreasing distance would prove that mergers and interactions are causing instabilities to funnel gas into the central regions of galaxies.

Appendix A: SPIRE Observations of the *Herschel*-BAT Sample

Table A.1: The *Herschel*-BAT Sample

Name	RA (J2000)	DEC (J2000)	z	Distance (Mpc)	Type	OD	OBSID
Mrk 335	00h06m19.5s	+20d12m10s	0.0258	112.62	Sy 1.2	949	1342234683
2MASX J00253292+6821442	00h25m32.9s	+68d21m44s	0.012	51.87	Sy 2	1022	1342239794
CGCG 535-012	00h36m21.0s	+45d39m54s	0.0476	211.45	Sy 1.2[a]	976	1342237509
NGC 235A	00h42m52.8s	-23d32m28s	0.0222	96.83	Sy 2	737	1342221462
MCG -02-02-095	00h43m08.8s	-11d36m04s	0.0189	81.99	Sy 2	949	1342234695
Mrk 348	00h48m47.1s	+31d57m25s	0.015	65.13	Sy 1.9	603	1342212368
MCG +05-03-013	00h51m35.0s	+29d24m05s	0.036	158.22	Sy 1[a]	977	1342237559
Mrk 352	00h59m53.3s	+31d49m37s	0.0149	64.39	Sy 1.2	964	1342236244
ESO 195-IG021 NED03	01h00m35.0s	-47d52m04s	0.0482	214.22	Sy 2	949	1342234727
MCG -07-03-007	01h05m26.8s	-42d12m58s	0.0299	130.92	Sy 2	949	1342234725
2MASX J01064523+0638015	01h06m45.3s	+06d38m02s	0.041	181.09	Sy 2	976	1342237549
2MASX J01073963-1139117	01h07m39.6s	-11d39m12s	0.0475	210.61	Sy 2	977	1342237554
NGC 424	01h11m27.6s	-38d05m00s	0.0118	50.84	Sy 1.9	949	1342234724
Mrk 975	01h13m51.0s	+13d16m18s	0.0496	220.6	Sy 1.5	976	1342237498
IC 1657	01h14m07.0s	-32d39m03s	0.012	51.66	Sy 2	949	1342234723
Fairall 9	01h23m45.8s	-58d48m21s	0.047	208.57	Sy 1.2	963	1342236209
NGC 526A	01h23m54.4s	-35d03m56s	0.0191	82.99	Sy 2	949	1342234722
NGC 513	01h24m26.9s	+33d47m58s	0.0195	84.96	Sy 2	976	1342237506
Mrk 359	01h27m32.6s	+19d10m44s	0.0174	75.45	Sy 1.5	977	1342237557
MCG -03-04-072	01h28m06.7s	-18d48m31s	0.046	203.92	Sy 1[a]	949	1342234711
ESO 244-IG030	01h29m51.2s	-42d19m35s	0.0256	111.78	Sy 2	976	1342237522
ESO 297-018	01h38m37.2s	-40d00m41s	0.0252	110.13	Sy 2	976	1342237523
MCG -01-05-047	01h52m49.0s	-03d26m49s	0.0172	74.63	Sy 2	976	1342237537
UGC 01479	02h00m19.1s	+24d28m25s	0.0164	71.28	Sy 2[a]	989	1342238264
NGC 788	02h01m06.4s	-06d48m56s	0.0136	58.87	Sy 2	976	1342237536
Mrk 1018	02h06m16.0s	-00d17m29s	0.0424	187.63	Sy 1.2	976	1342237542
LEDA 138501	02h09m34.3s	+52d26m33s	0.0492	218.61	Sy 1[a]	1022	1342239798
ESO 197-G027	02h10m52.5s	-49d41m55s	0.0481	213.5	Sy 2	963	1342236212
Mrk 590	02h14m33.6s	-00d46m00s	0.0264	115.29	Sy 1.5	976	1342237544
NGC 931	02h28m14.5s	+31d18m42s	0.0167	72.23	Sy 1.5	989	1342238263
IC 1816	02h31m51.0s	-36d40m19s	0.0169	73.52	Sy 1.9	963	1342236221
NGC 985	02h34m37.8s	-08d47m15s	0.0431	190.85	Sy 1.5	989	1342238278
ESO 198-024	02h38m19.7s	-52d11m33s	0.0455	201.63	Sy 1[a]	963	1342236214
NGC 1052	02h41m04.8s	-08d15m21s	0.005	19.4	Sy 2	989	1342238279
Mrk 595	02h41m34.9s	+07d11m14s	0.027	117.95	Sy 1.5[a]	989	1342238272
ESO 479-G031	02h44m47.7s	-24d30m50s	0.0235	102.58	LINER[a]	963	1342236224
[HB89] 0241+622	02h44m57.7s	+62d28m07s	0.044	194.77	Sy 1.2	1022	1342239795
NGC 1106	02h50m40.5s	+41d40m17s	0.0145	62.65	Sy 2[a]	1022	1342239820
2MFGC 02280	02h50m42.6s	+54d42m18s	0.0152	65.66	Sy 2	1022	1342239800
NGC 1125	02h51m40.3s	-16d39m04s	0.0109	47.21	Sy 2	989	1342238282
MCG -02-08-014	02h52m23.4s	-08d30m37s	0.0168	72.67	Sy 2	989	1342238280
ESO 417-G006	02h56m21.5s	-32d11m08s	0.0163	70.65	Sy 2	963	1342236222
MCG -02-08-038	03h00m04.3s	-10d49m29s	0.0326	143.05	Sy 1.5	989	1342238281
NGC 1194	03h03m49.1s	-01d06m13s	0.0136	58.84	Sy 2	1022	1342239837
ESO 031-G008	03h07m35.3s	-72d50m03s	0.0276	120.79	Sy 1.2	861	1342229230
MCG +00-09-042	03h17m02.2s	+01d15m18s	0.0238	103.62	Sy 2	1022	1342239841

Table A.1 – continued from previous page

Name	RA (J2000)	DEC (J2000)	z	Distance (Mpc)	Type	OD	OBSID
IRAS 03219+4031	03h25m13.2s	+40d41m55s	0.0477	211.83	Sy 2[a]	1022	1342239818
2MASX J03305218+0538253	03h30m52.2s	+05d38m26s	0.046	203.92	Sy 1.9	1023	1342239939
MCG -01-09-045	03h31m23.0s	-05d08m30s	0.0128	55.46	Sy 2	1022	1342239846
NGC 1365	03h33m36.4s	-36d08m25s	0.0055	18	Sy 2	427	1342201436
2MASX J03342453-1513402	03h34m24.5s	-15d13m40s	0.0349	153.63	Sy 1.5	989	1342238285
ESO 548-G081	03h42m03.7s	-21d14m39s	0.0145	62.71	Sy 1	989	1342238286
LCRS B034324.7-394349	03h45m12.5s	-39d34m29s	0.0428	189.21	Sy 1.9	963	1342236218
2MASX J03502377-5018354	03h50m23.8s	-50d18m36s	0.0365	160.65	Sy 2	1022	1342239868
2MASX J03534246+3714077	03h53m42.5s	+37d14m07s	0.0186	81	Sy 2	1022	1342239817
2MASX J03540948+0249307	03h54m09.5s	+02d49m31s	0.036	158.43	Sy 1.5	1022	1342239849
ESO 549-G049	04h02m25.7s	-18d02m51s	0.0263	114.87	Sy 1.9	1022	1342239856
IRAS 04124-0803	04h14m52.7s	-07d55m40s	0.0382	168.2	Sy 1.5	1022	1342239852
3C 111.0	04h18m21.3s	+38d01m36s	0.0485	215.39	Sy 1.2	861	1342229105
ESO 157-G023	04h22m24.2s	-56d13m33s	0.0435	192.62	Sy 2	861	1342229232
2MASX J04234080+0408017	04h23m40.8s	+04d08m02s	0.045	199.34	Sy 2	1023	1342239937
3C 120	04h33m11.1s	+05d21m16s	0.033	144.95	Sy 1.5	1023	1342239936
Mrk 618	04h36m22.2s	-10d22m34s	0.0356	156.39	Sy 1.5	1023	1342239927
MCG -02-12-050	04h38m14.2s	-10d47m45s	0.0364	160.02	Sy 1.2	1023	1342239926
1RXS J044154.5-082639	04h41m54.1s	-08d26m34s	0.044	194.77	Sy 1[a]	1025	1342241125
UGC 03142	04h43m46.8s	+28d58m19s	0.0217	94.29	Sy 1[a]	861	1342229103
2MASX J04440903+2813003	04h44m09.0s	+28d13m01s	0.0113	48.68	Sy 1.9	861	1342229102
MCG -01-13-025	04h51m41.5s	-03d48m33s	0.0159	68.9	Sy 1.2	861	1342229242
1RXS J045205.0+493248	04h52m05.0s	+49d32m45s	0.029	126.96	Sy 1.5	861	1342229109
CGCG 420-015	04h53m25.8s	+04d03m42s	0.0294	128.71	Sy 2	862	1342229656
ESO 033-G002	04h55m59.0s	-75d32m28s	0.0181	78.6	Sy 2	861	1342229229
2MASX J05020903+0331499	05h02m09.0s	+03d31m50s	0.016	69.32	Sy 1[a]	862	1342229658
2MASX J05054575-2351139	05h05m45.7s	-23d51m14s	0.035	154.1	Sy 2	829	1342226989
CGCG 468-002 NED01	05h08m19.7s	+17d21m48s	0.0175	75.98	Sy 1.9	841	1342227712
IRAS 05078+1626	05h10m45.5s	+16d29m56s	0.0179	77.63	Sy 1.5	841	1342227713
ESO 553-G022	05h11m57.8s	-18d29m38s	0.0421	186	Sy 2	861	1342229241
Ark 120	05h16m11.4s	-00d08m59s	0.0327	143.61	Sy 1	841	1342227715
MCG -02-14-009	05h16m21.2s	-10d33m41s	0.0285	124.52	Sy 1.2	862	1342229660
ESO 362-18	05h19m35.8s	-32d39m28s	0.0124	53.81	Sy 1.5	862	1342229664
Pictor A	05h19m49.7s	-45d46m44s	0.0351	154.17	Sy 1.9	861	1342229235
IRAS0 5218-1212	05h24m06.5s	-12d10m00s	0.049	217.69	Sy 1.5	862	1342229662
ESO 553-G043	05h26m27.3s	-21d17m12s	0.0278	121.4	Sy 2	829	1342226988
NGC 2110	05h52m11.4s	-07d27m22s	0.0078	35.6	Sy 2	841	1342227709
MCG +08-11-011	05h54m53.6s	+46d26m22s	0.0205	89.11	Sy 1.5	861	1342229113
2MASX J05580206-3820043	05h58m02.0s	-38d20m05s	0.0339	148.82	Sy 1.2	841	1342227702
IRAS0 5589+2828	06h02m10.7s	+28d28m22s	0.033	144.9	Sy 1.2	861	1342229101
ESO 005-G004	06h05m41.6s	-86d37m55s	0.0062	22	Sy 2	861	1342229228
Mrk 3	06h15m36.3s	+71d02m15s	0.0135	58.5	Sy 1.9	1024	1342240031
ESO 121-IG028	06h23m45.6s	-60d58m44s	0.0405	178.91	Sy 2	825	1342226640
ESO 426-G002	06h23m46.4s	-32d13m00s	0.0224	97.71	Sy 2	829	1342226983
6dF J0626586-370559	06h26m58.6s	-37d05m59s	0.0385	169.82	Sy 1.5	829	1342226982
VII Zw 073	06h30m25.6s	+63d40m41s	0.0413	182.6	Sy 2	861	1342229118
UGC 03478	06h32m47.2s	+63d40m25s	0.0128	55.23	Sy 1.2[a]	861	1342229117
ESO 490-IG026	06h40m11.7s	-25d53m43s	0.0249	108.46	Sy 1.9	841	1342227705
2MASX J06411806+3249313	06h41m18.0s	+32d49m32s	0.047	208.5	Sy 2	861	1342229100
Mrk 6	06h52m12.3s	+74d25m37s	0.0188	81.74	Sy 1.5	861	1342229129
UGC 03601	06h55m49.5s	+40d00m01s	0.0171	74.3	Sy 1.9	862	1342229650
2MASX J06561197-4919499	06h56m12.0s	-49d19m50s	0.041	181.1	Sy 2	829	1342226980
MCG +06-16-028	07h14m03.9s	+35d16m45s	0.0157	68.03	Sy 1.9	880	1342230761
2MASX J07262635-3554214	07h26m26.4s	-35d54m22s	0.0294	128.77	Sy 2[a]	841	1342227704
Mrk 79	07h42m32.8s	+49d48m35s	0.0222	96.65	Sy 1.5	862	1342229646
UGC 03995A	07h44m07.0s	+29d14m57s	0.0158	68.54	Sy 2	862	1342229473
Mrk 10	07h47m29.1s	+60d56m01s	0.0293	128.1	Sy 1.5	861	1342229119
2MASS J07594181-3843560	07h59m41.7s	-38d43m57s	0.04	176.55	Sy 1.2[a]	862	1342229676
2MASX J07595347+2323241	07h59m53.5s	+23d23m24s	0.0292	127.78	Sy 1.9	862	1342229468
IC0 486	08h00m21.0s	+26d36m49s	0.0269	117.47	Sy 1.9	862	1342229470
ESO 209-G012	08h01m58.0s	-49d46m42s	0.0405	178.79	Sy 1.5[a]	862	1342229673
2MASX J08032736+0841523	08h03m27.4s	+08d41m52s	0.0468	207.58	Sy 1.5	880	1342230783
Mrk 1210	08h04m05.9s	+05d06m50s	0.0135	58.4	Sy 1.9	880	1342230791
MCG +02-21-013	08h04m46.4s	+10d46m36s	0.0344	151.36	Sy 2	880	1342230782

Table A.1 – continued from previous page

Name	RA (J2000)	DEC (J2000)	z	Distance (Mpc)	Type	OD	OBSID
Fairall 272	08h23m01.1s	-04d56m05s	0.0218	95	Sy 2	880	1342230789
Fairall 1146	08h38m30.8s	-35d59m33s	0.0316	138.51	Sy 1.5[a]	880	1342230800
MCG +11-11-032	08h55m12.5s	+64d23m46s	0.0363	159.56	Sy 2	861	1342229121
NGC 2655	08h55m37.7s	+78d13m23s	0.0047	23.8	Sy 2	862	1342229633
Mrk 18	09h01m58.4s	+60d09m06s	0.0111	47.89	Sy 1.9	862	1342229641
2MASX J09023729-4813339	09h02m37.3s	-48d13m34s	0.0391	172.46	Sy 1[a]	829	1342226977
2MASX J09043699+5536025	09h04m36.9s	+55d36m03s	0.0371	163.59	Sy 1.2	862	1342229494
Mrk 704	09h18m26.0s	+16d18m19s	0.0292	128.01	Sy 1.2	1093	1342245565
SBS 0915+556	09h19m13.2s	+55d27m55s	0.0494	219.53	Sy 1.9	862	1342229495
IC 2461	09h19m58.0s	+37d11m29s	0.0075	25.5	Sy 2	1093	1342245569
MCG -01-24-012	09h20m46.2s	-08d03m22s	0.0196	85.4	Sy 2	1082	1342245154
MCG +04-22-042	09h23m43.0s	+22d54m33s	0.0323	141.98	Sy 1.5	1116	1342246606
2MASX J09235371-3141305	09h23m53.7s	-31d41m31s	0.0424	187.31	Sy 2	948	1342234834
2MASX J09254750+6927532	09h25m47.5s	+69d27m53s	0.039	172.01	Sy 1[a]	861	1342229123
NGC 2885	09h27m18.5s	+23d01m12s	0.0263	114.98	Sy 1.2	1116	1342246607
CGCG 312-012	09h29m37.9s	+62d32m39s	0.0256	111.84	Sy 1.9	862	1342229638
ESO 565-G019	09h34m43.6s	-21d55m40s	0.0163	70.62	Sy 2[a]	948	1342234836
2MASX J09360622-6548336	09h36m06.3s	-65d48m33s	0.0392	173	Sy 1.9	825	1342226635
CGCG 122-055	09h42m04.8s	+23d41m07s	0.0214	93.03	Sy 1.5	904	1342231843
NGC 2992	09h45m42.1s	-14d19m35s	0.0077	31.6	Sy 1.9	403	1342198866
MCG -05-23-016	09h47m40.2s	-30d56m55s	0.0085	36.58	Sy 1.9	948	1342234833
NGC 3035	09h51m55.0s	-06d49m23s	0.0145	62.89	Sy 1.5	1116	1342246593
NGC 3081	09h59m29.5s	-22d49m35s	0.008	32.5	Sy 2	558	1342210523
2MASX J09594263-3112581	09h59m42.6s	-31d12m58s	0.037	162.95	Sy 1[a]	948	1342234832
NGC 3079	10h01m57.8s	+55d40m47s	0.0037	25.8	Sy 1.9	880	1342230873
ESO 499-G041	10h05m55.4s	-23d03m25s	0.0128	55.43	Sy 1.5	948	1342234837
ESO 263-G013	10h09m48.2s	-42d48m40s	0.0335	147.32	Sy 2	963	1342236206
ESO 374-G044	10h13m19.9s	-35d58m58s	0.0285	124.52	Sy 2	948	1342234830
ARK 241	10h21m40.2s	-03d27m14s	0.0408	180.39	Sy 1.2	948	1342234845
NGC 3227	10h23m30.6s	+19d51m54s	0.0039	26.4	Sy 1.5	381	1342197318
NGC 3281	10h31m52.1s	-34d51m13s	0.0107	46.09	Sy 2	428	1342201483
2MASX J10402231-4625264	10h40m22.5s	-46d25m26s	0.0239	104.34	Sy 2	963	1342236205
SDSS J104326.47+110524.2	10h43m26.5s	+11d05m24s	0.0476	211.16	Sy 1.5	948	1342234868
MCG +12-10-067	10h44m08.5s	+70d24m19s	0.0336	147.5	Sy 2	862	1342229636
MCG +06-24-008	10h44m49.0s	+38d10m52s	0.0259	113.04	Sy 2	1265	1342254049
UGC 05881	10h46m42.5s	+25d55m54s	0.0206	89.58	Sy 2	1136	1342247228
NGC 3393	10h48m23.5s	-25d09m43s	0.0125	54.09	Sy 2	948	1342234827
Mrk 417	10h49m30.9s	+22d57m52s	0.0328	143.81	Sy 1.9	763	1342222670
NGC 3431	10h51m15.0s	-17d00m29s	0.0175	76.06	Sy 2	948	1342234840
Mrk 728	11h01m01.8s	+11d02m49s	0.0356	156.82	Sy 1.5	768	1342222888
NGC 3516	11h06m47.5s	+72d34m07s	0.0088	38.9	Sy 1.2	862	1342229629
IC 2637	11h13m49.7s	+09d35m11s	0.0292	127.99	Sy 1.9	948	1342234874
ARP 151	11h25m36.2s	+54d22m57s	0.0211	91.79	Sy 1.5	763	1342222659
ESO 439-G009	11h27m23.4s	-29d15m27s	0.0239	104.19	Sy 2[a]	948	1342234824
NGC 3718	11h32m34.9s	+53d04m05s	0.0033	17.1	Sy 1.9	880	1342230870
IC 2921	11h32m49.3s	+10d17m47s	0.044	194.94	Sy 1.5	948	1342234876
Mrk 739E	11h36m29.4s	+21d35m46s	0.0297	130.17	Sy 1.2	776	1342223231
IGR J11366-6002	11h36m42.0s	-60d03m07s	0.014	60.61	Sy 2[a]	825	1342226632
NGC 3783	11h39m01.8s	-37d44m19s	0.0097	38.5	Sy 1.5	447	1342202198
NGC 3786	11h39m42.6s	+31d54m33s	0.0089	40	Sy 1.9	776	1342223233
KUG 1141+371	11h44m29.9s	+36d53m09s	0.0381	167.74	Sy 1.5	776	1342223235
UGC 06728	11h45m16.0s	+79d40m53s	0.0065	28.06	Sy 1.2	862	1342229626
2MASX J11454045-1827149	11h45m40.5s	-18d27m16s	0.0329	144.67	Sy 1.5	948	1342234854
MCG +05-28-032	11h48m45.9s	+29d38m28s	0.023	100.32	LINER[a]	776	1342223232
MCG -01-30-041	11h52m38.2s	-05d12m26s	0.0188	81.75	Sy 1.8[a]	948	1342234860
2MASX J12005792+0648226	12h00m57.9s	+06d48m23s	0.036	158.63	Sy 2	948	1342234894
Mrk 1310	12h01m14.4s	-03d40m41s	0.0196	85.03	Sy 1.5	948	1342234859
LEDA 38038	12h02m47.6s	-53d50m08s	0.028	122.34	Sy 2	829	1342226975
NGC 4051	12h03m09.6s	+44d31m53s	0.0023	17.1	Sy 1.5	558	1342210502
ARK 347	12h04m29.7s	+20d18m58s	0.0224	97.79	Sy 1.9	776	1342223254
UGC 07064	12h04m43.3s	+31d10m38s	0.025	109.11	Sy 1.9	776	1342223251
NGC 4102	12h06m23.0s	+52d42m40s	0.0028	17.1	Sy 2	776	1342223239
Mrk 198	12h09m14.1s	+47d03m30s	0.0242	105.66	Sy 2	776	1342223245
NGC 4138	12h09m29.8s	+43d41m07s	0.003	13.8	Sy 2	776	1342223246

Table A.1 – continued from previous page

Name	RA (J2000)	DEC (J2000)	z	Distance (Mpc)	Type	OD	OBSID
NGC 4151	12h10m32.6s	+39d24m21s	0.0033	11.2	Sy 1.5	226	1342188588
KUG 1208+386	12h10m44.3s	+38d20m10s	0.0228	99.32	Sy 1.5	776	1342223248
NGC 4180	12h13m03.0s	+07d02m20s	0.007	31.5	Sy 2[a]	948	1342234893
NGC 4235	12h17m09.9s	+07d11m30s	0.008	31.5	Sy 1.5	948	1342234892
Mrk 202	12h17m55.0s	+58d39m35s	0.021	91.46	Sy 1[a]	880	1342230868
Mrk 766	12h18m26.5s	+29d48m46s	0.0129	55.92	Sy 1.5	948	1342234910
M 106	12h18m57.5s	+47d18m14s	0.0015	7.61	Sy 2	763	1342222664
Mrk 50	12h23m24.1s	+02d40m45s	0.0234	102.17	Sy 1	948	1342234881
NGC 4388	12h25m46.7s	+12d39m44s	0.0084	16.8	Sy 2	1166	1342248482
2MASX J12313717-4758019	12h31m37.2s	-47d58m02s	0.0277	120.94	Sy 1.5	948	1342234820
2MASX J12335145-2103448	12h33m51.4s	-21d03m45s	0.023	100.4	Sy 1[a]	963	1342236194
NGC 4507	12h35m36.6s	-39d54m33s	0.0118	51	Sy 1.9	948	1342234818
ESO 506-G027	12h38m54.6s	-27d18m28s	0.025	109.23	Sy 2	963	1342236197
LEDA 170194	12h39m06.3s	-16d10m47s	0.0367	161.48	Sy 2	948	1342234812
Mrk 653	12h39m51.7s	+34d58m30s	0.0431	190.51	Sy 2	948	1342234909
WKK 1263	12h41m25.7s	-57d50m04s	0.0244	106.59	Sy 1.5[a]	829	1342226973
NGC 4619	12h41m44.5s	+35d03m46s	0.0231	100.71	Sy 1.2	948	1342234908
2MASX J12475784-5829599	12h47m57.8s	-58d30m00s	0.028	122.49	Sy 1.9[a]	829	1342226972
NGC 4748	12h52m12.5s	-13d24m53s	0.0146	63.36	Sy 1.5	948	1342234811
MCG -01-33-063	13h00m19.1s	-08d05m15s	0.0263	114.87	Sy 2[a]	948	1342234805
SBS 1301+540	13h03m59.5s	+53d47m30s	0.0299	130.99	Sy 1.5	880	1342230865
NGC 4941	13h04m13.1s	-05d33m06s	0.0037	14	Sy 1.9	948	1342234804
NGC 4939	13h04m14.4s	-10d20m23s	0.0104	44.79	Sy 2	948	1342234806
ESO 323-077	13h06m26.1s	-40d24m53s	0.015	65.05	Sy 1.5	963	1342236202
NGC 4992	13h09m05.6s	+11d38m03s	0.0251	109.73	Sy 2	963	1342236172
II SZ 010	13h13m05.8s	-11d07m42s	0.0343	150.61	Sy 1.5	948	1342234808
NGC 5033	13h13m27.5s	+36d35m38s	0.0029	18.5	Sy 1.5	948	1342234905
UGC 08327 NED02	13h15m17.3s	+44d24m26s	0.0366	160.92	Sy 1.9	910	1342232707
NGC 5106	13h20m59.6s	+08d58m42s	0.0319	140.15	LINER[a]	963	1342236171
MCG -03-34-064	13h22m24.5s	-16d43m42s	0.0165	71.74	Sy 1.9	963	1342236179
Cen A	13h25m27.6s	-43d01m09s	0.0018	3.57	Sy 2	227	1342188663
ESO 509-G038	13h31m13.9s	-25d24m10s	0.026	113.45	Sy 1.5	963	1342236192
ESO 383-18	13h33m26.1s	-34d00m53s	0.0124	53.67	Sy 2	963	1342236200
ESO 509-IG066NED01	13h34m39.6s	-23d26m48s	0.0343	150.79	Sy 1.9	963	1342236190
NGC 5231	13h35m48.2s	+02d59m56s	0.0218	94.75	Sy 1.9	948	1342234796
MCG -06-30-015	13h35m53.7s	-34d17m44s	0.0077	33.39	Sy 1.5	963	1342236199
NGC 5252	13h38m16.0s	+04d32m33s	0.023	100.13	Sy 2	948	1342234795
2MASX J13411287-1438407	13h41m12.9s	-14d38m41s	0.0418	184.69	Sy 1.5	963	1342236177
NGC 5273	13h42m08.3s	+35d39m15s	0.0035	16.5	Sy 1.5	963	1342236143
CGCG 102-048	13h44m15.7s	+19d34m00s	0.0271	118.32	Sy 2	976	1342237514
NGC 5290	13h45m19.2s	+41d42m45s	0.0086	30.9	Sy 1.9	910	1342232712
4U 1344-60	13h47m36.0s	-60d37m04s	0.0129	55.71	Sy 1.5[a]	829	1342226968
IC 4329A	13h49m19.3s	-30d18m34s	0.0161	69.61	Sy 1.5	963	1342236198
UM 614	13h49m52.8s	+02d04m45s	0.0327	143.55	Sy 1.5	963	1342236166
2MASX J13512953-1813468	13h51m29.5s	-18d13m47s	0.0122	52.82	Sy 1.5	963	1342236187
Mrk 279	13h53m03.4s	+69d18m30s	0.0305	133.46	Sy 1.5	862	1342229617
ESO 578-G009	13h56m36.7s	-19d31m45s	0.035	154.01	Sy 1.5	963	1342236189
2MASX J14080674-3023537	14h08m06.8s	-30d23m54s	0.0235	102.27	Sy 1.5	976	1342237519
NGC 5506	14h13m14.9s	-03d12m27s	0.0062	21.7	Sy 1.9	626	1342213466
NGC 5548	14h17m59.5s	+25d08m12s	0.0172	74.53	Sy 1.5	948	1342234784
ESO 511-G030	14h19m22.4s	-26d38m41s	0.0224	97.54	Sy 1	976	1342237518
NGC 5610	14h24m22.9s	+24d36m51s	0.0169	73.27	Sy 2	948	1342234783
NGC 5674	14h33m52.2s	+05d27m30s	0.0249	108.82	Sy 2	963	1342236157
NGC 5683	14h34m52.4s	+48d39m43s	0.0362	159.43	Sy 1.2	910	1342232719
Mrk 817	14h36m22.1s	+58d47m39s	0.0315	137.96	Sy 1.2	862	1342229517
Mrk 477	14h40m38.1s	+53d30m16s	0.0377	166.23	Sy 1.9	862	1342229519
NGC 5728	14h42m23.9s	-17d15m11s	0.0094	24.8	Sy 2	626	1342213476
WKK 4374	14h51m33.1s	-55d40m38s	0.018	78.16	Sy 2[a]	861	1342229204
2MASX J14530794+2554327	14h53m07.9s	+25d54m33s	0.0465	206.21	Sy 1	948	1342234780
WKK 4438	14h55m17.4s	-51d34m15s	0.016	69.37	Sy 1 NL[a]	861	1342229203
IC 4518A	14h57m41.2s	-43d07m56s	0.0163	70.51	Sy 2[a]	1022	1342239895
Mrk 841	15h04m01.2s	+10d26m16s	0.0364	160.33	Sy 1.5	989	1342238323
Mrk 1392	15h05m56.6s	+03d42m26s	0.0361	159.04	Sy 1.5	989	1342238318
2MASX J15064412+0351444	15h06m44.1s	+03d51m44s	0.0377	166.11	Sy 2	989	1342238319

Table A.1 – continued from previous page

Name	RA (J2000)	DEC (J2000)	z	Distance (Mpc)	Type	OD	OBSID
2MASX J15115979-2119015	15h11m59.8s	-21d19m02s	0.0446	197.54	Sy 1.5	989	1342238298
NGC 5899	15h15m03.2s	+42d02m59s	0.0085	43.5	Sy 2	862	1342229533
CGCG 319-007	15h19m33.7s	+65d35m59s	0.044	194.77	Sy 1.9[a]	862	1342229616
MCG -01-40-001	15h33m20.7s	-08d42m02s	0.0227	98.94	Sy 1.9	989	1342238305
Mrk 290	15h35m52.4s	+57d54m09s	0.0296	129.54	Sy 1.5	862	1342229524
2MASX J15462424+6929102	15h46m24.3s	+69d29m10s	0.0374	164.71	Sy 2	862	1342229615
NGC 5995	15h48m25.0s	-13d45m28s	0.0252	109.99	Sy 1.9	1022	1342239776
WKK 6092	16h11m51.4s	-60d37m55s	0.0156	67.78	Sy 1.5	861	1342229211
WKK 6471	16h18m36.4s	-59d27m17s	0.0346	152.23	Sy 1	861	1342229212
CGCG 367-009	16h19m19.3s	+81d02m48s	0.0239	104.31	Sy 2	747	1342221919
Mrk 885	16h29m48.3s	+67d22m42s	0.0253	110.58	Sy 1[a]	862	1342229613
ESO 137-34	16h35m14.1s	-58d04m48s	0.0091	39.44	Sy 2	861	1342229214
2MASX J16481523-3035037	16h48m15.3s	-30d35m04s	0.031	135.92	Sy 1[a]	861	1342229198
LEDA 214543	16h50m42.7s	+04d36m18s	0.0321	140.67	Sy 2	862	1342229574
UGC 10593	16h52m18.9s	+55d54m20s	0.0292	127.63	Sy 2[a]	862	1342229610
NGC 6221	16h52m46.1s	-59d13m07s	0.005	15.6	Sy 2[a]	861	1342229215
NGC 6240	16h52m58.9s	+02d24m03s	0.0245	106.81	Sy 1.9	467	1342203586
NGC 6300	17h16m59.5s	-62d49m14s	0.0037	13.1	Sy 2	861	1342229218
ARP 102B	17h19m14.5s	+48d58m49s	0.0242	105.42	Sy 2	861	1342229154
AX J1737.4-2907	17h37m28.4s	-29d08m03s	0.0214	93.16	Sy 1[a]	840	1342227689
ESO 139-G012	17h37m39.1s	-59d56m27s	0.017	73.84	Sy 2[a]	861	1342229217
2E 1739.1-1210	17h41m55.3s	-12d11m57s	0.037	162.95	Sy 1[a]	861	1342229191
CGCG 300-062	17h43m17.4s	+62d50m21s	0.033	144.9	Sy 2[a]	861	1342229145
2MASS J17485512-3254521	17h48m55.1s	-32d54m52s	0.02	86.97	Sy 1[a]	861	1342229196
NGC 6552	18h00m07.3s	+66d36m54s	0.0265	115.77	Sy 2[a]	861	1342229135
2MASXi J1802473-145454	18h02m47.3s	-14d54m55s	0.0034	14.6	Sy 1[a]	861	1342229192
UGC 11185 NED02	18h16m11.5s	+42d39m37s	0.0412	182.02	Sy 2	861	1342229164
IC 4709	18h24m19.4s	-56d22m09s	0.0169	73.34	Sy 2	861	1342229223
Fairall 49	18h36m58.3s	-59d24m09s	0.02	87.07	Sy 1.9	861	1342229221
ESO 103-035	18h38m20.3s	-65d25m39s	0.0133	57.48	Sy 2	861	1342229219
Fairall 51	18h44m54.0s	-62d21m53s	0.0142	61.38	Sy 1.5	861	1342229220
CGCG 341-006	18h45m26.2s	+72d11m02s	0.0463	205.29	Sy 2[a]	861	1342229133
2MASX J18570768-7828212	18h57m07.8s	-78d28m21s	0.042	185.64	Sy 1[a]	880	1342230809
CGCG 229-015	19h05m25.9s	+42d27m40s	0.0279	121.95	Sy 1[a]	862	1342229607
ESO 141-G055	19h21m14.1s	-58d40m13s	0.0371	163.44	Sy 1.2	861	1342229225
2MASX J19373299-0613046	19h37m33.0s	-06d13m05s	0.0103	44.26	Sy 1.5	880	1342230836
2MASX J19380437-5109497	19h38m04.4s	-51d09m50s	0.04	176.63	Sy 1.2	880	1342230812
NGC 6814	19h42m40.6s	-10d19m25s	0.0052	22	Sy 1.5	880	1342230834
2MASX J20005575-1810274	20h00m55.7s	-18d10m27s	0.0371	163.48	Sy 1.9	880	1342230831
ESO 399-20	20h06m57.7s	-34d32m58s	0.025	108.91	Sy 1.2	880	1342230822
NGC 6860	20h08m46.9s	-61d06m01s	0.0149	64.48	Sy 1.5	515	1342206209
2MASX J20101740+4800214	20h10m17.4s	+48d00m21s	0.0256	111.92	Sy 2	880	1342230854
2MASX J20183871+4041003	20h18m38.7s	+40d41m00s	0.0144	62.36	Sy 2[a]	880	1342230852
II Zw 083	20h26m55.9s	-02d16m39s	0.0291	127.6	Sy 2[a]	1064	1342244150
MCG +04-48-002	20h28m35.1s	+25d44m00s	0.0139	60.17	Sy 2	931	1342233321
Mrk 509	20h44m09.7s	-10d43m25s	0.0344	151.19	Sy 1.5	1064	1342244151
IC 5063	20h52m02.3s	-57d04m08s	0.0113	49.03	Sy 2	515	1342206208
ESO 464-G016	21h02m23.8s	-28d10m29s	0.0364	160.02	AGN[a]	1064	1342244155
2MASX J21090996-0940147	21h09m10.0s	-09d40m15s	0.0265	115.87	Sy 1.2	1064	1342244152
SWIFT J212745.6+565636	21h27m45.8s	+56d57m07s	0.0147	63.67	Sy 1[a]	725	1342220628
6dF J2132022-334254	21h32m02.2s	-33d42m54s	0.03	131.32	Sy 1.5	1064	1342244156
2MASX J21355399+4728217	21h35m54.0s	+47d28m22s	0.025	109.12	Sy 1[a]	725	1342220632
CGCG 493-002	21h38m33.4s	+32d05m06s	0.0248	108.24	Sy 1.5[a]	722	1342219966
NGC 7172	22h02m01.9s	-31d52m11s	0.0087	33.9	Sy 2	544	1342209301
NGC 7213	22h09m16.3s	-47d10m00s	0.0058	14.5	Sy 2	1064	1342244160
MCG +02-57-002	22h23m45.0s	+11d50m09s	0.029	126.96	Sy 1.5	725	1342220638
MCG +06-49-019	22h27m05.8s	+36d21m42s	0.0213	92.84	Sy 2[a]	725	1342220634
ESO 533-G050	22h34m49.8s	-25d40m37s	0.0264	115.56	Sy 2	949	1342234743
MCG +01-57-016	22h40m17.0s	+08d03m14s	0.025	109.01	Sy 1.5	725	1342220641
UGC 12237	22h54m19.7s	+11d46m57s	0.0283	123.71	Sy 2[a]	949	1342234761
UGC 12282	22h58m55.5s	+40d55m53s	0.017	73.73	Sy 2	949	1342234677
KAZ 320	22h59m32.9s	+24d55m06s	0.0345	151.66	Sy 1.5	949	1342234767
NGC 7465	23h02m01.0s	+15d57m53s	0.0066	26.5	LINER[a]	949	1342234763
NGC 7469	23h03m15.6s	+08d52m26s	0.0163	70.76	Sy 1.5	565	1342210572

Table A.1 – continued from previous page

Name	RA (J2000)	DEC (J2000)	z	Distance (Mpc)	Type	OD	OBSID
Mrk 926	23h04m43.5s	-08d41m09s	0.0469	207.86	Sy 1.5	949	1342234673
NGC 7479	23h04m56.7s	+12d19m22s	0.0079	31.5	Sy 1.9	949	1342234760
PG 2304+042	23h07m02.9s	+04d32m57s	0.042	185.64	Sy 1.2	949	1342234757
NGC 7582	23h18m23.5s	-42d22m14s	0.0053	18.7	Sy 2	558	1342210529
NGC 7603	23h18m56.6s	+00d14m38s	0.0295	129.31	Sy 1	949	1342234753
LCRS B232242.2-384320	23h25m24.2s	-38d26m49s	0.0359	157.97	Sy 2	949	1342234739
2MASX J23272195+1524375	23h27m22.0s	+15d24m37s	0.0457	202.62	Sy 1.5	949	1342234764
NGC 7679	23h28m46.7s	+03d30m41s	0.0171	74.37	Sy 1.9	949	1342234754
IGR J23308+7120	23h30m37.7s	+71d22m46s	0.037	162.85	Sy 2	862	1342229621
PKS 2331-240	23h33m55.2s	-23d43m41s	0.0477	211.71	Sy 2[a]	949	1342234747
UGC 12741	23h41m55.5s	+30d34m54s	0.0174	75.72	Sy 2	948	1342234920

Notes – *Column 1:* Name of the source. *Column 2:* Right ascension in J2000 coordinates. *Column 3:* Declination in J2000 coordinates. *Column 4:* Redshift of the source. *Column 5:* Luminosity distance of the source in Mpc. *Column 6:* AGN classification. Sources marked with an [a] are from the 70 month *Swift*/BAT catalog; all others are from the BASS survey (Berney et al., 2015). *Column 7: Herschel* Operational Day number for when the observation started. *Column 7: Herschel* Observation Identification number.

Appendix B: SPIRE Maps

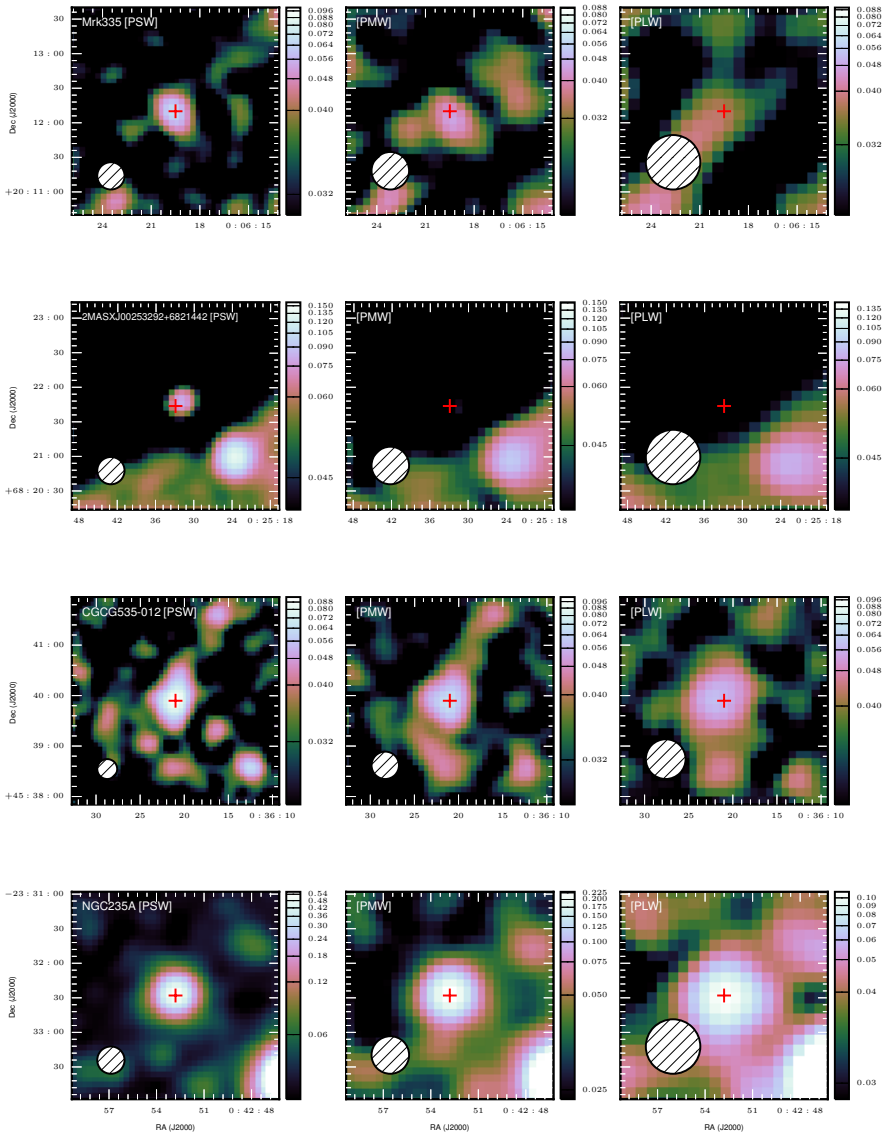

Figure B.1: SPIRE maps for all of the *Herschel*-BAT AGN. Each row is a separate AGN and each column is a separate waveband. Left: PSW or 250 μm. Middle: PMW or 350 μm. Right: PLW or 500 μm. All images have been smoothed for aesthetic purposes using a 2D Gaussian kernel with $\sigma = 1.5$ pixels, slightly smaller than the beam size. Pixel intensity units are Jy/beam and are displayed with an arcsinh stretch. The range in intensity is from the maximum pixel value near the BAT position or 5 times the median global background (whichever is larger) to the median global background level measured during the aperture photometry process. The white hatched circle in the lower left corner shows the FWHM of the *Herschel* beam convolved with the same Gaussian as the image. The red cross plots the known position of the BAT AGN from Table A.1.

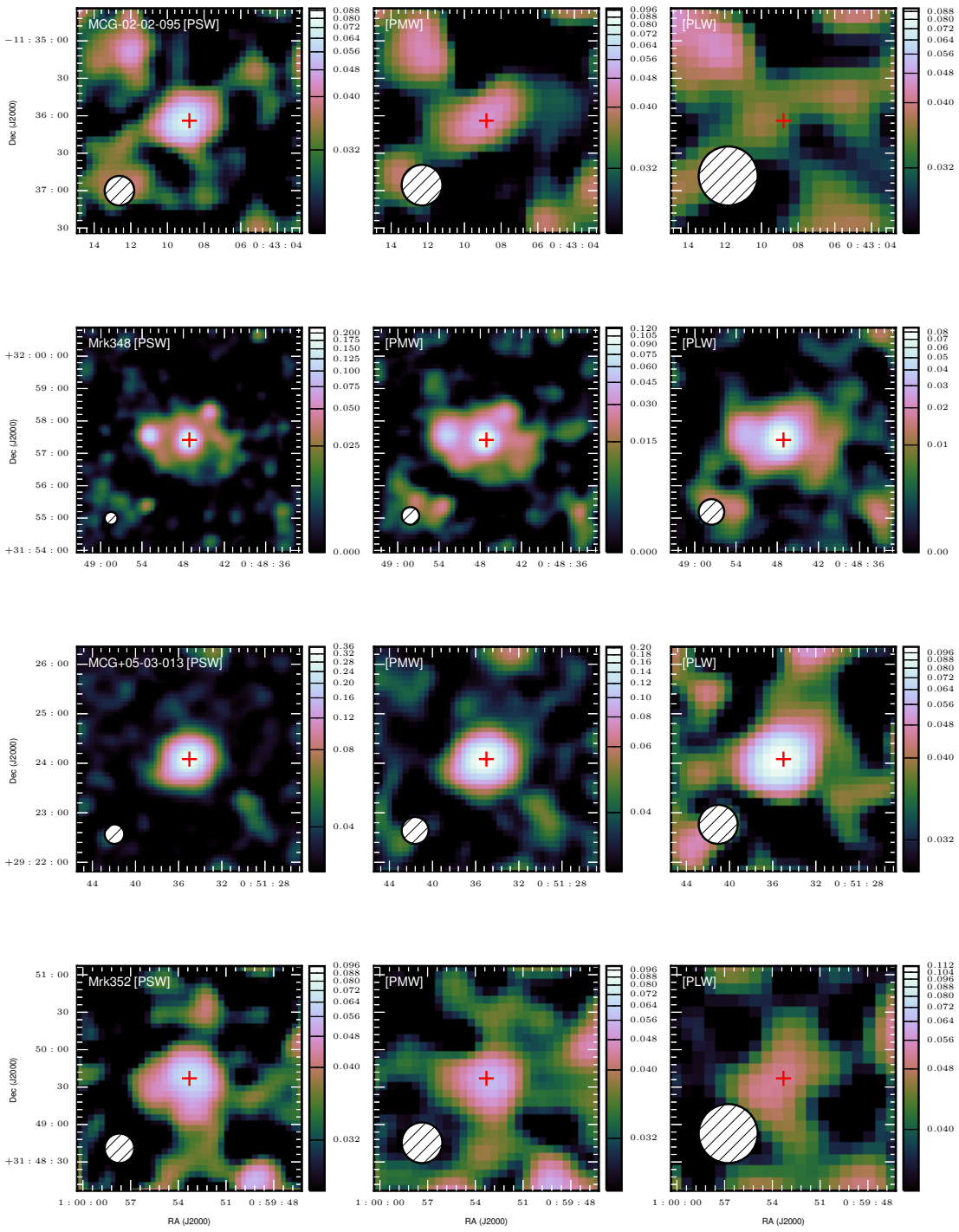
MCG-02-02-095 [PSW]
[PMW]
[PLW]
Mrk348 [PSW]
[PMW]
[PLW]
MCG+05-03-013 [PSW]
[PMW]
[PLW]
Mrk352 [PSW]
[PMW]
[PLW]
Dec (J2000)
RA (J2000)

Figure B.2

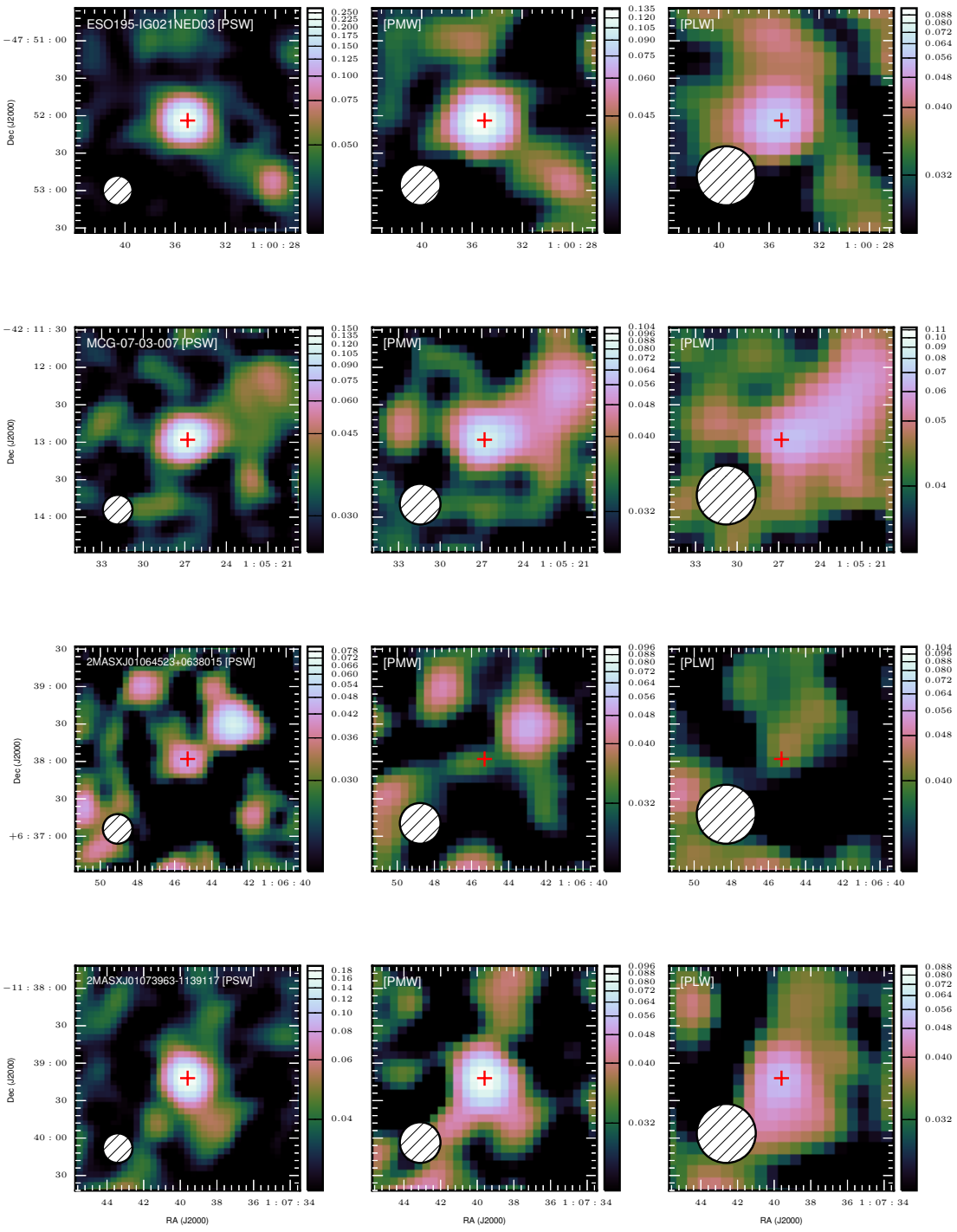
ESO195-IG021NED03 [PSW]
[PMW]
[PLW]
MCG-07-03-007 [PSW]
[PMW]
[PLW]
2MASXJ01064523+0638015 [PSW]
[PMW]
[PLW]
2MASXJ01073963-1139117 [PSW]
[PMW]
[PLW]
Dec (J2000)
RA (J2000)

Figure B.3

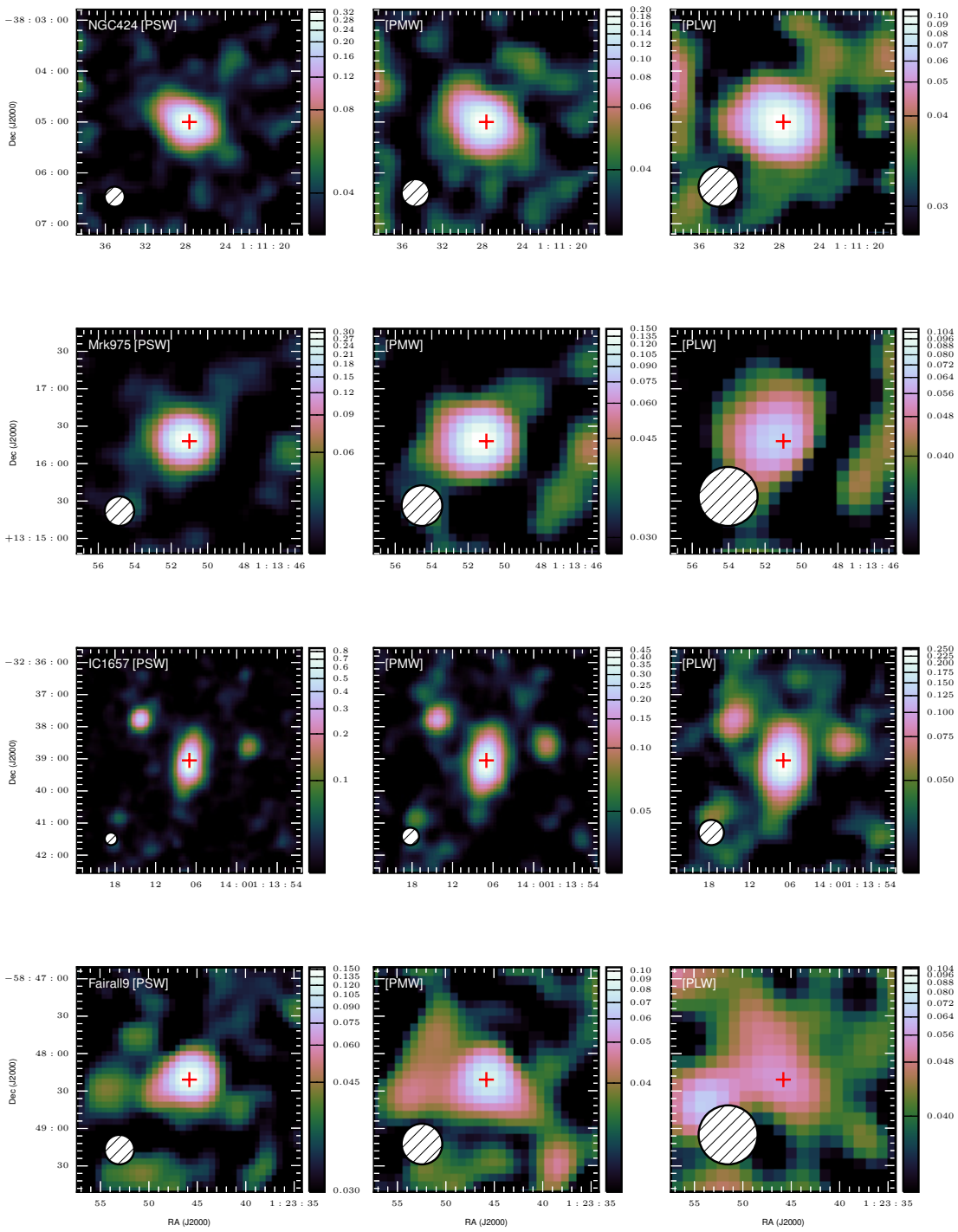
NGC424 [PSW]
[PMW]
[PLW]
Mrk975 [PSW]
[PMW]
[PLW]
IC1657 [PSW]
[PMW]
[PLW]
Fairall9 [PSW]
[PMW]
[PLW]
Dec (J2000)
RA (J2000)

Figure B.4

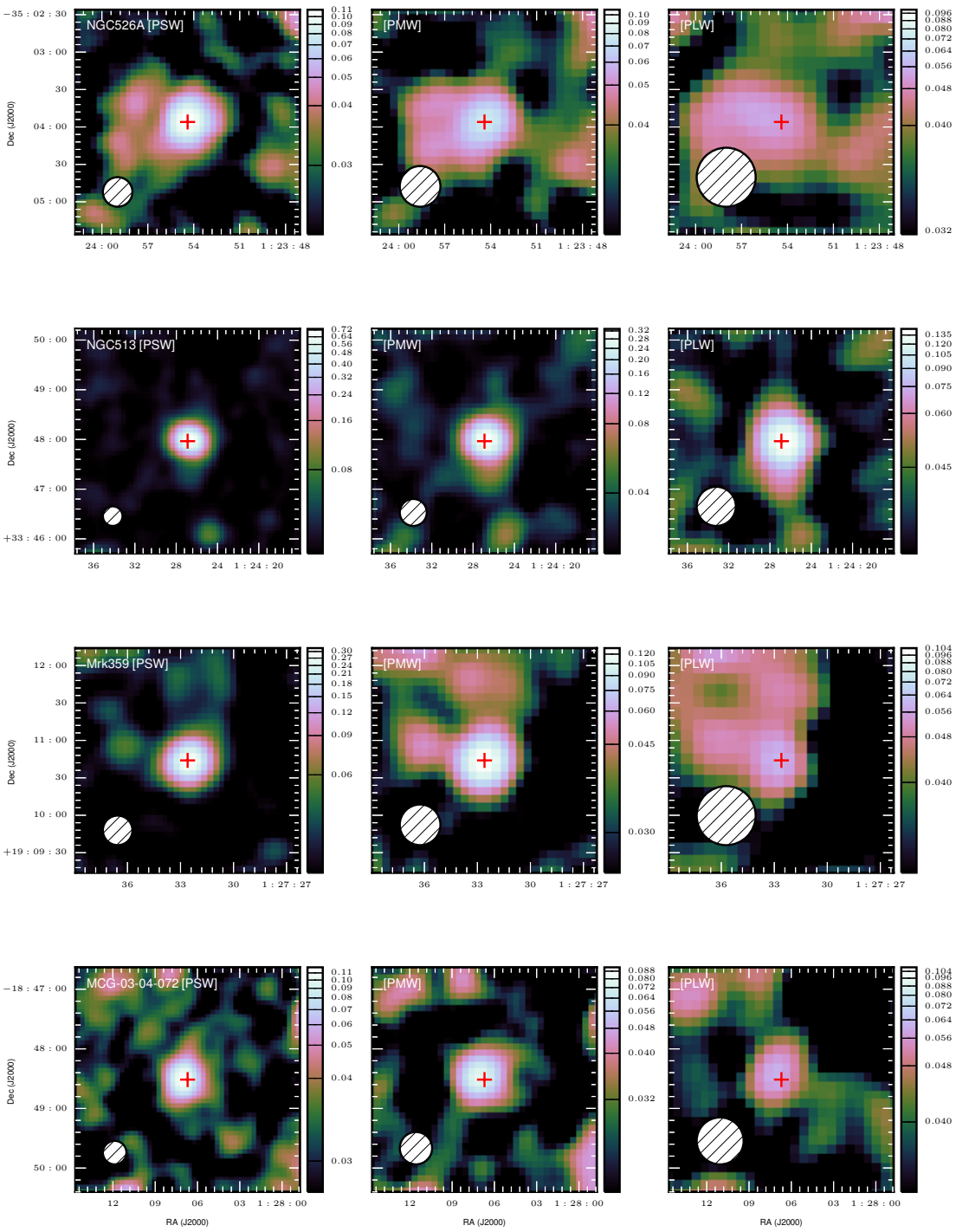
NGC526A [PSW]
[PMW]
[PLW]
NGC513 [PSW]
[PMW]
[PLW]
Mrk359 [PSW]
[PMW]
[PLW]
MCG-03-04-072 [PSW]
[PMW]
[PLW]
Dec (J2000)
RA (J2000)

Figure B.5

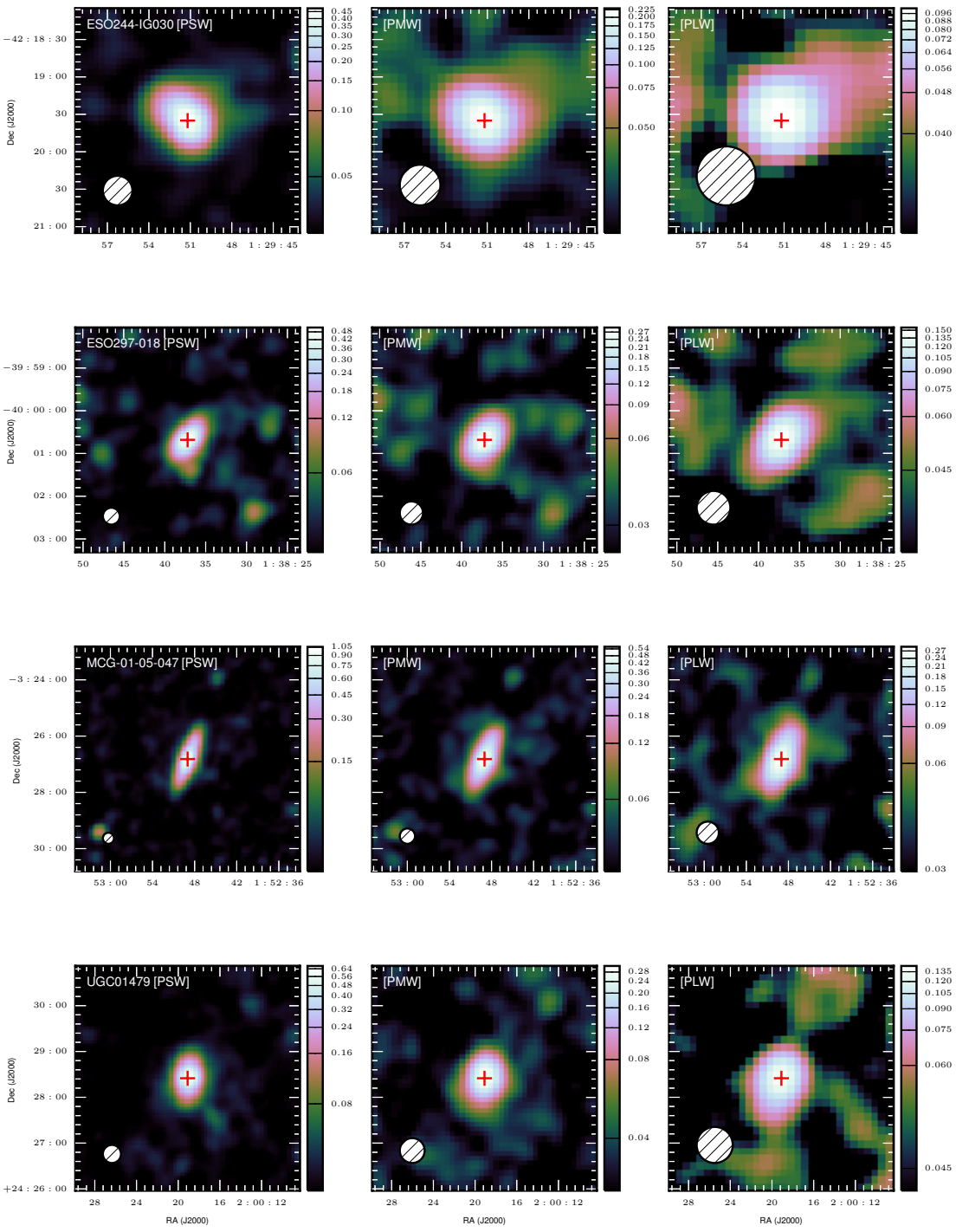
ESO244-IG030 [PSW]
[PMW]
[PLW]
ESO297-018 [PSW]
[PMW]
[PLW]
MCG-01-05-047 [PSW]
[PMW]
[PLW]
UGC01479 [PSW]
[PMW]
[PLW]
Dec (J2000)
RA (J2000)

Figure B.6

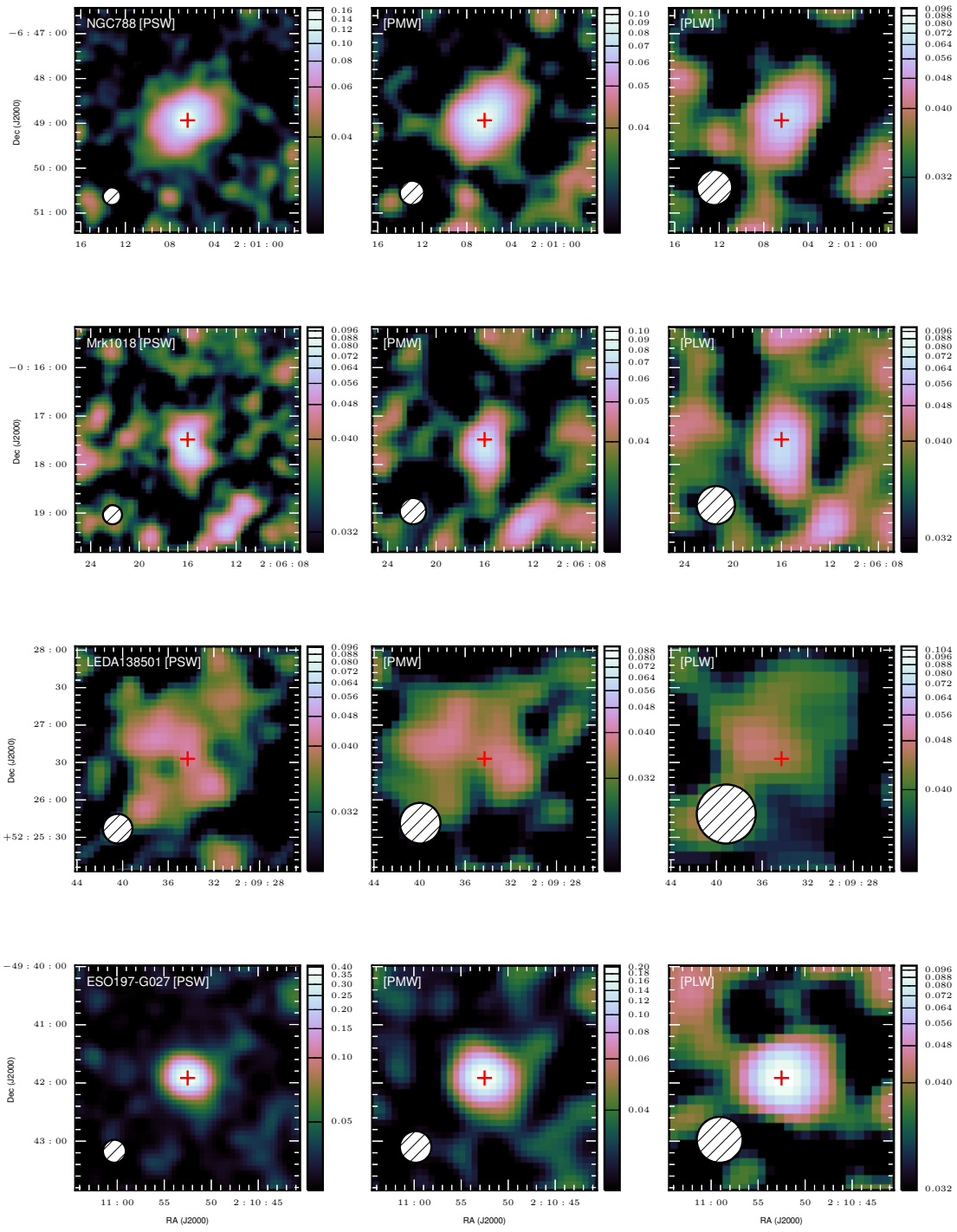
NGC788 [PSW]
[PMW]
[PLW]
Mrk1018 [PSW]
[PMW]
[PLW]
LEDA138501 [PSW]
[PMW]
[PLW]
ESO197-G027 [PSW]
[PMW]
[PLW]
Dec (J2000)
RA (J2000)

Figure B.7

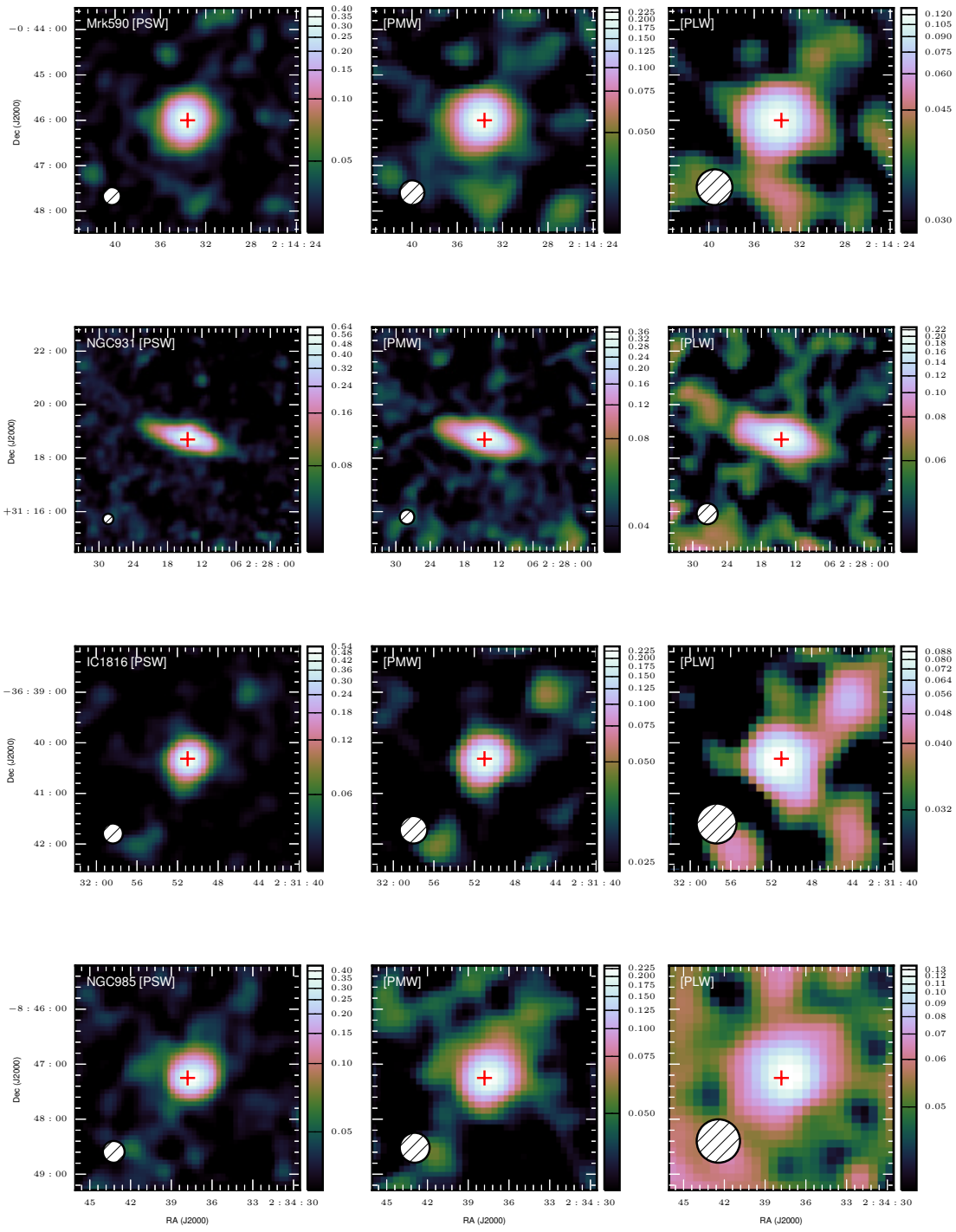
Mrk590 [PSW]
[PMW]
[PLW]
NGC931 [PSW]
[PMW]
[PLW]
IC1816 [PSW]
[PMW]
[PLW]
NGC985 [PSW]
[PMW]
[PLW]
Dec (J2000)
RA (J2000)

Figure B.8

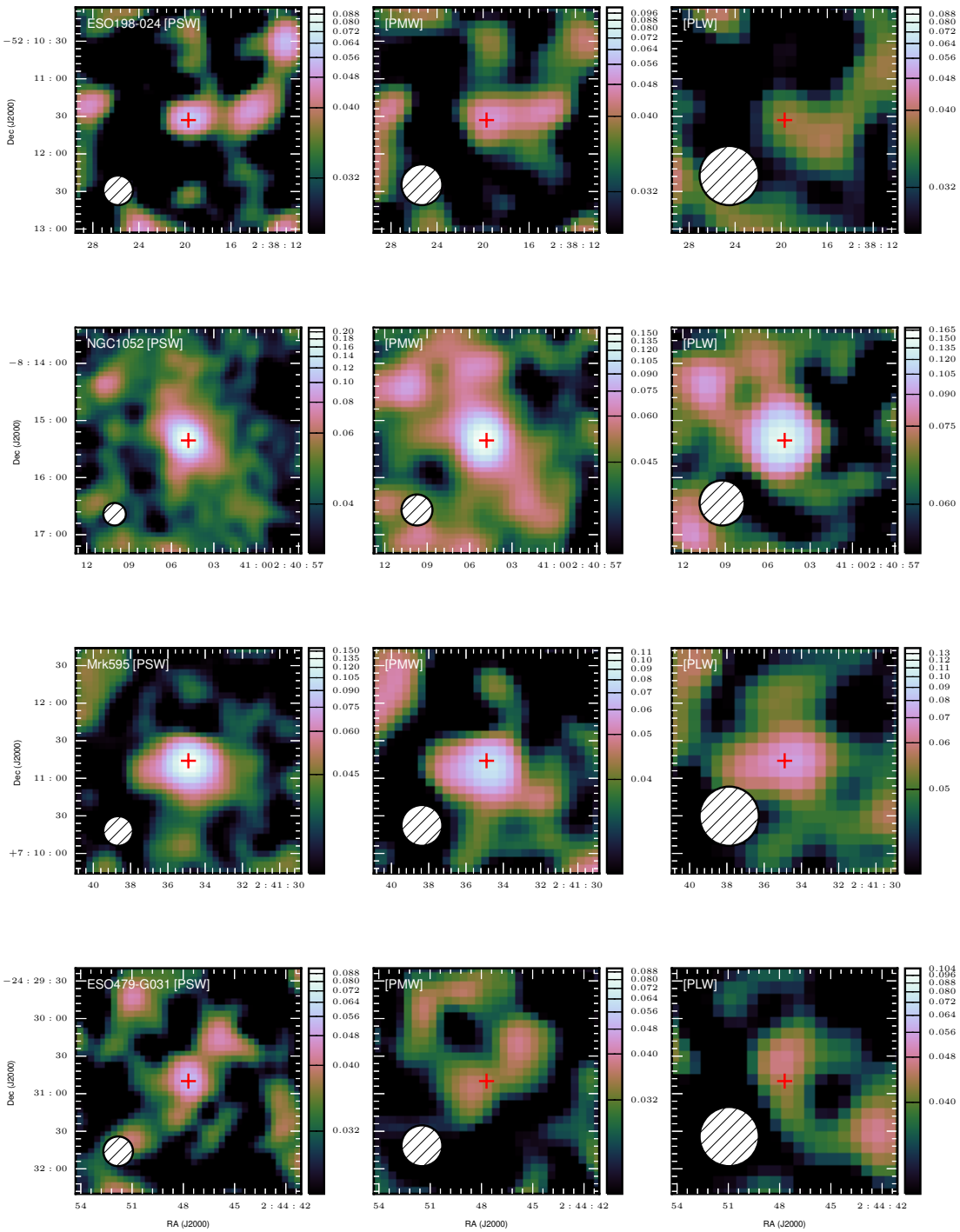
ESO198-024 [PSW]
[PMW]
[PLW]
NGC1052 [PSW]
[PMW]
[PLW]
Mrk595 [PSW]
[PMW]
[PLW]
ESO479-G031 [PSW]
[PMW]
[PLW]
Dec (J2000)
RA (J2000)

Figure B.9

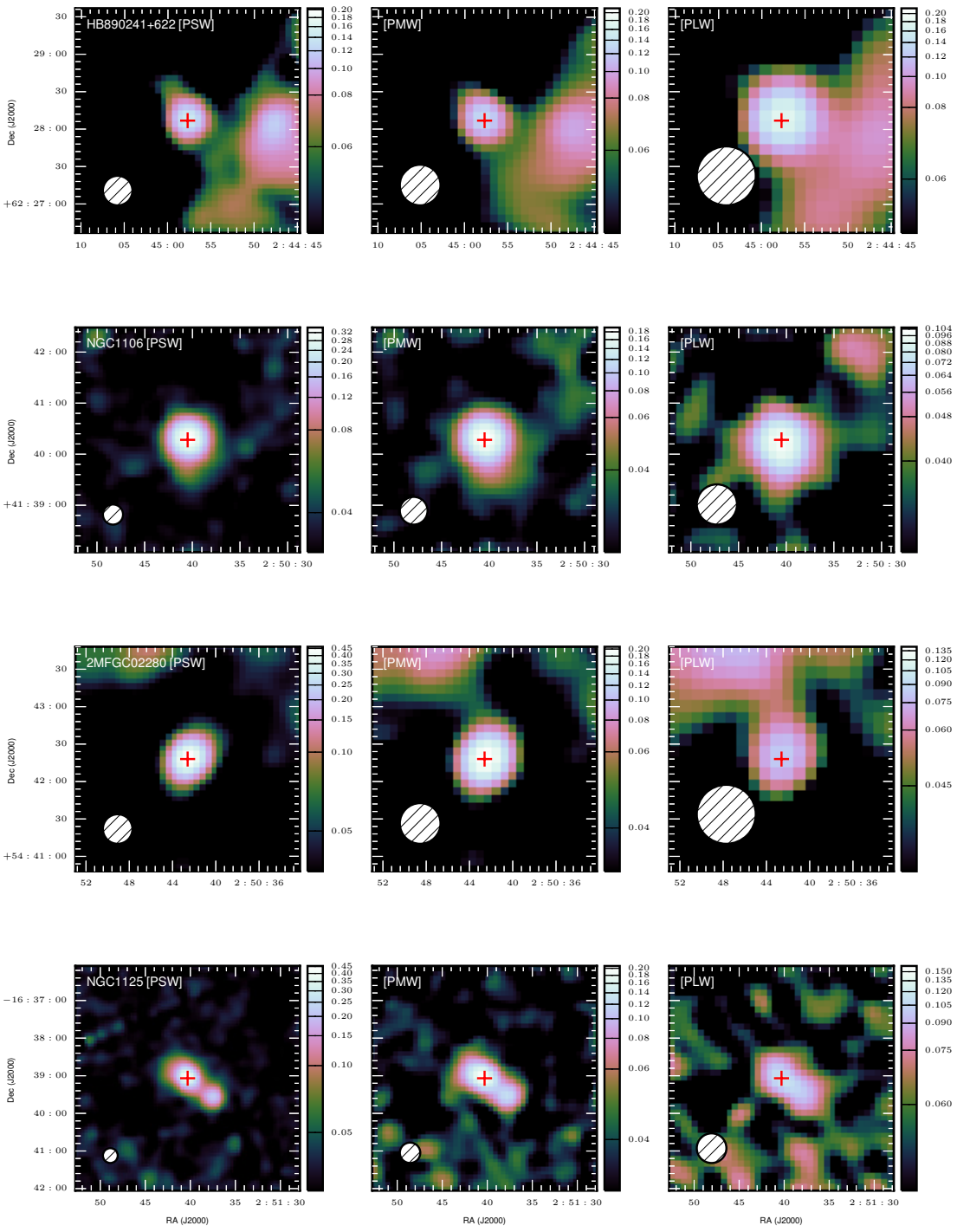
HB890241+622 [PSW]
[PMW]
[PLW]
NGC1106 [PSW]
[PMW]
[PLW]
2MFGC02280 [PSW]
[PMW]
[PLW]
NGC1125 [PSW]
[PMW]
[PLW]
Dec (J2000)
RA (J2000)

Figure B.10

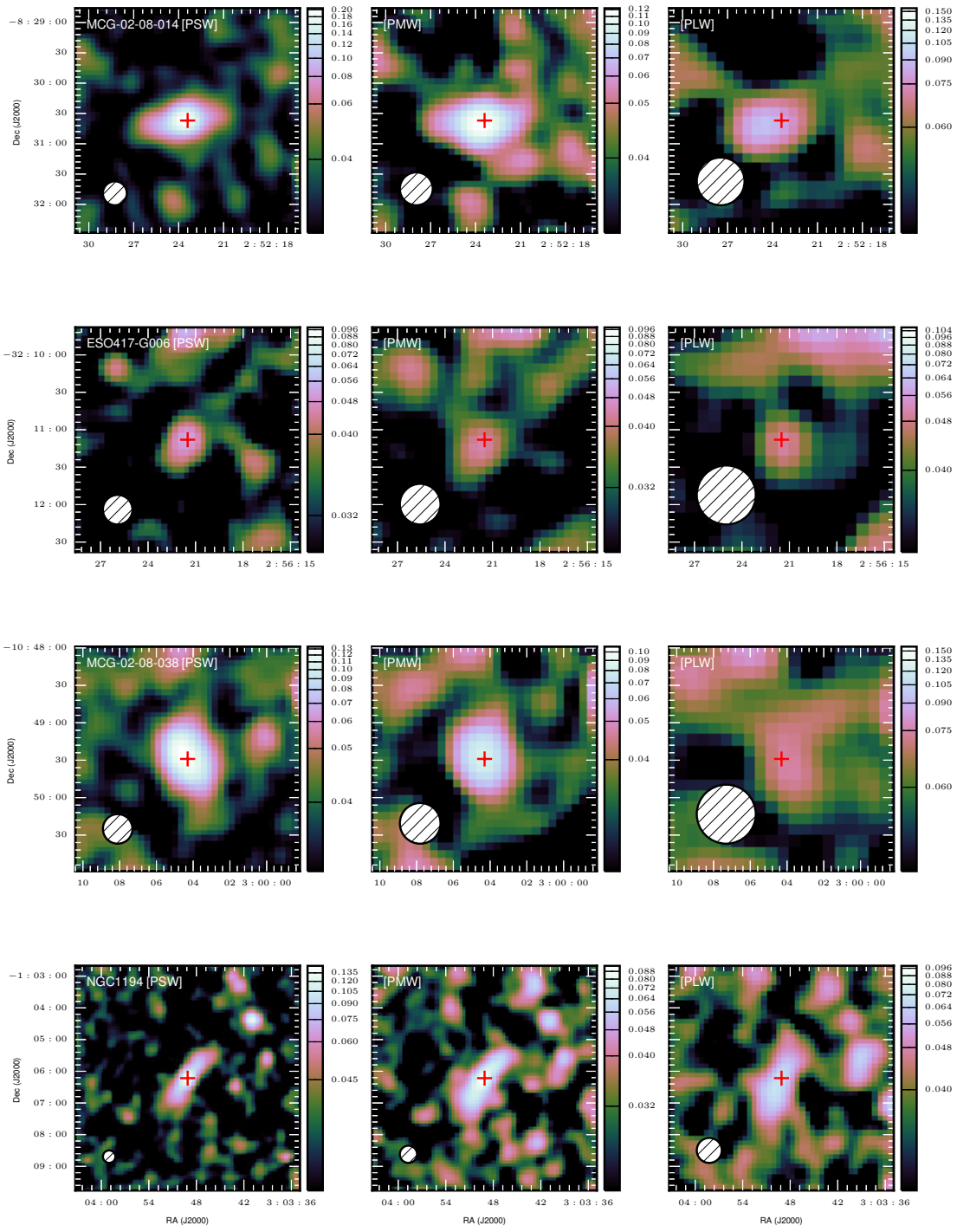
MCG-02-08-014 [PSW]
[PMW]
[PLW]
ESO417-G006 [PSW]
[PMW]
[PLW]
MCG-02-08-038 [PSW]
[PMW]
[PLW]
NGC1194 [PSW]
[PMW]
[PLW]
Dec (J2000)
RA (J2000)

Figure B.11

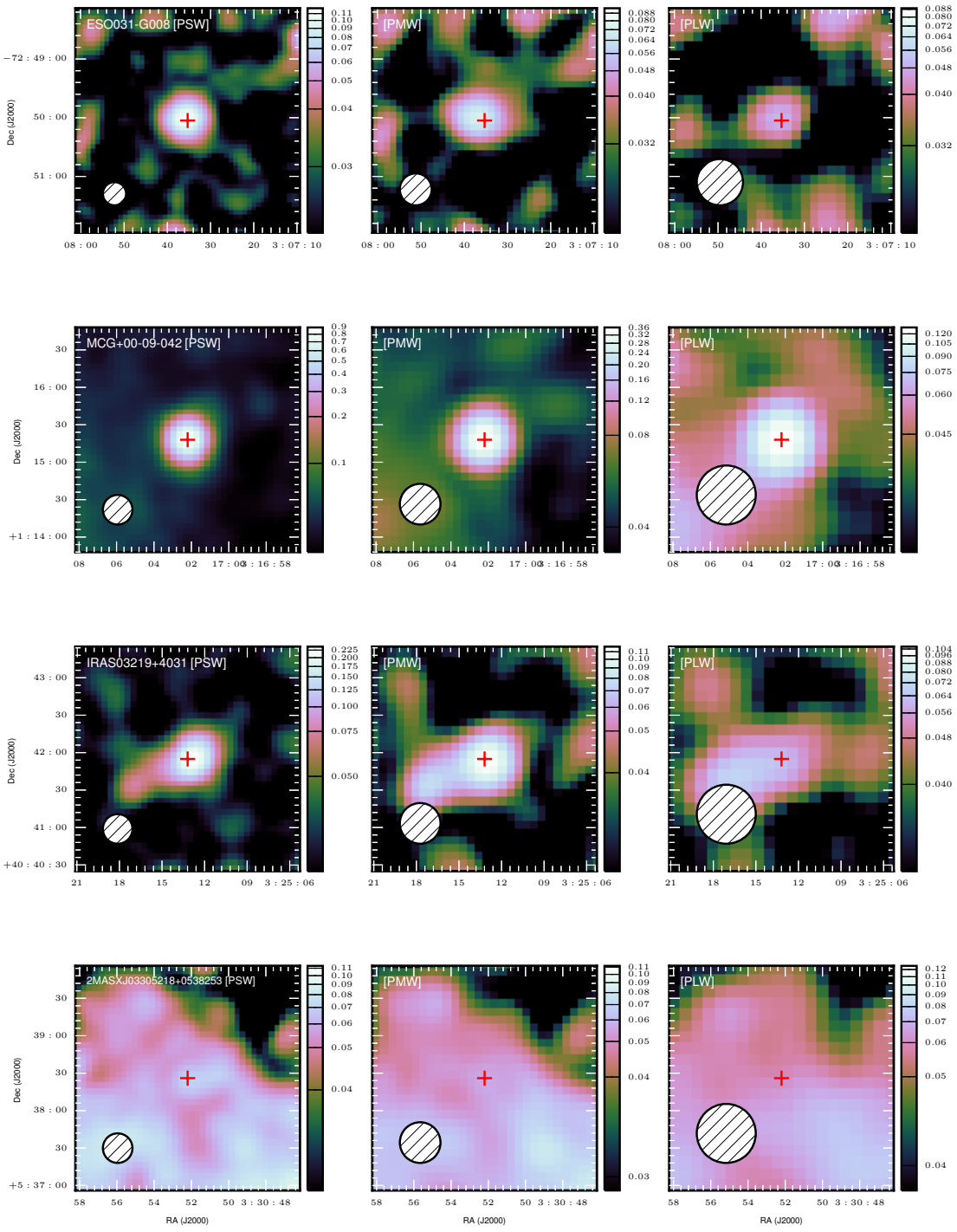
ESO031-G008 [PSW]
[PMW]
[PLW]
MCG+00-09-042 [PSW]
[PMW]
[PLW]
IRAS03219+4031 [PSW]
[PMW]
[PLW]
2MASXJ03305218+0538253 [PSW]
[PMW]
[PLW]
Dec (J2000)
RA (J2000)

Figure B.12

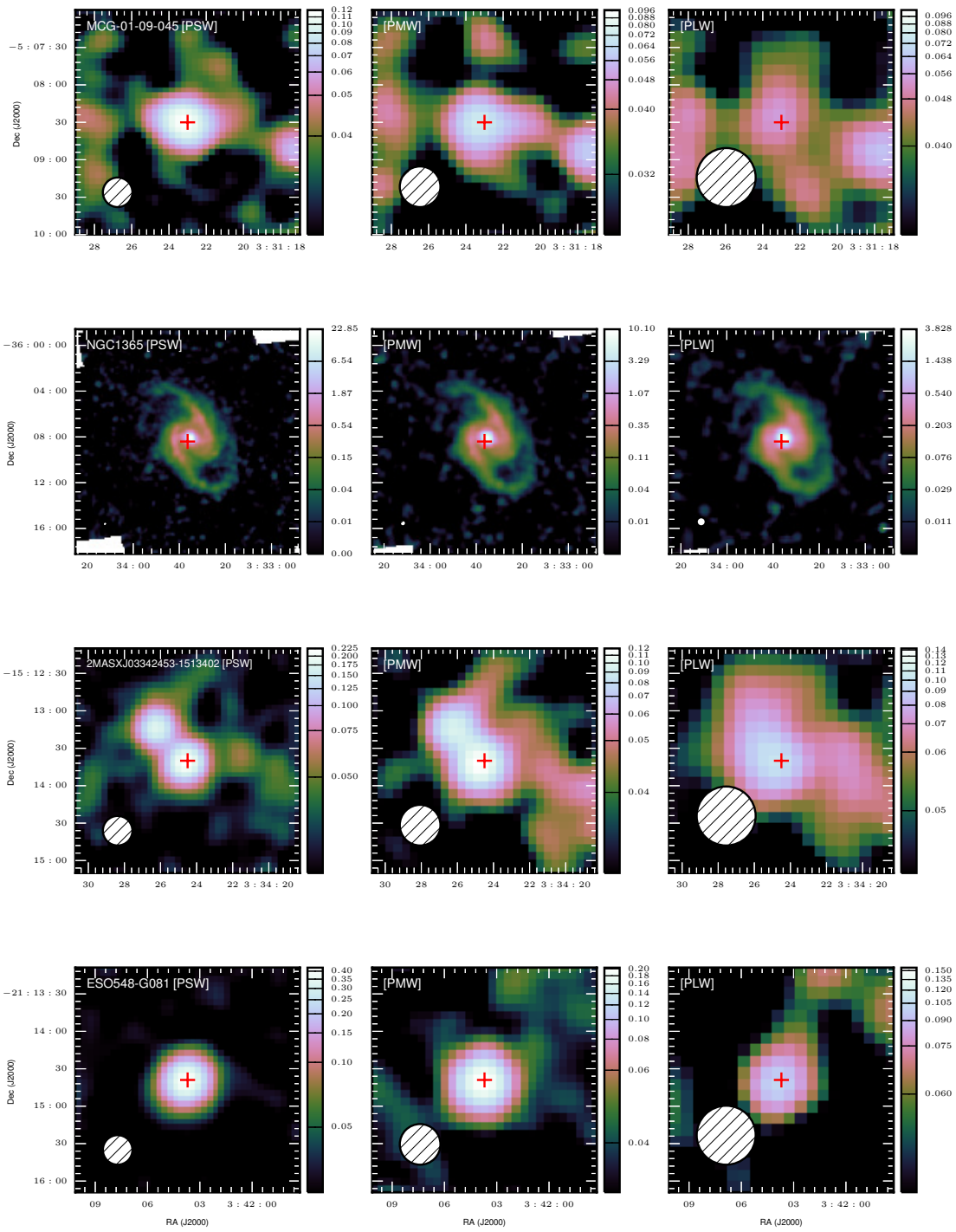
MCG-01-09-045 [PSW]
[PMW]
[PLW]
NGC1365 [PSW]
[PMW]
[PLW]
2MASXJ03342453-1513402 [PSW]
[PMW]
[PLW]
ESO548-G081 [PSW]
[PMW]
[PLW]
Dec (J2000)
RA (J2000)

Figure B.13

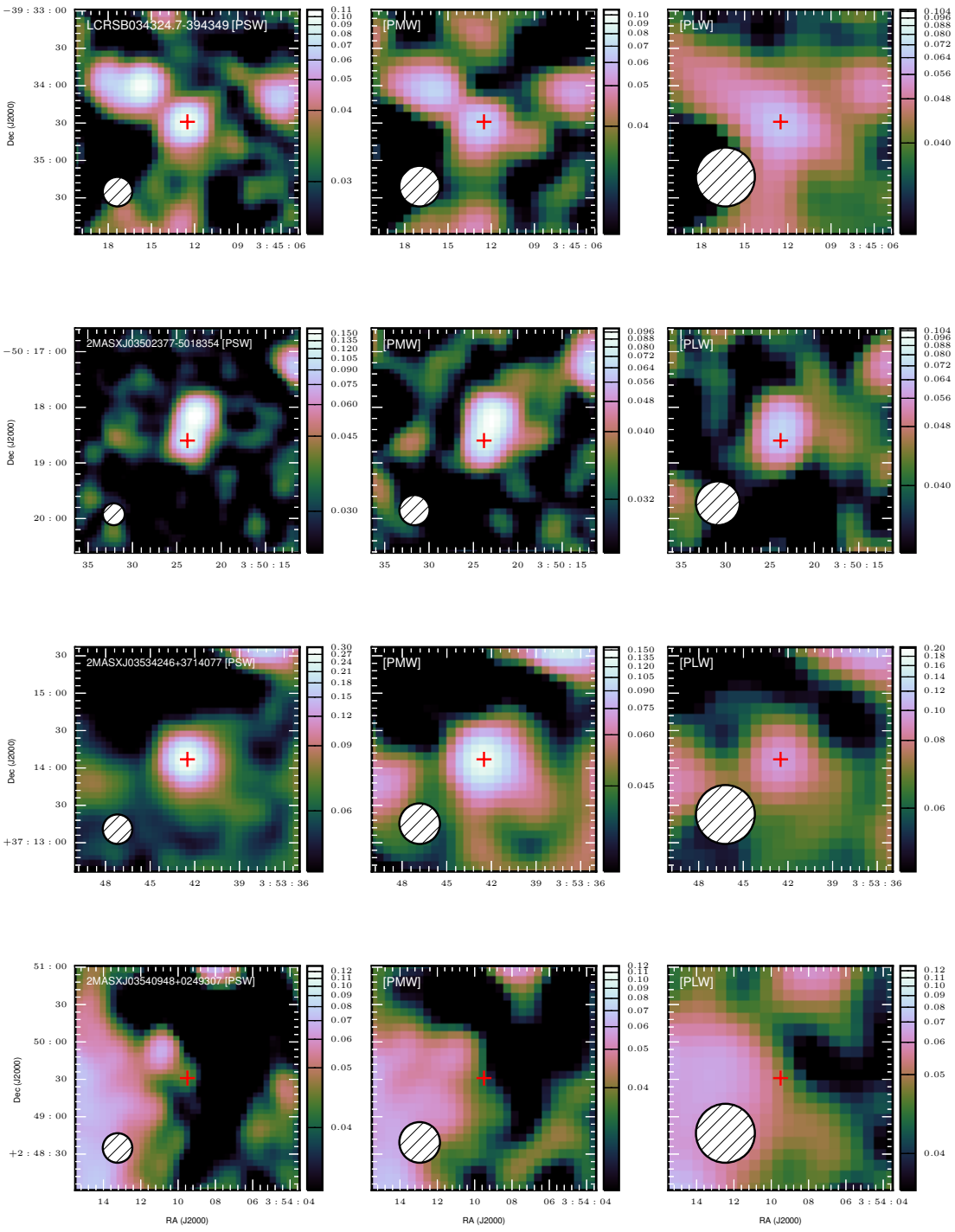
LCRSB034324.7-394349 [PSW]
[PMW]
[PLW]
2MASXJ03502377-5018354 [PSW]
[PMW]
[PLW]
2MASXJ03534246+3714077 [PSW]
[PMW]
[PLW]
2MASXJ03540948+0249307 [PSW]
[PMW]
[PLW]
Dec (J2000)
RA (J2000)

Figure B.14

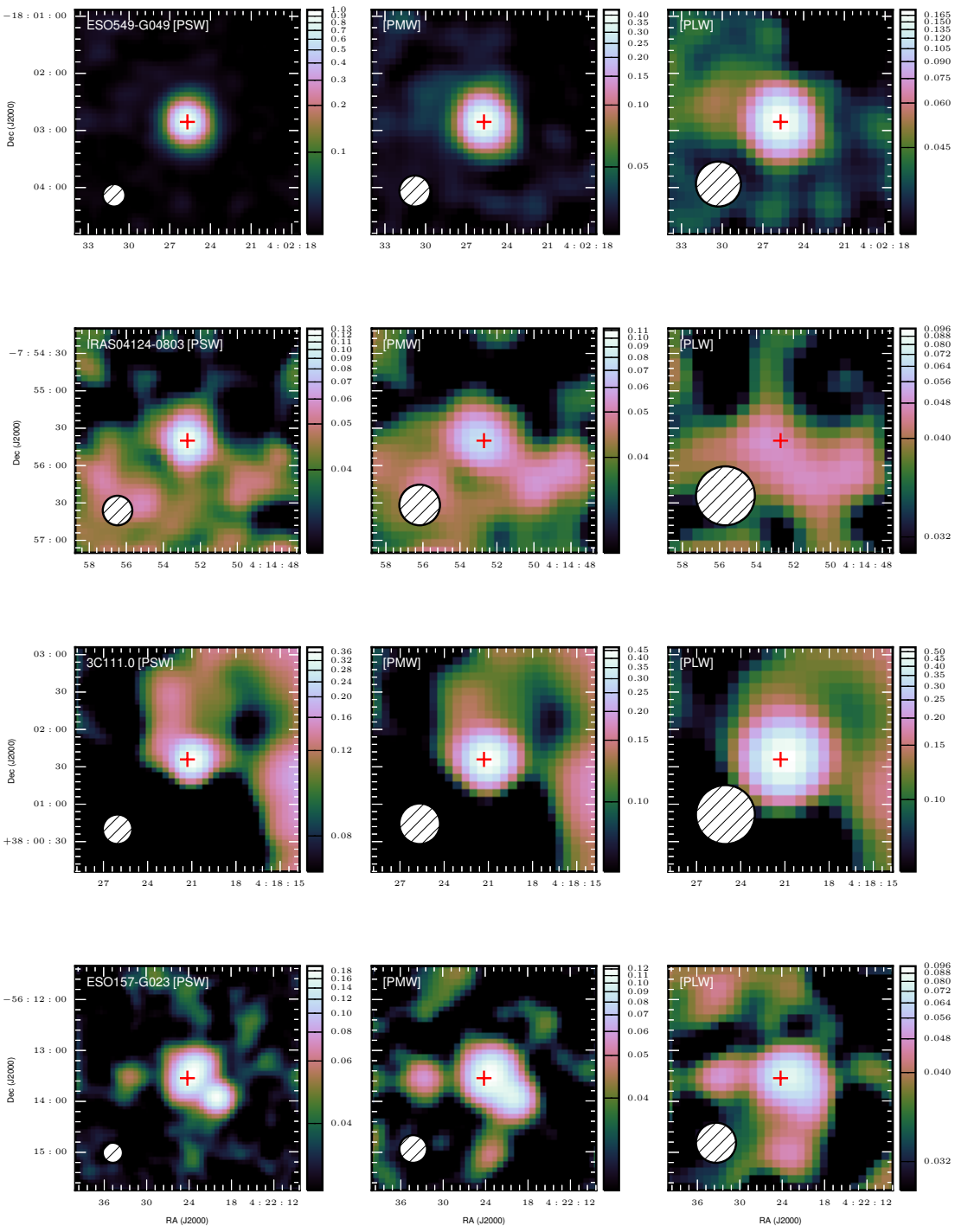
ESO549-G049 [PSW]
[PMW]
[PLW]
[RAS04124-0803 [PSW]
[PMW]
[PLW]
3C111.0 [PSW]
[PMW]
[PLW]
ESO157-G023 [PSW]
[PMW]
[PLW]
Dec (J2000)
RA (J2000)

Figure B.15

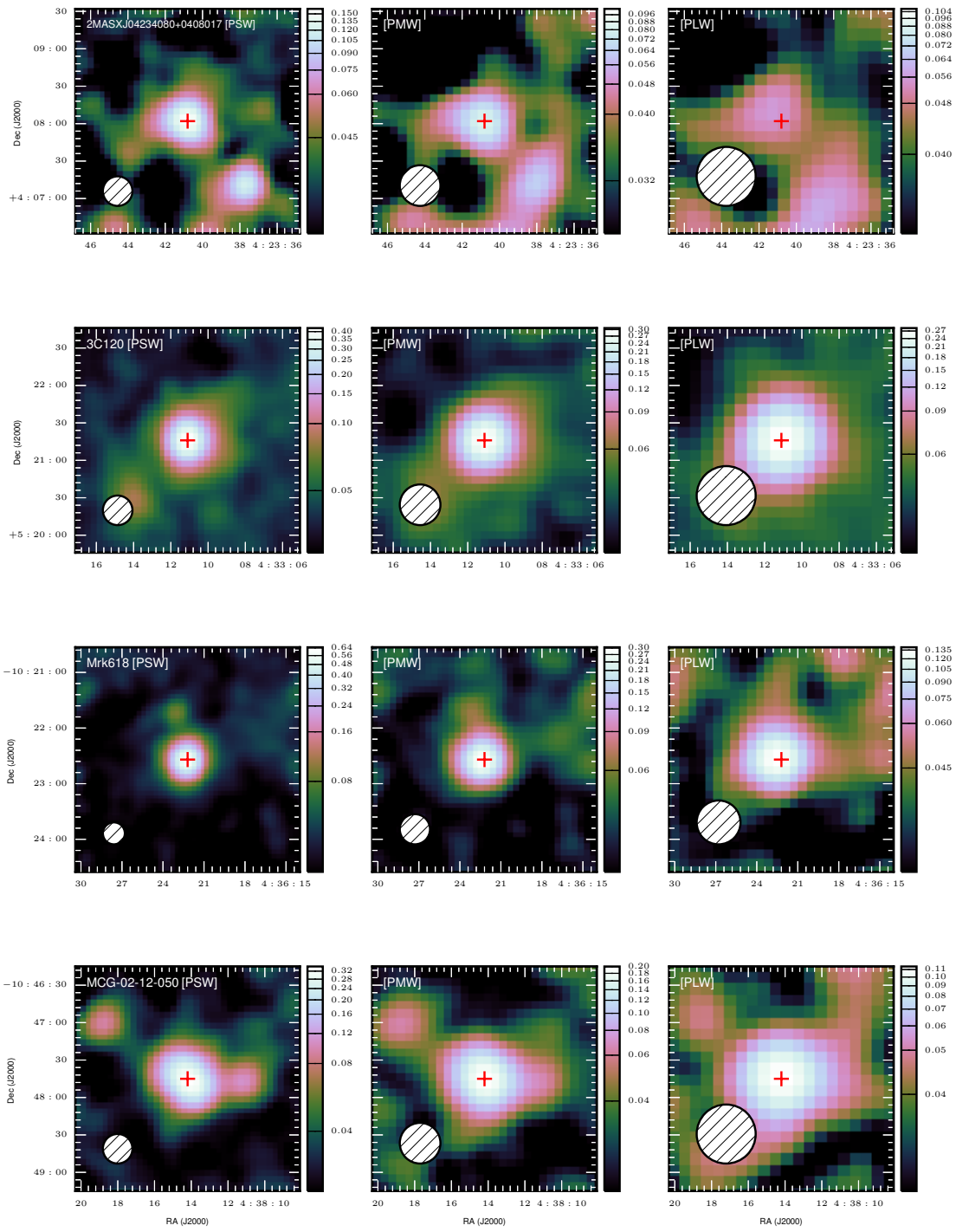
2MASXJ04234080+0408017 [PSW]
[PMW]
[PLW]
3C120 [PSW]
[PMW]
[PLW]
Mrk618 [PSW]
[PMW]
[PLW]
MCG-02-12-050 [PSW]
[PMW]
[PLW]
Dec (J2000)
RA (J2000)

Figure B.16

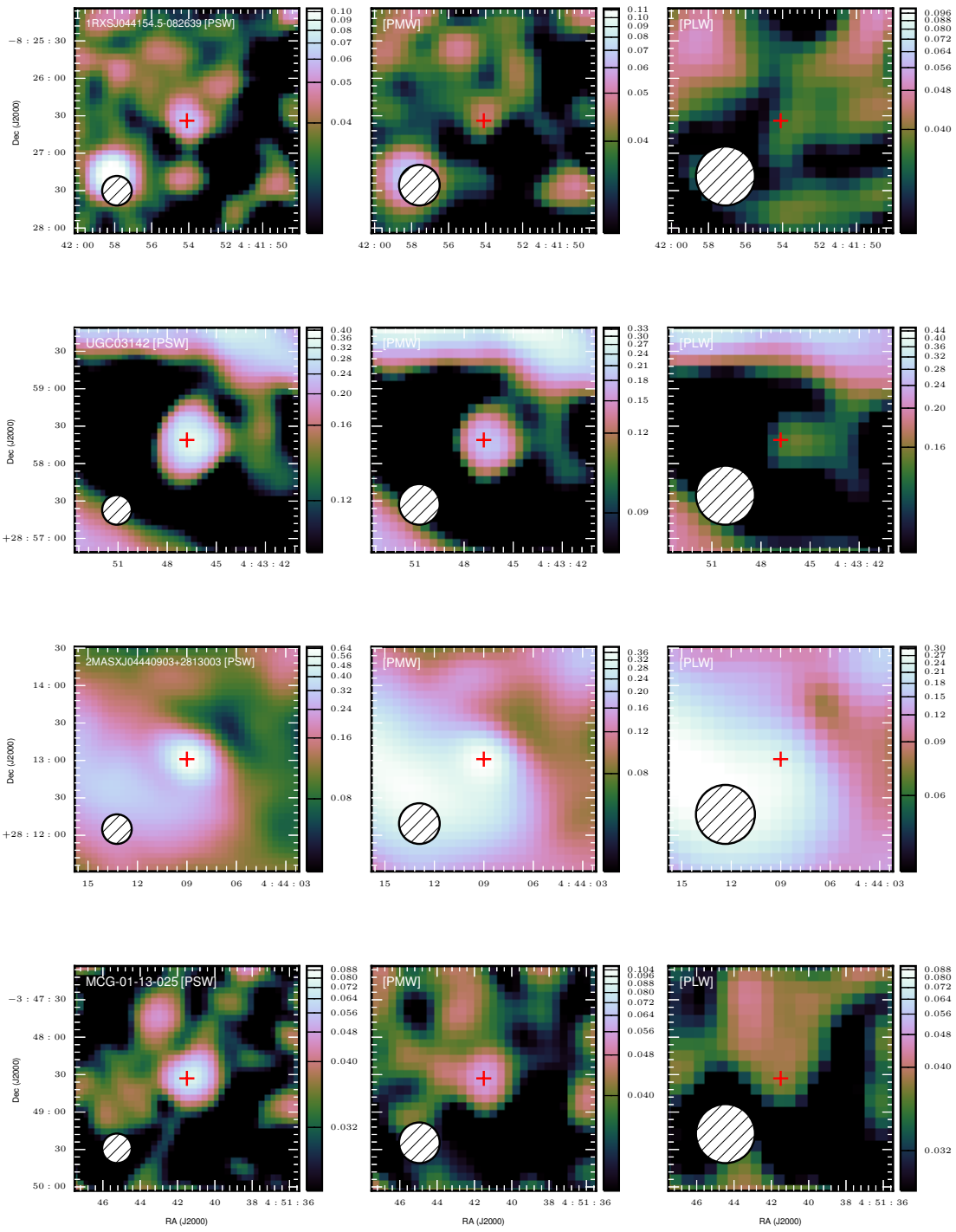
1RXSJ044154.5-082639 [PSW]
[PMW]
[PLW]
UGC03142 [PSW]
[PMW]
[PLW]
2MASXJ04440903+2813003 [PSW]
[PMW]
[PLW]
MCG-01-13-025 [PSW]
[PMW]
[PLW]
Dec (J2000)
RA (J2000)

Figure B.17

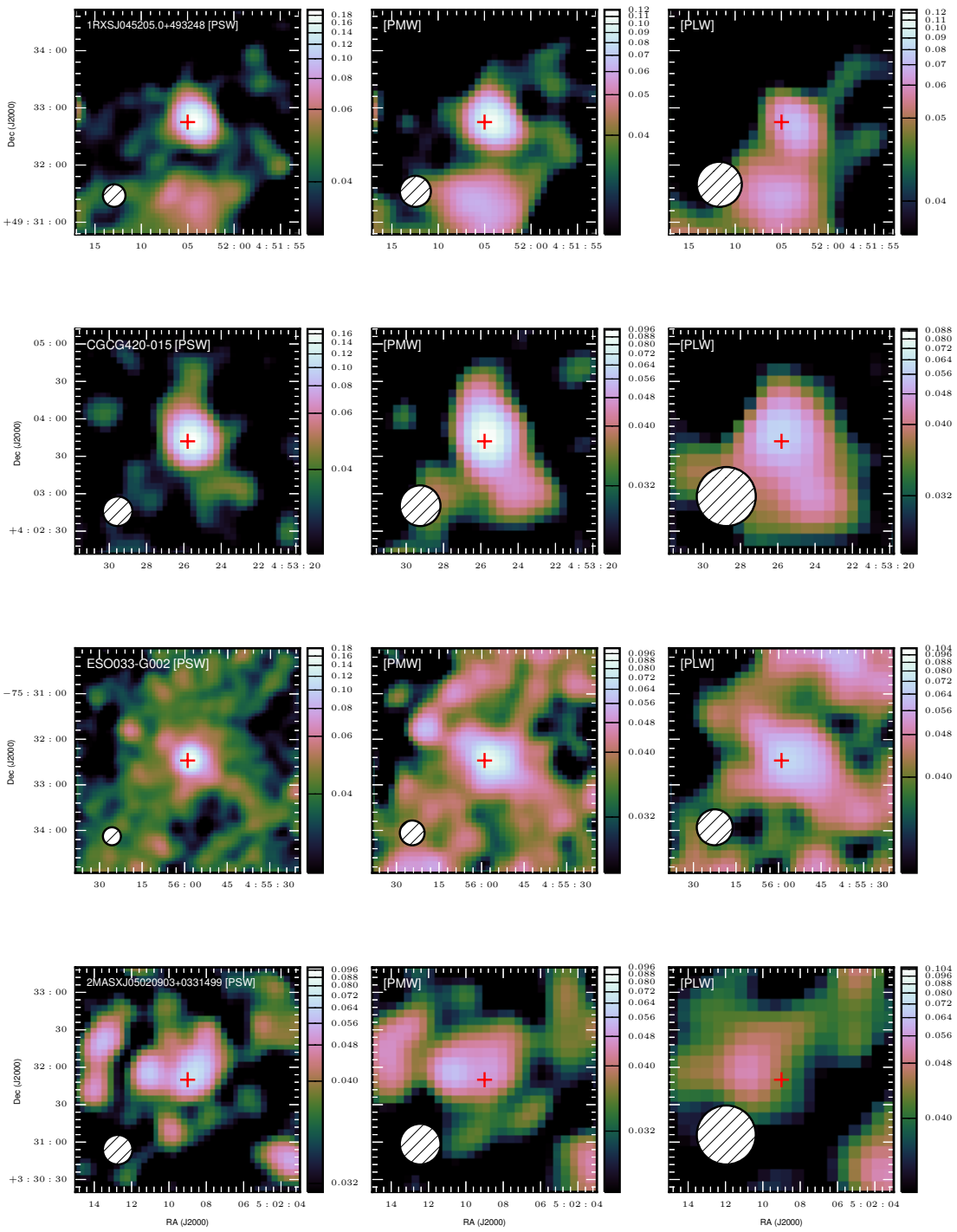
1RXSJ045205.0+493248 [PSW]
[PMW]
[PLW]
CGCG420-015 [PSW]
[PMW]
[PLW]
ESO033-G002 [PSW]
[PMW]
[PLW]
2MASXJ05020903+0331499 [PSW]
[PMW]
[PLW]
Dec (J2000)
RA (J2000)

Figure B.18

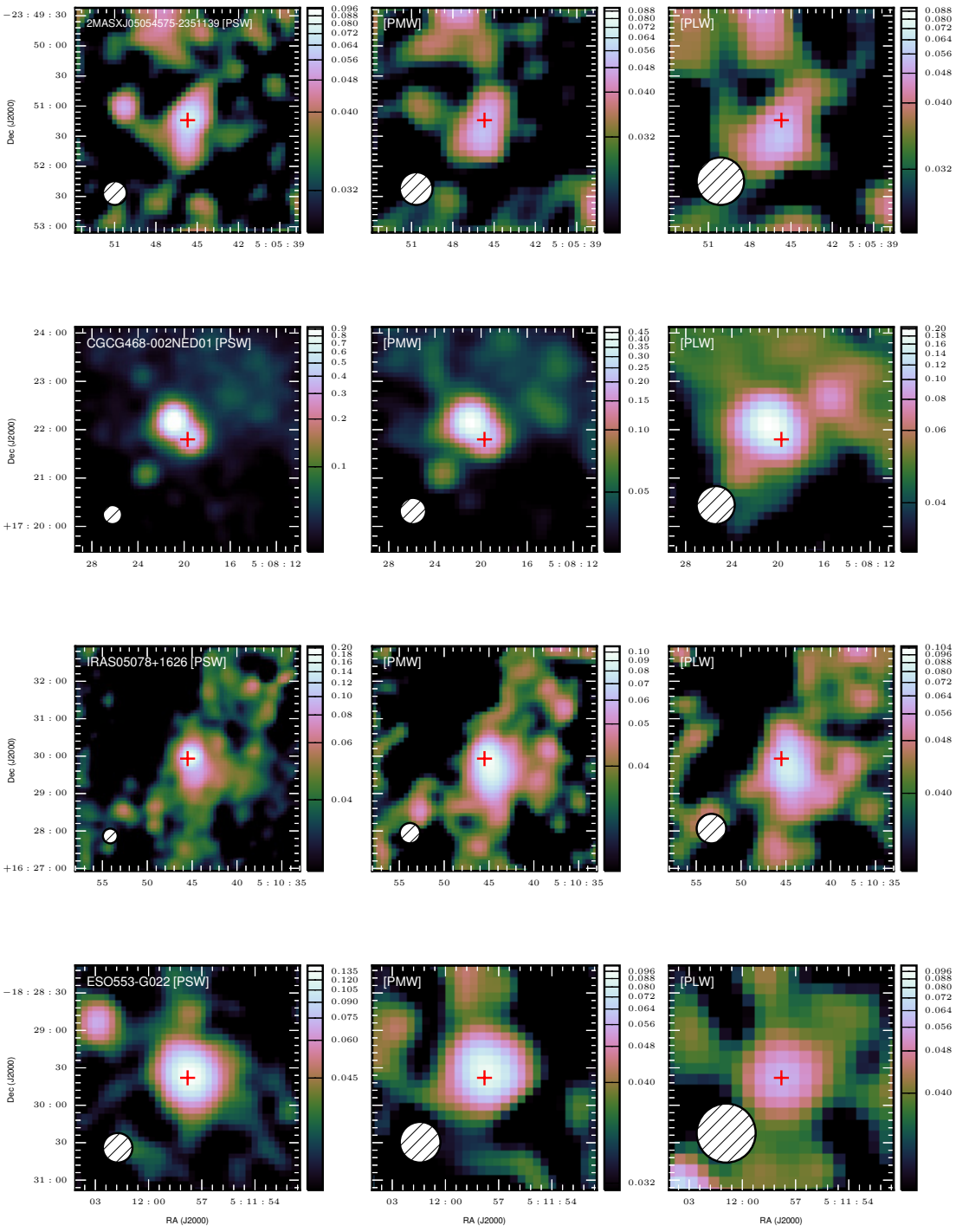
2MASXJ05054575-2351139 [PSW]
[PMW]
[PLW]
CGCG468-002NED01 [PSW]
[PMW]
[PLW]
IRAS05078+1626 [PSW]
[PMW]
[PLW]
ESO553-G022 [PSW]
[PMW]
[PLW]
Dec (J2000)
RA (J2000)

Figure B.19

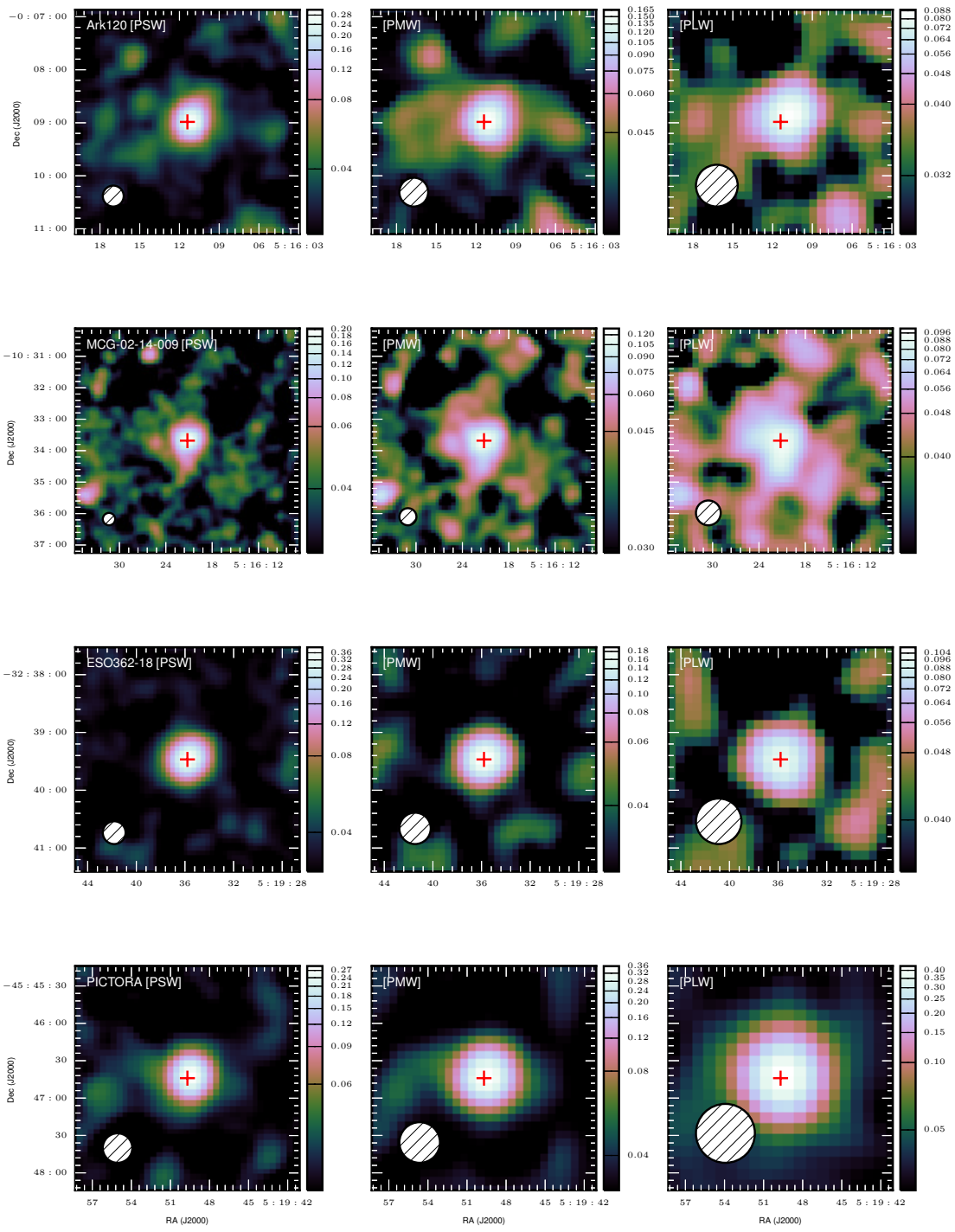
Ark120 [PSW]
[PMW]
[PLW]
MCG-02-14-009 [PSW]
[PMW]
[PLW]
ESO362-18 [PSW]
[PMW]
[PLW]
PICTORA [PSW]
[PMW]
[PLW]
Dec (J2000)
RA (J2000)

Figure B.20

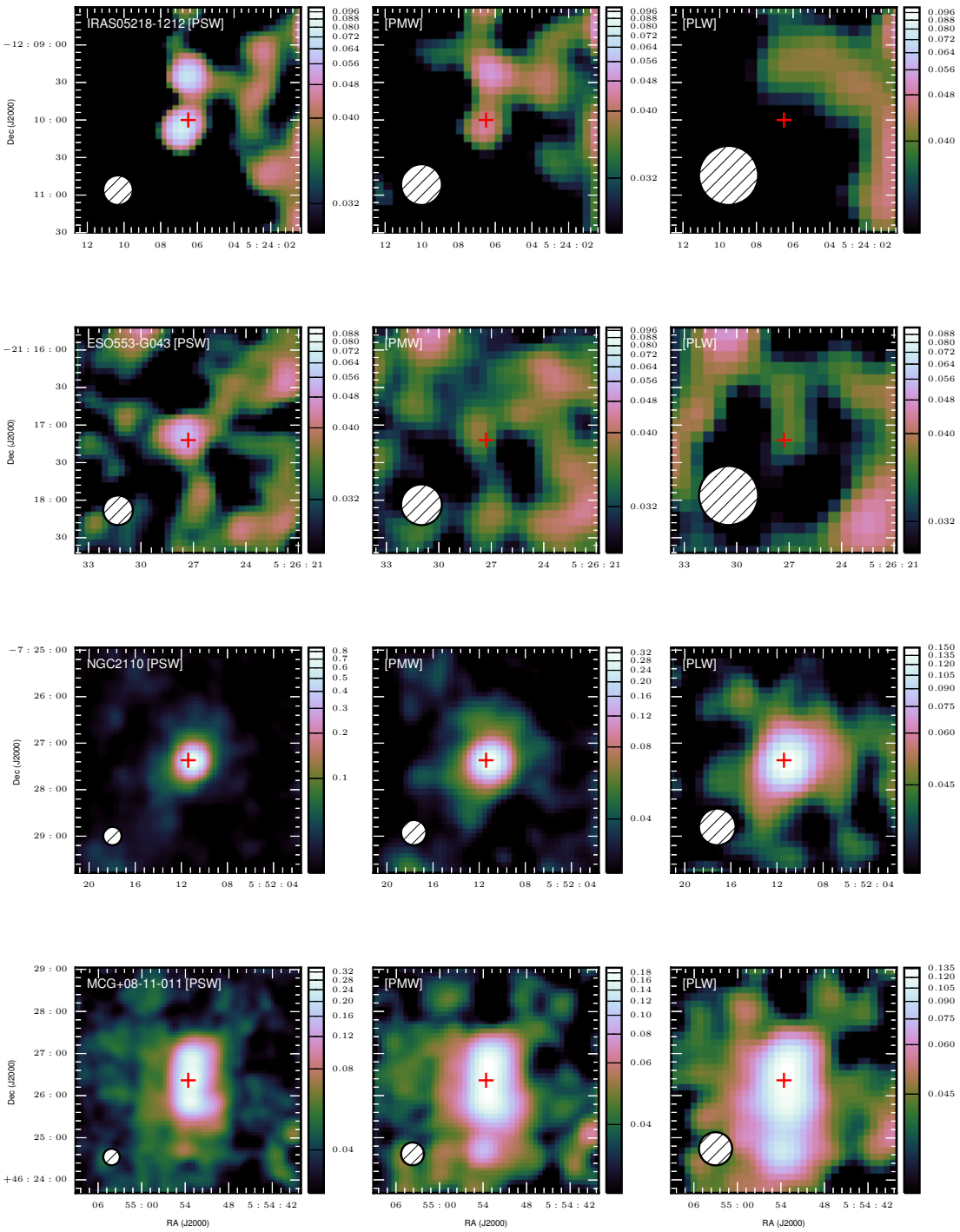
IRAS05218-1212 [PSW]
[PMW]
[PLW]
ESO553-G043 [PSW]
[PMW]
[PLW]
NGC2110 [PSW]
[PMW]
[PLW]
MCG+08-11-011 [PSW]
[PMW]
[PLW]
Dec (J2000)
RA (J2000)

Figure B.21

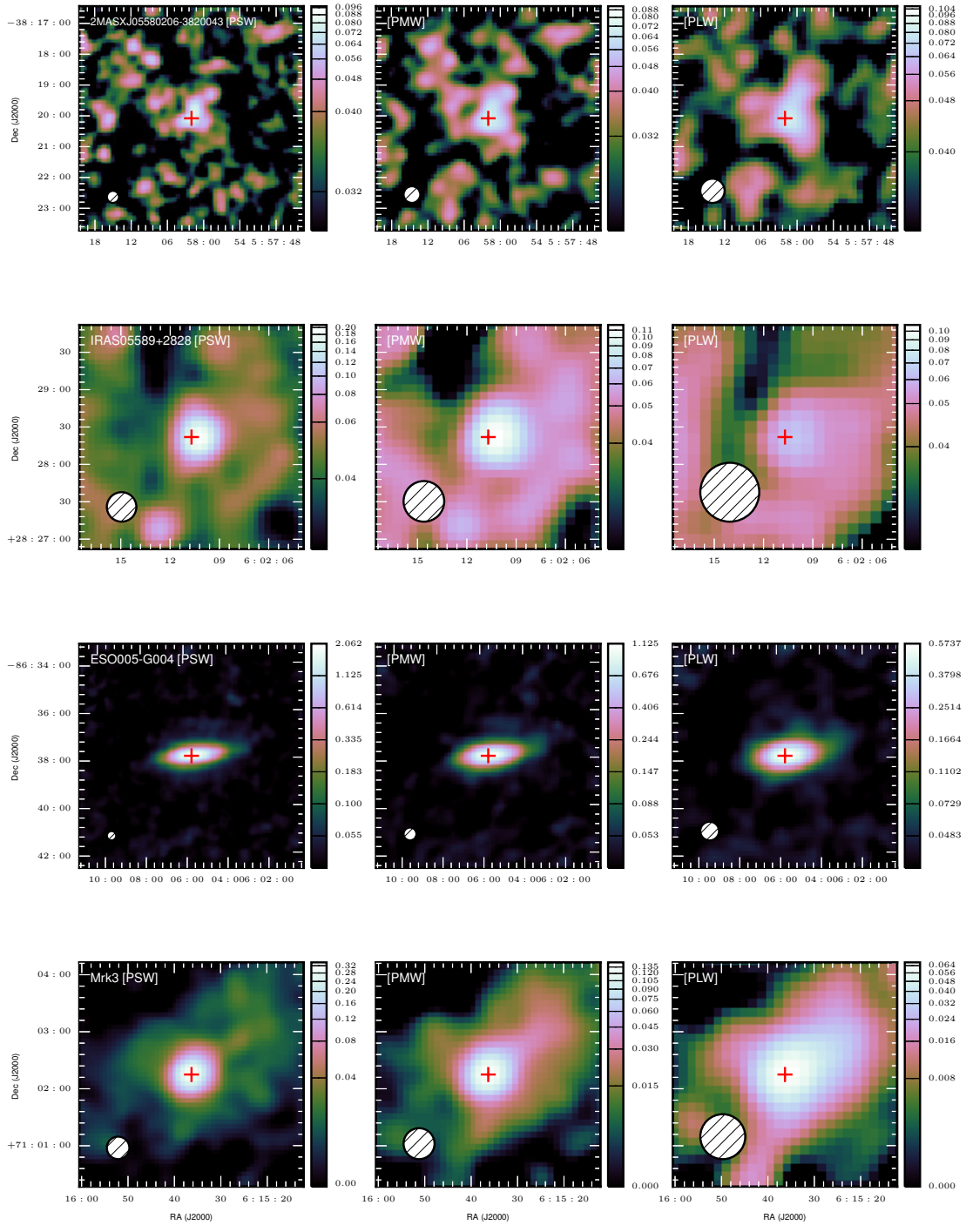
2MASXJ05580206-3820043 [PSW]
[PMW]
[PLW]
IRAS05589+2828 [PSW]
[PMW]
[PLW]
ESO005-G004 [PSW]
[PMW]
[PLW]
Mrk3 [PSW]
[PMW]
[PLW]
Dec (J2000)
RA (J2000)

Figure B.22

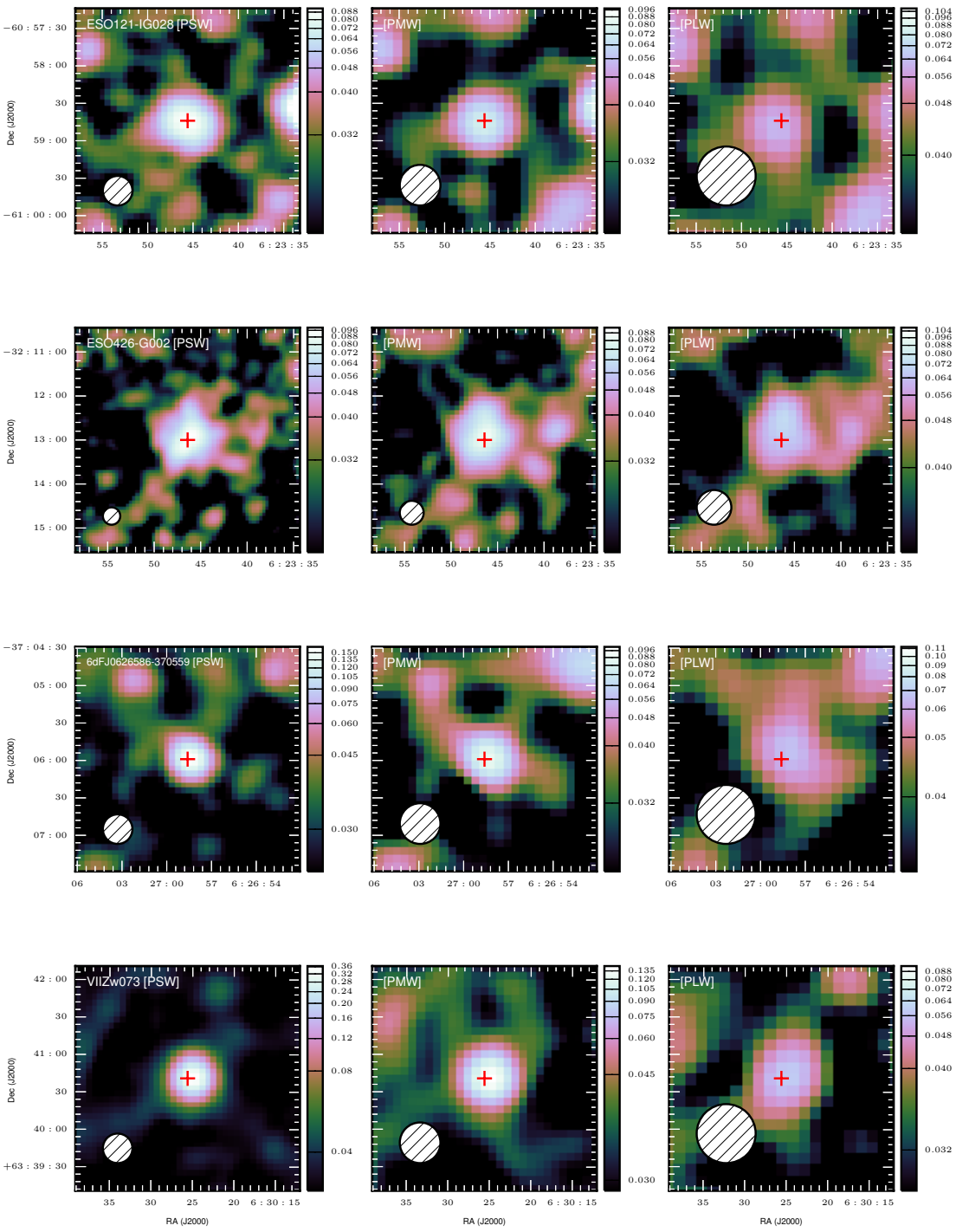
ESO121-IG028 [PSW]
[PMW]
[PLW]
ESO426-G002 [PSW]
[PMW]
[PLW]
6dFJ0626586-370559 [PSW]
[PMW]
[PLW]
VIIZw073 [PSW]
[PMW]
[PLW]
Dec (J2000)
RA (J2000)

Figure B.23

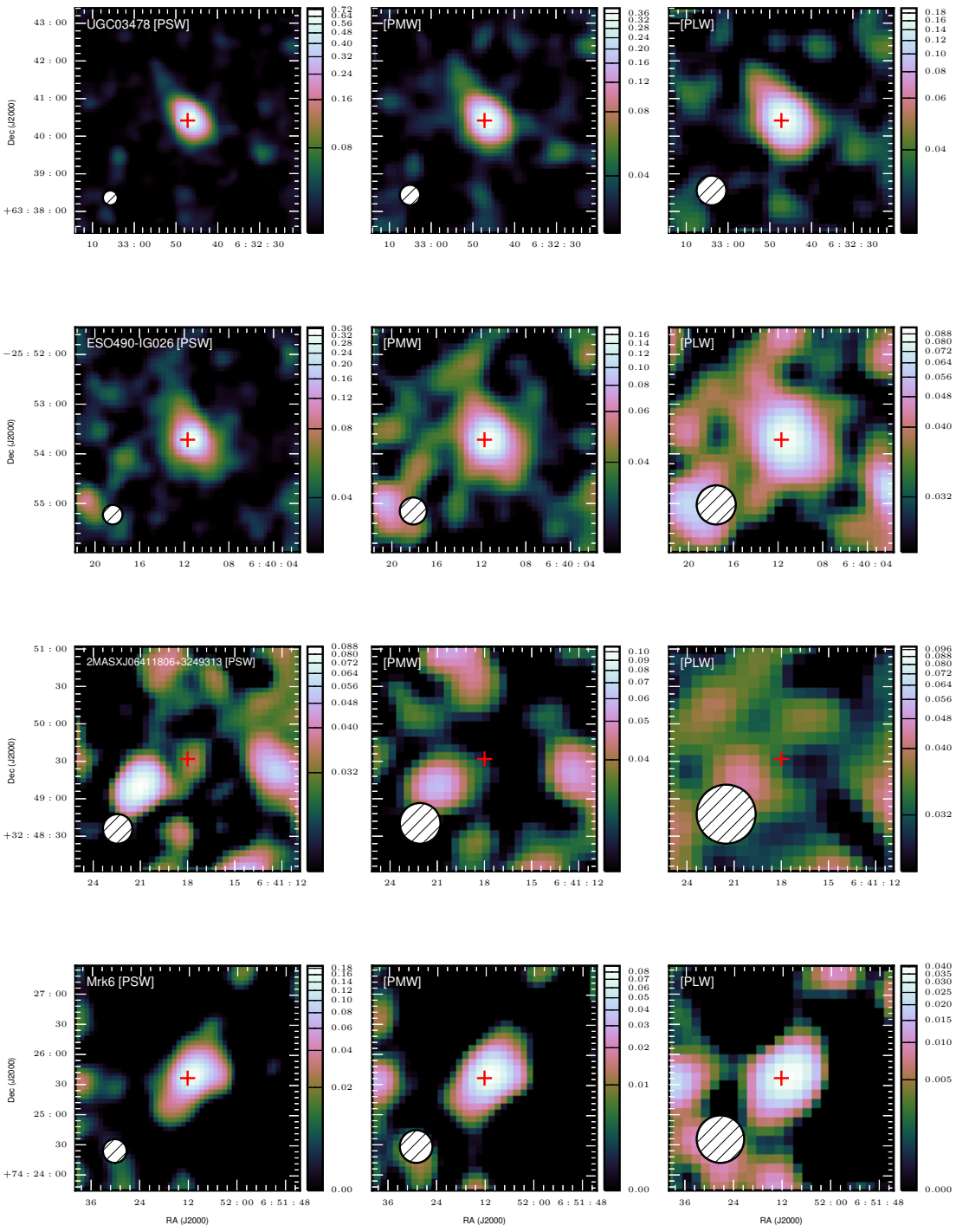
UGC03478 [PSW]
[PMW]
[PLW]
ESO490-IG026 [PSW]
[PMW]
[PLW]
2MASXJ06411806+3249313 [PSW]
[PMW]
[PLW]
Mrk6 [PSW]
[PMW]
[PLW]
Dec (J2000)
RA (J2000)

Figure B.24

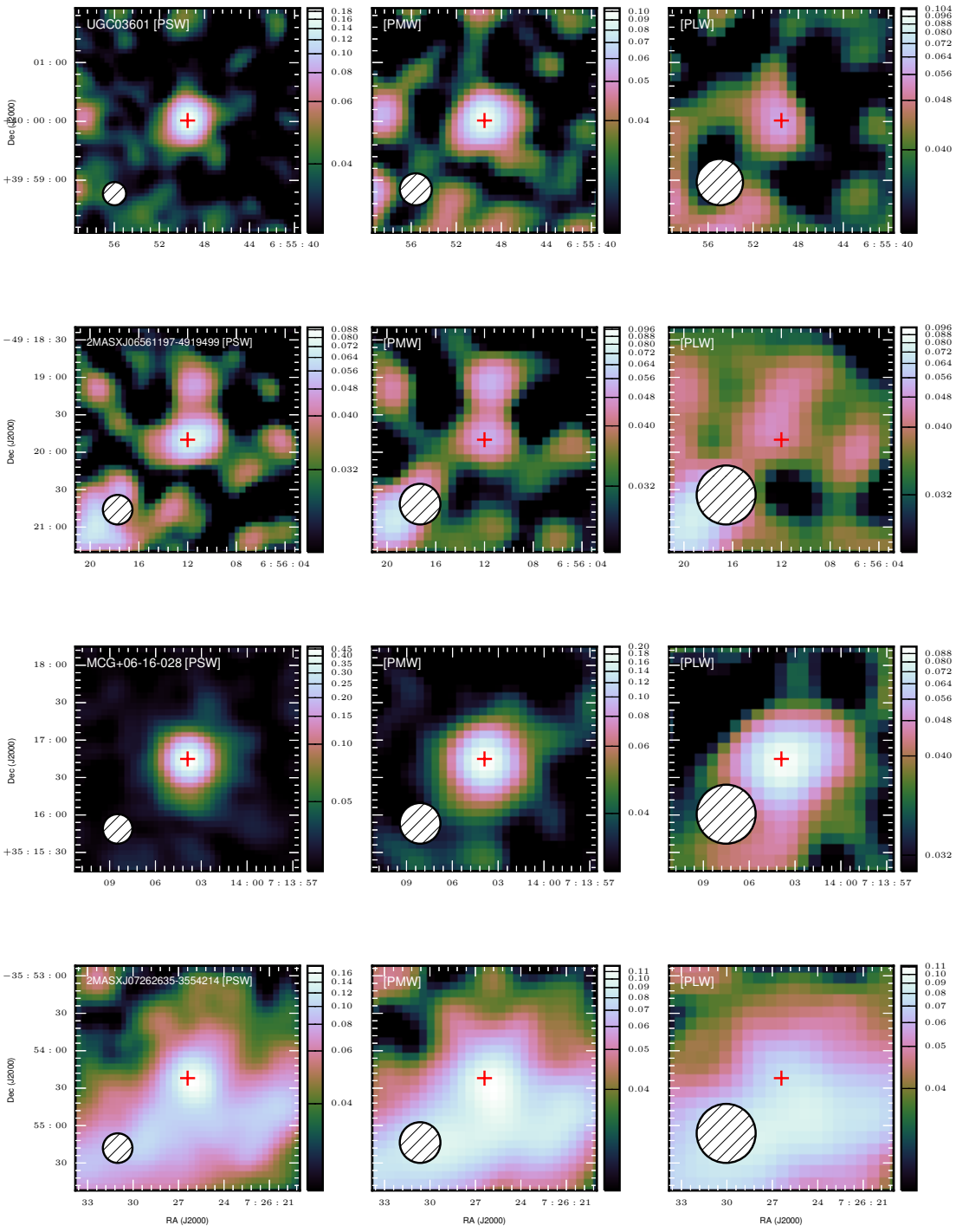
UGC03601 [PSW]
[PMW]
[PLW]
2MASXJ06561197-4919499 [PSW]
[PMW]
[PLW]
MCG+06-16-028 [PSW]
[PMW]
[PLW]
2MASXJ07262635-3554214 [PSW]
[PMW]
[PLW]
Dec (J2000)
RA (J2000)

Figure B.25

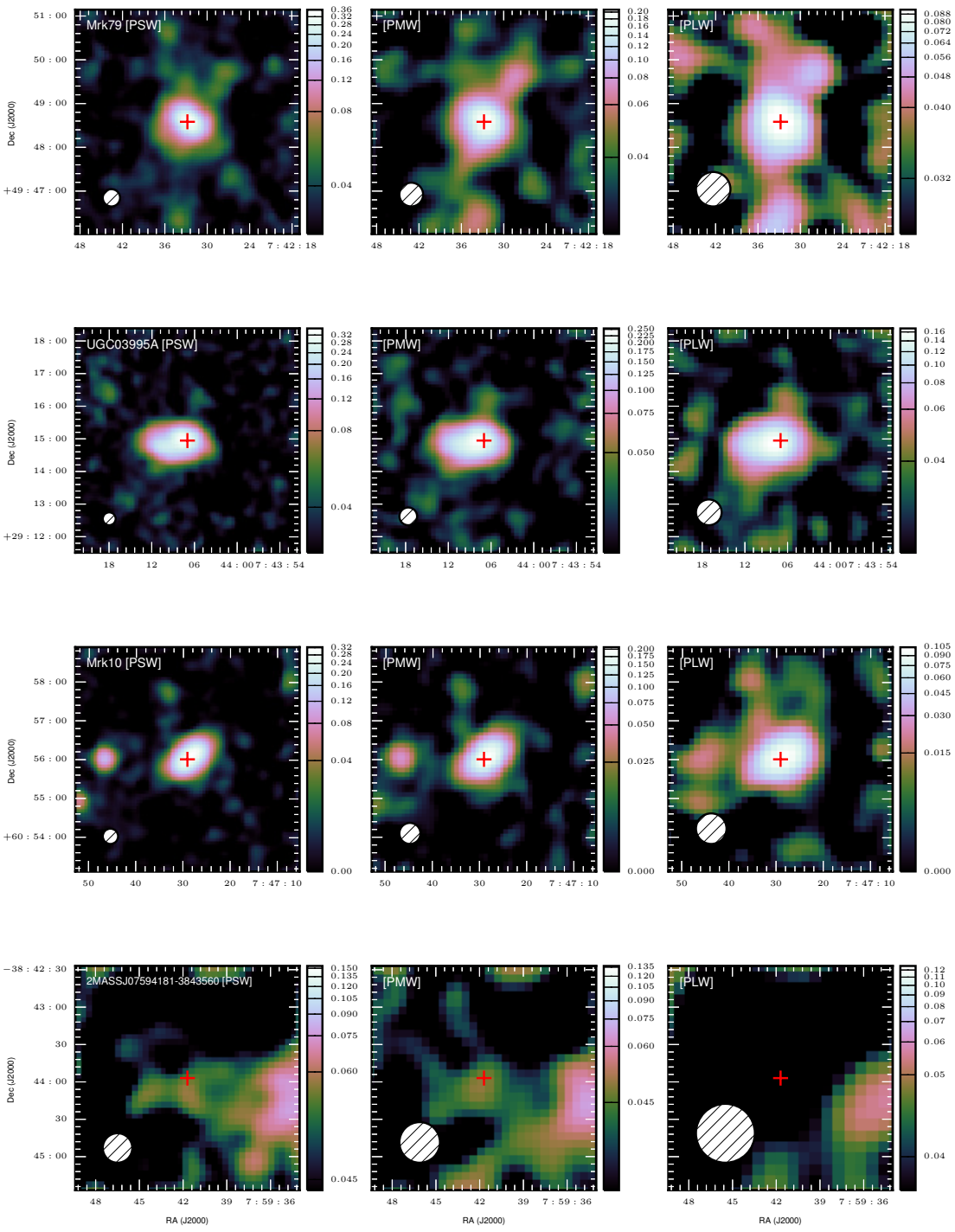
Mrk79 [PSW]
[PMW]
[PLW]
UGC03995A [PSW]
[PMW]
[PLW]
Mrk10 [PSW]
[PMW]
[PLW]
2MASSJ07594181-3843560 [PSW]
[PMW]
[PLW]
Dec (J2000)
RA (J2000)

Figure B.26

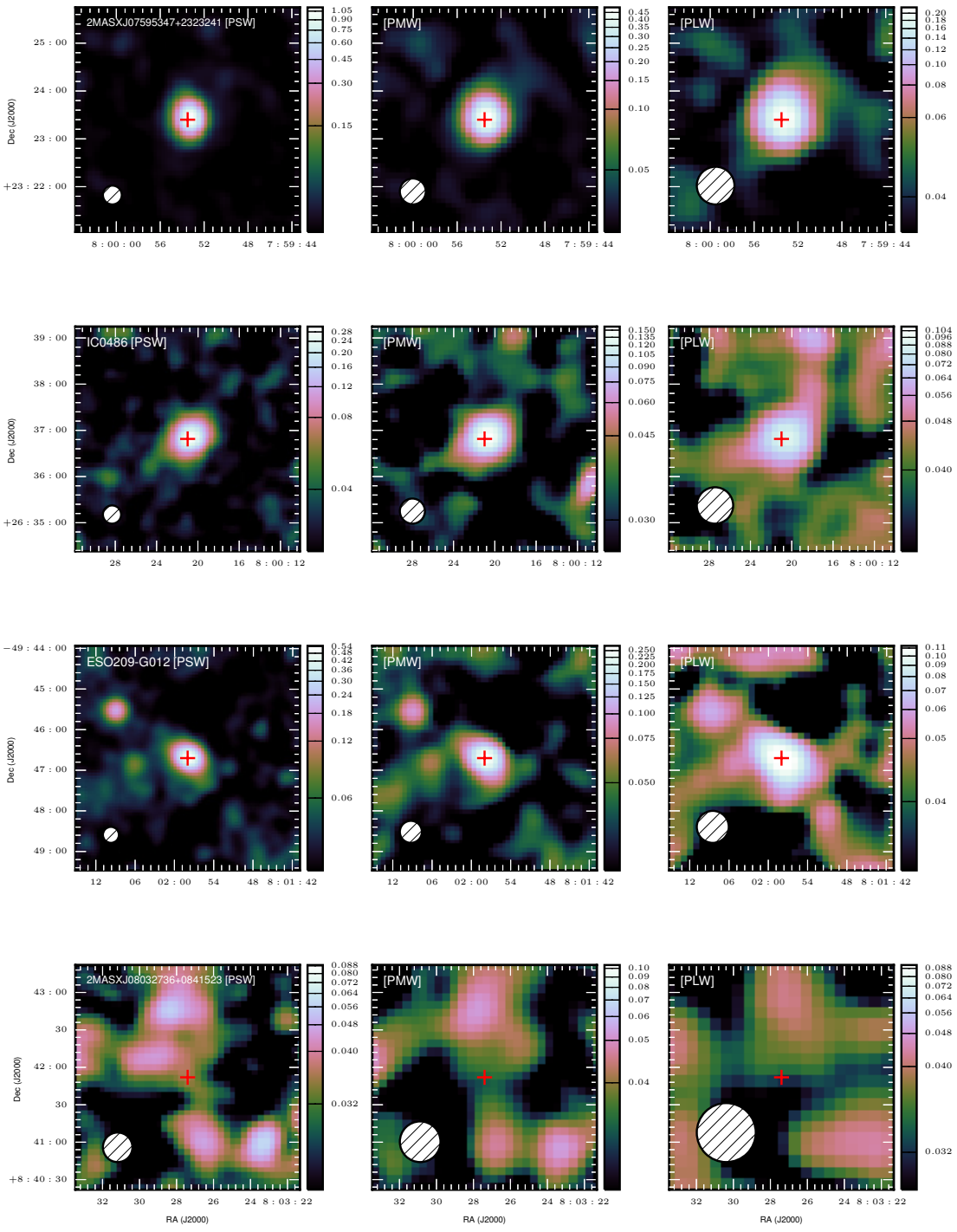
2MASXJ07595347+2323241 [PSW]
[PMW]
[PLW]
IC0486 [PSW]
[PMW]
[PLW]
ESO209-G012 [PSW]
[PMW]
[PLW]
2MASXJ08032736+0841523 [PSW]
[PMW]
[PLW]
Dec (J2000)
RA (J2000)

Figure B.27

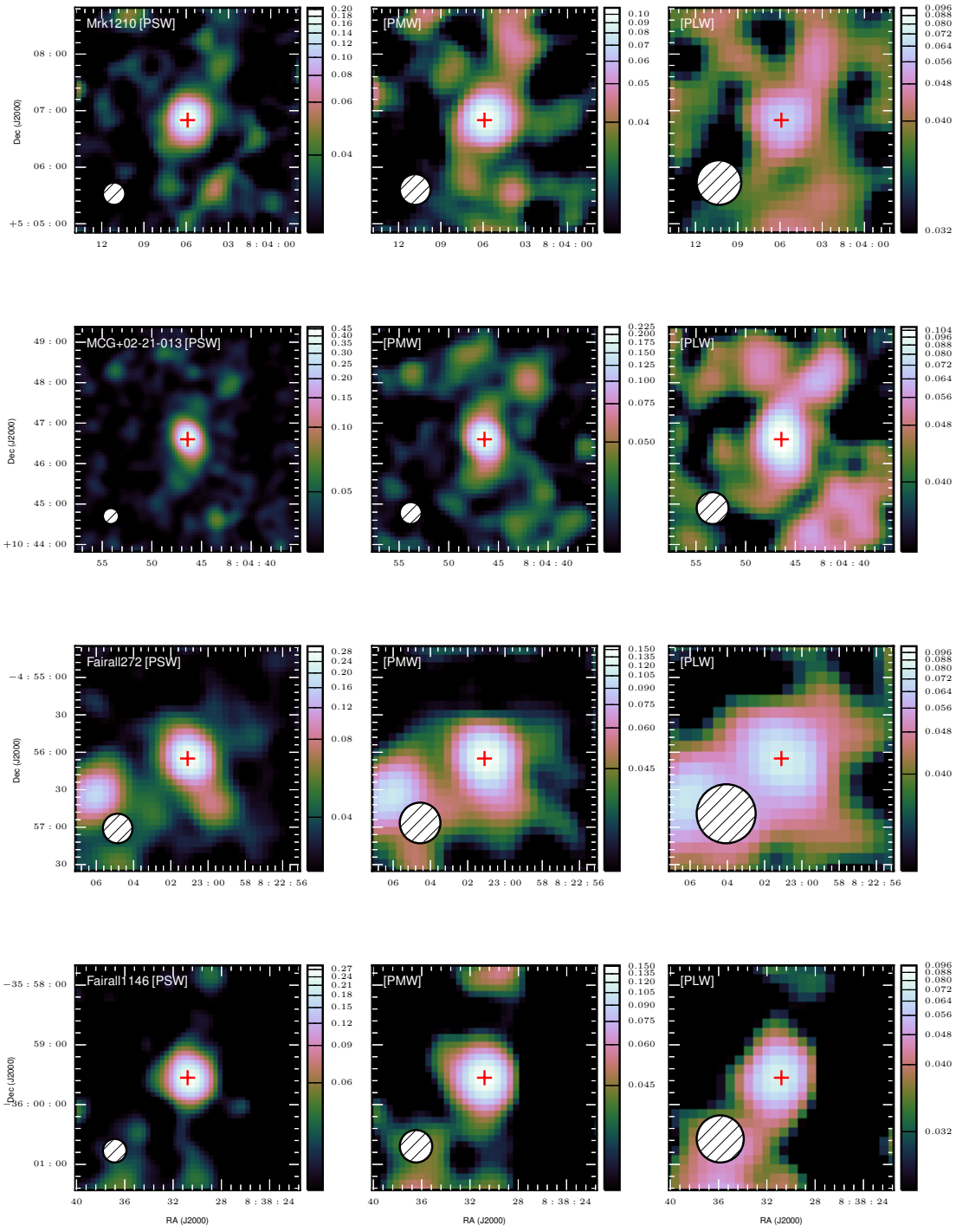
Mrk1210 [PSW]
[PMW]
[PLW]
MCG+02-21-013 [PSW]
[PMW]
[PLW]
Fairall272 [PSW]
[PMW]
[PLW]
Fairall1146 [PSW]
[PMW]
[PLW]
Dec (J2000)
RA (J2000)

Figure B.28

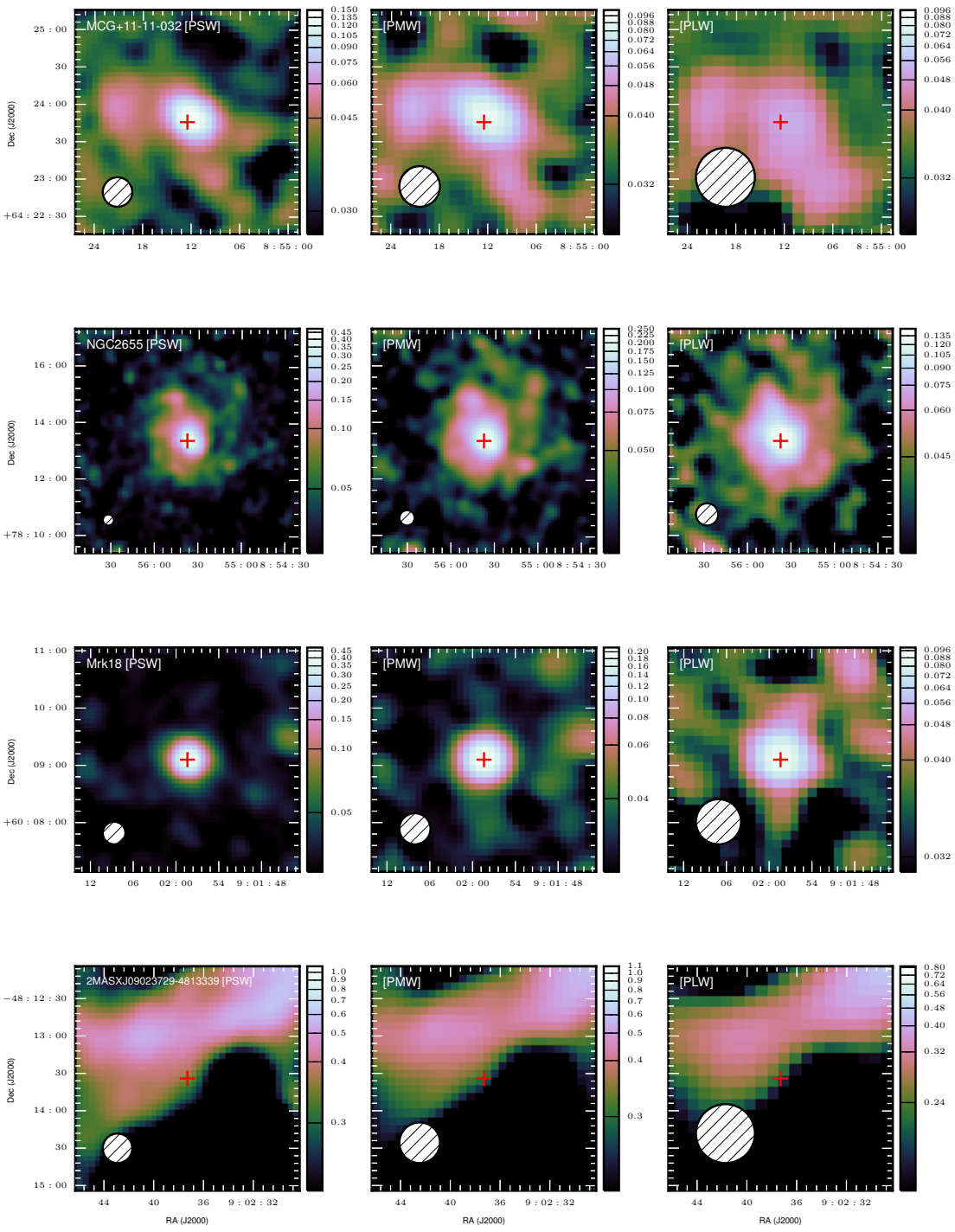
MCG+11-11-032 [PSW]
[PMW]
[PLW]
NGC2655 [PSW]
[PMW]
[PLW]
Mrk18 [PSW]
[PMW]
[PLW]
2MASXJ09023729-4813339 [PSW]
[PMW]
[PLW]
Dec (J2000)
RA (J2000)

Figure B.29

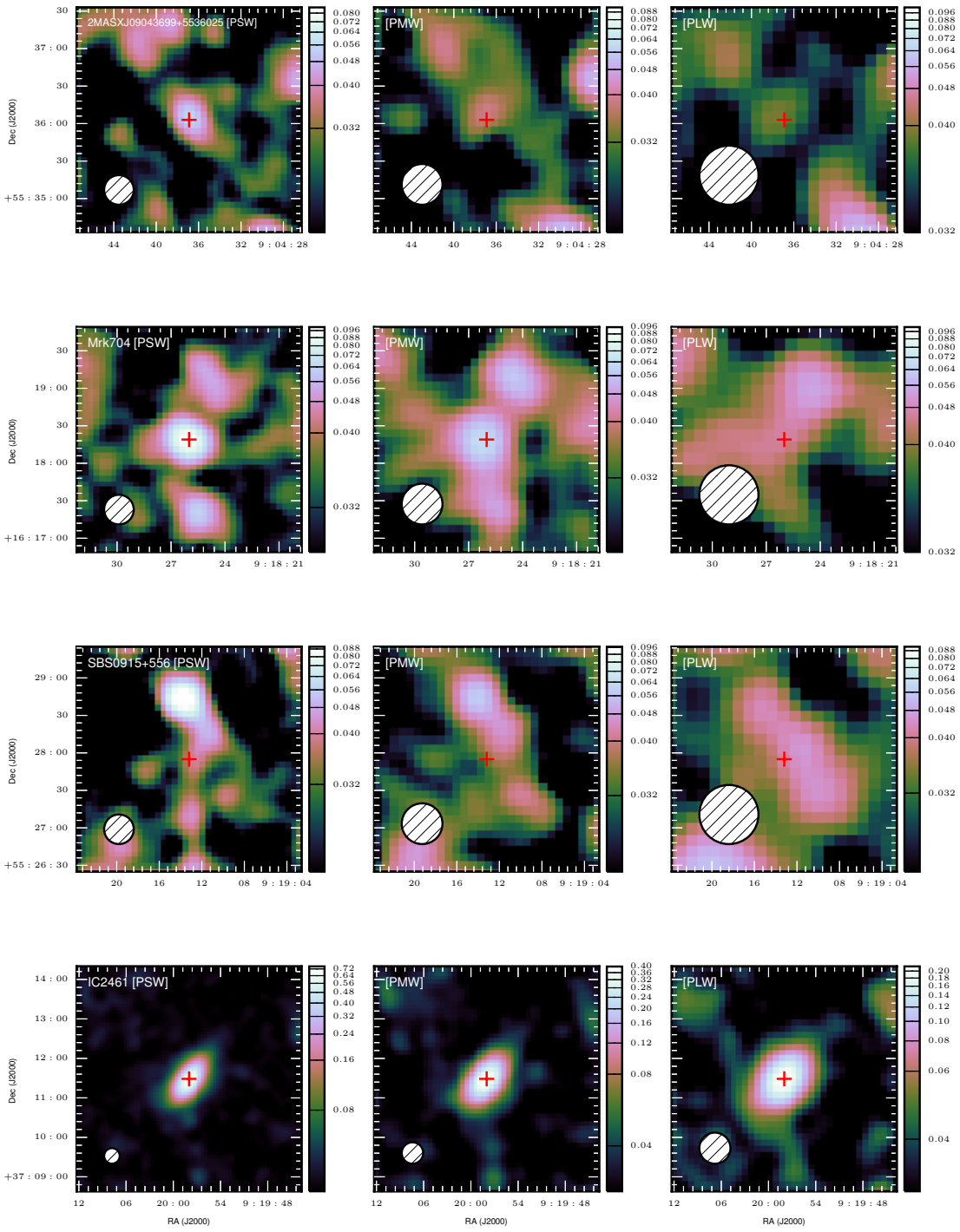
2MASXJ09043699+5536025 [PSW]
[PMW]
[PLW]
Mrk704 [PSW]
[PMW]
[PLW]
SBS0915+556 [PSW]
[PMW]
[PLW]
IC2461 [PSW]
[PMW]
[PLW]
Dec (J2000)
RA (J2000)

Figure B.30

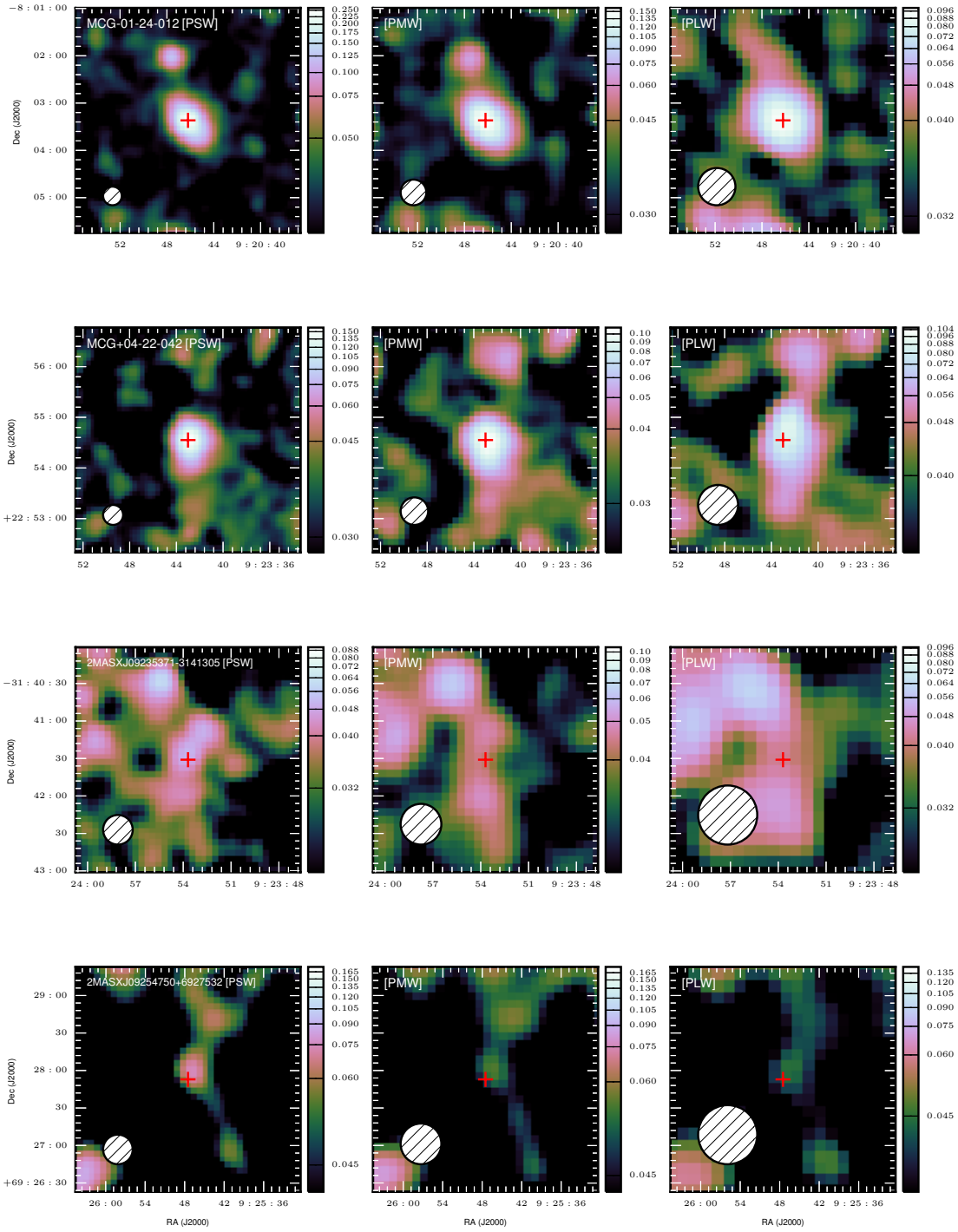
MCG-01-24-012 [PSW]
[PMW]
[PLW]
MCG+04-22-042 [PSW]
[PMW]
[PLW]
2MASXJ09235371-3141305 [PSW]
[PMW]
[PLW]
2MASXJ09254750+6927532 [PSW]
[PMW]
[PLW]
Dec (J2000)
RA (J2000)

Figure B.31

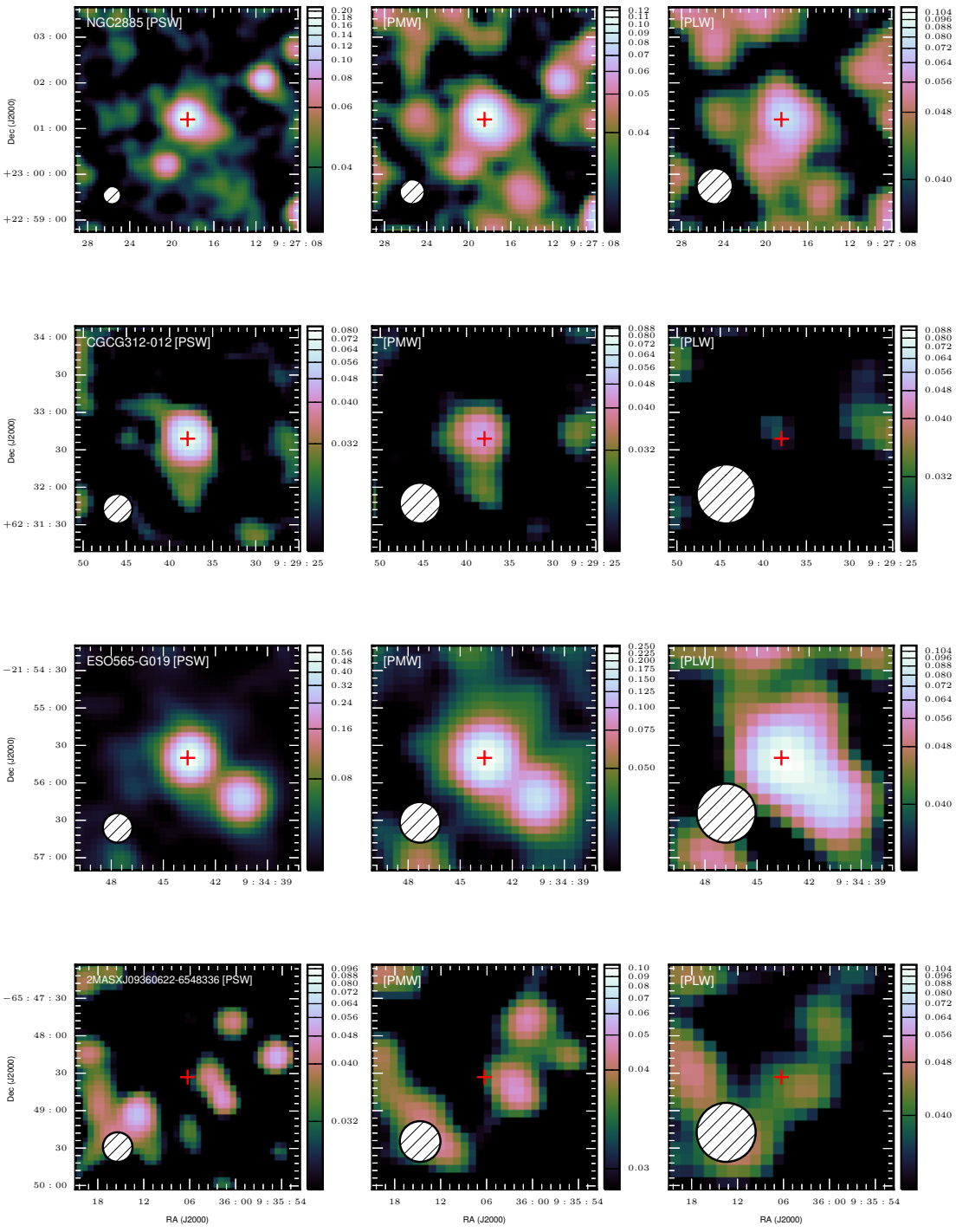
NGC2885 [PSW]
[PMW]
[PLW]
CGCG312-012 [PSW]
[PMW]
[PLW]
ESO565-G019 [PSW]
[PMW]
[PLW]
2MASXJ09360622-6548336 [PSW]
[PMW]
[PLW]
Dec (J2000)
RA (J2000)

Figure B.32

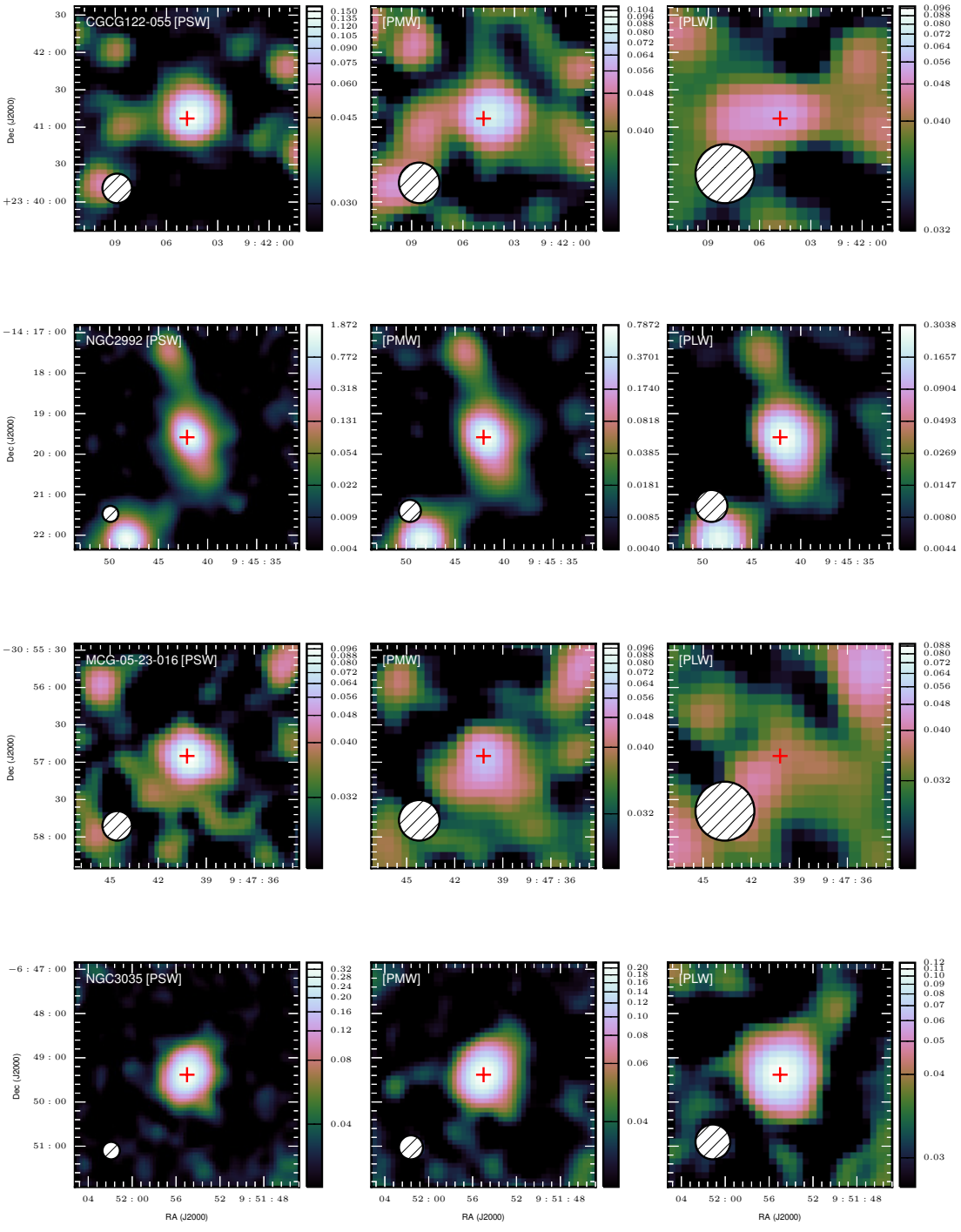
CGCG122-055 [PSW]
[PMW]
[PLW]
NGC2992 [PSW]
[PMW]
[PLW]
MCG-05-23-016 [PSW]
[PMW]
[PLW]
NGC3035 [PSW]
[PMW]
[PLW]
Dec (J2000)
RA (J2000)

Figure B.33

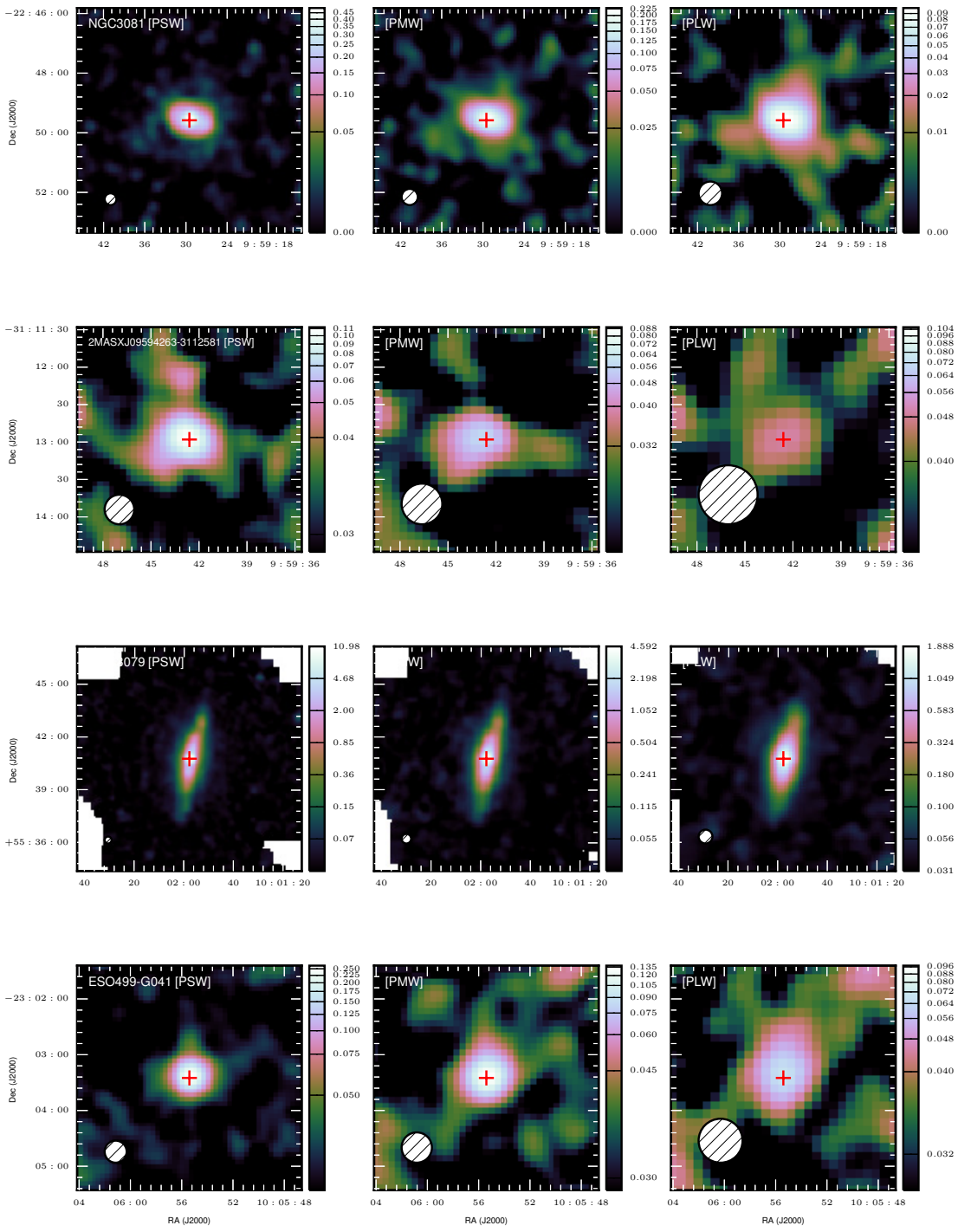
NGC3081 [PSW]
[PMW]
[PLW]
2MASXJ09594263-3112581 [PSW]
[PMW]
[PLW]
079 [PSW]
W]
LW]
ESO499-G041 [PSW]
[PMW]
[PLW]
Dec (J2000)
RA (J2000)

Figure B.34

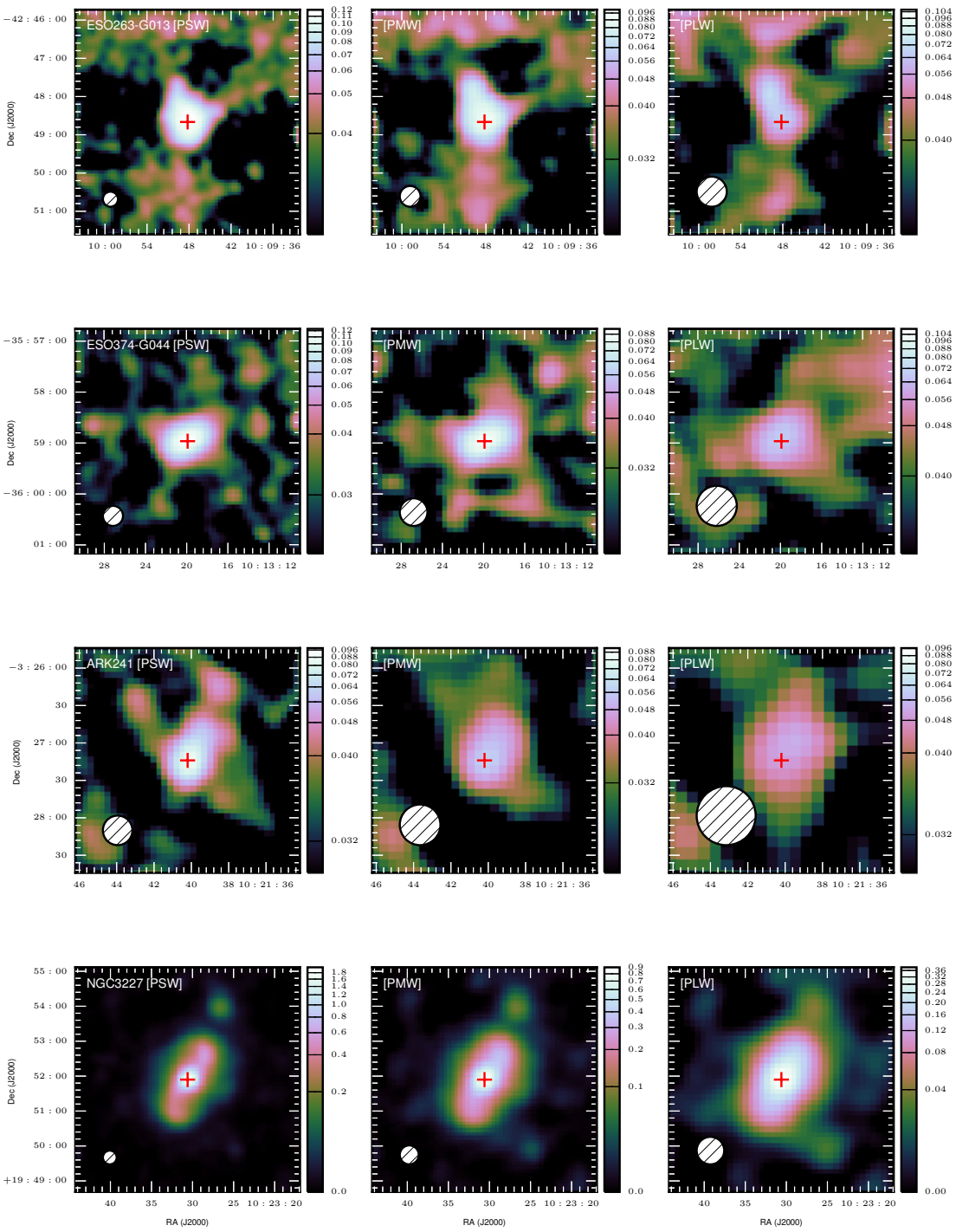
ESO263-G013 [PSW]
[PMW]
[PLW]
ESO374-G044 [PSW]
[PMW]
[PLW]
ARK241 [PSW]
[PMW]
[PLW]
NGC3227 [PSW]
[PMW]
[PLW]
Dec (J2000)
RA (J2000)

Figure B.35

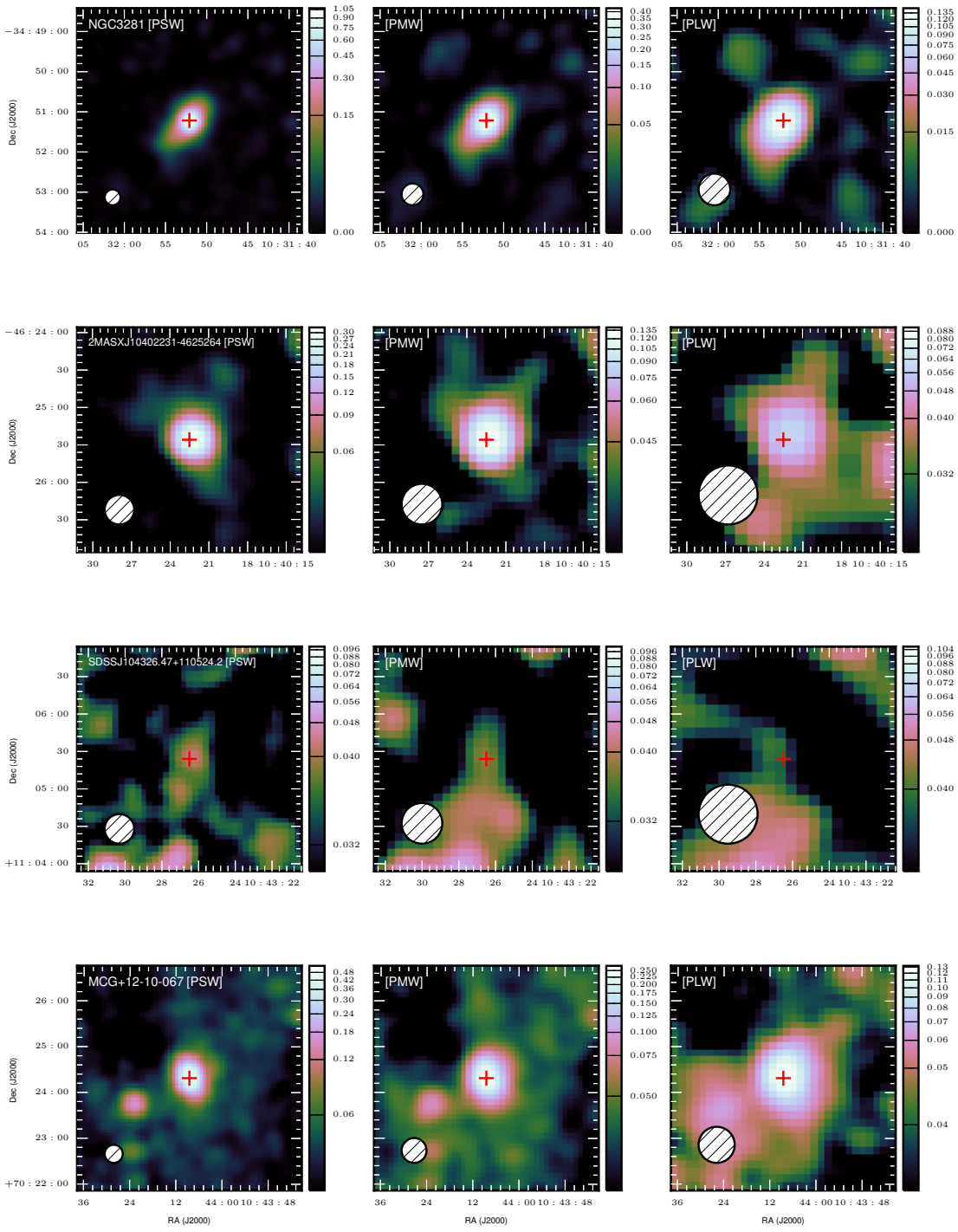
NGC3281 [PSW]
[PMW]
[PLW]
2MASXJ10402231-4625264 [PSW]
[PMW]
[PLW]
SDSSJ104326.47+110524.2 [PSW]
[PMW]
[PLW]
MCG+12-10-067 [PSW]
[PMW]
[PLW]
Dec (J2000)
RA (J2000)

Figure B.36

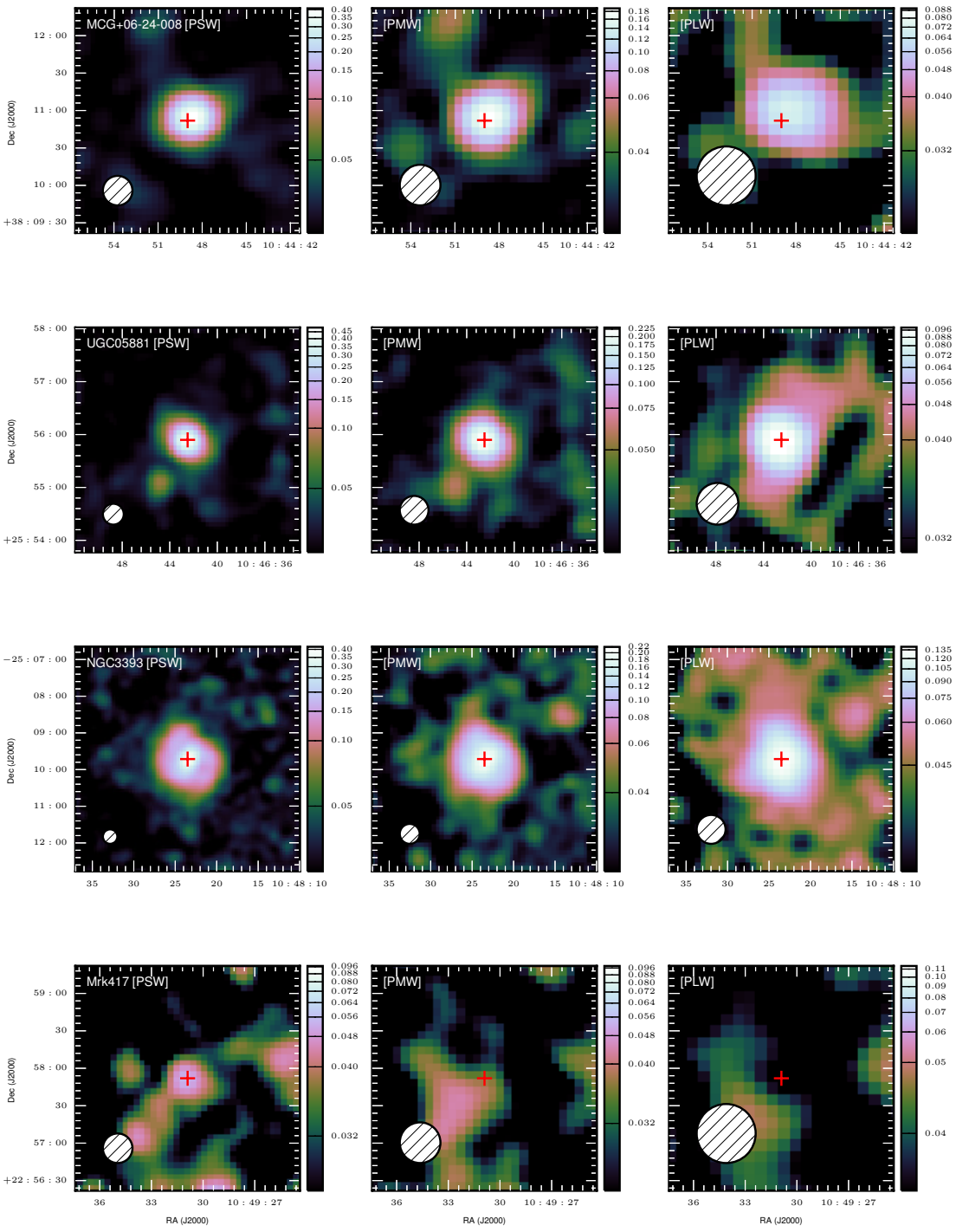
MCG+06-24-008 [PSW]
[PMW]
[PLW]
UGC05881 [PSW]
[PMW]
[PLW]
NGC3393 [PSW]
[PMW]
[PLW]
Mrk417 [PSW]
[PMW]
[PLW]
Dec (J2000)
RA (J2000)

Figure B.37

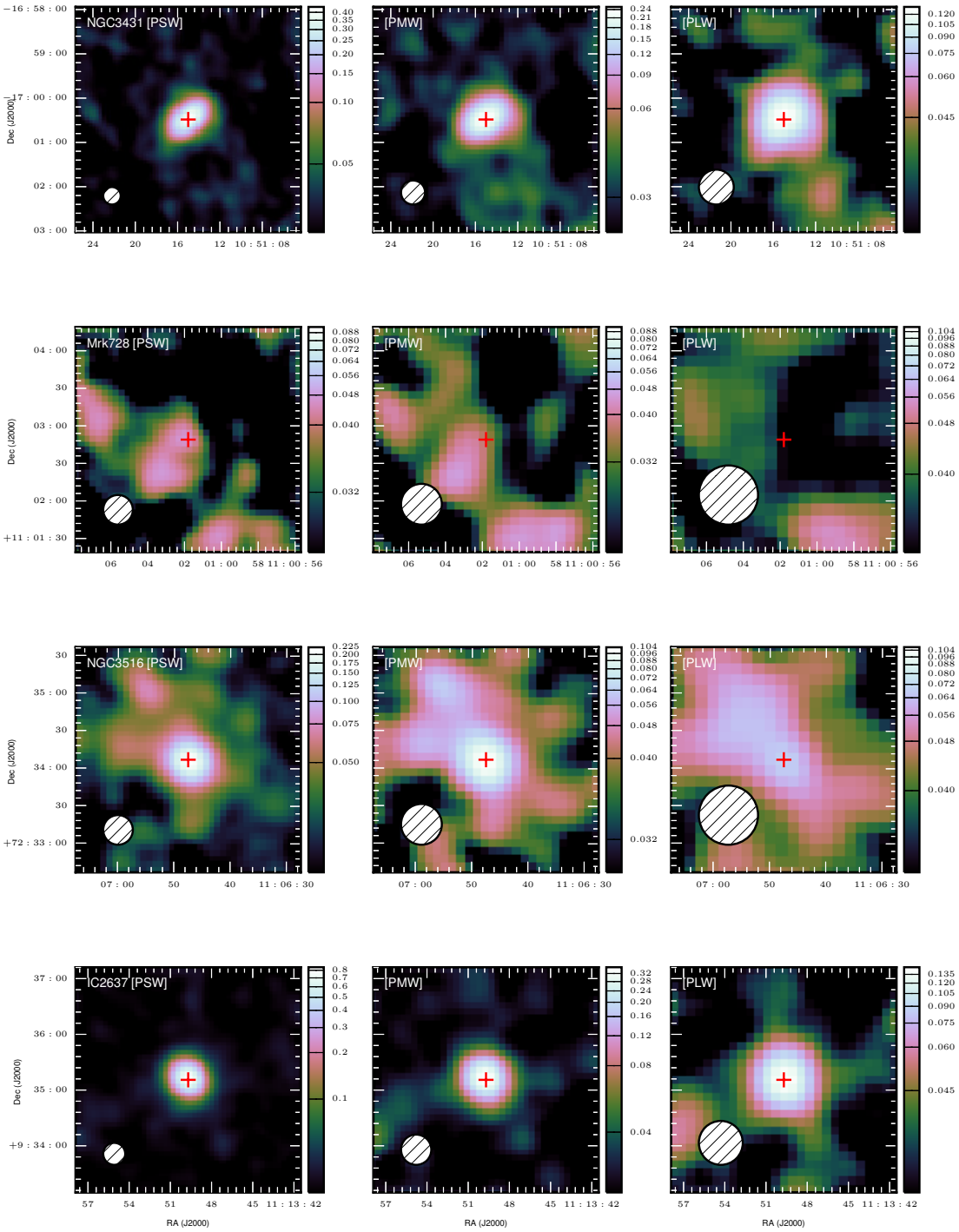
NGC3431 [PSW]
[PMW]
[PLW]
Mrk728 [PSW]
[PMW]
[PLW]
NGC3516 [PSW]
[PMW]
[PLW]
IC2637 [PSW]
[PMW]
[PLW]
Dec (J2000)
RA (J2000)

Figure B.38

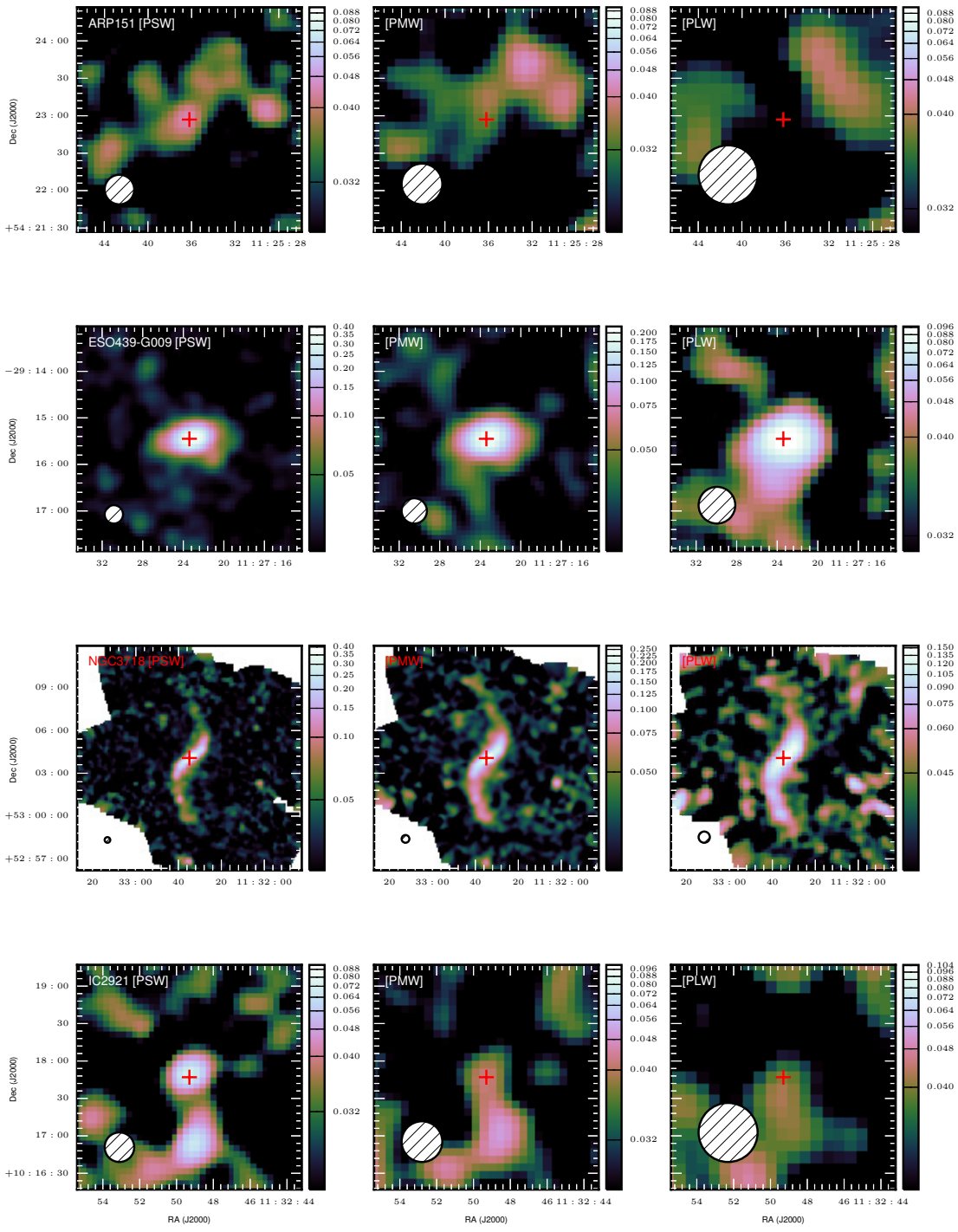
ARP151 [PSW]
[PMW]
[PLW]
ESO439-G009 [PSW]
[PMW]
[PLW]
NGC3718 [PSW]
[PMW]
[PLW]
IC2921 [PSW]
[PMW]
[PLW]
Dec (J2000)
RA (J2000)

Figure B.39

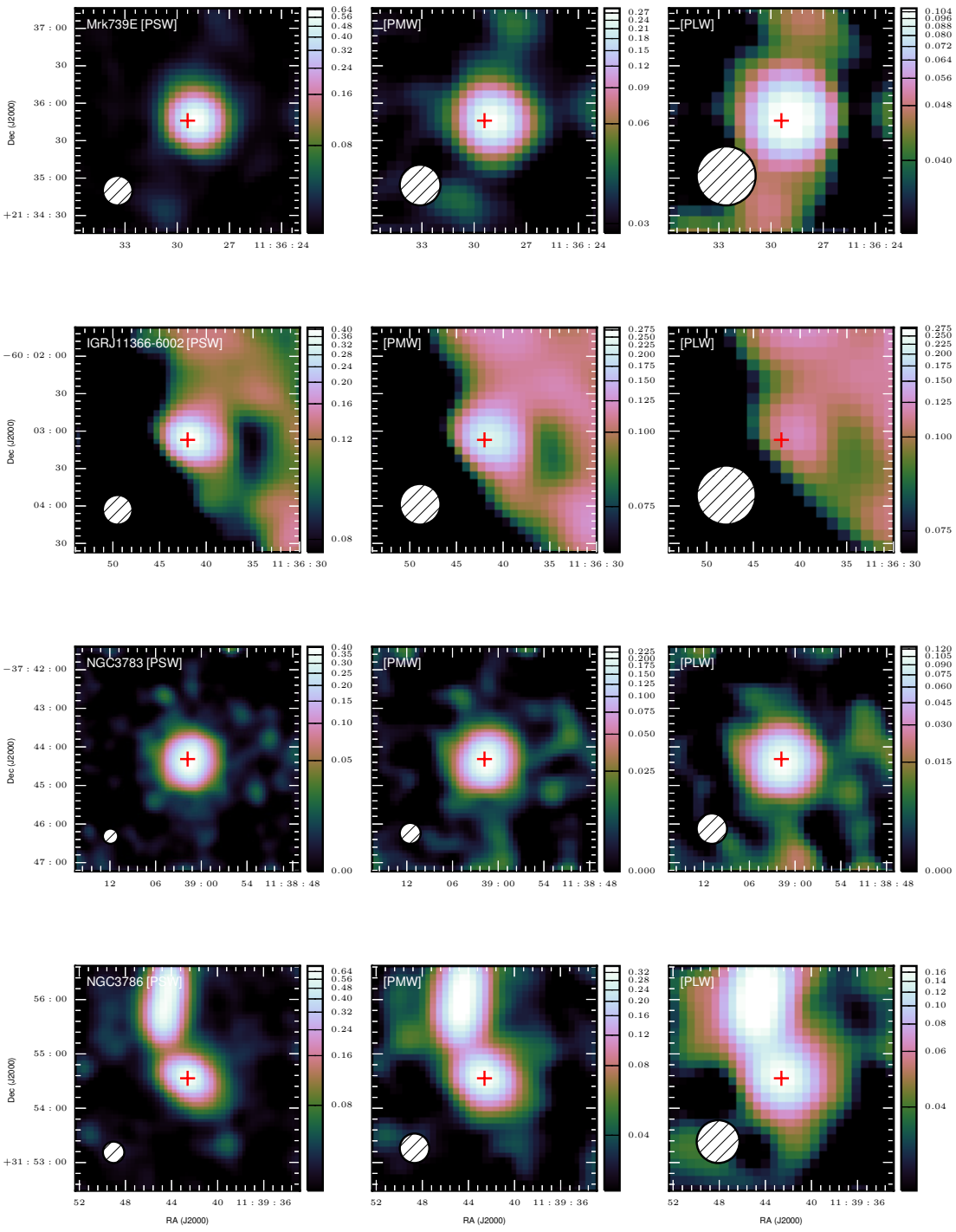
Mrk739E [PSW]
[PMW]
[PLW]
IGRJ11366-6002 [PSW]
[PMW]
[PLW]
NGC3783 [PSW]
[PMW]
[PLW]
NGC3786 [PSW]
[PMW]
[PLW]
Dec (J2000)
RA (J2000)

Figure B.40

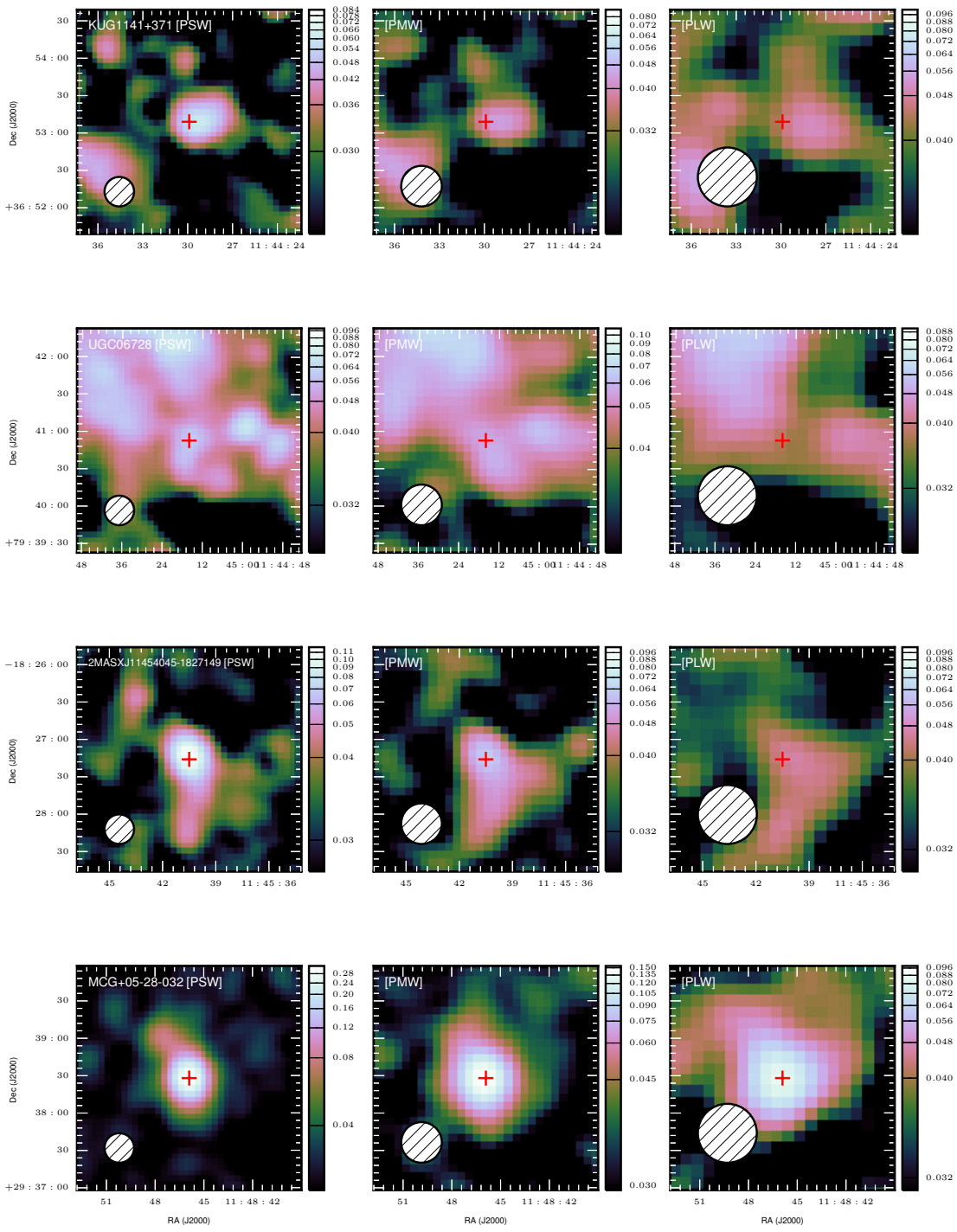
KUG1141+371 [PSW]
[PMW]
[PLW]
UGC06728 [PSW]
[PMW]
[PLW]
2MASXJ11454045-1827149 [PSW]
[PMW]
[PLW]
MCG+05-28-032 [PSW]
[PMW]
[PLW]
Dec (J2000)
RA (J2000)

Figure B.41

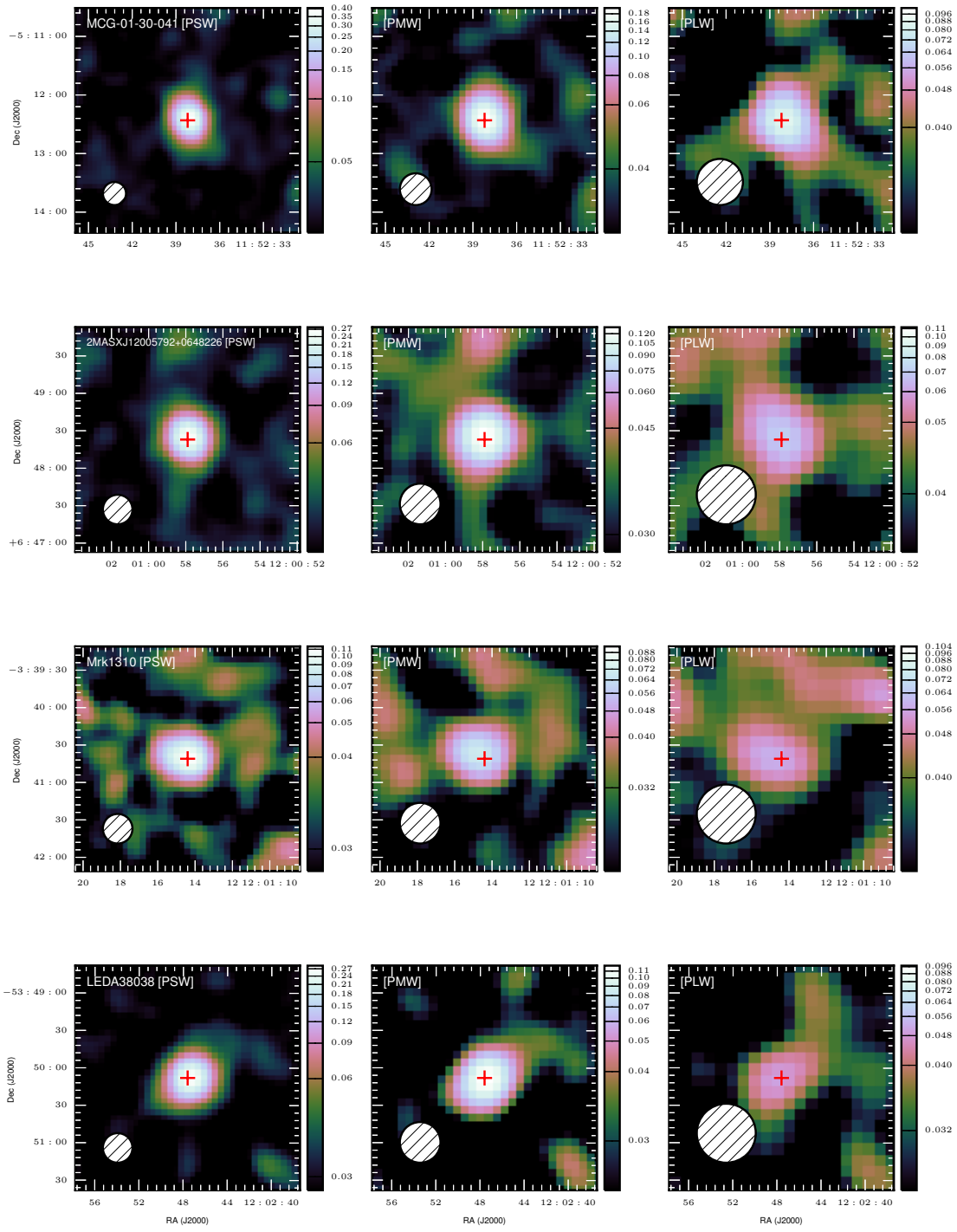
MCG-01-30-041 [PSW]
[PMW]
[PLW]
2MASXJ12005792+0648226 [PSW]
[PMW]
[PLW]
Mrk1310 [PSW]
[PMW]
[PLW]
LEDA38038 [PSW]
[PMW]
[PLW]
Dec (J2000)
RA (J2000)

Figure B.42

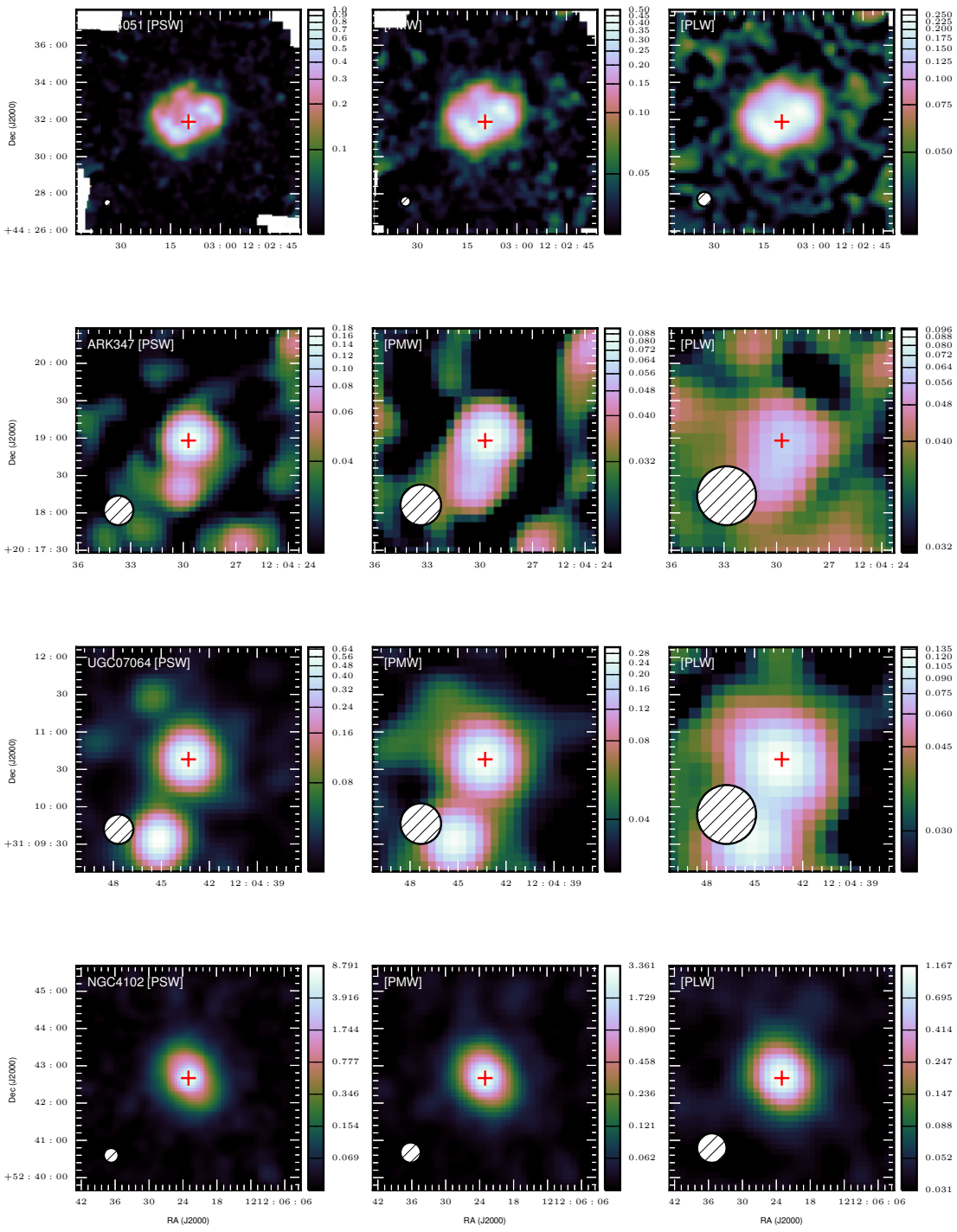
4051 [PSW]
[PMW]
[PLW]
ARK347 [PSW]
[PMW]
[PLW]
UGC07064 [PSW]
[PMW]
[PLW]
NGC4102 [PSW]
[PMW]
[PLW]
Dec (J2000)
RA (J2000)

Figure B.43

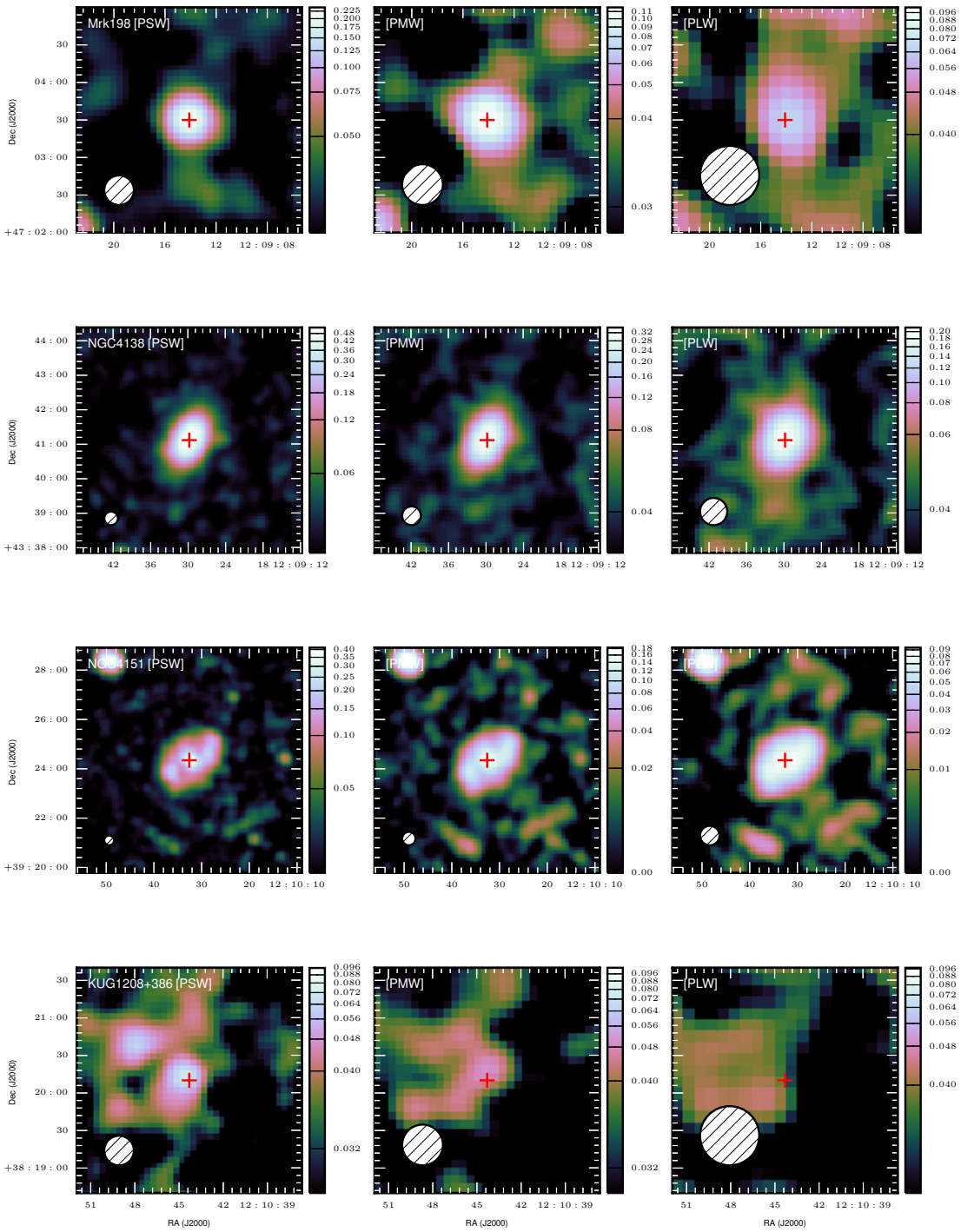
Mrk198 [PSW]
[PMW]
[PLW]
NGC4138 [PSW]
[PMW]
[PLW]
NGC4151 [PSW]
[PMW]
[PLW]
KUG1208+386 [PSW]
[PMW]
[PLW]
Dec (J2000)
RA (J2000)

Figure B.44

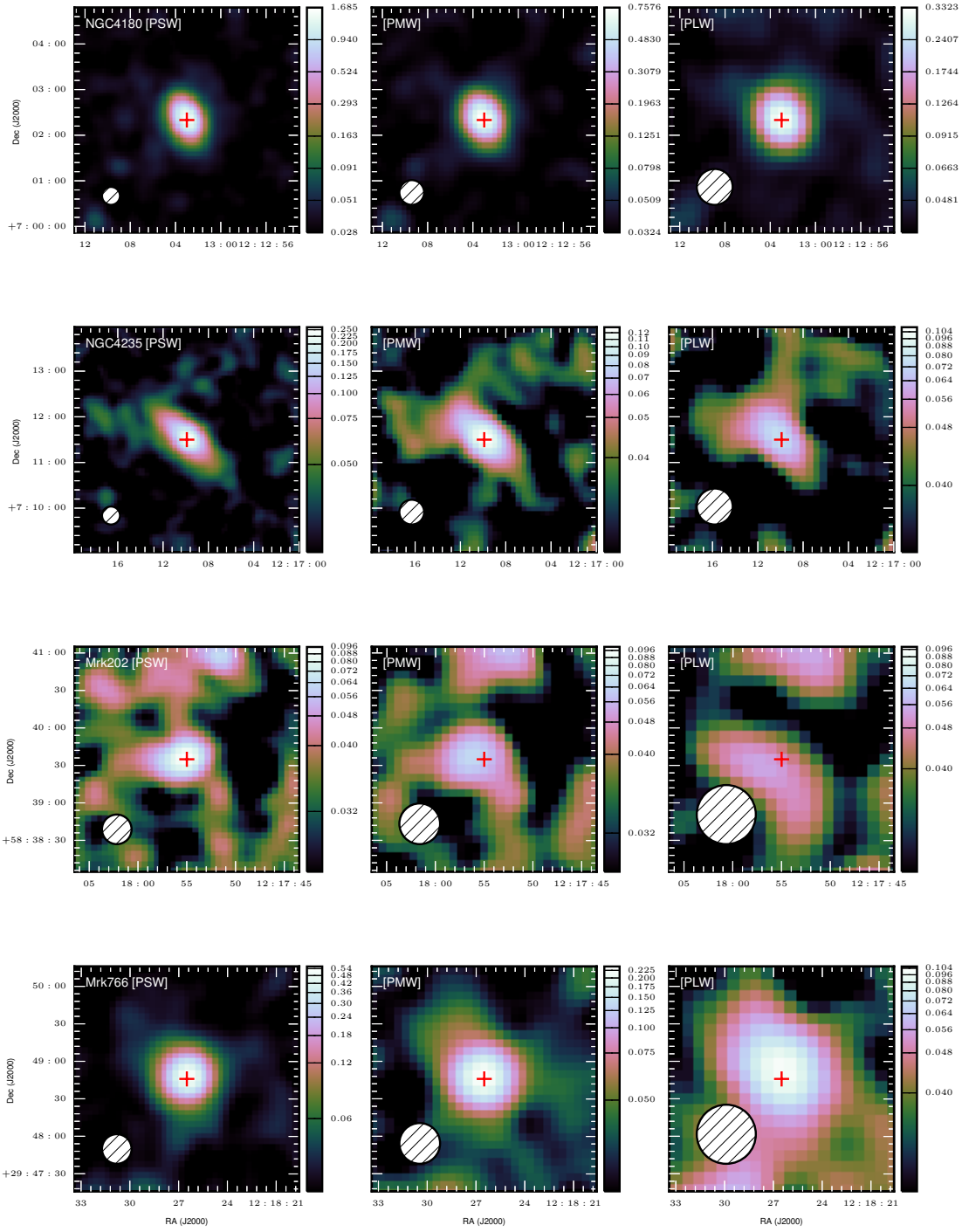
NGC4180 [PSW]
[PMW]
[PLW]
NGC4235 [PSW]
[PMW]
[PLW]
Mrk202 [PSW]
[PMW]
[PLW]
Mrk766 [PSW]
[PMW]
[PLW]
Dec (J2000)
RA (J2000)

Figure B.45

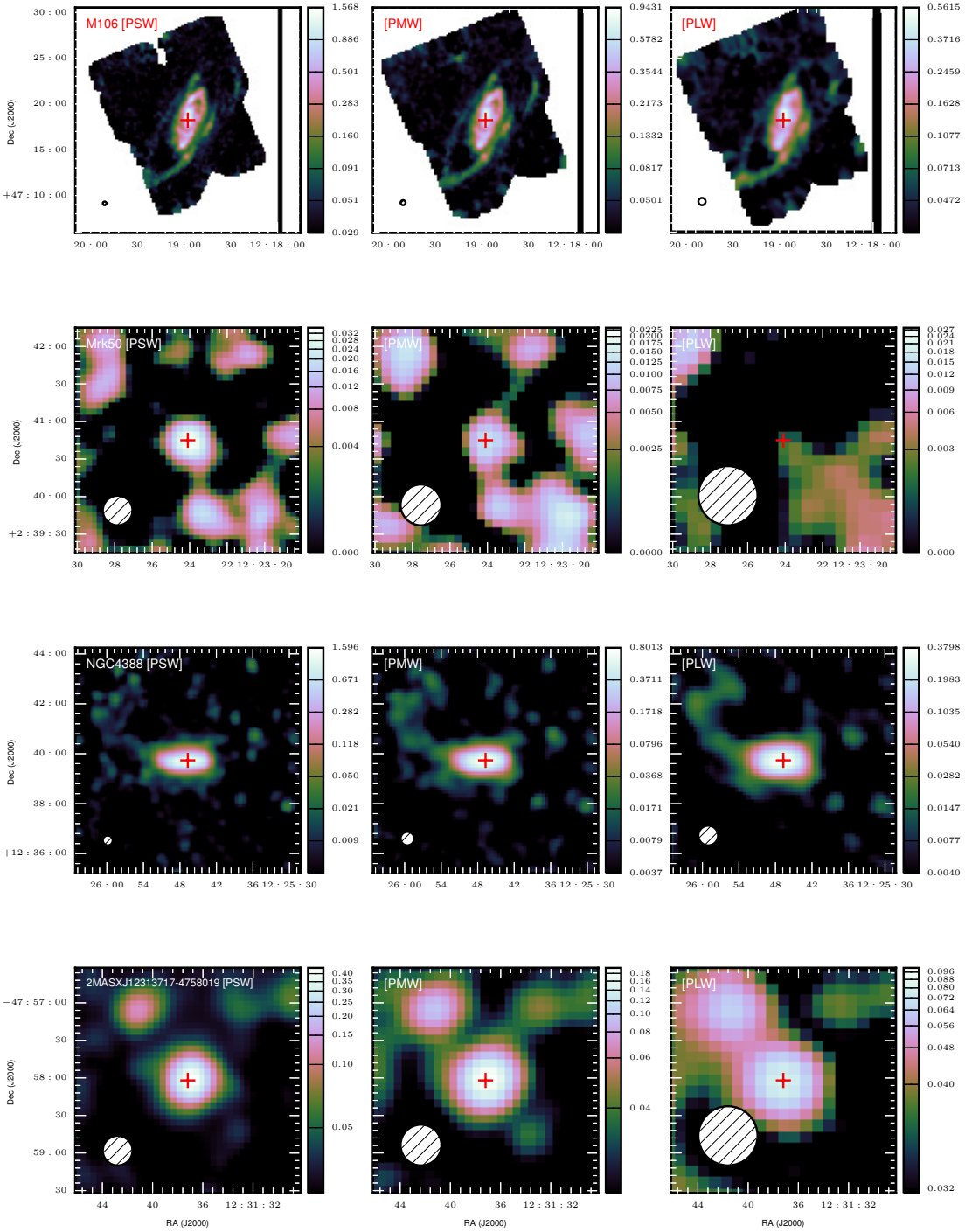
M106 [PSW]
[PMW]
[PLW]
Mrk50 [PSW]
[PMW]
[PLW]
NGC4388 [PSW]
[PMW]
[PLW]
2MASXJ12313717-4758019 [PSW]
[PMW]
[PLW]
Dec (J2000)
RA (J2000)

Figure B.46

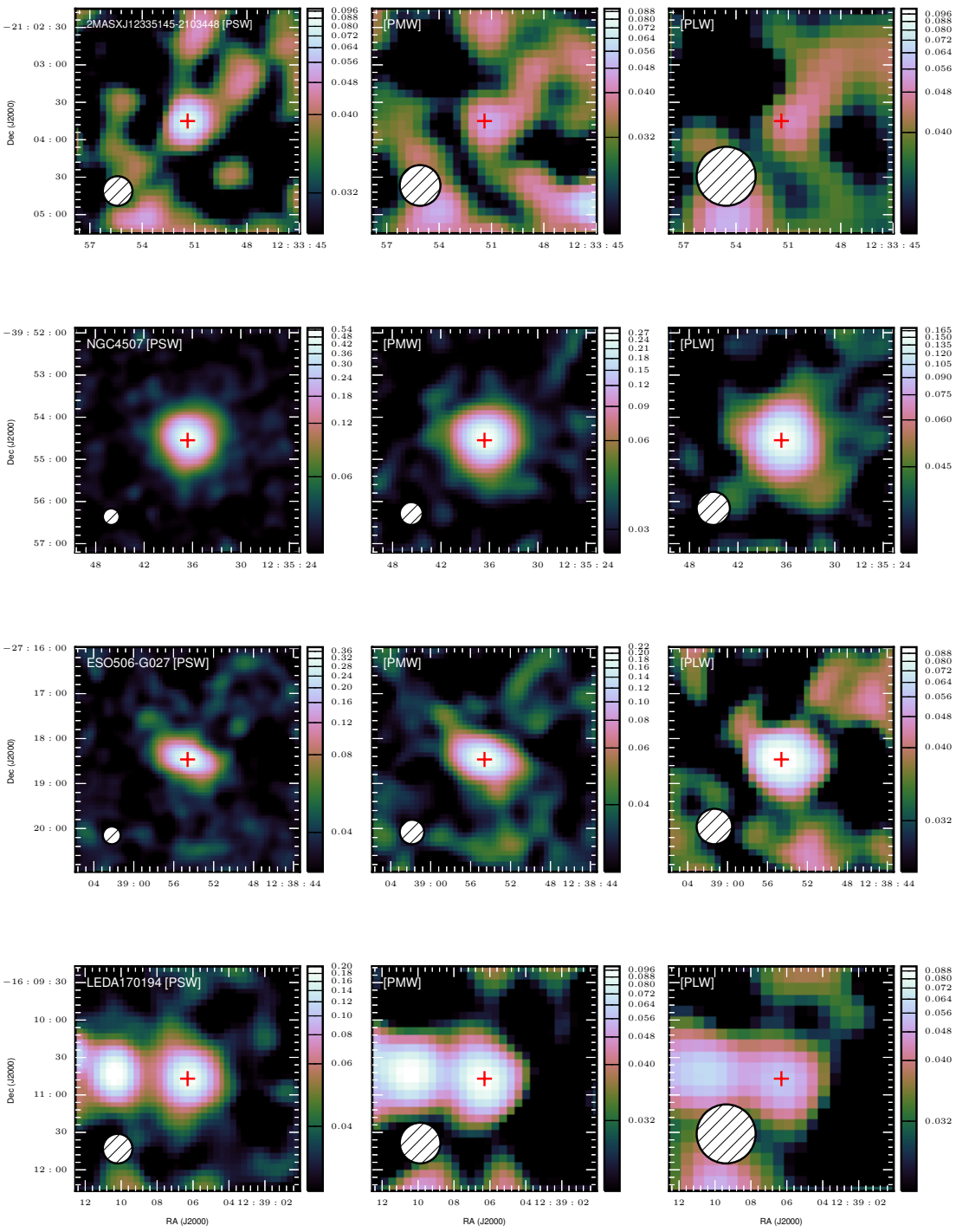
2MASXJ12335145-2103448 [PSW]
[PMW]
[PLW]
NGC4507 [PSW]
[PMW]
[PLW]
ESO506-G027 [PSW]
[PMW]
[PLW]
LEDA170194 [PSW]
[PMW]
[PLW]
Dec (J2000)
RA (J2000)

Figure B.47

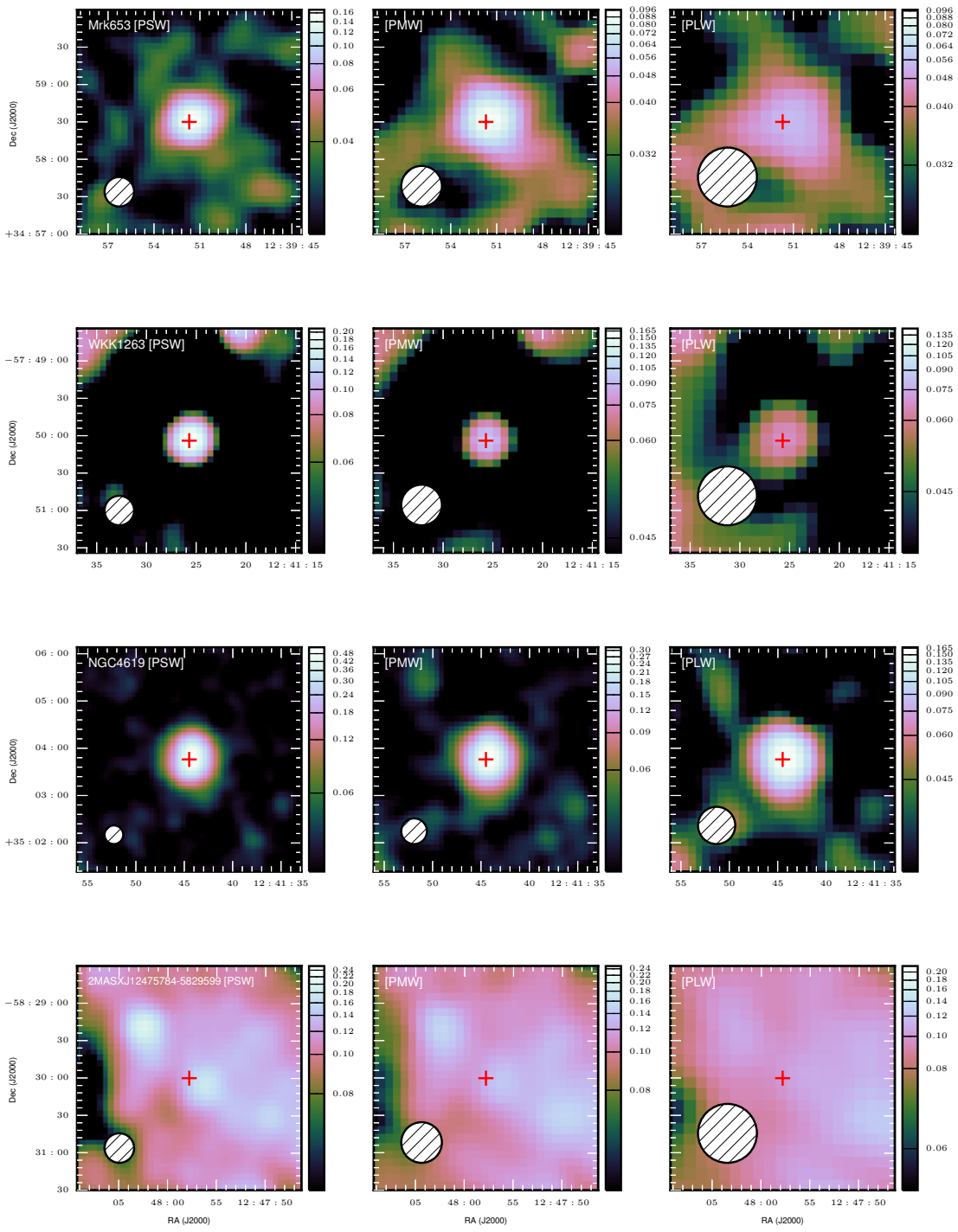
Mrk653 [PSW]
[PMW]
[PLW]
WKK1263 [PSW]
[PMW]
[PLW]
NGC4619 [PSW]
[PMW]
[PLW]
2MASXJ12475784-5829599 [PSW]
[PMW]
[PLW]
Dec (J2000)
RA (J2000)

Figure B.48

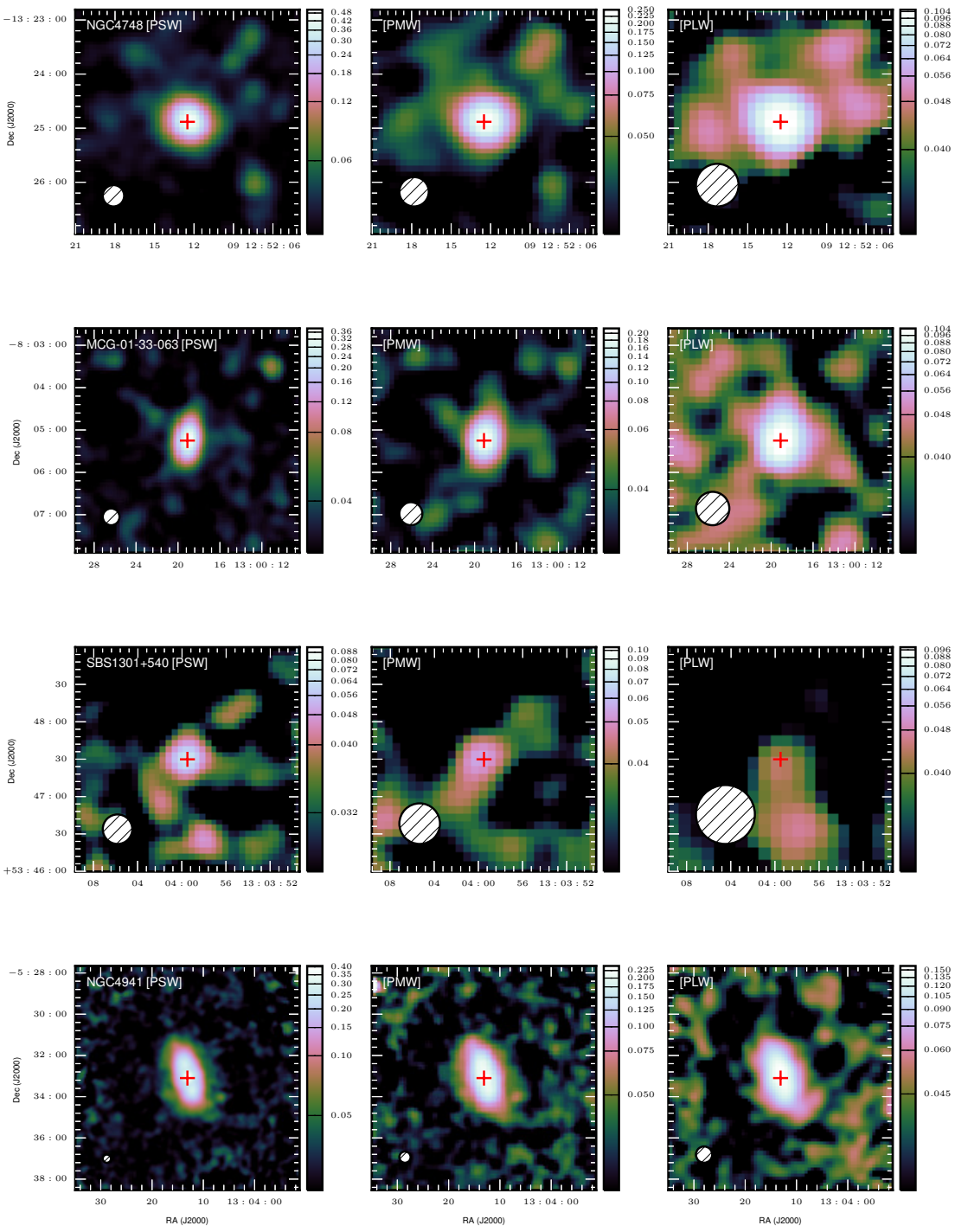
NGC4748 [PSW]
[PMW]
[PLW]
MCG-01-33-063 [PSW]
[PMW]
[PLW]
SBS1301+540 [PSW]
[PMW]
[PLW]
NGC4941 [PSW]
[PMW]
[PLW]
Dec (J2000)
RA (J2000)

Figure B.49

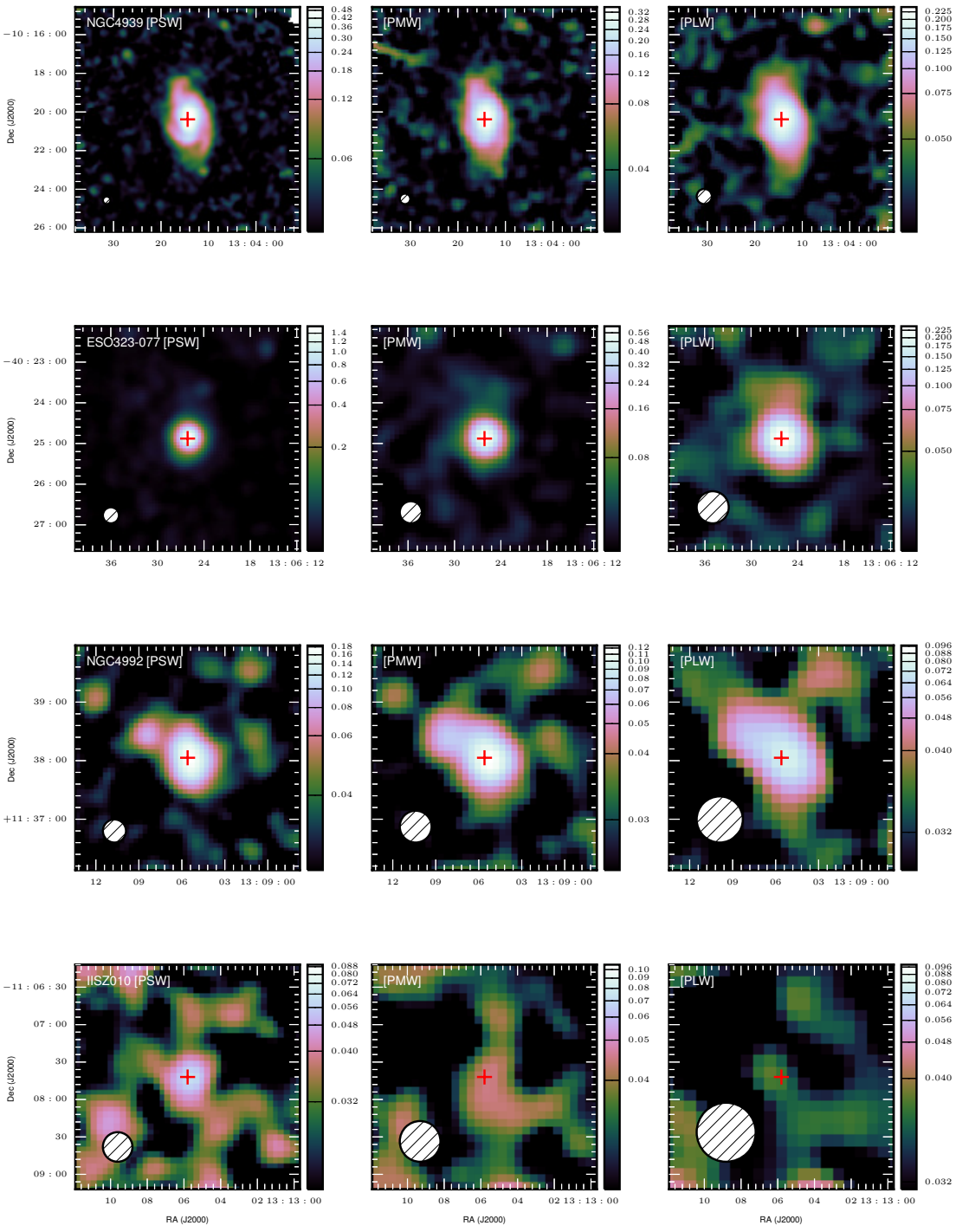
NGC4939 [PSW]
[PMW]
[PLW]
ESO323-077 [PSW]
[PMW]
[PLW]
NGC4992 [PSW]
[PMW]
[PLW]
IISZ010 [PSW]
[PMW]
[PLW]
Dec (J2000)
RA (J2000)

Figure B.50

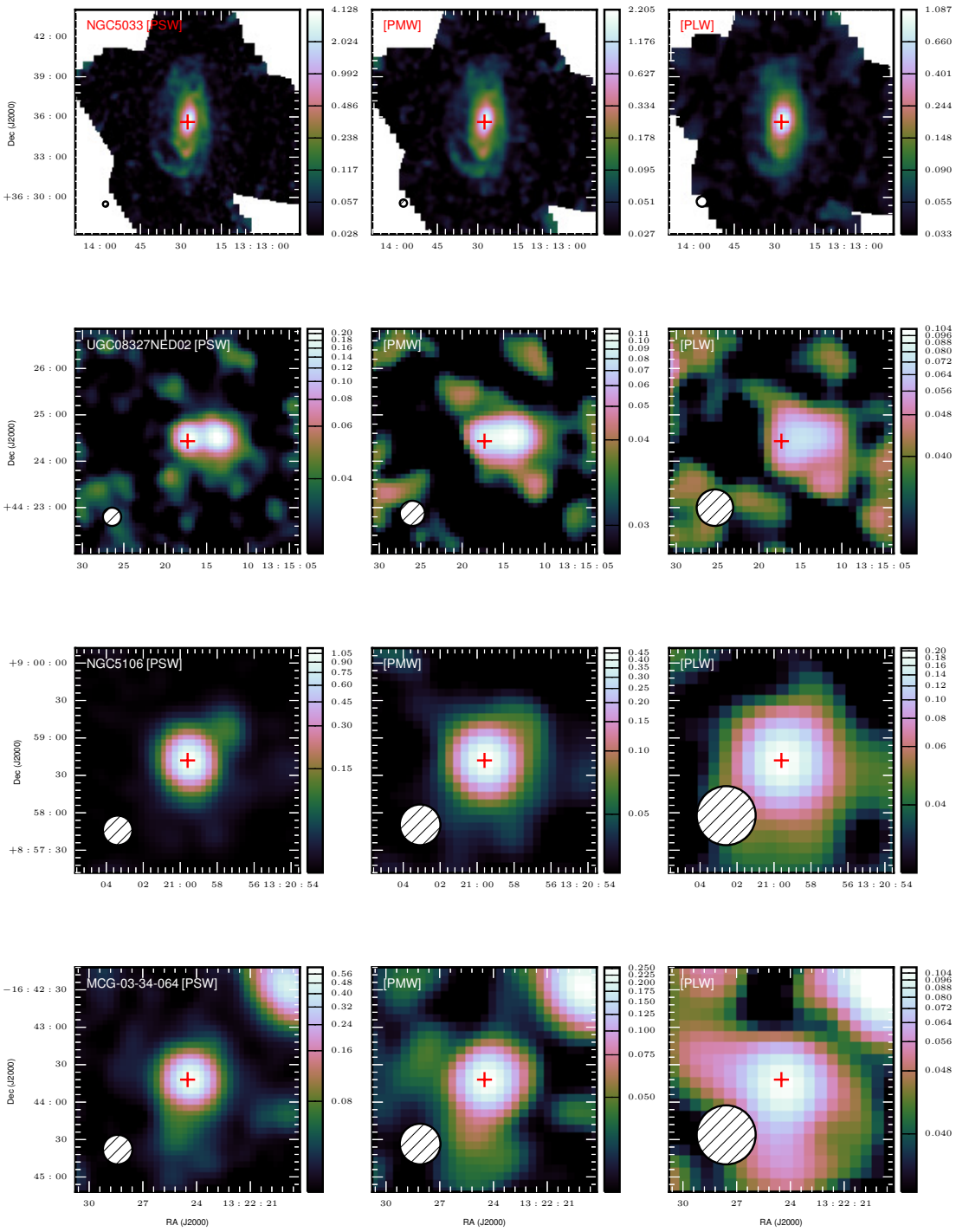
NGC5033 [PSW]
[PMW]
[PLW]
UGC08327NED02 [PSW]
[PMW]
[PLW]
NGC5106 [PSW]
[PMW]
[PLW]
MCG-03-34-064 [PSW]
[PMW]
[PLW]
Dec (J2000)
RA (J2000)

Figure B.51

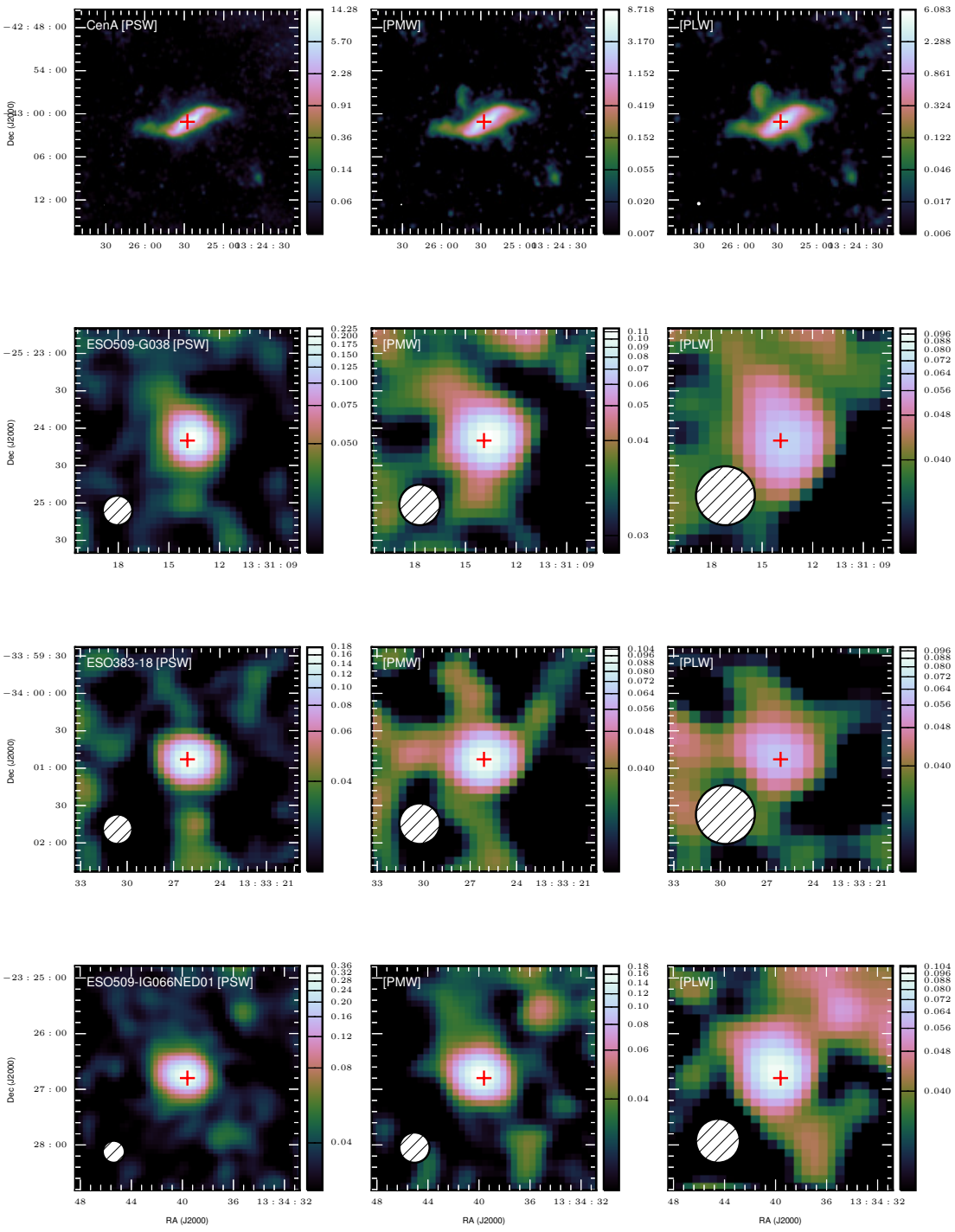
CenA [PSW]
[PMW]
[PLW]
ESO509-G038 [PSW]
[PMW]
[PLW]
ESO383-18 [PSW]
[PMW]
[PLW]
ESO509-IG066NED01 [PSW]
[PMW]
[PLW]
Dec (J2000)
RA (J2000)

Figure B.52

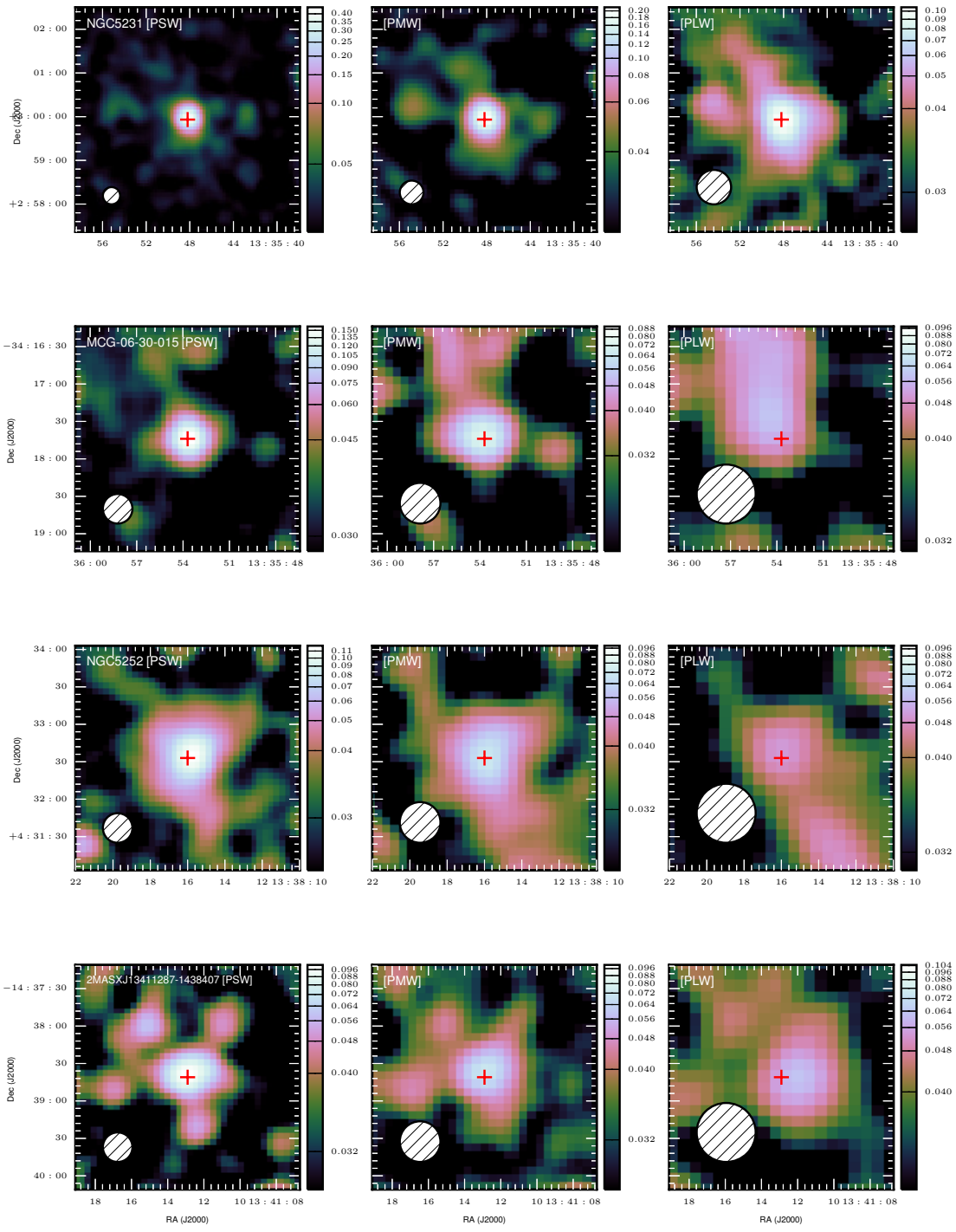
NGC5231 [PSW]
[PMW]
[PLW]
MCG-06-30-015 [PSW]
[PMW]
[PLW]
NGC5252 [PSW]
[PMW]
[PLW]
2MASXJ13411287-1438407 [PSW]
[PMW]
[PLW]
Dec (J2000)
RA (J2000)

Figure B.53

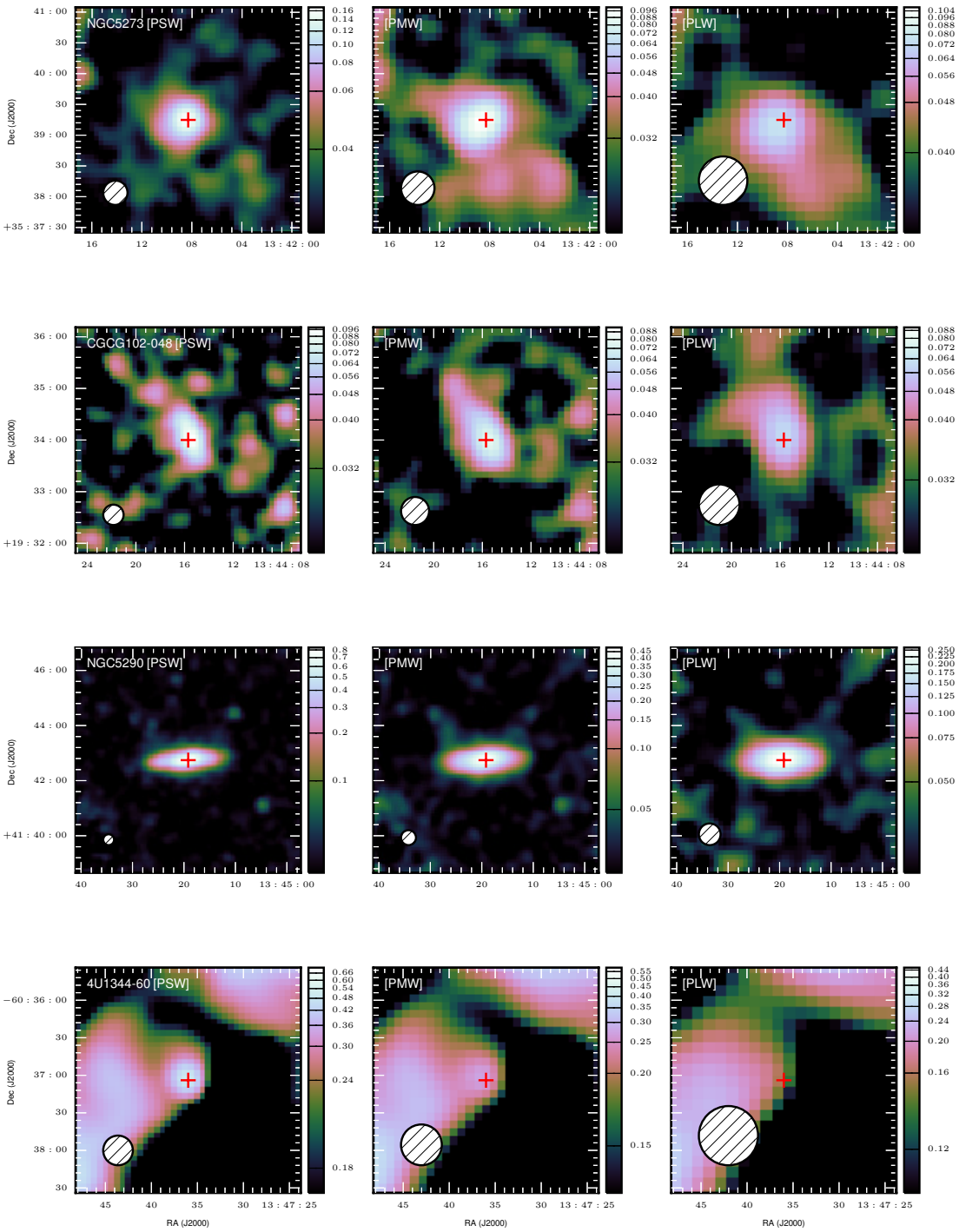
NGC5273 [PSW]
[PMW]
[PLW]
CGCG102-048 [PSW]
[PMW]
[PLW]
NGC5290 [PSW]
[PMW]
[PLW]
4U1344-60 [PSW]
[PMW]
[PLW]
Dec (J2000)
RA (J2000)

Figure B.54

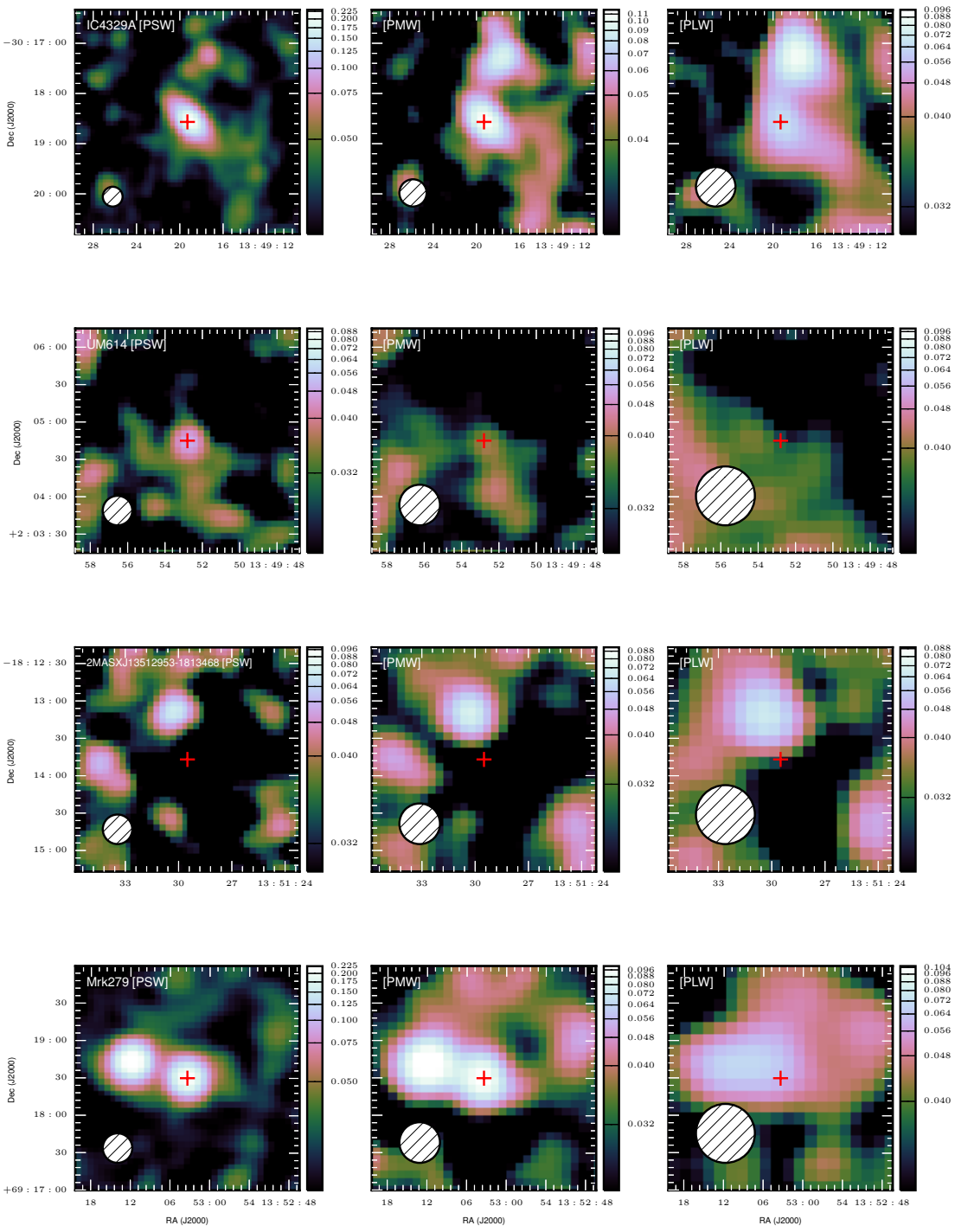
IC4329A [PSW]
[PMW]
[PLW]
UM614 [PSW]
[PMW]
[PLW]
2MASXJ13512953-1813468 [PSW]
[PMW]
[PLW]
Mrk279 [PSW]
[PMW]
[PLW]
Dec (J2000)
RA (J2000)

Figure B.55

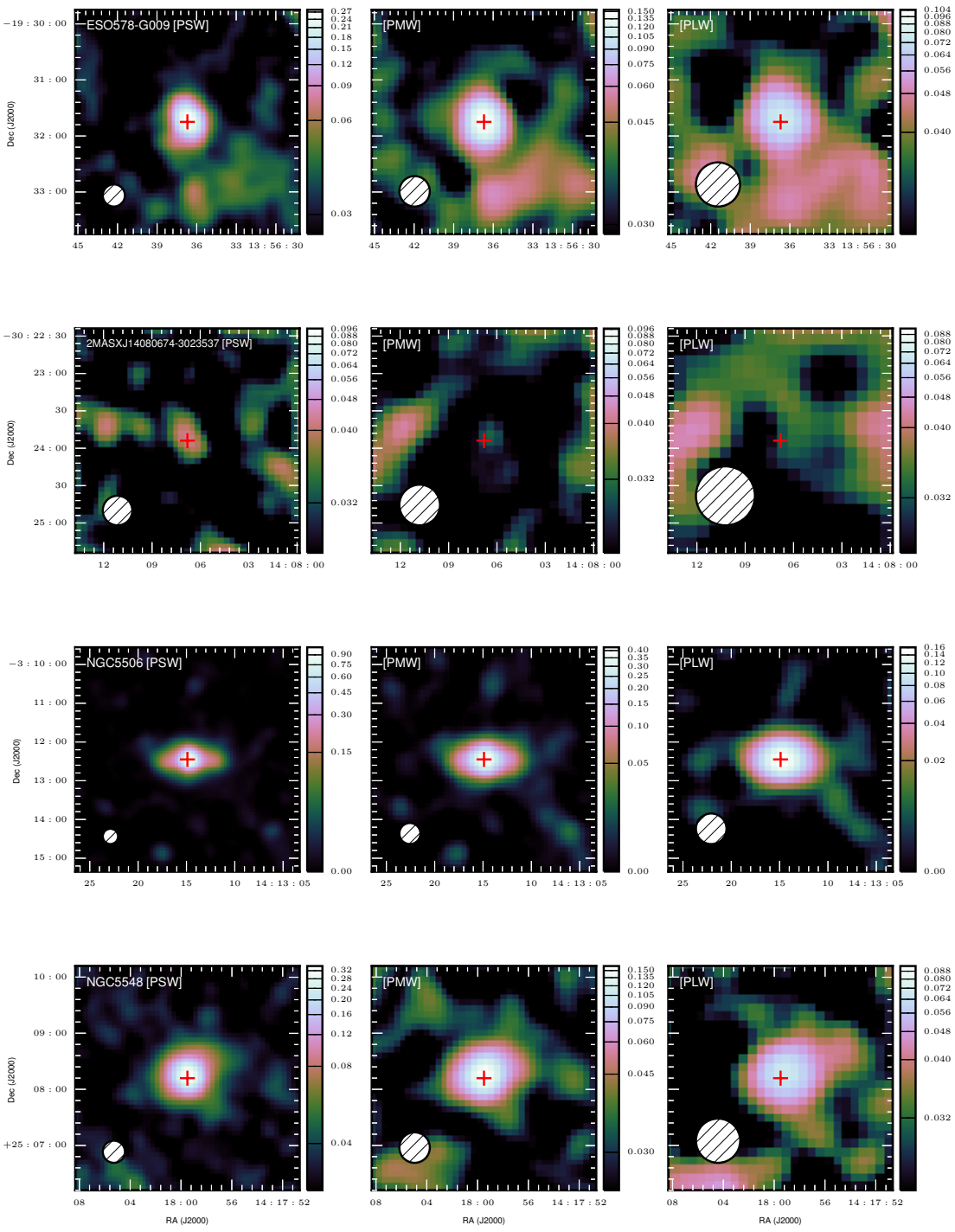
ESO578-G009 [PSW]
[PMW]
[PLW]
2MASXJ14080674-3023537 [PSW]
[PMW]
[PLW]
NGC5506 [PSW]
[PMW]
[PLW]
NGC5548 [PSW]
[PMW]
[PLW]
Dec (J2000)
RA (J2000)

Figure B.56

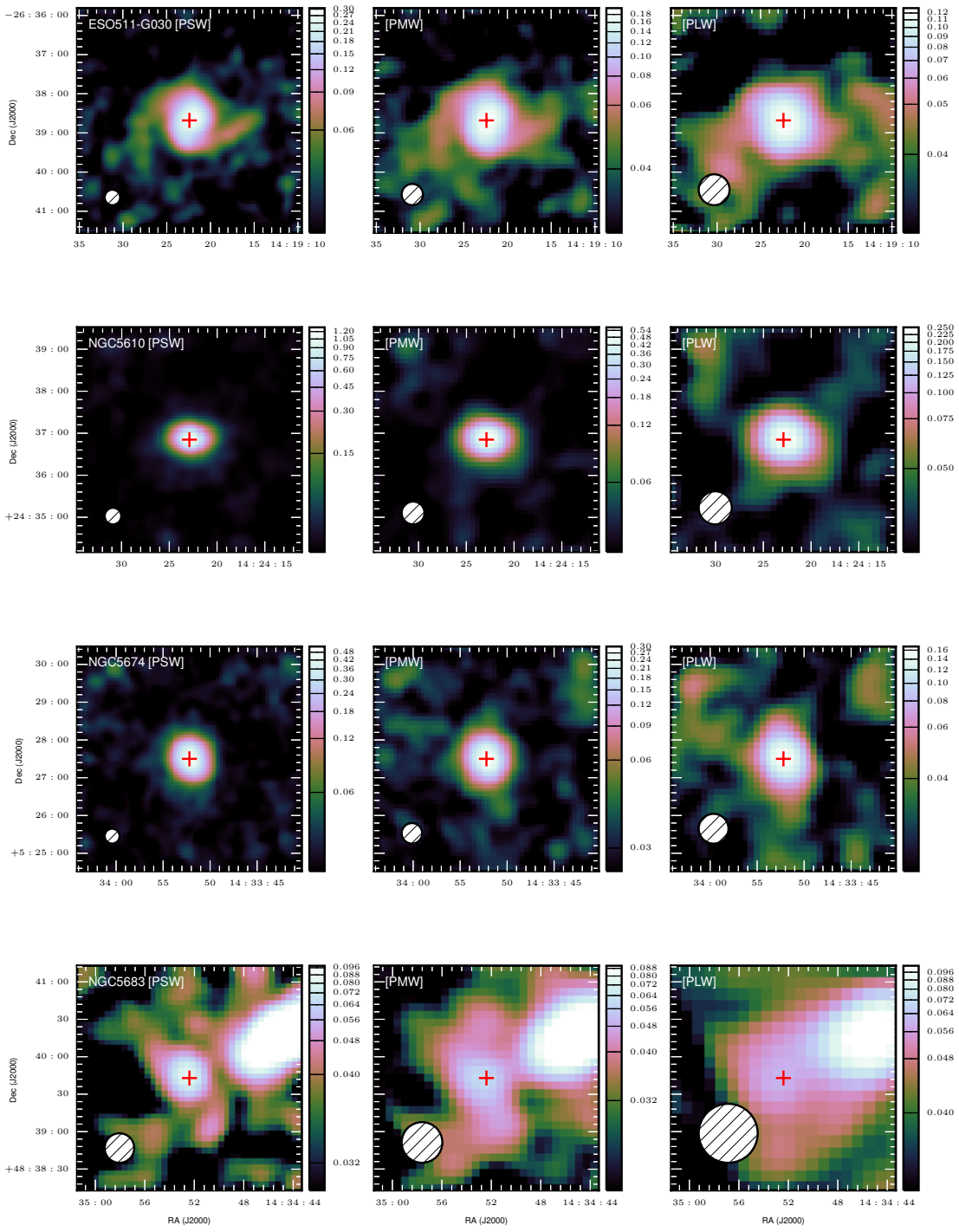
ESO511-G030 [PSW]
[PMW]
[PLW]
NGC5610 [PSW]
[PMW]
[PLW]
NGC5674 [PSW]
[PMW]
[PLW]
NGC5683 [PSW]
[PMW]
[PLW]
Dec (J2000)
RA (J2000)

Figure B.57

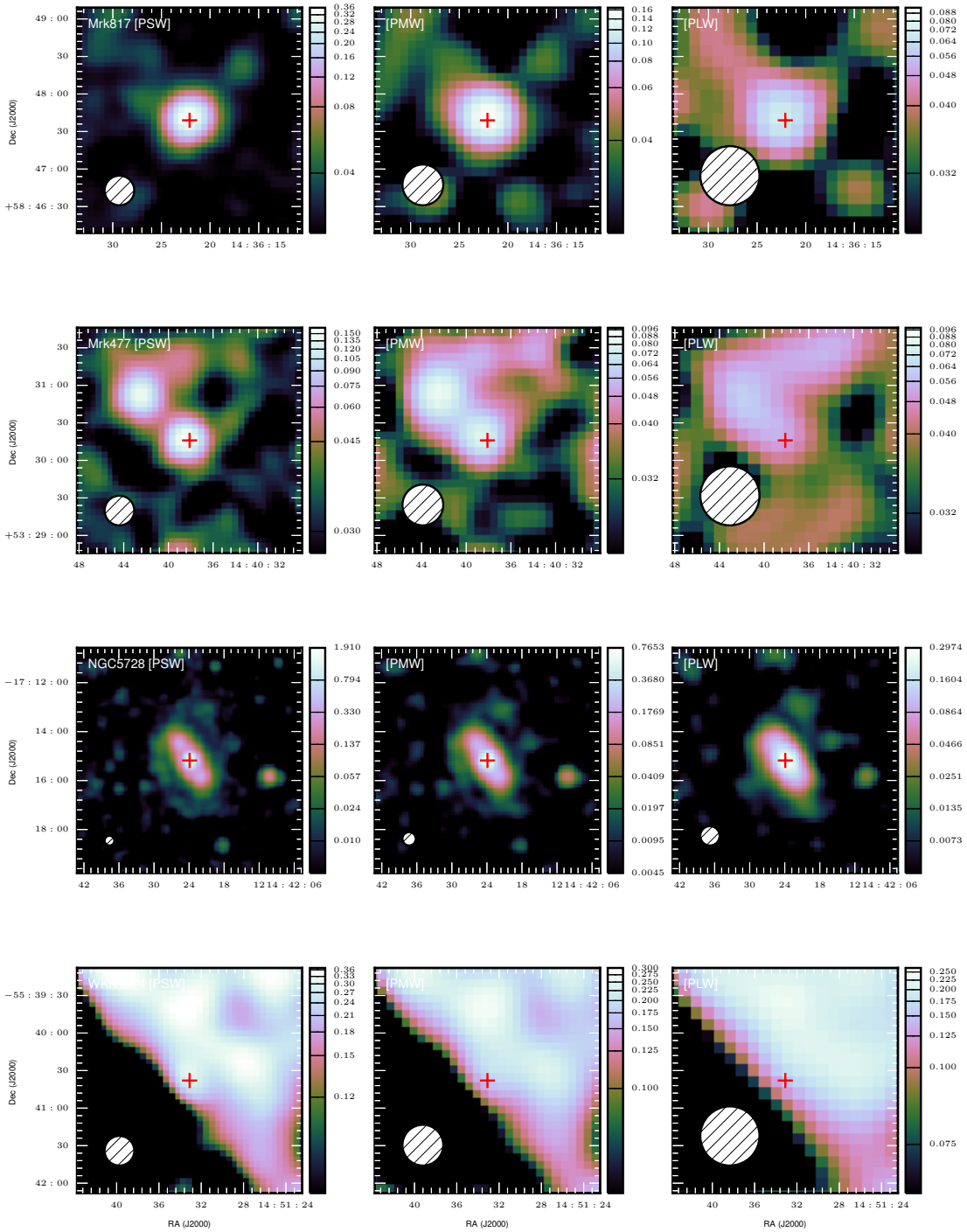
Mrk817 [PSW]
[PMW]
[PLW]
Mrk477 [PSW]
[PMW]
[PLW]
NGC5728 [PSW]
[PMW]
[PLW]
[PSW]
[PMW]
[PLW]
Dec (J2000)
RA (J2000)

Figure B.58

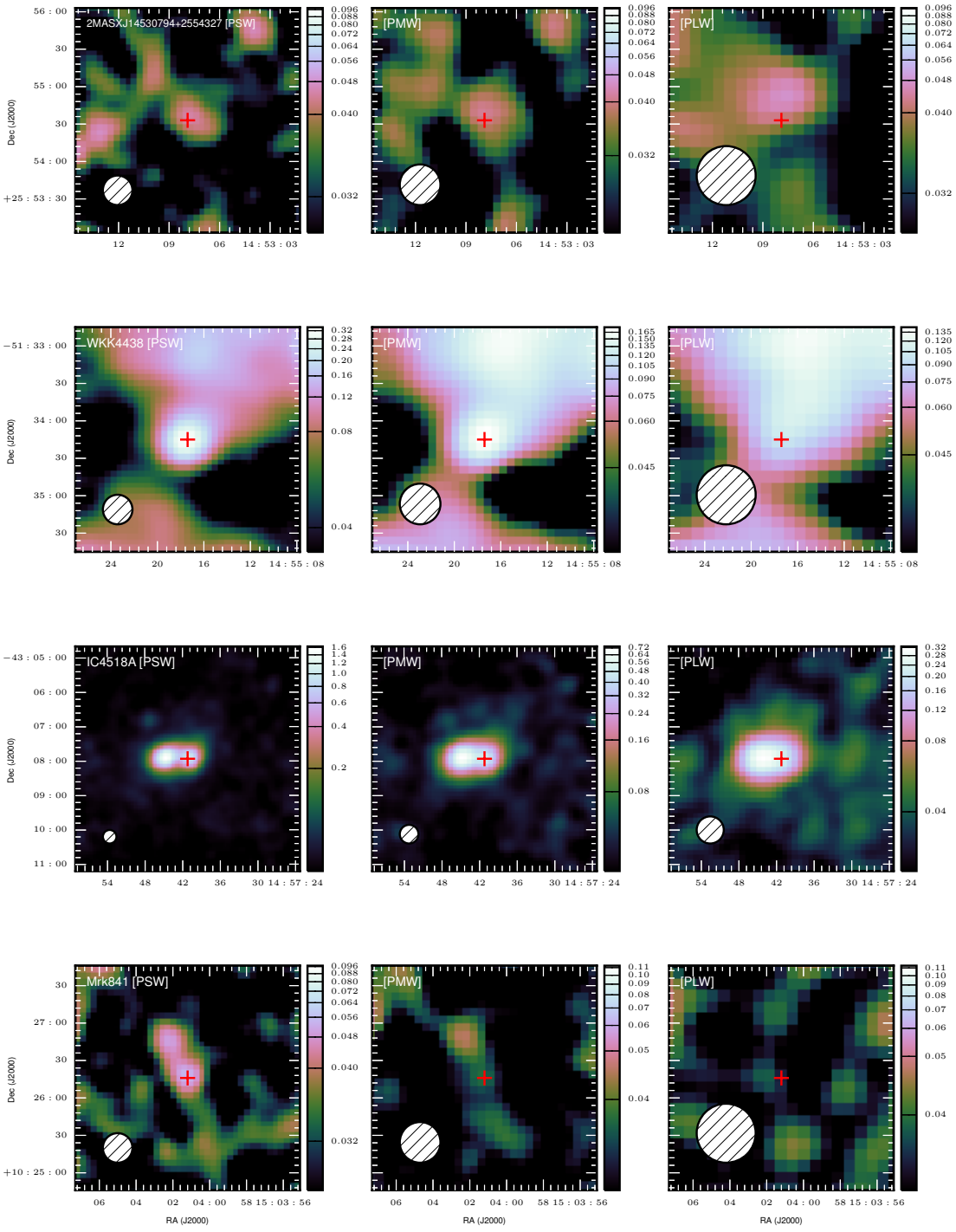
2MASXJ14530794+2554327 [PSW]
[PMW]
[PLW]
WKK4438 [PSW]
[PMW]
[PLW]
IC4518A [PSW]
[PMW]
[PLW]
Mrk841 [PSW]
[PMW]
[PLW]
Dec (J2000)
RA (J2000)

Figure B.59

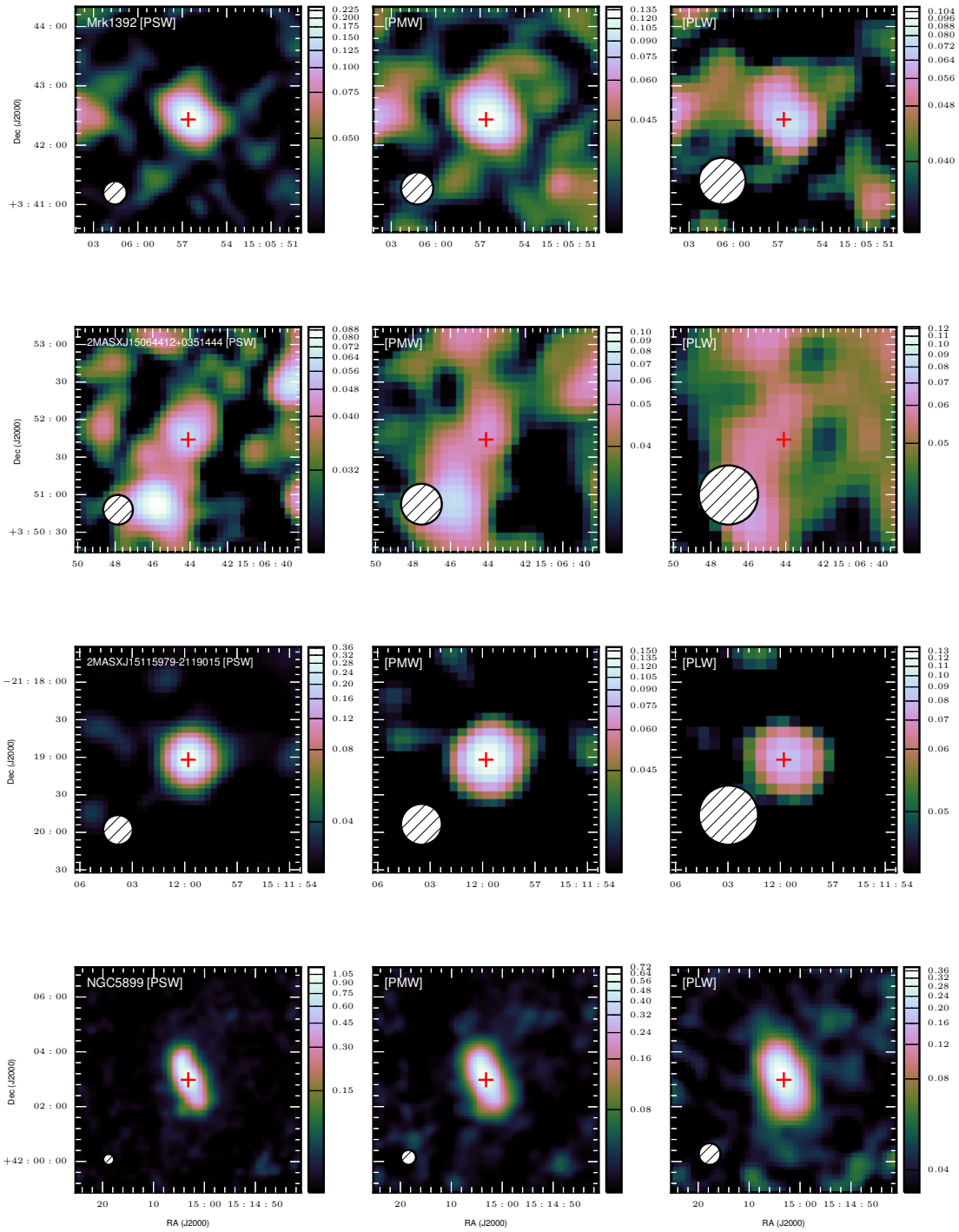
Mrk1392 [PSW]
[PMW]
[PLW]
2MASXJ15064412+0351444 [PSW]
[PMW]
[PLW]
2MASXJ15115979-2119015 [PSW]
[PMW]
[PLW]
NGC5899 [PSW]
[PMW]
[PLW]
Dec (J2000)
RA (J2000)

Figure B.60

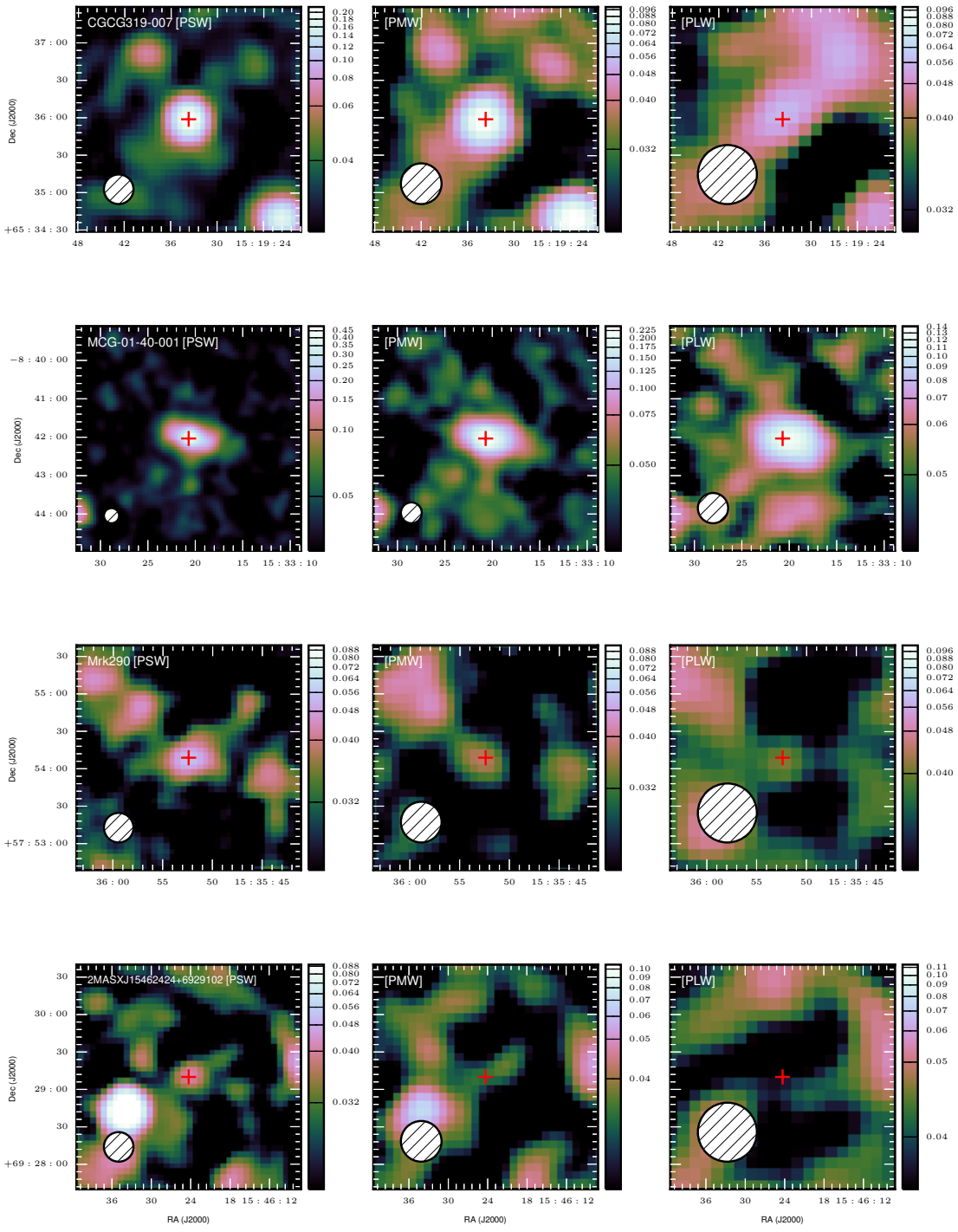
CGCG319-007 [PSW]
[PMW]
[PLW]
MCG-01-40-001 [PSW]
[PMW]
[PLW]
Mrk290 [PSW]
[PMW]
[PLW]
2MASXJ15462424+6929102 [PSW]
[PMW]
[PLW]
Dec (J2000)
RA (J2000)

Figure B.61

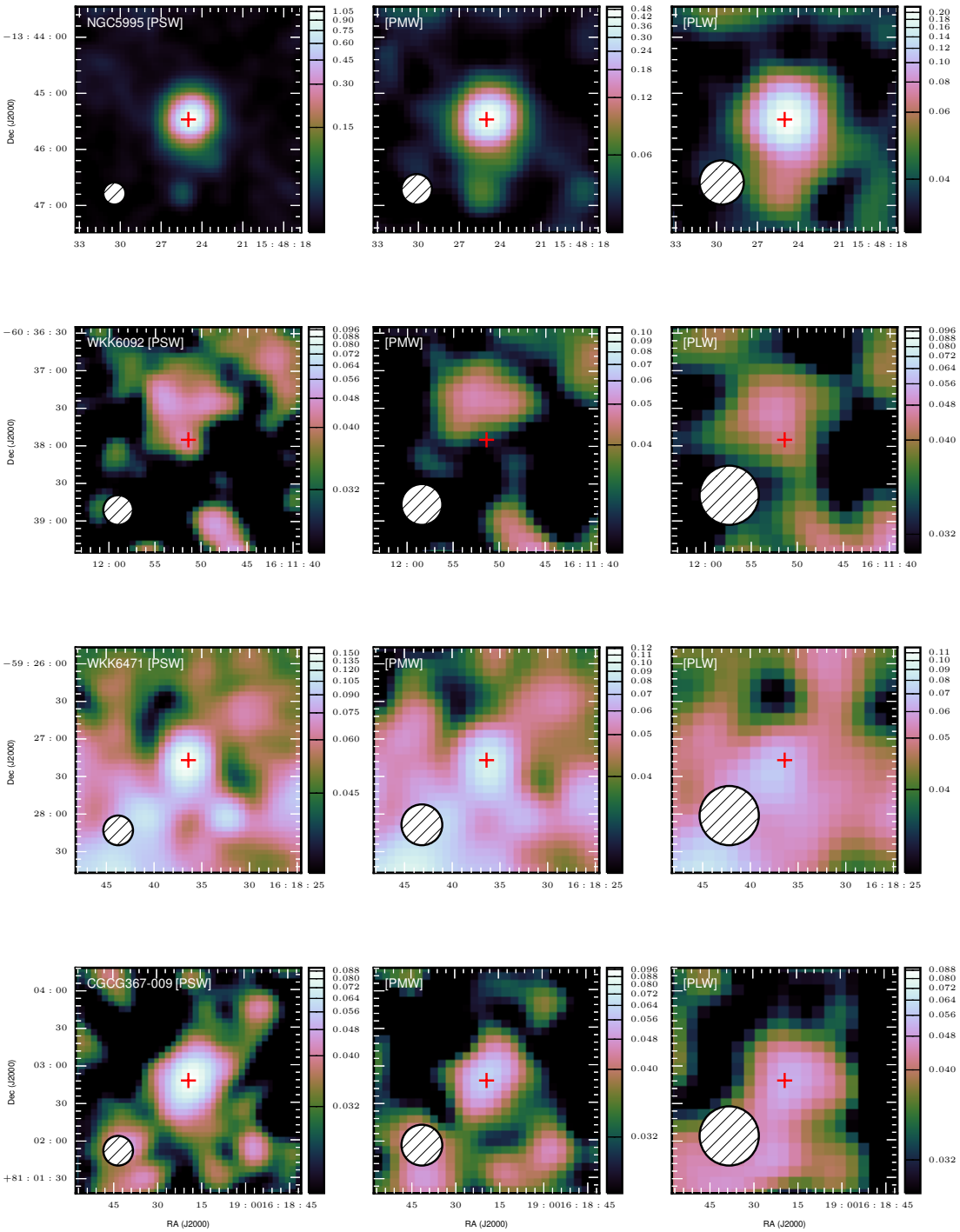
NGC5995 [PSW]
[PMW]
[PLW]
WKK6092 [PSW]
[PMW]
[PLW]
WKK6471 [PSW]
[PMW]
[PLW]
CGCG367-009 [PSW]
[PMW]
[PLW]
Dec (J2000)
RA (J2000)

Figure B.62

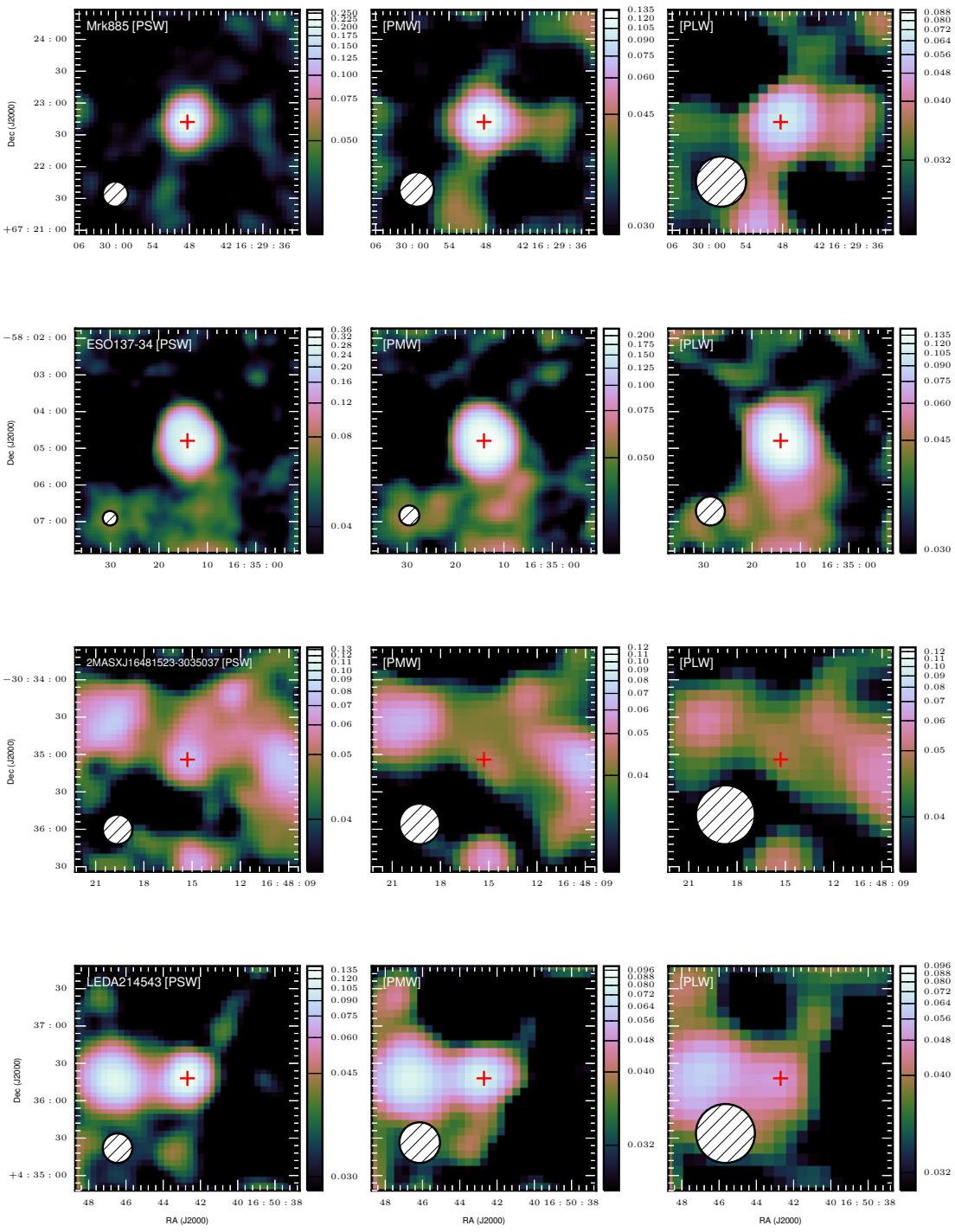
Mrk885 [PSW]
[PMW]
[PLW]
ESO137-34 [PSW]
[PMW]
[PLW]
2MASXJ16481523-3035037 [PSW]
[PMW]
[PLW]
LEDA214543 [PSW]
[PMW]
[PLW]
Dec (J2000)
RA (J2000)

Figure B.63

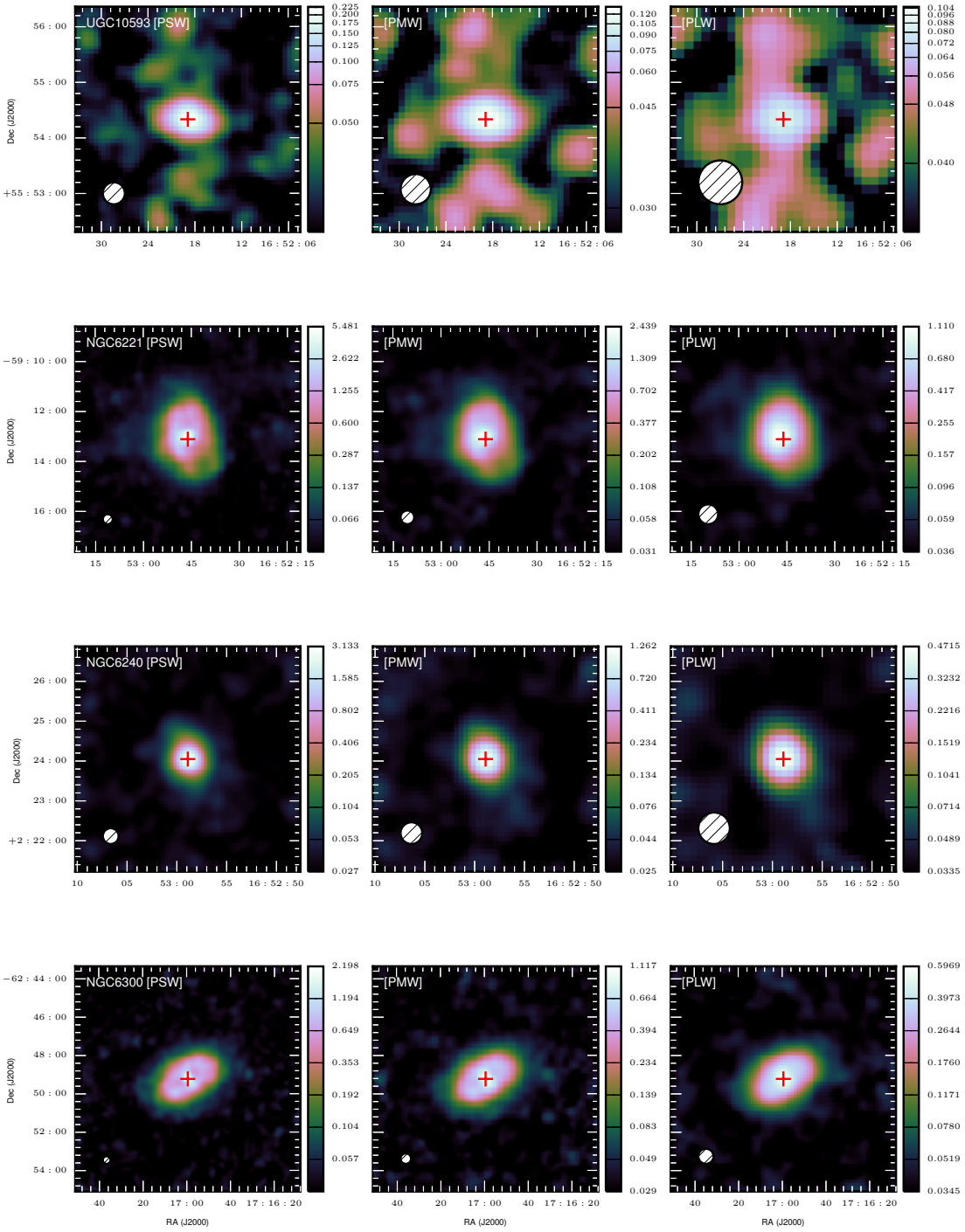
UGC10593 [PSW]
[PMW]
[PLW]
NGC6221 [PSW]
[PMW]
[PLW]
NGC6240 [PSW]
[PMW]
[PLW]
NGC6300 [PSW]
[PMW]
[PLW]
Dec (J2000)
RA (J2000)

Figure B.64

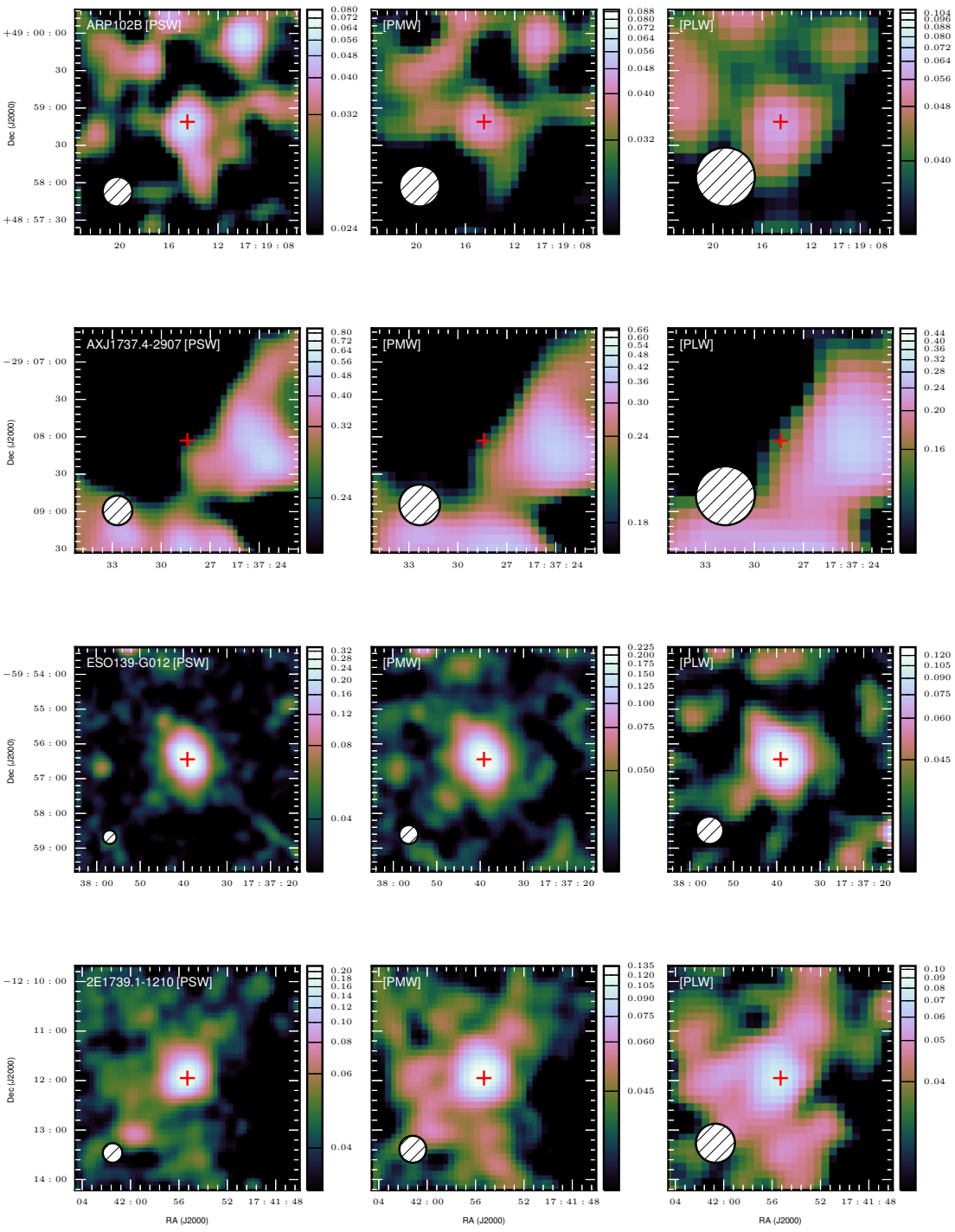
ARP102B [PSW]
[PMW]
[PLW]
AXJ1737.4-2907 [PSW]
[PMW]
[PLW]
ESO139-G012 [PSW]
[PMW]
[PLW]
2E1739.1-1210 [PSW]
[PMW]
[PLW]
Dec (J2000)
RA (J2000)

Figure B.65

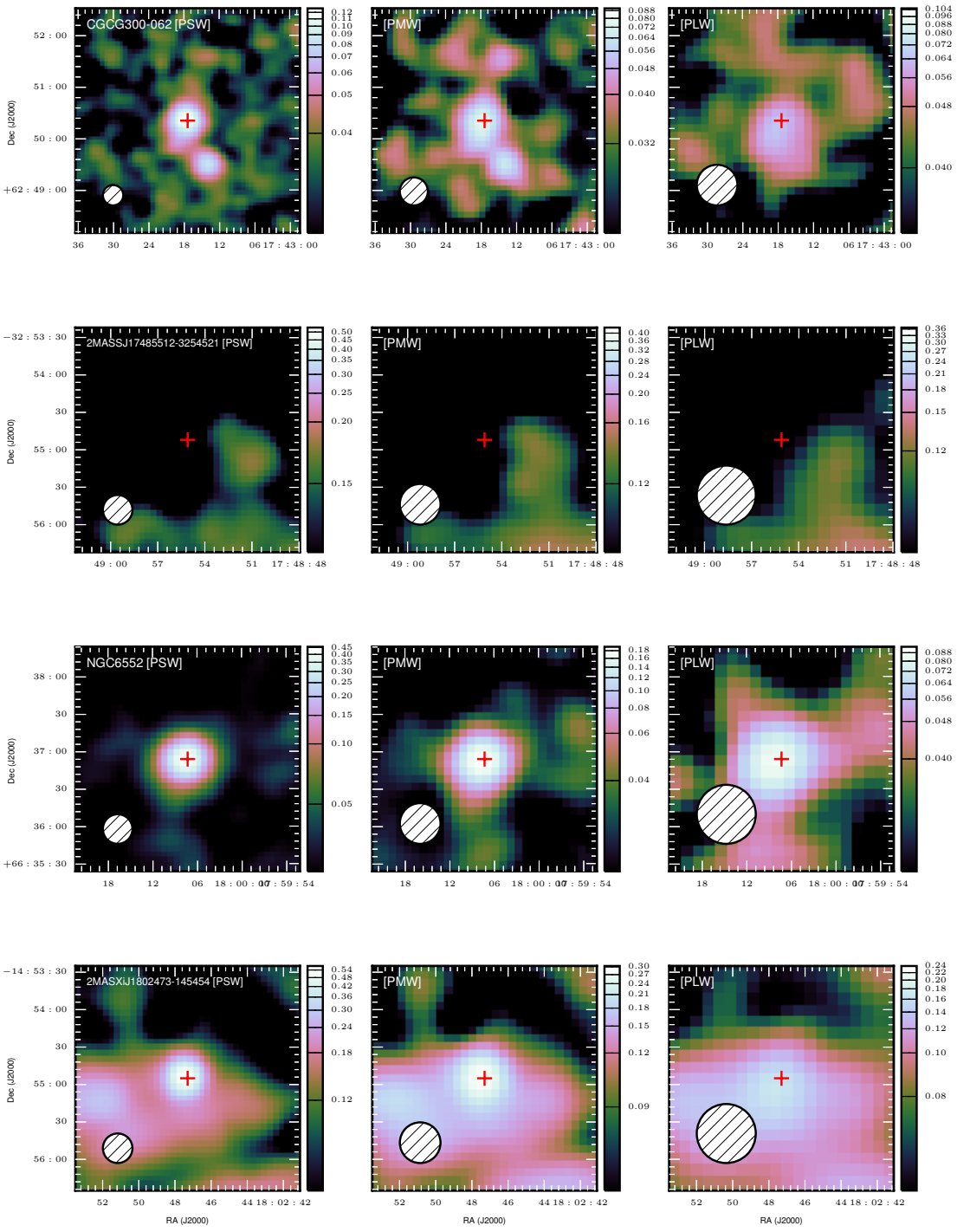
CGCG300-062 [PSW]
[PMW]
[PLW]
2MASSJ17485512-3254521 [PSW]
[PMW]
[PLW]
NGC6552 [PSW]
[PMW]
[PLW]
2MASXiJ1802473-145454 [PSW]
[PMW]
[PLW]
Dec (J2000)
RA (J2000)

Figure B.66

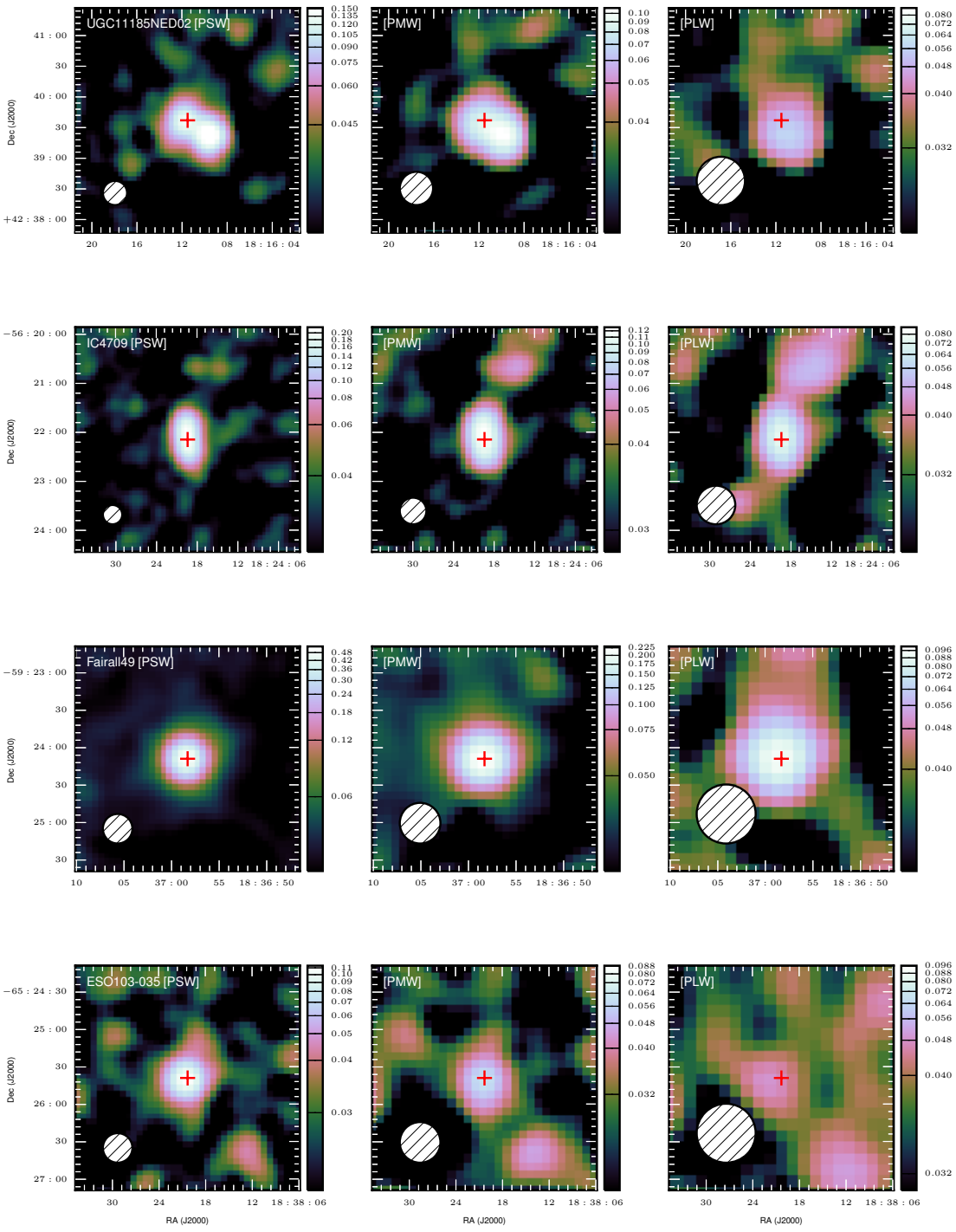
UGC11185NED02 [PSW]
[PMW]
[PLW]
IC4709 [PSW]
[PMW]
[PLW]
Fairall49 [PSW]
[PMW]
[PLW]
ESO103-035 [PSW]
[PMW]
[PLW]
Dec (J2000)
RA (J2000)

Figure B.67

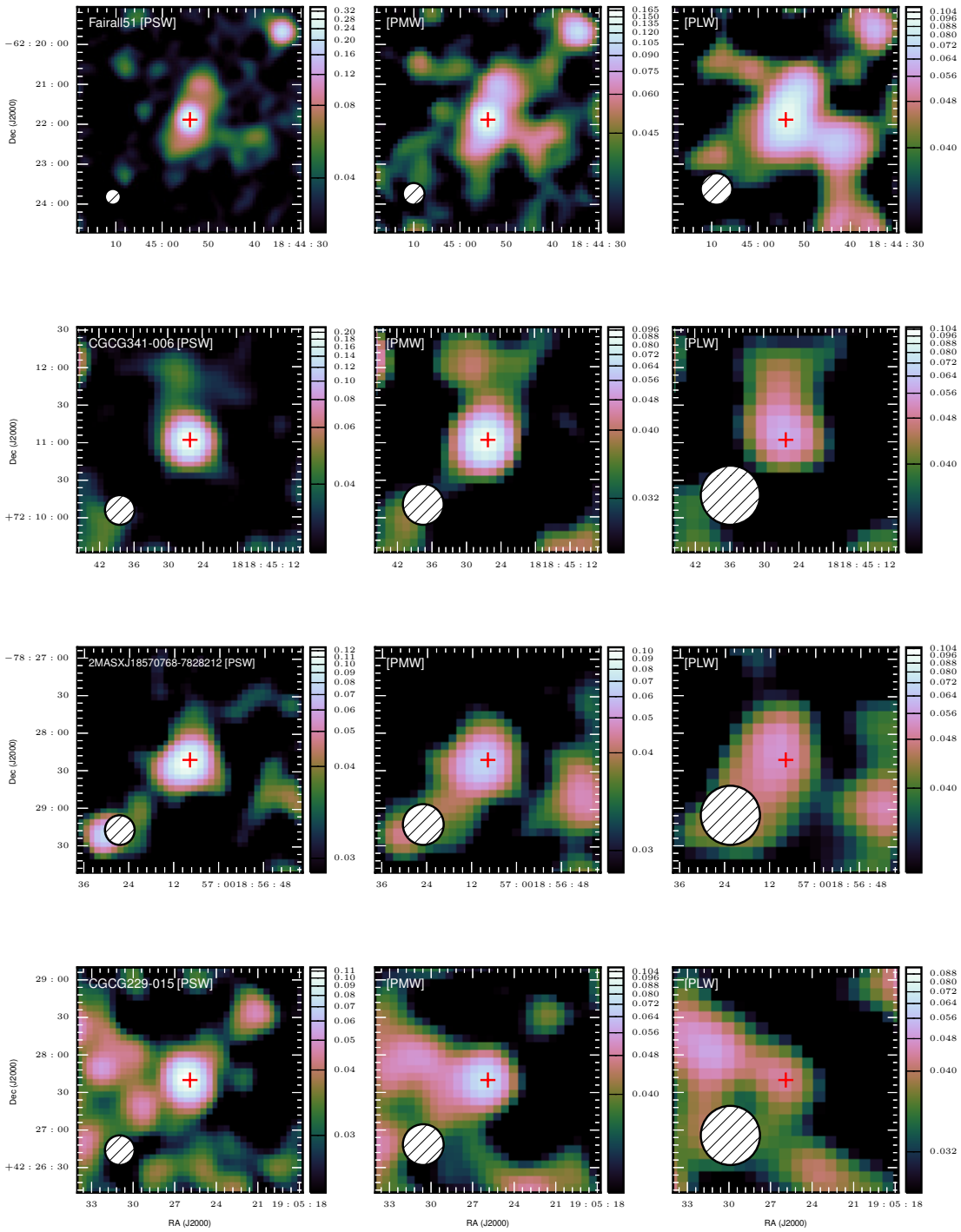
Fairall51 [PSW]
[PMW]
[PLW]
CGCG341-006 [PSW]
[PMW]
[PLW]
2MASXJ18570768-7828212 [PSW]
[PMW]
[PLW]
CGCG229-015 [PSW]
[PMW]
[PLW]
Dec (J2000)
RA (J2000)

Figure B.68

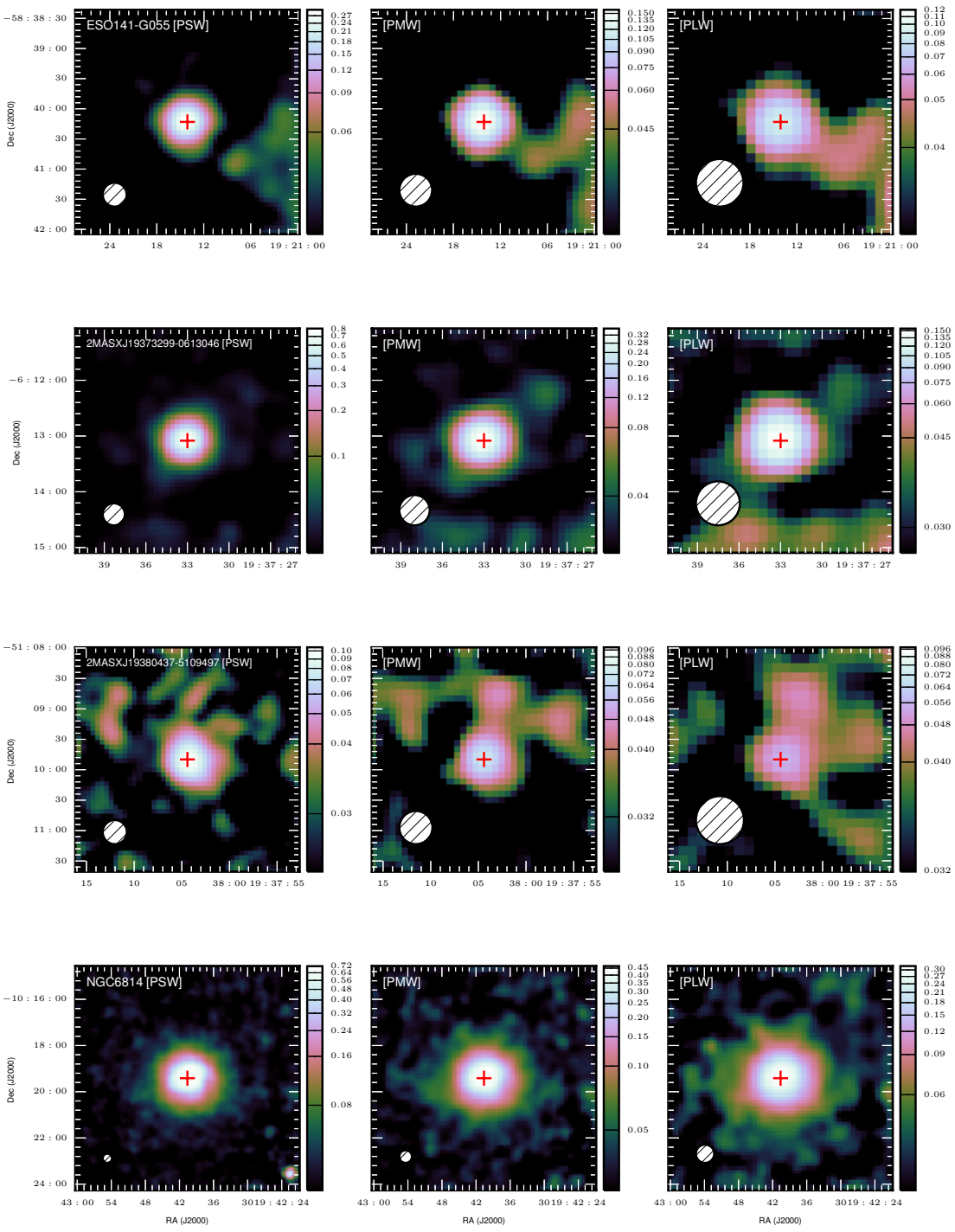
ESO141-G055 [PSW]
[PMW]
[PLW]
2MASXJ19373299-0613046 [PSW]
[PMW]
[PLW]
2MASXJ19380437-5109497 [PSW]
[PMW]
[PLW]
NGC6814 [PSW]
[PMW]
[PLW]
Dec (J2000)
RA (J2000)

Figure B.69

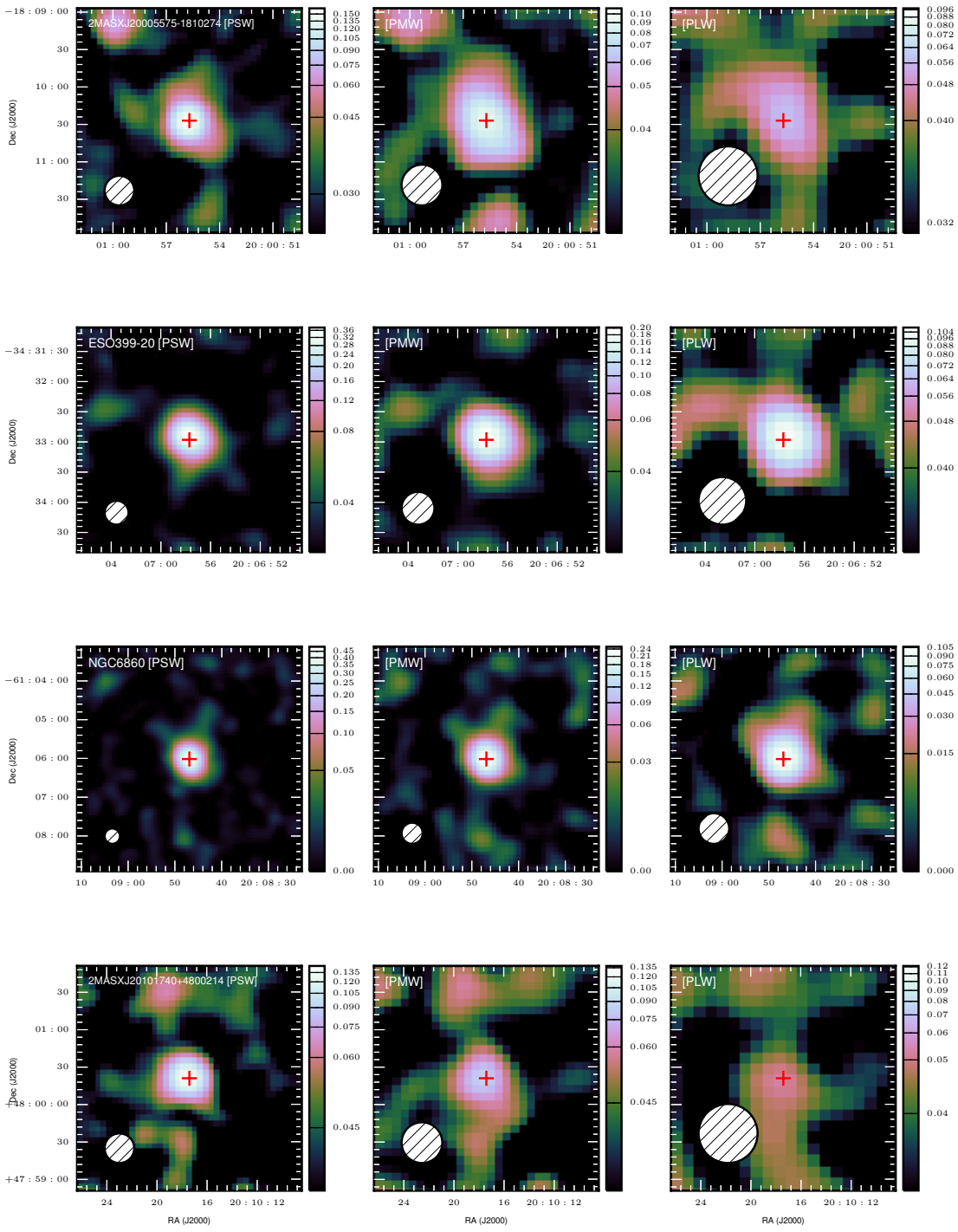
2MASXJ20005575-1810274 [PSW]
[PMW]
[PLW]
ESO399-20 [PSW]
[PMW]
[PLW]
NGC6860 [PSW]
[PMW]
[PLW]
2MASXJ20101740+4800214 [PSW]
[PMW]
[PLW]
Dec (J2000)
RA (J2000)

Figure B.70

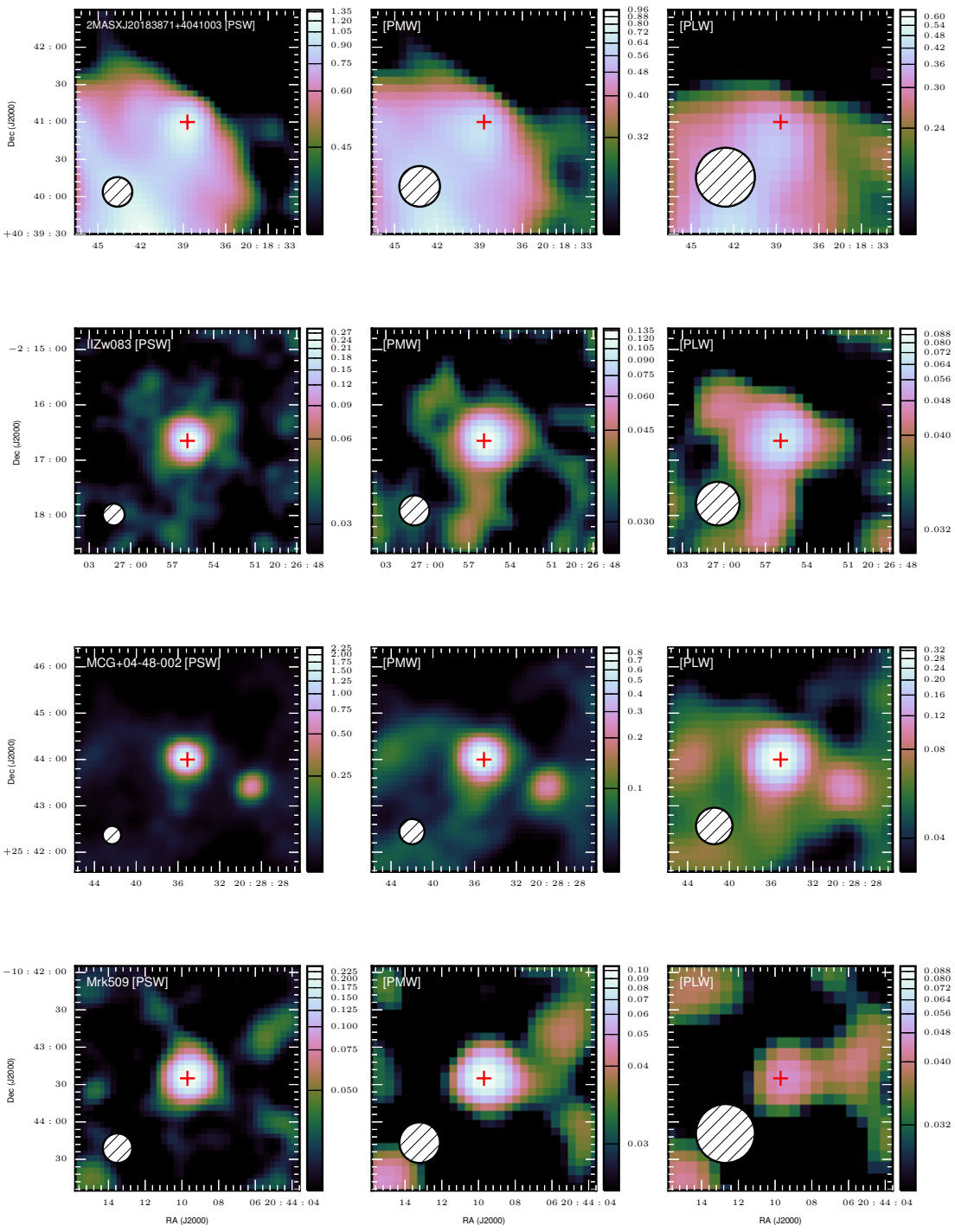
2MASXJ20183871+4041003 [PSW]
[PMW]
[PLW]
IZw083 [PSW]
[PMW]
[PLW]
MCG+04-48-002 [PSW]
[PMW]
[PLW]
Mrk509 [PSW]
[PMW]
[PLW]
Dec (J2000)
RA (J2000)

Figure B.71

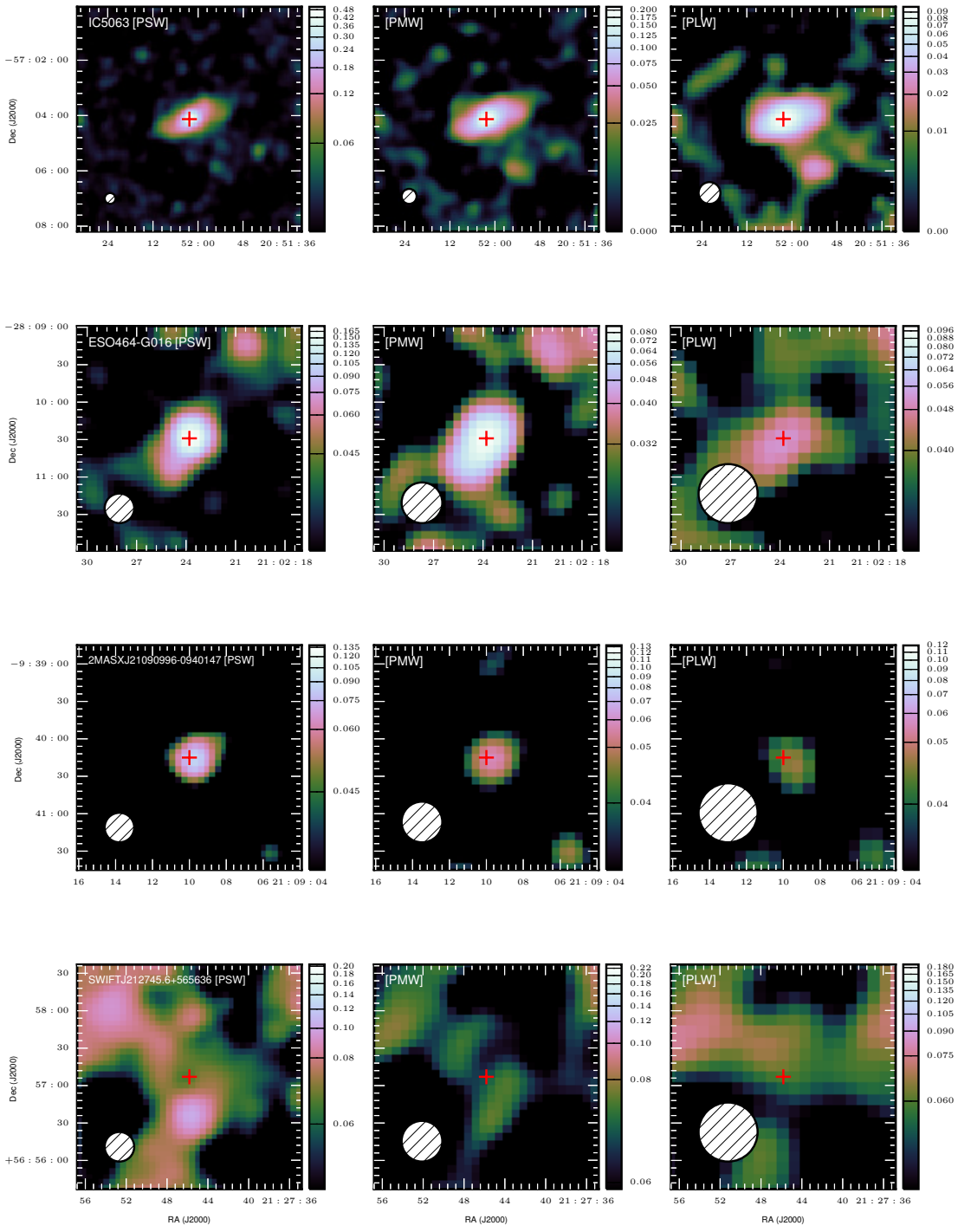
IC5063 [PSW]
[PMW]
[PLW]
ESO464-G016 [PSW]
[PMW]
[PLW]
2MASXJ21090996-0940147 [PSW]
[PMW]
[PLW]
SWIFTJ212745.6+565636 [PSW]
[PMW]
[PLW]
Dec (J2000)
RA (J2000)

Figure B.72

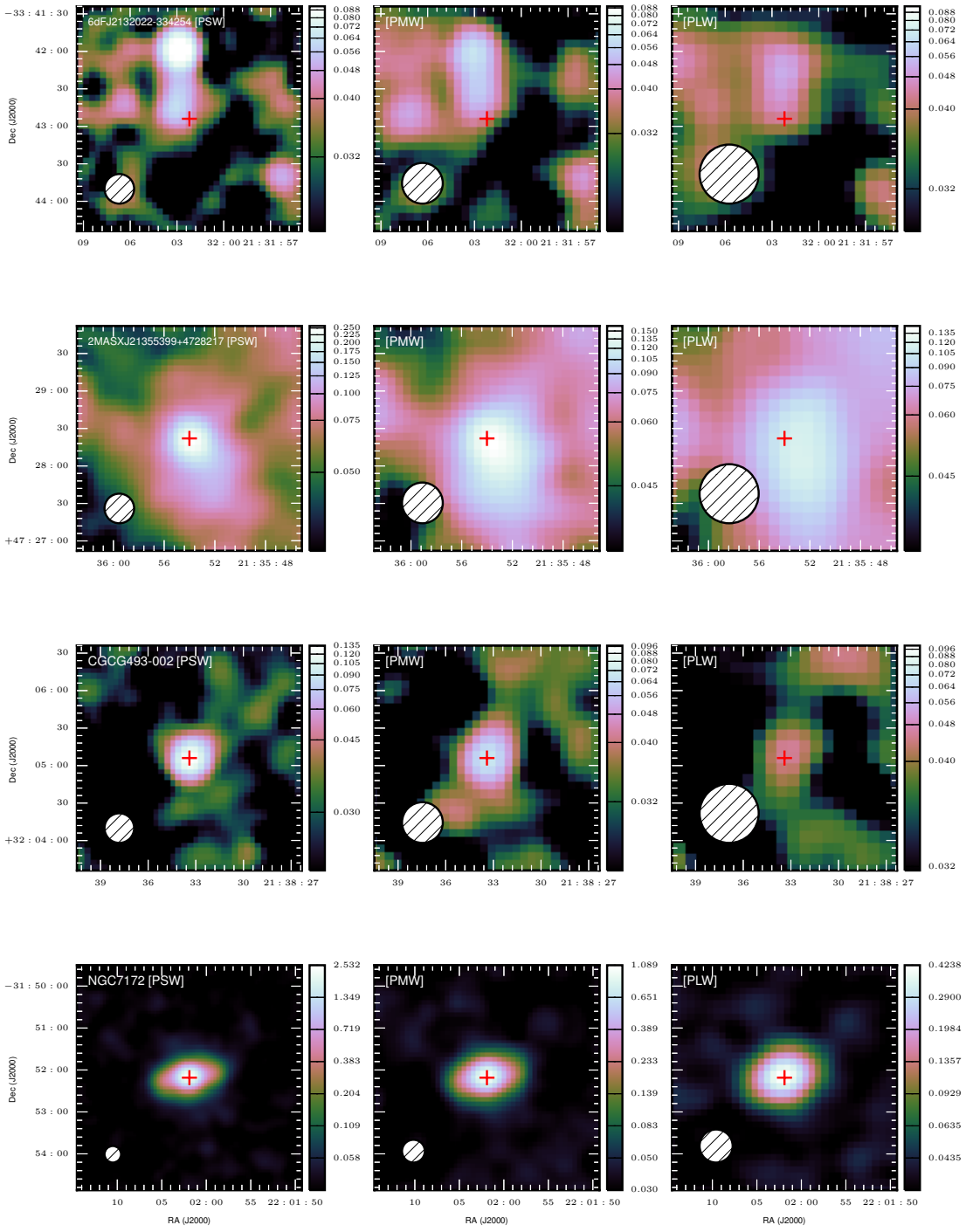
6dFJ2132022-334254 [PSW]
[PMW]
[PLW]
2MASXJ21355399+4728217 [PSW]
[PMW]
[PLW]
CGCG493-002 [PSW]
[PMW]
[PLW]
NGC7172 [PSW]
[PMW]
[PLW]
Dec (J2000)
RA (J2000)

Figure B.73

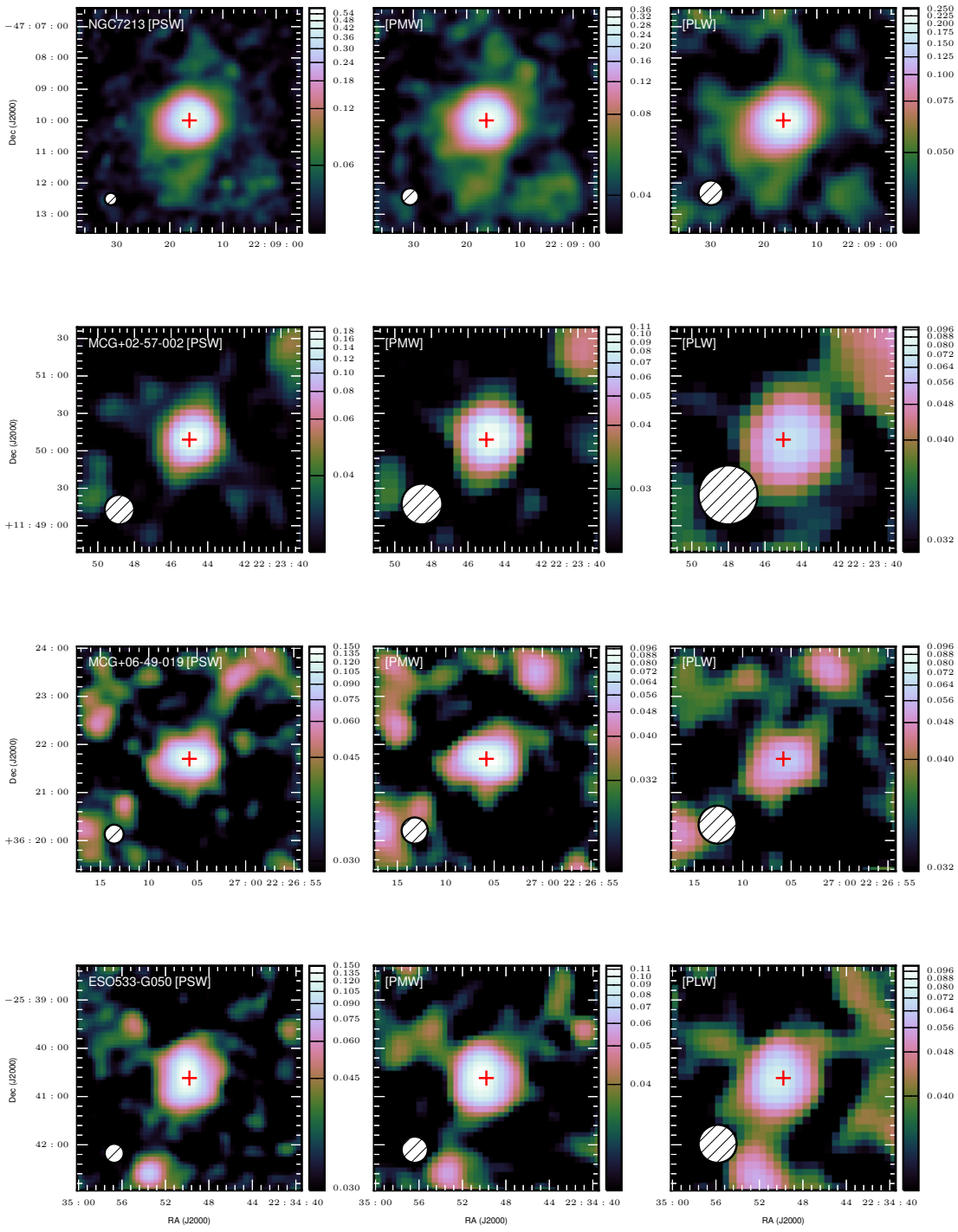
NGC7213 [PSW]
[PMW]
[PLW]
MCG+02-57-002 [PSW]
[PMW]
[PLW]
MCG+06-49-019 [PSW]
[PMW]
[PLW]
ESO533-G050 [PSW]
[PMW]
[PLW]
Dec (J2000)
RA (J2000)

Figure B.74

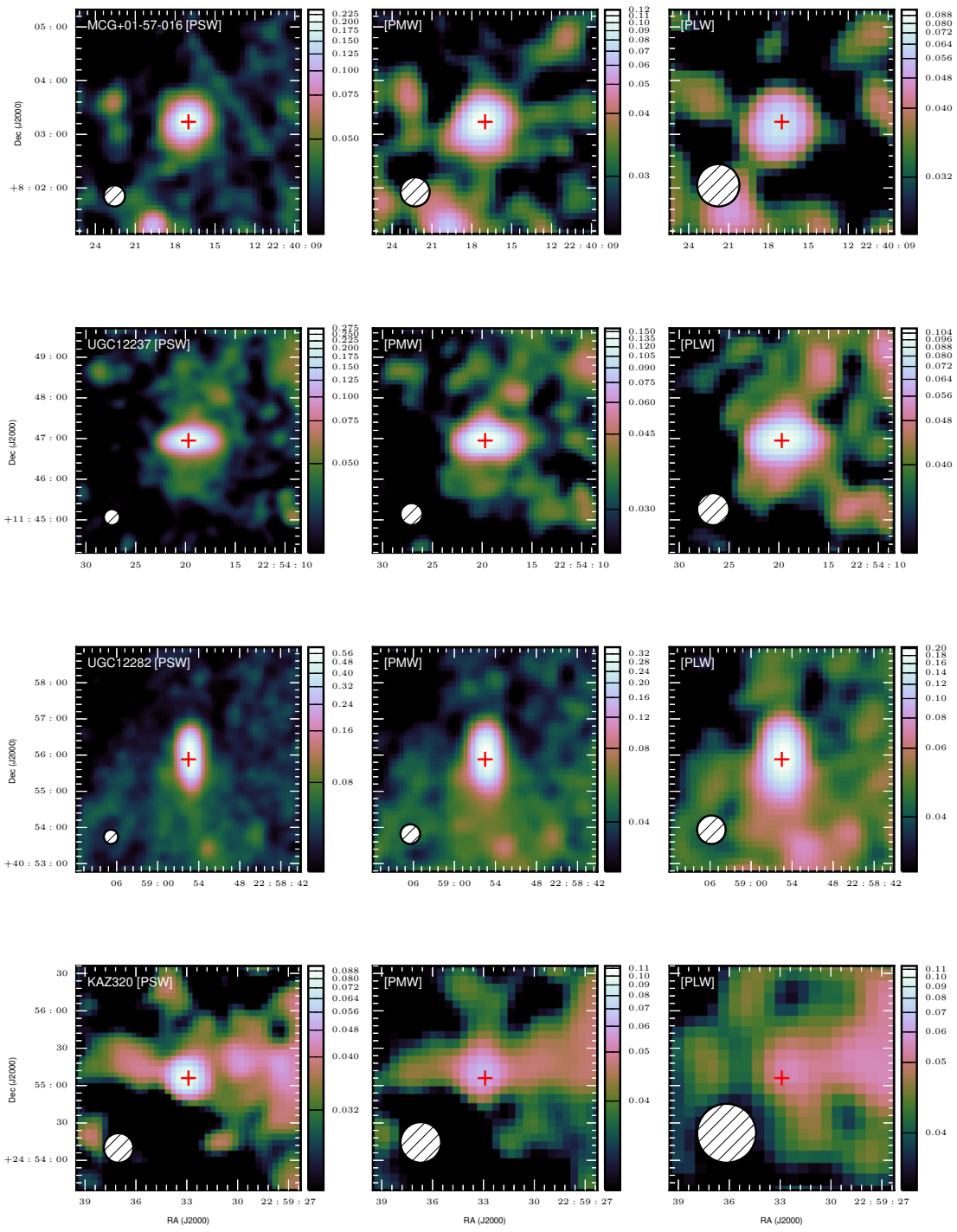
MCG+01-57-016 [PSW]
[PMW]
[PLW]
UGC12237 [PSW]
[PMW]
[PLW]
UGC12282 [PSW]
[PMW]
[PLW]
KAZ320 [PSW]
[PMW]
[PLW]
Dec (J2000)
RA (J2000)

Figure B.75

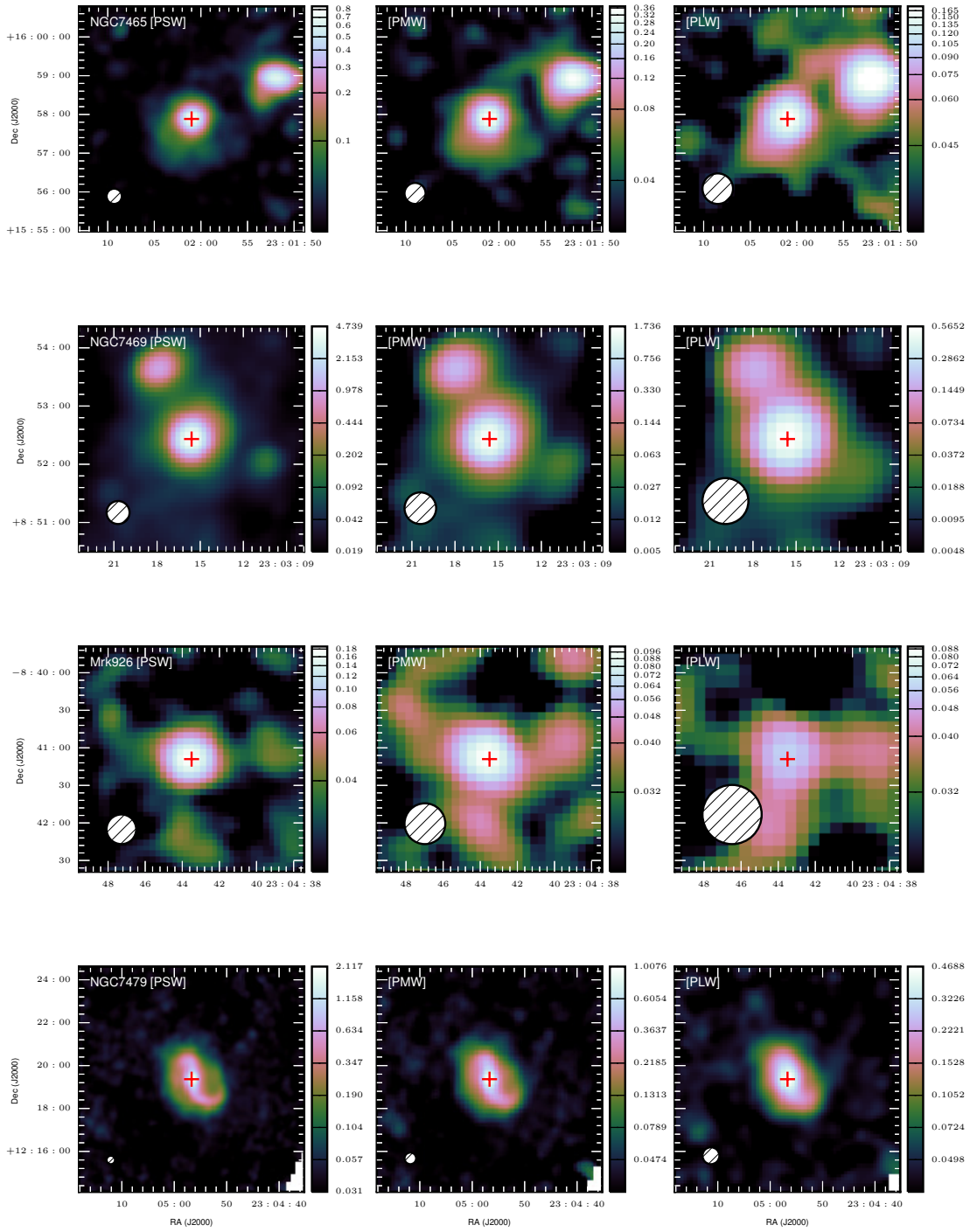
NGC7465 [PSW]
[PMW]
[PLW]
NGC7469 [PSW]
[PMW]
[PLW]
Mrk926 [PSW]
[PMW]
[PLW]
NGC7479 [PSW]
[PMW]
[PLW]
Dec (J2000)
RA (J2000)

Figure B.76

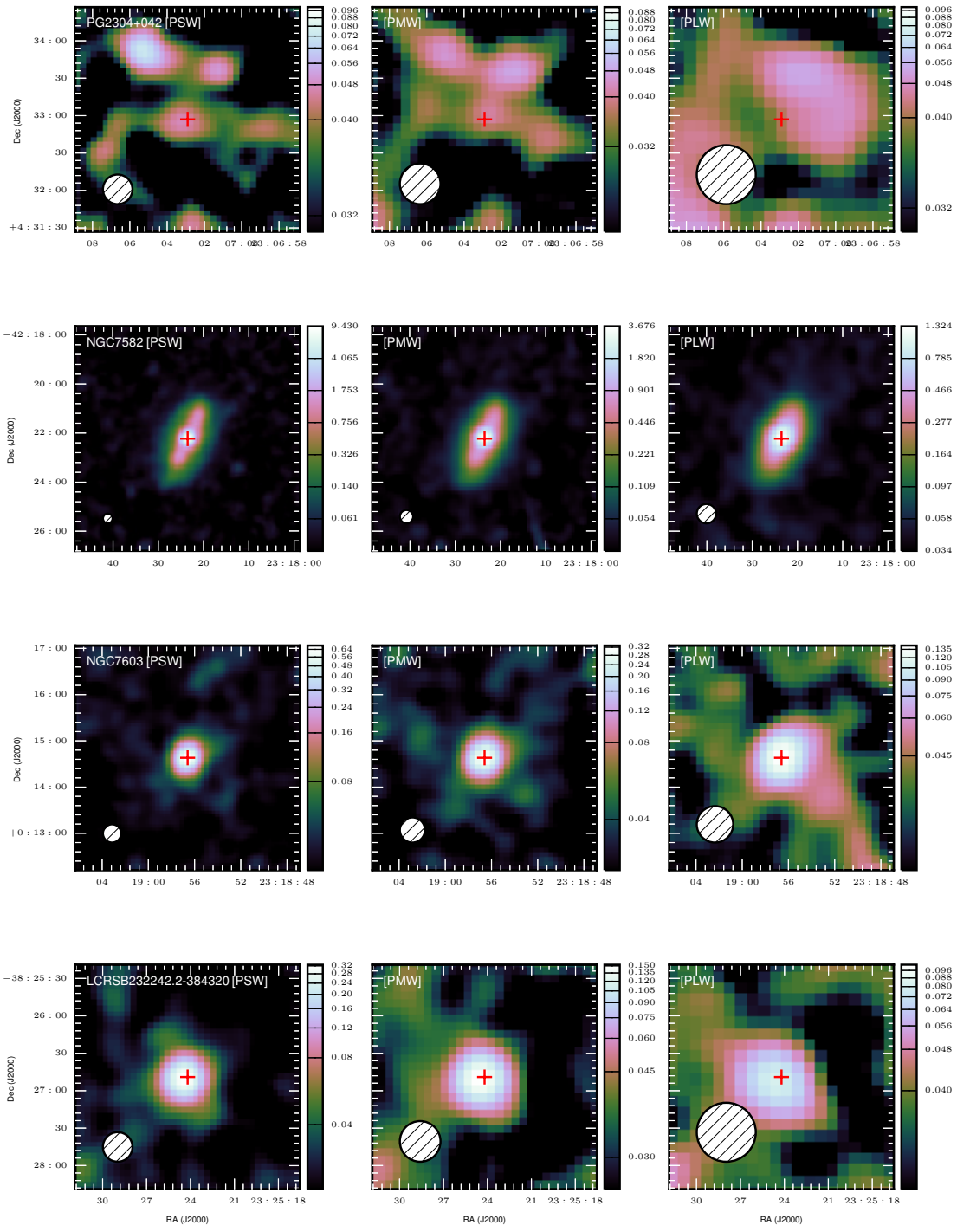
PG2304+042 [PSW]
[PMW]
[PLW]
NGC7582 [PSW]
[PMW]
[PLW]
NGC7603 [PSW]
[PMW]
[PLW]
LCRSB232242.2-384320 [PSW]
[PMW]
[PLW]
Dec (J2000)
RA (J2000)

Figure B.77

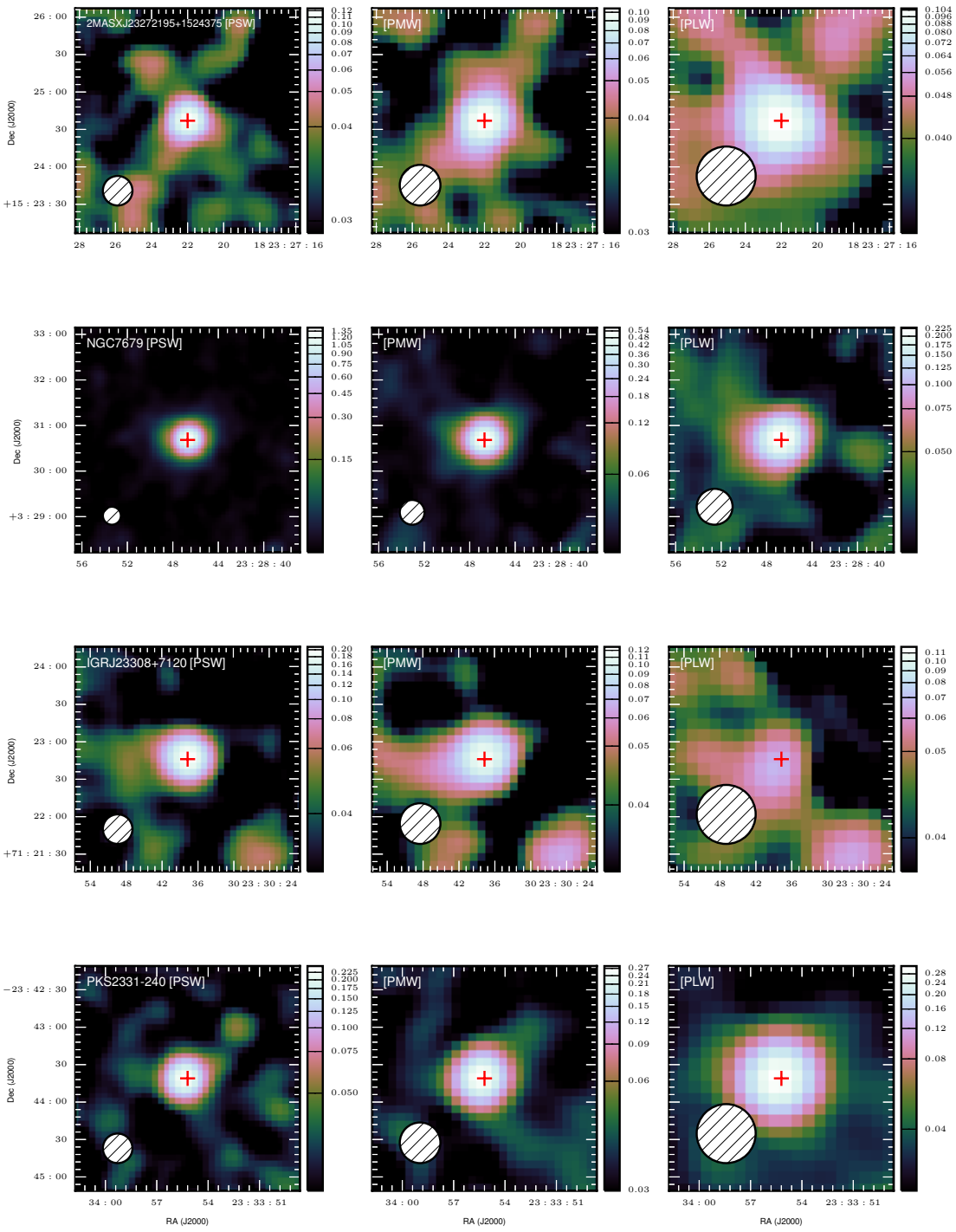
2MASXJ23272195+1524375 [PSW]
[PMW]
[PLW]
NGC7679 [PSW]
[PMW]
[PLW]
IGRJ23308+7120 [PSW]
[PMW]
[PLW]
PKS2331-240 [PSW]
[PMW]
[PLW]
Dec (J2000)
RA (J2000)

Figure B.78

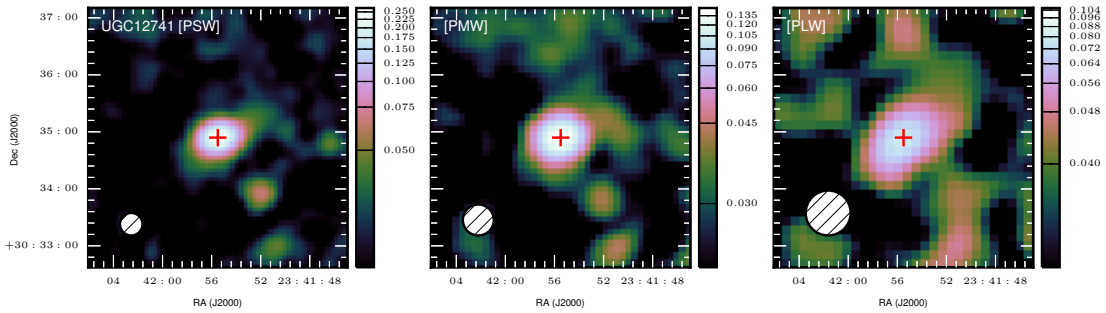
UGC12741 [PSW]
[PMW]
[PLW]
37 : 00
36 : 00
35 : 00
34 : 00
+30 : 33 : 00
Dec (J2000)
04 42 : 00 56 52 23 : 41 : 48
RA (J2000)
0.250
0.225
0.200
0.175
0.150
0.125
0.100
0.075
0.050
0.135
0.120
0.105
0.090
0.075
0.060
0.045
0.030
0.104
0.096
0.088
0.080
0.072
0.064
0.056
0.048
0.040

Figure B.79

Appendix C: SPIRE Flux Densities of the *Herschel*-BAT Sample

Table C.1: SPIRE Flux Densities

Name	RA (J2000)	DEC (J2000)	F_{250} (Jy)	Method 250	Flag 250	F_{350} (Jy)	Method 350	Flag 350	F_{500} (Jy)	Method 500	Flag 500
Mrk 335	00h06m19.5s	+20d12m10s	0.068 ± 0.007	TF	A	< 0.067	PAP	U	< 0.078	PAP	U
2MASX J00253292+6821442	00h25m32.9s	+68d21m44s	< 0.286	PAP	UC	< 0.364	PAP	UC	< 0.263	PAP	UC
CGCG 535-012	00h36m21.0s	+45d39m54s	0.178 ± 0.034	EAP	A	< 0.140	EAP	U	0.061 ± 0.011	EAP	A
NGC 235A	00h42m52.8s	-23d32m28s	0.955 ± 0.081	EAP	A	0.399 ± 0.060	EAP	A	< 0.126	PAP	U
MCG -02-02-095	00h43m08.8s	-11d36m04s	< 0.102	EAP	U	< 0.057	EAP	U	< 0.094	PAP	U
Mrk 348	00h48m47.1s	+31d57m25s	1.328 ± 0.179	EAP	AD	0.711 ± 0.109	EAP	AD	< 0.319	EAP	UD
MCG +05-03-013	00h51m35.0s	+29d24m05s	1.135 ± 0.086	EAP	A	0.512 ± 0.053	EAP	A	0.158 ± 0.030	EAP	A
Mrk 352	00h59m53.3s	+31d49m37s	0.127 ± 0.025	EAP	A	< 0.078	EAP	U	< 0.049	PAP	U
ESO 195-IG021 NED03	01h00m35.0s	-47d52m04s	0.415 ± 0.024	TF	A	0.194 ± 0.013	TF	A	0.072 ± 0.011	TF	A
MCG -07-03-007	01h05m26.8s	-42d12m58s	0.206 ± 0.013	TF	A	0.094 ± 0.009	TF	A	< 0.093	PAP	U
2MASX J01064523+0638015	01h06m45.3s	+06d38m02s	0.036 ± 0.006	TF	A	< 0.074	PAP	U	< 0.082	PAP	U
2MASX J01073963-1139117	01h07m39.6s	-11d39m12s	0.270 ± 0.016	TF	A	0.129 ± 0.010	TF	A	0.047 ± 0.009	TF	A
NGC 424	01h11m27.6s	-38d05m00s	1.004 ± 0.081	EAP	A	0.483 ± 0.047	EAP	A	0.177 ± 0.028	EAP	A
Mrk 975	01h13m51.0s	+13d16m18s	0.464 ± 0.026	TF	A	0.229 ± 0.014	TF	A	0.093 ± 0.012	TF	A
IC 1657	01h14m07.0s	-32d39m03s	3.035 ± 0.211	EAP	A	1.509 ± 0.146	EAP	A	0.607 ± 0.075	EAP	A
Fairall 9	01h23m45.8s	-58d48m21s	0.200 ± 0.012	TF	A	0.099 ± 0.009	TF	A	< 0.063	PAP	U
NGC 526A	01h23m54.4s	-35d03m56s	0.194 ± 0.028	EAP	A	< 0.157	EAP	U	< 0.077	PAP	U
NGC 513	01h24m26.9s	+33d47m58s	1.445 ± 0.099	EAP	A	0.630 ± 0.050	EAP	A	0.199 ± 0.019	EAP	A
Mrk 359	01h27m32.6s	+19d10m44s	0.488 ± 0.028	TF	A	0.187 ± 0.012	TF	A	0.062 ± 0.011	TF	A
MCG -03-04-072	01h28m06.7s	-18d48m31s	0.192 ± 0.022	EAP	A	0.110 ± 0.011	EAP	A	< 0.069	EAP	U
ESO 244-IG030	01h29m51.2s	-42d19m35s	1.035 ± 0.074	EAP	A	0.445 ± 0.050	EAP	A	0.140 ± 0.019	PAP	A
ESO 297-018	01h38m37.2s	-40d00m41s	1.358 ± 0.111	EAP	A	0.631 ± 0.058	EAP	A	0.241 ± 0.034	EAP	A

Table C.1 – continued from previous page

Name	RA (J2000)	DEC (J2000)	F_{250} (Jy)	Method 250	Flag 250	F_{350} (Jy)	Method 350	Flag$_{350}$ 350	F_{500} (Jy)	Method 500	Flag 500
MCG -01-05-047	01h52m49.0s	-03d26m49s	4.088 ± 0.296	EAP	A	1.970 ± 0.160	EAP	A	0.808 ± 0.063	EAP	A
UGC 01479	02h00m19.1s	+24d28m25s	1.390 ± 0.108	EAP	A	0.589 ± 0.049	EAP	A	0.180 ± 0.035	EAP	A
NGC 788	02h01m06.4s	-06d48m56s	0.851 ± 0.082	EAP	A	0.363 ± 0.052	EAP	A	< 0.158	EAP	U
Mrk 1018	02h06m16.0s	-00d17m29s	0.190 ± 0.029	EAP	A	0.122 ± 0.024	EAP	A	< 0.080	EAP	U
LEDA 138501	02h09m34.3s	+52d26m33s	< 0.074	PAP	U	< 0.059	PAP	U	< 0.063	PAP	U
ESO 197-G027	02h10m52.5s	-49d41m55s	0.753 ± 0.052	EAP	A	0.355 ± 0.031	EAP	A	0.125 ± 0.020	EAP	A
Mrk 590	02h14m33.6s	-00d46m00s	1.474 ± 0.109	EAP	A	0.643 ± 0.074	EAP	A	0.234 ± 0.026	EAP	A
NGC 931	02h28m14.5s	+31d18m42s	3.770 ± 0.289	EAP	A	1.766 ± 0.139	EAP	A	0.685 ± 0.085	EAP	A
IC 1816	02h31m51.0s	-36d40m19s	1.048 ± 0.072	EAP	A	0.403 ± 0.036	EAP	A	0.149 ± 0.026	EAP	A
NGC 985	02h34m37.8s	-08d47m15s	0.951 ± 0.067	EAP	A	0.486 ± 0.051	EAP	A	0.184 ± 0.025	EAP	A
ESO 198-024	02h38m19.7s	-52d11m33s	0.057 ± 0.007	TF	A	< 0.034	TF	U	< 0.061	PAP	U
NGC 1052	02h41m04.8s	-08d15m21s	0.558 ± 0.095	EAP	A	0.288 ± 0.048	EAP	A	< 0.152	EAP	U
Mrk 595	02h41m34.9s	+07d11m14s	0.295 ± 0.027	EAP	A	< 0.142	EAP	U	< 0.101	PAP	U
ESO 479-G031	02h44m47.7s	-24d30m50s	0.047 ± 0.007	TF	A	< 0.060	PAP	U	< 0.067	PAP	U
[HB89] 0241+622	02h44m57.7s	+62d28m07s	0.188 ± 0.012	TF	AC	0.192 ± 0.012	TF	AC	0.264 ± 0.018	TF	AC
NGC 1106	02h50m40.5s	+41d40m17s	1.034 ± 0.083	EAP	A	0.459 ± 0.033	EAP	A	0.138 ± 0.022	EAP	A
2MFGC 02280	02h50m42.6s	+54d42m18s	0.702 ± 0.062	EAP	A	0.279 ± 0.044	EAP	A	< 0.278	PAP	U
NGC 1125	02h51m40.3s	-16d39m04s	1.179 ± 0.093	EAP	AD	0.437 ± 0.059	EAP	AD	0.166 ± 0.027	EAP	AD
MCG -02-08-014	02h52m23.4s	-08d30m37s	0.460 ± 0.042	EAP	A	0.233 ± 0.043	EAP	A	< 0.115	EAP	U
ESO 417-G006	02h56m21.5s	-32d11m08s	0.044 ± 0.006	TF	A	< 0.094	PAP	U	< 0.105	PAP	U
MCG -02-08-038	03h00m04.3s	-10d49m29s	0.278 ± 0.047	EAP	A	< 0.158	EAP	U	< 0.101	PAP	U
NGC 1194	03h03m49.1s	-01d06m13s	0.546 ± 0.078	EAP	A	< 0.331	EAP	U	< 0.179	EAP	U
ESO 031-G008	03h07m35.3s	-72d50m03s	0.218 ± 0.022	EAP	A	0.115 ± 0.020	EAP	A	< 0.071	EAP	U
MCG +00-09-042	03h17m02.2s	+01d15m18s	1.308 ± 0.106	EAP	A	0.442 ± 0.046	EAP	A	< 0.156	PAP	U
IRAS 03219+4031	03h25m13.2s	+40d41m55s	0.430 ± 0.035	EAP	Ad	0.169 ± 0.018	EAP	Ad	< 0.062	PAP	UD
2MASX J03305218+0538253	03h30m52.2s	+05d38m26s	< 0.138	PAP	UC	< 0.259	PAP	UC	< 0.193	PAP	UC
MCG -01-09-045	03h31m23.0s	-05d08m30s	0.251 ± 0.048	EAP	A	< 0.190	EAP	U	< 0.100	PAP	U
NGC 1365	03h33m36.4s	-36d08m25s	99.193 ± 6.766	EAP	A	42.838 ± 2.999	EAP	A	15.216 ± 1.084	EAP	A
2MASX J03342453-1513402	03h34m24.5s	-15d13m40s	0.325 ± 0.019	TF	Ad	0.144 ± 0.012	TF	Ad	0.115 ± 0.023	PAP	AD
ESO 548-G081	03h42m03.7s	-21d14m39s	0.823 ± 0.059	EAP	A	0.315 ± 0.029	EAP	A	< 0.129	PAP	U
LCRS B034324.7-394349	03h45m12.5s	-39d34m29s	0.144 ± 0.011	TF	A	0.074 ± 0.008	TF	Ad	0.050 ± 0.009	TF	AD
2MASX J03502377-5018354	03h50m23.8s	-50d18m36s	0.264 ± 0.022	PAP	AD	0.186 ± 0.027	EAP	AD	< 0.072	EAP	UD
2MASX J03534246+3714077	03h53m42.5s	+37d14m07s	0.391 ± 0.022	TF	A	0.159 ± 0.011	TF	A	0.089 ± 0.011	TF	A
2MASX J03540948+0249307	03h54m09.5s	+02d49m31s	< 0.208	PAP	UC	< 0.183	PAP	UC	< 0.174	PAP	UC
ESO 549-G049	04h02m25.7s	-18d02m51s	1.822 ± 0.123	EAP	A	0.726 ± 0.051	EAP	A	0.212 ± 0.026	EAP	A
IRAS 04124-0803	04h14m52.7s	-07d55m40s	0.165 ± 0.011	TF	A	0.067 ± 0.008	TF	A	< 0.065	PAP	U
3C 111.0	04h18m21.3s	+38d01m36s	0.573 ± 0.033	TF	AC	0.737 ± 0.042	TF	AC	0.883 ± 0.050	TF	AC
ESO 157-G023	04h22m24.2s	-56d13m33s	0.502 ± 0.043	EAP	Ad	0.193 ± 0.020	EAP	AD	0.116 ± 0.018	EAP	AD
2MASX J04234080+0408017	04h23m40.8s	+04d08m02s	0.195 ± 0.013	TF	A	0.098 ± 0.009	TF	A	< 0.094	PAP	U
3C 120	04h33m11.1s	+05d21m16s	0.636 ± 0.036	TF	A	0.467 ± 0.027	TF	A	0.438 ± 0.026	TF	A

Table C.1 – continued from previous page

Name	RA (J2000)	DEC (J2000)	F_{250} (Jy)	Method 250	Flag 250	F_{350} (Jy)	Method 350	Flag$_{350}$ 350	F_{500} (Jy)	Method 500	Flag 500
Mrk 618	04h36m22.2s	-10d22m34s	1.197 ± 0.091	EAP	A	0.537 ± 0.050	EAP	Ad	0.184 ± 0.028	EAP	Ad
MCG -02-12-050	04h38m14.2s	-10d47m45s	0.858 ± 0.077	EAP	Ad	0.386 ± 0.034	EAP	Ad	0.169 ± 0.019	PAP	AD
1RXS J044154.5-082639	04h41m54.1s	-08d26m34s	0.059 ± 0.010	TF	A	< 0.096	PAP	U	< 0.103	PAP	U
UGC 03142	04h43m46.8s	+28d58m19s	0.808 ± 0.114	PAP	AC	< 0.702	PAP	UC	< 1.226	PAP	UC
2MASX J04440903+2813003	04h44m09.0s	+28d13m01s	< 1.688	PAP	UC	< 1.815	PAP	UC	< 1.390	PAP	UC
MCG -01-13-025	04h51m41.5s	-03d48m33s	< 0.107	EAP	U	< 0.065	PAP	U	< 0.072	PAP	U
1RXS J045205.0+493248	04h52m05.0s	+49d32m45s	0.367 ± 0.058	EAP	A	< 0.281	EAP	U	< 0.089	EAP	U
CGCG 420-015	04h53m25.8s	+04d03m42s	0.291 ± 0.027	EAP	A	0.175 ± 0.023	EAP	A	< 0.071	PAP	U
ESO 033-G002	04h55m59.0s	-75d32m28s	0.398 ± 0.073	EAP	A	< 0.266	EAP	U	< 0.249	EAP	U
2MASX J05020903+0331499	05h02m09.0s	+03d31m50s	0.086 ± 0.015	EAP	A	< 0.088	PAP	U	< 0.068	PAP	U
2MASX J05054575-2351139	05h05m45.7s	-23d51m14s	0.109 ± 0.021	EAP	A	< 0.137	EAP	U	< 0.052	EAP	U
CGCG 468-002 NED01	05h08m19.7s	+17d21m48s	1.166 ± 0.086	PAP	AD	0.720 ± 0.057	PAP	AD	0.308 ± 0.057	EAP	AD
IRAS 05078+1626	05h10m45.5s	+16d29m56s	< 1.405	EAP	U	< 0.524	EAP	U	< 0.240	EAP	U
ESO 553-G022	05h11m57.8s	-18d29m38s	0.318 ± 0.037	EAP	A	0.139 ± 0.021	PAP	A	< 0.087	PAP	U
Ark 120	05h16m11.4s	-00d08m59s	0.605 ± 0.054	EAP	A	0.302 ± 0.037	EAP	A	< 0.106	EAP	U
MCG -02-14-009	05h16m21.2s	-10d33m41s	< 0.763	EAP	U	< 0.809	EAP	U	< 0.382	EAP	U
ESO 362-18	05h19m35.8s	-32d39m28s	0.774 ± 0.053	EAP	A	0.300 ± 0.025	EAP	A	0.107 ± 0.018	EAP	A
Pictor A	05h19m49.7s	-45d46m44s	0.486 ± 0.028	TF	A	0.617 ± 0.035	TF	A	0.775 ± 0.044	TF	A
IRAS0 5218-1212	05h24m06.5s	-12d10m00s	0.094 ± 0.008	TF	A	< 0.126	PAP	U	< 0.106	PAP	U
ESO 553-G043	05h26m27.3s	-21d17m12s	< 0.078	PAP	U	< 0.067	EAP	U	< 0.065	PAP	U
NGC 2110	05h52m11.4s	-07d27m22s	1.932 ± 0.167	EAP	A	0.779 ± 0.062	EAP	A	0.238 ± 0.026	EAP	A
MCG +08-11-011	05h54m53.6s	+46d26m22s	2.531 ± 0.270	EAP	A	1.172 ± 0.134	EAP	Ad	0.409 ± 0.067	EAP	Ad
2MASX J05580206-3820043	05h58m02.0s	-38d20m05s	< 0.464	EAP	U	< 0.323	EAP	U	< 0.251	EAP	U
IRAS0 5589+2828	06h02m10.7s	+28d28m22s	0.265 ± 0.016	TF	A	0.130 ± 0.010	TF	A	< 0.058	TF	U
ESO 005-G004	06h05m41.6s	-86d37m55s	11.930 ± 0.811	EAP	A	5.492 ± 0.378	EAP	A	2.105 ± 0.178	EAP	A
Mrk 3	06h15m36.3s	+71d02m15s	0.795 ± 0.082	EAP	A	0.312 ± 0.042	EAP	A	0.118 ± 0.012	EAP	A
ESO 121-IG028	06h23m45.6s	-60d58m44s	0.183 ± 0.020	EAP	A	0.089 ± 0.015	EAP	A	< 0.090	PAP	U
ESO 426-G002	06h23m46.4s	-32d13m00s	0.552 ± 0.101	EAP	A	< 0.342	EAP	U	< 0.166	EAP	U
6dF J0626586-370559	06h26m58.6s	-37d05m59s	0.237 ± 0.015	TF	A	0.108 ± 0.009	TF	A	0.061 ± 0.011	TF	A
VII Zw 073	06h30m25.6s	+63d40m41s	0.606 ± 0.034	TF	A	0.221 ± 0.014	TF	A	0.073 ± 0.010	TF	A
UGC 03478	06h32m47.2s	+63d40m25s	2.213 ± 0.150	EAP	A	1.012 ± 0.086	EAP	A	0.372 ± 0.038	EAP	A
ESO 490-IG026	06h40m11.7s	-25d53m43s	0.907 ± 0.074	EAP	A	0.405 ± 0.057	EAP	A	< 0.144	EAP	U
2MASX J06411806+3249313	06h41m18.0s	+32d49m32s	< 0.083	PAP	U	< 0.093	PAP	U	< 0.073	PAP	U
Mrk 6	06h52m12.3s	+74d25m37s	0.612 ± 0.087	EAP	A	0.237 ± 0.039	EAP	A	< 0.068	EAP	U
UGC 03601	06h55m49.5s	+40d00m01s	0.339 ± 0.030	EAP	A	0.150 ± 0.020	EAP	A	< 0.051	EAP	U
2MASX J06561197-4919499	06h56m12.0s	-49d19m50s	0.097 ± 0.019	EAP	A	< 0.078	PAP	U	< 0.103	PAP	U
MCG +06-16-028	07h14m03.9s	+35d16m45s	0.844 ± 0.061	PAP	A	0.330 ± 0.027	PAP	A	0.108 ± 0.014	PAP	A
2MASX J07262635-3554214	07h26m26.4s	-35d54m22s	< 0.433	PAP	UC	< 0.406	PAP	UC	< 0.260	PAP	UC
Mrk 79	07h42m32.8s	+49d48m35s	1.313 ± 0.155	EAP	A	0.640 ± 0.074	EAP	AD	0.174 ± 0.028	EAP	A
UGC 03995A	07h44m07.0s	+29d14m57s	2.486 ± 0.209	EAP	AD	1.258 ± 0.130	EAP	AD	0.520 ± 0.057	EAP	AD

Table C.1 – continued from previous page

Name	RA (J2000)	DEC (J2000)	F_{250} (Jy)	Method 250	Flag 250	F_{350} (Jy)	Method 350	Flag$_{350}$ 350	F_{500} (Jy)	Method 500	Flag 500
Mrk 10	07h47m29.1s	+60d56m01s	1.418 ± 0.117	EAP	A	0.736 ± 0.071	EAP	A	0.306 ± 0.037	EAP	A
2MASS J07594181-3843560	07h59m41.7s	-38d43m57s	< 0.111	PAP	UC	< 0.126	PAP	UC	< 0.111	PAP	UC
2MASX J07595347+2323241	07h59m53.5s	+23d23m24s	2.078 ± 0.143	EAP	A	0.862 ± 0.061	EAP	A	0.329 ± 0.031	EAP	A
IC0 486	08h00m21.0s	+26d36m49s	0.721 ± 0.055	EAP	A	0.319 ± 0.044	EAP	A	< 0.120	EAP	U
ESO 209-G012	08h01m58.0s	-49d46m42s	1.246 ± 0.123	EAP	A	0.570 ± 0.066	EAP	A	< 0.218	EAP	U
2MASX J08032736+0841523	08h03m27.4s	+08d41m52s	< 0.080	PAP	U	< 0.081	PAP	U	< 0.061	PAP	U
Mrk 1210	08h04m05.9s	+05d06m50s	0.362 ± 0.032	EAP	A	0.149 ± 0.022	EAP	A	< 0.077	EAP	U
MCG +02-21-013	08h04m46.4s	+10d46m36s	0.899 ± 0.066	EAP	A	0.409 ± 0.051	EAP	A	< 0.190	EAP	U
Fairall 272	08h23m01.1s	-04d56m05s	0.465 ± 0.027	TF	Ad	0.215 ± 0.014	TF	Ad	0.103 ± 0.019	PAP	AD
Fairall 1146	08h38m30.8s	-35d59m33s	0.616 ± 0.058	EAP	A	0.283 ± 0.053	EAP	A	< 0.142	EAP	U
MCG +11-11-032	08h55m12.5s	+64d23m46s	0.258 ± 0.038	EAP	A	0.134 ± 0.023	EAP	A	< 0.055	PAP	U
NGC 2655	08h55m37.7s	+78d13m23s	4.638 ± 0.575	EAP	A	2.049 ± 0.288	EAP	A	0.599 ± 0.079	EAP	A
Mrk 18	09h01m58.4s	+60d09m06s	0.774 ± 0.058	EAP	A	0.312 ± 0.034	EAP	A	0.090 ± 0.013	EAP	A
2MASX J09023729-4813339	09h02m37.3s	-48d13m34s	< 2.473	PAP	UC	< 2.445	PAP	UC	< 1.655	PAP	UC
2MASX J09043699+5536025	09h04m36.9s	+55d36m03s	0.058 ± 0.008	TF	A	< 0.060	PAP	U	< 0.078	PAP	U
Mrk 704	09h18m26.0s	+16d18m19s	0.123 ± 0.019	EAP	A	< 0.080	EAP	U	< 0.086	PAP	U
SBS 0915+556	09h19m13.2s	+55d27m55s	< 0.076	PAP	U	< 0.099	PAP	U	< 0.090	PAP	U
IC 2461	09h19m58.0s	+37d11m29s	2.196 ± 0.150	EAP	A	1.006 ± 0.075	EAP	A	0.399 ± 0.035	EAP	A
MCG -01-24-012	09h20m46.2s	-08d03m22s	0.768 ± 0.074	EAP	A	0.367 ± 0.030	EAP	A	0.142 ± 0.025	EAP	A
MCG +04-22-042	09h23m43.0s	+22d54m33s	0.423 ± 0.074	EAP	A	0.211 ± 0.042	EAP	A	0.096 ± 0.017	EAP	A
2MASX J09235371-3141305	09h23m53.7s	-31d41m31s	0.032 ± 0.006	TF	A	< 0.112	PAP	U	< 0.137	PAP	U
2MASX J09254750+6927532	09h25m47.5s	+69d27m53s	0.080 ± 0.008	TF	A	< 0.206	PAP	U	< 0.174	PAP	U
NGC 2885	09h27m18.5s	+23d01m12s	0.534 ± 0.083	EAP	A	0.266 ± 0.035	EAP	A	< 0.121	EAP	U
CGCG 312-012	09h29m37.9s	+62d32m39s	0.094 ± 0.008	TF	A	0.044 ± 0.007	TF	A	< 0.062	PAP	U
ESO 565-G019	09h34m43.6s	-21d55m40s	1.031 ± 0.057	TF	Ad	0.407 ± 0.024	TF	Ad	0.137 ± 0.011	TF	Ad
2MASX J09360622-6548336	09h36m06.3s	-65d48m33s	< 0.112	PAP	U	< 0.086	PAP	U	< 0.103	PAP	U
CGCG 122-055	09h42m04.8s	+23d41m07s	0.226 ± 0.014	TF	A	0.110 ± 0.010	TF	A	< 0.050	TF	U
NGC 2992	09h45m42.1s	-14d19m35s	4.572 ± 0.301	EAP	Ad	1.912 ± 0.131	EAP	Ad	0.666 ± 0.075	EAP	Ad
MCG -05-23-016	09h47m40.2s	-30d56m55s	0.128 ± 0.009	TF	A	0.050 ± 0.007	TF	A	< 0.098	PAP	U
NGC 3035	09h51m55.0s	-06d49m23s	1.613 ± 0.121	EAP	A	0.702 ± 0.067	EAP	A	0.247 ± 0.031	EAP	A
NGC 3081	09h59m29.5s	-22d49m35s	2.330 ± 0.184	EAP	A	1.087 ± 0.106	EAP	A	0.435 ± 0.065	EAP	A
2MASX J09594263-3112581	09h59m42.6s	-31d12m58s	0.212 ± 0.032	EAP	A	< 0.078	EAP	U	< 0.091	PAP	U
NGC 3079	10h01m57.8s	+55d40m47s	46.418 ± 3.052	EAP	A	19.515 ± 1.297	EAP	A	6.897 ± 0.463	EAP	A
ESO 499-G041	10h05m55.4s	-23d03m25s	0.477 ± 0.037	EAP	A	0.213 ± 0.024	EAP	A	< 0.101	EAP	U
ESO 263-G013	10h09m48.2s	-42d48m40s	< 1.035	EAP	U	< 0.696	EAP	U	< 0.250	EAP	U
ESO 374-G044	10h13m19.9s	-35d58m58s	0.400 ± 0.059	EAP	A	0.199 ± 0.037	EAP	A	< 0.108	EAP	U
ARK 241	10h21m40.2s	-03d27m14s	0.145 ± 0.021	EAP	A	0.090 ± 0.017	EAP	A	< 0.076	PAP	U
NGC 3227	10h23m30.6s	+19d51m54s	11.141 ± 0.775	EAP	Ad	4.675 ± 0.331	EAP	Ad	1.530 ± 0.131	EAP	Ad
NGC 3281	10h31m52.1s	-34d51m13s	2.589 ± 0.174	EAP	A	1.014 ± 0.070	EAP	A	0.292 ± 0.033	EAP	A
2MASX J10402231-4625264	10h40m22.5s	-46d25m26s	0.542 ± 0.030	TF	A	0.211 ± 0.013	TF	A	0.077 ± 0.010	TF	A

Table C.1 – continued from previous page

Name	RA (J2000)	DEC (J2000)	F_{250} (Jy)	Method 250	Flag 250	F_{350} (Jy)	Method 350	Flag$_{350}$ 350	F_{500} (Jy)	Method 500	Flag 500
SDSS J104326.47+110524.2	10h43m26.5s	+11d05m24s	< 0.066	PAP	U	< 0.094	PAP	U	< 0.068	PAP	U
MCG +12-10-067	10h44m08.5s	+70d24m19s	1.242 ± 0.097	EAP	A	0.527 ± 0.070	EAP	A	0.206 ± 0.040	EAP	A
MCG +06-24-008	10h44m49.0s	+38d10m52s	0.650 ± 0.036	TF	A	0.283 ± 0.017	TF	A	0.088 ± 0.011	TF	A
UGC 05881	10h46m42.5s	+25d55m54s	0.887 ± 0.073	EAP	A	0.389 ± 0.034	EAP	A	0.134 ± 0.019	EAP	A
NGC 3393	10h48m23.5s	-25d09m43s	2.848 ± 0.285	EAP	A	1.197 ± 0.151	EAP	A	0.409 ± 0.076	EAP	A
Mrk 417	10h49m30.9s	+22d57m52s	0.048 ± 0.006	TF	A	< 0.096	PAP	U	< 0.088	PAP	U
NGC 3431	10h51m15.0s	-17d00m29s	1.229 ± 0.086	EAP	A	0.643 ± 0.071	EAP	A	0.260 ± 0.040	EAP	A
Mrk 728	11h01m01.8s	+11d02m49s	< 0.084	PAP	U	< 0.101	PAP	U	< 0.072	PAP	U
NGC 3516	11h06m47.5s	+72d34m07s	0.383 ± 0.045	EAP	A	0.128 ± 0.015	EAP	A	< 0.085	PAP	U
IC 2637	11h13m49.7s	+09d35m11s	1.442 ± 0.099	EAP	A	0.554 ± 0.041	EAP	A	0.189 ± 0.025	EAP	A
ARP 151	11h25m36.2s	+54d22m57s	< 0.062	PAP	U	< 0.053	PAP	U	< 0.063	PAP	U
ESO 439-G009	11h27m23.4s	-29d15m27s	1.206 ± 0.100	EAP	A	0.541 ± 0.056	EAP	A	0.168 ± 0.034	EAP	A
NGC 3718	11h32m34.9s	+53d04m05s	5.423 ± 0.842	EAP	A	3.170 ± 0.448	EAP	A	1.282 ± 0.233	EAP	A
IC 2921	11h32m49.3s	+10d17m47s	0.097 ± 0.009	TF	A	< 0.077	PAP	U	< 0.075	PAP	U
Mrk 739E	11h36m29.4s	+21d35m46s	1.007 ± 0.056	TF	A	0.459 ± 0.026	TF	A	0.166 ± 0.013	TF	A
IGR J11366-6002	11h36m42.0s	-60d03m07s	0.700 ± 0.104	PAP	A	< 0.539	PAP	U	< 0.573	PAP	U
NGC 3783	11h39m01.8s	-37d44m19s	2.864 ± 0.244	EAP	A	1.187 ± 0.101	EAP	A	0.402 ± 0.050	EAP	A
NGC 3786	11h39m42.6s	+31d54m33s	1.943 ± 0.231	EAP	AD	0.834 ± 0.116	EAP	AD	0.286 ± 0.044	EAP	AD
KUG 1141+371	11h44m29.9s	+36d53m09s	0.085 ± 0.016	EAP	A	< 0.075	EAP	U	< 0.082	PAP	U
UGC 06728	11h45m16.0s	+79d40m53s	< 0.122	PAP	UC	< 0.195	PAP	UC	< 0.189	PAP	UC
2MASX J11454045-1827149	11h45m40.5s	-18d27m16s	0.136 ± 0.009	TF	A	0.060 ± 0.006	TF	A	< 0.062	PAP	U
MCG +05-28-032	11h48m45.9s	+29d38m28s	0.500 ± 0.028	TF	Ad	0.214 ± 0.013	TF	AD	0.086 ± 0.009	TF	AD
MCG -01-30-041	11h52m38.2s	-05d12m26s	0.735 ± 0.053	EAP	A	0.321 ± 0.028	EAP	A	< 0.093	EAP	U
2MASX J12005792+0648226	12h00m57.9s	+06d48m23s	0.423 ± 0.024	TF	A	0.181 ± 0.012	TF	A	0.060 ± 0.010	TF	A
Mrk 1310	12h01m14.4s	-03d40m41s	0.154 ± 0.016	EAP	A	0.070 ± 0.014	EAP	A	< 0.082	PAP	U
LEDA 38038	12h02m47.6s	-53d50m08s	0.427 ± 0.024	TF	A	0.167 ± 0.011	TF	A	< 0.074	PAP	U
NGC 4051	12h03m09.6s	+44d31m53s	21.713 ± 1.666	EAP	A	9.679 ± 0.853	EAP	A	3.355 ± 0.321	EAP	A
ARK 347	12h04m29.7s	+20d18m58s	0.254 ± 0.015	TF	A	0.116 ± 0.009	TF	A	< 0.076	PAP	U
UGC 07064	12h04m43.3s	+31d10m38s	1.253 ± 0.089	EAP	Ad	0.555 ± 0.056	EAP	Ad	0.233 ± 0.030	PAP	AD
NGC 4102	12h06m23.0s	+52d42m40s	20.453 ± 1.343	EAP	A	7.792 ± 0.514	EAP	A	2.409 ± 0.168	EAP	A
Mrk 198	12h09m14.1s	+47d03m30s	0.342 ± 0.020	TF	A	0.152 ± 0.010	TF	A	0.064 ± 0.010	TF	A
NGC 4138	12h09m29.8s	+43d41m07s	3.642 ± 0.282	EAP	A	1.531 ± 0.128	EAP	A	0.589 ± 0.068	EAP	A
NGC 4151	12h10m32.6s	+39d24m21s	4.118 ± 0.368	EAP	A	1.804 ± 0.191	EAP	A	0.599 ± 0.104	EAP	A
KUG 1208+386	12h10m44.3s	+38d20m10s	0.070 ± 0.007	TF	A	0.033 ± 0.006	TF	A	< 0.082	PAP	U
NGC 4180	12h13m03.0s	+07d02m20s	3.908 ± 0.262	EAP	A	1.568 ± 0.109	EAP	A	0.545 ± 0.043	EAP	A
NGC 4235	12h17m09.9s	+07d11m30s	0.706 ± 0.058	EAP	A	0.307 ± 0.043	EAP	A	0.110 ± 0.020	EAP	A
Mrk 202	12h17m55.0s	+58d39m35s	0.123 ± 0.021	EAP	A	< 0.141	EAP	U	< 0.098	PAP	U
Mrk 766	12h18m26.5s	+29d48m46s	0.898 ± 0.050	TF	A	0.347 ± 0.020	TF	A	0.123 ± 0.011	TF	A
M 106	12h18m57.5s	+47d18m14s	53.312 ± 4.758	EAP	A	24.318 ± 2.817	EAP	A	9.355 ± 1.607	EAP	A
Mrk 50	12h23m24.1s	+02d40m45s	0.063 ± 0.007	TF	A	< 0.071	PAP	U	< 0.068	PAP	U

Table C.1 – continued from previous page

Name	RA (J2000)	DEC (J2000)	F_{250} (Jy)	Method 250	Flag 250	F_{350} (Jy)	Method 350	Flag$_{350}$ 350	F_{500} (Jy)	Method 500	Flag 500
NGC 4388	12h25m46.7s	+12d39m44s	7.866 ± 0.524	EAP	A	3.319 ± 0.242	EAP	A	1.245 ± 0.104	EAP	A
2MASX J12313717-4758019	12h31m37.2s	-47d58m02s	0.695 ± 0.039	TF	A	0.294 ± 0.017	TF	A	0.098 ± 0.010	TF	A
2MASX J12335145-2103448	12h33m51.4s	-21d03m45s	0.106 ± 0.009	TF	A	0.042 ± 0.008	TF	A	< 0.054	TF	U
NGC 4507	12h35m36.6s	-39d54m33s	2.686 ± 0.194	EAP	A	1.120 ± 0.095	EAP	A	0.423 ± 0.041	EAP	A
ESO 506-G027	12h38m54.6s	-27d18m28s	1.129 ± 0.091	EAP	A	0.547 ± 0.058	EAP	A	< 0.190	EAP	U
LEDA 170194	12h39m06.3s	-16d10m47s	0.377 ± 0.042	EAP	Ad	0.160 ± 0.028	EAP	Ad	< 0.098	PAP	Ud
Mrk 653	12h39m51.7s	+34d58m30s	0.271 ± 0.030	EAP	A	0.142 ± 0.025	EAP	A	< 0.067	PAP	U
WKK 1263	12h41m25.7s	-57d50m04s	0.313 ± 0.018	TF	AC	0.129 ± 0.012	TF	AC	< 0.144	PAP	UC
NGC 4619	12h41m44.5s	+35d03m46s	2.133 ± 0.146	EAP	A	0.892 ± 0.079	EAP	A	0.303 ± 0.030	EAP	A
2MASX J12475784-5829599	12h47m57.8s	-58d30m00s	< 0.337	PAP	UC	< 0.298	PAP	UC	< 0.236	PAP	UC
NGC 4748	12h52m12.5s	-13d24m53s	1.104 ± 0.089	EAP	A	0.474 ± 0.057	EAP	A	0.138 ± 0.020	EAP	A
MCG -01-33-063	13h00m19.1s	-08d05m15s	0.871 ± 0.068	EAP	A	0.400 ± 0.038	EAP	A	0.160 ± 0.024	EAP	A
SBS 1301+540	13h03m59.5s	+53d47m30s	0.087 ± 0.009	TF	A	0.055 ± 0.009	TF	A	< 0.087	PAP	U
NGC 4941	13h04m13.1s	-05d33m06s	5.442 ± 0.474	EAP	A	2.767 ± 0.256	EAP	A	0.992 ± 0.177	EAP	A
NGC 4939	13h04m14.4s	-10d20m23s	9.492 ± 0.750	EAP	A	4.582 ± 0.398	EAP	A	1.762 ± 0.154	EAP	A
ESO 323-077	13h06m26.1s	-40d24m53s	2.897 ± 0.201	EAP	A	1.149 ± 0.090	EAP	A	0.382 ± 0.033	EAP	A
NGC 4992	13h09m05.6s	+11d38m03s	0.512 ± 0.051	EAP	Ad	0.256 ± 0.024	EAP	AD	0.092 ± 0.012	EAP	AD
II SZ 010	13h13m05.8s	-11d07m42s	0.056 ± 0.007	TF	A	< 0.090	PAP	U	< 0.065	PAP	U
NGC 5033	13h13m27.5s	+36d35m38s	40.780 ± 2.852	EAP	A	18.221 ± 1.363	EAP	A	6.474 ± 0.574	EAP	A
UGC 08327 NED02	13h15m17.3s	+44d24m26s	0.316 ± 0.018	TF	AD	0.111 ± 0.008	TF	AD	0.117 ± 0.016	PAP	AD
NGC 5106	13h20m59.6s	+08d58m42s	1.871 ± 0.130	EAP	Ad	0.734 ± 0.051	EAP	Ad	0.330 ± 0.030	PAP	AD
MCG -03-34-064	13h22m24.5s	-16d43m42s	0.986 ± 0.055	TF	A	0.384 ± 0.023	TF	A	0.124 ± 0.011	TF	A
Cen A	13h25m27.6s	-43d01m09s	301.332 ± 21.138	EAP	A	123.527 ± 9.057	EAP	A	48.112 ± 3.648	EAP	A
ESO 509-G038	13h31m13.9s	-25d24m10s	0.344 ± 0.020	TF	A	0.150 ± 0.011	TF	A	0.060 ± 0.009	TF	A
ESO 383-18	13h33m26.1s	-34d00m53s	0.252 ± 0.015	TF	A	0.132 ± 0.010	TF	A	0.055 ± 0.009	TF	A
ESO 509-IG066NED01	13h34m39.6s	-23d26m48s	0.763 ± 0.068	EAP	A	0.319 ± 0.036	EAP	A	< 0.125	EAP	U
NGC 5231	13h35m48.2s	+02d59m56s	0.777 ± 0.061	EAP	A	0.348 ± 0.040	EAP	A	0.179 ± 0.030	EAP	A
MCG -06-30-015	13h35m53.7s	-34d17m44s	0.233 ± 0.014	TF	A	0.086 ± 0.008	TF	A	< 0.092	PAP	U
NGC 5252	13h38m16.0s	+04d32m33s	0.395 ± 0.065	EAP	A	< 0.158	EAP	U	< 0.092	PAP	U
2MASX J13411287-1438407	13h41m12.9s	-14d38m41s	0.176 ± 0.025	EAP	A	0.087 ± 0.015	EAP	A	< 0.089	PAP	U
NGC 5273	13h42m08.3s	+35d39m15s	0.327 ± 0.041	EAP	A	0.161 ± 0.027	EAP	A	< 0.069	EAP	U
CGCG 102-048	13h44m15.7s	+19d34m00s	0.225 ± 0.033	EAP	A	0.165 ± 0.031	EAP	A	< 0.081	EAP	U
NGC 5290	13h45m19.2s	+41d42m45s	4.998 ± 0.336	EAP	A	2.260 ± 0.173	EAP	A	0.788 ± 0.071	EAP	A
4U 1344-60	13h47m36.0s	-60d37m04s	< 2.141	PAP	UC	< 1.657	PAP	UC	< 1.295	PAP	UC
IC 4329A	13h49m19.3s	-30d18m34s	0.488 ± 0.073	EAP	A	0.170 ± 0.030	EAP	Ad	0.079 ± 0.014	EAP	AD
UM 614	13h49m52.8s	+02d04m45s	0.042 ± 0.006	TF	A	< 0.078	PAP	U	< 0.097	PAP	U
2MASX J13512953-1813468	13h51m29.5s	-18d13m47s	< 0.089	PAP	U	< 0.088	PAP	U	< 0.054	PAP	U
Mrk 279	13h53m03.4s	+69d18m30s	0.342 ± 0.020	TF	Ad	0.132 ± 0.010	TF	Ad	< 0.098	PAP	UD
ESO 578-G009	13h56m36.7s	-19d31m45s	0.571 ± 0.074	EAP	A	0.250 ± 0.045	EAP	A	< 0.096	EAP	U
2MASX J14080674-3023537	14h08m06.8s	-30d23m54s	< 0.060	PAP	U	< 0.076	PAP	U	< 0.128	PAP	U

Table C.1 – continued from previous page

Name	RA (J2000)	DEC (J2000)	F_{250} (Jy)	Method 250	Flag 250	F_{350} (Jy)	Method 350	Flag$_{350}$ 350	F_{500} (Jy)	Method 500	Flag 500
NGC 5506	14h13m14.9s	-03d12m27s	2.730 ± 0.185	EAP	A	1.149 ± 0.086	EAP	A	0.370 ± 0.032	EAP	A
NGC 5548	14h17m59.5s	+25d08m12s	0.809 ± 0.068	EAP	A	0.321 ± 0.040	EAP	A	< 0.089	EAP	U
ESO 511-G030	14h19m22.4s	-26d38m41s	2.035 ± 0.245	EAP	A	0.982 ± 0.139	EAP	A	< 0.342	EAP	U
NGC 5610	14h24m22.9s	+24d36m51s	2.989 ± 0.198	EAP	A	1.225 ± 0.094	EAP	A	0.434 ± 0.047	EAP	A
NGC 5674	14h33m52.2s	+05d27m30s	2.233 ± 0.155	EAP	A	0.964 ± 0.080	EAP	A	0.340 ± 0.031	EAP	A
NGC 5683	14h34m52.4s	+48d39m43s	< 0.140	EAP	UD	< 0.118	PAP	UD	< 0.086	PAP	UD
Mrk 817	14h36m22.1s	+58d47m39s	0.561 ± 0.031	TF	A	0.244 ± 0.015	TF	A	0.079 ± 0.010	TF	A
Mrk 477	14h40m38.1s	+53d30m16s	0.248 ± 0.015	TF	A	0.090 ± 0.009	TF	Ad	< 0.056	PAP	UD
NGC 5728	14h42m23.9s	-17d15m11s	7.103 ± 0.501	EAP	A	3.164 ± 0.241	EAP	A	1.038 ± 0.095	EAP	A
WKK 4374	14h51m33.1s	-55d40m38s	< 2.550	PAP	UC	< 1.839	PAP	UC	< 1.399	PAP	UC
2MASX J14530794+2554327	14h53m07.9s	+25d54m33s	< 0.068	PAP	U	< 0.079	PAP	U	< 0.075	PAP	U
WKK 4438	14h55m17.4s	-51d34m15s	< 0.740	PAP	UC	< 0.806	PAP	UC	< 0.536	PAP	UC
IC 4518A	14h57m41.2s	-43d07m56s	5.663 ± 0.390	EAP	AD	2.297 ± 0.175	EAP	AD	0.788 ± 0.094	EAP	AD
Mrk 841	15h04m01.2s	+10d26m16s	0.061 ± 0.009	TF	A	< 0.062	PAP	U	< 0.055	PAP	U
Mrk 1392	15h05m56.6s	+03d42m26s	0.552 ± 0.055	EAP	A	0.241 ± 0.036	EAP	A	< 0.083	EAP	U
2MASX J15064412+0351444	15h06m44.1s	+03d51m44s	0.056 ± 0.008	TF	A	< 0.093	PAP	U	< 0.095	PAP	U
2MASX J15115979-2119015	15h11m59.8s	-21d19m02s	0.612 ± 0.034	TF	A	0.240 ± 0.015	TF	A	0.088 ± 0.014	TF	A
NGC 5899	15h15m03.2s	+42d02m59s	8.324 ± 0.577	EAP	A	3.763 ± 0.291	EAP	A	1.337 ± 0.109	EAP	A
CGCG 319-007	15h19m33.7s	+65d35m59s	0.335 ± 0.020	TF	A	0.137 ± 0.011	TF	A	< 0.047	TF	U
MCG -01-40-001	15h33m20.7s	-08d42m02s	1.524 ± 0.135	EAP	A	0.707 ± 0.122	EAP	A	0.230 ± 0.045	EAP	A
Mrk 290	15h35m52.4s	+57d54m09s	0.049 ± 0.007	TF	A	< 0.084	PAP	U	< 0.069	PAP	U
2MASX J15462424+6929102	15h46m24.3s	+69d29m10s	< 0.043	TF	U	< 0.061	PAP	U	< 0.079	PAP	U
NGC 5995	15h48m25.0s	-13d45m28s	2.501 ± 0.172	EAP	A	1.002 ± 0.070	EAP	A	0.325 ± 0.027	EAP	Ad
WKK 6092	16h11m51.4s	-60d37m55s	< 0.079	PAP	U	< 0.092	PAP	U	< 0.082	PAP	U
WKK 6471	16h18m36.4s	-59d27m17s	< 0.361	PAP	UC	< 0.222	PAP	UC	< 0.165	PAP	UC
CGCG 367-009	16h19m19.3s	+81d02m48s	< 0.210	EAP	U	< 0.166	EAP	U	< 0.101	PAP	U
Mrk 885	16h29m48.3s	+67d22m42s	0.456 ± 0.040	EAP	A	0.189 ± 0.019	EAP	A	0.065 ± 0.013	EAP	A
ESO 137-34	16h35m14.1s	-58d04m48s	3.433 ± 0.471	EAP	A	1.415 ± 0.259	EAP	A	< 0.553	EAP	U
2MASX J16481523-3035037	16h48m15.3s	-30d35m04s	< 0.156	EAP	U	< 0.173	PAP	U	< 0.136	PAP	U
LEDA 214543	16h50m42.7s	+04d36m18s	0.182 ± 0.012	TF	Ad	0.099 ± 0.009	TF	Ad	< 0.099	PAP	Ud
UGC 10593	16h52m18.9s	+55d54m20s	0.464 ± 0.043	EAP	A	0.237 ± 0.033	EAP	A	< 0.107	EAP	U
NGC 6221	16h52m46.1s	-59d13m07s	41.624 ± 2.749	EAP	A	16.335 ± 1.120	EAP	A	5.319 ± 0.383	EAP	A
NGC 6240	16h52m58.9s	+02d24m03s	6.162 ± 0.411	EAP	A	2.451 ± 0.168	EAP	A	0.794 ± 0.062	EAP	A
NGC 6300	17h16m59.5s	-62d49m14s	29.767 ± 2.011	EAP	A	13.115 ± 0.981	EAP	A	4.559 ± 0.341	EAP	A
ARP 102B	17h19m14.5s	+48d58m49s	0.050 ± 0.006	TF	A	< 0.083	PAP	U	< 0.116	PAP	U
AX J1737.4-2907	17h37m28.4s	-29d08m03s	< 2.558	PAP	UC	< 2.054	PAP	UC	< 1.445	PAP	UC
ESO 139-G012	17h37m39.1s	-59d56m27s	2.311 ± 0.207	EAP	A	1.065 ± 0.118	EAP	A	0.333 ± 0.040	EAP	A
2E 1739.1-1210	17h41m55.3s	-12d11m57s	< 0.590	EAP	U	< 0.342	EAP	U	< 0.114	EAP	U
CGCG 300-062	17h43m17.4s	+62d50m21s	0.234 ± 0.027	EAP	Ad	0.112 ± 0.018	EAP	Ad	< 0.082	EAP	Ud
2MASS J17485512-3254521	17h48m55.1s	-32d54m52s	< 0.781	PAP	UC	< 0.707	PAP	UC	< 0.484	PAP	UC

Table C.1 – continued from previous page

Name	RA (J2000)	DEC (J2000)	F_{250} (Jy)	Method 250	Flag 250	F_{350} (Jy)	Method 350	Flag$_{350}$ 350	F_{500} (Jy)	Method 500	Flag 500
NGC 6552	18h00m07.3s	+66d36m54s	0.707 ± 0.039	TF	A	0.297 ± 0.018	TF	A	0.102 ± 0.010	TF	A
2MASXi J1802473-145454	18h02m47.3s	-14d54m55s	< 0.953	PAP	UC	< 0.651	PAP	UC	< 0.355	PAP	UC
UGC 11185 NED02	18h16m11.5s	+42d39m37s	0.269 ± 0.023	PAP	AD	0.220 ± 0.026	EAP	AD	< 0.062	EAP	UD
IC 4709	18h24m19.4s	-56d22m09s	0.623 ± 0.064	EAP	A	0.264 ± 0.046	EAP	A	< 0.103	EAP	U
Fairall 49	18h36m58.3s	-59d24m09s	0.872 ± 0.048	TF	A	0.339 ± 0.020	TF	A	0.123 ± 0.012	TF	A
ESO 103-035	18h38m20.3s	-65d25m39s	0.159 ± 0.011	TF	A	0.074 ± 0.009	TF	A	< 0.084	PAP	U
Fairall 51	18h44m54.0s	-62d21m53s	1.071 ± 0.118	EAP	A	0.560 ± 0.073	PAP	A	< 0.243	EAP	U
CGCG 341-006	18h45m26.2s	+72d11m02s	0.340 ± 0.020	TF	A	0.135 ± 0.010	TF	A	0.057 ± 0.009	TF	A
2MASX J18570768-7828212	18h57m07.8s	-78d28m21s	0.195 ± 0.024	EAP	A	< 0.103	EAP	U	< 0.086	PAP	U
CGCG 229-015	19h05m25.9s	+42d27m40s	0.149 ± 0.010	TF	A	0.080 ± 0.008	TF	A	< 0.082	PAP	U
ESO 141-G055	19h21m14.1s	-58d40m13s	0.629 ± 0.072	EAP	A	0.297 ± 0.052	EAP	A	< 0.150	EAP	U
2MASX J19373299-0613046	19h37m33.0s	-06d13m05s	1.901 ± 0.133	EAP	A	0.700 ± 0.057	EAP	A	0.203 ± 0.029	EAP	A
2MASX J19380437-5109497	19h38m04.4s	-51d09m50s	0.218 ± 0.035	EAP	A	0.093 ± 0.017	EAP	A	< 0.042	EAP	U
NGC 6814	19h42m40.6s	-10d19m25s	12.881 ± 0.977	EAP	A	5.960 ± 0.497	EAP	A	2.432 ± 0.229	EAP	A
2MASX J20005575-1810274	20h00m55.7s	-18d10m27s	0.269 ± 0.032	EAP	A	0.172 ± 0.025	EAP	A	< 0.064	PAP	U
ESO 399-20	20h06m57.7s	-34d32m58s	0.853 ± 0.061	EAP	A	0.404 ± 0.041	EAP	A	0.121 ± 0.020	EAP	A
NGC 6860	20h08m46.9s	-61d06m01s	1.555 ± 0.119	EAP	A	0.728 ± 0.076	EAP	A	0.253 ± 0.030	EAP	A
2MASX J20101740+4800214	20h10m17.4s	+48d00m21s	0.176 ± 0.032	EAP	A	< 0.097	EAP	U	< 0.088	PAP	U
2MASX J20183871+4041003	20h18m38.7s	+40d41m00s	< 4.476	PAP	UC	< 3.169	PAP	UC	< 1.648	PAP	UC
II Zw 083	20h26m55.9s	-02d16m39s	0.578 ± 0.054	EAP	A	0.240 ± 0.034	EAP	A	0.081 ± 0.014	EAP	A
MCG +04-48-002	20h28m35.1s	+25d44m00s	4.234 ± 0.330	EAP	AC	1.644 ± 0.194	EAP	AC	0.502 ± 0.088	EAP	AC
Mrk 509	20h44m09.7s	-10d43m25s	0.393 ± 0.023	TF	A	0.156 ± 0.011	TF	A	0.044 ± 0.009	TF	A
IC 5063	20h52m02.3s	-57d04m08s	2.205 ± 0.198	EAP	A	1.027 ± 0.121	EAP	A	0.354 ± 0.058	EAP	A
ESO 464-G016	21h02m23.8s	-28d10m29s	0.244 ± 0.015	TF	Ad	0.136 ± 0.019	PAP	AD	< 0.096	PAP	UD
2MASX J21090996-0940147	21h09m10.0s	-09d40m15s	0.156 ± 0.012	PAP	AC	0.085 ± 0.012	PAP	AC	< 0.109	PAP	UC
SWIFT J212745.6+565636	21h27m45.8s	+56d57m07s	< 0.135	PAP	UC	< 0.131	PAP	UC	< 0.133	PAP	UC
6dF J2132022-334254	21h32m02.2s	-33d42m54s	< 0.074	PAP	U	< 0.089	PAP	U	< 0.061	PAP	U
2MASX J21355399+4728217	21h35m54.0s	+47d28m22s	0.408 ± 0.066	PAP	AC	< 0.244	PAP	UC	< 0.176	PAP	UC
CGCG 493-002	21h38m33.4s	+32d05m06s	0.192 ± 0.012	TF	A	0.093 ± 0.009	TF	A	< 0.064	PAP	U
NGC 7172	22h02m01.9s	-31d52m11s	6.012 ± 0.399	EAP	A	2.477 ± 0.172	EAP	A	0.802 ± 0.057	EAP	A
NGC 7213	22h09m16.3s	-47d10m00s	6.537 ± 0.574	EAP	A	2.725 ± 0.405	EAP	A	0.834 ± 0.067	EAP	A
MCG +02-57-002	22h23m45.0s	+11d50m09s	0.265 ± 0.016	TF	A	0.166 ± 0.012	TF	A	0.071 ± 0.009	TF	A
MCG +06-49-019	22h27m05.8s	+36d21m42s	0.523 ± 0.070	EAP	A	0.241 ± 0.038	EAP	A	< 0.076	EAP	U
ESO 533-G050	22h34m49.8s	-25d40m37s	0.658 ± 0.076	EAP	A	0.314 ± 0.058	EAP	A	< 0.169	EAP	U
MCG +01-57-016	22h40m17.0s	+08d03m14s	0.544 ± 0.050	EAP	A	0.212 ± 0.035	EAP	A	< 0.088	EAP	U
UGC 12237	22h54m19.7s	+11d46m57s	0.909 ± 0.123	EAP	A	0.434 ± 0.066	EAP	A	< 0.183	EAP	U
UGC 12282	22h58m55.5s	+40d55m53s	2.595 ± 0.231	EAP	A	1.241 ± 0.137	EAP	A	0.455 ± 0.070	EAP	A
KAZ 320	22h59m32.9s	+24d55m06s	0.110 ± 0.009	TF	A	0.048 ± 0.007	TF	A	< 0.101	PAP	U
NGC 7465	23h02m01.0s	+15d57m53s	2.496 ± 0.245	EAP	A	1.068 ± 0.159	EAP	A	0.339 ± 0.066	EAP	A
NGC 7469	23h03m15.6s	+08d52m26s	11.345 ± 0.847	EAP	A	4.491 ± 0.363	EAP	Ad	1.381 ± 0.130	EAP	AD

Table C.1 – continued from previous page

Name	RA (J2000)	DEC (J2000)	F_{250} (Jy)	Method 250	Flag 250	F_{350} (Jy)	Method 350	Flag$_{350}$ 350	F_{500} (Jy)	Method 500	Flag 500
Mrk 926	23h04m43.5s	-08d41m09s	0.325 ± 0.038	EAP	A	0.127 ± 0.016	EAP	A	< 0.074	PAP	U
NGC 7479	23h04m56.7s	+12d19m22s	17.341 ± 1.271	EAP	A	7.510 ± 0.648	EAP	A	2.692 ± 0.263	EAP	A
PG 2304+042	23h07m02.9s	+04d32m57s	< 0.083	PAP	U	< 0.084	PAP	U	< 0.113	PAP	U
NGC 7582	23h18m23.5s	-42d22m14s	29.800 ± 1.958	EAP	A	11.826 ± 0.781	EAP	A	3.798 ± 0.265	EAP	A
NGC 7603	23h18m56.6s	+00d14m38s	1.250 ± 0.089	EAP	A	0.540 ± 0.042	EAP	A	0.220 ± 0.028	EAP	A
LCRS B232242.2-384320	23h25m24.2s	-38d26m49s	0.498 ± 0.028	TF	A	0.221 ± 0.014	TF	A	0.082 ± 0.011	TF	A
2MASX J23272195+1524375	23h27m22.0s	+15d24m37s	0.171 ± 0.011	TF	A	0.142 ± 0.010	TF	A	0.150 ± 0.012	TF	A
NGC 7679	23h28m46.7s	+03d30m41s	2.960 ± 0.198	EAP	A	1.101 ± 0.079	EAP	A	0.379 ± 0.040	EAP	A
IGR J23308+7120	23h30m37.7s	+71d22m46s	0.370 ± 0.039	EAP	A	< 0.204	EAP	U	< 0.114	EAP	U
PKS 2331-240	23h33m55.2s	-23d43m41s	0.406 ± 0.023	TF	A	0.481 ± 0.027	TF	A	0.569 ± 0.033	TF	A
UGC 12741	23h41m55.5s	+30d34m54s	0.516 ± 0.049	EAP	A	0.248 ± 0.028	EAP	A	0.086 ± 0.017	EAP	A

Notes. – *Column 1:* Name of the source. *Column 2:* Right ascension in J2000 coordinates. *Column 3:* Declination in J2000 coordinates. *Column 4:* 250 μm flux density and 1σ uncertainty in units of Jy. 5σ upper limits are given for undetected sources. *Column 5:* Method used to extract the photometry. Either "TF" for timeline fitting, "PAP" for point sources aperture photometry, or "EAP" for extended source aperture photometry. See text for details on the differences. *Column 6:* Flag for the photometry. "A" = source was detected at greater than 5σ. "U" = 5σ upper limit. "C" = likely foreground cirrus contamination. "d" = nearby companion however unlikely to affect photometry. "D" = nearby companion that is likely strongly affecting photometry. *Columns 7–9:* Same as Columns 4–6 except for the 350 μm waveband. *Columns 10–12:* Same as Columns 4–6 except for the 500 μm waveband.

Appendix D: Table of Best Fit Parameters from SED Modeling

Table D.1: Best Fit C12 Model Parameters, Luminosities, and AGN Fractions

Name	log $M_{\rm dust}$ [$\rm M_\odot$]	$T_{\rm dust}$ [K]	α	$\lambda_{\rm c}$ [μm]	log $L_{\rm IR}$ [$\rm L_\odot$]	log $L_{\rm SF}$ [$\rm L_\odot$]	log $L_{\rm AGN,IR}$ [$\rm L_\odot$]	$f_{\rm AGN,C12}$
1RXSJ044154.5-082639	$6.80^{+0.21}_{-0.14}$	$27.98^{+2.45}_{-4.21}$	$1.70^{+0.46}_{-0.34}$	$47.71^{+18.85}_{-13.96}$	$10.36^{+0.03}_{-0.04}$	$9.99^{+0.12}_{-0.23}$	$9.99^{+0.12}_{-0.23}$	$0.58^{+0.18}_{-0.15}$
1RXSJ045205.0+493248	$7.47^{+0.12}_{-0.10}$	$23.27^{+0.99}_{-1.61}$	$1.44^{+0.59}_{-0.46}$	$39.95^{+14.82}_{-13.09}$	$10.48^{+0.03}_{-0.03}$	$10.19^{+0.04}_{-0.08}$	$10.19^{+0.04}_{-0.08}$	$0.49^{+0.09}_{-0.08}$
2E1739.1-1210	$7.55^{+0.22}_{-0.19}$	$25.11^{+2.11}_{-3.00}$	$1.46^{+0.51}_{-0.37}$	$45.22^{+16.42}_{-14.16}$	$10.82^{+0.03}_{-0.04}$	$10.46^{+0.07}_{-0.14}$	$10.46^{+0.07}_{-0.14}$	$0.57^{+0.12}_{-0.11}$
2MASSJ07594181-3843560	< 6.82	...	$1.15^{+0.48}_{-0.44}$	$38.46^{+6.97}_{-4.91}$	< 10.63	< 9.51	> 10.47	> 0.91
2MASSJ17485512-3254521	< 6.34	...	$1.37^{+0.47}_{-0.41}$	$47.45^{+18.52}_{-15.85}$	< 9.40	< 9.02	> 9.01	> 0.54
2MASXJ00253292+6821442	$6.16^{+0.39}_{-0.18}$	$25.34^{+2.79}_{-5.06}$	$1.46^{+0.53}_{-0.40}$	$45.40^{+16.38}_{-15.93}$	$9.62^{+0.04}_{-0.05}$	$9.10^{+0.10}_{-0.19}$	$9.10^{+0.10}_{-0.19}$	$0.70^{+0.11}_{-0.12}$
2MASXJ01064523+0638015	$6.81^{+0.69}_{-0.44}$	$21.56^{+9.09}_{-7.50}$	$1.86^{+0.53}_{-0.42}$	$44.58^{+10.57}_{-9.10}$	$10.46^{+0.05}_{-0.05}$	$9.31^{+0.52}_{-0.42}$	$9.31^{+0.52}_{-0.42}$	$0.93^{+0.04}_{-0.16}$
2MASXJ01073963-1139117	$7.66^{+0.09}_{-0.06}$	$25.52^{+1.27}_{-1.96}$	$2.05^{+0.58}_{-0.49}$	$41.53^{+20.19}_{-10.35}$	$10.87^{+0.03}_{-0.03}$	$10.63^{+0.06}_{-0.11}$	$10.63^{+0.06}_{-0.11}$	$0.44^{+0.13}_{-0.12}$
2MASXJ03305218+0538253	$6.76^{+0.69}_{-0.33}$	$28.20^{+6.57}_{-8.76}$	$2.46^{+0.78}_{-0.61}$	$33.77^{+8.47}_{-9.67}$	$10.81^{+0.06}_{-0.07}$	$10.02^{+0.21}_{-0.32}$	$10.02^{+0.21}_{-0.32}$	$0.84^{+0.08}_{-0.13}$
2MASXJ03342453-1513402	$7.43^{+0.05}_{-0.04}$	$26.61^{+0.61}_{-1.09}$	$1.69^{+0.58}_{-0.44}$	$43.00^{+24.14}_{-16.10}$	$10.59^{+0.03}_{-0.03}$	$10.51^{+0.03}_{-0.07}$	$10.51^{+0.03}_{-0.07}$	$0.18^{+0.14}_{-0.09}$
2MASXJ03502377-5018354	$7.20^{+0.12}_{-0.09}$	$27.00^{+1.17}_{-2.09}$	$2.10^{+0.51}_{-0.44}$	$49.32^{+20.01}_{-19.27}$	$10.36^{+0.03}_{-0.03}$	$10.31^{+0.05}_{-0.10}$	< 10.13	< 0.47
2MASXJ03534246+3714077	$6.99^{+0.07}_{-0.04}$	$26.47^{+0.73}_{-1.65}$	$1.73^{+0.43}_{-0.42}$	$52.42^{+29.97}_{-19.70}$	$10.11^{+0.03}_{-0.02}$	$10.05^{+0.04}_{-0.10}$	$10.05^{+0.04}_{-0.10}$	$0.13^{+0.20}_{-0.09}$
2MASXJ03540948+0249307	< 6.85	...	$1.65^{+0.43}_{-0.35}$	$53.89^{+12.86}_{-9.17}$	< 10.45	< 9.53	> 10.30	> 0.87
2MASXJ04234080+0408017	$7.44^{+0.17}_{-0.10}$	$26.29^{+2.14}_{-3.61}$	$1.67^{+0.55}_{-0.30}$	$50.48^{+28.28}_{-12.35}$	$10.92^{+0.03}_{-0.03}$	$10.48^{+0.11}_{-0.19}$	$10.48^{+0.11}_{-0.19}$	$0.64^{+0.13}_{-0.12}$
2MASXJ04440903+2813003	$7.06^{+0.11}_{-0.14}$	$24.22^{+1.02}_{-0.83}$	$0.96^{+0.58}_{-0.42}$	$45.07^{+19.18}_{-16.82}$	$9.92^{+0.03}_{-0.03}$	$9.89^{+0.04}_{-0.04}$	< 9.16	< 0.17
2MASXJ05020903+0331499	$6.45^{+0.57}_{-0.22}$	$20.60^{+3.06}_{-6.21}$	$1.62^{+0.37}_{-0.30}$	$58.47^{+16.68}_{-16.96}$	$9.21^{+0.03}_{-0.03}$	$8.84^{+0.18}_{-0.37}$	$8.84^{+0.18}_{-0.37}$	$0.59^{+0.22}_{-0.22}$
2MASXJ05054575-2351139	$7.29^{+0.35}_{-0.39}$	$19.26^{+4.76}_{-3.13}$	$1.56^{+0.46}_{-0.35}$	$52.21^{+13.78}_{-9.95}$	$10.39^{+0.03}_{-0.04}$	$9.53^{+0.20}_{-0.14}$	$9.53^{+0.20}_{-0.14}$	$0.86^{+0.04}_{-0.08}$
2MASXJ05580206-3820043	< 6.75	...	$0.69^{+0.37}_{-0.34}$	$51.88^{+12.54}_{-7.51}$	< 11.03	< 9.39	> 10.88	> 0.97
2MASXJ06411806+3249313	< 6.49	...	$1.47^{+0.41}_{-0.34}$	$50.01^{+10.85}_{-7.19}$	< 10.50	< 9.21	> 10.36	> 0.94

Table D.1 – continued from previous page

Name	log $M_{\rm dust}$ [$M_\odot$]	$T_{\rm dust}$ [K]	α	$\lambda_{\rm c}$ [μm]	log $L_{\rm IR}$ [$L_\odot$]	log $L_{\rm SF}$ [$L_\odot$]	log $L_{\rm AGN,IR}$ [$L_\odot$]	$f_{\rm AGN}$
2MASXJ06561197-4919499	$7.34^{+0.33}_{-0.45}$	$19.56^{+5.69}_{-2.98}$	$1.93^{+0.48}_{-0.48}$	$41.99^{+9.57}_{-5.98}$	$10.78^{+0.06}_{-0.05}$	$9.62^{+0.23}_{-0.13}$	$9.62^{+0.23}_{-0.13}$	$0.93^{+0.02}_{-0.05}$
2MASXJ07262635-3554214	< 7.19	...	$1.99^{+0.47}_{-0.40}$	$48.47^{+10.88}_{-6.99}$	< 11.04	< 9.91	> 10.88	> 0.91
2MASXJ07595347+2323241	$8.18^{+0.03}_{-0.03}$	$24.36^{+0.33}_{-0.36}$	$1.26^{+0.52}_{-0.43}$	$44.50^{+18.59}_{-16.21}$	$11.01^{+0.02}_{-0.02}$	$11.03^{+0.01}_{-0.02}$	< 10.01	< 0.10
2MASXJ08032736+0841523	< 6.75	...	$1.52^{+0.61}_{-0.45}$	$43.15^{+19.37}_{-16.23}$	< 10.01	< 9.40	> 9.66	> 0.71
2MASXJ09023729-4813339	< 7.29	...	$1.20^{+0.40}_{-0.32}$	$57.14^{+15.79}_{-17.67}$	< 10.26	< 9.98	> 9.84	> 0.41
2MASXJ09043699+5536025	$6.72^{+0.54}_{-0.23}$	$25.56^{+4.92}_{-8.05}$	$2.18^{+0.45}_{-0.35}$	$51.93^{+14.12}_{-14.73}$	$10.14^{+0.03}_{-0.04}$	$9.67^{+0.25}_{-0.47}$	$9.67^{+0.25}_{-0.47}$	$0.67^{+0.22}_{-0.31}$
2MASXJ09235371-3141305	$6.37^{+0.15}_{-0.17}$	$30.80^{+2.18}_{-2.25}$	$1.63^{+0.48}_{-0.43}$	$46.95^{+19.81}_{-16.78}$	$9.96^{+0.03}_{-0.03}$	$9.84^{+0.05}_{-0.10}$	$9.84^{+0.05}_{-0.10}$	$0.23^{+0.18}_{-0.11}$
2MASXJ09254750+6927532	$7.12^{+0.39}_{-0.15}$	$21.92^{+2.54}_{-5.21}$	$0.99^{+0.54}_{-0.34}$	$50.12^{+17.56}_{-17.12}$	$10.30^{+0.04}_{-0.04}$	$9.67^{+0.16}_{-0.32}$	$9.67^{+0.16}_{-0.32}$	$0.77^{+0.12}_{-0.12}$
2MASXJ09360622-6548336	< 6.64	...	$1.06^{+0.56}_{-0.55}$	$45.65^{+18.02}_{-16.06}$	< 9.54	< 9.31	> 9.05	> 0.38
2MASXJ09594263-3112581	$7.44^{+0.19}_{-0.23}$	$21.04^{+2.96}_{-2.04}$	$1.28^{+0.38}_{-0.33}$	$51.92^{+12.14}_{-8.55}$	$10.71^{+0.04}_{-0.04}$	$9.90^{+0.12}_{-0.09}$	$9.90^{+0.12}_{-0.09}$	$0.85^{+0.03}_{-0.05}$
2MASXJ10402231-4625264	$7.29^{+0.06}_{-0.04}$	$27.14^{+0.82}_{-1.35}$	$1.76^{+0.68}_{-0.42}$	$43.71^{+20.95}_{-17.07}$	$10.56^{+0.03}_{-0.03}$	$10.42^{+0.04}_{-0.08}$	$10.42^{+0.04}_{-0.08}$	$0.29^{+0.14}_{-0.11}$
2MASXJ11454045-1827149	$6.99^{+0.09}_{-0.07}$	$26.76^{+1.31}_{-1.86}$	$1.19^{+0.45}_{-0.36}$	$47.98^{+19.49}_{-14.51}$	$10.44^{+0.03}_{-0.03}$	$10.07^{+0.06}_{-0.10}$	$10.07^{+0.06}_{-0.10}$	$0.58^{+0.09}_{-0.09}$
2MASXJ12005792+0648226	$7.65^{+0.05}_{-0.04}$	$24.42^{+0.68}_{-0.99}$	$1.50^{+0.49}_{-0.38}$	$48.46^{+17.16}_{-13.80}$	$10.64^{+0.02}_{-0.03}$	$10.50^{+0.04}_{-0.06}$	$10.50^{+0.04}_{-0.06}$	$0.27^{+0.10}_{-0.10}$
2MASXJ12313717-4758019	$7.54^{+0.05}_{-0.03}$	$27.15^{+0.57}_{-1.18}$	$2.03^{+0.66}_{-0.49}$	$39.37^{+21.42}_{-13.52}$	$10.76^{+0.03}_{-0.03}$	$10.67^{+0.03}_{-0.06}$	$10.67^{+0.03}_{-0.06}$	$0.20^{+0.12}_{-0.09}$
2MASXJ12335145-2103448	$6.50^{+0.11}_{-0.08}$	$28.47^{+1.66}_{-2.53}$	$1.83^{+0.48}_{-0.42}$	$42.97^{+14.87}_{-10.49}$	$10.09^{+0.04}_{-0.03}$	$9.75^{+0.07}_{-0.13}$	$9.75^{+0.07}_{-0.13}$	$0.55^{+0.13}_{-0.11}$
2MASXJ12475784-5829599	< 6.18	...	$1.57^{+0.53}_{-0.40}$	$45.87^{+18.40}_{-15.44}$	< 9.60	< 8.92	> 9.26	> 0.75
2MASXJ13411287-1438407	$7.85^{+0.14}_{-0.15}$	$17.17^{+1.31}_{-1.14}$	$1.14^{+0.43}_{-0.36}$	$49.88^{+10.82}_{-7.98}$	$10.68^{+0.04}_{-0.04}$	$9.78^{+0.06}_{-0.06}$	$9.78^{+0.06}_{-0.06}$	$0.87^{+0.02}_{-0.02}$
2MASXJ13512953-1813468	< 5.50	...	$0.84^{+0.56}_{-0.43}$	$45.63^{+18.92}_{-17.56}$	< 8.96	< 8.16	> 8.74	> 0.82
2MASXJ14080674-3023537	< 6.01	...	$1.40^{+0.71}_{-0.53}$	$36.02^{+12.48}_{-11.61}$	< 9.72	< 8.71	> 9.51	> 0.88
2MASXJ14530794+2554327	< 6.73	...	$0.52^{+0.52}_{-0.43}$	$45.93^{+18.19}_{-16.94}$	< 9.81	< 9.54	> 9.43	> 0.48
2MASXJ15064412+0351444	$6.78^{+0.11}_{-0.12}$	$24.61^{+1.06}_{-1.35}$	$1.60^{+0.50}_{-0.50}$	$51.64^{+18.16}_{-17.20}$	$9.68^{+0.03}_{-0.03}$	$9.64^{+0.05}_{-0.08}$	< 9.39	< 0.42
2MASXJ15115979-2119015	$7.85^{+0.09}_{-0.07}$	$27.56^{+1.84}_{-2.16}$	$1.85^{+0.48}_{-0.30}$	$51.26^{+19.38}_{-13.33}$	$11.32^{+0.03}_{-0.03}$	$11.02^{+0.10}_{-0.12}$	$11.02^{+0.10}_{-0.12}$	$0.50^{+0.13}_{-0.15}$
2MASXJ15462424+6929102	$6.24^{+0.35}_{-0.30}$	$31.75^{+4.71}_{-7.68}$	$2.66^{+0.61}_{-0.67}$	$37.70^{+18.44}_{-9.85}$	$10.17^{+0.05}_{-0.05}$	$9.77^{+0.16}_{-0.40}$	$9.77^{+0.16}_{-0.40}$	$0.61^{+0.24}_{-0.22}$
2MASXJ16481523-3035037	< 6.86	...	$1.23^{+0.29}_{-0.28}$	$69.83^{+13.42}_{-11.58}$	< 9.97	< 9.57	> 9.68	> 0.57
2MASXJ18570768-7828212	$7.42^{+0.18}_{-0.18}$	$23.83^{+2.98}_{-2.54}$	$1.42^{+0.38}_{-0.33}$	$51.80^{+14.00}_{-10.89}$	$10.77^{+0.03}_{-0.04}$	$10.21^{+0.13}_{-0.12}$	$10.21^{+0.13}_{-0.12}$	$0.72^{+0.07}_{-0.11}$
2MASXJ19373299-0613046	$7.12^{+0.03}_{-0.03}$	$26.70^{+0.41}_{-0.53}$	$1.97^{+0.75}_{-0.61}$	$32.15^{+12.19}_{-9.71}$	$10.34^{+0.03}_{-0.03}$	$10.20^{+0.02}_{-0.03}$	$10.20^{+0.02}_{-0.03}$	$0.27^{+0.07}_{-0.07}$
2MASXJ19380437-5109497	$7.79^{+0.13}_{-0.16}$	$17.60^{+1.41}_{-1.15}$	$1.36^{+0.38}_{-0.29}$	$55.25^{+13.25}_{-9.88}$	$10.20^{+0.03}_{-0.04}$	$9.79^{+0.06}_{-0.06}$	$9.79^{+0.06}_{-0.06}$	$0.61^{+0.05}_{-0.06}$
2MASXJ20005575-1810274	$7.48^{+0.16}_{-0.16}$	$25.31^{+3.05}_{-2.81}$	$1.21^{+0.43}_{-0.30}$	$53.38^{+17.36}_{-12.28}$	$11.11^{+0.03}_{-0.04}$	$10.41^{+0.15}_{-0.14}$	$10.41^{+0.15}_{-0.14}$	$0.80^{+0.06}_{-0.09}$
2MASXJ20101740+4800214	$6.97^{+0.11}_{-0.09}$	$24.09^{+0.96}_{-1.67}$	$1.70^{+0.50}_{-0.41}$	$46.99^{+16.94}_{-16.49}$	$9.90^{+0.03}_{-0.03}$	$9.78^{+0.04}_{-0.09}$	$9.78^{+0.04}_{-0.09}$	$0.25^{+0.16}_{-0.10}$
2MASXJ20183871+4041003	< 7.26	...	$0.96^{+0.51}_{-0.43}$	$45.56^{+19.68}_{-17.11}$	< 10.04	< 9.91	> 9.39	> 0.22
2MASXJ21090996-0940147	$7.36^{+0.14}_{-0.14}$	$18.13^{+1.59}_{-1.46}$	$1.21^{+0.38}_{-0.29}$	$56.85^{+13.27}_{-9.29}$	$10.48^{+0.04}_{-0.04}$	$9.42^{+0.10}_{-0.09}$	$9.42^{+0.10}_{-0.09}$	$0.91^{+0.02}_{-0.02}$

Table D.1 – continued from previous page

Name	log $M_{\rm dust}$ [$M_\odot$]	$T_{\rm dust}$ [K]	α	$\lambda_{\rm c}$ [μm]	log $L_{\rm IR}$ [$L_\odot$]	log $L_{\rm SF}$ [$L_\odot$]	log $L_{\rm AGN,IR}$ [$L_\odot$]	$f_{\rm AGN}$
2MASXJ21355399+4728217	$7.35^{+0.19}_{-0.15}$	$23.19^{+2.04}_{-2.58}$	$1.58^{+0.42}_{-0.32}$	$51.11^{+14.51}_{-13.50}$	$10.42^{+0.03}_{-0.03}$	$10.06^{+0.09}_{-0.12}$	$10.06^{+0.09}_{-0.12}$	$0.56^{+0.13}_{-0.12}$
2MASXJ23272195+1524375	$9.16^{+0.30}_{-0.28}$	$9.23^{+1.48}_{-1.28}$	$1.17^{+0.13}_{-0.10}$	$131.95^{+16.95}_{-22.95}$	$10.42^{+0.03}_{-0.03}$	$9.47^{+0.13}_{-0.09}$	$9.47^{+0.13}_{-0.09}$	$0.88^{+0.03}_{-0.03}$
2MASXiJ1802473-145454	$7.81^{+0.11}_{-0.11}$	$26.02^{+1.05}_{-1.14}$	$1.35^{+0.51}_{-0.43}$	$44.39^{+19.31}_{-15.12}$	$10.91^{+0.03}_{-0.03}$	$10.82^{+0.03}_{-0.05}$	$10.82^{+0.03}_{-0.05}$	$0.18^{+0.09}_{-0.07}$
2MFGC02280	$7.04^{+0.05}_{-0.04}$	$27.10^{+0.55}_{-0.75}$	$1.70^{+0.64}_{-0.47}$	$43.73^{+23.32}_{-16.70}$	$10.16^{+0.02}_{-0.02}$	$10.16^{+0.02}_{-0.03}$	< 9.67	< 0.21
3C111.0	$9.98^{+0.01}_{-0.02}$	$8.92^{+0.10}_{-0.08}$	$1.05^{+0.12}_{-0.10}$	$104.00^{+11.96}_{-14.03}$	$10.84^{+0.03}_{-0.03}$	$10.20^{+0.02}_{-0.02}$	$10.20^{+0.02}_{-0.02}$	$0.77^{+0.01}_{-0.02}$
3C120	$9.80^{+0.12}_{-0.15}$	$7.45^{+0.56}_{-0.41}$	$1.26^{+0.09}_{-0.09}$	$132.76^{+5.59}_{-5.85}$	$11.06^{+0.03}_{-0.03}$	$9.55^{+0.05}_{-0.04}$	$9.55^{+0.05}_{-0.04}$	$0.97^{+0.00}_{-0.00}$
4U1344-60	< 7.09	...	$1.84^{+0.34}_{-0.24}$	$63.90^{+12.85}_{-9.92}$	< 10.38	< 9.76	> 10.23	> 0.75
6dFJ0626586-370559	$7.59^{+0.08}_{-0.08}$	$21.89^{+1.20}_{-1.21}$	$1.30^{+0.38}_{-0.29}$	$56.73^{+16.97}_{-13.78}$	$10.42^{+0.02}_{-0.03}$	$10.16^{+0.06}_{-0.08}$	$10.16^{+0.06}_{-0.08}$	$0.46^{+0.10}_{-0.10}$
6dFJ2132022-334254	< 6.23	...	$1.83^{+0.51}_{-0.51}$	$41.63^{+9.53}_{-5.42}$	< 10.20	< 8.91	> 10.00	> 0.94
ARK241	$8.06^{+0.25}_{-0.26}$	$14.38^{+2.38}_{-1.92}$	$1.21^{+0.37}_{-0.30}$	$55.00^{+12.77}_{-8.70}$	$10.34^{+0.04}_{-0.04}$	$9.54^{+0.14}_{-0.14}$	$9.54^{+0.14}_{-0.14}$	$0.84^{+0.04}_{-0.06}$
ARK347	$7.15^{+0.07}_{-0.08}$	$22.10^{+1.20}_{-1.12}$	$1.49^{+0.43}_{-0.35}$	$51.85^{+14.03}_{-8.93}$	$10.25^{+0.04}_{-0.04}$	$9.75^{+0.06}_{-0.07}$	$9.75^{+0.06}_{-0.07}$	$0.69^{+0.05}_{-0.05}$
ARP102B	$6.48^{+0.55}_{-0.24}$	$22.17^{+4.59}_{-6.88}$	$1.51^{+0.47}_{-0.35}$	$49.20^{+13.04}_{-13.51}$	$9.83^{+0.04}_{-0.04}$	$9.09^{+0.23}_{-0.41}$	$9.09^{+0.23}_{-0.41}$	$0.83^{+0.11}_{-0.15}$
ARP151	< 5.85	...	$1.14^{+0.59}_{-0.47}$	$39.80^{+15.26}_{-13.23}$	< 9.57	< 8.55	> 9.36	> 0.89
AXJ1737.4-2907	< 7.01	...	$1.67^{+0.39}_{-0.34}$	$51.93^{+11.49}_{-7.73}$	< 10.41	< 9.66	> 10.24	> 0.80
Ark120	$7.77^{+0.10}_{-0.07}$	$23.37^{+1.13}_{-1.55}$	$0.83^{+0.35}_{-0.35}$	$55.87^{+15.98}_{-15.70}$	$10.89^{+0.03}_{-0.03}$	$10.50^{+0.06}_{-0.07}$	$10.50^{+0.06}_{-0.07}$	$0.59^{+0.07}_{-0.09}$
CGCG102-048	$8.14^{+0.16}_{-0.17}$	$12.50^{+1.05}_{-0.97}$	$1.64^{+0.34}_{-0.25}$	$64.28^{+13.42}_{-10.88}$	$9.60^{+0.03}_{-0.03}$	$9.24^{+0.07}_{-0.08}$	$9.24^{+0.07}_{-0.08}$	$0.56^{+0.06}_{-0.06}$
CGCG122-055	$6.90^{+0.14}_{-0.10}$	$25.46^{+2.18}_{-2.67}$	$1.97^{+0.58}_{-0.43}$	$47.66^{+26.32}_{-10.69}$	$10.30^{+0.04}_{-0.04}$	$9.86^{+0.12}_{-0.16}$	$9.86^{+0.12}_{-0.16}$	$0.65^{+0.10}_{-0.12}$
CGCG229-015	$7.21^{+0.09}_{-0.10}$	$20.55^{+1.34}_{-1.18}$	$1.83^{+0.48}_{-0.42}$	$47.34^{+12.89}_{-7.83}$	$10.05^{+0.04}_{-0.04}$	$9.61^{+0.07}_{-0.07}$	$9.61^{+0.07}_{-0.07}$	$0.63^{+0.07}_{-0.07}$
CGCG300-062	$7.71^{+0.12}_{-0.13}$	$17.81^{+1.24}_{-1.06}$	$1.63^{+0.35}_{-0.26}$	$59.51^{+12.92}_{-9.94}$	$10.04^{+0.02}_{-0.02}$	$9.74^{+0.05}_{-0.05}$	$9.74^{+0.05}_{-0.05}$	$0.50^{+0.05}_{-0.06}$
CGCG312-012	$6.82^{+0.08}_{-0.06}$	$22.28^{+0.73}_{-1.18}$	$1.22^{+0.45}_{-0.41}$	$48.48^{+17.94}_{-15.72}$	$9.61^{+0.03}_{-0.03}$	$9.42^{+0.04}_{-0.07}$	$9.42^{+0.04}_{-0.07}$	$0.35^{+0.11}_{-0.09}$
CGCG319-007	$7.71^{+0.05}_{-0.04}$	$24.37^{+0.52}_{-0.90}$	$1.76^{+0.76}_{-0.56}$	$34.46^{+14.65}_{-12.08}$	$10.73^{+0.03}_{-0.03}$	$10.56^{+0.03}_{-0.05}$	$10.56^{+0.03}_{-0.05}$	$0.34^{+0.09}_{-0.09}$
CGCG341-006	$7.64^{+0.15}_{-0.09}$	$27.48^{+2.48}_{-3.87}$	$2.09^{+0.47}_{-0.26}$	$55.44^{+22.15}_{-17.47}$	$11.08^{+0.03}_{-0.03}$	$10.81^{+0.12}_{-0.25}$	$10.81^{+0.12}_{-0.25}$	$0.47^{+0.24}_{-0.18}$
CGCG367-009	$6.91^{+0.55}_{-0.32}$	$19.90^{+3.03}_{-4.30}$	$1.58^{+0.55}_{-0.45}$	$42.77^{+12.13}_{-13.13}$	$9.70^{+0.04}_{-0.05}$	$9.21^{+0.10}_{-0.11}$	$9.21^{+0.10}_{-0.11}$	$0.67^{+0.08}_{-0.10}$
CGCG420-015	$7.37^{+0.12}_{-0.13}$	$23.96^{+2.38}_{-1.96}$	$1.74^{+0.51}_{-0.51}$	$41.75^{+11.13}_{-7.76}$	$10.84^{+0.04}_{-0.05}$	$10.17^{+0.11}_{-0.11}$	$10.17^{+0.11}_{-0.11}$	$0.79^{+0.05}_{-0.07}$
CGCG468-002NED01	$7.26^{+0.15}_{-0.09}$	$27.13^{+1.48}_{-2.64}$	$2.11^{+0.49}_{-0.39}$	$50.01^{+20.33}_{-18.21}$	$10.50^{+0.03}_{-0.03}$	$10.38^{+0.06}_{-0.13}$	$10.38^{+0.06}_{-0.13}$	$0.24^{+0.21}_{-0.15}$
CGCG493-002	$7.04^{+0.10}_{-0.09}$	$23.51^{+1.54}_{-1.53}$	$1.42^{+0.46}_{-0.33}$	$53.18^{+16.04}_{-10.48}$	$10.39^{+0.04}_{-0.04}$	$9.79^{+0.09}_{-0.08}$	$9.79^{+0.09}_{-0.08}$	$0.75^{+0.04}_{-0.06}$
CGCG535-012	$8.43^{+0.18}_{-0.18}$	$13.23^{+1.40}_{-1.38}$	$1.42^{+0.33}_{-0.26}$	$60.27^{+12.50}_{-9.32}$	$10.56^{+0.03}_{-0.04}$	$9.68^{+0.11}_{-0.13}$	$9.68^{+0.11}_{-0.13}$	$0.87^{+0.03}_{-0.03}$
CenA	$7.27^{+0.03}_{-0.02}$	$24.48^{+0.30}_{-0.30}$	$0.75^{+0.74}_{-0.57}$	$45.98^{+19.17}_{-19.01}$	$10.12^{+0.02}_{-0.02}$	$10.13^{+0.01}_{-0.02}$	< 9.12	< 0.10
ESO005-G004	$7.58^{+0.03}_{-0.03}$	$21.62^{+0.27}_{-0.35}$	$1.02^{+0.48}_{-0.38}$	$51.55^{+18.51}_{-19.00}$	$10.10^{+0.01}_{-0.01}$	$10.11^{+0.02}_{-0.02}$	< 9.10	< 0.10
ESO031-G008	$7.67^{+0.20}_{-0.21}$	$16.31^{+2.28}_{-1.83}$	$1.34^{+0.36}_{-0.29}$	$57.03^{+12.88}_{-10.98}$	$9.85^{+0.03}_{-0.03}$	$9.48^{+0.13}_{-0.12}$	$9.48^{+0.13}_{-0.12}$	$0.57^{+0.09}_{-0.14}$
ESO033-G002	$7.07^{+0.27}_{-0.24}$	$22.60^{+3.61}_{-3.25}$	$1.46^{+0.40}_{-0.33}$	$52.95^{+14.21}_{-11.49}$	$10.35^{+0.03}_{-0.03}$	$9.71^{+0.17}_{-0.13}$	$9.71^{+0.17}_{-0.13}$	$0.77^{+0.06}_{-0.11}$

Table D.1 – continued from previous page

Name	log $M_{\rm dust}$ [$M_\odot$]	$T_{\rm dust}$ [K]	α	$\lambda_{\rm c}$ [μm]	log $L_{\rm IR}$ [$L_\odot$]	log $L_{\rm SF}$ [$L_\odot$]	log $L_{\rm AGN,IR}$ [$L_\odot$]	$f_{\rm AGN}$
ESO103-035	$5.98^{+0.13}_{-0.10}$	$36.45^{+3.87}_{-4.10}$	$2.94^{+0.69}_{-0.69}$	$29.96^{+5.93}_{-5.67}$	$10.60^{+0.06}_{-0.08}$	$9.87^{+0.16}_{-0.17}$	$9.87^{+0.16}_{-0.17}$	$0.82^{+0.07}_{-0.10}$
ESO121-IG028	$7.89^{+0.21}_{-0.19}$	$16.50^{+2.12}_{-2.00}$	$1.70^{+0.64}_{-0.48}$	$39.81^{+15.64}_{-13.11}$	$10.06^{+0.06}_{-0.07}$	$9.72^{+0.13}_{-0.14}$	$9.72^{+0.13}_{-0.14}$	$0.53^{+0.11}_{-0.13}$
ESO137-34	$7.42^{+0.06}_{-0.06}$	$22.93^{+0.53}_{-0.65}$	$1.12^{+0.43}_{-0.41}$	$49.75^{+17.07}_{-16.37}$	$10.18^{+0.02}_{-0.02}$	$10.10^{+0.02}_{-0.03}$	$10.10^{+0.02}_{-0.03}$	$0.16^{+0.08}_{-0.06}$
ESO139-G012	$8.05^{+0.05}_{-0.04}$	$18.37^{+0.39}_{-0.49}$	$1.19^{+0.54}_{-0.38}$	$47.32^{+15.89}_{-15.25}$	$10.19^{+0.02}_{-0.02}$	$10.15^{+0.02}_{-0.02}$	< 9.44	< 0.17
ESO141-G055	$7.90^{+0.09}_{-0.06}$	$23.47^{+0.79}_{-1.24}$	$1.14^{+0.54}_{-0.41}$	$42.71^{+15.16}_{-14.04}$	$10.93^{+0.03}_{-0.03}$	$10.65^{+0.04}_{-0.06}$	$10.65^{+0.04}_{-0.06}$	$0.49^{+0.08}_{-0.07}$
ESO157-G023	$8.20^{+0.08}_{-0.07}$	$18.36^{+0.60}_{-0.72}$	$1.01^{+0.60}_{-0.46}$	$40.36^{+12.37}_{-12.75}$	$10.51^{+0.03}_{-0.03}$	$10.31^{+0.03}_{-0.03}$	$10.31^{+0.03}_{-0.03}$	$0.38^{+0.05}_{-0.06}$
ESO195-IG021NED03	$8.00^{+0.10}_{-0.07}$	$22.50^{+1.27}_{-1.74}$	$1.74^{+0.40}_{-0.32}$	$57.95^{+16.88}_{-15.50}$	$10.80^{+0.02}_{-0.02}$	$10.63^{+0.08}_{-0.11}$	$10.63^{+0.08}_{-0.11}$	$0.33^{+0.14}_{-0.14}$
ESO197-G027	$8.22^{+0.07}_{-0.06}$	$23.24^{+0.89}_{-1.04}$	$2.01^{+0.52}_{-0.37}$	$47.48^{+19.40}_{-13.29}$	$11.02^{+0.02}_{-0.02}$	$10.94^{+0.05}_{-0.05}$	$10.94^{+0.05}_{-0.05}$	$0.18^{+0.11}_{-0.11}$
ESO198-024	$7.01^{+0.41}_{-0.23}$	$22.76^{+4.17}_{-5.52}$	$1.24^{+0.37}_{-0.32}$	$55.32^{+13.51}_{-13.74}$	$10.38^{+0.03}_{-0.04}$	$9.68^{+0.21}_{-0.30}$	$9.68^{+0.21}_{-0.30}$	$0.80^{+0.10}_{-0.14}$
ESO209-G012	$8.37^{+0.09}_{-0.09}$	$21.23^{+1.15}_{-1.02}$	$1.88^{+0.45}_{-0.40}$	$47.27^{+11.09}_{-7.87}$	$11.18^{+0.03}_{-0.03}$	$10.86^{+0.05}_{-0.04}$	$10.86^{+0.05}_{-0.04}$	$0.52^{+0.06}_{-0.07}$
ESO244-IG030	$7.67^{+0.04}_{-0.04}$	$25.50^{+0.46}_{-0.55}$	$1.57^{+0.48}_{-0.40}$	$48.56^{+18.19}_{-17.33}$	$10.62^{+0.02}_{-0.02}$	$10.63^{+0.02}_{-0.03}$	< 9.83	< 0.12
ESO263-G013	< 6.92	...	$1.60^{+0.42}_{-0.38}$	$50.57^{+13.17}_{-7.62}$	< 10.42	< 9.64	> 10.24	> 0.81
ESO297-018	$8.16^{+0.07}_{-0.08}$	$18.84^{+0.90}_{-0.79}$	$1.61^{+0.26}_{-0.23}$	$71.45^{+12.98}_{-10.75}$	$10.53^{+0.02}_{-0.02}$	$10.33^{+0.04}_{-0.04}$	$10.33^{+0.04}_{-0.04}$	$0.37^{+0.05}_{-0.07}$
ESO323-077	$7.62^{+0.05}_{-0.04}$	$27.38^{+0.70}_{-1.10}$	$1.55^{+0.48}_{-0.39}$	$49.42^{+20.03}_{-16.92}$	$10.88^{+0.02}_{-0.03}$	$10.76^{+0.03}_{-0.06}$	$10.76^{+0.03}_{-0.06}$	$0.24^{+0.12}_{-0.10}$
ESO362-18	$6.93^{+0.05}_{-0.04}$	$26.12^{+0.62}_{-0.91}$	$2.01^{+0.65}_{-0.51}$	$35.49^{+11.14}_{-9.98}$	$10.16^{+0.03}_{-0.03}$	$9.96^{+0.03}_{-0.05}$	$9.96^{+0.03}_{-0.05}$	$0.38^{+0.09}_{-0.08}$
ESO374-G044	$7.76^{+0.18}_{-0.19}$	$18.59^{+2.54}_{-2.18}$	$2.24^{+0.50}_{-0.49}$	$39.48^{+7.71}_{-5.65}$	$10.48^{+0.05}_{-0.05}$	$9.91^{+0.14}_{-0.15}$	$9.91^{+0.14}_{-0.15}$	$0.73^{+0.08}_{-0.10}$
ESO383-18	$6.56^{+0.14}_{-0.10}$	$24.37^{+2.13}_{-2.70}$	$0.96^{+0.52}_{-0.29}$	$55.83^{+25.18}_{-15.39}$	$10.08^{+0.03}_{-0.04}$	$9.40^{+0.13}_{-0.17}$	$9.40^{+0.13}_{-0.17}$	$0.79^{+0.07}_{-0.08}$
ESO399-20	$7.75^{+0.07}_{-0.06}$	$21.84^{+0.81}_{-0.97}$	$1.21^{+0.35}_{-0.34}$	$59.15^{+14.45}_{-14.08}$	$10.46^{+0.02}_{-0.02}$	$10.31^{+0.04}_{-0.05}$	$10.31^{+0.04}_{-0.05}$	$0.29^{+0.09}_{-0.08}$
ESO417-G006	$5.72^{+0.21}_{-0.13}$	$31.50^{+2.56}_{-5.81}$	$1.93^{+0.43}_{-0.37}$	$51.01^{+22.04}_{-17.00}$	$9.50^{+0.03}_{-0.03}$	$9.23^{+0.12}_{-0.30}$	$9.23^{+0.12}_{-0.30}$	$0.47^{+0.28}_{-0.18}$
ESO426-G002	$7.72^{+0.24}_{-0.20}$	$18.00^{+2.12}_{-2.55}$	$1.77^{+0.53}_{-0.51}$	$41.47^{+11.13}_{-9.37}$	$10.21^{+0.04}_{-0.05}$	$9.75^{+0.14}_{-0.18}$	$9.75^{+0.14}_{-0.18}$	$0.65^{+0.11}_{-0.12}$
ESO439-G009	$8.00^{+0.07}_{-0.08}$	$19.66^{+0.94}_{-0.86}$	$1.73^{+0.44}_{-0.34}$	$50.31^{+12.03}_{-9.13}$	$10.51^{+0.03}_{-0.03}$	$10.28^{+0.05}_{-0.05}$	$10.28^{+0.05}_{-0.05}$	$0.42^{+0.06}_{-0.08}$
ESO464-G016	$7.29^{+0.09}_{-0.06}$	$26.56^{+1.11}_{-1.63}$	$1.95^{+0.39}_{-0.39}$	$53.62^{+14.76}_{-15.33}$	$10.45^{+0.02}_{-0.02}$	$10.36^{+0.05}_{-0.08}$	$10.36^{+0.05}_{-0.08}$	$0.19^{+0.15}_{-0.12}$
ESO479-G031	$6.26^{+0.25}_{-0.15}$	$25.68^{+1.84}_{-4.57}$	$1.47^{+0.46}_{-0.46}$	$54.24^{+18.45}_{-21.43}$	$9.47^{+0.04}_{-0.04}$	$9.22^{+0.08}_{-0.29}$	$9.22^{+0.08}_{-0.29}$	$0.44^{+0.29}_{-0.13}$
ESO490-IG026	$7.79^{+0.10}_{-0.10}$	$21.67^{+1.43}_{-1.36}$	$2.18^{+0.37}_{-0.28}$	$54.70^{+11.04}_{-8.31}$	$10.88^{+0.03}_{-0.03}$	$10.33^{+0.07}_{-0.07}$	$10.33^{+0.07}_{-0.07}$	$0.72^{+0.04}_{-0.06}$
ESO499-G041	$6.88^{+0.08}_{-0.07}$	$23.17^{+0.94}_{-1.43}$	$1.41^{+0.38}_{-0.38}$	$53.51^{+17.45}_{-15.45}$	$9.78^{+0.03}_{-0.02}$	$9.59^{+0.05}_{-0.09}$	$9.59^{+0.05}_{-0.09}$	$0.36^{+0.13}_{-0.11}$
ESO506-G027	$8.10^{+0.08}_{-0.08}$	$18.42^{+0.89}_{-0.85}$	$1.27^{+0.32}_{-0.24}$	$60.94^{+11.87}_{-9.80}$	$10.57^{+0.03}_{-0.03}$	$10.22^{+0.05}_{-0.04}$	$10.22^{+0.05}_{-0.04}$	$0.56^{+0.04}_{-0.06}$
ESO509-G038	$7.37^{+0.08}_{-0.08}$	$22.86^{+1.47}_{-1.43}$	$1.74^{+0.46}_{-0.38}$	$49.99^{+16.48}_{-11.51}$	$10.34^{+0.03}_{-0.03}$	$10.05^{+0.09}_{-0.09}$	$10.05^{+0.09}_{-0.09}$	$0.49^{+0.10}_{-0.13}$
ESO509-IG066NED01	$7.87^{+0.06}_{-0.05}$	$24.25^{+0.73}_{-1.19}$	$2.79^{+0.65}_{-0.64}$	$32.25^{+9.56}_{-7.53}$	$10.88^{+0.04}_{-0.04}$	$10.70^{+0.04}_{-0.07}$	$10.70^{+0.04}_{-0.07}$	$0.34^{+0.11}_{-0.10}$
ESO511-G030	$8.31^{+0.09}_{-0.09}$	$17.25^{+0.76}_{-0.74}$	$1.02^{+0.44}_{-0.38}$	$53.55^{+17.37}_{-19.10}$	$10.30^{+0.03}_{-0.03}$	$10.25^{+0.03}_{-0.03}$	< 9.62	< 0.20
ESO533-G050	$7.95^{+0.08}_{-0.07}$	$17.94^{+0.56}_{-0.64}$	$1.34^{+0.48}_{-0.41}$	$48.01^{+17.87}_{-16.18}$	$9.98^{+0.02}_{-0.02}$	$10.00^{+0.03}_{-0.02}$	< 8.98	< 0.10
ESO548-G081	$7.17^{+0.03}_{-0.03}$	$24.40^{+0.33}_{-0.34}$	$0.15^{+0.52}_{-0.41}$	$41.71^{+18.88}_{-14.23}$	$10.21^{+0.02}_{-0.03}$	$10.02^{+0.02}_{-0.02}$	$10.02^{+0.02}_{-0.02}$	$0.35^{+0.04}_{-0.05}$

Table D.1 – continued from previous page

Name	log $M_{\rm dust}$ [$M_\odot$]	$T_{\rm dust}$ [K]	α	$\lambda_{\rm c}$ [μm]	log $L_{\rm IR}$ [$L_\odot$]	log $L_{\rm SF}$ [$L_\odot$]	log $L_{\rm AGN,IR}$ [$L_\odot$]	$f_{\rm AGN}$
ESO549-G049	$7.91^{+0.11}_{-0.04}$	$26.82^{+0.72}_{-3.30}$	$1.90^{+0.46}_{-0.43}$	$56.67^{+35.53}_{-26.20}$	$11.04^{+0.03}_{-0.02}$	$11.00^{+0.04}_{-0.23}$	< 10.95	< 0.69
ESO553-G022	$7.93^{+0.08}_{-0.07}$	$19.48^{+0.58}_{-0.79}$	$1.16^{+0.44}_{-0.40}$	$47.40^{+17.31}_{-15.83}$	$10.23^{+0.02}_{-0.02}$	$10.19^{+0.04}_{-0.05}$	< 9.64	< 0.26
ESO553-G043	< 6.35	...	$2.12^{+0.45}_{-0.47}$	$42.68^{+9.02}_{-5.03}$	< 10.15	< 9.08	> 9.97	> 0.91
ESO565-G019	$7.21^{+0.05}_{-0.03}$	$28.52^{+0.72}_{-1.60}$	$2.02^{+0.49}_{-0.39}$	$47.10^{+31.24}_{-16.00}$	$10.52^{+0.02}_{-0.02}$	$10.46^{+0.04}_{-0.11}$	$10.46^{+0.04}_{-0.11}$	$0.12^{+0.21}_{-0.10}$
ESO578-G009	$7.88^{+0.08}_{-0.07}$	$21.68^{+0.68}_{-0.97}$	$1.96^{+0.63}_{-0.48}$	$40.33^{+13.84}_{-13.96}$	$10.49^{+0.03}_{-0.03}$	$10.42^{+0.03}_{-0.05}$	$10.42^{+0.03}_{-0.05}$	$0.14^{+0.10}_{-0.09}$
Fairall1146	$7.64^{+0.11}_{-0.09}$	$25.59^{+1.61}_{-1.79}$	$1.68^{+0.46}_{-0.41}$	$43.72^{+13.73}_{-9.68}$	$10.99^{+0.03}_{-0.03}$	$10.62^{+0.07}_{-0.09}$	$10.62^{+0.07}_{-0.09}$	$0.58^{+0.09}_{-0.10}$
Fairall272	$7.22^{+0.03}_{-0.03}$	$25.95^{+0.42}_{-0.49}$	$0.85^{+0.45}_{-0.40}$	$49.38^{+18.86}_{-16.86}$	$10.29^{+0.02}_{-0.02}$	$10.23^{+0.02}_{-0.03}$	$10.23^{+0.02}_{-0.03}$	$0.13^{+0.06}_{-0.05}$
Fairall49	$7.28^{+0.08}_{-0.05}$	$29.39^{+1.31}_{-2.25}$	$1.51^{+0.67}_{-0.39}$	$43.99^{+25.30}_{-13.33}$	$10.95^{+0.03}_{-0.03}$	$10.61^{+0.07}_{-0.12}$	$10.61^{+0.07}_{-0.12}$	$0.55^{+0.12}_{-0.10}$
Fairall51	$7.56^{+0.11}_{-0.11}$	$19.24^{+1.28}_{-1.24}$	$1.68^{+0.36}_{-0.25}$	$60.08^{+12.64}_{-9.64}$	$10.52^{+0.03}_{-0.03}$	$9.80^{+0.06}_{-0.07}$	$9.80^{+0.06}_{-0.07}$	$0.81^{+0.03}_{-0.03}$
Fairall9	$7.40^{+0.06}_{-0.04}$	$28.74^{+0.83}_{-1.31}$	$1.25^{+0.80}_{-0.57}$	$31.96^{+12.84}_{-10.84}$	$11.20^{+0.04}_{-0.04}$	$10.68^{+0.03}_{-0.06}$	$10.68^{+0.03}_{-0.06}$	$0.70^{+0.06}_{-0.05}$
HB890241+622	$9.91^{+0.07}_{-0.23}$	$6.92^{+0.70}_{-0.19}$	$0.45^{+0.12}_{-0.09}$	$141.21^{+7.16}_{-14.57}$	$11.21^{+0.04}_{-0.05}$	$9.47^{+0.03}_{-0.03}$	$9.47^{+0.03}_{-0.03}$	$0.98^{+0.00}_{-0.00}$
IC0486	$7.64^{+0.09}_{-0.08}$	$24.09^{+1.23}_{-1.47}$	$1.82^{+0.48}_{-0.35}$	$49.28^{+17.23}_{-12.77}$	$10.64^{+0.03}_{-0.03}$	$10.45^{+0.06}_{-0.08}$	$10.45^{+0.06}_{-0.08}$	$0.35^{+0.13}_{-0.11}$
IC1657	$7.64^{+0.06}_{-0.04}$	$23.04^{+0.49}_{-0.92}$	$1.42^{+0.59}_{-0.46}$	$60.14^{+17.22}_{-18.35}$	$10.32^{+0.01}_{-0.02}$	$10.33^{+0.03}_{-0.05}$	< 10.00	< 0.32
IC1816	$7.34^{+0.04}_{-0.03}$	$25.99^{+0.47}_{-0.61}$	$2.20^{+0.64}_{-0.58}$	$33.36^{+12.58}_{-8.75}$	$10.45^{+0.03}_{-0.02}$	$10.36^{+0.02}_{-0.04}$	$10.36^{+0.02}_{-0.04}$	$0.19^{+0.08}_{-0.07}$
IC2461	$6.97^{+0.03}_{-0.03}$	$21.75^{+0.31}_{-0.34}$	$1.09^{+0.41}_{-0.39}$	$52.99^{+18.98}_{-18.20}$	$9.48^{+0.01}_{-0.02}$	$9.51^{+0.02}_{-0.02}$	< 8.48	< 0.10
IC2637	$7.92^{+0.03}_{-0.03}$	$26.73^{+0.34}_{-0.38}$	$1.28^{+0.59}_{-0.43}$	$42.28^{+19.35}_{-15.56}$	$10.98^{+0.02}_{-0.02}$	$11.00^{+0.02}_{-0.02}$	< 9.98	< 0.10
IC2921	$7.54^{+0.39}_{-0.29}$	$18.35^{+4.02}_{-3.84}$	$1.23^{+0.40}_{-0.37}$	$49.93^{+13.70}_{-9.85}$	$10.44^{+0.04}_{-0.04}$	$9.65^{+0.23}_{-0.23}$	$9.65^{+0.23}_{-0.23}$	$0.84^{+0.06}_{-0.12}$
IC4329A	$6.91^{+0.15}_{-0.17}$	$25.71^{+3.48}_{-2.75}$	$1.25^{+0.48}_{-0.39}$	$46.68^{+11.01}_{-8.77}$	$10.87^{+0.04}_{-0.04}$	$9.89^{+0.16}_{-0.15}$	$9.89^{+0.16}_{-0.15}$	$0.90^{+0.03}_{-0.05}$
IC4518A	$7.59^{+0.37}_{-0.16}$	$26.06^{+2.78}_{-5.26}$	$2.56^{+0.59}_{-0.43}$	$45.09^{+17.22}_{-15.65}$	$10.83^{+0.04}_{-0.04}$	$10.62^{+0.10}_{-0.20}$	$10.62^{+0.10}_{-0.20}$	$0.39^{+0.24}_{-0.22}$
IC4709	$7.35^{+0.10}_{-0.11}$	$20.35^{+1.33}_{-1.10}$	$1.84^{+0.40}_{-0.32}$	$52.87^{+11.42}_{-8.34}$	$10.13^{+0.03}_{-0.03}$	$9.73^{+0.06}_{-0.05}$	$9.73^{+0.06}_{-0.05}$	$0.61^{+0.05}_{-0.07}$
IC5063	$7.61^{+0.08}_{-0.09}$	$20.11^{+1.10}_{-0.93}$	$2.23^{+0.47}_{-0.48}$	$43.60^{+9.12}_{-5.44}$	$10.75^{+0.04}_{-0.04}$	$9.96^{+0.06}_{-0.06}$	$9.96^{+0.06}_{-0.06}$	$0.84^{+0.02}_{-0.03}$
IGRJ11366-6002	$7.01^{+0.10}_{-0.08}$	$25.35^{+1.01}_{-1.60}$	$1.89^{+0.47}_{-0.40}$	$47.47^{+17.74}_{-15.61}$	$10.05^{+0.03}_{-0.02}$	$9.95^{+0.04}_{-0.07}$	$9.95^{+0.04}_{-0.07}$	$0.21^{+0.15}_{-0.12}$
IGRJ23308+7120	$7.62^{+0.06}_{-0.06}$	$24.21^{+0.60}_{-0.69}$	$1.55^{+0.63}_{-0.45}$	$42.37^{+19.97}_{-16.96}$	$10.46^{+0.02}_{-0.02}$	$10.45^{+0.03}_{-0.03}$	< 9.81	< 0.18
IISZ010	$6.69^{+0.13}_{-0.09}$	$25.13^{+1.35}_{-2.16}$	$1.52^{+0.71}_{-0.53}$	$33.35^{+9.22}_{-10.44}$	$10.32^{+0.05}_{-0.05}$	$9.60^{+0.06}_{-0.11}$	$9.60^{+0.06}_{-0.11}$	$0.81^{+0.05}_{-0.05}$
IIZw083	$7.55^{+0.10}_{-0.08}$	$25.56^{+1.68}_{-1.71}$	$1.80^{+0.62}_{-0.49}$	$38.77^{+10.32}_{-9.19}$	$11.02^{+0.04}_{-0.04}$	$10.51^{+0.09}_{-0.09}$	$10.51^{+0.09}_{-0.09}$	$0.69^{+0.07}_{-0.09}$
IRAS03219+4031	$7.69^{+0.09}_{-0.06}$	$29.40^{+1.18}_{-2.21}$	$3.32^{+0.67}_{-0.67}$	$34.14^{+13.73}_{-8.49}$	$11.11^{+0.04}_{-0.03}$	$11.02^{+0.05}_{-0.10}$	$11.02^{+0.05}_{-0.10}$	$0.21^{+0.17}_{-0.15}$
IRAS04124-0803	$7.08^{+0.09}_{-0.09}$	$29.46^{+2.12}_{-2.12}$	$1.43^{+0.53}_{-0.44}$	$41.43^{+12.14}_{-9.48}$	$11.02^{+0.04}_{-0.04}$	$10.42^{+0.09}_{-0.10}$	$10.42^{+0.09}_{-0.10}$	$0.75^{+0.06}_{-0.07}$
IRAS05078+1626	$6.79^{+0.58}_{-0.31}$	$26.67^{+5.92}_{-7.29}$	$2.49^{+0.61}_{-0.58}$	$36.68^{+8.57}_{-9.45}$	$10.60^{+0.05}_{-0.06}$	$9.86^{+0.23}_{-0.25}$	$9.86^{+0.23}_{-0.25}$	$0.82^{+0.08}_{-0.15}$
IRAS05218-1212	$7.01^{+0.12}_{-0.08}$	$30.22^{+1.66}_{-2.60}$	$1.70^{+0.67}_{-0.66}$	$34.53^{+12.54}_{-9.59}$	$11.00^{+0.04}_{-0.05}$	$10.42^{+0.07}_{-0.13}$	$10.42^{+0.07}_{-0.13}$	$0.74^{+0.07}_{-0.07}$
IRAS05589+2828	$7.34^{+0.20}_{-0.14}$	$25.67^{+3.50}_{-4.16}$	$1.24^{+0.46}_{-0.26}$	$57.54^{+26.58}_{-17.42}$	$10.98^{+0.03}_{-0.03}$	$10.31^{+0.21}_{-0.27}$	$10.31^{+0.21}_{-0.27}$	$0.79^{+0.10}_{-0.13}$
KAZ320	$6.86^{+0.11}_{-0.07}$	$28.77^{+1.68}_{-2.51}$	$1.55^{+0.53}_{-0.42}$	$43.59^{+18.03}_{-13.49}$	$10.53^{+0.03}_{-0.04}$	$10.13^{+0.08}_{-0.13}$	$10.13^{+0.08}_{-0.13}$	$0.60^{+0.12}_{-0.10}$

Table D.1 – continued from previous page

Name	log $M_{\rm dust}$ [$M_\odot$]	$T_{\rm dust}$ [K]	α	$\lambda_{\rm c}$ [μm]	log $L_{\rm IR}$ [$L_\odot$]	log $L_{\rm SF}$ [$L_\odot$]	log $L_{\rm AGN,IR}$ [$L_\odot$]	$f_{\rm AGN}$
KUG1141+371	$7.68^{+0.47}_{-0.47}$	$14.70^{+4.04}_{-2.98}$	$1.39^{+0.37}_{-0.32}$	$55.19^{+13.26}_{-9.75}$	$9.91^{+0.04}_{-0.05}$	$9.21^{+0.21}_{-0.16}$	$9.21^{+0.21}_{-0.16}$	$0.80^{+0.06}_{-0.11}$
KUG1208+386	$6.62^{+0.36}_{-0.28}$	$21.54^{+5.52}_{-4.77}$	$1.30^{+0.36}_{-0.30}$	$56.69^{+13.92}_{-12.34}$	$10.03^{+0.03}_{-0.04}$	$9.14^{+0.32}_{-0.31}$	$9.14^{+0.32}_{-0.31}$	$0.87^{+0.06}_{-0.15}$
LCRSB034324.7-394349	$7.61^{+0.11}_{-0.11}$	$19.65^{+1.44}_{-1.30}$	$0.92^{+0.32}_{-0.26}$	$59.71^{+13.62}_{-9.78}$	$10.59^{+0.03}_{-0.04}$	$9.89^{+0.08}_{-0.08}$	$9.89^{+0.08}_{-0.08}$	$0.80^{+0.04}_{-0.04}$
LCRSB232242.2-384320	$7.72^{+0.03}_{-0.03}$	$25.01^{+0.38}_{-0.47}$	$1.44^{+0.57}_{-0.44}$	$43.69^{+22.60}_{-15.73}$	$10.63^{+0.02}_{-0.02}$	$10.63^{+0.02}_{-0.03}$	< 10.08	< 0.15
LEDA138501	< 6.64	...	$0.89^{+0.53}_{-0.43}$	$47.31^{+19.30}_{-18.52}$	< 10.13	< 9.41	> 9.86	> 0.78
LEDA170194	$7.69^{+0.13}_{-0.13}$	$22.21^{+1.76}_{-1.76}$	$1.56^{+0.37}_{-0.31}$	$56.67^{+15.86}_{-13.42}$	$10.58^{+0.02}_{-0.03}$	$10.29^{+0.08}_{-0.08}$	$10.29^{+0.08}_{-0.08}$	$0.48^{+0.09}_{-0.13}$
LEDA214543	$7.42^{+0.08}_{-0.08}$	$20.60^{+1.07}_{-0.99}$	$1.40^{+0.47}_{-0.36}$	$48.86^{+14.11}_{-10.19}$	$10.12^{+0.03}_{-0.03}$	$9.82^{+0.05}_{-0.06}$	$9.82^{+0.05}_{-0.06}$	$0.50^{+0.07}_{-0.08}$
LEDA38038	$7.18^{+0.08}_{-0.05}$	$31.35^{+1.31}_{-2.49}$	$2.04^{+0.66}_{-0.63}$	$36.60^{+17.34}_{-10.64}$	$11.02^{+0.04}_{-0.04}$	$10.69^{+0.06}_{-0.14}$	$10.69^{+0.06}_{-0.14}$	$0.54^{+0.13}_{-0.10}$
M106	$7.30^{+0.02}_{-0.02}$	$21.88^{+0.17}_{-0.23}$	$0.69^{+0.61}_{-0.55}$	$46.03^{+18.23}_{-16.49}$	$9.85^{+0.02}_{-0.02}$	$9.86^{+0.01}_{-0.01}$	< 8.85	< 0.10
MCG+00-09-042	$7.59^{+0.03}_{-0.03}$	$29.42^{+0.50}_{-0.55}$	$1.55^{+0.60}_{-0.49}$	$43.88^{+24.92}_{-16.51}$	$10.89^{+0.02}_{-0.02}$	$10.92^{+0.02}_{-0.02}$	< 9.89	< 0.10
MCG+01-57-016	$7.46^{+0.13}_{-0.13}$	$23.46^{+2.31}_{-2.18}$	$1.90^{+0.37}_{-0.33}$	$54.71^{+13.41}_{-12.23}$	$10.56^{+0.03}_{-0.03}$	$10.21^{+0.12}_{-0.13}$	$10.21^{+0.12}_{-0.13}$	$0.57^{+0.12}_{-0.16}$
MCG+02-21-013	$7.99^{+0.05}_{-0.05}$	$23.11^{+0.48}_{-0.57}$	$1.42^{+0.49}_{-0.42}$	$50.28^{+18.71}_{-17.91}$	$10.69^{+0.02}_{-0.02}$	$10.70^{+0.02}_{-0.03}$	< 9.91	< 0.12
MCG+02-57-002	$7.65^{+0.12}_{-0.11}$	$19.72^{+1.79}_{-1.69}$	$1.97^{+0.31}_{-0.19}$	$68.55^{+14.95}_{-13.36}$	$10.43^{+0.02}_{-0.02}$	$9.95^{+0.10}_{-0.11}$	$9.95^{+0.10}_{-0.11}$	$0.67^{+0.07}_{-0.08}$
MCG+04-22-042	$8.12^{+0.09}_{-0.11}$	$15.87^{+0.76}_{-0.62}$	$1.15^{+0.41}_{-0.38}$	$47.57^{+10.11}_{-6.48}$	$10.53^{+0.04}_{-0.04}$	$9.85^{+0.03}_{-0.03}$	$9.85^{+0.03}_{-0.03}$	$0.79^{+0.02}_{-0.02}$
MCG+04-48-002	$7.68^{+0.03}_{-0.03}$	$27.90^{+0.43}_{-0.48}$	$1.30^{+0.53}_{-0.43}$	$47.11^{+18.79}_{-17.99}$	$10.84^{+0.02}_{-0.02}$	$10.87^{+0.02}_{-0.02}$	< 9.84	< 0.10
MCG+05-03-013	$8.18^{+0.08}_{-0.06}$	$22.10^{+0.85}_{-1.21}$	$1.96^{+0.42}_{-0.34}$	$55.40^{+15.71}_{-15.16}$	$10.81^{+0.02}_{-0.02}$	$10.77^{+0.04}_{-0.07}$	< 10.36	< 0.33
MCG+05-28-032	$7.25^{+0.05}_{-0.04}$	$26.36^{+0.57}_{-0.89}$	$1.68^{+0.54}_{-0.44}$	$42.04^{+20.66}_{-13.41}$	$10.36^{+0.02}_{-0.02}$	$10.30^{+0.03}_{-0.04}$	$10.30^{+0.03}_{-0.04}$	$0.14^{+0.10}_{-0.07}$
MCG+06-16-028	$7.07^{+0.04}_{-0.03}$	$28.87^{+0.62}_{-0.96}$	$1.43^{+0.54}_{-0.41}$	$42.86^{+19.10}_{-13.64}$	$10.51^{+0.02}_{-0.03}$	$10.36^{+0.03}_{-0.05}$	$10.36^{+0.03}_{-0.05}$	$0.30^{+0.09}_{-0.08}$
MCG+06-24-008	$7.57^{+0.03}_{-0.02}$	$24.61^{+0.34}_{-0.34}$	$1.14^{+0.57}_{-0.45}$	$41.94^{+19.87}_{-14.96}$	$10.40^{+0.02}_{-0.02}$	$10.44^{+0.02}_{-0.02}$	< 9.40	< 0.10
MCG+06-49-019	$7.55^{+0.08}_{-0.07}$	$19.37^{+0.56}_{-0.97}$	$1.47^{+0.52}_{-0.45}$	$44.89^{+17.60}_{-14.65}$	$9.85^{+0.03}_{-0.03}$	$9.79^{+0.04}_{-0.07}$	$9.79^{+0.04}_{-0.07}$	$0.14^{+0.11}_{-0.07}$
MCG+08-11-011	$8.24^{+0.07}_{-0.08}$	$18.88^{+0.81}_{-0.73}$	$1.72^{+0.40}_{-0.33}$	$51.58^{+10.29}_{-7.47}$	$11.06^{+0.03}_{-0.03}$	$10.42^{+0.04}_{-0.04}$	$10.42^{+0.04}_{-0.04}$	$0.77^{+0.02}_{-0.03}$
MCG+11-11-032	$7.67^{+0.13}_{-0.10}$	$20.17^{+1.06}_{-1.60}$	$1.12^{+0.39}_{-0.32}$	$55.07^{+16.58}_{-19.15}$	$10.21^{+0.02}_{-0.03}$	$10.01^{+0.07}_{-0.10}$	$10.01^{+0.07}_{-0.10}$	$0.37^{+0.13}_{-0.11}$
MCG+12-10-067	$8.25^{+0.09}_{-0.09}$	$20.39^{+1.05}_{-1.01}$	$1.82^{+0.35}_{-0.26}$	$59.41^{+14.06}_{-10.72}$	$10.85^{+0.02}_{-0.02}$	$10.64^{+0.05}_{-0.06}$	$10.64^{+0.05}_{-0.06}$	$0.40^{+0.07}_{-0.08}$
MCG-01-05-047	$8.21^{+0.04}_{-0.04}$	$21.17^{+0.42}_{-0.63}$	$1.33^{+0.42}_{-0.41}$	$57.79^{+17.99}_{-19.11}$	$10.68^{+0.02}_{-0.02}$	$10.68^{+0.03}_{-0.04}$	< 10.00	< 0.16
MCG-01-09-045	$6.83^{+0.19}_{-0.19}$	$19.12^{+1.92}_{-1.66}$	$0.97^{+0.53}_{-0.44}$	$46.13^{+19.71}_{-16.45}$	$9.06^{+0.05}_{-0.04}$	$9.05^{+0.06}_{-0.06}$	< 8.25	< 0.13
MCG-01-13-025	$6.20^{+0.21}_{-0.20}$	$24.20^{+1.64}_{-2.46}$	$1.02^{+0.61}_{-0.42}$	$44.05^{+18.96}_{-17.06}$	$9.42^{+0.04}_{-0.04}$	$9.00^{+0.06}_{-0.11}$	$9.00^{+0.06}_{-0.11}$	$0.62^{+0.10}_{-0.07}$
MCG-01-24-012	$7.73^{+0.08}_{-0.08}$	$18.65^{+1.06}_{-1.03}$	$2.28^{+0.49}_{-0.46}$	$43.76^{+9.25}_{-6.00}$	$10.35^{+0.05}_{-0.04}$	$9.88^{+0.07}_{-0.07}$	$9.88^{+0.07}_{-0.07}$	$0.66^{+0.05}_{-0.06}$
MCG-01-30-041	$7.24^{+0.06}_{-0.04}$	$26.55^{+0.74}_{-1.20}$	$1.89^{+0.46}_{-0.42}$	$49.19^{+18.58}_{-17.37}$	$10.38^{+0.02}_{-0.02}$	$10.31^{+0.04}_{-0.07}$	$10.31^{+0.04}_{-0.07}$	$0.15^{+0.14}_{-0.12}$
MCG-01-33-063	$7.93^{+0.04}_{-0.04}$	$20.18^{+0.35}_{-0.40}$	$1.01^{+0.48}_{-0.40}$	$49.24^{+18.22}_{-16.68}$	$10.25^{+0.02}_{-0.02}$	$10.29^{+0.02}_{-0.03}$	< 9.25	< 0.10
MCG-01-40-001	$8.03^{+0.09}_{-0.10}$	$20.18^{+1.19}_{-1.12}$	$2.78^{+0.42}_{-0.29}$	$54.32^{+11.65}_{-8.39}$	$10.73^{+0.02}_{-0.02}$	$10.38^{+0.05}_{-0.06}$	$10.38^{+0.05}_{-0.06}$	$0.55^{+0.06}_{-0.06}$
MCG-02-02-095	< 6.47	...	$1.98^{+0.44}_{-0.37}$	$48.91^{+11.27}_{-8.39}$	< 9.47	< 9.16	> 9.09	> 0.48

Table D.1 – continued from previous page

Name	log $M_{\rm dust}$ [$M_\odot$]	$T_{\rm dust}$ [K]	α	$\lambda_{\rm c}$ [μm]	log $L_{\rm IR}$ [$L_\odot$]	log $L_{\rm SF}$ [$L_\odot$]	log $L_{\rm AGN,IR}$ [$L_\odot$]	$f_{\rm AGN}$
MCG-02-08-014	$7.50^{+0.11}_{-0.12}$	$16.91^{+1.09}_{-0.96}$	$1.81^{+0.29}_{-0.24}$	$62.47^{+12.89}_{-9.01}$	$9.87^{+0.02}_{-0.02}$	$9.39^{+0.05}_{-0.05}$	$9.39^{+0.05}_{-0.05}$	$0.67^{+0.04}_{-0.04}$
MCG-02-08-038	$7.61^{+0.22}_{-0.24}$	$19.24^{+2.37}_{-1.93}$	$1.42^{+0.44}_{-0.37}$	$47.77^{+12.18}_{-10.97}$	$10.26^{+0.03}_{-0.04}$	$9.84^{+0.07}_{-0.06}$	$9.84^{+0.07}_{-0.06}$	$0.63^{+0.05}_{-0.09}$
MCG-02-12-050	$8.14^{+0.08}_{-0.08}$	$20.87^{+1.06}_{-1.02}$	$1.79^{+0.31}_{-0.28}$	$61.70^{+14.45}_{-11.53}$	$10.73^{+0.02}_{-0.02}$	$10.58^{+0.05}_{-0.06}$	$10.58^{+0.05}_{-0.06}$	$0.31^{+0.09}_{-0.10}$
MCG-02-14-009	$7.58^{+0.26}_{-0.14}$	$22.05^{+1.52}_{-2.68}$	$1.30^{+0.54}_{-0.40}$	$46.99^{+17.35}_{-17.45}$	$10.46^{+0.03}_{-0.04}$	$10.17^{+0.05}_{-0.09}$	$10.17^{+0.05}_{-0.09}$	$0.49^{+0.11}_{-0.09}$
MCG-03-04-072	$8.05^{+0.09}_{-0.10}$	$16.72^{+0.84}_{-0.80}$	$1.22^{+0.38}_{-0.28}$	$57.51^{+13.17}_{-9.69}$	$10.55^{+0.03}_{-0.04}$	$9.91^{+0.04}_{-0.04}$	$9.91^{+0.04}_{-0.04}$	$0.77^{+0.02}_{-0.03}$
MCG-03-34-064	$7.08^{+0.06}_{-0.03}$	$32.50^{+0.75}_{-1.82}$	$2.43^{+0.82}_{-0.91}$	$29.79^{+15.93}_{-8.40}$	$10.97^{+0.04}_{-0.04}$	$10.68^{+0.03}_{-0.09}$	$10.68^{+0.03}_{-0.09}$	$0.50^{+0.12}_{-0.08}$
MCG-05-23-016	$5.43^{+0.09}_{-0.06}$	$39.66^{+1.95}_{-3.71}$	$2.41^{+0.75}_{-0.60}$	$28.88^{+6.78}_{-7.58}$	$10.17^{+0.05}_{-0.05}$	$9.53^{+0.08}_{-0.15}$	$9.53^{+0.08}_{-0.15}$	$0.77^{+0.07}_{-0.07}$
MCG-06-30-015	$5.80^{+0.08}_{-0.05}$	$32.01^{+1.26}_{-2.35}$	$1.56^{+0.72}_{-0.52}$	$36.54^{+14.59}_{-12.12}$	$9.82^{+0.04}_{-0.04}$	$9.35^{+0.06}_{-0.12}$	$9.35^{+0.06}_{-0.12}$	$0.67^{+0.09}_{-0.08}$
MCG-07-03-007	$7.18^{+0.08}_{-0.07}$	$24.44^{+1.37}_{-1.35}$	$2.20^{+0.59}_{-0.59}$	$37.44^{+11.09}_{-9.54}$	$10.37^{+0.04}_{-0.04}$	$10.04^{+0.07}_{-0.07}$	$10.04^{+0.07}_{-0.07}$	$0.55^{+0.08}_{-0.12}$
Mrk10	$8.33^{+0.08}_{-0.08}$	$19.08^{+1.01}_{-0.94}$	$1.92^{+0.36}_{-0.26}$	$61.79^{+16.61}_{-12.17}$	$10.71^{+0.02}_{-0.02}$	$10.54^{+0.06}_{-0.07}$	$10.54^{+0.06}_{-0.07}$	$0.32^{+0.09}_{-0.10}$
Mrk1018	$8.36^{+0.13}_{-0.15}$	$13.11^{+0.80}_{-0.71}$	$0.90^{+0.34}_{-0.28}$	$57.32^{+11.93}_{-9.41}$	$10.41^{+0.03}_{-0.04}$	$9.59^{+0.04}_{-0.04}$	$9.59^{+0.04}_{-0.04}$	$0.85^{+0.02}_{-0.02}$
Mrk1210	$6.58^{+0.12}_{-0.13}$	$28.09^{+3.09}_{-2.71}$	$3.15^{+0.60}_{-0.61}$	$30.46^{+4.67}_{-4.67}$	$10.57^{+0.06}_{-0.07}$	$9.78^{+0.15}_{-0.13}$	$9.78^{+0.15}_{-0.13}$	$0.84^{+0.05}_{-0.09}$
Mrk1310	$6.75^{+0.11}_{-0.08}$	$22.78^{+0.94}_{-1.49}$	$1.12^{+0.44}_{-0.41}$	$54.67^{+18.39}_{-18.34}$	$9.60^{+0.03}_{-0.03}$	$9.41^{+0.04}_{-0.07}$	$9.41^{+0.04}_{-0.07}$	$0.35^{+0.11}_{-0.09}$
Mrk1392	$7.86^{+0.08}_{-0.07}$	$21.99^{+0.92}_{-1.07}$	$1.90^{+0.58}_{-0.51}$	$37.07^{+9.90}_{-9.46}$	$10.71^{+0.03}_{-0.03}$	$10.44^{+0.04}_{-0.06}$	$10.44^{+0.04}_{-0.06}$	$0.46^{+0.07}_{-0.09}$
Mrk18	$6.75^{+0.06}_{-0.04}$	$28.18^{+0.87}_{-1.44}$	$2.22^{+0.54}_{-0.41}$	$45.32^{+20.41}_{-14.85}$	$10.04^{+0.02}_{-0.03}$	$9.97^{+0.05}_{-0.09}$	$9.97^{+0.05}_{-0.09}$	$0.13^{+0.17}_{-0.11}$
Mrk198	$7.12^{+0.04}_{-0.03}$	$27.61^{+0.61}_{-1.00}$	$1.34^{+0.45}_{-0.40}$	$49.41^{+23.85}_{-18.01}$	$10.38^{+0.02}_{-0.02}$	$10.29^{+0.03}_{-0.06}$	$10.29^{+0.03}_{-0.06}$	$0.18^{+0.12}_{-0.07}$
Mrk202	$6.61^{+0.08}_{-0.08}$	$25.54^{+0.83}_{-1.07}$	$1.27^{+0.50}_{-0.41}$	$48.21^{+17.34}_{-17.53}$	$9.70^{+0.03}_{-0.03}$	$9.58^{+0.03}_{-0.05}$	$9.58^{+0.03}_{-0.05}$	$0.24^{+0.10}_{-0.07}$
Mrk279	$7.29^{+0.08}_{-0.06}$	$27.07^{+1.50}_{-1.79}$	$1.77^{+0.56}_{-0.47}$	$42.22^{+13.47}_{-12.22}$	$10.78^{+0.03}_{-0.04}$	$10.40^{+0.09}_{-0.10}$	$10.40^{+0.09}_{-0.10}$	$0.59^{+0.09}_{-0.13}$
Mrk290	$6.37^{+0.20}_{-0.17}$	$27.83^{+3.61}_{-3.33}$	$1.63^{+0.59}_{-0.50}$	$39.84^{+9.85}_{-9.00}$	$10.34^{+0.04}_{-0.04}$	$9.57^{+0.15}_{-0.14}$	$9.57^{+0.15}_{-0.14}$	$0.83^{+0.05}_{-0.08}$
Mrk335	$6.46^{+0.18}_{-0.20}$	$26.11^{+3.93}_{-2.94}$	$1.02^{+0.41}_{-0.29}$	$52.82^{+12.85}_{-10.05}$	$10.48^{+0.04}_{-0.04}$	$9.49^{+0.16}_{-0.14}$	$9.49^{+0.16}_{-0.14}$	$0.90^{+0.03}_{-0.05}$
Mrk348	$7.02^{+0.40}_{-0.23}$	$23.23^{+3.44}_{-4.29}$	$1.56^{+0.52}_{-0.45}$	$43.16^{+13.08}_{-12.99}$	$10.37^{+0.04}_{-0.04}$	$9.74^{+0.13}_{-0.13}$	$9.74^{+0.13}_{-0.13}$	$0.77^{+0.06}_{-0.11}$
Mrk352	< 5.74	...	$0.84^{+0.59}_{-0.45}$	$46.44^{+19.00}_{-18.26}$	< 8.85	< 8.40	> 8.56	> 0.62
Mrk359	$6.92^{+0.06}_{-0.04}$	$28.80^{+0.77}_{-1.64}$	$1.66^{+0.56}_{-0.39}$	$44.71^{+27.01}_{-15.52}$	$10.34^{+0.03}_{-0.03}$	$10.20^{+0.04}_{-0.09}$	$10.20^{+0.04}_{-0.09}$	$0.28^{+0.15}_{-0.10}$
Mrk417	$6.51^{+0.21}_{-0.14}$	$26.78^{+2.73}_{-3.89}$	$1.71^{+0.58}_{-0.54}$	$38.00^{+10.52}_{-10.09}$	$10.33^{+0.05}_{-0.05}$	$9.59^{+0.13}_{-0.20}$	$9.59^{+0.13}_{-0.20}$	$0.82^{+0.07}_{-0.07}$
Mrk477	$7.14^{+0.09}_{-0.06}$	$32.57^{+1.75}_{-2.55}$	$2.63^{+0.63}_{-0.58}$	$34.43^{+9.77}_{-8.41}$	$11.05^{+0.05}_{-0.04}$	$10.75^{+0.08}_{-0.14}$	$10.75^{+0.08}_{-0.14}$	$0.52^{+0.13}_{-0.15}$
Mrk50	< 6.57	...	$0.80^{+0.79}_{-0.50}$	$38.05^{+17.76}_{-15.51}$	< 9.56	< 9.26	> 9.08	> 0.42
Mrk509	$7.35^{+0.06}_{-0.04}$	$30.65^{+0.95}_{-1.57}$	$1.56^{+0.62}_{-0.52}$	$37.56^{+17.21}_{-10.75}$	$11.12^{+0.04}_{-0.03}$	$10.79^{+0.04}_{-0.08}$	$10.79^{+0.04}_{-0.08}$	$0.54^{+0.10}_{-0.08}$
Mrk590	$8.21^{+0.06}_{-0.06}$	$18.84^{+0.67}_{-0.63}$	$1.51^{+0.38}_{-0.32}$	$53.98^{+12.22}_{-9.05}$	$10.61^{+0.02}_{-0.02}$	$10.39^{+0.04}_{-0.04}$	$10.39^{+0.04}_{-0.04}$	$0.40^{+0.05}_{-0.06}$
Mrk595	$7.28^{+0.16}_{-0.15}$	$22.85^{+2.19}_{-2.16}$	$1.74^{+0.39}_{-0.28}$	$56.31^{+14.99}_{-13.24}$	$10.27^{+0.03}_{-0.03}$	$9.96^{+0.10}_{-0.10}$	$9.96^{+0.10}_{-0.10}$	$0.52^{+0.11}_{-0.14}$
Mrk6	$7.24^{+0.12}_{-0.14}$	$22.77^{+2.09}_{-1.61}$	$1.67^{+0.45}_{-0.37}$	$49.40^{+11.64}_{-8.10}$	$10.55^{+0.04}_{-0.04}$	$9.91^{+0.09}_{-0.08}$	$9.91^{+0.09}_{-0.08}$	$0.77^{+0.05}_{-0.06}$
Mrk618	$7.98^{+0.08}_{-0.05}$	$27.49^{+1.07}_{-1.78}$	$1.53^{+0.47}_{-0.37}$	$49.69^{+23.59}_{-17.87}$	$11.34^{+0.03}_{-0.03}$	$11.15^{+0.05}_{-0.10}$	$11.15^{+0.05}_{-0.10}$	$0.36^{+0.15}_{-0.10}$

Table D.1 – continued from previous page

Name	log $M_{\rm dust}$ [$M_\odot$]	$T_{\rm dust}$ [K]	α	$\lambda_{\rm c}$ [μm]	log $L_{\rm IR}$ [$L_\odot$]	log $L_{\rm SF}$ [$L_\odot$]	log $L_{\rm AGN,IR}$ [$L_\odot$]	$f_{\rm AGN}$
Mrk653	$7.88^{+0.10}_{-0.12}$	$19.69^{+1.27}_{-1.01}$	$1.60^{+0.46}_{-0.43}$	$44.45^{+11.67}_{-7.56}$	$10.52^{+0.03}_{-0.03}$	$10.17^{+0.05}_{-0.05}$	$10.17^{+0.05}_{-0.05}$	$0.55^{+0.05}_{-0.07}$
Mrk704	$6.81^{+0.24}_{-0.20}$	$26.01^{+3.89}_{-3.56}$	$1.13^{+0.54}_{-0.46}$	$41.72^{+11.56}_{-10.65}$	$10.78^{+0.04}_{-0.04}$	$9.83^{+0.16}_{-0.17}$	$9.83^{+0.16}_{-0.17}$	$0.89^{+0.04}_{-0.06}$
Mrk728	< 6.46	...	$1.73^{+0.35}_{-0.27}$	$60.84^{+12.71}_{-10.15}$	< 9.70	< 9.17	> 9.48	> 0.69
Mrk739E	$7.84^{+0.03}_{-0.03}$	$25.92^{+0.34}_{-0.42}$	$1.03^{+0.61}_{-0.41}$	$43.99^{+22.50}_{-15.90}$	$10.88^{+0.02}_{-0.02}$	$10.85^{+0.02}_{-0.02}$	< 10.21	< 0.19
Mrk766	$6.89^{+0.12}_{-0.05}$	$30.42^{+1.54}_{-3.89}$	$2.32^{+0.72}_{-0.58}$	$39.70^{+37.32}_{-11.29}$	$10.57^{+0.03}_{-0.03}$	$10.31^{+0.08}_{-0.23}$	$10.31^{+0.08}_{-0.23}$	$0.46^{+0.22}_{-0.13}$
Mrk79	$7.83^{+0.09}_{-0.09}$	$22.12^{+1.37}_{-1.19}$	$1.53^{+0.42}_{-0.37}$	$49.11^{+13.74}_{-10.12}$	$10.83^{+0.03}_{-0.03}$	$10.42^{+0.07}_{-0.07}$	$10.42^{+0.07}_{-0.07}$	$0.61^{+0.06}_{-0.09}$
Mrk817	$7.51^{+0.09}_{-0.07}$	$28.46^{+2.11}_{-2.50}$	$2.06^{+0.69}_{-0.59}$	$40.92^{+18.52}_{-10.51}$	$11.18^{+0.04}_{-0.04}$	$10.75^{+0.12}_{-0.14}$	$10.75^{+0.12}_{-0.14}$	$0.63^{+0.10}_{-0.12}$
Mrk841	$6.44^{+0.18}_{-0.13}$	$34.21^{+3.67}_{-4.41}$	$1.97^{+0.57}_{-0.56}$	$35.03^{+9.44}_{-7.78}$	$10.87^{+0.05}_{-0.05}$	$10.18^{+0.13}_{-0.18}$	$10.18^{+0.13}_{-0.18}$	$0.80^{+0.07}_{-0.08}$
Mrk885	$7.44^{+0.04}_{-0.04}$	$23.36^{+0.41}_{-0.51}$	$1.52^{+0.46}_{-0.41}$	$44.60^{+17.98}_{-14.27}$	$10.18^{+0.02}_{-0.02}$	$10.17^{+0.02}_{-0.03}$	< 9.44	< 0.16
Mrk926	$7.66^{+0.10}_{-0.08}$	$26.11^{+1.37}_{-1.86}$	$1.24^{+0.38}_{-0.34}$	$49.67^{+15.45}_{-13.63}$	$11.05^{+0.03}_{-0.03}$	$10.68^{+0.07}_{-0.09}$	$10.68^{+0.07}_{-0.09}$	$0.57^{+0.09}_{-0.10}$
Mrk975	$7.94^{+0.06}_{-0.04}$	$25.93^{+0.74}_{-1.26}$	$1.42^{+0.61}_{-0.44}$	$40.35^{+18.62}_{-13.04}$	$11.20^{+0.03}_{-0.03}$	$10.94^{+0.04}_{-0.08}$	$10.94^{+0.04}_{-0.08}$	$0.45^{+0.11}_{-0.08}$
NGC1052	$6.36^{+0.14}_{-0.16}$	$18.16^{+1.71}_{-1.34}$	$1.57^{+0.35}_{-0.27}$	$58.77^{+12.16}_{-9.00}$	$9.21^{+0.03}_{-0.03}$	$8.44^{+0.09}_{-0.08}$	$8.44^{+0.09}_{-0.08}$	$0.83^{+0.03}_{-0.04}$
NGC1106	$7.42^{+0.06}_{-0.07}$	$21.12^{+0.98}_{-0.88}$	$2.22^{+0.48}_{-0.40}$	$47.88^{+10.81}_{-7.65}$	$10.22^{+0.03}_{-0.03}$	$9.89^{+0.05}_{-0.06}$	$9.89^{+0.05}_{-0.06}$	$0.54^{+0.06}_{-0.07}$
NGC1125	$6.74^{+0.16}_{-0.11}$	$29.30^{+1.94}_{-3.20}$	$3.04^{+0.63}_{-0.64}$	$36.11^{+11.63}_{-9.46}$	$10.27^{+0.04}_{-0.04}$	$10.06^{+0.07}_{-0.14}$	$10.06^{+0.07}_{-0.14}$	$0.40^{+0.18}_{-0.15}$
NGC1194	$7.56^{+0.15}_{-0.19}$	$15.00^{+1.18}_{-0.86}$	$1.50^{+0.39}_{-0.31}$	$54.43^{+10.95}_{-8.22}$	$10.16^{+0.03}_{-0.04}$	$9.14^{+0.03}_{-0.03}$	$9.14^{+0.03}_{-0.03}$	$0.90^{+0.01}_{-0.01}$
NGC1365	$8.20^{+0.05}_{-0.04}$	$23.96^{+0.63}_{-0.91}$	$2.06^{+0.40}_{-0.41}$	$54.32^{+17.69}_{-14.89}$	$11.02^{+0.02}_{-0.02}$	$11.00^{+0.04}_{-0.06}$	< 10.53	< 0.28
NGC2110	$6.91^{+0.04}_{-0.03}$	$28.02^{+0.53}_{-0.78}$	$1.37^{+0.56}_{-0.42}$	$44.91^{+21.27}_{-17.31}$	$10.22^{+0.02}_{-0.03}$	$10.11^{+0.03}_{-0.04}$	$10.11^{+0.03}_{-0.04}$	$0.21^{+0.10}_{-0.08}$
NGC235A	$7.46^{+0.07}_{-0.05}$	$27.73^{+0.81}_{-1.52}$	$2.71^{+0.79}_{-0.65}$	$34.94^{+16.85}_{-10.52}$	$10.73^{+0.03}_{-0.03}$	$10.64^{+0.04}_{-0.08}$	$10.64^{+0.04}_{-0.08}$	$0.20^{+0.15}_{-0.11}$
NGC2655	$7.26^{+0.09}_{-0.08}$	$20.06^{+1.23}_{-1.44}$	$0.31^{+0.41}_{-0.38}$	$48.60^{+18.31}_{-15.43}$	$9.62^{+0.06}_{-0.08}$	$9.59^{+0.09}_{-0.12}$	< 8.86	< 0.21
NGC2885	$7.84^{+0.12}_{-0.13}$	$18.03^{+1.35}_{-1.08}$	$1.72^{+0.31}_{-0.24}$	$63.37^{+13.38}_{-10.79}$	$10.14^{+0.02}_{-0.02}$	$9.91^{+0.06}_{-0.06}$	$9.91^{+0.06}_{-0.06}$	$0.42^{+0.07}_{-0.10}$
NGC2992	$7.26^{+0.05}_{-0.04}$	$26.31^{+0.62}_{-1.25}$	$1.97^{+0.49}_{-0.39}$	$47.76^{+23.04}_{-18.23}$	$10.34^{+0.02}_{-0.02}$	$10.30^{+0.03}_{-0.08}$	< 9.97	< 0.38
NGC3035	$7.63^{+0.05}_{-0.04}$	$20.88^{+0.49}_{-0.61}$	$1.70^{+0.43}_{-0.36}$	$52.46^{+16.95}_{-15.83}$	$10.07^{+0.02}_{-0.02}$	$10.07^{+0.02}_{-0.03}$	< 9.26	< 0.13
NGC3079	$8.14^{+0.02}_{-0.02}$	$24.74^{+0.27}_{-0.26}$	$1.06^{+0.50}_{-0.41}$	$51.30^{+18.18}_{-18.09}$	$10.97^{+0.01}_{-0.01}$	$11.03^{+0.01}_{-0.02}$	< 9.97	< 0.10
NGC3081	$7.31^{+0.07}_{-0.07}$	$20.00^{+0.85}_{-0.88}$	$1.98^{+0.41}_{-0.34}$	$54.29^{+13.47}_{-8.71}$	$10.05^{+0.03}_{-0.03}$	$9.63^{+0.05}_{-0.05}$	$9.63^{+0.05}_{-0.05}$	$0.62^{+0.04}_{-0.05}$
NGC3227	$7.61^{+0.04}_{-0.03}$	$23.07^{+0.48}_{-0.69}$	$1.55^{+0.46}_{-0.39}$	$48.77^{+16.09}_{-15.47}$	$10.38^{+0.02}_{-0.02}$	$10.31^{+0.03}_{-0.04}$	$10.31^{+0.03}_{-0.04}$	$0.16^{+0.09}_{-0.08}$
NGC3281	$7.23^{+0.04}_{-0.03}$	$28.51^{+0.65}_{-1.02}$	$2.12^{+0.65}_{-0.59}$	$34.51^{+12.67}_{-9.50}$	$10.69^{+0.03}_{-0.03}$	$10.48^{+0.03}_{-0.05}$	$10.48^{+0.03}_{-0.05}$	$0.38^{+0.09}_{-0.08}$
NGC3393	$7.84^{+0.08}_{-0.08}$	$19.03^{+0.85}_{-0.74}$	$2.11^{+0.44}_{-0.38}$	$50.11^{+12.05}_{-7.45}$	$10.35^{+0.03}_{-0.03}$	$10.04^{+0.04}_{-0.04}$	$10.04^{+0.04}_{-0.04}$	$0.51^{+0.05}_{-0.06}$
NGC3431	$7.89^{+0.08}_{-0.09}$	$18.09^{+0.91}_{-0.81}$	$1.81^{+0.27}_{-0.23}$	$70.06^{+13.38}_{-11.17}$	$10.18^{+0.02}_{-0.02}$	$9.96^{+0.05}_{-0.04}$	$9.96^{+0.05}_{-0.04}$	$0.39^{+0.06}_{-0.07}$
NGC3516	$6.15^{+0.07}_{-0.06}$	$31.72^{+1.09}_{-1.84}$	$1.58^{+0.68}_{-0.51}$	$36.85^{+16.55}_{-11.22}$	$10.02^{+0.04}_{-0.04}$	$9.68^{+0.04}_{-0.09}$	$9.68^{+0.04}_{-0.09}$	$0.54^{+0.10}_{-0.08}$
NGC3718	$7.52^{+0.14}_{-0.12}$	$15.18^{+1.28}_{-1.30}$	$-0.05^{+0.47}_{-0.40}$	$48.49^{+18.36}_{-16.63}$	$9.10^{+0.08}_{-0.08}$	$9.13^{+0.10}_{-0.11}$	< 8.10	< 0.10
NGC3783	$7.45^{+0.06}_{-0.06}$	$20.65^{+0.83}_{-0.75}$	$1.69^{+0.39}_{-0.37}$	$47.93^{+9.83}_{-5.97}$	$10.42^{+0.03}_{-0.03}$	$9.87^{+0.05}_{-0.04}$	$9.87^{+0.05}_{-0.04}$	$0.72^{+0.03}_{-0.04}$

Table D.1 – continued from previous page

Name	log $M_{\rm dust}$ [$M_\odot$]	$T_{\rm dust}$ [K]	α	$\lambda_{\rm c}$ [μm]	log $L_{\rm IR}$ [$L_\odot$]	log $L_{\rm SF}$ [$L_\odot$]	log $L_{\rm AGN,IR}$ [$L_\odot$]	$f_{\rm AGN}$
NGC3786	$6.88^{+0.11}_{-0.14}$	$26.15^{+1.30}_{-1.08}$	$1.13^{+0.48}_{-0.43}$	$47.98^{+18.02}_{-16.62}$	$9.92^{+0.03}_{-0.03}$	$9.90^{+0.04}_{-0.04}$	< 9.15	< 0.16
NGC4051	$7.61^{+0.04}_{-0.03}$	$21.50^{+0.36}_{-0.48}$	$1.26^{+0.43}_{-0.38}$	$49.57^{+16.56}_{-16.13}$	$10.15^{+0.02}_{-0.02}$	$10.13^{+0.02}_{-0.03}$	< 9.42	< 0.17
NGC4102	$7.29^{+0.04}_{-0.03}$	$28.07^{+0.57}_{-1.02}$	$2.61^{+0.66}_{-0.49}$	$38.21^{+17.38}_{-11.50}$	$10.53^{+0.02}_{-0.02}$	$10.50^{+0.03}_{-0.05}$	< 10.12	< 0.34
NGC4138	$6.63^{+0.03}_{-0.03}$	$21.53^{+0.28}_{-0.31}$	$0.34^{+0.49}_{-0.40}$	$50.48^{+18.12}_{-19.21}$	$9.14^{+0.02}_{-0.02}$	$9.15^{+0.02}_{-0.02}$	< 8.14	< 0.10
NGC4151	$6.40^{+0.08}_{-0.08}$	$24.10^{+1.33}_{-1.21}$	$1.79^{+0.57}_{-0.48}$	$40.36^{+9.25}_{-7.92}$	$9.67^{+0.04}_{-0.04}$	$9.21^{+0.06}_{-0.06}$	$9.21^{+0.06}_{-0.06}$	$0.65^{+0.05}_{-0.08}$
NGC4180	$7.23^{+0.02}_{-0.03}$	$24.91^{+0.30}_{-0.29}$	$0.88^{+0.52}_{-0.39}$	$47.36^{+18.40}_{-17.40}$	$10.09^{+0.01}_{-0.01}$	$10.13^{+0.02}_{-0.02}$	< 9.09	< 0.10
NGC4235	$6.68^{+0.05}_{-0.05}$	$20.91^{+0.43}_{-0.62}$	$0.84^{+0.47}_{-0.41}$	$51.26^{+18.02}_{-18.67}$	$9.23^{+0.02}_{-0.03}$	$9.12^{+0.03}_{-0.04}$	$9.12^{+0.03}_{-0.04}$	$0.22^{+0.08}_{-0.06}$
NGC424	$7.36^{+0.08}_{-0.08}$	$19.43^{+1.09}_{-1.03}$	$1.11^{+0.36}_{-0.26}$	$59.24^{+12.94}_{-9.59}$	$10.50^{+0.03}_{-0.04}$	$9.61^{+0.07}_{-0.07}$	$9.61^{+0.07}_{-0.07}$	$0.87^{+0.02}_{-0.02}$
NGC4388	$7.03^{+0.05}_{-0.04}$	$24.33^{+0.80}_{-0.93}$	$2.10^{+0.58}_{-0.46}$	$43.44^{+15.23}_{-12.15}$	$10.00^{+0.02}_{-0.03}$	$9.87^{+0.04}_{-0.06}$	$9.87^{+0.04}_{-0.06}$	$0.27^{+0.10}_{-0.11}$
NGC4507	$7.66^{+0.06}_{-0.06}$	$21.00^{+0.83}_{-0.86}$	$1.79^{+0.35}_{-0.24}$	$59.42^{+11.06}_{-9.37}$	$10.64^{+0.03}_{-0.02}$	$10.12^{+0.05}_{-0.06}$	$10.12^{+0.05}_{-0.06}$	$0.70^{+0.04}_{-0.04}$
NGC4619	$8.02^{+0.03}_{-0.03}$	$22.49^{+0.29}_{-0.31}$	$0.49^{+0.48}_{-0.39}$	$53.57^{+17.61}_{-19.31}$	$10.63^{+0.01}_{-0.01}$	$10.65^{+0.01}_{-0.02}$	< 9.63	< 0.10
NGC4748	$7.29^{+0.05}_{-0.05}$	$24.50^{+0.64}_{-0.86}$	$2.20^{+0.63}_{-0.55}$	$38.93^{+13.94}_{-11.58}$	$10.24^{+0.03}_{-0.03}$	$10.15^{+0.04}_{-0.05}$	$10.15^{+0.04}_{-0.05}$	$0.20^{+0.10}_{-0.09}$
NGC4939	$8.34^{+0.08}_{-0.07}$	$17.62^{+0.97}_{-0.99}$	$1.12^{+0.51}_{-0.43}$	$47.68^{+18.42}_{-17.86}$	$10.36^{+0.05}_{-0.06}$	$10.34^{+0.08}_{-0.08}$	< 9.56	< 0.16
NGC4941	$7.19^{+0.10}_{-0.10}$	$16.60^{+1.12}_{-1.10}$	$1.32^{+0.43}_{-0.35}$	$48.27^{+17.54}_{-14.57}$	$9.15^{+0.05}_{-0.06}$	$9.03^{+0.08}_{-0.09}$	$9.03^{+0.08}_{-0.09}$	$0.23^{+0.10}_{-0.09}$
NGC4992	$7.66^{+0.11}_{-0.10}$	$19.68^{+0.94}_{-1.29}$	$1.31^{+0.55}_{-0.40}$	$43.70^{+13.77}_{-12.18}$	$10.20^{+0.03}_{-0.03}$	$9.94^{+0.05}_{-0.08}$	$9.94^{+0.05}_{-0.08}$	$0.45^{+0.10}_{-0.08}$
NGC5033	$8.03^{+0.07}_{-0.07}$	$20.28^{+1.14}_{-1.22}$	$0.72^{+0.45}_{-0.39}$	$48.62^{+17.93}_{-17.14}$	$10.36^{+0.07}_{-0.08}$	$10.40^{+0.08}_{-0.10}$	< 9.36	< 0.10
NGC5106	$8.13^{+0.03}_{-0.03}$	$26.05^{+0.36}_{-0.36}$	$1.26^{+0.49}_{-0.43}$	$46.13^{+20.30}_{-16.11}$	$11.11^{+0.02}_{-0.02}$	$11.15^{+0.02}_{-0.02}$	< 10.11	< 0.10
NGC513	$7.59^{+0.03}_{-0.03}$	$26.79^{+0.36}_{-0.40}$	$1.14^{+0.54}_{-0.43}$	$43.52^{+19.78}_{-15.40}$	$10.65^{+0.02}_{-0.02}$	$10.68^{+0.02}_{-0.02}$	< 9.65	< 0.10
NGC5231	$7.58^{+0.04}_{-0.04}$	$23.04^{+0.43}_{-0.56}$	$1.35^{+0.47}_{-0.40}$	$48.24^{+17.48}_{-16.07}$	$10.30^{+0.02}_{-0.02}$	$10.28^{+0.02}_{-0.03}$	< 9.62	< 0.17
NGC5252	$7.12^{+0.18}_{-0.13}$	$23.78^{+1.40}_{-2.42}$	$0.91^{+0.41}_{-0.41}$	$55.65^{+17.86}_{-18.53}$	$10.22^{+0.03}_{-0.03}$	$9.88^{+0.06}_{-0.10}$	$9.88^{+0.06}_{-0.10}$	$0.53^{+0.11}_{-0.08}$
NGC526A	$6.95^{+0.22}_{-0.23}$	$20.54^{+2.72}_{-2.33}$	$1.34^{+0.51}_{-0.45}$	$42.81^{+10.24}_{-7.56}$	$10.18^{+0.04}_{-0.04}$	$9.34^{+0.12}_{-0.09}$	$9.34^{+0.12}_{-0.09}$	$0.85^{+0.03}_{-0.05}$
NGC5273	$5.46^{+0.07}_{-0.06}$	$27.20^{+0.80}_{-1.14}$	$1.32^{+0.47}_{-0.43}$	$53.76^{+17.19}_{-18.47}$	$8.67^{+0.02}_{-0.02}$	$8.59^{+0.03}_{-0.05}$	$8.59^{+0.03}_{-0.05}$	$0.16^{+0.11}_{-0.08}$
NGC5290	$7.54^{+0.03}_{-0.03}$	$20.49^{+0.38}_{-0.40}$	$0.40^{+0.46}_{-0.40}$	$50.21^{+17.56}_{-17.31}$	$9.91^{+0.02}_{-0.03}$	$9.93^{+0.03}_{-0.03}$	< 8.91	< 0.10
NGC5506	$6.73^{+0.06}_{-0.06}$	$25.56^{+1.12}_{-1.15}$	$1.83^{+0.44}_{-0.38}$	$49.21^{+13.16}_{-7.46}$	$10.15^{+0.04}_{-0.03}$	$9.70^{+0.06}_{-0.06}$	$9.70^{+0.06}_{-0.06}$	$0.65^{+0.06}_{-0.06}$
NGC5548	$7.28^{+0.08}_{-0.08}$	$23.90^{+1.29}_{-1.28}$	$1.68^{+0.44}_{-0.40}$	$46.89^{+12.24}_{-8.92}$	$10.45^{+0.03}_{-0.03}$	$10.07^{+0.06}_{-0.07}$	$10.07^{+0.06}_{-0.07}$	$0.59^{+0.07}_{-0.08}$
NGC5610	$7.87^{+0.07}_{-0.07}$	$23.87^{+1.26}_{-1.38}$	$2.40^{+0.26}_{-0.28}$	$61.17^{+10.52}_{-10.13}$	$10.83^{+0.02}_{-0.02}$	$10.66^{+0.07}_{-0.08}$	$10.66^{+0.07}_{-0.08}$	$0.33^{+0.12}_{-0.14}$
NGC5674	$8.09^{+0.03}_{-0.03}$	$23.31^{+0.30}_{-0.32}$	$0.44^{+0.53}_{-0.39}$	$48.19^{+19.69}_{-18.90}$	$10.80^{+0.01}_{-0.02}$	$10.82^{+0.01}_{-0.02}$	< 9.80	< 0.10
NGC5683	< 6.94	...	$1.64^{+0.34}_{-0.29}$	$57.92^{+13.11}_{-9.31}$	< 10.10	< 9.64	> 9.87	> 0.63
NGC5728	$7.30^{+0.05}_{-0.04}$	$24.43^{+0.58}_{-0.89}$	$1.74^{+0.41}_{-0.39}$	$56.78^{+14.97}_{-18.42}$	$10.16^{+0.02}_{-0.02}$	$10.15^{+0.03}_{-0.06}$	< 9.65	< 0.25
NGC5899	$7.99^{+0.05}_{-0.04}$	$21.40^{+0.45}_{-0.71}$	$1.23^{+0.47}_{-0.44}$	$63.82^{+14.92}_{-17.47}$	$10.51^{+0.01}_{-0.01}$	$10.50^{+0.03}_{-0.04}$	< 9.83	< 0.18
NGC5995	$8.06^{+0.05}_{-0.04}$	$25.26^{+0.83}_{-0.96}$	$1.56^{+0.45}_{-0.34}$	$50.36^{+16.36}_{-12.61}$	$11.17^{+0.02}_{-0.02}$	$11.00^{+0.04}_{-0.06}$	$11.00^{+0.04}_{-0.06}$	$0.33^{+0.09}_{-0.10}$

Table D.1 – continued from previous page

Name	log $M_{\rm dust}$ [$M_\odot$]	$T_{\rm dust}$ [K]	α	$\lambda_{\rm c}$ [μm]	log $L_{\rm IR}$ [$L_\odot$]	log $L_{\rm SF}$ [$L_\odot$]	log $L_{\rm AGN,IR}$ [$L_\odot$]	$f_{\rm AGN}$
NGC6221	$7.64^{+0.04}_{-0.03}$	$24.65^{+0.60}_{-0.78}$	$1.73^{+0.40}_{-0.38}$	$54.54^{+15.83}_{-15.37}$	$10.56^{+0.02}_{-0.02}$	$10.51^{+0.04}_{-0.05}$	$10.51^{+0.04}_{-0.05}$	$0.10^{+0.11}_{-0.09}$
NGC6240	$8.27^{+0.11}_{-0.04}$	$30.66^{+1.07}_{-3.88}$	$2.81^{+0.87}_{-0.44}$	$40.29^{+34.89}_{-12.95}$	$11.78^{+0.03}_{-0.03}$	$11.71^{+0.06}_{-0.26}$	< 11.64	< 0.67
NGC6300	$7.53^{+0.07}_{-0.06}$	$21.23^{+1.22}_{-1.25}$	$1.35^{+0.45}_{-0.42}$	$48.44^{+18.64}_{-16.12}$	$10.06^{+0.07}_{-0.06}$	$10.02^{+0.09}_{-0.09}$	< 9.47	< 0.25
NGC6552	$7.44^{+0.07}_{-0.05}$	$29.39^{+1.15}_{-1.74}$	$3.25^{+0.60}_{-0.67}$	$31.86^{+7.76}_{-6.91}$	$11.02^{+0.05}_{-0.05}$	$10.77^{+0.05}_{-0.10}$	$10.77^{+0.05}_{-0.10}$	$0.44^{+0.13}_{-0.13}$
NGC6814	$7.63^{+0.05}_{-0.04}$	$21.08^{+0.37}_{-0.55}$	$1.03^{+0.49}_{-0.41}$	$58.78^{+16.89}_{-18.83}$	$10.10^{+0.01}_{-0.01}$	$10.10^{+0.02}_{-0.03}$	< 9.35	< 0.14
NGC6860	$7.55^{+0.06}_{-0.05}$	$22.75^{+0.63}_{-0.84}$	$0.99^{+0.40}_{-0.36}$	$52.98^{+16.77}_{-16.16}$	$10.39^{+0.02}_{-0.02}$	$10.21^{+0.03}_{-0.05}$	$10.21^{+0.03}_{-0.05}$	$0.34^{+0.08}_{-0.08}$
NGC7172	$7.49^{+0.02}_{-0.02}$	$24.42^{+0.29}_{-0.30}$	$1.05^{+0.48}_{-0.41}$	$47.34^{+17.33}_{-15.87}$	$10.32^{+0.01}_{-0.02}$	$10.34^{+0.02}_{-0.02}$	< 9.32	< 0.10
NGC7213	$6.89^{+0.03}_{-0.04}$	$21.39^{+0.31}_{-0.40}$	$0.78^{+0.44}_{-0.40}$	$48.50^{+18.27}_{-16.12}$	$9.47^{+0.02}_{-0.02}$	$9.40^{+0.02}_{-0.03}$	$9.40^{+0.02}_{-0.03}$	$0.16^{+0.06}_{-0.05}$
NGC7465	$6.73^{+0.04}_{-0.04}$	$26.53^{+0.52}_{-0.56}$	$1.24^{+0.47}_{-0.42}$	$52.28^{+17.45}_{-17.34}$	$9.79^{+0.02}_{-0.02}$	$9.80^{+0.02}_{-0.02}$	< 8.79	< 0.10
NGC7469	$8.29^{+0.08}_{-0.07}$	$26.77^{+1.53}_{-1.62}$	$2.69^{+0.51}_{-0.41}$	$44.98^{+14.81}_{-9.22}$	$11.55^{+0.03}_{-0.03}$	$11.38^{+0.07}_{-0.09}$	$11.38^{+0.07}_{-0.09}$	$0.34^{+0.13}_{-0.15}$
NGC7479	$8.06^{+0.09}_{-0.08}$	$21.21^{+1.56}_{-1.56}$	$2.19^{+0.49}_{-0.42}$	$46.54^{+16.42}_{-14.70}$	$10.69^{+0.07}_{-0.09}$	$10.53^{+0.12}_{-0.11}$	$10.53^{+0.12}_{-0.11}$	$0.27^{+0.15}_{-0.14}$
NGC7582	$7.57^{+0.04}_{-0.03}$	$27.05^{+0.53}_{-0.93}$	$2.09^{+0.59}_{-0.43}$	$43.57^{+20.54}_{-14.94}$	$10.71^{+0.02}_{-0.02}$	$10.69^{+0.03}_{-0.05}$	< 10.29	< 0.31
NGC7603	$7.98^{+0.04}_{-0.03}$	$24.02^{+0.40}_{-0.54}$	$0.46^{+0.45}_{-0.40}$	$49.75^{+19.20}_{-18.14}$	$10.99^{+0.03}_{-0.03}$	$10.78^{+0.02}_{-0.03}$	$10.78^{+0.02}_{-0.03}$	$0.37^{+0.06}_{-0.05}$
NGC7679	$7.68^{+0.03}_{-0.03}$	$29.20^{+0.46}_{-0.59}$	$1.51^{+0.52}_{-0.42}$	$45.13^{+23.12}_{-15.06}$	$10.99^{+0.02}_{-0.02}$	$11.00^{+0.02}_{-0.03}$	< 10.48	< 0.15
NGC788	$7.32^{+0.14}_{-0.09}$	$20.49^{+1.29}_{-1.97}$	$1.66^{+0.54}_{-0.44}$	$42.61^{+11.87}_{-11.24}$	$10.07^{+0.03}_{-0.04}$	$9.71^{+0.09}_{-0.12}$	$9.71^{+0.09}_{-0.12}$	$0.57^{+0.11}_{-0.11}$
NGC931	$8.23^{+0.11}_{-0.10}$	$19.46^{+1.72}_{-1.64}$	$1.41^{+0.44}_{-0.39}$	$50.14^{+17.39}_{-16.78}$	$10.78^{+0.06}_{-0.07}$	$10.48^{+0.13}_{-0.13}$	$10.48^{+0.13}_{-0.13}$	$0.48^{+0.12}_{-0.13}$
NGC985	$8.32^{+0.08}_{-0.07}$	$21.73^{+1.08}_{-1.15}$	$1.66^{+0.39}_{-0.28}$	$56.13^{+14.54}_{-10.04}$	$11.29^{+0.03}_{-0.03}$	$10.86^{+0.05}_{-0.06}$	$10.86^{+0.05}_{-0.06}$	$0.63^{+0.05}_{-0.06}$
PG2304+042	< 6.05	...	$1.35^{+0.70}_{-0.48}$	$38.09^{+13.14}_{-13.24}$	< 9.89	< 8.72	> 9.66	> 0.92
PICTORA	$9.78^{+0.09}_{-0.10}$	$8.39^{+0.38}_{-0.32}$	$0.69^{+0.13}_{-0.10}$	$130.08^{+14.43}_{-17.31}$	$10.42^{+0.03}_{-0.04}$	$9.84^{+0.02}_{-0.02}$	$9.84^{+0.02}_{-0.02}$	$0.73^{+0.02}_{-0.02}$
PKS2331-240	$9.95^{+0.04}_{-0.07}$	$8.34^{+0.27}_{-0.16}$	$1.23^{+0.12}_{-0.11}$	$137.74^{+9.34}_{-10.52}$	$10.54^{+0.02}_{-0.03}$	$9.99^{+0.02}_{-0.02}$	$9.99^{+0.02}_{-0.02}$	$0.71^{+0.02}_{-0.02}$
SBS0915+556	< 6.89	...	$1.66^{+0.44}_{-0.37}$	$49.66^{+10.92}_{-7.85}$	< 10.52	< 9.65	> 10.36	> 0.85
SBS1301+540	$7.64^{+0.22}_{-0.20}$	$13.85^{+1.53}_{-1.51}$	$0.94^{+0.45}_{-0.42}$	$48.39^{+18.85}_{-17.33}$	$9.53^{+0.06}_{-0.06}$	$9.02^{+0.09}_{-0.10}$	$9.02^{+0.09}_{-0.10}$	$0.70^{+0.07}_{-0.07}$
SDSSJ104326.47+110524.2	< 7.01	...	$1.77^{+0.39}_{-0.29}$	$55.74^{+12.59}_{-9.91}$	< 10.09	< 9.69	> 9.83	> 0.59
SWIFTJ212745.6+565636	< 6.01	...	$1.15^{+0.50}_{-0.50}$	$42.48^{+9.30}_{-5.67}$	< 10.18	< 8.74	> 10.02	> 0.96
UGC01479	$7.50^{+0.07}_{-0.06}$	$23.90^{+0.91}_{-1.26}$	$2.09^{+0.37}_{-0.39}$	$57.96^{+13.43}_{-12.84}$	$10.34^{+0.02}_{-0.02}$	$10.29^{+0.05}_{-0.07}$	< 9.91	< 0.35
UGC03142	$7.60^{+0.05}_{-0.05}$	$24.61^{+0.48}_{-0.49}$	$1.04^{+0.54}_{-0.41}$	$43.40^{+19.02}_{-15.44}$	$10.50^{+0.02}_{-0.02}$	$10.47^{+0.02}_{-0.02}$	< 9.73	< 0.16
UGC03478	$7.66^{+0.06}_{-0.05}$	$21.13^{+0.70}_{-0.76}$	$1.46^{+0.34}_{-0.33}$	$59.57^{+16.50}_{-13.42}$	$10.22^{+0.02}_{-0.02}$	$10.13^{+0.04}_{-0.05}$	$10.13^{+0.04}_{-0.05}$	$0.20^{+0.08}_{-0.08}$
UGC03601	$6.95^{+0.06}_{-0.05}$	$23.71^{+0.66}_{-1.08}$	$1.70^{+0.60}_{-0.46}$	$43.26^{+16.80}_{-14.95}$	$9.84^{+0.02}_{-0.03}$	$9.72^{+0.03}_{-0.06}$	$9.72^{+0.03}_{-0.06}$	$0.23^{+0.12}_{-0.08}$
UGC03995A	$7.77^{+0.12}_{-0.11}$	$20.52^{+0.80}_{-1.00}$	$1.04^{+0.47}_{-0.38}$	$45.78^{+18.90}_{-15.19}$	$10.29^{+0.03}_{-0.03}$	$10.16^{+0.04}_{-0.05}$	$10.16^{+0.04}_{-0.05}$	$0.25^{+0.07}_{-0.06}$
UGC05881	$7.48^{+0.11}_{-0.08}$	$24.81^{+1.61}_{-2.05}$	$2.30^{+0.28}_{-0.30}$	$60.28^{+12.52}_{-12.72}$	$10.55^{+0.02}_{-0.02}$	$10.38^{+0.09}_{-0.13}$	$10.38^{+0.09}_{-0.13}$	$0.32^{+0.19}_{-0.18}$
UGC06728	< 5.10	...	$1.24^{+0.40}_{-0.28}$	$59.17^{+14.15}_{-10.08}$	< 8.81	< 7.80	> 8.66	> 0.89

Table D.1 – continued from previous page

Name	log $M_{\rm dust}$ [$\rm M_\odot$]	$T_{\rm dust}$ [K]	α	$\lambda_{\rm c}$ [μm]	log $L_{\rm IR}$ [$\rm L_\odot$]	log $L_{\rm SF}$ [$\rm L_\odot$]	log $L_{\rm AGN,IR}$ [$\rm L_\odot$]	$f_{\rm AGN}$
UGC07064	$7.80^{+0.05}_{-0.04}$	$25.05^{+0.51}_{-0.76}$	$1.93^{+0.61}_{-0.50}$	$38.27^{+17.46}_{-11.43}$	$10.78^{+0.02}_{-0.02}$	$10.72^{+0.02}_{-0.04}$	$10.72^{+0.02}_{-0.04}$	$0.14^{+0.10}_{-0.07}$
UGC08327NED02	$7.14^{+0.14}_{-0.13}$	$33.02^{+2.30}_{-4.20}$	$2.05^{+0.71}_{-0.46}$	$41.76^{+32.70}_{-14.74}$	$11.01^{+0.03}_{-0.03}$	$10.78^{+0.08}_{-0.27}$	$10.78^{+0.08}_{-0.27}$	$0.42^{+0.27}_{-0.16}$
UGC10593	$7.57^{+0.11}_{-0.08}$	$23.19^{+1.16}_{-1.70}$	$1.68^{+0.41}_{-0.36}$	$53.94^{+16.49}_{-14.87}$	$10.44^{+0.03}_{-0.03}$	$10.29^{+0.05}_{-0.09}$	$10.29^{+0.05}_{-0.09}$	$0.30^{+0.14}_{-0.13}$
UGC11185NED02	$7.31^{+0.22}_{-0.13}$	$26.60^{+2.50}_{-3.76}$	$2.31^{+0.51}_{-0.35}$	$47.79^{+21.50}_{-14.83}$	$10.60^{+0.03}_{-0.03}$	$10.38^{+0.10}_{-0.16}$	$10.38^{+0.10}_{-0.16}$	$0.40^{+0.19}_{-0.21}$
UGC12237	$8.14^{+0.11}_{-0.11}$	$17.77^{+1.08}_{-0.96}$	$2.48^{+0.36}_{-0.28}$	$56.89^{+11.98}_{-8.71}$	$10.50^{+0.02}_{-0.02}$	$10.17^{+0.05}_{-0.05}$	$10.17^{+0.05}_{-0.05}$	$0.54^{+0.05}_{-0.05}$
UGC12282	$7.96^{+0.09}_{-0.06}$	$20.58^{+0.64}_{-1.12}$	$1.25^{+0.47}_{-0.47}$	$64.59^{+15.07}_{-18.12}$	$10.39^{+0.02}_{-0.02}$	$10.36^{+0.03}_{-0.05}$	< 9.83	< 0.25
UGC12741	$7.21^{+0.05}_{-0.04}$	$22.86^{+0.50}_{-0.74}$	$1.59^{+0.47}_{-0.41}$	$51.42^{+18.01}_{-18.49}$	$9.90^{+0.02}_{-0.02}$	$9.89^{+0.03}_{-0.04}$	< 9.25	< 0.19
UM614	< 6.69	...	$1.82^{+0.79}_{-0.59}$	$31.82^{+9.49}_{-9.83}$	< 10.05	< 9.39	> 9.72	> 0.71
VIIZw073	$7.69^{+0.08}_{-0.04}$	$30.13^{+1.01}_{-2.33}$	$2.78^{+0.85}_{-0.73}$	$35.01^{+30.58}_{-11.81}$	$11.21^{+0.03}_{-0.03}$	$11.09^{+0.05}_{-0.14}$	$11.09^{+0.05}_{-0.14}$	$0.27^{+0.20}_{-0.14}$
WKK1263	$7.07^{+0.06}_{-0.04}$	$27.60^{+0.66}_{-1.33}$	$1.84^{+0.64}_{-0.53}$	$35.80^{+18.10}_{-10.96}$	$10.43^{+0.03}_{-0.03}$	$10.24^{+0.03}_{-0.07}$	$10.24^{+0.03}_{-0.07}$	$0.36^{+0.12}_{-0.09}$
WKK4374	< 7.02	...	$1.57^{+0.42}_{-0.30}$	$57.52^{+14.77}_{-14.64}$	< 9.94	< 9.71	> 9.49	> 0.38
WKK4438	$7.22^{+0.15}_{-0.12}$	$23.79^{+1.26}_{-2.02}$	$1.84^{+0.63}_{-0.45}$	$40.64^{+15.11}_{-12.89}$	$10.23^{+0.03}_{-0.04}$	$9.99^{+0.04}_{-0.08}$	$9.99^{+0.04}_{-0.08}$	$0.42^{+0.12}_{-0.10}$
WKK6092	< 5.59	...	$1.61^{+0.36}_{-0.30}$	$56.70^{+12.07}_{-8.59}$	< 9.73	< 8.25	> 9.61	> 0.96
WKK6471	$7.79^{+0.11}_{-0.09}$	$19.40^{+0.60}_{-0.76}$	$0.75^{+0.51}_{-0.42}$	$43.29^{+17.57}_{-15.07}$	$10.19^{+0.03}_{-0.03}$	$10.04^{+0.04}_{-0.04}$	$10.04^{+0.04}_{-0.04}$	$0.29^{+0.06}_{-0.06}$

Appendix E: 12 – 500 μm Spectral Energy Distributions of the *Herschel*-BAT Sample

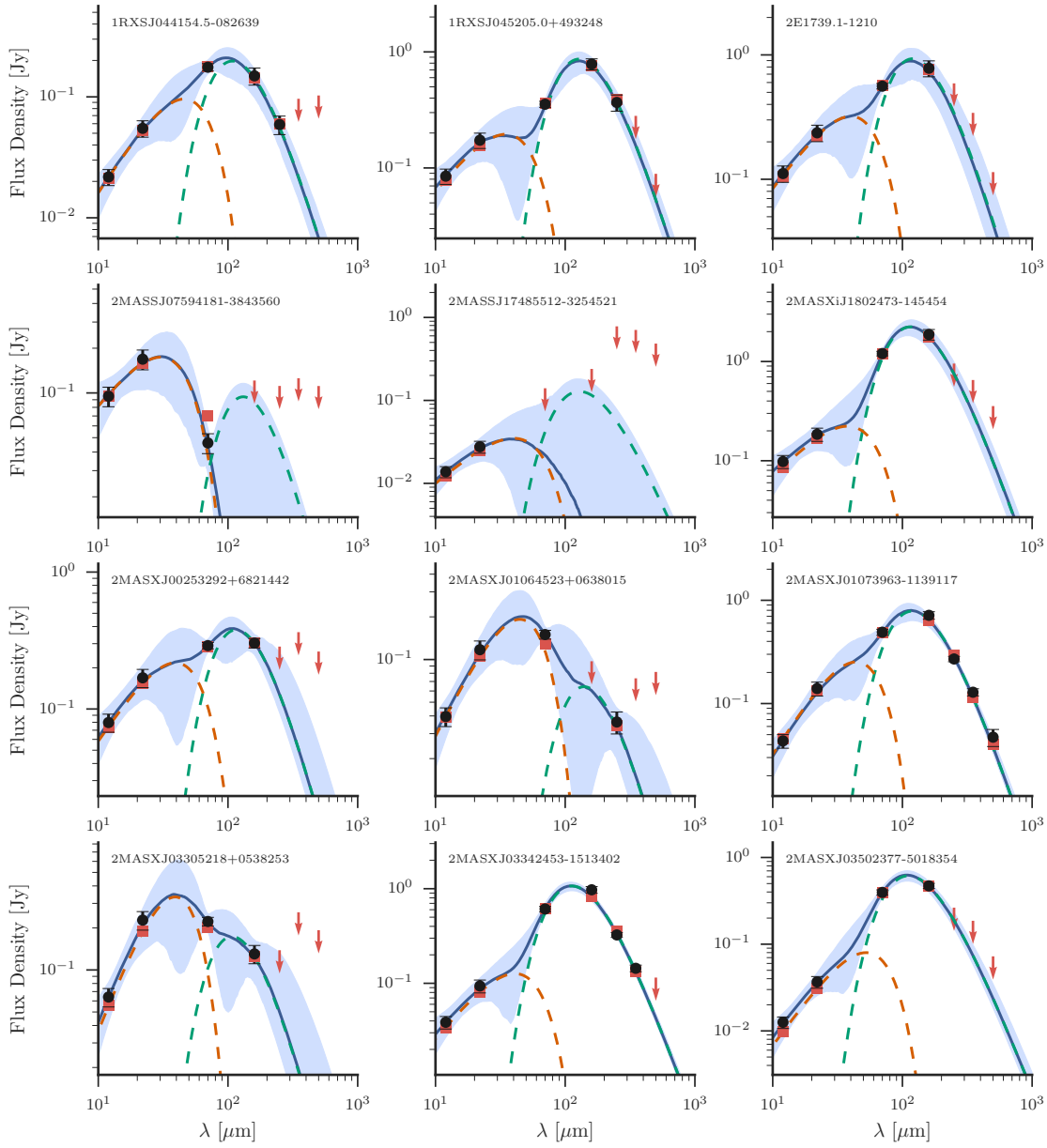

Figure E.1: Observed frame 12–500 μm SEDs for all of the *Herschel*-BAT sample. Black points plot the observed flux densities with downward-pointing red arrows indicating 5σ upper limits. The solid blue line and shaded region shows the best-fit C12 model with a 95 percent confidence interval. The red squares are the model flux densities after convolving the best-fit model SED with each instrument's transmission curve. The orange and green dashed lines show the best-fit PL and MBB components, respectively.

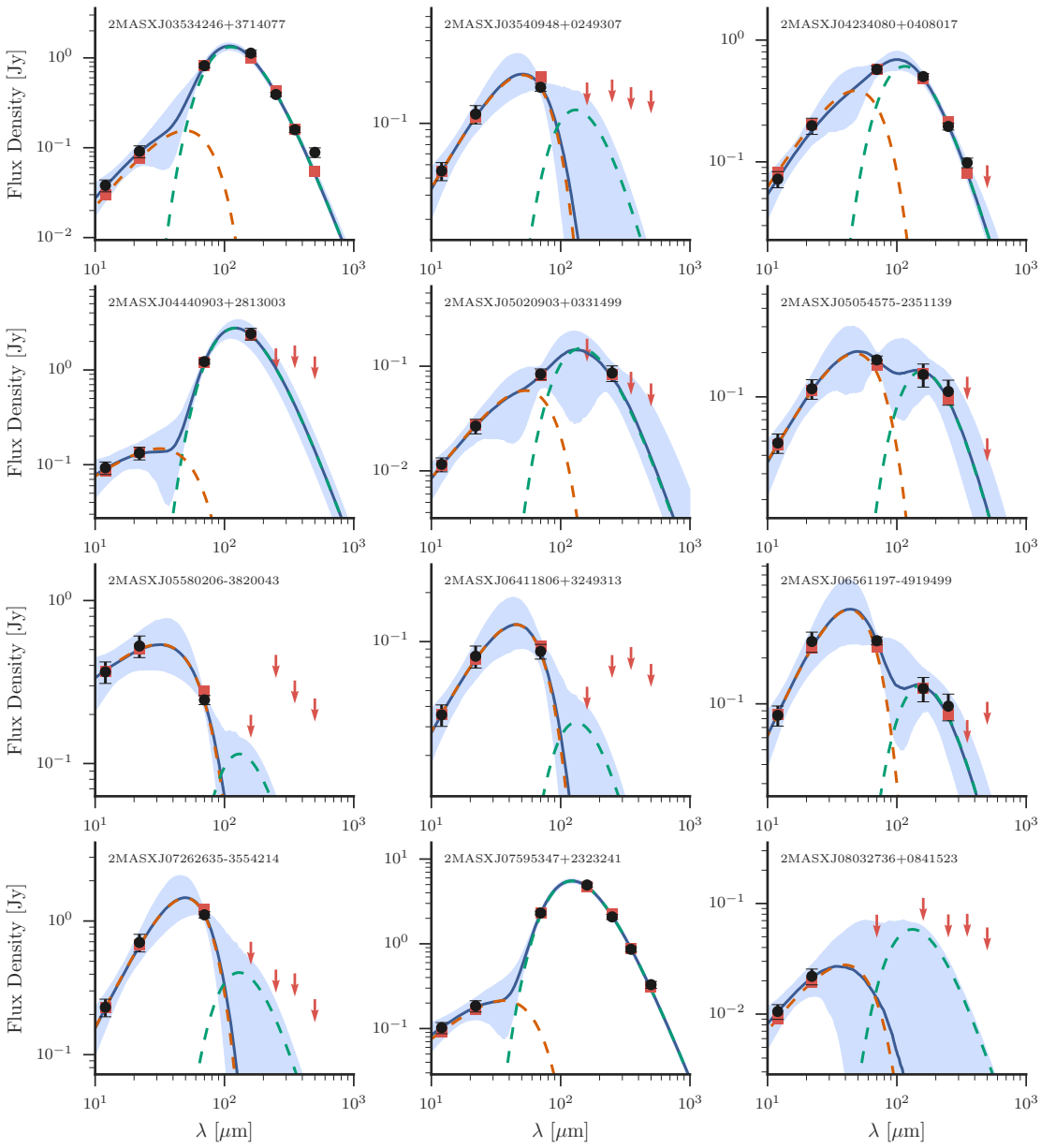
2MASXJ03534246+3714077
2MASXJ03540948+0249307
2MASXJ04234080+0408017
2MASXJ04440903+2813003
2MASXJ05020903+0331499
2MASXJ05054575-2351139
2MASXJ05580206-3820043
2MASXJ06411806+3249313
2MASXJ06561197-4919499
2MASXJ07262635-3554214
2MASXJ07595347+2323241
2MASXJ08032736+0841523
Flux Density [Jy]
λ [μm]

Figure E.2

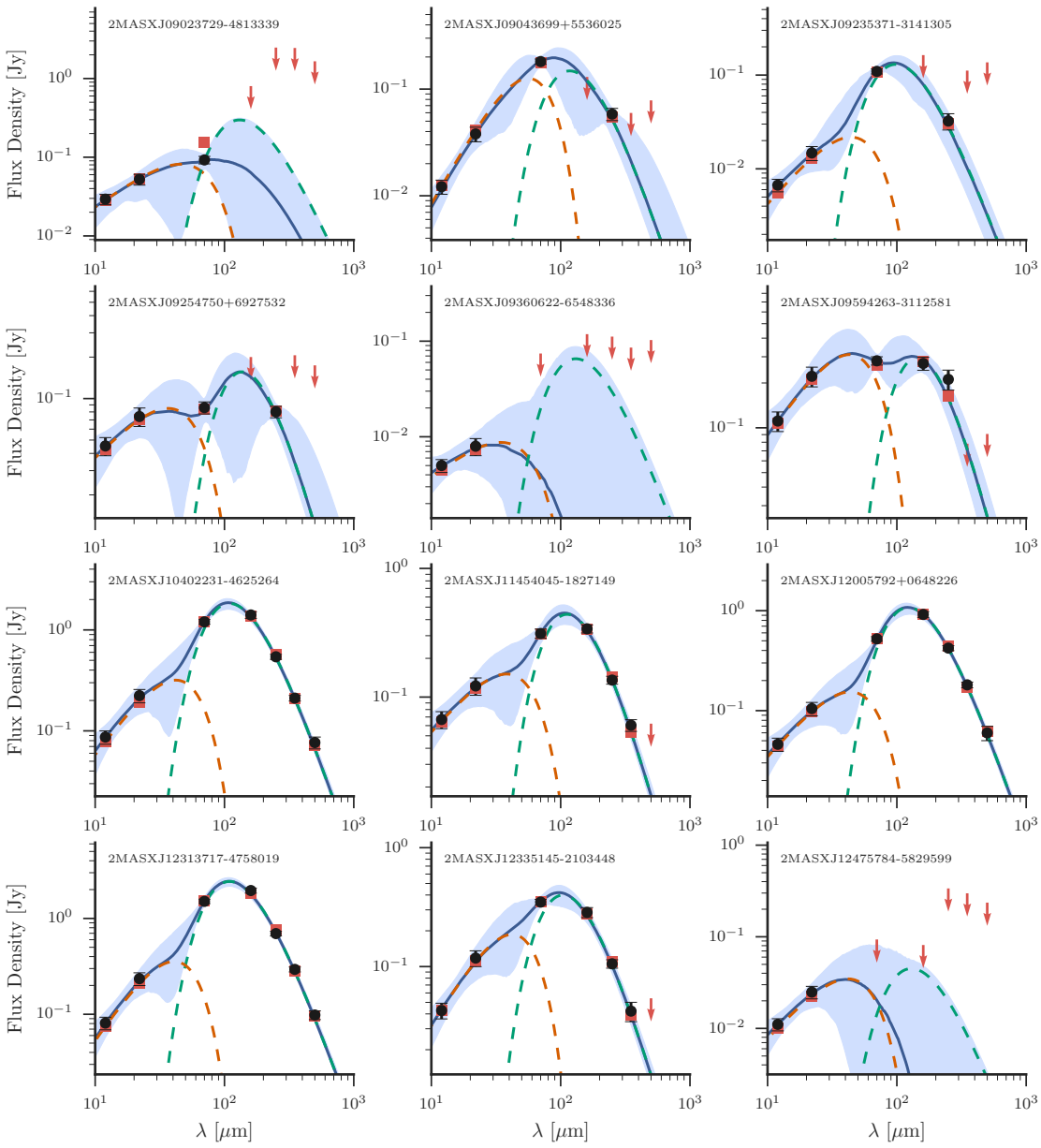
2MASXJ09023729-4813339
2MASXJ09043699+5536025
2MASXJ09235371-3141305
2MASXJ09254750+6927532
2MASXJ09360622-6548336
2MASXJ09594263-3112581
2MASXJ10402231-4625264
2MASXJ11454045-1827149
2MASXJ12005792+0648226
2MASXJ12313717-4758019
2MASXJ12335145-2103448
2MASXJ12475784-5829599
Flux Density [Jy]
λ [μm]

Figure E.3

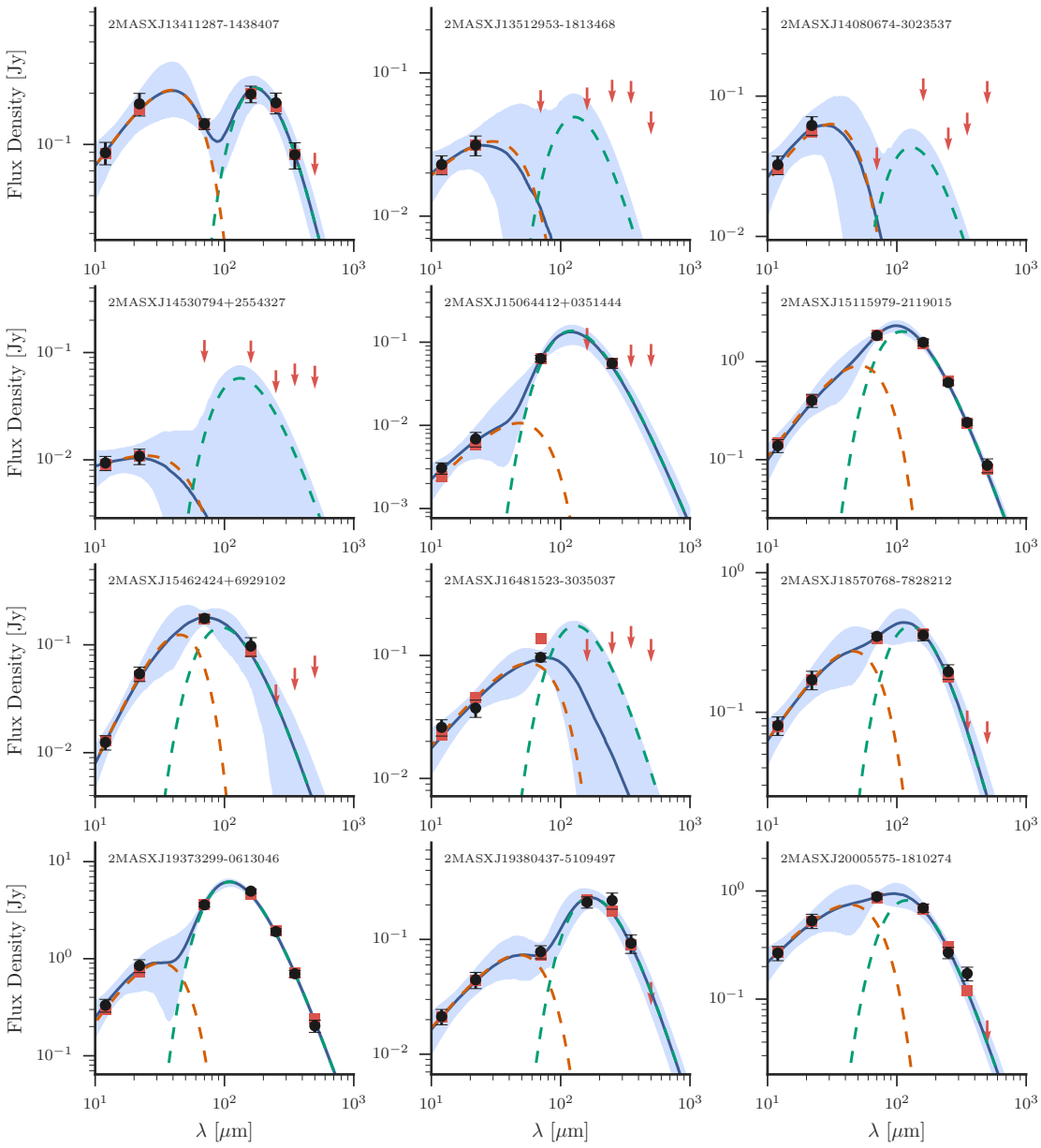
2MASXJ13411287-1438407
2MASXJ13512953-1813468
2MASXJ14080674-3023537
2MASXJ14530794+2554327
2MASXJ15064412+0351444
2MASXJ15115979-2119015
2MASXJ15462424+6929102
2MASXJ16481523-3035037
2MASXJ18570768-7828212
2MASXJ19373299-0613046
2MASXJ19380437-5109497
2MASXJ20005575-1810274
Flux Density [Jy]
λ [μm]

Figure E.4

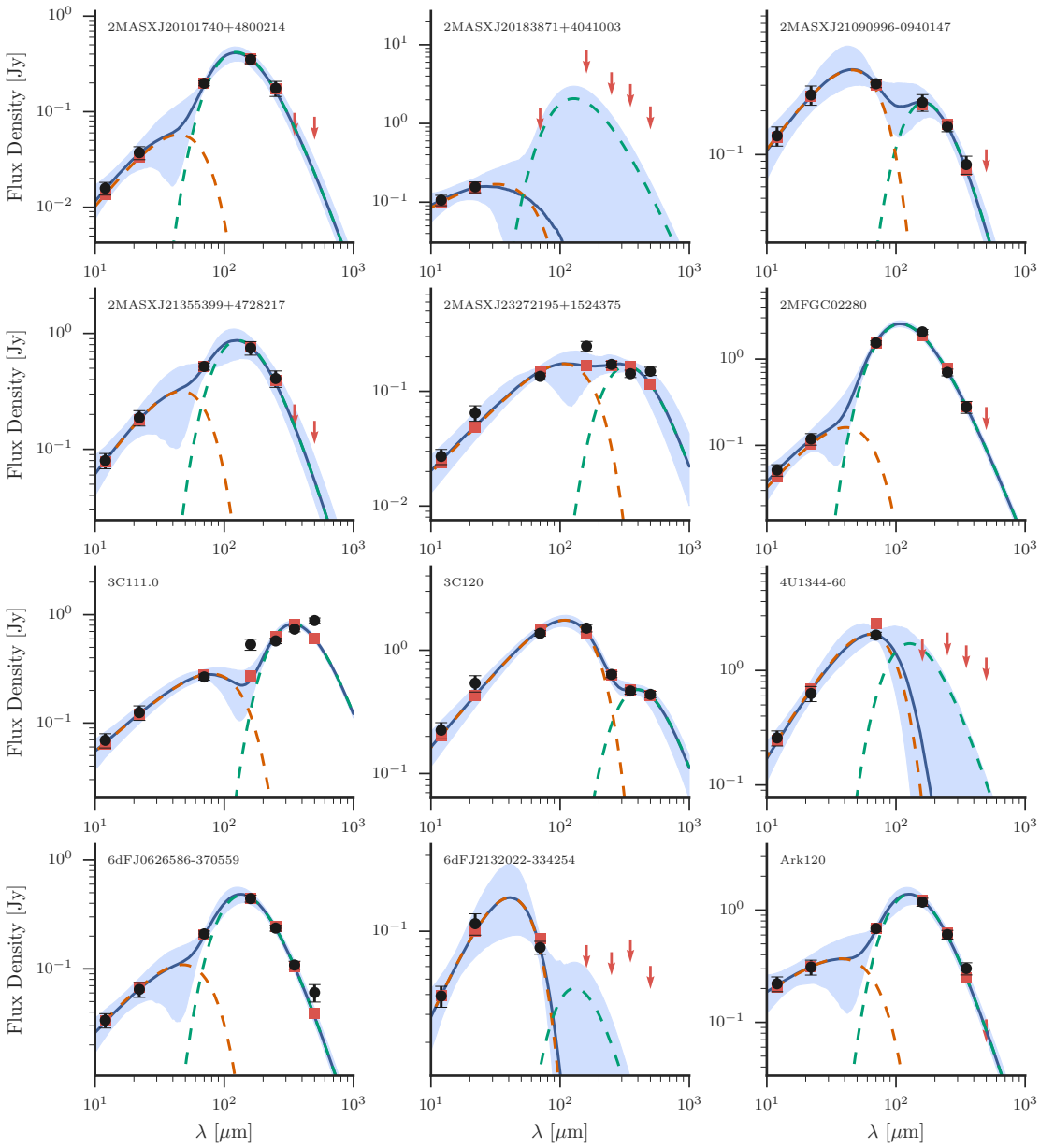
2MASXJ20101740+4800214
2MASXJ20183871+4041003
2MASXJ21090996-0940147
2MASXJ21355399+4728217
2MASXJ23272195+1524375
2MFGC02280
3C111.0
3C120
4U1344-60
6dFJ0626586-370559
6dFJ2132022-334254
Ark120
Flux Density [Jy]
λ [μm]

Figure E.5

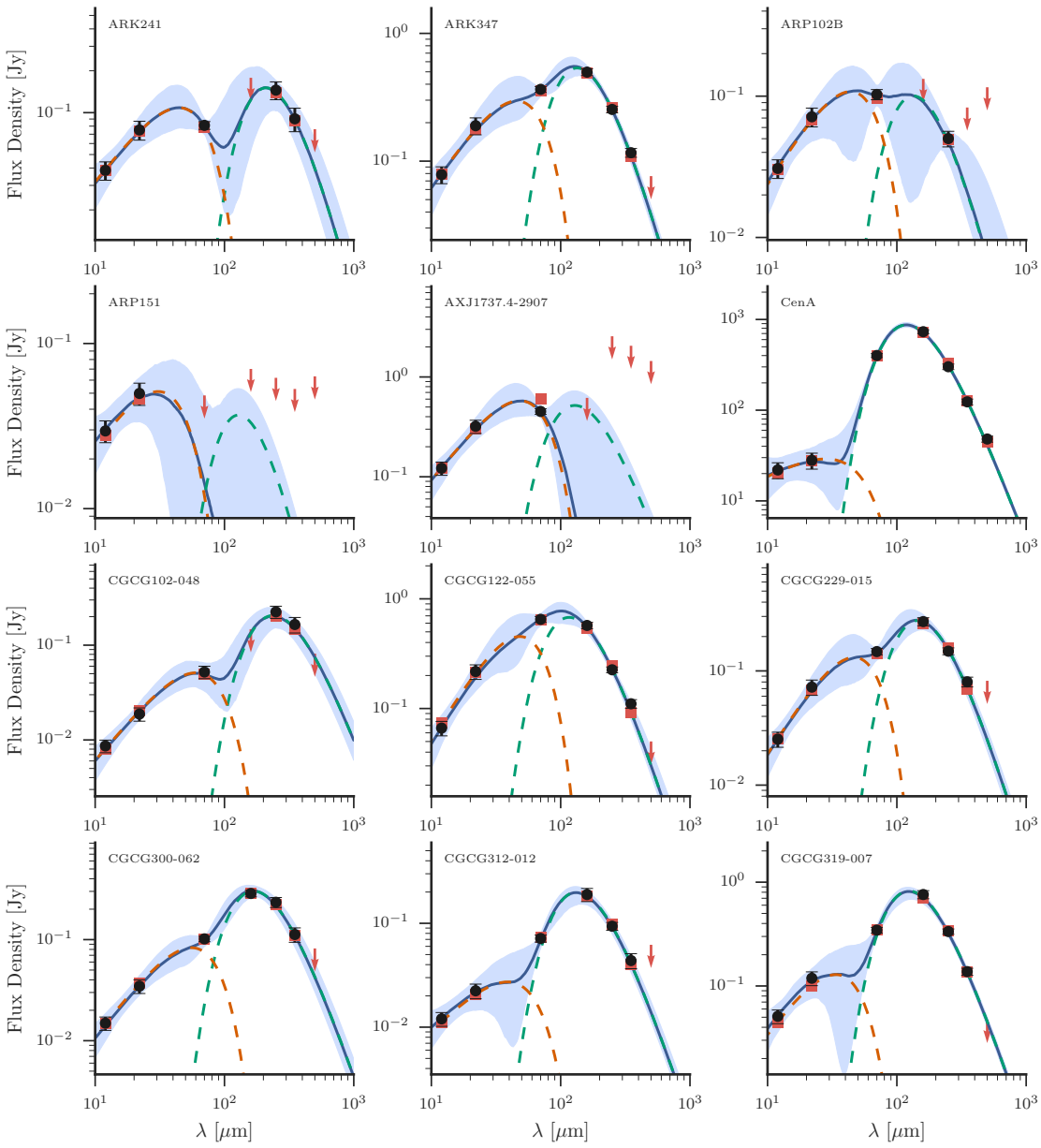
ARK241
ARK347
ARP102B
ARP151
AXJ1737.4-2907
CenA
CGCG102-048
CGCG122-055
CGCG229-015
CGCG300-062
CGCG312-012
CGCG319-007
Flux Density [Jy]
λ [μm]

Figure E.6

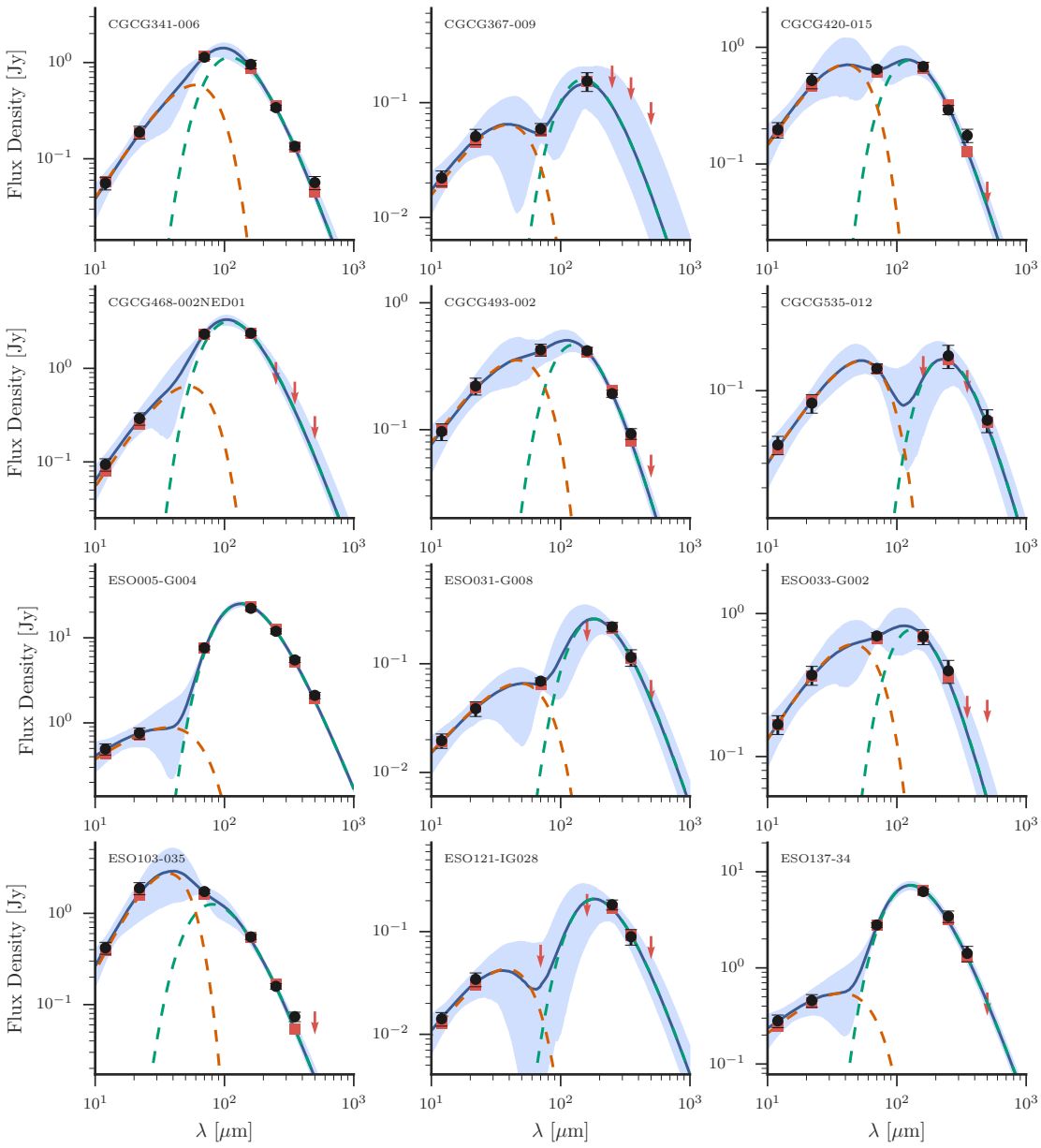
CGCG341-006
CGCG367-009
CGCG420-015
CGCG468-002NED01
CGCG493-002
CGCG535-012
ESO005-G004
ESO031-G008
ESO033-G002
ESO103-035
ESO121-IG028
ESO137-34
Flux Density [Jy]
λ [μm]

Figure E.7

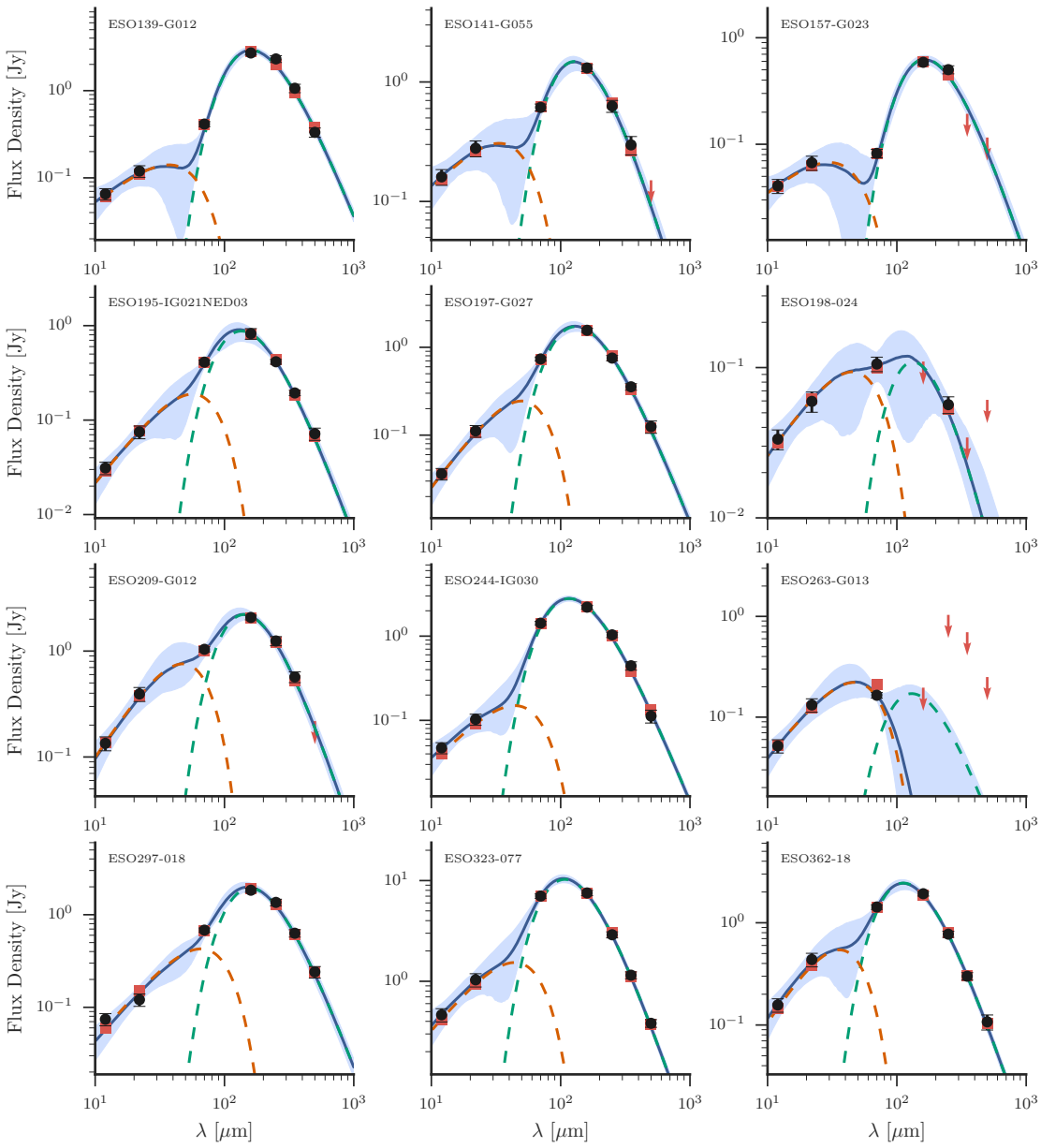
ESO139-G012
ESO141-G055
ESO157-G023
ESO195-IG021NED03
ESO197-G027
ESO198-024
ESO209-G012
ESO244-IG030
ESO263-G013
ESO297-018
ESO323-077
ESO362-18
Flux Density [Jy]
λ [μm]

Figure E.8

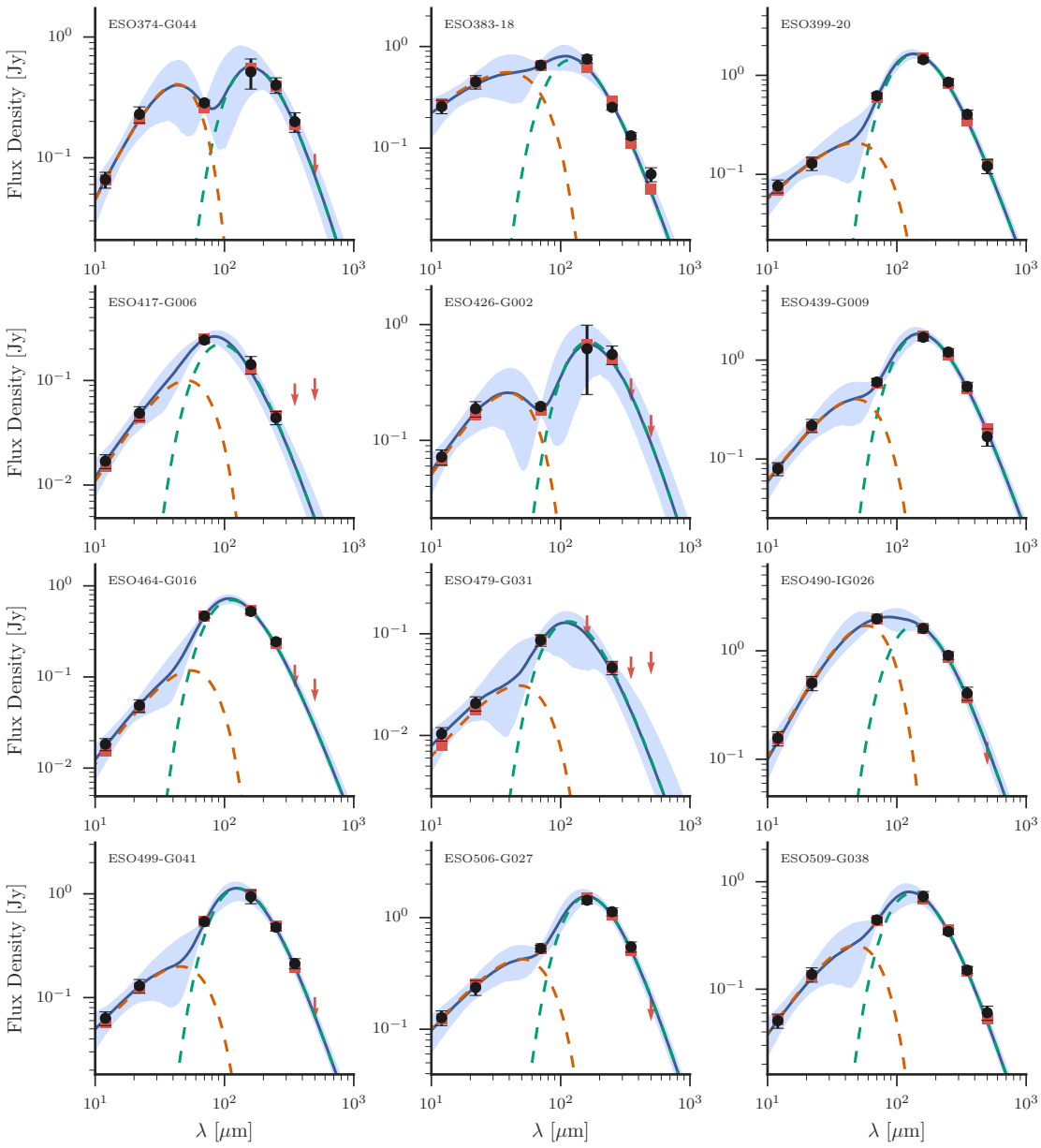
ESO374-G044
ESO383-18
ESO399-20
ESO417-G006
ESO426-G002
ESO439-G009
ESO464-G016
ESO479-G031
ESO490-IG026
ESO499-G041
ESO506-G027
ESO509-G038
Flux Density [Jy]
λ [μm]

Figure E.9

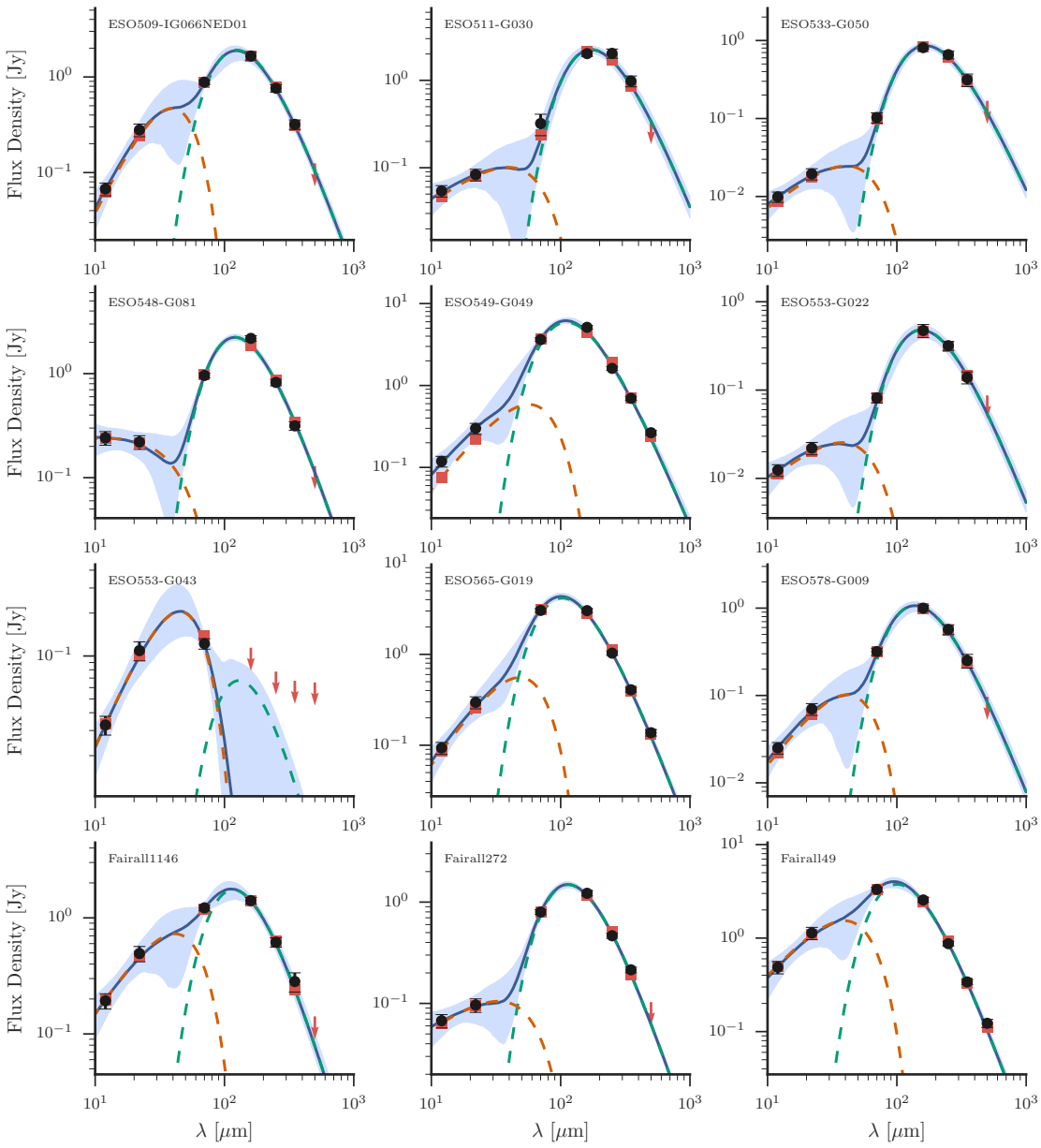
ESO509-IG066NED01
ESO511-G030
ESO533-G050
ESO548-G081
ESO549-G049
ESO553-G022
ESO553-G043
ESO565-G019
ESO578-G009
Fairall1146
Fairall272
Fairall49
Flux Density [Jy]
λ [μm]

Figure E.10

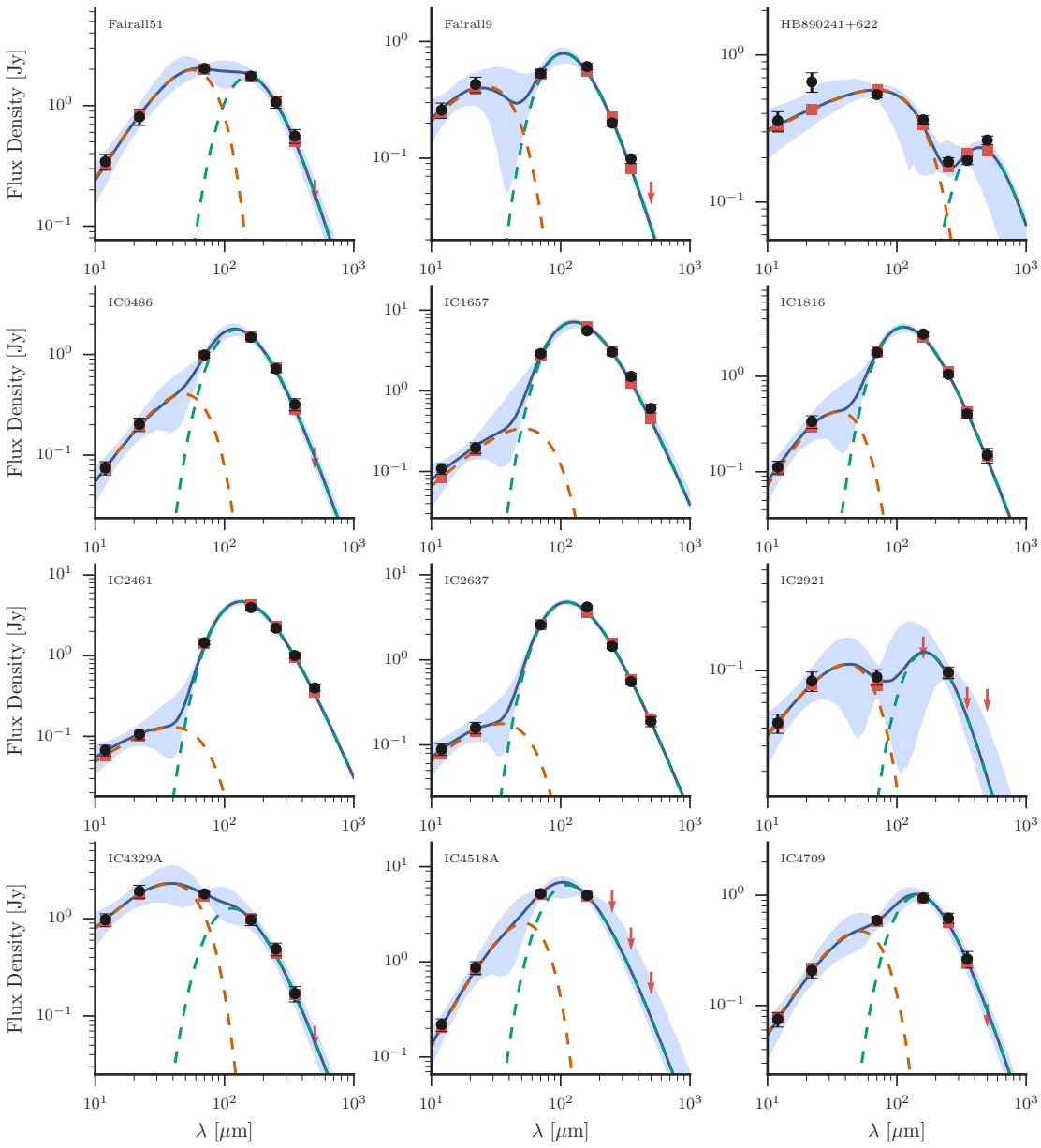
Fairall51
Fairall9
HB890241+622
IC0486
IC1657
IC1816
IC2461
IC2637
IC2921
IC4329A
IC4518A
IC4709
Flux Density [Jy]
λ [μm]

Figure E.11

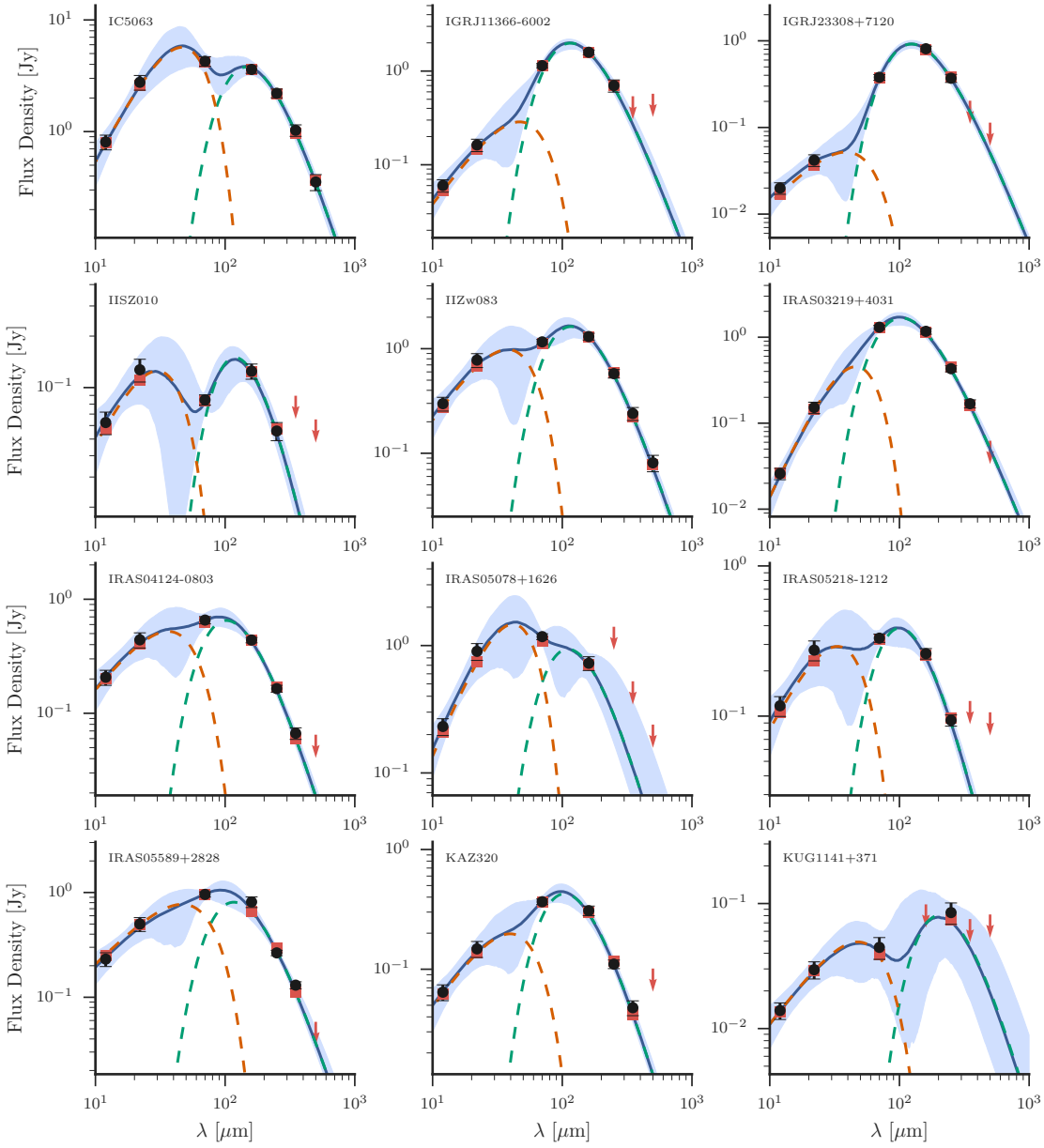
IC5063
IGRJ11366-6002
IGRJ23308+7120
IISZ010
IIZw083
IRAS03219+4031
IRAS04124-0803
IRAS05078+1626
IRAS05218-1212
IRAS05589+2828
KAZ320
KUG1141+371
Flux Density [Jy]
λ [μm]

Figure E.12

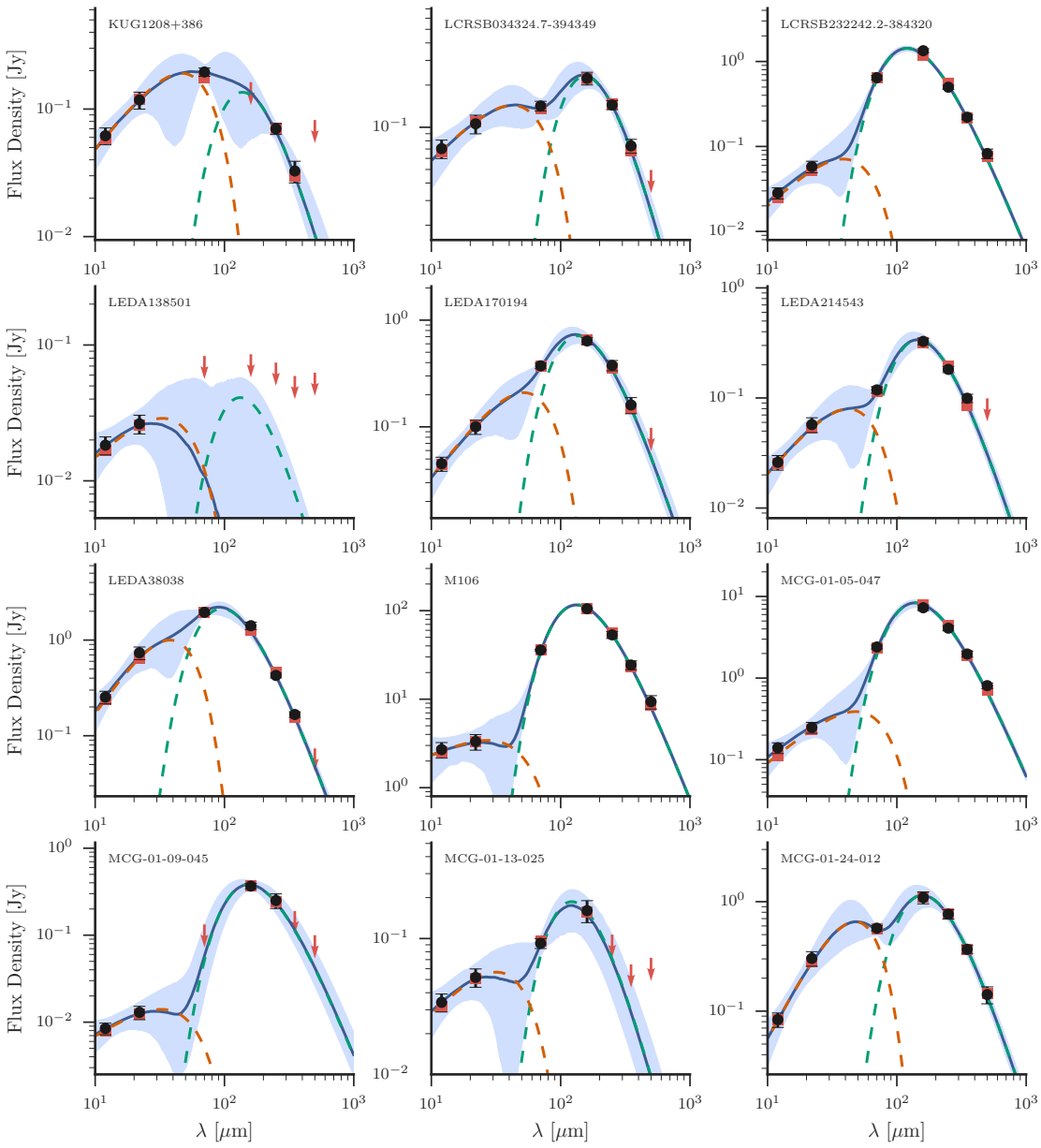
KUG1208+386
LCRSB034324.7-394349
LCRSB232242.2-384320
LEDA138501
LEDA170194
LEDA214543
LEDA38038
M106
MCG-01-05-047
MCG-01-09-045
MCG-01-13-025
MCG-01-24-012
Flux Density [Jy]
λ [μm]

Figure E.13

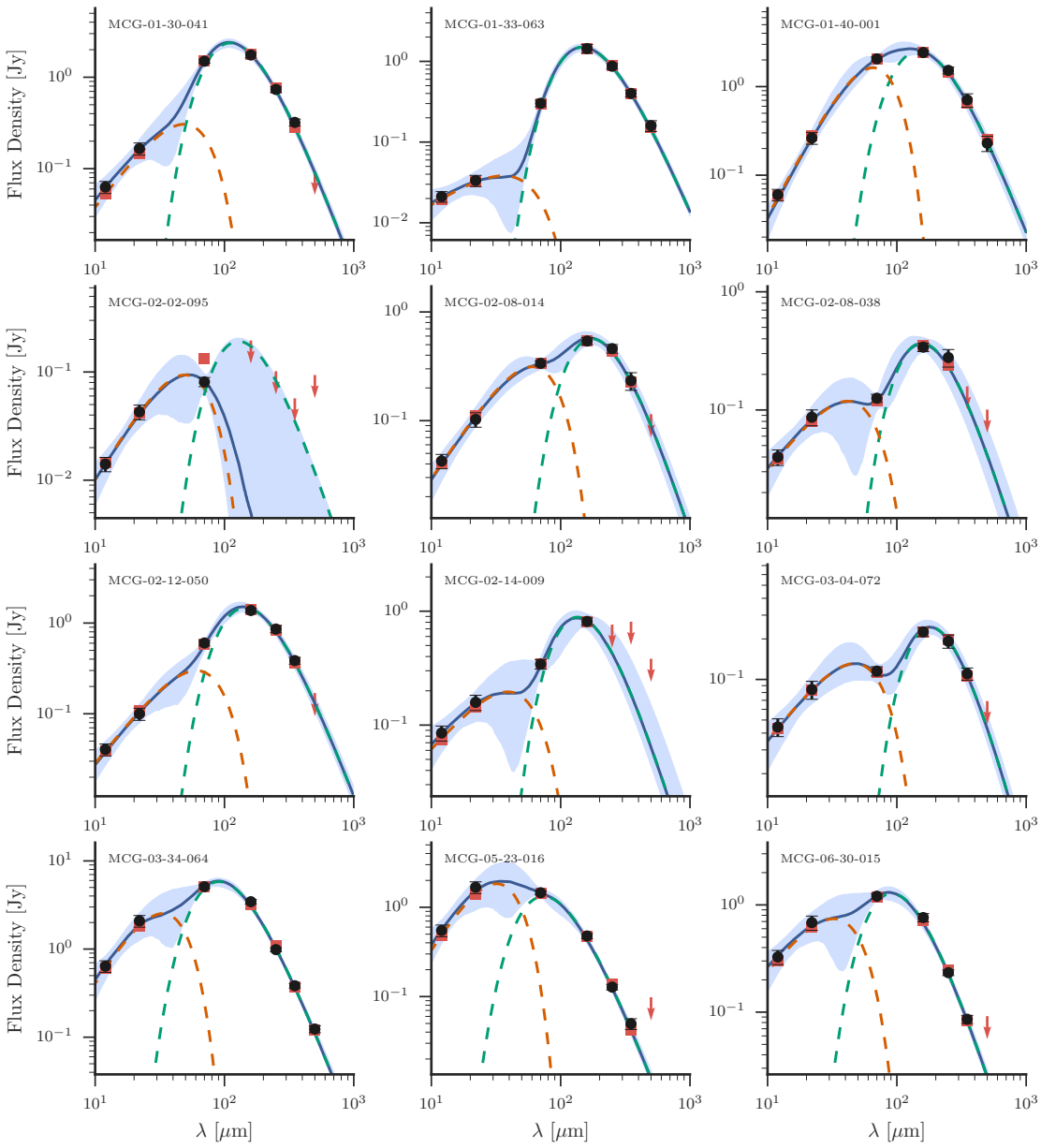
MCG-01-30-041
MCG-01-33-063
MCG-01-40-001
MCG-02-02-095
MCG-02-08-014
MCG-02-08-038
MCG-02-12-050
MCG-02-14-009
MCG-03-04-072
MCG-03-34-064
MCG-05-23-016
MCG-06-30-015
Flux Density [Jy]
λ [μm]

Figure E.14

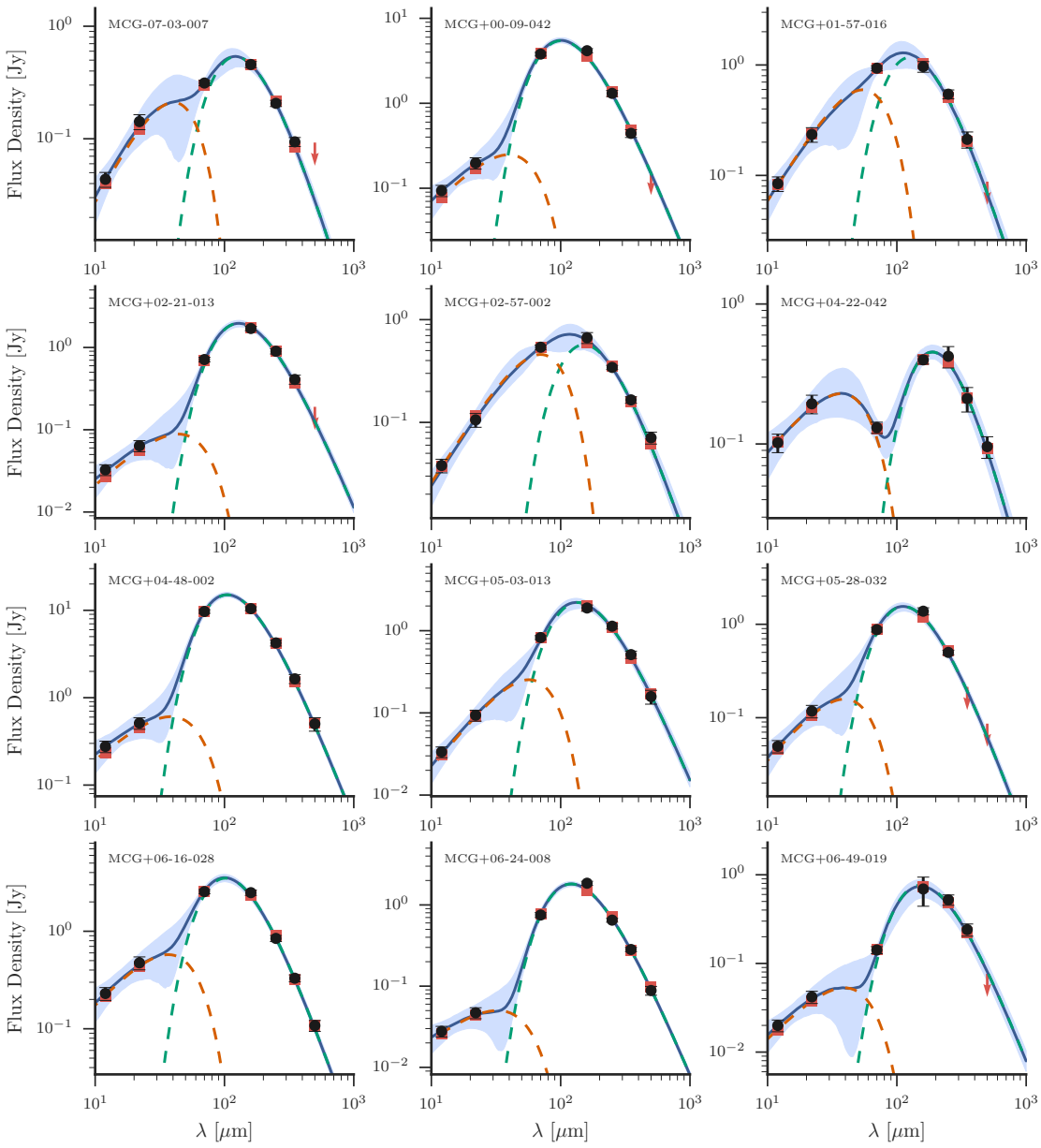
MCG-07-03-007
MCG+00-09-042
MCG+01-57-016
MCG+02-21-013
MCG+02-57-002
MCG+04-22-042
MCG+04-48-002
MCG+05-03-013
MCG+05-28-032
MCG+06-16-028
MCG+06-24-008
MCG+06-49-019
Flux Density [Jy]
λ [μm]

Figure E.15

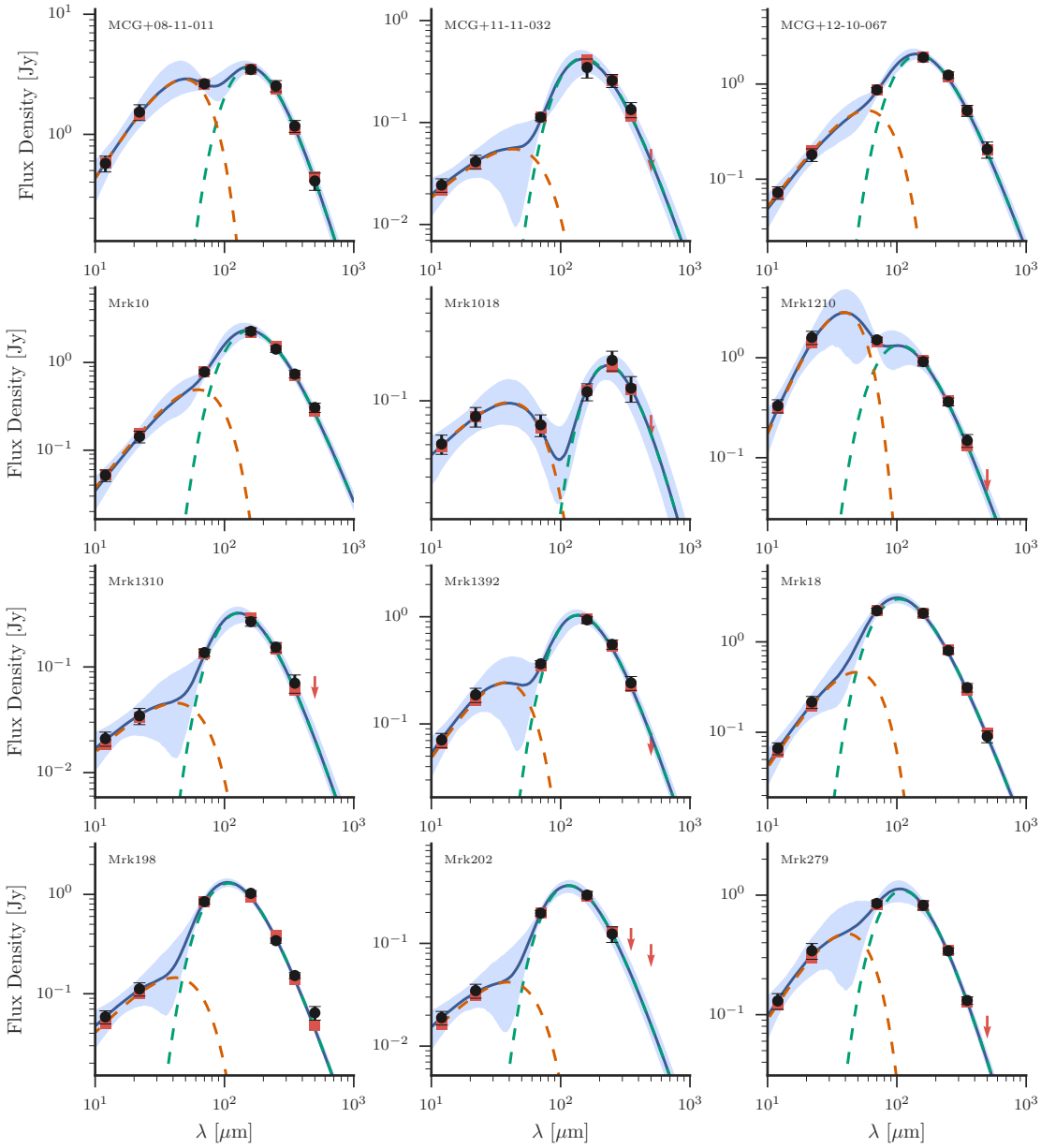
MCG+08-11-011
MCG+11-11-032
MCG+12-10-067
Mrk10
Mrk1018
Mrk1210
Mrk1310
Mrk1392
Mrk18
Mrk198
Mrk202
Mrk279
Flux Density [Jy]
λ [μm]

Figure E.16

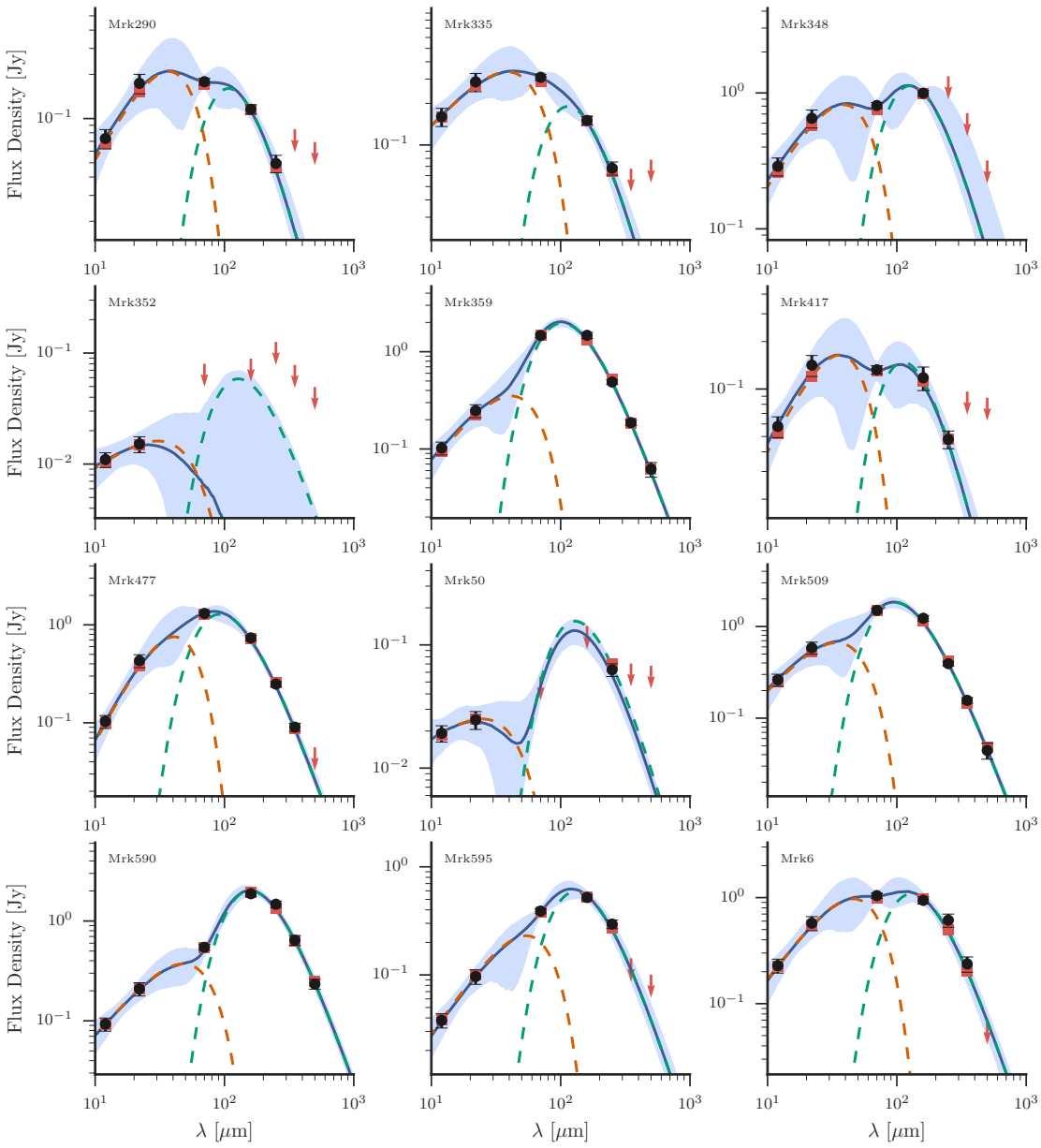
Mrk290
Mrk335
Mrk348
Mrk352
Mrk359
Mrk417
Mrk477
Mrk50
Mrk509
Mrk590
Mrk595
Mrk6
Flux Density [Jy]
λ [μm]

Figure E.17

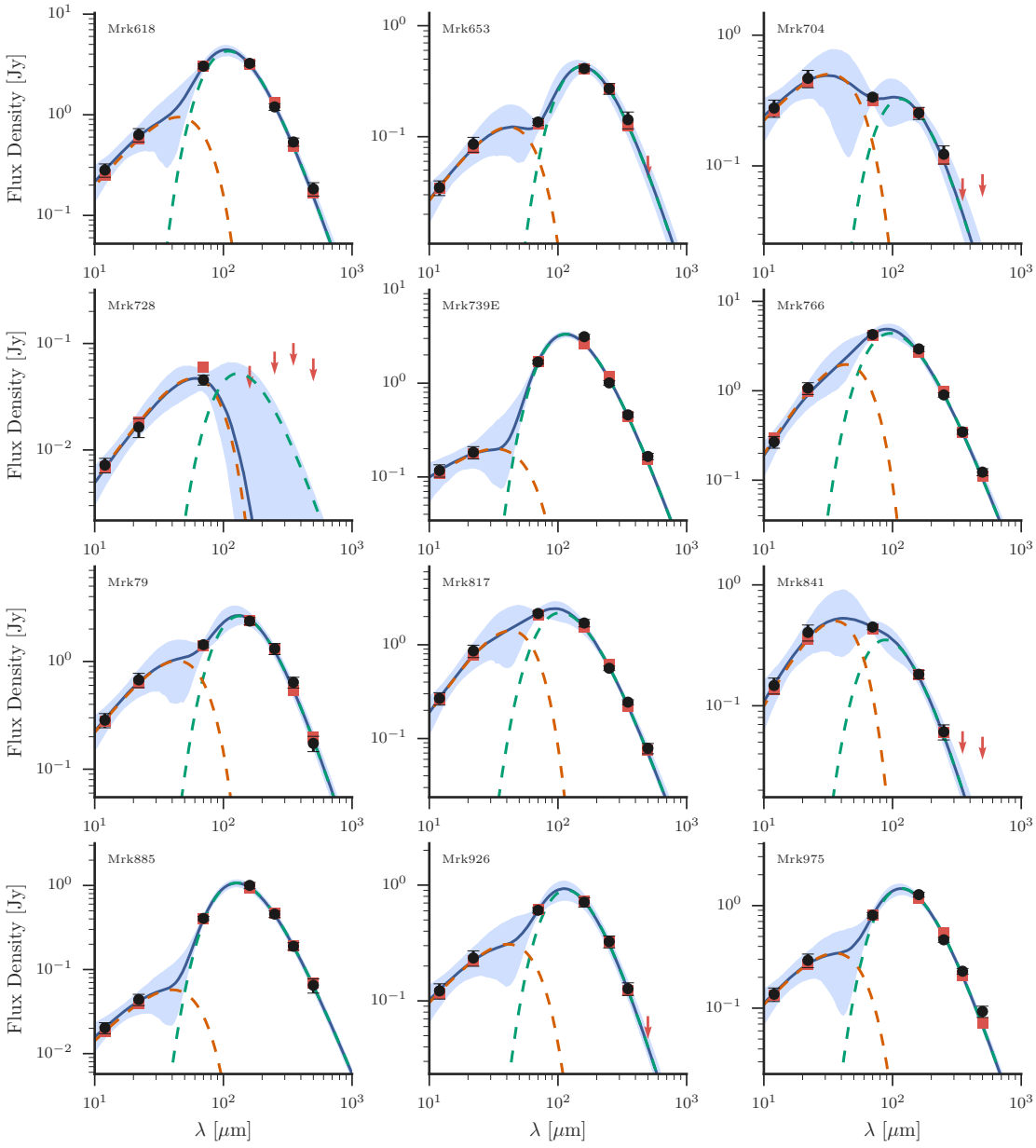
Mrk618
Mrk653
Mrk704
Mrk728
Mrk739E
Mrk766
Mrk79
Mrk817
Mrk841
Mrk885
Mrk926
Mrk975
Flux Density [Jy]
λ [μm]

Figure E.18

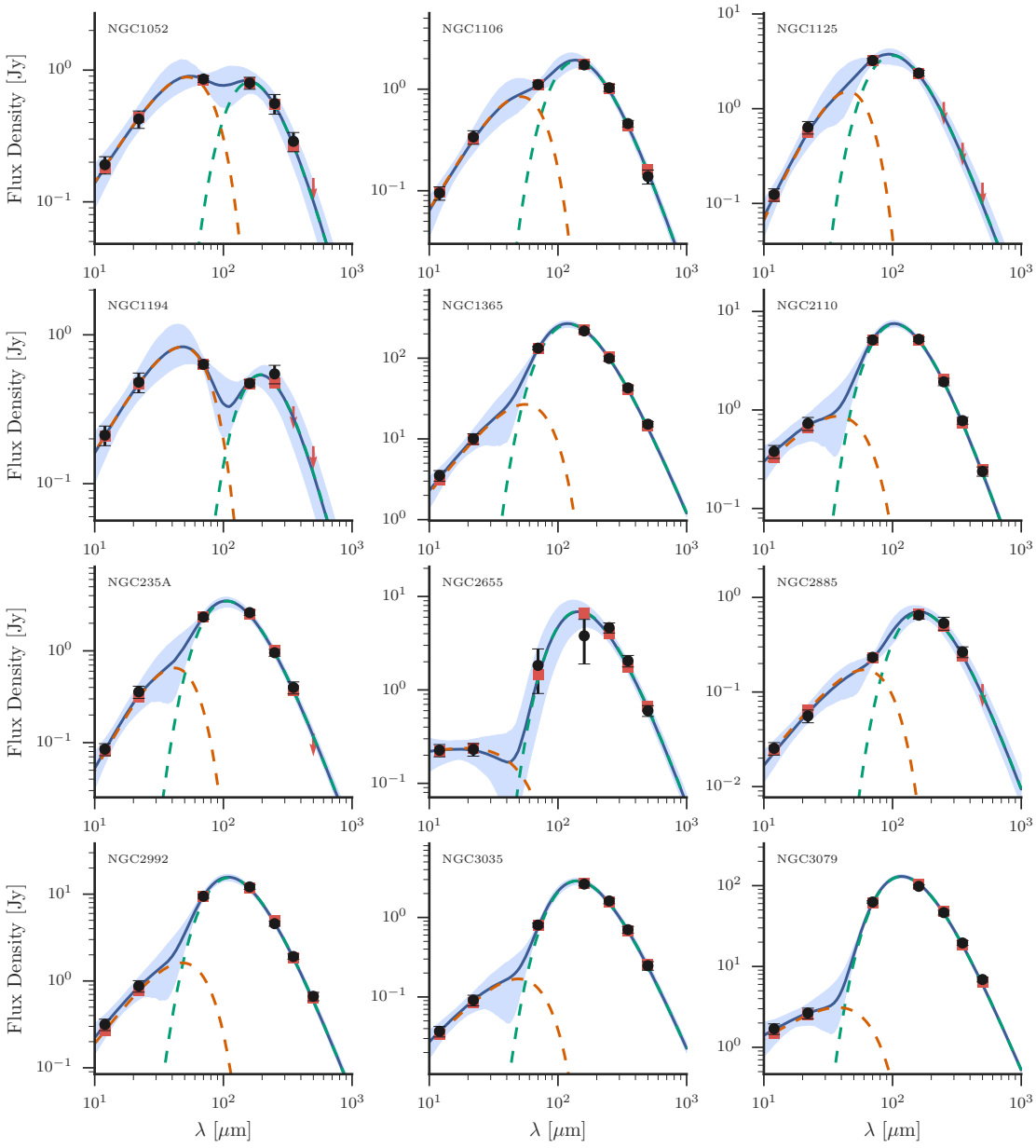
NGC1052
NGC1106
NGC1125
NGC1194
NGC1365
NGC2110
NGC235A
NGC2655
NGC2885
NGC2992
NGC3035
NGC3079
Flux Density [Jy]
λ [μm]

Figure E.19

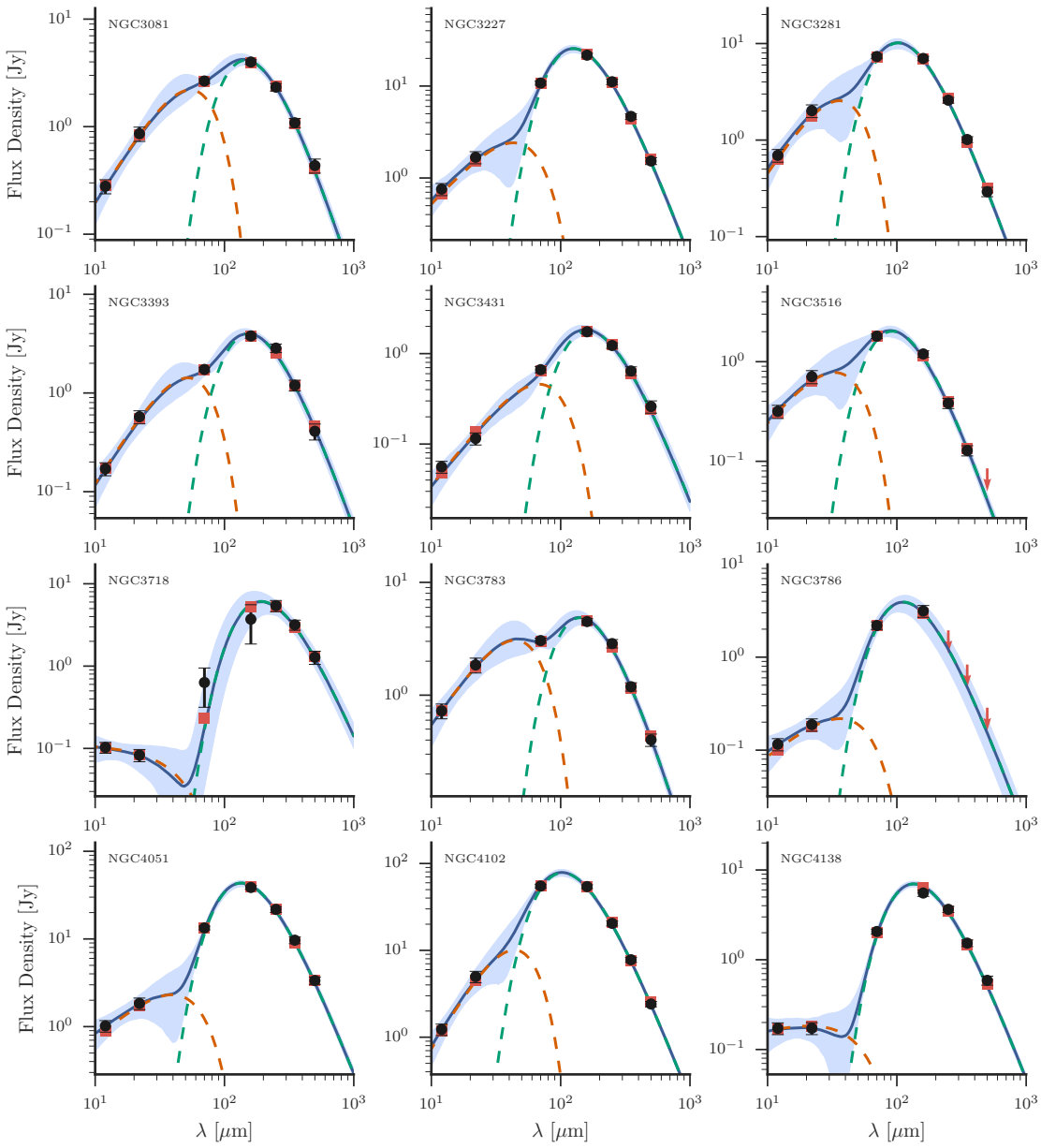
NGC3081
NGC3227
NGC3281
NGC3393
NGC3431
NGC3516
NGC3718
NGC3783
NGC3786
NGC4051
NGC4102
NGC4138
Flux Density [Jy]
λ [μm]

Figure E.20

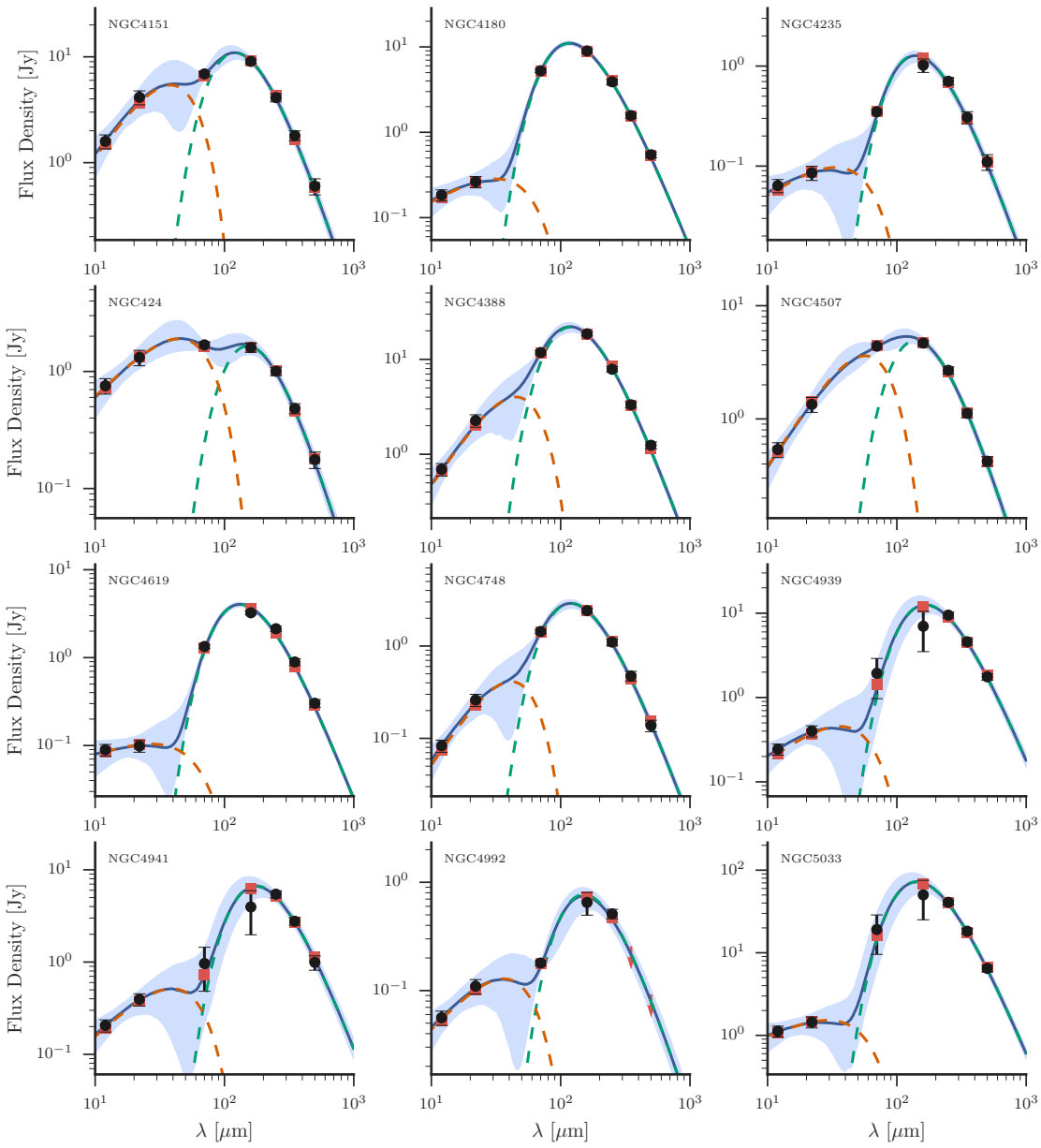
NGC4151
NGC4180
NGC4235
NGC424
NGC4388
NGC4507
NGC4619
NGC4748
NGC4939
NGC4941
NGC4992
NGC5033
Flux Density [Jy]
λ [μm]

Figure E.21

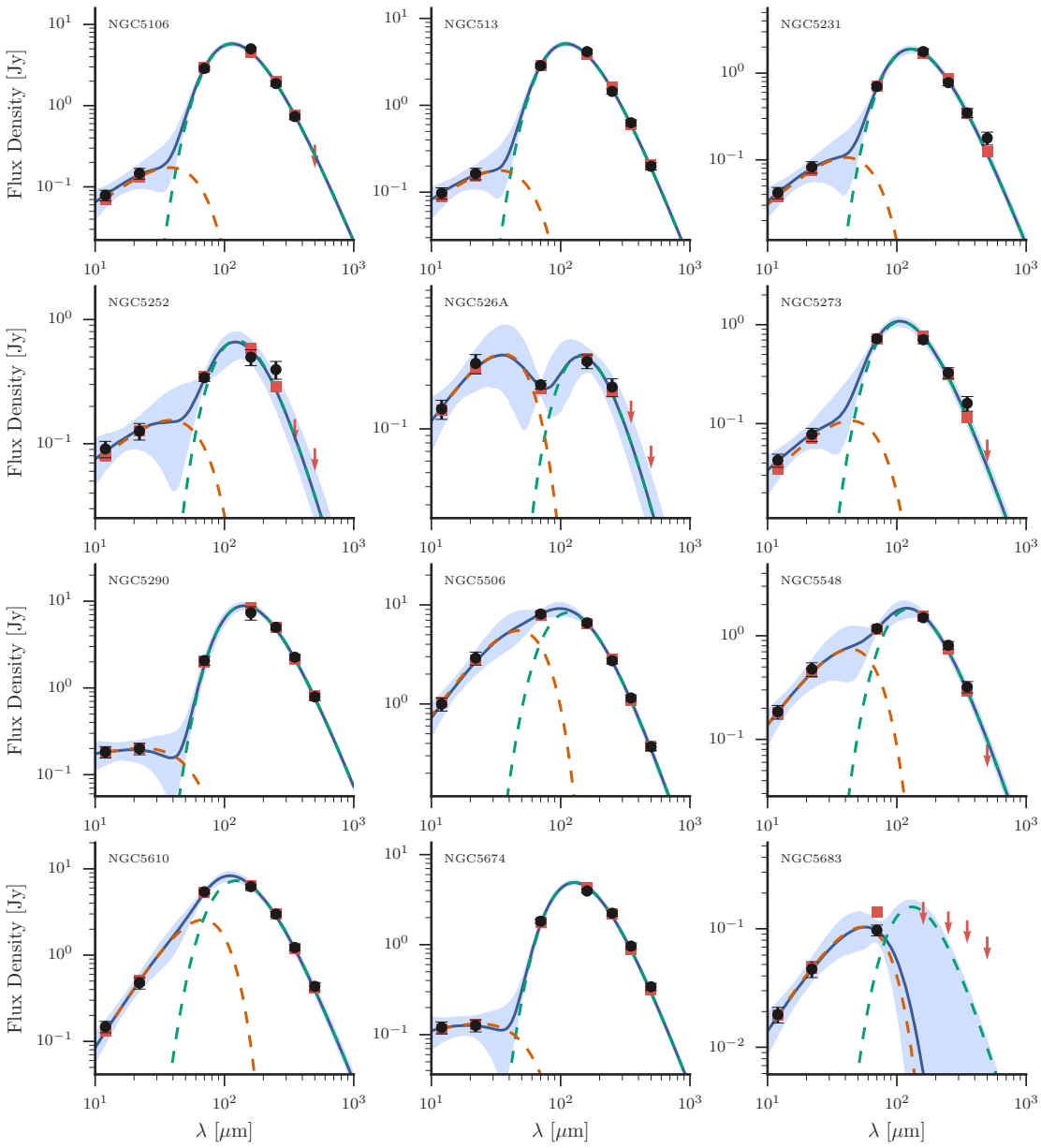
NGC5106
NGC513
NGC5231
NGC5252
NGC526A
NGC5273
NGC5290
NGC5506
NGC5548
NGC5610
NGC5674
NGC5683
Flux Density [Jy]
λ [μm]

Figure E.22

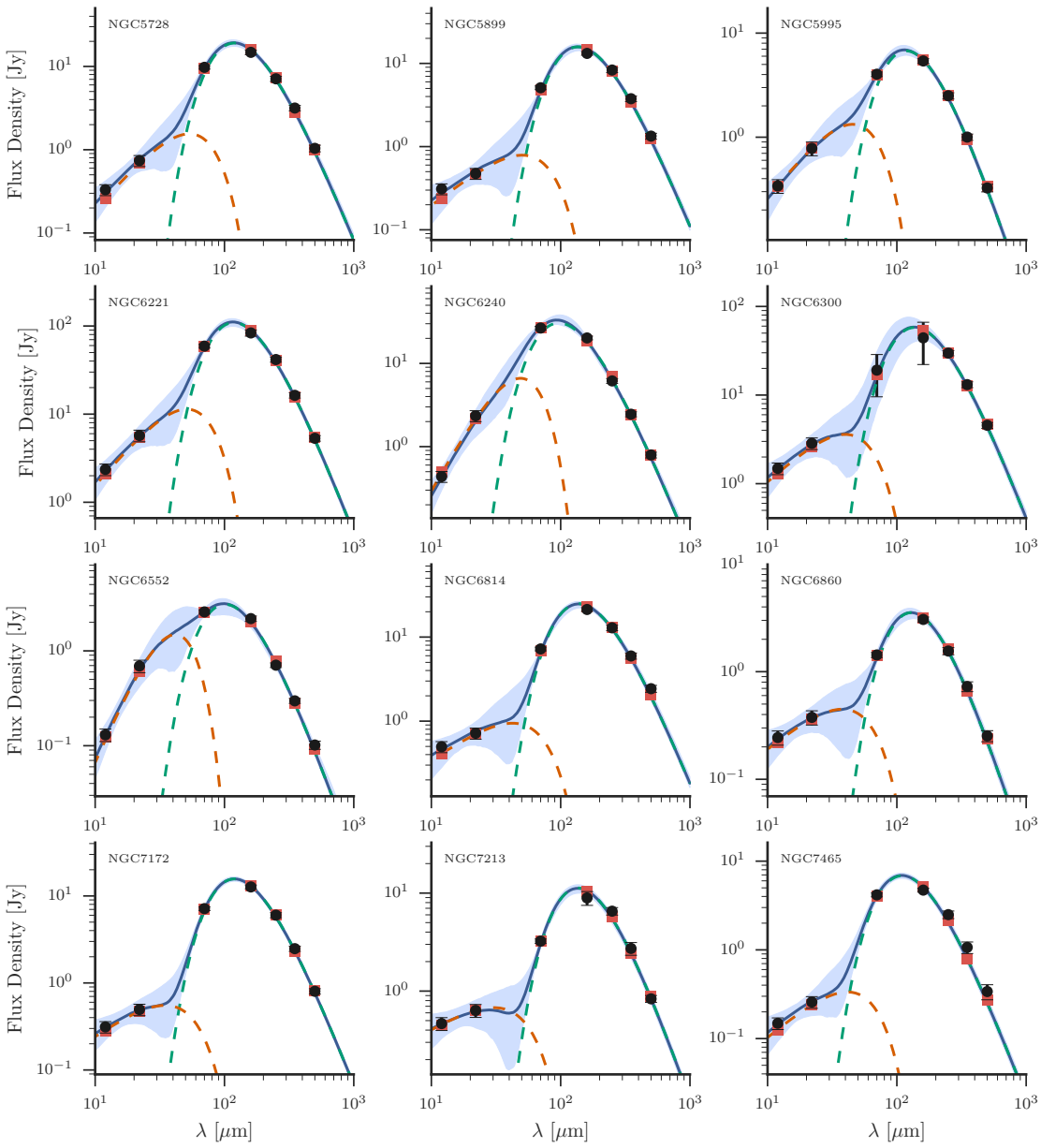
NGC5728
NGC5899
NGC5995
NGC6221
NGC6240
NGC6300
NGC6552
NGC6814
NGC6860
NGC7172
NGC7213
NGC7465
Flux Density [Jy]
λ [μm]

Figure E.23

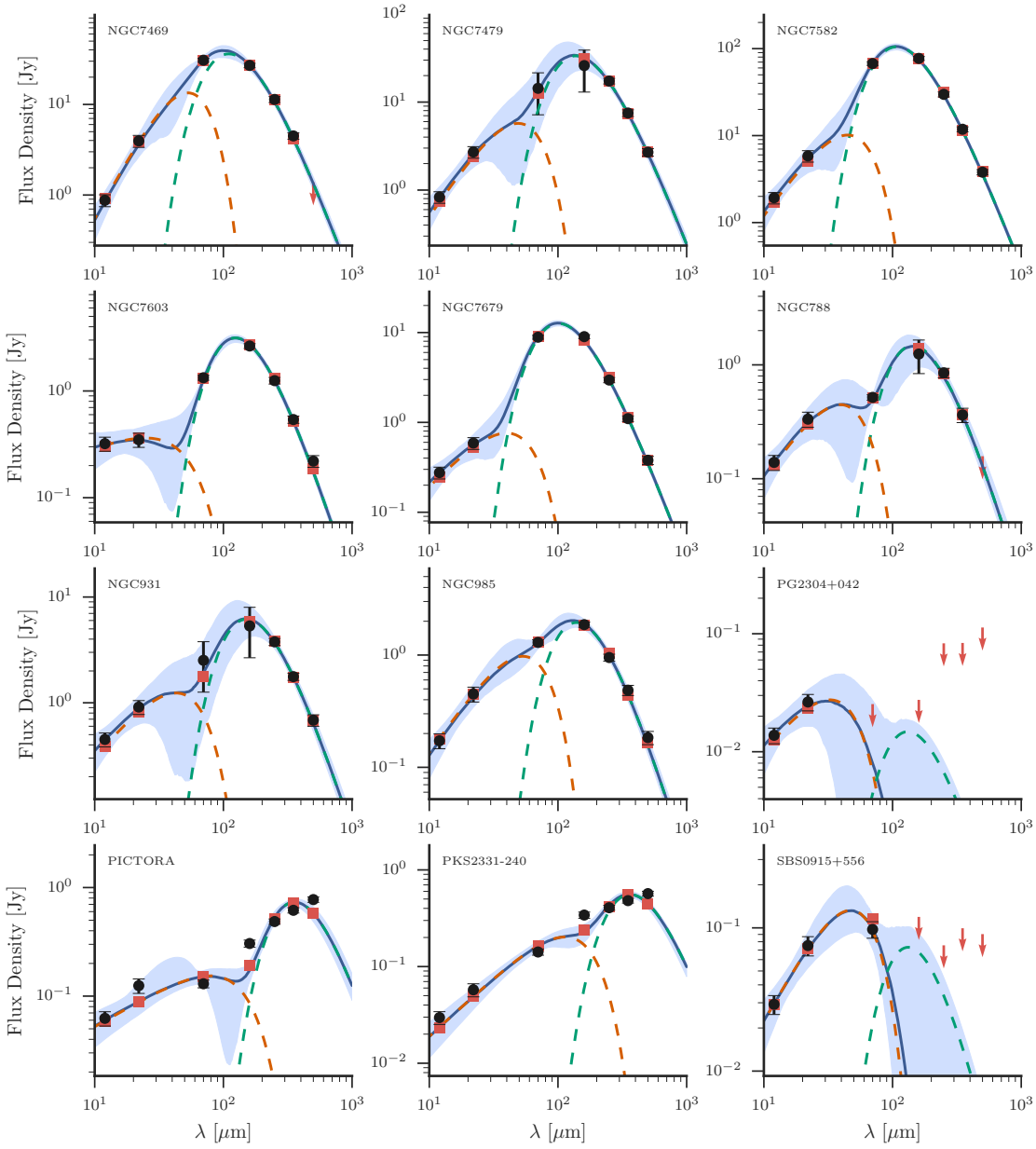
NGC7469
NGC7479
NGC7582
NGC7603
NGC7679
NGC788
NGC931
NGC985
PG2304+042
PICTORA
PKS2331-240
SBS0915+556
Flux Density [Jy]
λ [μm]

Figure E.24

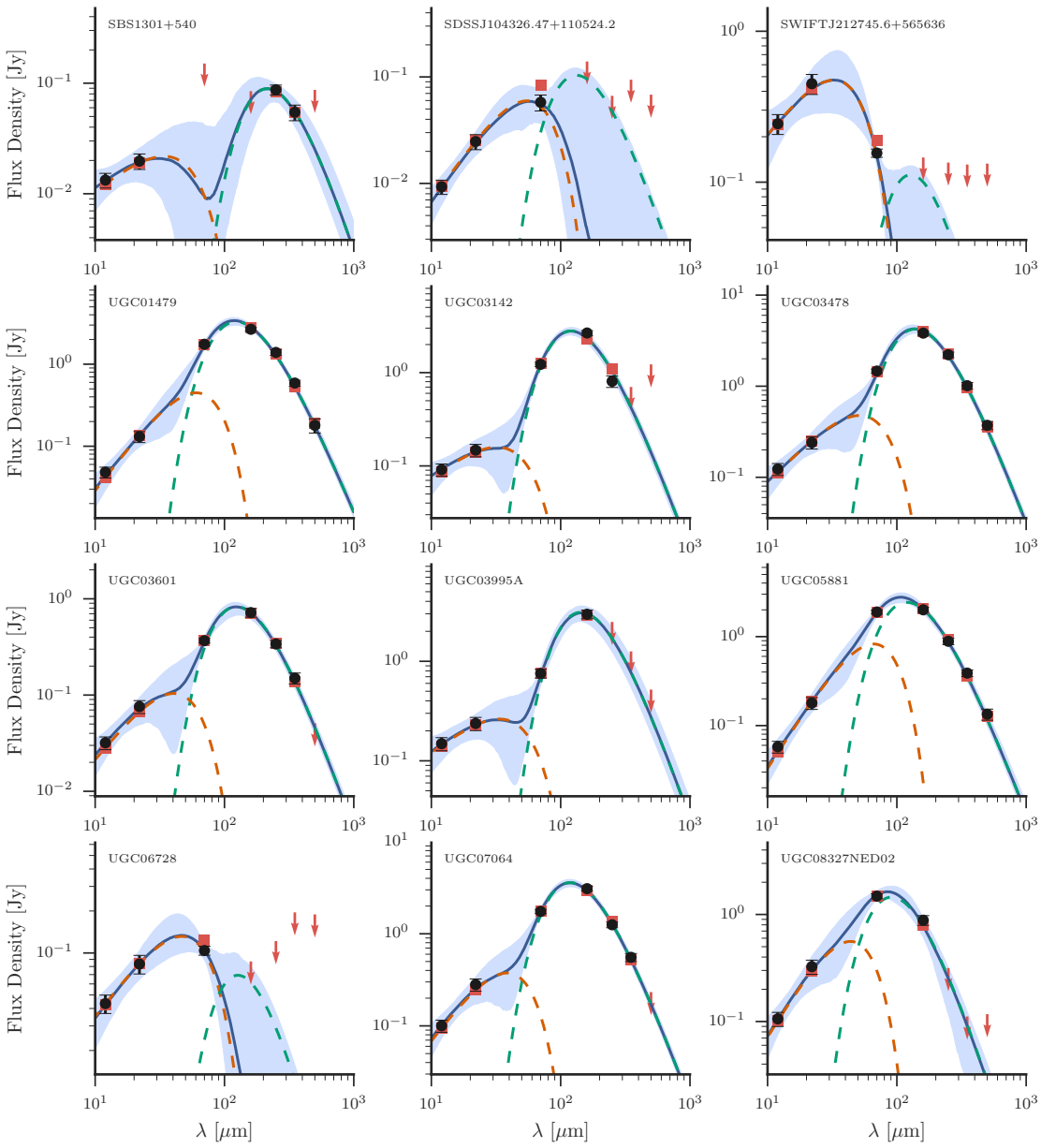
SBS1301+540
SDSSJ104326.47+110524.2
SWIFTJ212745.6+565636
UGC01479
UGC03142
UGC03478
UGC03601
UGC03995A
UGC05881
UGC06728
UGC07064
UGC08327NED02
Flux Density [Jy]
λ [μm]

Figure E.25

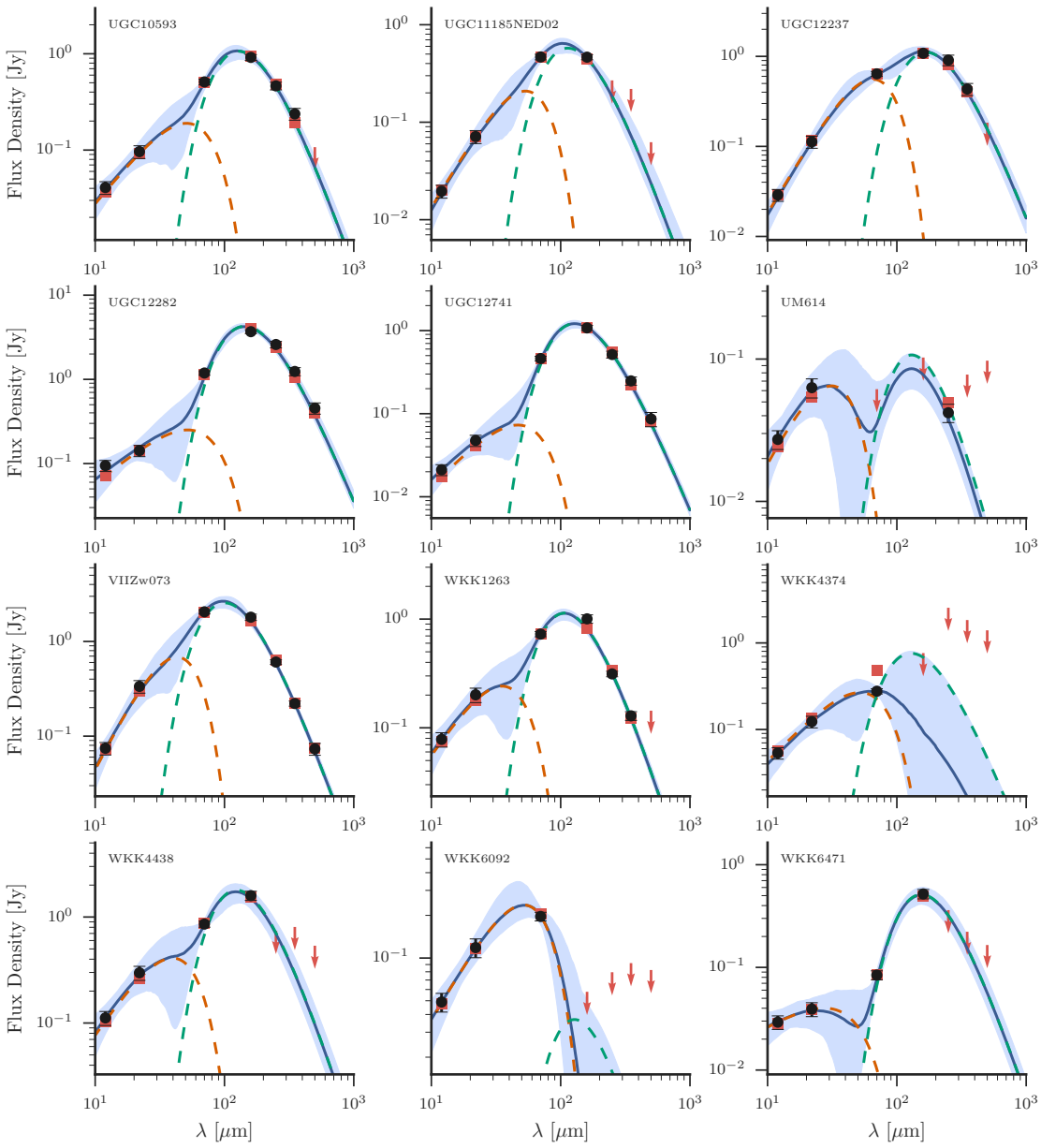
UGC10593
UGC11185NED02
UGC12237
UGC12282
UGC12741
UM614
VIIZw073
WKK1263
WKK4374
WKK4438
WKK6092
WKK6471
Flux Density [Jy]
λ [μm]

Figure E.26

Bibliography

Aird, J., Nandra, K., Laird, E. S., et al. 2010, MNRAS, 401, 2531

Akritas, M. G., & Siebert, J. 1996, MNRAS, 278, 919

Alatalo, K., Blitz, L., Young, L. M., et al. 2011, ApJ, 735, 88

Aniano, G., Draine, B. T., Gordon, K. D., & Sandstrom, K. 2011, PASP, 123, 1218

Antonucci, R. 1993, ARA&A, 31, 473

Asmus, D., Hönig, S. F., Gandhi, P., Smette, A., & Duschl, W. J. 2012, Journal of Physics Conference Series, 372, 012034

—. 2014, MNRAS, 439, 1648

Astropy Collaboration, Robitaille, T. P., Tollerud, E. J., et al. 2013, A&A, 558, A33

Azadi, M., Aird, J., Coil, A. L., et al. 2015, ApJ, 806, 187

Baes, M., Clemens, M., Xilouris, E. M., et al. 2010, A&A, 518, L53

Baldwin, J. A., Phillips, M. M., & Terlevich, R. 1981, PASP, 93, 5

Barger, A. J., Cowie, L. L., Owen, F. N., et al. 2015, ApJ, 801, 87

Barthelmy, S. D., Barbier, L. M., Cummings, J. R., et al. 2005, Space Sci. Rev., 120, 143

Barvainis, R. 1987, ApJ, 320, 537

Bastian, T. S., Benz, A. O., & Gary, D. E. 1998, ARA&A, 36, 131

Baum, S. A., Gallimore, J. F., O'Dea, C. P., et al. 2010, ApJ, 710, 289

Baumgartner, W. H., Tueller, J., Markwardt, C. B., et al. 2013, ApJS, 207, 19

Becker, R. H., White, R. L., & Edwards, A. L. 1991, ApJS, 75, 1

Becker, R. H., White, R. L., & Helfand, D. J. 1995, ApJ, 450, 559

Behar, E., Baldi, R. D., Laor, A., et al. 2015, MNRAS, 451, 5036

Bell, E. F., van der Wel, A., Papovich, C., et al. 2012, ApJ, 753, 167

Bendo, G. J., Wilson, C. D., Pohlen, M., et al. 2010, A&A, 518, L65

Bendo, G. J., Boselli, A., Dariush, A., et al. 2012, MNRAS, 419, 1833

Bendo, G. J., Griffin, M. J., Bock, J. J., et al. 2013, MNRAS, 433, 3062

Bendo, G. J., Baes, M., Bianchi, S., et al. 2015, MNRAS, 448, 135

Benson, A. J., Bower, R. G., Frenk, C. S., et al. 2003, ApJ, 599, 38

Berney, S., Koss, M., Trakhtenbrot, B., et al. 2015, MNRAS, 454, 3622

Bertin, E., & Arnouts, S. 1996, A&AS, 117, 393

Best, P. N. 2007, New A Rev., 51, 168

Bianchi, L., Conti, A., & Shiao, B. 2014, Advances in Space Research, 53, 900

Bianchi, S. 2013, A&A, 552, A89

Bock, D. C.-J., Large, M. I., & Sadler, E. M. 1999, AJ, 117, 1578

Boquien, M., Calzetti, D., Combes, F., et al. 2011, AJ, 142, 111

Boselli, A., Boissier, S., Cortese, L., et al. 2006, ApJ, 651, 811

Boselli, A., Gavazzi, G., & Sanvito, G. 2003, Astronomy and Astrophysics, 402, 37

Boselli, A., Hughes, T. M., Cortese, L., Gavazzi, G., & Buat, V. 2013, A&A, 550, A114

Boselli, A., Ciesla, L., Buat, V., et al. 2010a, A&A, 518, L61

Boselli, A., Eales, S., Cortese, L., et al. 2010b, PASP, 122, 261

Boselli, A., Ciesla, L., Cortese, L., et al. 2012, A&A, 540, A54

Bot, C., Ysard, N., Paradis, D., et al. 2010, A&A, 523, A20

Bouwens, R. J., Illingworth, G. D., Oesch, P. A., et al. 2012, ApJ, 754, 83

Bower, R. G., Benson, A. J., Malbon, R., et al. 2006, MNRAS, 370, 645

Boyle, B. J., & Terlevich, R. J. 1998, MNRAS, 293, L49

Brandl, B. R., Bernard-Salas, J., Spoon, H. W. W., et al. 2006, ApJ, 653, 1129

Brinchmann, J., Charlot, S., White, S. D. M., et al. 2004, MNRAS, 351, 1151

Bruzual, G., & Charlot, S. 2003, MNRAS, 344, 1000

Buchanan, C. L., Gallimore, J. F., O'Dea, C. P., et al. 2006, AJ, 132, 401

Burgarella, D., Buat, V., Gruppioni, C., et al. 2013, Astronomy & Astrophysics, 554, A70

Burlon, D., Ajello, M., Greiner, J., et al. 2011, ApJ, 728, 58

Calzetti, D., Armus, L., Bohlin, R. C., et al. 2000, ApJ, 533, 682

Calzetti, D., Kinney, A. L., & Storchi-Bergmann, T. 1994, ApJ, 429, 582

Calzetti, D., Wu, S.-Y., Hong, S., et al. 2010, ApJ, 714, 1256

Cardamone, C. N., Urry, C. M., Schawinski, K., et al. 2010, ApJ, 721, L38

Casey, C. M. 2012, MNRAS, 425, 3094

Catinella, B., Schiminovich, D., Kauffmann, G., et al. 2010, MNRAS, 403, 683

Chapman, S. C., Helou, G., Lewis, G. F., & Dale, D. A. 2003, ApJ, 588, 186

Charlot, S., & Longhetti, M. 2001, MNRAS, 323, 887

Chen, B., Dai, X., Kochanek, C. S., et al. 2011, ApJ, 740, L34

Chen, C.-T. J., Hickox, R. C., Alberts, S., et al. 2013, ApJ, 773, 3

Cicone, C., Maiolino, R., Sturm, E., et al. 2014, A&A, 562, A21

Cid Fernandes, R., Heckman, T., Schmitt, H., González Delgado, R. M., & Storchi-Bergmann, T. 2001, ApJ, 558, 81

Ciesla, L., Boselli, A., Smith, M. W. L., et al. 2012, A&A, 543, A161

Ciesla, L., Boquien, M., Boselli, A., et al. 2014a, ArXiv e-prints

—. 2014b, A&A, 565, A128

Ciesla, L., Charmandaris, V., Georgakakis, A., et al. 2015, A&A, 576, A10

Cimatti, A., Brusa, M., Talia, M., et al. 2013, ApJ, 779, L13

Cirasuolo, M., Celotti, A., Magliocchetti, M., & Danese, L. 2003a, MNRAS, 346, 447

Cirasuolo, M., Magliocchetti, M., Celotti, A., & Danese, L. 2003b, MNRAS, 341, 993

Condon, J. J., Cotton, W. D., Greisen, E. W., et al. 1998, AJ, 115, 1693

Cortese, L., Davies, J. I., Pohlen, M., et al. 2010, A&A, 518, L49

Cortese, L., Ciesla, L., Boselli, A., et al. 2012a, A&A, 540, A52

Cortese, L., Boissier, S., Boselli, A., et al. 2012b, A&A, 544, A101

Cortese, L., Fritz, J., Bianchi, S., et al. 2014, MNRAS, 440, 942

Cowie, L. L., Barger, A. J., Bautz, M. W., Brandt, W. N., & Garmire, G. P. 2003, ApJ, 584, L57

Cowie, L. L., Songaila, A., Hu, E. M., & Cohen, J. G. 1996, AJ, 112, 839

Croton, D. J., Springel, V., White, S. D. M., et al. 2006, MNRAS, 365, 11

da Cunha, E., Eminian, C., Charlot, S., & Blaizot, J. 2010, MNRAS, 403, 1894

Dai, Y. S., Wilkes, B. J., Bergeron, J., et al. 2015, ArXiv e-prints

Dale, D. A., & Helou, G. 2002, ApJ, 576, 159

Dale, D. A., Helou, G., Magdis, G. E., et al. 2014, ApJ, 784, 83

Dale, D. A., Gil de Paz, A., Gordon, K. D., et al. 2007, ApJ, 655, 863

Dale, D. A., Aniano, G., Engelbracht, C. W., et al. 2012, ApJ, 745, 95

Davies, R. I., Müller Sánchez, F., Genzel, R., et al. 2007, ApJ, 671, 1388

de Grijp, M. H. K., Miley, G. K., Lub, J., & de Jong, T. 1985, Nature, 314, 240

Devereux, N. A., & Young, J. S. 1990, ApJ, 350, L25

Di Matteo, P., Combes, F., Melchior, A.-L., & Semelin, B. 2007, A&A, 468, 61

Di Matteo, T., Springel, V., & Hernquist, L. 2005, Nature, 433, 604

di Serego Alighieri, S., Bianchi, S., Pappalardo, C., et al. 2013, A&A, 552, A8

Diamond-Stanic, A. M., & Rieke, G. H. 2010, ApJ, 724, 140

—. 2012, ApJ, 746, 168

Dixon, T. G., & Joseph, R. D. 2011, ApJ, 740, 99

Doi, A., Kameno, S., & Inoue, M. 2005, MNRAS, 360, 119

Doi, A., Nakanishi, K., Nagai, H., Kohno, K., & Kameno, S. 2011, AJ, 142, 167

Domínguez Sánchez, H., Bongiovanni, A., Lara-López, M. A., et al. 2014, MNRAS, 441, 2

Donley, J. L., Koekemoer, A. M., Brusa, M., et al. 2012, ApJ, 748, 142

Draine, B. T. 2003, ARA&A, 41, 241

—. 2011, Physics of the Interstellar and Intergalactic Medium

Draine, B. T., & Hensley, B. 2012, ApJ, 757, 103

Draine, B. T., & Lee, H. M. 1984, ApJ, 285, 89

Draine, B. T., Dale, D. A., Bendo, G., et al. 2007, ApJ, 663, 866

Dubois, Y., Gavazzi, R., Peirani, S., & Silk, J. 2013, MNRAS, 433, 3297

Efstathiou, A., & Rowan-Robinson, M. 1995, MNRAS, 273, 649

Elbaz, D., Daddi, E., Le Borgne, D., et al. 2007, A&A, 468, 33

Elbaz, D., Dickinson, M., Hwang, H. S., et al. 2011, A&A, 533, A119

Ellison, S. L., Patton, D. R., Mendel, J. T., & Scudder, J. M. 2011, MNRAS, 418, 2043

Elvis, M., Wilkes, B. J., McDowell, J. C., et al. 1994, ApJS, 95, 1

Esquej, P., Alonso-Herrero, A., González-Martín, O., et al. 2014, ApJ, 780, 86

Fabian, A. C. 1999, MNRAS, 308, L39

—. 2012, ARA&A, 50, 455

Fabian, A. C., Sanders, J. S., Allen, S. W., et al. 2003, MNRAS, 344, L43

Feigelson, E. D., & Nelson, P. I. 1985, ApJ, 293, 192

Ferrarese, L., & Merritt, D. 2000, ApJ, 539, L9

Foreman-Mackey, D., Hogg, D. W., Lang, D., & Goodman, J. 2013, PASP, 125, 306

Franceschini, A., Hasinger, G., Miyaji, T., & Malquori, D. 1999, MNRAS, 310, L5

Fritz, J., Franceschini, A., & Hatziminaoglou, E. 2006, MNRAS, 366, 767

Galametz, M., Madden, S. C., Galliano, F., et al. 2011, A&A, 532, A56

Galametz, M., Madden, S., Galliano, F., et al. 2009, A&A, 508, 645

Galametz, M., Kennicutt, R. C., Albrecht, M., et al. 2012, MNRAS, 425, 763

Gandhi, P., Horst, H., Smette, A., et al. 2009, A&A, 502, 457

García-González, J., Alonso-Herrero, A., Hernán-Caballero, A., et al. 2016, MNRAS, 458, 4512

Gebhardt, K., Bender, R., Bower, G., et al. 2000, ApJ, 539, L13

Gehrels, N., Chincarini, G., Giommi, P., et al. 2004, ApJ, 611, 1005

Goodman, J., & Weare, J. 2010, Communications in Applied Mathematics and Computational Science, 5, 65

Gordon, K. D., Galliano, F., Hony, S., et al. 2010, A&A, 518, L89

Gould, R. J., & Salpeter, E. E. 1963, ApJ, 138, 393

Griffin, M. J., Abergel, A., Abreu, A., et al. 2010, A&A, 518, L3

Griffith, M. R., & Wright, A. E. 1993, AJ, 105, 1666

Gültekin, K., Richstone, D. O., Gebhardt, K., et al. 2009, ApJ, 698, 198

Häring, N., & Rix, H.-W. 2004, ApJ, 604, L89

Harrison, C. M., Alexander, D. M., Mullaney, J. R., & Swinbank, A. M. 2014, MNRAS, 441, 3306

Hasinger, G., Miyaji, T., & Schmidt, M. 2005, A&A, 441, 417

Hauser, M. G., & Dwek, E. 2001, Annual Review of Astronomy and Astrophysics, 39, 249

Heckman, T. M. 2001, in Astronomical Society of the Pacific Conference Series, Vol. 240, Gas and Galaxy Evolution, ed. J. E. Hibbard, M. Rupen, & J. H. van Gorkom, 345

Heckman, T. M., Blitz, L., Wilson, A. S., Armus, L., & Miley, G. K. 1989, ApJ, 342, 735

Heinis, S., Buat, V., Béthermin, M., et al. 2014, MNRAS, 437, 1268

Hernán-Caballero, A., Alonso-Herrero, A., Hatziminaoglou, E., et al. 2015, ArXiv e-prints

Hickox, R. C., Mullaney, J. R., Alexander, D. M., et al. 2014, ApJ, 782, 9

Hickox, R. C., Jones, C., Forman, W. R., et al. 2009, ApJ, 696, 891

Ho, L. C., & Peng, C. Y. 2001, ApJ, 555, 650

Hönig, S. F., & Kishimoto, M. 2010, A&A, 523, A27

Hönig, S. F., Kishimoto, M., Tristram, K. R. W., et al. 2013, ApJ, 771, 87

Hopkins, P. F., Hernquist, L., Cox, T. J., et al. 2006, ApJS, 163, 1

Hopkins, P. F., & Quataert, E. 2010, MNRAS, 407, 1529

Hunt, L. K., Draine, B. T., Bianchi, S., et al. 2015, A&A, 576, A33

Ichikawa, K., Ueda, Y., Terashima, Y., et al. 2012, ApJ, 754, 45

Imanishi, M., & Wada, K. 2004, ApJ, 617, 214

Isobe, T., Feigelson, E. D., Akritas, M. G., & Babu, G. J. 1990, ApJ, 364, 104

Jaffe, W., Meisenheimer, K., Röttgering, H. J. A., et al. 2004, Nature, 429, 47

Kauffmann, G., Heckman, T. M., White, S. D. M., et al. 2003a, MNRAS, 341, 54

Kauffmann, G., Heckman, T. M., Tremonti, C., et al. 2003b, MNRAS, 346, 1055

Kaviraj, S., Schawinski, K., Silk, J., & Shabala, S. S. 2011, MNRAS, 415, 3798

Keating, S. K., Everett, J. E., Gallagher, S. C., & Deo, R. P. 2012, ApJ, 749, 32

Keel, W. C., Chojnowski, S. D., Bennert, V. N., et al. 2012, MNRAS, 420, 878

Keel, W. C., Maksym, W. P., Bennert, V. N., et al. 2014, ArXiv e-prints

Kellermann, K. I., Sramek, R., Schmidt, M., Shaffer, D. B., & Green, R. 1989, AJ, 98, 1195

Kelly, B. C. 2007, ApJ, 665, 1489

Kennicutt, R. C., & Evans, N. J. 2012, ARA&A, 50, 531

Kennicutt, R. C., Calzetti, D., Aniano, G., et al. 2011, PASP, 123, 1347

Kennicutt, Jr., R. C. 1998, ARA&A, 36, 189

Kennicutt, Jr., R. C., Tamblyn, P., & Congdon, C. E. 1994, ApJ, 435, 22

Kessler, M. F., Steinz, J. A., Anderegg, M. E., et al. 1996, A&A, 315, L27

Kewley, L. J., Dopita, M. A., Sutherland, R. S., Heisler, C. A., & Trevena, J. 2001, ApJ, 556, 121

Kewley, L. J., Groves, B., Kauffmann, G., & Heckman, T. 2006, MNRAS, 372, 961

Kirkpatrick, A., Calzetti, D., Kennicutt, R., et al. 2014, ApJ, 789, 130

Kocevski, D. D., Faber, S. M., Mozena, M., et al. 2012, ApJ, 744, 148

Kormendy, J., & Ho, L. C. 2013, ARA&A, 51, 511

Kormendy, J., & Richstone, D. 1995, ARA&A, 33, 581

Koss, M., Mushotzky, R., Veilleux, S., & Winter, L. 2010, ApJ, 716, L125

Koss, M., Mushotzky, R., Veilleux, S., et al. 2011, ApJ, 739, 57

Lacy, M., Storrie-Lombardi, L. J., Sajina, A., et al. 2004, ApJS, 154, 166

LaMassa, S. M., Heckman, T. M., Ptak, A., & Urry, C. M. 2013, ApJ, 765, L33

Lanz, L., Ogle, P. M., Evans, D., et al. 2015, ApJ, 801, 17

Laor, A. 2003, ArXiv Astrophysics e-prints

Lebouteiller, V., Barry, D. J., Spoon, H. W. W., et al. 2011, ApJS, 196, 8

Leslie, S. K., Kewley, L. J., Sanders, D. B., & Lee, N. 2016, MNRAS, 455, L82

Li, Y., Calzetti, D., Kennicutt, R. C., et al. 2010, ApJ, 725, 677

Li, Y., Crocker, A. F., Calzetti, D., et al. 2013, ApJ, 768, 180

Lilly, S. J., Carollo, C. M., Pipino, A., Renzini, A., & Peng, Y. 2013, ApJ, 772, 119

Lintott, C. J., Schawinski, K., Slosar, A., et al. 2008, MNRAS, 389, 1179

Lintott, C. J., Schawinski, K., Keel, W., et al. 2009, MNRAS, 399, 129

Lonsdale Persson, C. J., & Helou, G. 1987, ApJ, 314, 513

Lutz, D., Maiolino, R., Spoon, H. W. W., & Moorwood, A. F. M. 2004, A&A, 418, 465

Lutz, D., Sturm, E., Tacconi, L. J., et al. 2008, ApJ, 684, 853

Lutz, D., Berta, S., Contursi, A., et al. 2016, A&A, 591, A136

Lynden-Bell, D. 1969, Nature, 223, 690

Madau, P., Pozzetti, L., & Dickinson, M. 1998, ApJ, 498, 106

Magnelli, B., Lutz, D., Saintonge, A., et al. 2014, A&A, 561, A86

Magorrian, J., Tremaine, S., Richstone, D., et al. 1998, AJ, 115, 2285

Maiolino, R., Ruiz, M., Rieke, G. H., & Keller, L. D. 1995, ApJ, 446, 561

Marconi, A., & Hunt, L. K. 2003, ApJ, 589, L21

Martin, D. C., Fanson, J., Schiminovich, D., et al. 2005, ApJ, 619, L1

Martin, D. C., Wyder, T. K., Schiminovich, D., et al. 2007, ApJS, 173, 342

Matsuoka, Y., Strauss, M. A., Shen, Y., et al. 2015, ApJ, 811, 91

Matsuta, K., Gandhi, P., Dotani, T., et al. 2012, ApJ, 753, 104

McConnell, N. J., & Ma, C.-P. 2013, ApJ, 764, 184

Meléndez, M., Kraemer, S. B., Schmitt, H. R., et al. 2008, ApJ, 689, 95

Meléndez, M., Mushotzky, R. F., Shimizu, T. T., Barger, A. J., & Cowie, L. L. 2014, ApJ, 794, 152

Merloni, A., & Heinz, S. 2013, Evolution of Active Galactic Nuclei, ed. T. D. Oswalt & W. C. Keel, 503

Mor, R., & Netzer, H. 2012, MNRAS, 420, 526

Mouri, H., & Taniguchi, Y. 2002, ApJ, 565, 786

Mullaney, J. R., Alexander, D. M., Goulding, A. D., & Hickox, R. C. 2011, MNRAS, 414, 1082

Mullaney, J. R., Pannella, M., Daddi, E., et al. 2012a, MNRAS, 419, 95

Mullaney, J. R., Daddi, E., Béthermin, M., et al. 2012b, ApJ, 753, L30

Mullaney, J. R., Alexander, D. M., Aird, J., et al. 2015, MNRAS, 453, L83

Murphy, E. J., Condon, J. J., Schinnerer, E., et al. 2011, ApJ, 737, 67

Mushotzky, R. 2004, in Astrophysics and Space Science Library, Vol. 308, Supermassive Black Holes in the Distant Universe, ed. A. J. Barger, 53

Mushotzky, R. F., Shimizu, T. T., Meléndez, M., & Koss, M. 2014, ApJ, 781, L34

Nandra, K., Georgakakis, A., Willmer, C. N. A., et al. 2007, ApJ, 660, L11

Nenkova, M., Ivezić, Ž., & Elitzur, M. 2002, ApJ, 570, L9

Nenkova, M., Sirocky, M. M., Ivezić, Ž., & Elitzur, M. 2008a, ApJ, 685, 147

Nenkova, M., Sirocky, M. M., Nikutta, R., Ivezić, Ž., & Elitzur, M. 2008b, ApJ, 685, 160

Netzer, H. 2009, MNRAS, 399, 1907

Netzer, H., Lutz, D., Schweitzer, M., et al. 2007, ApJ, 666, 806

Neugebauer, G., Habing, H. J., van Duinen, R., et al. 1984, ApJ, 278, L1

Nikutta, R., Elitzur, M., & Lacy, M. 2009, ApJ, 707, 1550

Noeske, K. G., Weiner, B. J., Faber, S. M., et al. 2007, ApJ, 660, L43

Novak, G. S., Ostriker, J. P., & Ciotti, L. 2011, ApJ, 737, 26

O'Halloran, B., Galametz, M., Madden, S. C., et al. 2010, A&A, 518, L58

Osterbrock, D. E. 1977, ApJ, 215, 733

—. 1981, ApJ, 249, 462

Osterbrock, D. E., & Ferland, G. J. 2006, Astrophysics of gaseous nebulae and active galactic nuclei

Ott, S. 2010, in Astronomical Society of the Pacific Conference Series, Vol. 434, Astronomical Data Analysis Software and Systems XIX, ed. Y. Mizumoto, K.-I. Morita, & M. Ohishi, 139

Page, M. J., Symeonidis, M., Vieira, J. D., et al. 2012, Nature, 485, 213

Papadopoulos, P. P., & Allen, M. L. 2000, ApJ, 537, 631

Papadopoulos, P. P., & Seaquist, E. R. 1999, ApJ, 514, L95

Paradis, D., Bernard, J.-P., & Mény, C. 2009, A&A, 506, 745

Paradis, D., Paladini, R., Noriega-Crespo, A., et al. 2012, A&A, 537, A113

Patton, D. R., & Atfield, J. E. 2008, ApJ, 685, 235

Patton, D. R., Torrey, P., Ellison, S. L., Mendel, J. T., & Scudder, J. M. 2013, MNRAS, 433, L59

Peebles, P. J. E. 1972, ApJ, 178, 371

Peng, C. Y., Ho, L. C., Impey, C. D., & Rix, H.-W. 2002, AJ, 124, 266

Peng, Y., Maiolino, R., & Cochrane, R. 2015, Nature, 521, 192

Peng, Y.-j., Lilly, S. J., Kovač, K., et al. 2010, ApJ, 721, 193

Pereira-Santaella, M., Diamond-Stanic, A. M., Alonso-Herrero, A., & Rieke, G. H. 2010, ApJ, 725, 2270

Petric, A. O., Ho, L. C., Flagey, N. J. M., & Scoville, N. Z. 2015, ApJS, 219, 22

Pier, E. A., & Krolik, J. H. 1992, ApJ, 401, 99

Pierce, C. M., Lotz, J. M., Salim, S., et al. 2010, MNRAS, 408, 139

Pilbratt, G. L., Riedinger, J. R., Passvogel, T., et al. 2010, A&A, 518, L1

Planck Collaboration, Ade, P. A. R., Aghanim, N., et al. 2011, A&A, 536, A17

—. 2014, A&A, 571, A28

Poglitsch, A., Waelkens, C., Geis, N., et al. 2010, A&A, 518, L2

Puget, J. L., & Leger, A. 1989, ARA&A, 27, 161

Rémy-Ruyer, A., Madden, S. C., Galliano, F., et al. 2013, A&A, 557, A95

Richards, G. T., Fan, X., Schneider, D. P., et al. 2001, AJ, 121, 2308

Richards, G. T., Lacy, M., Storrie-Lombardi, L. J., et al. 2006, ApJS, 166, 470

Rodighiero, G., Cimatti, A., Gruppioni, C., et al. 2010, A&A, 518, L25

Rosario, D. J., Santini, P., Lutz, D., et al. 2012, A&A, 545, A45

—. 2013a, ApJ, 771, 63

Rosario, D. J., Mozena, M., Wuyts, S., et al. 2013b, ApJ, 763, 59

Roussel, H. 2013, PASP, 125, 1126

Roussel, H., Sauvage, M., Vigroux, L., & Bosma, A. 2001, A&A, 372, 427

Rovilos, E., Comastri, A., Gilli, R., et al. 2012, A&A, 546, A58

Rush, B., Malkan, M. A., & Edelson, R. A. 1996, ApJ, 473, 130

Saintonge, A., Kauffmann, G., Kramer, C., et al. 2011a, MNRAS, 415, 32

Saintonge, A., Kauffmann, G., Wang, J., et al. 2011b, MNRAS, 415, 61

Saintonge, A., Tacconi, L. J., Fabello, S., et al. 2012, ApJ, 758, 73

Salim, S., Rich, R. M., Charlot, S., et al. 2007, ApJS, 173, 267

Sánchez, S. F., Kennicutt, R. C., Gil de Paz, A., et al. 2012, A&A, 538, A8

Sanders, D. B., & Mirabel, I. F. 1996, ARA&A, 34, 749

Sanders, D. B., Soifer, B. T., Elias, J. H., et al. 1988a, ApJ, 325, 74

Sanders, D. B., Soifer, B. T., Elias, J. H., Neugebauer, G., & Matthews, K. 1988b, ApJ, 328, L35

Sargsyan, L. A., & Weedman, D. W. 2009, ApJ, 701, 1398

Schartmann, M., Meisenheimer, K., Camenzind, M., et al. 2008, A&A, 482, 67

Scharwächter, J., Combes, F., Salomé, P., Sun, M., & Krips, M. 2015, ArXiv e-prints

Schawinski, K., Virani, S., Simmons, B., et al. 2009, ApJ, 692, L19

Schawinski, K., Urry, C. M., Virani, S., et al. 2010, ApJ, 711, 284

Schawinski, K., Urry, C. M., Simmons, B. D., et al. 2014, MNRAS, 440, 889

Schaye, J., Crain, R. A., Bower, R. G., et al. 2015, MNRAS, 446, 521

Scott, D. W. 1992, Multivariate Density Estimation

Seyfert, C. K. 1943, ApJ, 97, 28

Shao, L., Lutz, D., Nordon, R., et al. 2010, A&A, 518, L26

Shi, Y., Helou, G., Armus, L., Stierwalt, S., & Dale, D. 2013, ApJ, 764, 28

Shi, Y., Rieke, G. H., Ogle, P. M., Su, K. Y. L., & Balog, Z. 2014, ApJS, 214, 23

Shi, Y., Rieke, G. H., Hines, D. C., et al. 2005, ApJ, 629, 88

Shimizu, T. T., Meléndez, M., Mushotzky, R. F., et al. 2016, MNRAS, 456, 3335

Shimizu, T. T., Mushotzky, R. F., Meléndez, M., Koss, M., & Rosario, D. J. 2015, MNRAS, 452, 1841

Shipley, H. V., Papovich, C., Rieke, G. H., Brown, M. J. I., & Moustakas, J. 2016, ApJ, 818, 60

Silk, J., & Mamon, G. A. 2012, Research in Astronomy and Astrophysics, 12, 917

Silk, J., & Rees, M. J. 1998, A&A, 331, L1

Silverman, J. D., Mainieri, V., Lehmer, B. D., et al. 2008, ApJ, 675, 1025

Silverman, J. D., Lamareille, F., Maier, C., et al. 2009, ApJ, 696, 396

Simard, L., Mendel, J. T., Patton, D. R., Ellison, S. L., & McConnachie, A. W. 2011, ApJS, 196, 11

Smith, J. D. T., Draine, B. T., Dale, D. A., et al. 2007, ApJ, 656, 770

Smith, M. W. L., Eales, S. A., Gomez, H. L., et al. 2012, ApJ, 756, 40

Speagle, J. S., Steinhardt, C. L., Capak, P. L., & Silverman, J. D. 2014, ApJS, 214, 15

Spinoglio, L., Andreani, P., & Malkan, M. A. 2002, ApJ, 572, 105

Spoon, H. W. W., Marshall, J. A., Houck, J. R., et al. 2007, ApJ, 654, L49

Springel, V., Di Matteo, T., & Hernquist, L. 2005a, ApJ, 620, L79

—. 2005b, MNRAS, 361, 776

Stanley, F., Harrison, C. M., Alexander, D. M., et al. 2015, MNRAS, 453, 591

Stern, D., Assef, R. J., Benford, D. J., et al. 2012, ApJ, 753, 30

Stone, M., Veilleux, S., Melendez, M., et al. 2016, ArXiv e-prints

Strateva, I., Ivezić, Ž., Knapp, G. R., et al. 2001, AJ, 122, 1861

Symeonidis, M., Vaccari, M., Berta, S., et al. 2013, MNRAS, 431, 2317

Temi, P., Brighenti, F., & Mathews, W. G. 2007, ApJ, 660, 1215

Terashima, Y., & Wilson, A. S. 2003, ApJ, 583, 145

Thacker, R. J., MacMackin, C., Wurster, J., & Hobbs, A. 2014, MNRAS, 443, 1125

Toba, Y., Oyabu, S., Matsuhara, H., et al. 2014, ApJ, 788, 45

Tombesi, F., Meléndez, M., Veilleux, S., et al. 2015, Nature, 519, 436

Treister, E., Schawinski, K., Urry, C. M., & Simmons, B. D. 2012, ApJ, 758, L39

Tremonti, C. A., Heckman, T. M., Kauffmann, G., et al. 2004, ApJ, 613, 898

Treyer, M., Schiminovich, D., Johnson, B. D., et al. 2010, ApJ, 719, 1191

Trump, J. R., Sun, M., Zeimann, G. R., et al. 2015, ArXiv e-prints

Tueller, J., Mushotzky, R. F., Barthelmy, S., et al. 2008, ApJ, 681, 113

Tueller, J., Baumgartner, W. H., Markwardt, C. B., et al. 2010, ApJS, 186, 378

Ueda, Y., Akiyama, M., Hasinger, G., Miyaji, T., & Watson, M. G. 2014, ApJ, 786, 104

Urry, C. M., & Padovani, P. 1995, PASP, 107, 803

Vasudevan, R. V., Brandt, W. N., Mushotzky, R. F., et al. 2013, ApJ, 763, 111

Vasudevan, R. V., & Fabian, A. C. 2007, MNRAS, 381, 1235

Veilleux, S., & Osterbrock, D. E. 1987, ApJS, 63, 295

Veilleux, S., Meléndez, M., Sturm, E., et al. 2013, ApJ, 776, 27

Viero, M. P., Asboth, V., Roseboom, I. G., et al. 2014, ApJS, 210, 22

Villforth, C., Hamann, F., Rosario, D. J., et al. 2014, MNRAS, 439, 3342

Vito, F., Maiolino, R., Santini, P., et al. 2014, MNRAS, 441, 1059

Vogelsberger, M., Genel, S., Springel, V., et al. 2014, MNRAS, 444, 1518

Weaver, K. A., Meléndez, M., Mushotzky, R. F., et al. 2010, ApJ, 716, 1151

Werner, M. W., Roellig, T. L., Low, F. J., et al. 2004, ApJS, 154, 1

Whitaker, K. E., van Dokkum, P. G., Brammer, G., & Franx, M. 2012, ApJ, 754, L29

White, R. L., Becker, R. H., Gregg, M. D., et al. 2000, ApJS, 126, 133

White, S. D. M., & Frenk, C. S. 1991, ApJ, 379, 52

Winter, L. M., Lewis, K. T., Koss, M., et al. 2010, ApJ, 710, 503

Winter, L. M., Mushotzky, R. F., Reynolds, C. S., & Tueller, J. 2009, ApJ, 690, 1322

Winter, L. M., Veilleux, S., McKernan, B., & Kallman, T. R. 2012, ApJ, 745, 107

Wright, E. L., Eisenhardt, P. R. M., Mainzer, A. K., et al. 2010, AJ, 140, 1868

Wu, Y., Charmandaris, V., Huang, J., Spinoglio, L., & Tommasin, S. 2009, ApJ, 701, 658

Wuyts, S., Förster Schreiber, N. M., van der Wel, A., et al. 2011, ApJ, 742, 96

Xu, C., Livio, M., & Baum, S. 1999, AJ, 118, 1169

Xu, L., Rieke, G. H., Egami, E., et al. 2015, ApJ, 808, 159

Xue, Y. Q., Brandt, W. N., Luo, B., et al. 2010, ApJ, 720, 368

York, D. G., Adelman, J., Anderson, Jr., J. E., et al. 2000, AJ, 120, 1579

Zibetti, S., Charlot, S., & Rix, H.-W. 2009, MNRAS, 400, 1181